



THE ISO HANDBOOK

Volume I:

ISO – Mission & Satellite Overview

Martin F. Kessler^{1,2}, Thomas G. Müller^{1,4}, Kieron Leech¹, Christophe Arviset¹, Pedro García-Lario¹, Leo Metcalfe¹, Andy M. T. Pollock^{1,3}, Timo Prusti^{1,2} and Alberto Salama¹

SAI-2000-035/Dc, Version 2.0

November, 2003

- ¹ ISO Data Centre, Science Operations and Data Systems Division
Research and Scientific Support Department of ESA,
Villafranca del Castillo, P.O. Box 50727, E-28080 Madrid, Spain
- ² ESTEC, Science Operations and Data Systems Division
Research and Scientific Support Department of ESA,
Keplerlaan 1, Postbus 299, 2200 AG Noordwijk, The Netherlands
- ³ Computer & Scientific Co. Ltd.,
230 Graham Road, Sheffield S10 3GS, England
- ⁴ Max-Planck-Institut für extraterrestrische Physik,
Giessenbachstraße, D-85748 Garching, Germany

Document Information

Document:	The ISO Handbook
Volume:	I
Title:	ISO - Mission & Satellite Overview
Reference Number:	SAI/2000-035/Dc
Issue:	Version 2.0
Issue Date:	November 2003
Authors:	M.F. Kessler, T. Müller, K. Leech et al.
Editors:	T. Müller, J. Blommaert & P. García-Lario
Web-Editor:	J. Matagne

Document History

The **ISO Handbook, Volume I: ISO – Mission & Satellite Overview** is mainly based on the following documents:

- *The ISO Handbook, Volume I: ISO – Mission Overview*, Kessler M.F., Müller T.G., Arviset C. et al., earlier versions, SAI-2000-035/Dc.
- *The ISO Handbook, Volume II: ISO – The Satellite and its Data*, K. Leech & A.M.T. Pollock, earlier versions, SAI-99-082/Dc.
- The following ESA Bulletin articles:
 - The ISO Mission – A Scientific Overview*, M.F. Kessler, A. Heske, L. Metcalfe & A. Salama, ESA Bulletin No. 84, November 1995, p.43
 - The ISO Spacecraft*, S. Ximénez de Ferrán, ESA Bulletin No. 84, November 1995, p.51
 - The ISO Scientific Instruments – Technical Highlights*, H. Eggel, H. Schaap & G. Bagnasco, ESA Bulletin No. 84, November 1995, p.59
 - The ISO Programme*, J. Steinz & A. Linszen, ESA Bulletin No. 84, November 1995, p.67
 - Using ISO*, M.F. Kessler, ESA Bulletin No. 84, November 1995, p.73
 - Looking Back at ISO Operations*, M.F. Kessler, J. Clavel & J. Faelker, ESA Bulletin No. 95, August 1998, p. 87
 - The ISO Data Archive*, C. Arviset & T. Prusti, ESA Bulletin No. 98, June 1999, p.133
- The following ISO summary articles:
 - The Infrared Space Observatory (ISO) mission*, M.F. Kessler, J.A. Steinz, M.E. Anderegg et al. 1996, *Astronomy & Astrophysics* 315, 27
 - Overview of the ISO Mission*, M.F. Kessler, in ‘Infrared space astronomy, today and tomorrow’, Les Houches Session LXX F. Casoli, J. Lequeux & F. David (Eds.), Springer 1998, p.29
 - The ISO Mission: Past and Future*, M.F. Kessler 1999, in: Proceedings of the Paris Conference ‘The Universe as Seen by ISO’, P. Cox & M.F. Kessler (Eds.), ESA SP-427, 23
 - ISO: The mission and its Results*, M.F. Kessler, 2001, in: Proceedings of the Toledo Conference ‘The Promise of the Herschel Space Observatory’, ESA SP-460, p.53
- The following technical reports (available from the ISO web page):
 - ISO Scientific Instrument In-Orbit Commissioning Report*, ISO-RP-Z-12573, 24 January 1996, P. Estaria & H. Schaap, ISO Project, ESA/ESTEC
 - ISO Data Archive, Physical Data Model*, SAI/97-107/Dc, Version 4.0, J.L. Dowson, 2001

Post-Operations Cross-Calibration Status Reports, P. García-Lario, 1999 - 2002

Final reports of the Polarisation, Beam Profile & Pointing, Spectral Matching, Glitches, Photometry, Transients, Line Profile and Interactive Analysis Working Groups

Additional documents are listed in the bibliography chapter. Most of the documents are available in electronic format from the ISO web page: <http://www.iso.vilspa.esa.es/>

Document Change Record

Date	Revision	Comments
07/07/00	Draft 1.0	Initial Draft for comments
01/11/00	Version 1.0	First Version of the ISO Handbook, Volume I: ISO – Mission Overview
31/07/01	Version 1.1	update
31/12/01	Version 1.2	Merging with the Satellite Handbook (previously Volume II) and update
19/11/03	Version 2.0	update, printed version

Acknowledgements

During the history of ISO, countless engineers and scientists have contributed to its development, launch and operation and scientific use. Without their expertise, enthusiasm, dedication, professionalism and sheer hard work, the success of ISO, the results discussed in many scientific articles and the data contained in the archive would not have been possible. The following pages list the names of many of these individuals. We apologize to any of who may have been inadvertently omitted. The ISO Handbook has been written on their behalf and serves, we hope, as a testament to their efforts.

Wim Aalders	SWS	
Alain Abergel	ISOCAM	CIST/Collaborator
Jack Abolins	ISOPHOT	RAL
Peter Ábrahám	ISOPHOT	PHT Team
José Acosta Pulido	SOC	PIDT
Juan José Adán	TOS/GMV - INSA	
Peter Ade	LWS	
Patrick Agnese	ISOCAM	Collaborator
Matthew Ahier	ESOC-Software	Logica
Michela Alberti-Merri	ESOC-Software	TOS-GCI/Logicasiel
Günter Albrecht	ISOPHOT	Zeiss
Francisco Alcaraz	TOS/OV-INSA	
Godfrey Alexander	ESOC-Network Operations	TOS-ONC/Thorn
Ricardo Alonso	TOS/OV-INSA	
María Teresa Alonso	TOS/OV-INSA	
Bruno Altieri	SOC	CIDT
Jürgen Altmann	ISOPHOT	Zeiss
Rubén Álvarez	TOS/OV-INSA	
Manfred Amann	ISOPHOT	Dornier
Dieter Amend	ESOC-Network Operations	TOS-ONN
Ángel Anaya	TOS/OV-INSA	
Michel Anderegg	IST	Project
Immo Appenzeller	OTAC	
Tomás Aragonés	TOS/OV-INSA	
Birgit Arkestijn	SOC	S/W dev- U
Christiane Armand	LWS	LIDT
José Antonio Arteaga	TOS/OV-INSA	
Christophe Arviset	SOC	
Jacques Audric	SOC	
Jean-Louis Augueres	ISOCAM	CIST/Collaborator
Hervé Aussel	ISOCAM	CIST/Collaborator
Debbi Backhaus	SOC	SOST
Eliseo Balaguer	Project	
Cristiano Baldoni	ESOC-Flight Operations	TOS-OFC/Vitrociset
Jean-Paul Baluteau	LWS	OTAC/LIST
Christian Bambula	ESOC-Network Operations	TOS-ONF/Thorn
Mary Ellen Barba	IPAC	
Xavier Barcons	OTAC	
Lothar Barl	SWS	MPE
Mike Barlow	OTAC	LIST

Paul Barr	SOC	
Michael Barrett	ESOC-Network Operations	TOS-ONN
David Bass	SOC	S/W dev- U
Hans Peter Batroff	ISOPHOT	Zeiss
Alan Batten	ESOC-FD	(ex FDD)
Otto H. Bauer	SWS	MPE
Harald Baumgartner	SWS	MPE
Kurt Becher	SWS	MPE
Ron Beck	IPAC	
Steven Beckwith	ISOPHOT	MPIA
Lars Behrend	ESOC-FD	(ex FDD)
Chas Beichman	IPAC	
Douwe Beintema	SWS	SIDT
Heinrich Bellemann	ISOPHOT	MPIA
Jean Beresne	ISOCAM	Collaborator
Jean-Claude Berges	LWS	LIST
Jan Berkhout	Project	
Neil Berry	SOC	S/W dev- U
Johann Bestler	ISOPHOT	Dornier
Peter Biermann	OTAC	
Andrea Biviano	ISOCAM	CIDT/Collaborator
Jaime Blanco	TOS/OV-INSA	
David Bleakley	ESOC-Flight Operations	TOS-OF
Joris Blommaert	SOC	CIDT/Collaborator
Nicolas Bobrinsky	ESOC-Network Operations	TOS-ONN
Stefan Bogun	ISOPHOT	PHT Team
Catherine Boisson	OTAC	
Antoni Bolagistua	TOS/OV-INSA	
Wolfgang Bollinger	ISOPHOT	Zeiss
Reinhold Bolz	ISOPHOT	Antec
Jean Francois Bonnal	ISOCAM	Collaborator
Sylvain Bontemps	ISOCAM	Collaborator
Albert-Jan Boonstra	SWS	SRON-Utrecht
Ken Booty	ESOC-Sim	(ex Anite)
Fabio Bortoletto	ISOCAM	Collaborator
Ignacio Botana	TOS/OV-INSA	
André Bouere	ISOCAM	Collaborator
Olivier Boulade	ISOCAM	CIDT/Collaborator
Francois Boulanger	ISOCAM	CIST/Collaborator
John Bowers	ESOC-Software	Logica
Danny Boxhoorn	SWS	SIDT
Huib Braafhart	SWS	SRON-Utrecht
Jim Brauher	IPAC	
Michael Braun	ISOPHOT	PIDT
Michel Breitfellner	SOC	
Walter Breitling	ISOPHOT	Dornier
Christine Breneol	SOC	
Kurt Brenner	ISOPHOT	Zeiss
Francine van Bruggen	Project	
Jon Brumfitt	SOC	
Mark Buckley	LWS	LIST
Guillermo Buenadicha	ESOC-Flight Operations	TOS-OFC/INSA

Valentín Bujarrabal	OTAC	
Martin Burgdorf	SOC	LIDT
Maria Busetta	SOC	SOST
Marko Butkovic	ESOC-Network Operations	TOS-ONF/Thorn
Heiko Bäurle	ISOPHOT	Zeiss
Armin Böhm	ISOPHOT	MPIA
Pedro Calderón	TOS/OV-INSA	
Cristina Calderón	TOS/OV-INSA	
Fuencisla Camargo	TOS/OV-INSA	
Octavio Camino-Ramos	ESOC-Network Operations	TOS-ONN
Richard Carr	SOC	
Santos Carretero	TOS/OV-INSA	
David Carter	SOC	
Mauro Casale	ESOC-Flight Operations	TOS-OFC
Hector Castañeda	ISOPHOT	PIDT
Francisco Javier Castro	TOS/GMV-INSA	
Peter Catterall	ESOC-Network Operations	TOS-ONC/Tecnodata
Emmanuel Caux	LWS	LIST
Cecilia Ceccarelli	LWS	LIST
José Cernicharo	OTAC	LWS
Ricardo Cerulli	LWS	
Diego Cesarsky	ISOCAM	CIDT/CIST
Catherine Cesarsky	IST	CIST
Jean-Paul Chabaud	LWS	
José Chamorro	TOS/OV-INSA	
Neil Cheek	ESOC-Flight Operations	TOS-OFC/Serco
Uwe Christ	ESOC-Software	TOS-GME
Sarah Church	LWS	LIST
Peter Claes	SOC	
Arnaud Claret	ISOCAM	CIDT/Collaborator
Valeriano Claros	TOS/OV	
Jean Clavel	SOC	
Peter Clegg	IST	LIST
Mike Clendining	ESOC-Software	(ex TOS-GCI)
Martin Cohen	Calibration	
Francoise Combes	OTAC	
Jim Condon	OTAC	
Angioletta Coradini	OTAC	
Angel Corbasí	TOS/OV-INSA	
Linda Cornwall	ISOPHOT	PIDT
Carlos Correia	LWS	LIST
Stefan Cos	ISOPHOT	IMEC
Francis Cotin	LWS	
Matthew Couch	ESOC-Software	TOS-GLI/Logica
Peter Coulter	SOC	
Pierre Cox	LWS	LIST
Jacky Cretolle	ISOCAM	Collaborator
Anthony Crowson	ESOC-Software	TOS-OGC/Anite
Paul Cruvellier	LWS	
Stephan Czempiel	SWS	MPE
Francesca D'Antona	OTAC	
Luigi Danese	OTAC	

John Danziger	OTAC	
John K. Davies	ISOCAM	Collaborator
Gary Davis	LWS	LIST
Catherine de Bergh	OTAC	
Franck de Bruin	SOC	S/W dev- U
Marcus de Deus Silva	SOC	
Thijs de Graauw	IST	
Piet de Groene	SWS	SRON-Utrecht
Raquel de la Cruz	TOS/GMV-INSA	
Antonio de la Fuente	TOS/GMV-INSA	
Rob de la Rie	SWS	SRON-Utrecht
Francisco Javier de Miguel	TOS/GMV-INSA	
Daniel de Pablo	TOS/GMV	
Shuji Deguchi	OTAC	
Matt Delaney	ISOCAM	CIDT-Associated
Christophe Deletrez	LWS	
Emilio Deleyto	TOS/OV-INSA	
Fabienne Delhaise	ESOC-FD	TOS-GFI/EDS
Francois-Xavier Désert	ISOCAM	CIST/Collaborator
Anna di Giorgio	LWS	LIDT
Pierre Didelon	ISOCAM	CIST
Bart Dierickx	ISOPHOT	IMEC
Trevor Dimbylow	LWS	
Peter Dinges	ISOPHOT	Antec
Brian Diplock	LWS	
Stephen Dodsworth	ESOC-Flight Operations	TOS-OFC
Henk Doedens	SWS	SRON-Groningen
Jürgen Dohm	ESOC-Network Operations	TOS-ONF
Rhona Donald	SOC	
Stefan Dornheim	ISOPHOT	Zeiss
Eric Doumayrou	ISOCAM	Collaborator
John Dowson	SOC	
Siegfried Drapatz	SWS	MPE
Gilbert Drechsel	SOC	
Frank Dreger	ESOC-FD	TOS-GFO
Duncan Drummond	LWS	LIST
Luke Drury	ISOPHOT	DIAS
Cees du Maine	SWS	SRON-Utrecht
Eric Dunford	LWS	
Hervé Dzitko	ISOCAM	CIST
Derek Eaton	Project	
Ricardo J. Ebert	IPAC	
Albert Ebert	ISOPHOT	Zeiss
Andreas Efstathiou	ISOPHOT	PHT Team
David Elbaz	ISOCAM	CIST/Collaborator
Martin Ellam	ESOC-Network Operations	TOS-ONF/Thorn
Hans Elsässer	ISOPHOT	MPIA
Roger Emery	LWS	LIST
Thérèse Encrenaz	IST	OTAC
Jean Jacques Engelmann	ISOCAM	Collaborator
Gérard Epstein	ISOCAM	Collaborator
Pierre Estaria	Project	

Colin Evans	ESOC-Network Operations	TOS-ONF/Thorn
Jaap Evers	SWS	SRON-Groningen
David Ewart	LWS	LIDT
Dario Fadda	ISOCAM	Collaborator
Jürgen Fälker	ESOC-Flight Operations	TOS-OFC
Alan Falla	ESOC-CompOps	TOS-GMC/Serco
Yuhong Fan	SOC	CIDT
Jorge Fauste	TOS/OV-INSA	
Jürgen Fay	ESOC-Network Operations	TOS-ONF
Rudolf Faymonville	ISOPHOT	Antec
Reiner Felten	ISOPHOT	Antec
María Teresa Fernández	TOS/OV-INSA	
J. Manuel Fernández Cuenca	TOS/OV-INSA	
Helmut Feuchtgruber	SWS	SIDT
Harald Feuer	ISOPHOT	Dornier
Edgar Fink	ISOPHOT	MPIA
Jacqueline Fisher	LWS	LIST
Ursula Flock	ISOPHOT	MPIA
Vic Fonderie	ISOPHOT	IMEC
Renée Fontaine	SOC	
Luc Fraiture	ESOC-FD	(ex FDD/ESA)
Jürgen Frank	ISOPHOT	Dornier
Peter Franke	ISOPHOT	MPIA
Danny Frederickx	ISOPHOT	IMEC
Otto Frenzl	ISOPHOT	Antec
Martin Frericks	SWS	SRON-Utrecht
Wolfgang Fricke	ISOPHOT	Dornier
Ian Furniss	LWS	LIST
Carlos Gabriel	SOC	PIDT
Pascal Gallais	ISOCAM	CIDT/Collaborator
Carlos Gallo	TOS/OV-INSA	
Fernando Gallo	TOS/OV-INSA	
Kevin Galloway	SOC	ESOC-Software
Ken Ganga	IPAC	
Arturo García	TOS/OV-INSA	
Carlos García	TOS/OV-INSA	
Faustino García	TOS/OV-INSA	
Pedro García-Lario	SOC	SOST/IDC
Francisco Garzón	ISOPHOT	IAC
Rene Gastaud	ISOCAM	CIST/Collaborator
Hans-Peter Gemünd	ISOPHOT	MPIfR
Reinhard Genzel	SWS	OTAC
Juan-Carlos Gil	ESOC-Software	GMV/Logica
Patrick Gladney	ESOC-FD	TOS-GFS/CR
Bill Glencross	LWS	
Nick Godfrey	ESOC-ComOps	TOS-GMC/Serco
Paul Godfrey	ESOC-ComOps	TOS-GMC/Serco
Werner Goebel	SWS	MPE
Hans Golstein	SWS	SRON-Groningen
Pedro Gómez Cambronero	TOS/OV-INSA	
Salvador González	TOS/OV-INSA	
Michel Gorisse	ISOCAM	Collaborator

Ron van Gorp	Project	
Naoteru Gouda	SOC	
Hans Goulooze	SWS	SRON-Utrecht
Peter Gray	LWS	
Matt Greenhouse	LWS	
Derek Greer	SOC	
Matt Griffin	LWS	LIST
Phil Griffiths	LWS	
Harry Gritter	SWS	
Amanda Grunes	SOC	
Cécile Gry	SOC	LIDT/IDC
Ulrich Grözinger	ISOPHOT	PHT Team
Eberhard Grün	ISOPHOT	MPIK
Steve Guest	ISOCAM	CIDT/Collaborator
Bernard Guillaume	Project	
Jean-Jaques Gujer	ESOC-Sim	TOS-GMS
Theo Gunsing	SWS	SRON-Utrecht
Vippin Gupta	ESOC-FD	(ex FDD)
Bengt Gustafsson	OTAC	
Hans Göhringer	ISOPHOT	Zeiss
Joachim Gürtler	ISOPHOT	Friedrich S
Arnt Haaland	ESOC-Network Operations	(ex TOS-OFS)
Martin Haas	ISOPHOT	PHT Team
Harm Habing	IST	
Peter Hackel	ISOPHOT	Zeiss
Gerhard Haerendel	SWS	MPE
Christian Hajduk	ISOPHOT	PHT Team
Graham Hall	ISOPHOT	RAL
Peter Hammersley	Calibration	ISOPHOT
Mark Hampson	ESOC-Software	Logica
Lars Hansson	SOC	
Phil Harper	ESOC-Flight Operations	TOS-OFC/Vega
Michael Harr	ISOPHOT	Antec
Booth Hartley	IPAC	
Gernot Hartmann	ISOPHOT	DLR
Martin Harwit	IST	
Andrew Harwood	LWS	LIDT
Leo Haser	SWS	MPE
Adam Hazell	SOC	
Angela Head	ESOC-Software	TOS-GMS
Peter Heal	Project	
Norbert Heinecke	SWS	MPE
Ingolf Heinrichsen	ISOPHOT	PIDT
Danielle Heinzer	ESOC-ComOps	TOS-GMC
Hannelore Heissler	ISOPHOT	MPIA
George Helou	IST	
Peter Henneberg	ISOPHOT	Zeiss
Thomas Henning	ISOPHOT	Friedrich S
Ana Heras	SOC	SIDT
Edgar Herbst	ISOPHOT	Dornier
Uwe Herbstmeier	ISOPHOT	PHT Team
Lou Hermans	ISOPHOT	IMEC

Domingo Hermoso	ESOC-Flight Operations	TOS-OFC/INSA
José Hernández	SOC	
Silvia Hernández	SOC	
Ottmar Hertel	ISOPHOT	Antec
Astrid Heske	SOC	
Steven Hickey	ESOC-FD	(ex FDD)
Phil Hingston	LWS	
Hans Hippelein	ISOPHOT	MPIA
Reinhard Hofacker	ISOPHOT	MPIK
Hermann Hohl	ISOPHOT	Zeiss
John Holmes	LWS	
Hilary Hope	IPAC	
Wim Horinga	SWS	SRON-Groningen
Alan Hughes	SOC	
Stephan Huth	ISOPHOT	PIDT
Rik Huygen	SWS	KU-Leuven
Manfred von Högen	Project	
Danielle Imbault	ISOCAM	Collaborator
Freek van Ingen	Project	
Herman Jacobs	SWS	SRON-Utrecht
Gerd Jakob	SWS	MPE
Guy Janin	ESOC-Flight Operations	TOS-OFA
Wim Jansen	SWS	SRON-Utrecht
Alex Jeanes	SOC	ESOC-Software
Neil Jenkins	SOC	
Per Jensen	ESOC-Network Operations	TOS-ONF
Bob Joseph	ISOPHOT	IRTF
Annelies José-Veldkamp	SWS	SRON-Utrecht
Martine Joubert	LWS	LIST
Marie Jourdain de Muizon	Calibration	
Blanca Juárez	ESOC-Flight Operations	TOS-OFC/INSA
Joachim Junghans	ISOPHOT	Zeiss
Amanda Kaas	ISOCAM	Collaborator
Aman Kabir	ESOC-Network Operations	TOS-ONF
Norbert Kamm	SWS	MPE
Theo Kamperman	SWS	SRON-Utrecht
Reinhard Katterloher	SWS	MPE
Kimiaki Kawara	SOC	SOST
Hartmut Kehrer	ESOC-ComOps	TOS-GMC/Serco
Uwe Keller	OTAC	
Martin Kessler	IST	SOC
Iffat Khan	IPAC	
Sabine Kielbassa	ESOC-FD	TOS-GFI/EDS
Ken King	LWS	LIST
Ulrich Kinkel	ISOPHOT	PIDT
Ulrich Klaas	ISOPHOT	PIDT
Wolfgang Klück	ISOPHOT	Antec
Mary Koksvik	SOC	
Bernard Komasa	ESOC-ComOps	TOS-GMC
Sasha Konechni	SOC	S/W dev- U
Mihseh Kong	IPAC	
Adriaan Koning	SWS	

Axel Koppe	ISOPHOT	Dornier
Thilo Kranz	ISOPHOT	PHT Team
Rainer Kresken	ESOC-FD	TOS-GF/EDS
Ernst Kreysa	ISOPHOT	MPIfR
Anders Krogvig	ESOC-Sim	TOS-GMS
Wolfgang Krätschmer	ISOPHOT	MPIK
Harald Krüger	ISOPHOT	PHT Team
Heribert Krüger	ISOPHOT	Antec
Henk Kuiper	SWS	
Michael Kunkel	ISOPHOT	PHT Team
Dietmar Kunze	SWS	MPE
Hans Köppen	ISOPHOT	Zeiss
Fred Lahuis	SWS	SIDT
David Lambert	OTAC	
David Landriu	ISOCAM	CIST/Collaborator
Stephen Lane	ESOC-ComOps	TOS-GMC/SSL
Jacques Lapegue	ISOCAM	Collaborator
Tomás Lara	TOS/OV-INSA	
Gary Lattimer	ESOC-Network Operations	TOS-ONF/Thorn
Rene Laureijs	SOC	PIDT
Olivier Laurent	ISOCAM	CIST
Kieron Leech	SOC	SIDT
Sarah Leeks	LWS	LIST
Koos Leertouwer	Project	
Alain Léger	LWS	
Hansjörg Lehle	ISOPHOT	Zeiss
Christoph Leinert	ISOPHOT	MPIA
Dietrich Lemke	IST	
Peter Lemke	ESOC-Network Operations	TOS-ON
Ludovic Lemonon	ISOCAM	CIST
Werner Lenz	ISOPHOT	Dornier
Rafael León	TOS/OV-INSA	
James Lequeux	OTAC	
Klaus Lethaus	ISOPHOT	Dornier
Deborah Levine	IPAC	
Jing Li	IPAC	
Jean Li Kam Ti	SOC	S/W dev- U
Kate Lidiard	LWS	
Tanya Lim	LWS	LIDT
Dominic Lindars	ESOC-Software	Logica
Michael Linden-Voernle	ISOPHOT	PIDT
Reinhard Link	ISOPHOT	Zeiss
Ton Linssen	Project	
Rene Liseau	LWS	
Anne Litzelmann	ISOPHOT	Zeiss
Xiaowei Liu	LWS	LIST
Álvaro Llorente	TOS/OV-INSA	
Santiago Llorente	ESOC-ComOps	TOS-GMC
Antonio Lobato	TOS/GMV-INSA	
Tim Lock	SOC	
Diane Locke	IPAC	
Hans Loidl	SWS	MPE

Judy Long	LWS	LIST
Ray Long	SOC	SOST
Pedro López	TOS/OV-INSA	
Steve D. Lord	IPAC	
Rosario Lorente	TOS/OV-INSA	SIDT/IDC
Dario Lorenzetti	LWS	
Nanyao Lu	IPAC	
Ángeles Luchena	TOS/OV-INSA	
Reinhard Ludewig	ISOPHOT	Zeiss
Georg Luichtel	ISOPHOT	Zeiss
Willem Luinge	SWS	SRON-Groningen
Dieter Lutz	SWS	MPE
Peter Lützow-Wentzky	ISOPHOT	PHT Team
Susan Madden	ISOCAM	CIST
André Maeder	OTAC	
Pierre Maigne	ESOC-Software	TOS-GCI
Paolo Maldari	ESOC-Flight Operations	TOS-OGI
Silvano Manganeli	ESOC-Flight Operations	TOS-OFC/Vitrociset
Francisco Manso	ESOC-Flight Operations	TOS-OFC/INSA
Miguel Ángel Manzanares	TOS/OV-INSA	
Francisco Marcelo	TOS/OV-INSA	
Kevin Marston	ESOC-Software	Logica
Horst Martens	ESOC-Site	ADM-GC
Begoa Martín	TOS/OV-INSA	
Tarsicio Martín	TOS/GMV-INSA	
Fernando Martín Parra	TOS/OV-INSA	
Diego Martínez	Project	
Luis Martínez	TOS/OV-INSA	
Juan Gabriel Martínez Arcas	TOS/GMV-INSA	
Francisco Martínez-Fadrique	ESOC-FD	TOS-GF/GMV
Alberto Martos	TOS/OV-INSA	
Giuseppe Mastrominico	ESOC-Software	Logicasiel
Jean Matagne	SOC	SOST/IDC
Kalevi Mattila	ISOPHOT	Helsinki
Joe Mazarella	IPAC	
Alastair McDonald	ESOC-FD	TOS-GF/Logica
Steve McNally	ESOC-Network Operations	TOS-ONF/Thorn
Hans Jürgen Meier	ISOPHOT	Zeiss
P. Meijering	SOC	
Klaus Meisenheimer	ISOPHOT	MPIA
Michael Meister	ESOC-FD	(ex FDD)
Stig Mejnertsen	Project	
Fiedhelm Melzner	SWS	MPE
David Merricks	ESOC-Flight Operations	TOS-OFC/Serco
Bernhard Merz	SWS	MPE
Leo Metcalfe	SOC	CIDT
Klaus Meyer	ISOPHOT	Antec
Peter Mezger	ISOPHOT	MPIfR
Alberto Micol	SOC	SOST
Ole Mikkelsen	ESOC-FD	(ex FDD)
George Miley	OTAC	
Nigel Minchin	LWS	LIST

Kiana Mohseni	ESOC-Software	Logica
Sergio Molinari	IPAC	LIDT
Esther Moll	TOS/OV-INSA	
Andrea Moneti	SOC	
Judith Mood	ESOC-Flight Operations	TOS-O/Serco
Phillip Moore	ESOC-Network Operations	TOS-ONF/Thorn
Alan Moorwood	IST	
Victoria Morales	TOS/OV-INSA	
Allan Morecroft	ESOC-Network Operations	TOS-ONF/Thorn
Keith Morgan	SOC	
Trevor Morley	ESOC-FD	TOS-GFI
Patrick Morris	SWS	SIDT
Huw Morris	ISOPHOT	RAL
Christian Müller	ESOC-Software	Logica
Roland Müller	ISOPHOT	Dornier
Thomas Müller	SOC	ISOPHOT
Rolf Münch	ESOC-FD	TOS-GF
Jesús Municio	TOS/OV-INSA	
Ramón Muñoz Peiró	SOC	S/W dev- U
Wim Muysert	SWS	SRON-Utrecht
Bob Narron	IPAC	
Antonella Natta	OTAC	
David Naylor	LWS	LIST
Ture Nesgaard	ESOC-FD	(ex FDD)
Peter Neumeister	ESOC-ComOps	TOS-GMC
Stephan Nicklas	ISOPHOT	PHT Team
Jörg Niekerke	SWS	MPE
Marco Nijdam	SOC	S/W dev- U
Brunella Nisini	LWS	Calibration
Javier Noguero	ESOC-Software	GMV/Logica
John Nolan	SOC	
Lennard Nordh	ISOCAM	Collaborator
Hans Ulrik Norgaard-Nielsen	ISOPHOT	DSRI
Alberto Noriega-Crespo	IPAC	
Keith Norman	LWS	
Howard Nye	ESOC-Flight Operations	TOS-OF
Eduardo Ojero	TOS/GMV-INSA	
Haruyuki Okuda	IST	
Koryo Okumura	ISOCAM	CIDT/Collaborator
Alejandro Olazábal	TOS/OV-INSA	
Peter Oldeman	SOC	
Bert Oldenburger	SWS	
Graeme Oldham	LWS	LIST
Ernesto Oliva	OTAC	
Sebastian Oliver	ISOPHOT	ICSTM
Goran Olofsson	ISOCAM	Collaborator
Rob Oremus	Project	
Renato Orfei	LWS	
Alain Ormont	LWS	
Luciano Orsini	SOC	
Georg Orthuber	SWS	MPE
Sabine Osterhage	SWS	MPE

Linna Osterman	SOC	
Pedro Osuna	TOS/OV-INSA	
Stephan Ott	SOC	CIDT/Collaborator
Manfred Otterbein	ISOPHOT	DLR
Uwe Pagel	SWS	MPE
Siegmar Pallaschke	ESOC-FD	TOS-GFM
Tim Panton	SOC	S/W dev- U
Santiago Pascual	TOS/OV-INSA	
Reinhold Passenheim	ISOPHOT	Zeiss
Thomas Passvogel	Project	
Tom Patrick	LWS	
Soren Paulsen	SOC	S/W dev- U
Guido Pelz	ISOPHOT	PIDT
Alejandro Pena	ESOC-Flight Operations	TOS-OFC/INSA
Fany Peña	TOS/OV	
Daniel Pequignot	LWS	
Michel Pérault	ISOCAM	CIST/Collaborator
Diego Pérez	SOC	
Miguel Pérez	TOS/OV-INSA	
Francisco Pérez	TOS/OV-INSA	
Diego Pérez-Olea	TOS/OV-INSA	
Christian Peschel	ISOPHOT	Zeiss
Sibylle Peschke	SOC	
Wolfgang Peterhänsel	ESOC-FD	TOS-GF/EDS
Ton Peters	SWS	SRON-Utrecht
Carsten Petersen	ESOC-FD	TOS-GF/Terma
Stefano Pezzuto	LWS	LIDT
Günther Pfaller	SWS	MPE
Cees Pieters	SWS	
Max Pignede	ESOC-Software	TOS-GCM
Juan Piñeiro	ESOC-Flight Operations	TOS-OFC/Vitrociset
Pita Leira	SOC	
Ger Ploeger	SWS	SRON-Groningen
Arno Plug	SOC	
José Poblet	TOS/OV-INSA	
Luis Pociña	TOS/OV-INSA	
Elizabeth Poindron	ISOCAM	Collaborator
Andy Pollock	SOC	CIDT
Daniel Ponz	TOS/GMV	
Emil Popow	ISOPHOT	AIP
Jesús Portero	TOS/GMV-INSA	
Dominique Pouliquen	LWS	
Justo Povedano	TOS/OV-INSA	
Mariano Pozas	TOS/OV-INSA	
Karl Prantl-Baumann	ESOC-Site	ADM-GCG
Mark Price	LWS	LIDT
Steve Price	SWS	AFRL/VSBC
Klaus Proetel	ISOPHOT	DLR
Timo Prusti	SOC	
Jean-Loup Puget	IST	
Pascal Puget	ISOCAM	Collaborator
Julio Pulido	TOS/OV-INSA	

Terry Purkins	ISOCAM	Collaborator
Carlos Queija	TOS/OV-INSA	
Eusebio Quijada	TOS/OV-INSA	
Mario Radovich	ISOPHOT	PIDT
Robert Rae	ESOC-Network Operations	TOS-ONF/Thorn
María Ramírez	TOS/OV-INSA	
Raquel Ramos	TOS/OV-INSA	
Ib Rasmussen	ISOPHOT	DSRI
Tom Ray	OTAC	
Peter Reiss	SWS	MPE
Tomás Reneses	ESOC-Flight Operations	TOS-OFC/INSA
Lisa Retbøll	ESOC-Software	Logica
Steen Retbøll	ESOC-FD	(ex FDD)
José Revuelta	TOS/OV-INSA	
Pascal Richard	ESOC-Flight Operations	TOS-OFC/Thomson
Phil Richards	ISOPHOT	RAL
Gotthard Richter	ISOPHOT	AIP
Johannes Riedinger	SOC	
Rieu N’Guyen-Quang	LWS	
Yvon Rio	ISOCAM	CIST/Collaborator
Thérèse Robert	ISOCAM	Collaborator
David Robinson	LWS	
Andrew Robson	ESOC-Flight Operations	TOS-OF
Brigitte Rocca-Volmerange	OTAC	
Adolfo Rodero Cosano	ESOC-Flight Operations	TOS-OFC/INSA
José Miguel Rodríguez Espinosa	ISOPHOT	IAC
Peter Roelfsema	SWS	SIDT
Alan Rogers	LWS	LIST
Pilar Román	TOS/OV-INSA	CIDT/PIDT
Diego Romero	ESOC-Flight Operations	TOS-OFC/INSA
Steph Rosser	ESOC-Flight Operations	TOS-OFC/Serco
Daniel Rouan	ISOCAM	CIST/Collaborator
Helene Roussel	ISOCAM	Collaborator
Michael Rowan-Robinson	OTAC	ISOPHOT
André Roy	ISOCAM	Collaborator
Georges Rudaz	ESOC-Software	TOS-GSP
Jesús Ruiz	TOS/GMV-INSA	
Alison Rushworth	ISOPHOT	PHT Team
Michael Röser	ISOPHOT	Antec
Olivier Saint-Pe	ISOCAM	Collaborator
Michel Saisse	LWS	LIST
Alberto Salama	SOC	SIDT/IDC
Jesús Salgado	TOS/OV-INSA	
Monica Salomone	SOC	
Jacqui Sam-Lone	ISOCAM	CIST
David Sánchez	TOS/OV-INSA	
Miguel Sánchez	TOS/OV-INSA	
Sergio Sanjuan	ESOC-Flight Operations	TOS-OFC/INSA
Paolo Saraceno	LWS	LIST
Lakshmi Sastry	LWS	
Yasunori Sato	SOC	SOST
Marc Sauvage	ISOCAM	CIST/Collaborator

Aymeric Sauvageon	ISOCAM	CIDT
Richard Saxton	SOC	
Harm Schaap	Project	
Stephan Schaeidt	SWS	SIDT
Madelaine Schäfer	ESOC-FD	TOS-GF
Bernhard Scheiner	SWS	MPE
Rudolf Schlegelmilch	ISOPHOT	Zeiss
Michael Schmidt	ESOC-Flight Operations	TOS-OFC
Herbert Schnopper	ISOPHOT	DSRI
Pedro Schoch	ESOC-Software	GMV/Logica
Rosanne Scholey	IPAC	
Joseph Schubert	ISOPHOT	PHT Team
Bernhard Schulz	SOC	PIDT
Rita Schulz	OTAC	
Alain Schütz	ESOC-FD	TOS-GFS
Heike Schweitzer	ESOC-Flight Operations	TOS-OF
Christel Schäfer	SWS	MPE
Alex Scohier	SOC	
Andrés Scola	TOS/OV-INSA	
Günter Seger	ISOPHOT	Antec
Ramon Segura-Oto	ESOC-Network Operations	TOS-ONN
Karla Seidenschwang	SWS	MPE
Guy Serra	LWS	
Pierre Servan	ESOC-Flight Operations	TOS-OFC/Thomson
Giancarlo Setti	OTAC	
Mike Sheldon	ESOC-Network Operations	TOS-ONF/Thorn
Francois Sibille	ISOCAM	Collaborator
Roger Sidey	LWS	
Sunil Sidher	LWS	LIDT
Ralf Siebenmorgen	SOC	CIDT
Nico Sijm	SWS	SRON-Utrecht
Nancy Silbermann	IPAC	
Frances Sirou	ISOCAM	Collaborator
Sjef Kikken	SWS	
Boris Smeds	ESOC-Network Operations	TOS-OFS
Ursule Smissaert van de Haere	SWS	SRON-Utrecht
Alan Smith	LWS	LIST
Alan Smith	ESOC-Flight Operations	TOS-OF
Howard Smith	LWS	LIST
Raymond Smith	ESOC-ComOps	TOS-GMC/Serco
Kees Smoorenburg	SWS	TNO-TU Delft
Martyn Snelling	Project	
Axel Sohn	ISOPHOT	Antec
Anders Sørensen	ESOC-FD	(ex FDD)
Richard Southworth	ESOC-Flight Operations	TOS-OFC/Vega
Jan Spakman	SWS	SRON-Groningen
Karlheinz Spindler	ESOC-FD	(ex FDD)
Luigi Spinoglio	LWS	
Henrik Spoon	SWS	MPE
Phil Spurrett	LWS	
Heinrich Späth	SWS	MPE
Gordon Stacey	LWS	

Jean-Luc Starck	ISOCAM	CIST/Collaborator
Rick Starczewski	SOC	
Michael Steinmayer	SWS	MPE
Johan Steinz	Project	
Silke Stenzel	ESOC-Site	ADM-GC
Craig Stephenson	ESOC-FD	TOS-GFI/SSL
Julian Sternberg	SOC	
Manfred Stickel	ISOPHOT	PHT Team
Eckhard Sturm	SWS	MPE
Wilhelm Stöberl	SWS	MPE
Jakob Stöcker	SWS	MPE
Eva Suárez	TOS/OV-INSA	
Frank Sürth	ESOC-Network Operations	TOS-ONF/Thorn
Jean-Pierre Swings	OTAC	
Bruce Swinyard	LWS	LIST
Bill Sydenham	Project	
Roger Sylvester	LWS	LIST
Brian Taylor	Project	
Andrés Teijo	TOS/OV-INSA	
Oscar Tejedor	ESOC-Software	GMV/Logica
Charles Telesco	ISOPHOT	Univ. Florida
Francisco Terleira	TOS/OV-INSA	
Roberto Terlevich	OTAC	
Damien Texier	SOC	LIDT
Götz Thieme	ISOPHOT	Dornier
Mark Thomas	SOC	
Graham Thomas	ESOC-FD	(ex FDD)
Mark Thompson	ESOC-Network Operations	TOS-ONF/Thorn
Clemens Tilgner	ISOPHOT	PHT Team
Didier Tiphéne	ISOCAM	Collaborator
Colin Todd	SOC	
Laura Tomás Calderón	SOC	
Elisabetta Tommasi	LWS	LIDT
Steve Tonkmor	SOC	
Carlos Topham	TOS/OV-INSA	
José Torrente	TOS/OV-INSA	
Norman Trams	SOC	LIDT
Dan Tran	ISOCAM	CIST
Ulrike Trautwein	ESOC-Network Operations	TOS-ON/Tecnodata
Friedrich Trebstein	ISOPHOT	Zeiss
Philip Tregoning	ESOC-ComOps	TOS-GMC/SSL
Michael Trunz	ISOPHOT	Zeiss
Takashi Tsuji	IST	
Richard Tuffs	ISOPHOT	MPIK
Mark Tuttlebee	ESOC-Sim	TOS-GMS/Anite
David Twynam	ESOC-FD	(ex FDD)
Victor Tóth	ISOPHOT	PHT Team
Sarah Unger	LWS	LIST/IPAC
Javier Unzalu	ESOC-Software	TOS-GCI
Edwin Valentijn	SWS	SIDT
Juan-Carlos Vallejo	ESOC-Software	GMV/Logica
Herman van Agthoven	SWS	TNO-TU Delft

David van Buren	IPAC	
Ruud van de Haar	SWS	SRON-Utrecht
Nicole van der Blik	Calibration	
Karel van der Hucht	SWS	SRON-Utrecht
Siep van der Lei	SWS	SRON-Utrecht
Rien van der Linden	SWS	SRON-Utrecht
Peter van der Plas	SOC	
Rob van der Schuur	SWS	
Carel van Dijkhuizen	SWS	SRON-Utrecht
Jan van Geffen	SWS	SRON-Utrecht
John van Genechten	SWS	SRON-Utrecht
Frans van Gool	SOC	S/W dev- U
Duc van Nguyen	SWS	SRON-Groningen
Gertjan van Oosten	SOC	S/W dev- U
Jelle van Zeijl	SOC	S/W dev- U
Bart Vandenbussche	SWS	SIDT
Pedro Vargas	ESOC-Flight Operations	TOS-OFC/INSA
Peter Vaughan	ISOPHOT	RAL
Jesús Vázquez	ESOC-Flight Operations	TOS-OFC/INSA
Stephane Veillat	SOC	
Kees Veldkamp	SWS	SRON-Utrecht
Adolfo Ventero	TOS/OV-INSA	
Giulio Ventura	ISOCAM	Collaborator
Eva Verdugo	TOS/OV-INSA	IDC
Jan Vermeiren	ISOPHOT	IMEC
Rob Verschoor	SOC	
Pierre Viau	SOC	
Derek Vickers	LWS	
Laurent Vigroux	ISOCAM	CIDT/Collaborator
Osmi Vilhu	OTAC	
Javier Villanueva	TOS/OV-INSA	
Huib Visser	SWS	TNO-TU Delft
Florence Vivares	ISOCAM/LWS	CIST/LIST
Berthold Vogt	ISOPHOT	Dornier
Heinrich Völk	ISOPHOT	MPIK
Christoffel Waelkens	SWS/OTAC	KU-Leuven
Hans Wagenaar	SWS	SRON-Utrecht
Helen Walker	ISOPHOT	RAL
Gustav Wallum	ESOC-Site	ADM-GCT
Ray Walsh	SOC	
Mark Walter	ESOC-ComOps	TOS-GMC/Serco
Martin Ward	OTAC	
Rens Waters	SWS	UvA
Karsten Weber	ESOC-Network Operations	TOS-ONF/Thorn
Erhard Wedel	ISOPHOT	Dornier
Ann E. Wehrle	IPAC	
Martin Wells	ISOPHOT	ROE
Johan Wensink	SWS	SRON-Groningen
Paul Wesselius	SWS	SRON-Groningen
Bengt Westerlund	OTAC	
Inge van de Wetering	Project	
Glenn White	LWS	

Peter White	ESOC-Network Operations	TOS-ONF/Thorn
Ekkehard Wieprecht	SWS	SIDT
Erich Wieszorrek	SWS	MPE
Jan Wijnbergen	SWS	SRON-Groningen
Klaas Wildeman	SWS	SRON-Groningen
Hans Willaczek	ISOPHOT	Zeiss
G. William	SOC	
Iwan Williams	OTAC	
Peter Williams	ESOC-FD	(ex FDD)
Rupert Williams	ESOC-ComOps	TOS-GMC/Serco
Ana Willis	INSA/SOC	IDC
Derek Wilson	Project	
Gary Wilson	ESOC-Sim	TOS-GMS/Anite
Tom Wilson	OTAC	
Yvonne Windsor	LWS	
Henny Witjes	Studio Blanche	
Günter Wittig	ESOC-Network Operations	TOS-ONN
Jürgen Wolf	ISOPHOT	PHT Team
Lo Woltjer	OTAC	
Andy Woodcock	SOC	
Santiago Ximénez de Ferrán	Project	
Erick Young	SWS	Steward Obs.
Ignacio Yurrita	TOS/OV-INSA	
Carlos Yuste	TOS/OV-INSA	
Rafael Zarza	ESOC-Software	GMV/Logica
Rob Zondag	SOC	
Frans Zwart	SWS	SRON-Utrecht

Contents

List of Figures	xxix
List of Tables	xxxiii
Preface	1
1 Introduction	3
1.1 ISO – The Infrared Space Observatory	3
1.2 The ISO Legacy	5
1.3 How to Refer to the ISO Documentation	6
1.3.1 References	6
1.3.2 Acknowledgements	7
1.3.3 Guidelines	9
1.4 ISO Support	9
1.4.1 Data Centres	9
1.4.2 ISO Data Analysis Software	11
1.5 Document Guide	12
2 The ISO Project	13
2.1 The Project Organisation	13
2.2 Satellite Development	14
2.2.1 Industrial consortium	14
2.2.2 Model development and costs	16
2.3 Principal Investigators and Science Team	17
2.4 Science and Spacecraft Operations	19
2.5 Operational Activities	20
2.5.1 Launch and Early Orbit Phase	20
2.5.2 Commissioning Phase	20
2.5.3 Performance Verification Phase	22
2.5.4 Routine Phase	22
2.5.5 From end of helium to switch off	24
2.6 Post-Operational Activities	25
2.6.1 Transition Phase to Post-Operations	25
2.6.2 Post-Operations Phase	25

2.7	Active Archive Phase	26
2.8	Outlook: ISO and the Virtual Observatory	27
2.9	Chronology of the ISO Mission	28
3	The ISO Spacecraft	29
3.1	Payload Module	30
3.2	Service Module	30
3.3	Spacecraft subsystems	32
3.3.1	The cryostat subsystem	32
3.3.1.1	Design of the cryostat	33
3.3.1.2	Cryostat operations	34
3.3.2	The optical subsystem	34
3.3.2.1	Telescope mirrors	35
3.3.2.2	Focal plane geometry	35
3.3.3	Attitude and Orbit Control Subsystem (AOCS)	37
3.3.3.1	AOCS system components	37
3.3.3.2	AOCS operation	39
3.4	The Scientific Instruments	40
3.4.1	The ISO Camera: ISOCAM	41
3.4.2	The ISO Long Wavelength Spectrometer: LWS	43
3.4.3	The ISO Imaging Photo-Polarimeter: ISOPHOT	44
3.4.4	The ISO Short Wavelength Spectrometer: SWS	47
4	ISO Operations	49
4.1	The ISO Orbit	49
4.1.1	Orbit phases	50
4.1.2	Pointing constraints	50
4.2	The Ground Segment	51
4.2.1	Ground stations	52
4.2.2	The Spacecraft Control Centre (SCC)	52
4.2.3	The Science Operations Centre (SOC)	56
4.3	Observing with ISO	58
4.3.1	Observing strategy	58
4.3.2	Guaranteed time and open time programmes	58
4.3.3	The ISO observing cycle	59
4.3.3.1	Calls for proposals	59
4.3.3.2	Proposal evaluation and selection	60
4.3.3.3	Proposal data entry	61
4.3.4	Community Support	62
4.4	Overview of the Scientific Programme	62
4.4.1	Large survey programmes	62
4.4.2	Target of opportunity programmes	64
4.4.3	Discretionary time programmes	64

4.4.4	Parallel and serendipity programmes	64
4.5	Overview of Satellite Observing Modes	66
4.6	Overview of Instrument Observing Modes and AOTs	70
5	ISO In-Orbit Performance	73
5.1	Satellite Operation Performance	73
5.2	Cryostat Performance	73
5.3	Optical Performance	74
5.3.1	ISO Point Spread Function	74
5.3.2	Straylight	77
5.4	Pointing Performance	79
5.4.1	Pointing accuracy	79
5.4.2	Tracking of solar system objects	81
5.4.3	Guide stars and effects on pointing	81
5.5	Satellite Timing	82
5.6	Detector Performance	84
5.6.1	Radiation effects	84
5.6.1.1	Space radiation environment	84
5.6.1.2	Glitches in ISO detectors	86
5.6.1.3	Other radiation induced effects on the detectors	89
5.6.2	Detector transients	91
5.6.2.1	Si:Ga detectors	93
5.6.2.2	Ge:Ga detectors	97
5.6.2.3	Other detectors	107
5.7	Events and Conflicts during Operations	112
6	ISO Cross-Calibration	117
6.1	Cross-Calibration Strategy	117
6.1.1	Definition of cross-calibration sources	118
6.1.2	Limitations and caveats	118
6.2	Internal Cross-Calibration	120
6.2.1	Between the ISO spectrometers	120
6.2.1.1	SWS versus PHT-S	120
6.2.1.2	SWS versus CAM-CVF	122
6.2.1.3	CAM-CVF versus PHT-S	123
6.2.1.4	SWS/LWS overlap region	124
6.2.2	Filter measurements versus spectroscopy	126
6.2.2.1	ISOCAM filters versus chopped PHT-S	126
6.2.2.2	ISOCAM filters versus SWS	128
6.2.2.3	ISOPHOT filters versus ISO spectroscopy	129
6.2.2.4	ISOPHOT filters versus LWS	130
6.3	External Cross-Calibration	134
6.3.1	Comparison with IRAS	134

6.3.1.1	SWS versus IRAS photometry	134
6.3.1.2	LWS versus IRAS photometry	137
6.3.1.3	ISO composite SWS+LWS spectra versus IRAS photometry at 60 and 100 μm	142
6.3.1.4	LWS raster scans of extended sources versus IRAS photometry	145
6.3.1.5	ISOPHOT-P and -C versus IRAS photometry	146
6.3.2	Comparison with MSX	148
6.3.3	Comparison with COBE/DIRBE	153
6.3.3.1	PHT-S spectroscopy versus COBE/DIRBE photometry	153
6.3.3.2	PHT-C versus COBE/DIRBE photometry	155
6.4	Comparison with Models	158
6.4.1	ISOCAM	158
6.4.2	LWS	159
6.4.3	ISOPHOT	167
6.4.4	SWS	172
6.5	Conclusions	176
7	The ISO Data Archive (IDA)	177
7.1	Introduction	177
7.2	IDA Contents	179
7.2.1	Off-Line products	179
7.2.1.1	Scientific validation and accuracy	180
7.2.1.2	Quality control	180
7.2.2	Browse products after OLP	181
7.2.3	Highly Processed Data Products	181
7.2.4	Other products	181
7.3	Database Architecture	181
7.4	User Interface	183
7.5	Business Logic/Middle-Tier	183
7.6	Publication Tracking	183
7.7	Interoperability Aspects	183
7.8	Using the ISO Data Archive	184
7.9	Historical Aspects	189
7.10	IDA usage statistics	189
A	Infrared Astronomy	193
A.1	Infrared Units	193
A.2	Astronomical Background Radiation	194
A.2.1	The celestial background	194
A.2.2	Source Confusion	196
A.3	Infrared Astronomical Calibrators	197

B ISO Scientific Observations	199
B.1 Performed Guaranteed Time Proposals	200
B.1.1 Solar System	200
B.1.2 Stellar/Circumstellar Physics	200
B.1.3 Interstellar Matter	201
B.1.4 Extragalactic Systems	203
B.1.5 Cosmology	204
B.2 Performed Open Time Proposals	205
B.2.1 Solar System	205
B.2.2 Stellar/Circumstellar Physics	206
B.2.3 Interstellar Matter	215
B.2.4 Extragalactic Systems	222
B.2.5 Cosmology	229
B.3 Performed Discretionary Time Proposals/Calibration	231
C List of Solar System Objects	233
D Satellite Files	235
D.1 Attitude and Orbit Control System (AOCS)	235
D.1.1 Primary header	235
D.1.2 Records	235
D.2 ISO Operational Guide-Star List (APHSTAR)	238
D.2.1 Primary header	238
D.2.2 Records	239
D.3 Aperture Pointing History (APPH)	240
D.3.1 Primary header	240
D.3.2 Records	241
D.4 Aperture Programmed Pointing History (APPM)	242
D.4.1 Primary header	242
D.4.2 Records	243
D.5 Executed Observation History per AOT (EOHA)	244
D.5.1 Primary header	244
D.5.2 Records	245
D.5.3 CAM AOT specific information	246
D.5.4 LWS AOT specific information	246
D.5.5 PHT AOT specific information	247
D.5.6 SWS AOT specific information	247
D.6 Continuous Executed Observation History (EOHC)	248
D.6.1 Primary header	248
D.6.2 Records	249
D.7 Executed Observation History per ICS (EOHI)	250
D.7.1 Primary header	250
D.7.2 Records	250

D.7.3	CAM AOT specific information	250
D.7.4	LWS AOT specific information	251
D.7.5	PHT AOT specific information	252
D.7.6	SWS AOT specific information	252
D.8	General Housekeeping (GEHK)	253
D.8.1	Primary header	253
D.8.2	Records	254
D.8.3	CAM frame 8	255
D.8.4	LWS frame 8	255
D.8.5	PHT frame 8	255
D.8.6	SWS frame 8	255
D.9	General Housekeeping (Sampled) (GSHH)	256
D.10	ISO Guide-Star Hipparcos Catalogue Data (HIPPARCHOS)	257
D.10.1	Primary header	257
D.10.2	Records	258
D.11	ISO Focal Plane Geometry (IFPG)	260
D.11.1	Primary header	260
D.11.2	Records	260
D.12	Instrument Instantaneous Pointing History (IIPH)	261
D.12.1	Primary header	261
D.12.2	Records	263
D.13	Instrument Reference Pointing History (IRPH)	264
D.13.1	Primary header	264
D.13.2	Records	266
D.14	ISO Star-Tracker Calibration Data (ISTR)	267
D.14.1	Primary header	267
D.14.2	Records	267
D.15	ORBIT	268
D.15.1	Primary header	268
D.15.2	Records	269
D.15.3	MC_ORBIT subroutine	269
D.16	ISO Guide-Star Tycho Catalogue Data (TYCHO)	275
D.16.1	Primary header	275
D.16.2	Records	275
E	IDA content details	277
E.1	Off-Line Products	277
E.1.1	Quality flags	280
E.2	Browse Products after OLP	281
E.2.1	Survey products	281
E.2.2	Icons and postcards	281
E.3	Other Products	283

E.3.1	Auxiliary data	283
E.3.2	Ancillary data	283
E.3.3	Observation details and associated files	284
E.3.4	Calibration data	284
E.3.5	Historical and chronological data	284
E.3.6	Documentation	284
E.3.7	Software	284
F	Quaternions	285
G	IDA SQL-Queries: Worked Examples	287
H	Acronyms	295
	Bibliography	303
	Index	313

List of Figures

1.1	The ISO satellite flight model	4
1.2	The ISO Data Centre at VILSPA	10
2.1	ISO project organisation	13
2.2	Structure of the industrial consortium	15
2.3	Industrial contractors by country contribution	16
2.4	The pre-launch ISO project schedule	17
2.5	Principal Investigator (PI) organisations by country and instrument	18
2.6	The ISO Spacecraft Control Room	20
2.7	The ISO Instrument Control Room	23
3.1	Cut-away schematic of the ISO satellite	29
3.2	Definition of the spacecraft axes	31
3.3	Cryostat and telescope design	32
3.4	Helium flow diagram for ISO in orbit	34
3.5	ISO telescope optical layout.	35
3.6	ISO focal plane map	37
3.7	Attitude and Orbit Control Subsystem	38
3.8	Schematic of the Camera (ISOCAM)	42
3.9	Schematic of the Long Wavelength Spectrometer (LWS)	43
3.10	Schematic of the Photo-polarimeter (ISOPHOT)	45
3.11	Schematic of the Short Wavelength Spectrometer (SWS)	48
4.1	The ISO orbit	49
4.2	Visibility constraints of ISO	51
4.3	ESA's Villafranca Satellite Tracking Station in Spain	52
4.4	Skeleton schedule of ISO activities along an orbit	53
4.5	The ISO Mission Control System	55
4.6	Data flow within the Spacecraft Control Centre at Villafranca	56
4.7	Distribution of observing time	59
4.8	Distribution of ISO observation pointings	63
4.9	Mapping with ISO: Orientation 0°	68
4.10	Mapping with ISO: Orientation 47°	69
4.11	Usage of the instrument observing modes by time and number	72

5.1	Image of the ISOCAM PSF	75
5.2	Plot of the ISOCAM PSF	76
5.3	Straylight observed in a PHT22 raster map	78
5.4	Straylight observed in a CAM parallel image	79
5.5	Trapped electron fluxes as a function of ISO orbital time	85
5.6	Daily proton fluence during the ISO mission	86
5.7	Effect of the solar proton event of November 1997 on ISOCAM images	87
5.8	Example of a <i>fader</i> glitch in ISOCAM data	90
5.9	Example of a <i>dipper</i> glitch in ISOCAM data	90
5.10	Short term transient and long term drift in ISOCAM LW detectors	94
5.11	Raster observation suffering from long term drift and the correction	95
5.12	Transients in ISOPHOT-P1 detector	96
5.13	Transients in SWS detectors	98
5.14	Transients in ISOPHOT-P3 detector at intermediate flux level	99
5.15	Transients in ISOPHOT-P3 detector at low flux level	100
5.16	Transients in ISOPHOT-C100 detector	101
5.17	Transients in ISOPHOT-C200 detector	102
5.18	Transients in LWS-SW4 detector	103
5.19	Transients in LWS-LW2 detector	104
5.20	Transients in LWS-LW5 detector	104
5.21	Forward and backward scans in LWS-SW4 detector	105
5.22	Forward and backward scans in LWS-LW2 detector	105
5.23	Forward and backward scans of Uranus in LWS-LW2 detector after transient correction	106
5.24	Memory effects in ISOCAM SW detectors	107
5.25	ISOPHOT-P2 detector transients induced by chopper modulation	108
5.26	Transients in LWS-SW1 detector	109
5.27	Forward and backward scans of Uranus in LWS-SW1 detector	109
5.28	Forward and backward scans of Uranus in LWS-SW1 detector after transient correction	110
5.29	Forward and backward scans of NGC 6302 in LWS-SW1 detector	110
5.30	Forward and backward scans of NGC 6302 in LWS-SW1 detector after transient correction	111
5.31	Memory effects in band 4 of SWS	112
6.1	Bad pointing and extended source effects in SWS spectra	119
6.2	SWS versus PHT-s cross-calibration comparison	121
6.3	SWS versus PHT-S cross-calibration comparison in two faint sources	122
6.4	SWS versus CAM-CVF cross-calibration comparison	123
6.5	CAM-CVF versus PHT-S cross-calibration comparison	124
6.6	Composite SWS+LWS spectra of sources used for cross-calibration	126
6.7	PHT-S versus ISOCAM LW2 and LW7 filter measurements	127
6.8	ISOCAM filter versus SWS cross-calibration comparison	128
6.9	ISOPHOT photometry versus PHT-S, SWS and LWS spectroscopy of Comet Hale-Bopp	129
6.10	LWS fixed grating versus LWS grating scan and ISOPHOT measurements of Ceres	132

6.11	LWS fixed grating versus ISOPHOT measurements of Pallas	133
6.12	LWS fixed grating versus ISOPHOT measurements of Vesta	133
6.13	LWS fixed grating versus LWS grating scan and ISOPHOT measurements of Hygiea	134
6.14	SWS versus IRAS photometry at 12 μm	135
6.15	SWS versus IRAS photometry at 25 μm	136
6.16	Distribution of discrepancies between ISO and IRAS photometry at 12 and 25 μm	137
6.17	LWS/IRAS flux density ratios versus IRAS flux density at 100 μm	139
6.18	LWS versus IRAS photometry at 100 μm	140
6.19	Difference between LWS and IRAS fluxes at 60 and 100 μm	141
6.20	LWS versus IRAS photometry at 60 and 100 μm for a sample of extragalactic sources	142
6.21	ISO/IRAS flux density ratios versus IRAS flux density at 60 μm	144
6.22	ISO/IRAS flux density ratios versus IRAS flux density at 100 μm	145
6.23	LWS raster scans versus IRAS photometry at 100 μm	146
6.24	Chopped PHT-P and -C photometry versus IRAS photometry	147
6.25	SWS versus MSX filter A photometry	149
6.26	SWS versus MSX filter C photometry	150
6.27	SWS versus MSX filter D photometry	151
6.28	SWS versus MSX filter E photometry	152
6.29	Distribution of discrepancies between SWS and MSX photometry	153
6.30	PHT-S sky background versus COBE/DIRBE photometry	154
6.31	ISOCAM photometry of HIC 67485 versus model predictions	159
6.32	ISOCAM photometry of HIC 77277 versus model predictions	159
6.33	LWS grating scan observations of Uranus versus model predictions (full spectral range)	160
6.34	LWS grating scan observations of Uranus versus model predictions (per detector)	161
6.35	LWS grating scan observations showing the SW1 conspicuous double-peaked shape	162
6.36	LWS fixed grating observations of Uranus versus model predictions (full spectral range)	163
6.37	LWS fixed grating observations of Neptune versus model predictions (full spectral range)	164
6.38	LWS fixed grating observations of Ceres versus model predictions	165
6.39	LWS fixed grating observations of α Boo versus model predictions	167
6.40	Staring PHT-S spectra versus model predictions	168
6.41	Chopped PHT-S spectra versus model predictions	169
6.42	PHT-P and PHT-C multi-filter photometry versus model predictions	169
6.43	PHT-P and PHT-C absolute photometry versus model predictions of γ Dra	170
6.44	PHT-P absolute photometry of Sirius versus model predictions	171
6.45	PHT-P absolute photometry of α Ari versus model predictions	171
6.46	C200 absolute photometry of Uranus versus model predictions	172
6.47	SWS01 observations of stars with different spectral types versus model predictions	173
6.48	SWS01 observations of stars with different brightness versus model predictions	174
6.49	SWS versus model predictions and other observational data for a sample of stars	175
7.1	ISO Data Archive 3-tier architecture	178
7.2	ISO pipeline products Quality Control statistics	182

7.3	ISO Data Archive main query panel	185
7.4	ISO Data Archive query results panel with associated browse products	186
7.5	ISO Data Archive users registration	189
7.6	ISO Data Archive users distribution by country	190
7.7	ISO Data Archive queries	190
7.8	ISO Data Archive active users	191
7.9	ISO Data Archive observations retrieval	191

List of Tables

3.1	Cryostat requirements	33
3.2	Optical parameters of the ISO telescope	36
3.3	Offset coordinates of the instrument apertures with reference to the QSS aperture	36
3.4	AOCS elements main specifications	39
3.5	Main characteristics of the ISO instruments	41
4.1	The largest ISO observing programmes	63
4.2	Summary of all performed ToO programmes	65
4.3	Summary of all performed parallel and serendipity programmes	66
4.4	Overview of instrument observing modes	71
4.5	Usage of the four ISO instruments by time and by number of observations	71
5.1	Pointing performance	81
5.2	Observed glitch rates and minimum deposited energy in the ISO detectors	88
5.3	List of IR detectors on board ISO	92
5.4	Time constants for the long term transients in P3, C100 and C200 detectors	99
6.1	LWS/SWS ratios at 44 μm	125
6.2	Cross-calibration comparison between PHT-C100 and LWS	130
6.3	Cross-calibration comparison between PHT-C200 and LWS	131
6.4	ISO versus IRAS photometry at 60 and 100 μm	143
6.5	Chopped PHT-P photometry compared to IRAS photometry and model predictions	147
6.6	Chopped PHT-C photometry compared to IRAS photometry and model predictions	148
6.7	Description of MSX photometric bands	148
6.8	C100 absolute sky brightness versus COBE/DIRBE photometry	156
6.9	C200 absolute sky brightness versus COBE/DIRBE photometry	157
6.10	Discrepancies between ISOCAM photometry and stellar models	158
6.11	LWS grating scan observations of Uranus versus model predictions (per detector)	160
6.12	LWS fixed grating observations of Uranus versus model predictions (per detector)	163
6.13	LWS grating scan observations of stars versus model predictions	166
A.1	Typical fluxes of celestial background	195
A.2	Maximum zodiacal light	196
C.1	Objects observed with ISO using the SSO tracking mode	234

D.1	APCS primary header	236
D.2	AOCS records	236
D.3	Description of AOCSFRAM field	237
D.4	APHSTAR primary header	238
D.5	APHSTAR records	239
D.6	APPH primary header	240
D.7	APPH records	241
D.8	APPM primary header	242
D.9	APPM records	243
D.10	EOHA primary header	244
D.11	EOHA records	245
D.12	AOTV information for CAM	246
D.13	AOTV information for LWS	246
D.14	AOTV information for PHT	247
D.15	AOTV information for SWS	247
D.16	EOHC primary header	248
D.17	EOHC records	249
D.18	EOHI primary header	250
D.19	EOHI records	250
D.20	:WS EOHIMSG1 contents	251
D.21	PHT EOHIMSG1 contents	252
D.22	SWS EOHIMSG1 contents	252
D.23	GEHK primary header	253
D.24	GEHK records	254
D.25	SWS frame 8 contents	255
D.26	HIPPARCHOS primary header	257
D.27	HIPPARCHOS records	258
D.28	IFOG primary header	260
D.29	IFPG records	260
D.30	IIPH primary header	261
D.31	IIPH records	263
D.32	IRPH primary header	264
D.33	IRPH records	266
D.34	ISTR primary header	267
D.35	ISTR records	267
D.36	ORBIT primary header	268
D.37	ORBIT records	269
D.38	TYCHO primary header	275
D.39	TYCHO records	275
E.1	List of files per product level ‘Raw Data’	278
E.2	List of files per product level ‘Basic Science’	279
E.3	List of files per product level ‘Fully Auto-Processed Products’	280

Preface

The European Space Agency's (ESA) Infrared Space Observatory (ISO) is an astronomical satellite that was operational between November 1995 and May 1998. It operated at wavelengths from 2.5 to 240 μm , in the infrared range of the electromagnetic spectrum. Because the atmosphere acts as an 'umbrella' for most infrared wavelengths — preventing them from reaching the ground — a space telescope is needed to detect this kind of radiation invisible to the human eye and to optical telescopes.

The ISO satellite essentially consisted of: a large liquid-helium cryostat; a telescope with a 60-cm diameter primary mirror; four scientific instruments and the service module. It was designed and constructed under ESA responsibility by a European industrial consortium led by Aerospatiale (F, now Alcatel), and launched by an Ariane IV rocket on 17 November 1995. Scientific observations were performed between February 1996 and April 1998, and communications with the satellite were terminated on 16 May 1998. All of the scientific goals motivating the mission's adoption were surpassed. ISO made during its lifetime more than 30 000 dedicated individual observations of all kind of astronomical objects, ranging from our own solar system out to the most distant galaxies. These observations were made with a wide variety of spectral and spatial resolving powers. The resulting database provides a treasure of information for further astronomical research.

The products of the ISO mission are available through the ISO Data Archive (IDA) from

<http://www.iso.vilspa.esa.es/>

The **ISO Handbook** (Volumes I to V) is, together with the ISO Data Archive, part of the legacy of the ISO Mission. It is a reference document with general information about the mission, the satellite, the instruments and the data products of the final ISO Archive:

- Volume I: ISO – Mission & Satellite Overview
- Volume II: CAM – The ISO Camera
- Volume III: LWS – The Long Wavelength Spectrometer
- Volume IV: PHT – The Imaging Photo-Polarimeter
- Volume V: SWS – The Short Wavelength Spectrometer

Chapter 1

Introduction

1.1 ISO – The Infrared Space Observatory

ISO was the world's first true orbiting infrared observatory (Figure 1.1). It was given a perfect launch on 17 November 1995 by an Ariane IV vehicle. Equipped with four sophisticated and versatile scientific instruments, it provided astronomers with a facility of unprecedented sensitivity and capabilities for an exploration of the universe at infrared wavelengths from 2.5 to 240 μm . The satellite was a great technical and scientific success with most of its sub-systems operating far better than their specifications and with its scientific results impacting practically all fields of astronomy. At a wavelength of 12 μm , ISO was one thousand times more sensitive and had one hundred times better angular resolution than its predecessor, the all-sky-surveying IRAS¹.

During its routine Operational Phase (4 February 1996 to 8 April 1998), which lasted almost a year longer than specified, ISO successfully made over 27 000 individual scientific observations and more than 4 000 calibration observations.

After termination of in-orbit operations, all observations were re-processed with the 'end-of-mission' calibration and pipeline. The ISO Data Archive opened to the world-wide astronomical community in December 1998 and all data had entered the public domain by August 1999. At the beginning of 2002, the data were again re-processed with the 'end-of-post-mission' calibration (final off-line processing software OLP Version 10) to create the ISO Legacy Archive.

ISO's Post-Operations Phase (POPS, 1998 – 2001) was designed to leave behind a homogeneous archive with improved calibration as a legacy to future generations of astronomers. From 2002 to 2006, an Active Archive Phase (AAP) takes place with the goal of maximising the scientific exploitation of ISO's vast data sets. In this latter period, the archive will be brought into its final form, including the concept of feeding back into the archive data reduced 'by hand' by experts (the so-called *Highly Processed Data Products* or HPDPs).

¹InfraRed Astronomical Satellite



Figure 1.1: *The ISO satellite flight model.*

1.2 The ISO Legacy

The ISO Legacy consists of:

- The ISO Data Archive:
(<http://www.iso.vilspa.esa.es/> → Access the Archive)
 - Over 27 000 science observations
 - More than 4 000 calibration observations
 - Thousands of serendipitous and parallel observations
 - Additional products and software
- The documentation:
 - The Explanatory Library:
(<http://www.iso.vilspa.esa.es/> → ISO Explanatory Library)
 - *The ISO Handbook*, T.G. Müller, J.A.D.L. Blommaert & P. García-Lario (Eds.), ESA SP-1262, 2003:
(<http://www.iso.vilspa.esa.es/> → ISO Handbook)
 - * Volume I: ISO – Mission & Satellite Overview (this volume)
 - * Volume II: CAM – The ISO Camera
 - * Volume III: LWS – The Long Wavelength Spectrometer
 - * Volume IV: PHT – The Imaging Photo-Polarimeter
 - * Volume V: SWS – The Short Wavelength Spectrometer
 - The following ISO conferences & proceedings:
 - First ISO Science Workshop*, ESTEC, Noordwijk, The Netherlands, 29–31 May 1996, Results published in the A&A Special Issue, Volume 315, Number 2, pp. L27–L400, 1996
 - Taking ISO to the limits: Exploring the faintest sources in the infrared*, ISO Science Operations Centre, Villafranca del Castillo, Madrid, Spain, 3–4 February 1997, Abstracts available from the ISO web pages at <http://www.iso.vilspa.esa.es/> → Conferences and Meetings
 - ESA SP-419: *First ISO Workshop on Analytical Spectroscopy*, ISO Science Operations Centre, Villafranca del Castillo, Madrid, Spain, 6–8 October 1997, 329 pages, A.M. Heras, K. Leech, N.R. Trams & M. Perry (Eds.)
 - ISO Detector Workshop*, Villafranca del Castillo, Madrid, Spain, 14–16 January 1998, Proceedings of this workshop published in *Exp. Astronomy*, Volume 10, Issue 2/3, August 2000
 - ESA SP-427: *The Universe as seen by ISO*, UNESCO, Paris, France, 20–23 October 1998, 1090 pages (2 Volumes), P. Cox & M.F. Kessler (Eds.)
 - ESA SP-435: *ISO Polarisation Observations*, ISO Data Centre, Villafranca del Castillo, Madrid, Spain, 25–28 May 1999, 56 pages, R.J. Laureijs & R. Siebenmorgen (Eds.)
 - ESA SP-455: *ISO Beyond Point Sources*, ISO Data Centre, Villafranca del Castillo, Madrid, Spain, 14–17 September 1999, 203 pages, R.J. Laureijs, K. Leech & M.F. Kessler (Eds.)
 - ESA SP-456: *ISO Beyond the Peaks*, Villafranca del Castillo, Madrid, Spain, 2–4 February 2000, 389 pages, A. Salama, M.F. Kessler, K. Leech & B. Schulz (Eds.)
 - ESA SP-481: *The Calibration Legacy of the ISO Mission*, ISO Data Centre, Villafranca del Castillo, Madrid, Spain, 5–9 February 2001, L. Metcalfe, A. Salama, S.B. Peschke & M.F. Kessler (Eds.)
 - ESA SP-482: *ISOPHOT Workshop on P32 Oversampled Mapping*, ISO Data Centre, Villafranca del Castillo, Madrid, Spain, 12–16 February 2001; Infrared Processing & Analysis Center

- IPAC, USA, 26–30 March 2001, B. Schulz, N. Lu & S.B. Peschke (Eds.)
- ESA SP-511: *Exploiting the ISO Data Archive – Infrared Astronomy in the Internet Age*, Parador de Sigüenza, Spain, 24–27 June 2002, C. Gry, S.B. Peschke, J. Matagne et al. (Eds.)
- A large number of refereed scientific publications based on ISO observations (at the end of 2002: approximately 1 000 ISO-related articles in total, with a peak publication rate of about 180 publications per year)
- Press releases by ESA, NASA, ISAS and many scientific institutes all over the world
- Background and summary articles
- The ISO Data Analysis Software Packages:
(<http://www.iso.vilspa.esa.es/> → ISO Data Analysis Software)
 - ISOPHOT Interactive Analysis (PIA)
 - ISOCAM Interactive Analysis (CIA)
 - ISO Spectroscopic Analysis Package (ISAP)
 - Observers SWS Interactive Analysis Package (OSIA)
 - LWS Interactive Analysis (LIA)
- Others:
 - Different sets of new calibrators for infrared wavelengths
 - Hardware, software, operational and calibration expertise

1.3 How to Refer to the ISO Documentation

1.3.1 References

1. References for general ISO topics, including the mission, satellite, instrument payload, orbit and operations, project organisation, observations and ISO data products:
 - *The ISO Handbook*, Volumes I–V, T.G. Müller, J.A.D.L. Blommaert & P. García-Lario (Eds.), ESA SP-1262, 2003:
 - Volume I: *ISO – Mission & Satellite Overview*, Kessler M.F., Müller T.G., Leech K. et al., Version 2.0, July 2003
 - Volume II: *CAM – The ISO Camera*, Blommaert J., Siebenmorgen R., Coulais A. et al., Version 2.0, June 2003
 - Volume III: *LWS – The Long Wavelength Spectrometer*, Gry C., Swinyard B., Harwood A. et al., Version 2.1, June 2003
 - Volume IV: *PHT – The Imaging Photo-Polarimeter*, Laureijs R.J., Klaas U., Richards P.J. et al., Version 2.0.1, June 2003
 - Volume V: *SWS – The Short Wavelength Spectrometer*, Leech K., Kester D., Shipman R. et al., Version 2.0.1, June 2003
 - Kessler M.F., Steinz J.A., Anderegg M. et al. 1996, *The Infrared Space Observatory (ISO) mission*, A&A 315, L27
 - Kessler M.F. 1999, *The ISO mission: past and future*, in ‘The Universe as Seen by ISO’. Eds. P. Cox & M.F. Kessler, ESA SP-427, 23
2. References for the ISO instruments in A&A Special Issue, Volume 315, Number 2, pp. L27–L400, 1996:

- Cesarsky C.J., Abergel A., Agnèsè P. et al. 1996, *ISOCAM in flight*, A&A 315, L32
- Clegg P.E., Ade P.A.R., Armand C. et al. 1996, *The ISO Long-Wavelength spectrometer*, A&A 315, L38
- Lemke D., Klaas U., Abolins J. et al. 1996, *ISOPHOT: Capabilities and performance*, A&A 315, L64
- De Graauw, Th., Haser, L.N., Beintema, D.A. et al. 1996, *Observing with the ISO Short Wavelength Spectrometer*, A&A 315, L49

Further instrument specific publications in *The Universe as Seen by ISO*, 1999, ESA SP-427, P. Cox & M.F. Kessler (Eds.):

- Cesarsky C.J. 1999, *ISOCAM: first assessment after the end of the mission*, in ‘The Universe as Seen by ISO’. Eds. P. Cox & M.F. Kessler, ESA SP-427, 45
- Clegg P.E. 1999, *The ISO Long-Wavelength Spectrometer: description, performance and highlights*, in ‘The Universe as Seen by ISO’. Eds. P. Cox & M.F. Kessler, ESA SP-427, 39
- Lemke D. & Klaas U. 1999, *ISOPHOT - performance, results and outlook*, in ‘The Universe as Seen by ISO’. Eds. P. Cox & M.F. Kessler, ESA SP-427, 51
- De Graauw Th. 1999, *Summary of ISO SWS performance and science highlights*, in ‘The Universe as Seen by ISO’. Eds. P. Cox & M.F. Kessler, ESA SP-427, 31

3. References for technical notes in the ISO Explanatory Library:

<http://www.iso.vilspa.esa/> → ISO Explanatory Library

4. References for Interactive Analysis (IA) software and data reduction procedures:

- **CAM:** *ISOCAM Interactive Analysis User’s Manual*, Version 5.0, SAI/96-5226/Dc, M. Delaney & S. Ott (Eds.), 2002
<http://www.iso.vilspa.esa.es/> → ISO Data Analysis Software
→ ISOCAM Interactive Analysis (CIA)
- **LWS:** <http://www.iso.vilspa.esa.es/> → ISO Data Analysis Software
→ ISO Spectroscopic Analysis Package (ISAP)
→ LWS Interactive Analysis (LIA)
- **PHT:** *PHT Interactive Analysis User Manual*, Version 9.0, C. Gabriel, 2000.
<http://www.iso.vilspa.esa.es/> → ISO Data Analysis Software
→ ISOPHOT Interactive Analysis (PIA)
- **SWS:** <http://www.iso.vilspa.esa.es/> → ISO Data Analysis Software
→ ISO Spectroscopic Analysis Package (ISAP)
→ Observers SWS Interactive Analysis Package (OSIA)

1.3.2 Acknowledgements

1. ISO

Any article based on ISO data should contain the following text, as a footnote to the title:

Based on observations with ISO, an ESA project with instruments funded by ESA Member States (especially the PI countries: France, Germany, the Netherlands and the United Kingdom) and with the participation of ISAS and NASA.

Should the journal in question not permit footnotes to the title, the above text should appear as a footnote the first time ISO is mentioned.

The preferred reference article for the ISO mission is:

Kessler M.F., Steinz J.A., Anderegg M. et al. 1996, *The Infrared Space Observatory (ISO) mission*, A&A 315, L27.

2. Scientific Instruments

You should acknowledge the instrument(s) you use with a reference to one (or more) of the following articles:

- Cesarsky C.J., Abergel A., Agnèsè P. et al. 1996, *ISOCAM in flight*, A&A 315, L32
- Clegg P.E., Ade P.A.R., Armand C. et al. 1996, *The ISO Long-Wavelength Spectrometer*, A&A 315, L38
- Lemke D., Klaas U., Abolins J. et al. 1996, *ISOPHOT: Capabilities and performance*, A&A 315, L64
- De Graauw Th., Haser L.N., Beintema D.A. et al. 1996, *Observing with the ISO Short Wavelength Spectrometer*, A&A 315, L49

3. CIA (ISOCAM Interactive Analysis)

If you use CIA to reduce your CAM data please write in the acknowledgments:

The ISOCAM data presented in this paper were analysed using ‘CIA’, a joint development by the ESA Astrophysics Division and the ISOCAM Consortium. The ISOCAM Consortium is led by the ISOCAM PI, C. Cesarsky.

The preferred reference to CIA is:

Ott S., Abergel A., Altieri B. et al. 1997, *Design and Implementation of CIA, the ISOCAM Interactive Analysis System*, in ASP Conf. Ser. Vol. 125, *Astronomical Data Analysis Software and Systems (ADASS) VI*, G. Hunt & H.E. Payne (Eds.), San Francisco: ASP, 34

4. ISAP (ISO Spectroscopic Analysis Package)

If you use ISAP to reduce your SWS or LWS data please write in the acknowledgments:

The ISO Spectral Analysis Package (ISAP) is a joint development by the LWS and SWS Instrument Teams and Data Centers. Contributing institutes are CESR, IAS, IPAC, MPE, RAL and SRON.

5. PIA (ISOPHOT Interactive Analysis)

If you use PIA to reduce your ISOPHOT data please write in the acknowledgments:

The ISOPHOT data presented in this paper were reduced using PIA, which is a joint development by the ESA Astrophysics Division and the ISOPHOT Consortium with the collaboration of the Infrared Processing and Analysis Center (IPAC). Contributing ISOPHOT Consortium institutes are DIAS, RAL, AIP, MPIK, and MPIA.

The preferred reference to PIA is:

Gabriel C., Acosta-Pulido J., Heinrichsen I. et al. 1997, *The ISOPHOT Interactive Analysis PIA, a calibration and scientific analysis tool*, in ASP Conf. Ser. Vol. 125, *Astronomical Data Analysis Software and Systems (ADASS) VI*, G. Hunt & H.E. Payne (Eds.), San Francisco: ASP, 108

6. OSIA (Observers SWS Interactive Analysis Package)

If you use OSIA to reduce your SWS data please write in the acknowledgements:

OSIA is a joint development of the SWS consortium. Contributing institutes are SRON, MPE, KUL and the ESA Astrophysics Division.

If you use IA3 to reduce your SWS data please write in the acknowledgements:

IA3 is a joint development of the SWS consortium. Contributing institutes are SRON, MPE, KUL and the ESA Astrophysics Division.

1.3.3 Guidelines

- Identifying ISO observations in a publication:

The ‘Observations’ section (or equivalent) of a paper using ISO data should clearly identify the observations on which the results presented in the publication are based. This is done uniquely by listing the TDT and AOT for each individual observation used. The TDT is an 8 digit number which you can see in the query results in the ISO Data Archive or in the filename of the retrieved observation. The AOT is a combination of a three letter code: CAM, LWS, PHT or SWS indicating the instrument (Camera, Long Wavelength Spectrometer, Imaging Photo-Polarimeter and Short Wavelength Spectrometer, respectively) and a two digit number indicating the instrument mode. The AOT can be found from query results in the archive or from the retrieved file headers of the data sets related to an observation. The authors should also include all additional information of the observations which has astronomical relevance in the studied case (e.g. the time the observations were made), but the TDT and AOT should never be omitted in order to give the possibility for future readers to find the original data in the ISO Data Archive.

- Inventory of ISO publications

In order to offer a complete bibliographic information to the ISO Data Archive users, we try to keep track of all publications involving ISO data, and of all observations used for these publications. The ISO Data Archive provides the references of the publications involving any selected observation and a link to their Astrophysics Data System (ADS) entry². Your contribution in this matter can greatly help keeping an information as comprehensive as possible and we therefore ask you to kindly provide the following information for each of your publications:

- complete reference of the article (or preprint)
- list of TDT numbers and instrument modes of the observations that you have exploited for the publication

You can send the information either by e-mail to:

helpdesk@iso.vilspa.esa.es

or by normal mail to:

**ISO Project Scientist
(ISO Preprints)
ESA Satellite Tracking Station
Villafranca del Castillo
P.O. Box 50727
28080 Madrid, Spain**

1.4 ISO Support

1.4.1 Data Centres

Reduction of ISO data was not always easy and new users were advised to seek guidance from ISO experts, particularly those specialised in providing community support at the various data centres:

- ISO Data Centre at Villafranca del Castillo, Spain (VILSPA, see Figure 1.2):
Responsible for the archive including user interfaces, the general off-line processing (‘pipeline’)

²<http://adswww.harvard.edu/>



Figure 1.2: *The ISO Data Centre at Villafranca del Castillo, Spain (VILSPA) during the Operational Phase.*

software, supporting the general European user community across all four instruments, and general co-ordination.

**ISO Data Centre
 ESA Satellite Tracking Station
 Villafranca del Castillo
 P.O. Box 50727
 28080 Madrid, Spain
 Telephone: +34 91 813 1100
 Fax: +34 91 813 1308**

- Five National Data Centres (NDC):
 - French ISO Centres, SAp/Saclay and IAS/Orsay, France³.
 Le projet ISOCAM,
 Service d’Astrophysique (SAp/Saclay),
 Orme des Merisiers,
 F-91191 Gif-sur-Yvette, France
 - ISOPHOT Data Centre at MPIA in Germany
 The ISOPHOT Data Centre,
 Max-Planck-Institut für Astronomie,
 Königstuhl 17,
 D-69117 Heidelberg, Germany

³inactive since 31 December 2001

- Dutch ISO Data Analysis Centre at SRON in the Netherlands
The Dutch ISO Data Analysis Centre (DIDAC),
SRON,
P.O. Box 800,
NL-9700 AV Groningen, The Netherlands
- ISO Spectrometer Data Centre at MPE in Germany
The ISO Spectrometer Data Centre (ISOSDC),
Max-Planck-Institut für extraterrestrische Physik,
Giessenbachstraße,
D-85748 Garching, Germany
- UK ISO Data Centre at RAL in the United Kingdom
The UK ISO Data Centre,
CCLRC - Rutherford Appleton Laboratory,
OX11 0QX Chilton, Didcot, Oxon, United Kingdom

Responsible for detailed instrument specific software and expertise, including provision of software modules for the pipeline, and for supporting their local and national user communities.

- ISO Support Center at IPAC in the United States ⁴:

The ISO U.S. Science Support Center,
IPAC – California Institute of Technology,
Mail Code 100-22,
770 South Wilson Avenue,
Pasadena, CA 91125, USA

Responsible for supporting the USA community plus provision of some data processing tools, like ‘First-look tools’ and the generation of ‘Browse Products’.

Most of these centres still provide direct support to users and welcome visitors during the Active Archive Phase.

1.4.2 ISO Data Analysis Software

The quality of the pipeline processed data in the archive may not always be sufficient for specific purposes. For further processing and analysis of ISO data the following software packages are available:

- The ISOPHOT Interactive Analysis (PIA) software package is distributed by the ISO Data Centre and the ISOPHOT Data Centre at Heidelberg, Germany.
- The ISOCAM Interactive Analysis (CIA) software package is distributed by the ISO Data Centre and the ISOCAM Data Centre at Saclay, France and is available upon request.
- The ISO Spectroscopic Analysis Package (ISAP) is distributed by the U.S. ISO Science Support Center at IPAC and the SWS Data Centre in Garching, Germany.
- The Observers SWS Interactive Analysis Package (OSIA) software package is distributed by the SWS consortium.
- The LWS Interactive Analysis (LIA) software package is distributed by the UK ISO Data Centre at RAL and the U.S. ISO Science Support Center at IPAC.

All these software packages can be obtained through the ISO Data Center web pages:

<http://www.iso.vilspa.esa.es/> → ISO Data Analysis Software

For questions and comments on the ISO software packages contact helpdesk@iso.vilspa.esa.es.

⁴inactive since 31 December 2001

1.5 Document Guide

This Volume I of the ISO Handbook tries to give the necessary background information to users of ISO Data, especially newcomers, on the ISO Mission and the way in which it was organised, the spacecraft operations and its in-orbit performance as well as on the data products which resulted from the scientific programme and how they can be retrieved from the ISO Data Archive.

Chapter 1 gives an introduction to the ISO, its legacy, references, acknowledgement statements and further ISO support. In Chapter 2, the general organisation of the ISO project is presented. Chapter 3 addresses the satellite design including a description of the Service Module and of the Payload Module components. Chapter 4 summarizes the key elements of the operations, including a description of the ground segment and of the ISO observing cycle, and it also gives an overview of the scientific programme and of the satellite/instrument observing modes. The in-orbit performance is described in Chapter 5. The ISO results are cross-calibrated with respect to other airborne and space missions in Chapter 6. Finally, a description of the ISO Data Archive is presented in Chapter 7, where we include an overview of its contents as well as some general guidelines on how to use it.

In the Appendix we give a general introduction to infrared astronomy and provide a list of all scientific programmes of ISO and of the observed solar system objects. We also give some technical information on the data products generated by the satellite and details on the contents of the ISO Data Archive. The section on the *quaternions* explains how the ISO pointing was calculated. Finally, a few SQL-query examples are provided showing that they can be a very powerful way of accessing all data in the ISO Data Archive.

Chapter 2

The ISO Project

2.1 The Project Organisation

ISO resulted from a proposal made to ESA in March 1979, [159]. After a number of studies (Assessment, 1979, [86]; Pre-Phase A, 1980, [88]; Phase A, 1982, [89]), ISO was selected in 1983 as the next new start in the ESA Scientific Programme. Following a ‘Call for Experiment and Mission Scientist Proposals’ in July 1984, [13], the four scientific instruments were selected in June 1985. The satellite design and main development phases started in 1986 and 1988, respectively with Aerospatiale (Cannes, F, now Alcatel) as prime contractor. The industrial team numbered 32 companies, including DASA (D, now part of the European Aeronautic Defence and Space Company, EADS) responsible for the Payload Module, Linde AG (D) for the helium sub-system, Aerospatiale (F) for the telescope, CASA (E, also part of EADS now) for the Service Module structure, thermal aspects and harness, and Fokker (NL) for the attitude and orbit control system.

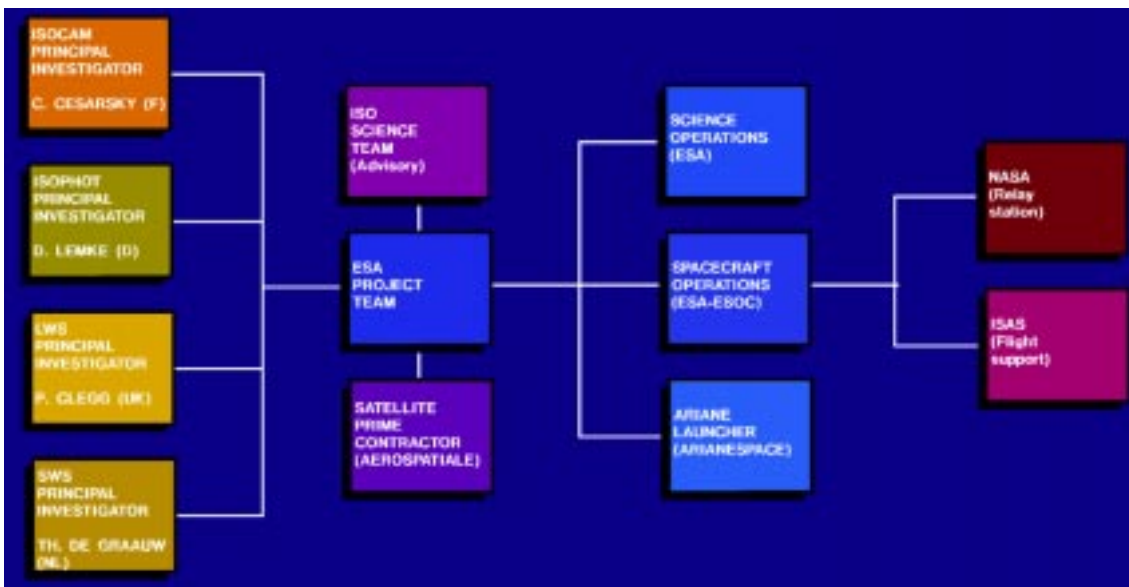


Figure 2.1: *ISO project organisation.*

The overall project organisation is shown in Figure 2.1. Central to this organisation was the ESA Project Team which was located at ESA’s European Research and Technology Centre, ESTEC, in Noordwijk,

The Netherlands. This project team, part of the ESA Scientific Projects Department in the Directorate of Scientific Programmes, was responsible for the management of the development, launch and in-orbit commissioning of the satellite. The team was headed by the Project Manager, initially Derek Eaton (from January 1984 until December 1986), succeeded at the start of the industrial phase by Johan A. Steinz, who was supported by:

- S. Ximénez de Ferrán - System and Spacecraft Manager
- M. Anderegg - Payload and Operations Manager
- K. Leertouwer - Assembly, Integration and Test Manager
- M. von Högen - Product Assurance Manager
- A. Linssen - Project Control and Administrative Manager
- A. Robson - Ground Segment Manager

The ESA Astrophysics Division, headed by Brian G. Taylor, of the Space Science Department (now Research and Scientific Support Department), was the home of the ISO Project Scientist Martin F. Kessler, who had an overseeing role of the ISO Development Phase and assumed this responsibility after the in-orbit Commissioning Phase, when the spacecraft operations were delegated to ESOC (Darmstadt, Germany and Villafranca, Spain).

Both the USA and Japan had great interest in using ISO. As a result, ESA made special agreements with NASA (USA's National Aeronautics and Space Administration) and ISAS (Japan's Institute of Space and Astronautical Sciences): NASA provided the second ground station and ISAS supported the flight operations; in return, NASA and ISAS were each allotted a half hour per day of ISO's time for use by their scientists.

2.2 Satellite Development

2.2.1 Industrial consortium

A number of specific features of ISO had to be taken into account to establish the industrial policy regarding the satellite development. In particular, there was little experience available anywhere in the world with respect to infrared astronomy. Only one major mission, IRAS, had been flown. The expertise available in the field of space cryogenics and the assembly, integration and verification of large superfluid helium cryostats, was also very limited. Only two companies in Europe had relevant experience: Aerospatiale/SNIAS (F) which had developed a laboratory model liquid-helium cryogenic facility, and DASA (D) which had manufactured a development model of a German infrared laboratory (GIRL).

ESA's Industrial Policy Committee (IPC) decided, in April 1984, that the Phase B should be carried out by one prime contractor, who would be responsible for the design and development of the satellite and for the integration and testing of the scientific instruments. The prime contractor would lead a consortium of companies formed by several subcontractors. It was also decided that critical technology items such as cryostat components and telescope mirrors would be developed in parallel to the Phase B design activities.

In November 1986, the IPC approved the placing of the Phase B contract with Aerospatiale as the satellite prime contractor and work started in industry in early December 1986. By the end of Phase B, 15 companies were involved in the work. Following the successful completion of Phase B, the Phase C/D contract was again placed with Aerospatiale and work started at the end of March 1988. The industrial consortium was extended to include a number of companies that had been selected through competitions



Figure 2.2: Structure of the industrial consortium that developed, manufactured, integrated and tested the ISO satellite.

that the prime contractor conducted in an effort to meet the overall geographical distribution and cost targets for Phase B and C/D.

Competitions were conducted for the following items:

- Parts procurement agent
- On-board data handling subsystem
- Optical subsystem
- Star-Tracker
- Central checkout equipment
- Service Module, Payload Module and system mechanical ground support equipment

At a later stage during Phase C/D, more competitions were held for the cryo-electronics unit and the data handling decoder. As a result, the final industrial consortium for ISO comprised 32 companies, with one prime contract and 44 sub-contracts. The final structure of the industrial consortium that developed, manufactured, integrated and tested the ISO satellite is depicted in Figures 2.2 and 2.3.

The total price for the Phase C/D was made up of cost-reimbursement prices associated with a cost-incentive scheme, and firm-fixed or fixed prices with variation. The percentage of the price consigned to a cost reimbursement was higher than in a typical scientific spacecraft mission, i.e. about 70%. This was due to the very advanced technology of the Payload Module and the greater-than-usual development risk. Also, the demanding mission requirements, such as those of the attitude and orbit control subsystem,

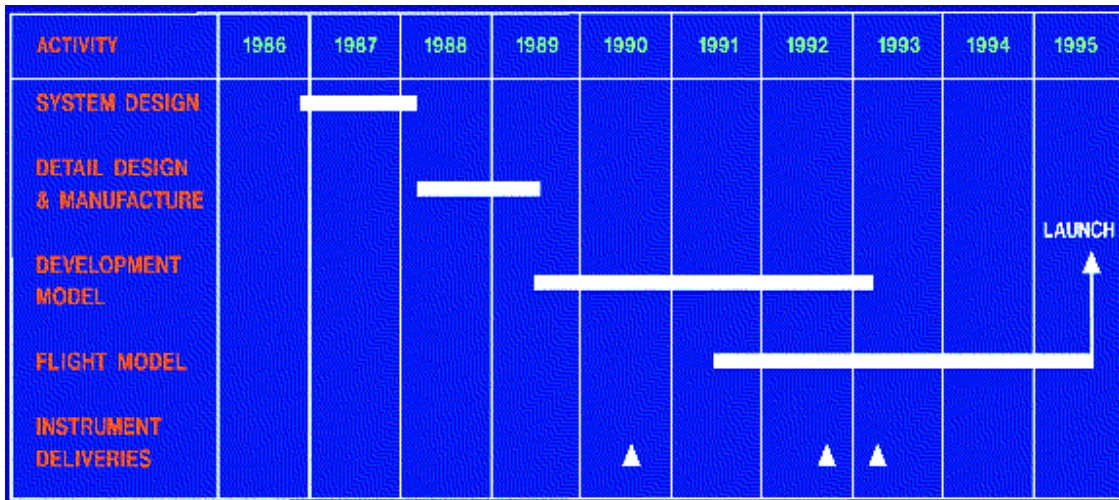


Figure 2.4: *The pre-launch ISO project schedule.*

All units were required to be delivered in two models, a flight model and a flight spare (which is generally a refurbished qualification model). The availability of flight spare units contributed greatly to the success of the programme: small problems could be easily resolved by simply exchanging units and thus avoiding any major delays. The scientific instruments also benefited because the flight model and flight spare could be alternately improved in parallel to the satellite development.

Arianespace provided the launch vehicle and all associated launch services. The interfaces and operations with ISO, however, were unusually complex because of ISO's need for frequent liquid helium cryogenic servicing until shortly before launch. Arianespace had to make special provisions to cope with the more complicated and longer duration launch campaign and combined operations with the launch vehicle.

ISO was approved in 1983 at a cost of 258 MAU, assuming 1982 economic conditions and 1983 exchange rates. During the Development Phase, there were a number of technical problems including the liquid helium valves, the telescope, the liquid helium tank, the attitude and orbit sub-system and science operations. These problems and the launch slip from May 1993 to November 1995 led to a number of cost increases. Additionally, the scope of the programme was extended by the extension of orbital operations by 1 year and the approval of Post-Operations and Active Archive Phases. The final cost of ISO was 615 Meuros at mixed economic conditions. This corresponds to 480.1 Meuros when backdated to the same economic conditions as the approval level of 258 Meuros in 1983. The final cost includes not only the effect of problems and delays in the development but also various enhancements to the mission such as a 1-year extension of operations and the addition of the Post-Operational (3.5 years) and Active Archive (5 years) phases.

2.3 Principal Investigators and Science Team

ISO had four Principal Investigators (PIs), one for each of the scientific instruments. The scientific instruments were developed under national funding, with each PI being responsible for his/her own scientific instrument. Each instrument was developed by a group involving many institutes and industries. Over 45 organisations in total were involved. Figure 2.5 lists these organisations by country and instrument name.

The PIs were responsible for the delivery of their scientific instruments to the ESA Project for integration and testing with the satellite. In return for the effort of developing the instrument, the PIs were



Figure 2.5: *Principal Investigator (PI) organisations by country and instrument.*

guaranteed the use of ISO for about one-third of its total operations time in orbit. The PIs planned this guaranteed time in great detail and shared it with their many Co-Investigators and Scientific Associates, about 100 astronomers in total. The remaining two-thirds of ISO's operations time was open to the scientific community, i.e. any scientist in Europe, the USA or Japan, through the submission of observing proposals.

An overview of the distribution of observing time per participating group is given in Figure 4.7.

The ISO Science Team advised ESA on all scientific aspects of the mission throughout the project's lifetime. The Team's main aims were to maximise the mission's scientific return and to ensure that ISO maintained its principal characteristic as an observatory satisfying the needs of the scientific community at large. The IST consisted of the ESA Project Scientist, the four instrument PIs, five Mission Scientists providing independent advice, and a representative from the ESA Project Team and both ISAS and NASA. The IST followed the development of the project and met quarterly to address the important scientific issues that arose during the period between the Development Phase and the end of the Post-Operations Phase.

The team consisted of:

- Instrument Principal Investigators:
 - C.J. Cesarsky, CEA, Saclay, F
 - P.E. Clegg, QMW, London, GB
 - Th. de Graauw, SRON, Groningen, NL
 - D. Lemke, MPIA, Heidelberg, D

- Mission Scientists:
 - Th. Encrenaz, Obs. de Meudon, Paris, F
 - H.J. Habing, Sterrewacht, Leiden, NL (Vice-chairman)
 - M.O. Harwit, Cornell University, USA
 - A.F.M. Moorwood, ESO, Garching, D
 - J.L. Puget, IAS, Orsay, F
- ESA Payload and Operations Manager:
 - M. Anderegg, ESTEC, Noordwijk, NL
- ESA Project Scientist:
 - M.F. Kessler, ESTEC, Noordwijk, NL (Chairman)¹
- NASA representative:
 - G. Helou, IPAC, USA
- ISAS representative:
 - H. Okuda, ISAS, Japan

The role of the Mission Scientists were to provide scientific input to the project and to represent the interests of the general astronomical community.

2.4 Science and Spacecraft Operations

The ESA Space Science Department (now Research and Scientific Support Department) was responsible for the science operations, i.e. the in-flight operations of the scientific instruments. It developed the necessary software at ESTEC, part of it (RTA/QLA², AOT³ logic, OLP⁴) in collaboration with the instrument teams. This software development was a difficult and challenging undertaking, mainly because of the high degree of automation required and the many constraints to be respected.

ESA's Space Operations Centre, ESOC in Darmstadt, Germany, was responsible for the overall ground segment and for operating the spacecraft. ESOC controlled the satellite from its Operations Control Centre at Darmstadt during the Launch and Early Orbit Phase (LEOP), i.e. the first four days after launch. ESOC was also coordinating its operations with NASA-JPL, which provided the second ground station for ISO at Goldstone, and with ISAS in Japan, which provided support for ISO's flight operations.

After this critical phase of the flight, ISO and its scientific instruments were controlled from the Spacecraft Control Centre (SCC) at Villafranca, Spain (VILSPA), which was co-located with the ISO Science Operations Centre (SOC). The roles and responsibilities of the SCC and the SOC are detailed in Section 4.2. The co-location of so many experts close to each other was a major factor in successfully carrying out ISO's complex operations.

Following attainment of the operational orbit and successful checkout, validation and calibration of the spacecraft and instruments, routine operations started — on schedule — on February 4, 1996 and continued until exhaustion of the liquid helium coolant on April 8, 1998.

¹At the last month of the Post-Operations Phase, L. Metcalfe took over the Project Scientist position (April 2001 – mid-May 2002). Since 15 May 2002, this role passed to A. Salama, leading the Active Archive Phase activities.

²Real-Time Technical Assessment & Quick-Look Analysis

³Astronomical Observation Template

⁴Off-Line Processing

2.5 Operational Activities

2.5.1 Launch and Early Orbit Phase

ISO was launched at 01:20 UTC on November 17, 1995 from Kourou (French Guiana) using an Ariane 44P (with 4 solid strap on boosters) launch vehicle on Flight V-80.

The trajectory was nominal and, after successful re-orientation of the composite Ariane 3rd stage/ISO, separation was reported by Arianespace at 01:40 UTC.

First orbit determination from Flight Dynamics revealed that the initial transfer orbit was very accurate and the dispersion of all elements much less than the standard deviation.

The apogee height was 71 577 km, about 43 km lower than the expected apogee of 71 620 km. The perigee height of 500 km and the inclination of 5.25° were as expected. The orbital period was 1 min. 15 sec. larger than expected.

A detailed summary of the events that took place during the 4 days of duration of this Phase (revolutions 0 to 3) can be found in the *ISO Launch and Early Orbit Phase & Satellite Commissioning Phase Report*, [87]



Figure 2.6: *The ISO Spacecraft Control Room*

2.5.2 Commissioning Phase

With the successfully performed handover of operations from ESOC/OCC to VILSPA/SCC, LEOP terminated and the Satellite Commissioning Phase (SCP) started. The SCP was carried out jointly by

the ISO Spacecraft Control Centre (SCC) and the Science Operations Centre (SOC), under the overall responsibility of the ISO Project from November 21, 1995 (revolution number 4) to December 9, 1995 (revolution number 21) inclusive.

The objectives of the SCP were the following:

- Continue with satellite control and monitoring activities
- Determine the status of the complete satellite after LEO-P
- Verify compliance with system specifications for parameters impossible to measure on ground (for instance pointing performance)
- Assess the effects of the in-orbit environment (radiation effects on the instrument detectors) and determine possible deviations from pre-launch predictions

The first step of the SCP was to continue with spacecraft check-out and subsystems performance verification, as initiated during LEO-P, to reach the mission orbit, and to eject the cryostat cover.

The second step of the SCP was to complete the overall check-out of the ISO payload, i.e. the scientific instruments. To validate the instrument activation and de-activation sequences, and initiate the study of the in-flight performance of each instrument, in order for the space segment to be ready to execute the Performance Verification (PV) phase and the Routine Phase (RP). In the process of executing the SCP, the overall integrated Ground Segment (SCC, SOC, Ground Stations, and communications network) was also validated.

In addition, all the nominal modes of the Service Module subsystems were successfully verified, including AACS units and functions, OBDH (On-Board Data Handling), RF (Radio Frequency), power conditioning and thermal control performance.

Similar to the Service Module subsystems, all nominal modes of the payload module were also successfully verified. There was no indication that the telescope was defocussed or suffering from aberrations. The performance of the four scientific instruments was nominal with respect to functionality of the hardware and software. The cool-down phase of the cryostat was determined to be well in line with the thermal model and the helium flow rate was found well within limits anticipating a lifetime of 24 ± 2 months, compared with the baseline of 18 months.

PHT was the first of ISO's four scientific instruments to be switched on at 09:56 UTC on November 21, 1995 (revolution 4). PHT-specific tasks during SCP comprised, among other activities, wheel commissioning, general instrument behaviour check-out, detector curing and determination of the PHT focal plane geometry offsets to measure the precise location of the instrument apertures with respect to the Quadrant Star Sensor (QSS) boresight. PHT was used as prime instrument in revolutions 4 to 9, 12, 13, 17 and 21.

CAM was switched on at 08:41 UTC on November 24, 1995 (revolution 7). Soon while instrument check-up was in progress, column 24 was reported missing in the Long Wavelength (LW) array, confirming the results obtained during testing on ground. Apart from the general instrument behaviour check-out, other CAM-specific tasks during SCP included detector transient measurements and determination of the CAM focal plane geometry offsets. CAM was used as prime instrument in revolutions 7, 8, 11, 13 to 16 and 21, and in parallel mode in revolutions 12 to 14 and 18 to 20.

LWS was switched on at 08:42 UTC on November 25, 1995 (revolution 8). LWS-specific tasks during SCP comprised, among other activities, general instrument behaviour check-out, detector curing and determination of the LWS focal plane geometry offsets. LWS was used as prime instrument in revolutions 8, 11 to 14 and 21.

SWS was the last of ISO's four scientific instruments to be switched on. The initial switch on of SWS took place at 08:08 UTC on November 26, 1995 (revolution 9). As for the other ISO instruments, SWS-specific tasks during SCP included general instrument behaviour check-out, detector performance

evaluation, detector curing, Fabry-Pérot parallelisation and determination of the focal plane geometry offsets. SWS was used as prime instrument in revolutions 9, 11 to 14 and 17 to 21.

Furthermore, the following general activities were performed: uplink time jitter buffer test, solar system object tracking, four instrument automatic activation and de-activation sequences validation, ground station ‘modulation index’ investigations and the verification of the overall observatory functionality.

During the course of the SCP several (minor) deviations from the flight operations plan were required in response to unexpected or unplanned events. But in general, no major problems occurred. All anomalies could be closed and the ISO observatory was declared ready to support the PV Phase.

A full description of the events that took place during this phase and of the few minor anomalies detected is given in the above mentioned *ISO Launch and Early Orbit Phase & Satellite Commissioning Phase Report*, [87].

2.5.3 Performance Verification Phase

After a successfully completed SCP, the Scientific Performance Verification Phase started on revolution 22 (December 9, 1995) and ended on revolution 78 (February 3, 1996).

The objectives of this phase were the following:

- Perform AOT functional and scientific verifications
- Establish the core scientific calibration of all instruments
- Collect the necessary data to scientifically validate the Off-Line Processing system.

It was anticipated that, contrary to the Routine Phase, re-planning of revolutions on short notice would be necessary. In order to allow quick re-planning it was decided to operate only one instrument per revolution.

With the exception of an anomaly in the scanning of the LWS long-wavelength Fabry-Pérot interferometer, the instruments appeared to operate functionally as expected from ground-based testing.

High energy particle impacts (glitches) adversely affected the sensitivity of the two spectrometers. Preliminary analyses showed sensitivity losses of up to around a factor of 4, depending on detector type; however, this loss was later reduced by optimised operating conditions and improved data processing.

The sensitivities of CAM and PHT appeared to be close to their pre-launch expectations, although, an additional set of procedures was needed for some detectors once per day to remove effects induced by high energy particle impacts.

From an operational point of view the PV phase consisted of two parts, the core PV part and the so-called Observatory Verification part. The core PV part covered revolutions 22 to 77, thus 56 revolutions, with a mid-term review held at VILSPA on January 12, 1996 to summarise the current status of instrument performance and to release some of the AOTs for use during the first weeks of the Routine Phase. The Observatory Verification part consisted of one revolution only, revolution 78, and marked the transition to the Routine Phase. This was the first time when all four instruments were activated and operated on the same revolution with the same operational SOC hardware and software used for the Routine Phase. The purpose of this revolution was to verify that ISO and the Ground System could successfully execute and generate a schedule as planned with the Mission Planning system in its nominal mode, and to commission and calibrate the PHT serendipity and the CAM parallel modes. At the end of the PV Phase 16 observing modes (AOTs), 80% of total, had been released for use by observers.

2.5.4 Routine Phase

The ISO Routine Phase comprised the period between revolution 79 (February 4, 1996) and revolution 875 (April 8, 1998).

During this phase the SCC was responsible for all spacecraft operations. This included:



Figure 2.7: *The ISO Instrument Control Room*

- Spacecraft telecommanding
- Spacecraft telemetry reception, handling and display
- Spacecraft mission planning
- Generation of spacecraft manoeuvres
- Orbit determination and maintenance
- Attitude control
- Generation, distribution to the SOC, archiving and logging of Telemetry Distribution Format (TDF)
- Monitoring of satellite subsystems
- Maintenance of the ground and on-board spacecraft software

The SCC was also responsible for the safety of the scientific instruments.

On the other hand, the SOC was responsible for the scientific aspects of the ISO mission and in particular for all activities related to the four instruments. This included the following tasks:

- Capture of observing proposals and support to OTAC and the scientific community
- Mission Data Base (MDB) operation and management
- Scientific mission planning
- Scientific real time operations
- Maintenance and assessment of the instruments performance
- Maintenance and design of the instrument observational modes (AOTs)
- Instrument microprocessor on-board S/W maintenance
- Routine pipeline processing of the scientific data and generation of the mission products
- Quality check of the mission products
- Management and operations of the mission products archive and data base
- Distribution of the mission products
- Instrument calibration
- Calibration coordination and cross-calibration of all instruments
- Maintenance, upgrade and configuration control of the Interactive Analysis and RTA/QLA system (B) S/W
- Maintenance of instrument specific requirements on the RTA/QLA S/W system (A)
- Maintenance of instrument specific requirements on the pipeline OLP S/W
- Maintenance, upgrade and testing of the SOC S/W
- Configuration control of the SOC S/W
- Computer Maintenance, system management and configuration control

A general description of the satellite and instruments performance and of the main events occurred during this Routine Phase is given in Chapter 5. More specific information on individual instruments performance can be found in the corresponding instrument specific volumes (II to VI) of the ISO Handbook.

2.5.5 From end of helium to switch off

At 07:00 UTC on April 8, 1998 (revolution 875) ISO's telescope started to warm up, which was the sign that ISO had exhausted the superfluid helium. Observations ceased at 23:07 UTC when the temperature of the instruments had risen above -269°C (4.2 K). Observations from revolutions 875 and later have to be taken with care because of the higher temperatures of the detectors. However, a few of the detectors in the Short Wavelength Spectrometer (SWS), could still be used after exhaustion of the liquid helium. Some 150 extra hours were used to measure nearly 300 stars at wavelengths between 2.4 and 4 microns (see Vandenbussche et al. 2002, [158]), interspersed between technology tests, where various software and hardware systems were subjected to detailed analysis under non-standard conditions.

Some of the main activities during this Technology Test Phase were testing the operation of the star trackers at low altitudes, i.e. in the radiation belts, use of the on-board redundant units that were not needed during the routine operations due to the superb performance of the satellite, and evaluation of the software intended to overcome multiple gyro failures.

The ISO satellite was switched off on May 16 at 12:00 h UTC, thereby bringing to a close the highly successful in-orbit operations.

2.6 Post-Operational Activities

2.6.1 Transition Phase to Post-Operations

The Transition Phase between the science and spacecraft Operations Phase and the Post-Operations Phase started already in February 1998, 2 months before helium depletion, and ended in July 1998, 3 months after helium depletion. The main tasks in the Transition Phase were:

- ‘Knowledge capture’ from instrument experts, IDC and NDCs
- Quality control of OLP (Version 7.0) products
- Interactive Analysis S/W development work
- Explanatory Supplement inputs and documentation
- Cross-Calibration Plan
- Testing and filling of the Post-Operations Archive
- Preparation of the Post-Operations Phase

2.6.2 Post-Operations Phase

The Post-Operations Phase started on August 1, 1998 and ended on December 31, 2001, about 3.5 years after helium depletion. The goal of the ISO Post-Operations was to facilitate a widespread, effective and extensive exploitation of the ISO data. This was achieved by:

(a) during the Post-Operations Phase:

- deepening the understanding of the satellite’s and instruments’ behaviour (including calibration),
- preparing and making available improved processing algorithms and data products at various levels,
- supporting the astronomical community to use ISO data during this entire phase by provision not only of software and data products (interim archive) but also of expertise, information and centres to visit for detailed assistance;

(b) by the end of the Post-Operations Phase:

- providing a final archive of data, documentation and software that permit continued exploitation of the ISO legacy by the astronomical community for the coming decades.

These objectives were achieved in close collaborations between the ISO Data Centre and all national data centres (see Section 1.4).

The ISO Post-Operations Phase (including some of the first months of the Active Archive Phase) left the ISO Data Archive (IDA), including data and documentation, in a well developed reference — ‘legacy’ — state. Automatically-generated data products were made available for the vast majority of observations, and comprehensive support documentation was provided. Links between ISO and other archives began to develop, as IDA asserted its ground-breaking role in the advancement of astronomical archive technology. The automatically-generated data products serve the vital need of facilitating exploration and ‘prospecting’ for interesting data in the archive. However, before data products can be fully exploited and interpreted scientifically they usually need to be assessed using the Interactive Analysis Software packages that are available for all ISO instruments (see Section 1.4.2).

2.7 Active Archive Phase

To retain the usefulness of the ISO Data Archive far into the future, an ‘Active Archive Phase’ was approved by ESA’s Science Programme Committee (SPC) for the ISO Data Centre. This phase started on January 1, 2002 and will last until December 31, 2006. During this phase the ESA ISO Data Centre continues to cooperate closely with the several national ISO data centres (see Section 1.4.1), in order to refine the archive data products. The goal at the end of this phase is that the archived data will then require no or only the absolute minimum use of additional IA intervention by the user before scientific exploitation.

The responsibilities of the ESA ISO Data Centre in the Active Archive Phase can be summarised as maintaining the central archive and providing expert support to the community across all instruments, via:

- **Archive maintenance and improvements:**
During this phase, the archive will be maintained, especially the user interface to maximise its usefulness and ease of use, and improved with the ingestion of new data and information. Major tasks will be: stimulating systematic data reduction by ISO experts and capturing the resulting data products into the archive; tracking of refereed ISO publications and incorporating this information; ingestion of new ISO catalogues and atlases; continuing the process of increasing the inter-operability of archives by linking to other data sets.
- **Support in data usage:**
The ISO Data Centre will continue to be the first line support to the general community on all matters regarding ISO data. This includes provision of advice; support for data reduction either remotely or via visits to the centre; and supply of, and assistance with, software for detailed data analysis.
- **Supply of general information:**
The existing Helpdesk and WWW services will be continued and updates made as needed to the ISO Handbooks.
- **Promotion of awareness of ISO data:**
General conferences and specific small ‘hands-on’ data reduction workshops will continue to be organised with the proceedings being made widely available.

The continuation of the cooperation between the ESA ISO Data Centre and most of the national data centres is of much benefit to the final archive and gives added value to the community. The ESA Centre in Villafranca is taking the responsibility for overall co-ordination of the managerially and financially independent data centres.

Activities of the national data centres involved in the Active Archive Phase include: maintenance and improvement of software packages for interactive data reduction, including making available new algorithms and calibration files; further work on instrument specific calibration; and focussed reduction of specific data sets to be ingested back into the archive as Highly Processed Data Products (HPDPs).

A mid-term review, in front of an independent Board, will be held in 2004 to review progress and make recommendations on any re-directions of effort.

2.8 Outlook: ISO and the Virtual Observatory

As of November 2003, the ISO Data Archive is still being intensively used by the astronomical community with typically more than 2000 queries executed every month. In its first five years of use, the equivalent of more than 8 times the total number of scientific observations in the archive has been downloaded. In total, there are nearly 1500 registered users, still increasing at an average rate of about one new user every two working days. About 50 to 70 users actually download data every month.

Looking further into the future, first steps have already been taken to prepare the ISO Data Archive for its future integration into the 'International Virtual Observatory' concept.

The Virtual Observatory is an international astronomical community-based initiative. It aims to allow global electronic access to the available astronomical data archives of space and ground-based observatories and sky survey databases. It also aims to enable data analysis techniques through a coordinating entity that will provide common standards, and state-of-the-art analysis tools.

With this spirit in mind, the ISO Data Archive currently provides links from individual observations to publications in the NASA ADS⁵ database; the list of ISO observations has been installed in VizieR⁶ (the most complete database of published astronomical catalogues) and links to the ISO Postcard Server (see Chapter 7) are provided from VizieR; and the feasibility to implement direct access to images from Aladin⁷ (an interactive software sky atlas allowing the user to visualize digitized images of any part of the sky and superimpose entries from astronomical catalogues or personal data files) is being assessed. More advanced, value-added functionalities are in preparation, in particular the cross-identification of the list of ISO observations with the astronomical database SIMBAD⁸, which will permit direct links between objects in SIMBAD and the ISO Data Archive, search by object types in the archive, etc.

At the end of the Active Archive Phase, maintenance of the historical archive is expected to be carried out in conjunction with the Herschel Science Centre, under the general auspices of the Research and Scientific Support Department. No additional funding, dedicated to the historical archive, is sought after 31 December 2006.

⁵<http://adswww.harvard.edu/>

⁶<http://vizier.u-strasbg.fr/>

⁷<http://aladin.u-strasbg.fr/>

⁸<http://simbad.u-strasbg.fr/>

2.9 Chronology of the ISO Mission

March 1979	Proposal to ESA for ISO
1979	Assessment Study
1980	Pre-Phase-A Study
1981–1982	Phase-A Study
March 1983	Selection of ISO for inclusion in ESA Scientific Programme
July 1984	Call for Experiment and Mission Scientist Proposals
June 1985	Selection of Scientific Instruments
December 1986	Start of Phase-B (Definition)
March 1988	Start of Phase-C/D (Main development)
April 1994	Call for Observing Proposals
17 November 1995	Launch
21 November 1995	Start of Commissioning Phase
9 December 1995	Start of Performance Verification Phase
4 February 1996	Start of Routine Phase
August 1996	Supplemental Call for Observing Proposals
February–July 1998	Transition Phase to Post-Operations
8 April 1998	Helium boil-off / End of Routine Phase
16 May 1998	Termination of satellite communication
9 December 1998	Opening of the ISO Data Archive
August 1998–December 2001	Post-Operations Phase
28 February 2002	Release of the ISO Legacy Archive
January 2002–December 2006	Active Archive Phase

Chapter 3

The ISO Spacecraft

The ISO satellite had a height of 5.3 m, a width of 3.6 m, a depth of 2.8 m and a launch mass of 2 498 kg (see Figure 1.1). It was conceived as two largely independent modules: the Payload Module and the Service Module (see Figure 3.1). The Payload Module was essentially a large cryostat containing superfluid helium which maintained the telescope and the scientific instruments at temperatures between 2 and 8 K for a lifetime of more than 28 months (the upper cylindrical part in Figure 3.1). The Service Module housed the warm electronics of the scientific instruments, the hydrazine propellant tank, and all the other classical spacecraft subsystems for the provision of the basic functions. The sun-shield, with its covering of solar cells, always faced the Sun to provide electrical power whilst at the same time protecting the Payload Module from direct insolation.

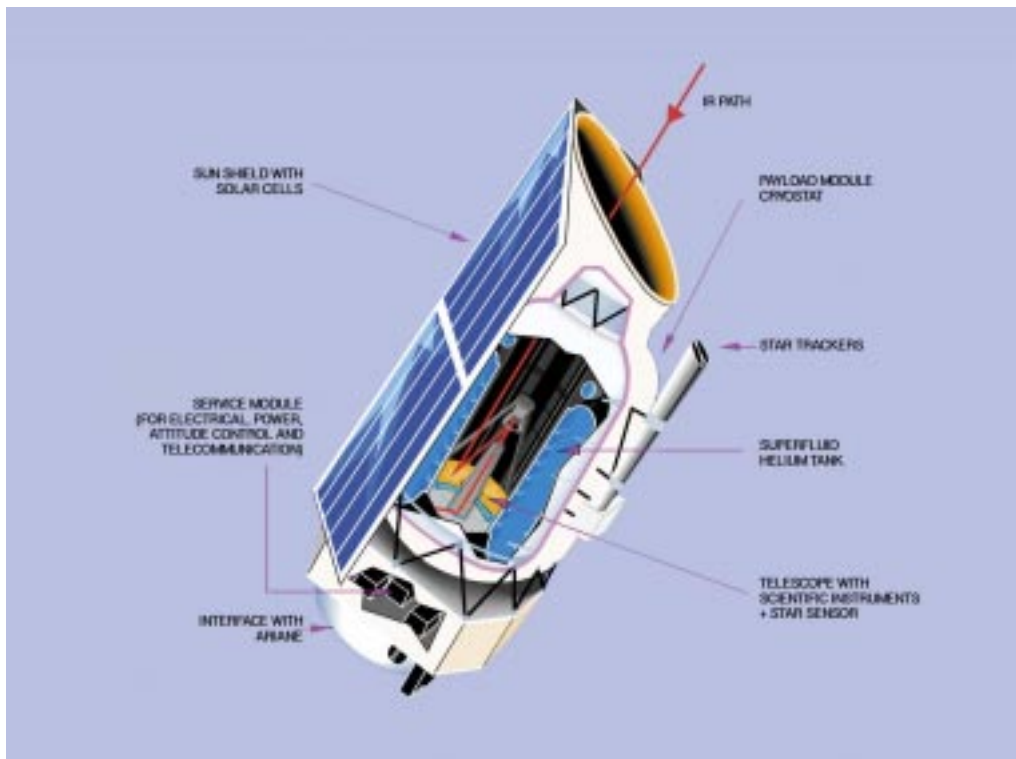


Figure 3.1: *Cut-away schematic of the ISO satellite.*

3.1 Payload Module

ISO's Payload Module (see Figure 3.1) consisted of the helium tank, the telescope and the four scientific instruments — a camera, ISOCAM, a photo-polarimeter, ISOPHOT, and the two spectrometers, LWS and SWS. Inside the vacuum vessel was a toroidal tank, which at launch was filled with 2286 litres of superfluid helium.

Some of the infrared detectors were directly coupled to the helium tank and were held at a temperature of around 1.8 K. All other units were cooled by means of the cold boil-off gas from the liquid helium. This was first routed through the optical support structure, where it cooled the telescope and the scientific instruments to temperatures of around 3 K. It was then passed along the baffles and radiation shields, before being vented to space. The cryogenic system enabled ISO observations of nearly 29 months (the design requirement was 18 months). Above the main helium tank was a small auxiliary tank (of volume about 60 litres); this contained normal liquid helium and met ISO's cooling needs on the launch pad for up to the last 100 hours before launch. Mounted on the outside of the vacuum vessel at the entrance of the telescope was a sunshade, which prevented direct sunlight from entering the cryostat. Cooling of the telescope and the instruments to close to absolute zero practically eliminated their thermal emission — an undesirable 'foreground' radiation source — and enabled observations to be made at high sensitivities.

The telescope itself, located at the centre of the cryostat, was a Ritchey-Chrétien Cassegrain telescope. This configuration was deemed to be the most appropriate for provision of a wide spectral range through a limited field of view, while remaining free from any coma or spherical aberration effects. The Ritchey-Chrétien telescope had an effective aperture of 60 cm and an f /ratio of 15. The optical quality of its mirrors was designed to be adequate for diffraction-limited performance at a wavelength of $5\ \mu\text{m}$. The optical system consisted of a weight-relieved fused silica primary mirror and a solid, fused silica secondary mirror with straylight control via baffles and imposition of viewing constraints. Stringent control over straylight, particularly that from bright infrared sources outside the telescope's field of view, was necessary to ensure that the system's sensitivity was not degraded. This was accomplished by means of the sunshade, the Cassegrain and main baffles, and a light-tight shield around the instruments. Additional straylight control was provided by constraining ISO from observing too close to the Sun, Earth and Moon.

The scientific instruments were mounted on an optical support structure (which carried the primary mirror on its opposite side). Each occupied an 80° segment of the cylindrical volume available. The $20'$ total unvignetted field of view of the telescope was distributed radially to the four instruments by a pyramid mirror. Each experiment received a $3'$ unvignetted field, centred on an axis at an angle of $8.5'$ to the main optical axis, i.e. the instruments viewed separate areas of the sky.

Data was gathered at the detectors and transferred to the 'warm' components in the Service Module for processing before downlink to the ground station.

3.2 Service Module

The Service Module (see Figure 3.1) supported the 'activities' of the Payload Module, acting as the link between the telescope and the ground control system.

It included: the interface with the Ariane launch vehicle, located at the base of the Service Module; the array of solar cells, mounted on the sun-shield, providing the power of approximately 600 W required by the spacecraft; subsystems for thermal control, data handling, power conditioning, telemetry and telecommand; and the Attitude and Orbit Control Subsystem. The last provided the three-axis stabilised accuracy of a few arcseconds and also the raster pointing facilities needed for the mission. The spacecraft axes are shown in Figure 3.2.

The Attitude and Orbit Control Subsystem (AOCS) consisted of Sun (SAS) and Earth (ELS) Sensors, one of two Star-Trackers (STRs), a Quadrant Star Sensor on the telescope axis, gyros and reaction wheels. It used a hydrazine reaction control system. The telecommand rate was 2 kbps while the data transmission rate from the satellite to the ground station, the downlink bit rate, was 32 kbps of which

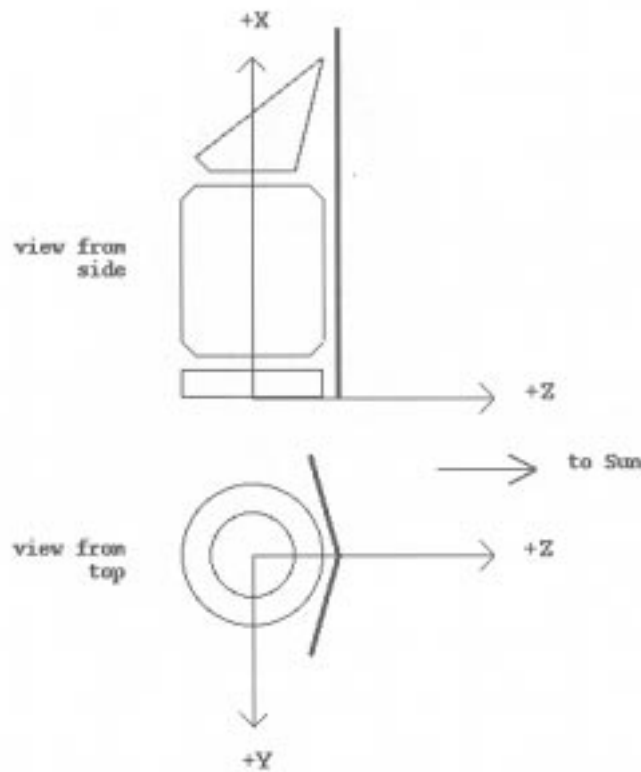


Figure 3.2: Definition of the spacecraft axes.

about 24 kbps were dedicated to scientific instruments. There was no on-board storage of telemetry; thus, while operating scientifically, ISO had to be in continuous real-time contact with a ground station.

All ‘warm’ electronics associated with the four scientific instruments were also housed in the Service Module. This was to minimise the amount of heat dissipated within the cryostat which, in turn, maximised the lifetime of the super-fluid helium.

Spacecrafts are normally not designed to *minimise* thermal emission, rather they are designed with thermal *balance* in mind. As a result, the Service Module, with its classical spacecraft sub-systems, was a significant source of heat and generated a considerable thermal gradient between the Service Module and the Payload Module (normally in the region of 20°C).

To prevent degradation of the effectiveness and lifetime of the cryostat, the Payload Module was thermally shielded from the Service Module by several different means:

- multi-layer insulation over the cryostat exterior;
- specially designed interfaces to minimise thermal conductivity between the Payload and the Service Module, and the Payload Module and the Star-Trackers;
- using low-conductivity glass-fibre struts filled with Ecofoam resin for the interface between Service and Payload Module.

3.3 Spacecraft subsystems

3.3.1 The cryostat subsystem

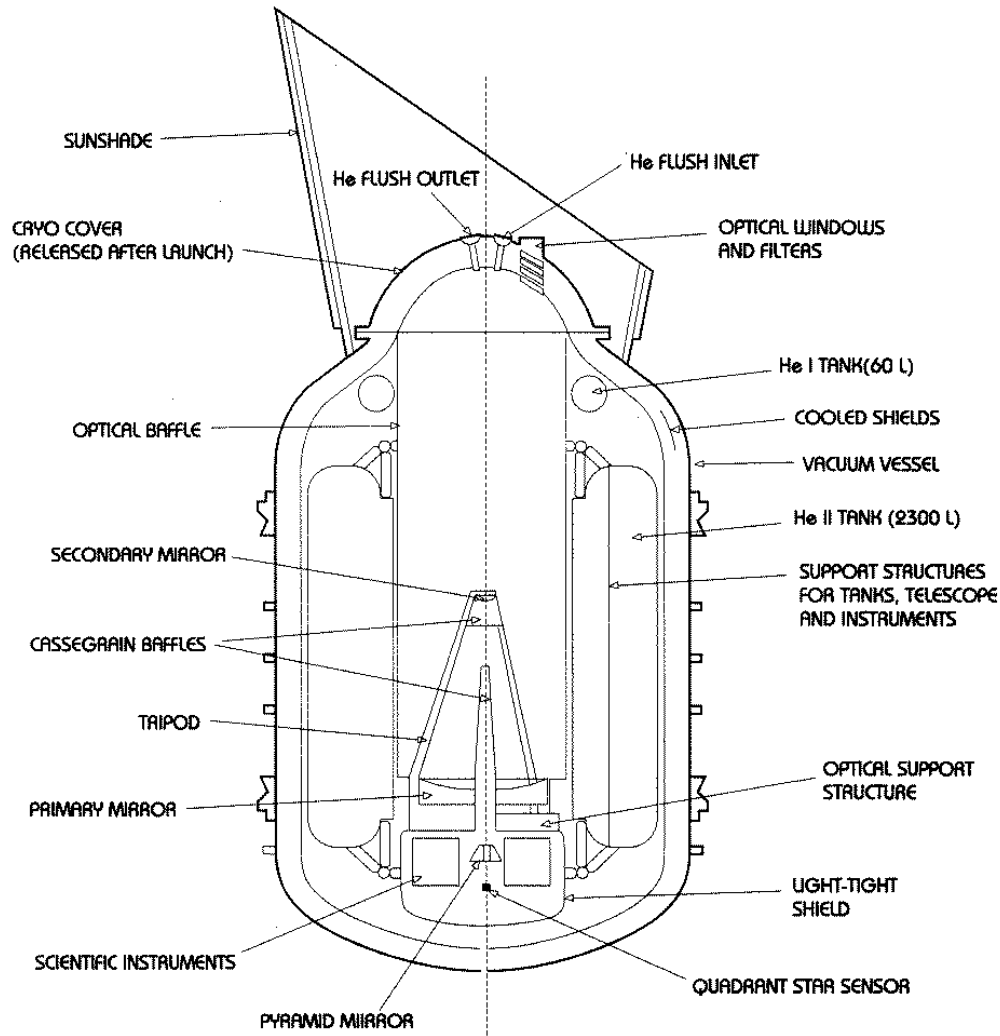


Figure 3.3: *Cryostat and telescope design, showing the location of important elements within, and attached to, the cryostat.*

The ISO spacecraft was designed around a large cryo vacuum vessel (cryostat) — effectively a very large thermos flask — cooled by the evaporation of super-fluid helium to an extremely low temperature. Figure 3.3 shows the general configuration of the cryostat. The cryostat provided an extremely cold stable environment for the ISO telescope, instruments and instrument detectors. This low temperature was required by the scientific instruments in order to obtain the extremely high degree of sensitivity; without this, the detectors (in combination with their electronics and the observing methods used) would only have been able to detect the thermal emissions of the spacecraft, telescope and detectors themselves. The original requirements on the cryostat (later on fulfilled) are given in Table 3.1.

Cryostats are not the only means available for cooling scientific instruments. They carry a significant mass penalty due to their large and heavy construction, they have the drawbacks in the need for complicated ground handling procedures, have difficult launcher interface problems and a lifetime limited by the capacity of the cryogen storage tanks. However, cryostats are capable of providing a significantly more stable environment than the alternatives and this was the driving requirement for the ISO mission.

Table 3.1: *Cryostat requirements.*

Component	Temperature [K]	Temperature stability [°]
Detectors interface	1.7<T<1.9	±0.05 in 1000 s
Optical Support Structure / Focal-Plane Unit interface	2.4<T< 3.4	±0.10 in 1000 s
Primary mirror	<3.2	±0.10 in 1000 s
Secondary mirror	<4	
Lower baffle	<5	
Upper baffle	<7.5	

3.3.1.1 Design of the cryostat

The cryostat surrounded the telescope and scientific instruments with a vacuum vessel, with cooled shields built into the vacuum vessel walls. A diagram of this can be seen in Figure 3.3. Inside these walls a toroidal tank containing up to 2300 liters of super-fluid helium surrounded the optical axis of the telescope including the telescope itself. At the ‘top’ of the cryo vacuum vessel, a cryo cover protected the thermal equilibrium of the cryostat and prevented atmospheric condensation inside the cold telescope until after the launch, at which time it was jettisoned.

The tank was insulated from external heat inputs by three Vapour-Cooled radiation Shields (VCS) equipped with Multi-Layer Insulation (MLI). The tank, radiation shields and telescope were suspended from the Cryo Vacuum Vessel (CVV) by low-conductivity straps. Cooling through the cryostat was achieved in different ways, depending on the subsystem requirements. The Optical Support Structure (OSS) and main baffle were cooled by cold helium gas, resulting in a 3.2 K temperature. The primary mirror was cooled through thermal straps to the OSS, and the secondary mirror was cooled by means of copper braids connecting it to the OSS. The instruments and detectors were either cooled by cooling straps connecting them to the OSS (giving them a temperature of 3.2 K) or by direct cooling straps connection to the helium tank, leading to 2 K temperatures. This is discussed in the *ISO telescope Design Specification* document, [90] and Ximénez de Ferrán 1995, [167]. A heat shield connected to the OSS enclosed all four focal-plane units and provided a light-tight environment.

The pressure inside the helium tank was 17 mbar, the equilibrium boiling point at a temperature of 1.8 K. This pressure was maintained in orbit by the impedance of the vent line, and on the ground prior to launch by continuous pumping of the tank exhaust. The gaseous-helium exit was located at the highest point of the tank, allowing separation by gravity of the liquid and gas phases during ground operations. Once in orbit, one of the remarkable properties of superfluid helium was exploited, the so-called ‘thermodynamic fountain effect’, by which a simple porous plug functions as a phase separator, keeping the liquid phase in the tank while allowing the gaseous helium to flow through the vent line. The vent lines were arranged so as not to impart a thrust to the satellite.

3.3.1.2 Cryostat operations

After the main helium tank had been topped-off, approximately 72–48 hours before launch, it was not possible to access the Ariane’s payload in order to pump the cooling system from an external source. In addition, the cryostat’s main helium tank was closed at this point resulting in a cessation of helium venting through the Vapour-Cooled radiation Shields (VCS). As the VCS could not be left without active cooling for such a period, it was necessary to provide another source of coolant for the VCS prior to launch. Adjacent to the cryostat cover was a smaller auxiliary tank containing 60 liters of normal liquid helium. This was used to vent cooling helium through the VCS and maintain the thermal equilibrium of the VCS until immediately before launch at which time the auxiliary tank was completely emptied. It had no further function.

During the launch of ISO, commands issued by Ariane’s electronics operated a set of cryogenic valves that opened the helium vent line, the main helium tank and its porous-plug phase separator to space. Initially, the vented helium mass flow rate was about 20 mg/s, rising to a peak of about 27 mg/s and then falling until, after about 20 days in orbit, it reached its in-orbit equilibrium point of 5 mg/s.

To cope with this range of flow rates the system was equipped with two sets of nozzles. Initially, both were opened to accommodate the high mass flow rate. As the rate fell and the temperatures decreased the larger nozzles were closed, leaving only the smaller set open (see Figure 3.4).

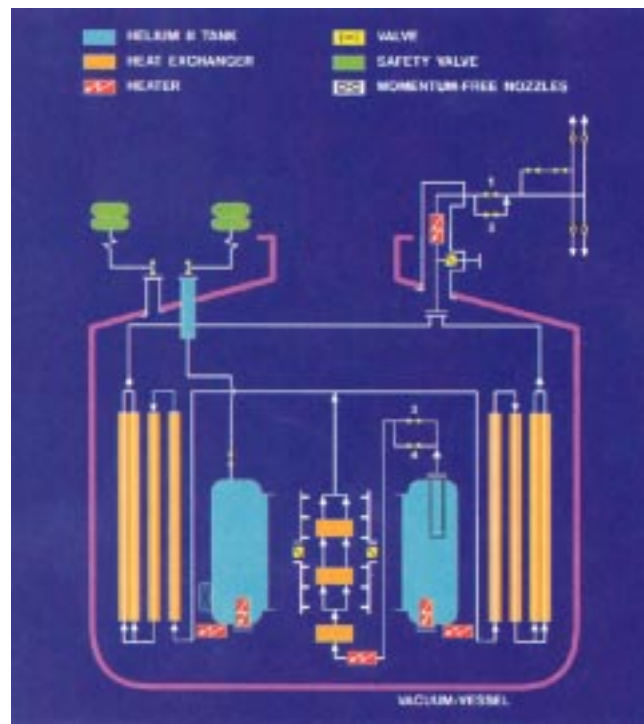


Figure 3.4: Helium flow diagram for ISO in orbit.

3.3.2 The optical subsystem

The ISO telescope was a 60 cm diameter aplanatic Richey-Chrétien system with an overall focal ratio of $f/15$. The main feature of this type of telescopes is the absence of coma and spherical aberration, leading to a larger field of view than the classical Cassegrain type. The optical quality of the primary and secondary mirrors provided diffraction limited performance at wavelengths beyond $5\ \mu\text{m}$, also limited by pointing

performance (Section 5.4.1). As already mentioned, stringent control of straylight was accomplished by a sunshade, the Cassegrain and main baffles and additional light-tight shields around instruments, as well as by imposition of viewing constraints (see Section 4.1). Figure 3.3 shows the configuration of the ISO optical subsystem within the cryostat and Figure 3.5 shows an expanded view of the telescope assembly.

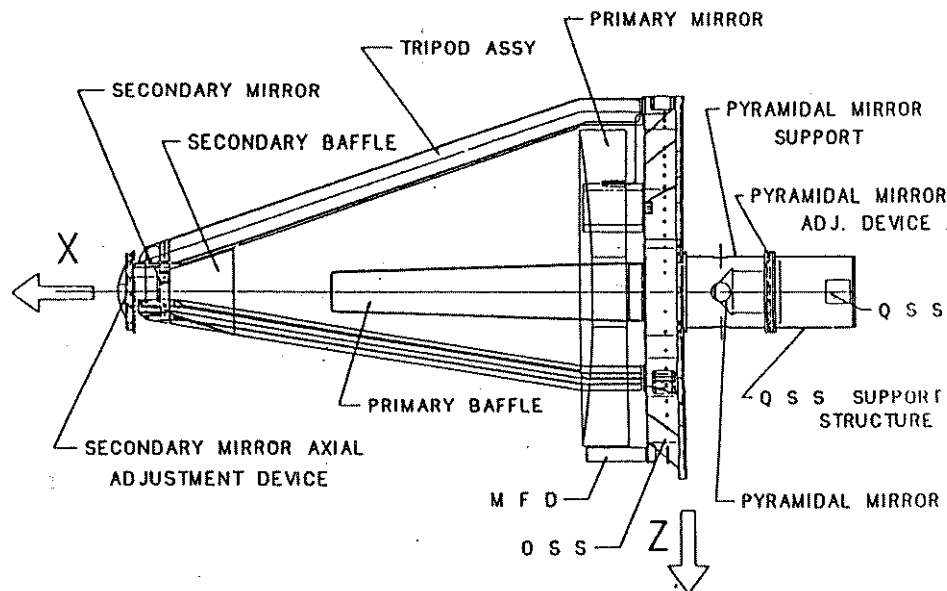


Figure 3.5: ISO telescope optical layout.

3.3.2.1 Telescope mirrors

The optically used diameter of the primary mirror is 634 mm, but the entrance pupil is defined by the secondary mirror which imposes the effective aperture of 600 mm. The central obscuration is imposed by the largest element centered on the optical axis, which is the largest part of the secondary baffle diameter. The tripod is mounted at 0° , 120° , 240° from the negative side of Z axis. Adjustment devices (with 5 degrees of freedom) on the secondary mirror were necessary to perform the internal alignment of the telescope, completed during ground tests.

Information on the mirrors is given in Table 3.2.

3.3.2.2 Focal plane geometry

A part of the $20'$ unvignetted field of view of the telescope (see Figure 3.6) was distributed into the entrance pupil of each of the four instruments by a pyramidical mirror located on the telescope axis. This resulted in a $3'$ unvignetted field of view for each instrument at an angle of $8.5'$ from the telescope optical axis, with the QSS aligned with this axis. The four instruments fields of view were centered around this axis. Since the four instruments viewed separate areas of the sky, switching an astronomical target between instruments required a repointing of the satellite. Figure 3.6 shows schematically how the individual apertures were used by the instruments.

The exact positions of all the apertures with respect to the QSS are given in the ISO Focal Plane Geometry data file (IFPG), see Section D.11, and are reproduced in Table 3.3.

Table 3.2: *Optical parameters of the ISO telescope.*

Object	Value
Primary mirror (M1)	
Total diameter	640 mm
Optically used outer diameter	634 mm
Diameter of central hole	145 mm
Optically not used inner diameter	150 mm
Radius of curvature	2 000 mm
Conic constant	-1.00422
Secondary mirror (M2)	
Optically used outer diameter	87.6 mm
Diameter of central hole	15 mm
Optically not used inner diameter	25 mm
Radius of curvature	-328.5 mm
Conic constant	-1.60366658
Telescope	
Focal length	9 000 ± 250 mm
Numerical aperture	f/15
Axial mirror separation	854 ± 1.8 mm
Entrance pupil	600 mm at 5849.3 mm behind M1
Exit pupil	87.6 mm at M2
Secondary baffle maximum diameter	173.9 mm at 742.4 mm before M1
Tripod width	20 mm
Linear obscuration (central + tripod)	0.36
Instrument field of view	8.5' off-axis
Unvignetted field of view	3' diameter
Pyramidal mirror tilt	44.515 °

Table 3.3: *Offset coordinates (in arcmin) of the instrument apertures with reference to the QSS aperture.*

Instrument	Y coordinates	Z coordinates
QSS ref.	+0.000000	+0.000000
CAM	+8.544170	+0.124167
LWS	+0.225000	-8.425000
PHT1 / PHT-P	-0.158333	+8.435000
PHT2 / PHT-C	-0.158333	+8.435000
PHT3 / PHT-S	-0.113333	+8.415000
SWS1	-8.475000	+1.173330
SWS2	-8.421670	-0.370000
SWS3	-8.345000	-1.908330
SWS4 ¹	-8.195000	-1.908330

Notes:

¹ This is the SWS virtual aperture 4, located approximately 10'' offset from the centre of aperture 3. It is not a real aperture, rather it indicates where the satellite pointed while observing with the FP.

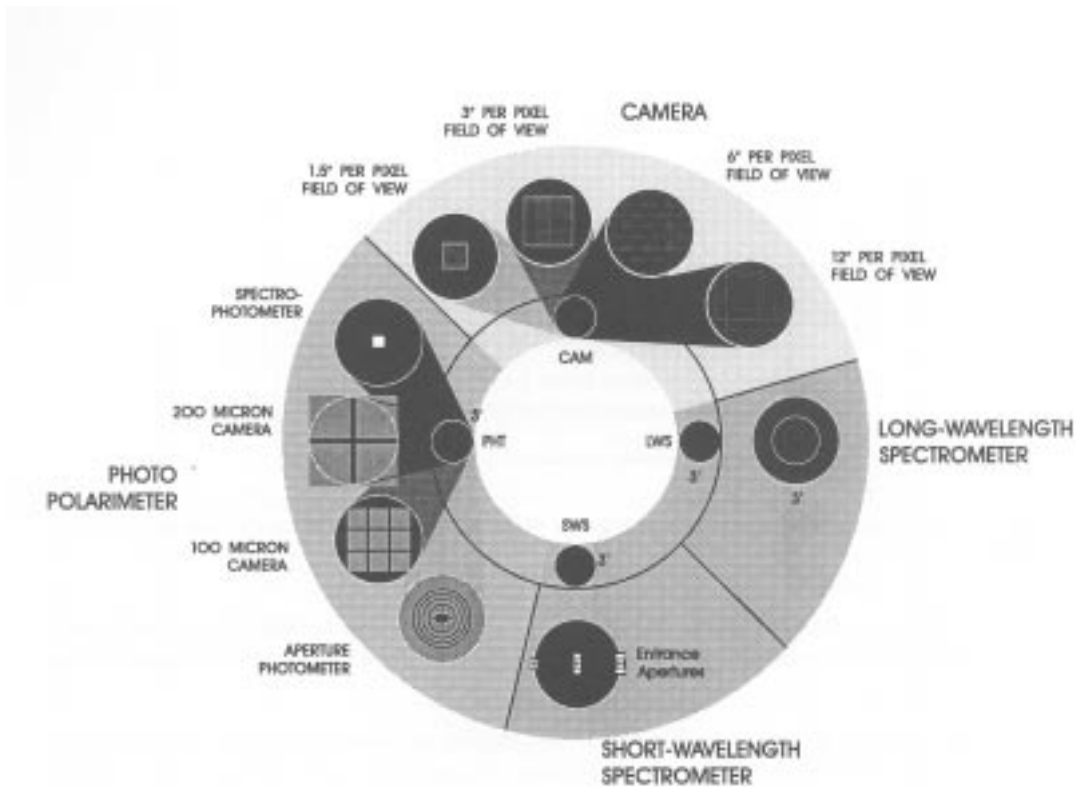


Figure 3.6: Focal plane map of all apertures of the four ISO instruments. Each of the four instruments had a $3'$ unvignetted field of view. LWS accepted the central $1.65'$ of its allocated field. The three possible SWS entrance apertures are shown. For CAM the four possible pixel fields of view (1.5 , 3 , 6 and $12''$) are plotted. The two larger fields of view extend into the vignetted region. For PHT the photometer and the spectrophotometer apertures are also shown. The $100\ \mu\text{m}$ camera filled the unvignetted field of view while the $200\ \mu\text{m}$ camera is somewhat larger. In the centre of the focal plane, not shown, is the Quadrant Star Sensor (QSS), used at the start of each revolution to determine any offset between the telescope boresight and the Star-Trackers.

3.3.3 Attitude and Orbit Control Subsystem (AOCS)

3.3.3.1 AOCS system components

The main elements of the AOCS are presented in Figure 3.7, which also shows the ISO spacecraft axes. The Quadrant Star Sensor (QSS) was aligned with the ISO telescope optical axis. The boresight of the QSS defined the x-axis of the ISO body coordinate system. The z-axis was defined by the Fine Sun Sensor (FSS), which provided control about the x-axis during pointings and about the x- and y-axis during slews. The Star-Tracker (STR), located outside the cryostat, provided two axis control about the y- and z-axis during pointings by the tracking of a single guide star. Slews were controlled by gyroscopes. The ISO attitude was constrained to limit heat input to the cryostat and straylight into the telescope. The Sun constraint was that the line of sight of the +x-axis must be within $90^\circ \pm 30^\circ$ of the Sun direction and the Sun vector must not be rotated by more than 5° around the x-axis from the +z half-plane of the satellite x-z plane. This was monitored by the FSS. The Earth constraint constrained the aspect angle

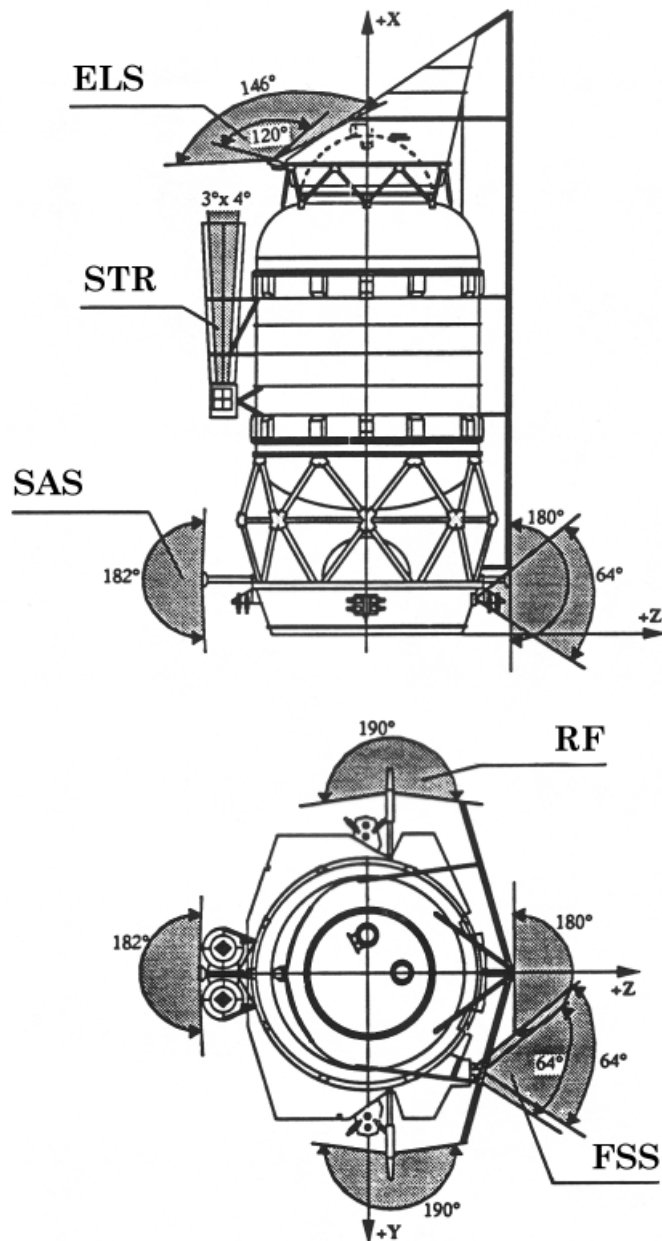


Figure 3.7: Schematic representation of the ISO spacecraft, locating the AOCS elements.

between the x-axis and the Earth in a non-linear manner. This was monitored by the Earth Limb Sensor (ELS). Other constraints were related to the Moon and Jupiter (see Section 4.1).

The AOCS elements were found to meet the specifications, summarised in Table 3.4. A more detailed description of the AOCS system can be found in Batten & Stephenson 1998, [9].

Table 3.4: *AOCS elements main specifications.*

Quadrant Star Sensor (QSS)	
Field of View	$4' \times 4'$
Sensitivity	$+7 > V_{mag} > +2$
Fine Sun Sensor (FSS)	
Field of View	$\pm 31^\circ$ about x- and y-axis
Accuracy about x-axis	$1'$
Accuracy about y-axis	$3'$
Noise Equivalent Angle	$2''$
Star-Tracker (STR)	
Field of View	$4^\circ \times 3^\circ$
Sensitivity	$+8 > V_{mag} > +2$
Bias error	$2''$ ($0.5''$ at f.o.v. centre)
Tracking speed	$5''/s$

3.3.3.2 AOCS operation

ISO was operated in a similar manner to a ground-based observatory, and therefore the spacecraft had to be able to manoeuvre smoothly from one celestial source to the next, and then maintain accurate pointing on that target. The spacecraft had also to be capable of pointing at any region of the sky that satisfied the straylight constraints. The slew speed between sights was set at $7^\circ/\text{min}$ in order to optimise observation time, and the duration of each observation ranged from a few seconds to up to 10 h, depending on the type of source.

The pointing requirements were satisfied by the spacecraft's Attitude and Orbit Control Subsystem (AOCS), in combination with careful spacecraft structural design, to avoid thermo-elastic deformation between the telescope's optical axis and the attitude sensors. Four operational pointing modes were defined:

- Fine pointing mode on a single point source
- Raster pointing mode, where the telescope axis was slewed through a rectangular pattern of pointings (up to 32×32 pointings)
- Solar System Objects tracking mode, implemented as a combination of one or more one-dimensional raster observations
- Calibration mode, in which any misalignment between the telescope and the spacecraft's attitude sensors was measured

For the high-accuracy pointing modes, the attitude errors were measured with gyroscopes, a Star-Tracker and the Fine Sun Sensors. In the calibration mode (activated nominally once per orbit), the Quadrant Star Sensor replaced the Star-Tracker.

A state-reconstructor in the AOCS computer produced minimum-variance estimates for the attitude, angular velocity and disturbance acceleration. This state-reconstructor also served as a sensor-data smoothing filter.

The control torques for high-performance slews and pointing modes were provided by a reaction-control wheel system, giving a maximum torque of 0.2Nm, with a total of 126 torque levels, and a maximum angular-momentum storage capability of some 18Nms. A so-called ‘dual control law’ was used together with a velocity controller that limited angular velocities to 8°/min. The ‘dual control law’ consisted of a non-linear time-optimal subcontroller and a linear state feedback subcontroller. For large errors during slewing, the time-optimal control prevails, whereas for fine pointing, the linear law predominates.

An important factor in achieving the requisite pointing accuracy for the ISO spacecraft was the limiting of the drift between the optical axis of the telescope and that of the Star-Tracker. Such drift can be induced by transient thermo-elastic deformations of structural elements linking the two optical axes. Consequently, the Star-Tracker support structure was mounted on the cryostat’s outer wall, rather than on the Service Module. This alone does not prevent local deformation due to temperature gradients in the cryo vacuum vessel from degrading pointing performance. It is also necessary to maintain a stable and uniform temperature distribution in these two structures.

This temperature stability was achieved by covering the cryo vacuum vessel with multi-layer insulation (MLI), even at the expense of a small penalty in the lifetime of the satellite. In addition, the Star-Tracker sensors (two for redundancy) were enclosed within a thermal housing, with heaters, which provided a constant sensor temperature and, even more importantly, maintained a constant temperature gradient between the mounting feet of the operational Star-Tracker (better than 0.1 °C over one orbit, except for 2 h around perigee). The specially stiffened fixing of the housing to the cryo vacuum vessel ensured that the thermal conductance between the two was less than 3mW/°C.

The in-orbit performance of the AOCS system and the final pointing accuracies are given in Section 5.4.1.

3.4 The Scientific Instruments

The scientific payload consisted of four instruments: a camera, ISOCAM; an imaging photo-polarimeter, ISOPHOT; a long wavelength spectrometer, LWS; and a short wavelength spectrometer, SWS. Each instrument was built by an international consortium of scientific institutes and industry, headed by a Principal Investigator, using national funding (see Section 2.3). Although developed separately, the four instruments were designed to form a complete, complementary and versatile common-user package. Table 3.5 summarizes the main characteristics of the instruments.

Only one instrument was operational in prime mode at a time. However, when the camera was not the main instrument, it was used in parallel mode to acquire extra astronomical data (Siebenmorgen et al. 1996, [151]). Whenever possible, the long-wavelength channel of the photometer was used during satellite slews. This serendipity mode (e.g. Stickel et al. 1999, [154]) led to a partial sky survey, covering approximately 15% of the sky, at wavelengths around 200 μm , a spectral region not covered by the IRAS survey. After launch, a parallel/serendipity mode was added for the LWS (e.g. Clegg 1999, [27]), in which narrow-band data were obtained at 10 fixed wavelengths in parallel with the main instrument and also during slews.

With ISO, photometry was possible in broad and narrow spectral bands across its entire wavelength range of 2.5 to around 240 μm . A variety of apertures, ranging from 5 to 180", was selectable out to 120 μm . For spectroscopy, resolving powers ranging from 50 to 30000 were available. ISO was capable of direct imaging in broad and narrow spectral bands across the complete wavelength range at spatial resolutions ranging from 1.5" (at the shortest wavelengths) to 90" (at the longer wavelengths). In addition, mapping could be carried out using sequences of pointings.

Each of the four instruments had a number of possible operating modes. To simplify the definition of an observation and to allow users to specify their observation in terms familiar to them, a set of

Table 3.5: *Main characteristics of the ISO instruments.*

Instrument (Principal Investigator)	Wavelength Range and Main Funct.	Outline Description	Spectral Resolution	Spatial Resolution
ISOCAM (C. Cesarsky, CEA-Saclay, F)	2.5–17 μm Camera and polarimeter	(i) 32×32 array for 2.5–5 μm (ii) 32×32 array for 4.5–17 μm	(i) 11 filters $2 \leq R \leq 20$ circ. var. filt. $R \sim 40$ (ii) 10 filt. $2 \leq R \leq 14$ circ. var. filt. $R \sim 40$	Choice of 1.5, 3, 6 or 12'' per pix.
ISOPHOT (D. Lemke, MPI für Astronomie Heidelberg, D)	2.5–240 μm Imaging photo- polarimeter	(i) Multi-aperture, multi-band photo-polarimeter (3–120 μm) (ii) Far-infrared camera 50–120 μm : 3×3 pix. 90–240 μm : 2×2 pix. (iii) Spectrophotometer (2.5–12 μm)	(i) 14 filters $2 \leq R \leq 15$ (ii) 6 filters $1 \leq R \leq 3$ 5 filters $2 \leq R \leq 3$ (iii) grating, $R \sim 90$	(i) Choice of diffraction- limited to 3' apertures (ii) 43'' per pix. 89'' per pix. (iii) 24'' \times 24'' aperture
ISO-SWS (Th. de Graauw, Lab. for Space Research, Groningen, NL)	2.38–45.2 μm Short wavel. spectrometer	(i) Two gratings 2.38–45.2 μm (ii) Two Fabry-Pérot interferometers 11.4–44.5 μm	(i) $R \sim 1000$ –2000 (ii) $R \sim 3 \times 10^4$	(i) 14'' \times 20'', 14'' \times 27'' 20'' \times 27'', and 20'' \times 33'' (ii) 10'' \times 39'', and 17'' \times 40''
ISO-LWS (P. Clegg, Queen Mary and Westfield College, London, UK)	43–196.7 μm Long wavel. spectrometer	(i) Grating (ii) Two Fabry-Pérot interferometers	(i) $R \sim 200$ (ii) $R \sim 10^4$	1.65' diameter aperture

astronomically-useful operating modes was defined and presented to users as a set of ‘Astronomical Observation Templates’ (AOTs). Each AOT was designed to carry out a specific type of astronomical observation. The observations resulting from the use of these AOTs are the basic building blocks of the ISO Data Archive. Note, however, that the AOTs consist of lower level structure, e.g. source, background, internal calibrator, dark current, etc. measurements. Further information on the individual AOTs, including engineering and calibration AOTs, is given in the following instrument specific subsections, where we give a short, compact high-level summary description of the 4 scientific instruments (CAM, LWS, PHT, SWS) on board ISO. More detailed instrument descriptions are given in volumes II to V of this Handbook.

3.4.1 The ISO Camera: ISOCAM

The ISOCAM instrument (Cesarsky et al. 1996, [16]; Cesarsky 1999, [17]) consisted of two optical channels, used one at a time, each with a 32×32 element detector array. These arrays operated, respectively, in the wavelength ranges 2.5–5.5 μm and 4–17 μm . The short wavelength (SW) array used an InSb detector with a Charge Injection Device (CID) readout and the long wavelength (LW) detector was made of Si:Ga with a direct readout. A selection wheel carried Fabry mirrors which directed the light beam of the ISO telescope towards one or other of the detectors; this wheel also carried an internal calibration source for flat-fielding purposes. Each channel contained two further selection wheels: one carried various filters (10–13 fixed and 1 or 2 Circular Variable Filters (CVF), with a resolution of ~ 45) and the other one carried lenses for choosing a pixel field of view of 1.5, 3, 6, or 12''. Polarizers were mounted on an entrance wheel — common to both channels — which also had a hole and a shutter. Figure 3.8 shows a schematic representation of ISOCAM.

ISOCAM observations were taken in four main modes. These are designated as CAM01 (General obser-

vation), CAM03 (Beam switching), CAM04 (Spectrophotometry) and CAM05 (Polarisation).

- CAM01 was dedicated to photometric imaging in one of the two channels, using one or more pixel field of views at one or more wavelengths. Observations could be made in the bandpass filters as well as at individual CVF positions. Use of the spacecraft's raster pointing capabilities gave the possibilities not only of mapping areas larger than the camera's field of view, but also of improving the flat-field accuracy. Micro-scanning techniques were employed to increase the redundancy and, thereby, improve detection limits and photometric accuracy.
- CAM03 was also dedicated to photometry and used a beam switching mode. An on-source measurement was made followed by a background measurement on a nearby empty reference field. The use of up to 4 different reference fields was possible.
- CAM04 allowed spectral imaging. The spectrum was observed by obtaining a series of spectral points. A complete CVF spectrum took at most 115 steps in the short wavelength channel and 85 steps for each of the two long wavelength CVFs.
- CAM05 allowed polarisation maps to be obtained by taking successive images through the three polarisers. (Operationally, it was implemented in a slightly different manner to the above AOTs).
- CAM60, CAM61, CAM62, CAM63: Engineering Data
- CAM99: Non-standard data, mainly used for special calibration purposes

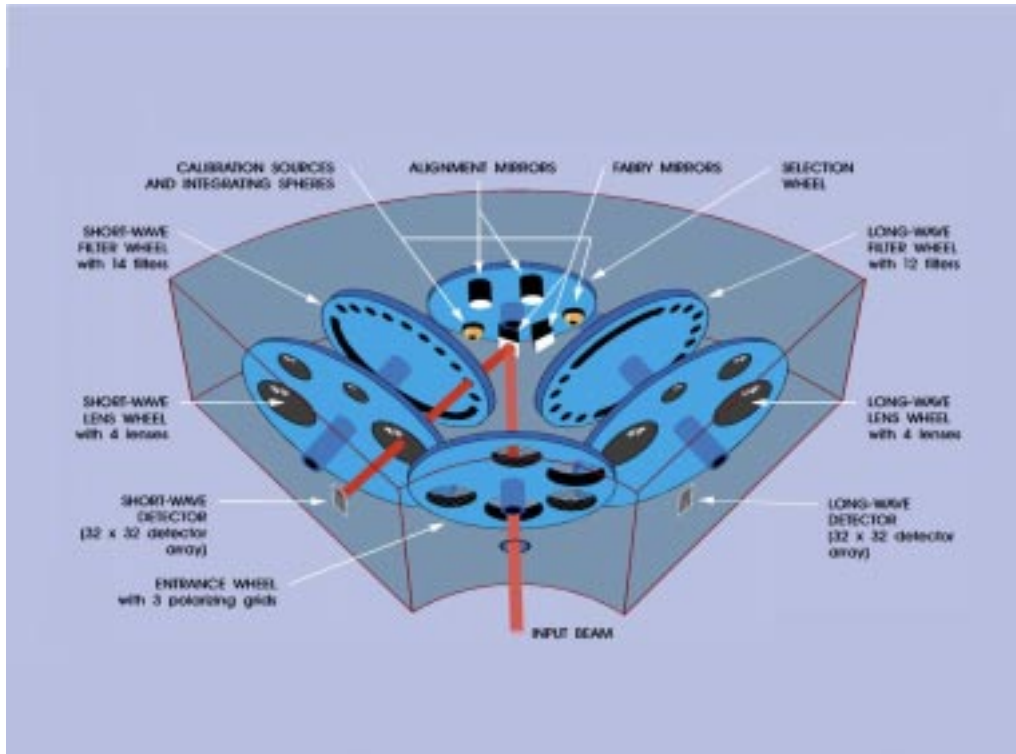


Figure 3.8: *Schematic of the Camera (ISOCAM).*

In orbit, the instrument behaved extremely well. Its sensitivity was as good (LW detector) or better (SW detector) than predicted from ground-based tests. In particular, ISOCAM was able to detect faint point

and extended sources through long observations. At $15\ \mu\text{m}$, good detections at the level of a few tens of μJy have been made. The broken readout cable for column 24 of the LW array found during pre-launch test, continued to render column 24 unreadable during operations (i.e., the detector was still active but no data were available). In common with the other instruments, ISOCAM experienced transients and glitches (see Sections 5.6.2 and 5.6.1); these have been tackled with increasingly sophisticated methods and ever-growing success. Work on minimising the effects of transients and glitches continues as do efforts relating to removing ghosts from CVF images and for detecting faint sources close to bright ones. The overall absolute calibration is better than 20% in practice with repeatability better than a few per cent. It is worth noting that a few camera settings have been used much more extensively than the rest, in particular the LW2 (around $7\ \mu\text{m}$) and LW3 (around $15\ \mu\text{m}$) filters, which became *the* ISOCAM colours, used with the $6''$ pixel field of view so as to take advantage of the whole field of view offered by the ISO satellite.

More details about ISOCAM are given in *The ISO Handbook, Volume II: CAM – The ISO Camera*, [11].

3.4.2 The ISO Long Wavelength Spectrometer: LWS

The LWS (Clegg et al. 1996, [26]; Clegg 1999 [27]) covered the wavelength range $43\text{--}196.7\ \mu\text{m}$ with a spectral resolving power of ~ 200 . Using also the Fabry-Pérot (FP) etalons, the resolution could be increased to around 10000.

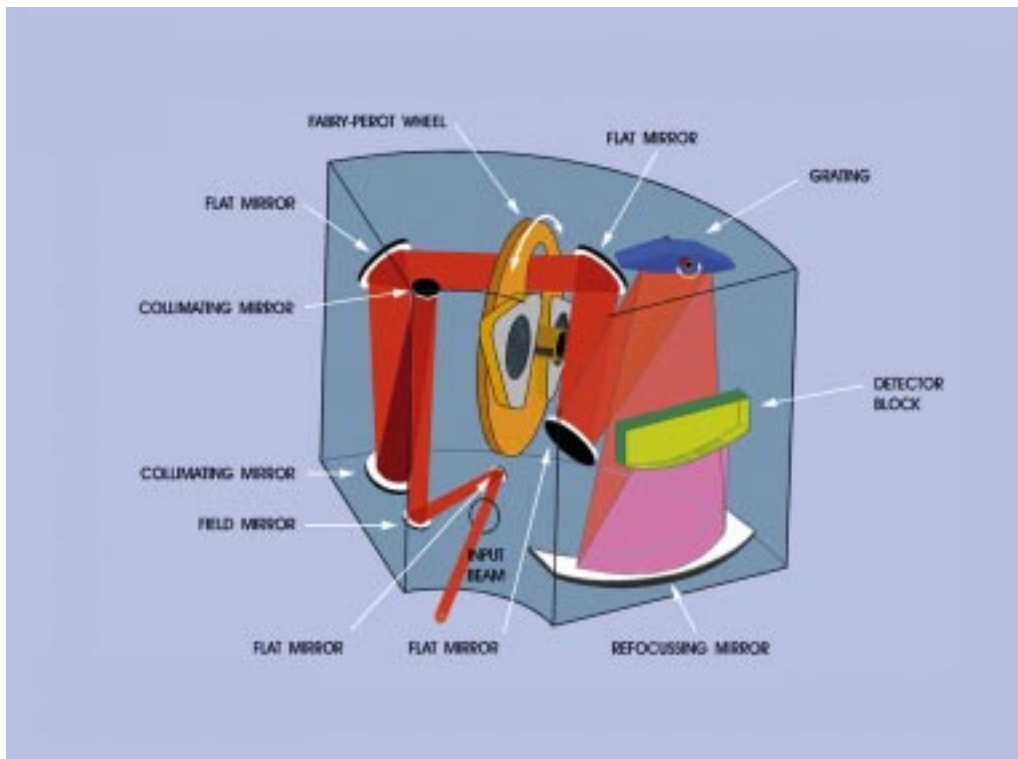


Figure 3.9: *Schematic of the Long Wavelength Spectrometer (LWS).*

The LWS instrument consisted essentially of a reflection diffraction grating, two FP etalons and an array of 10 discrete detectors. The grating was ruled with 7.9 lines per millimetre at a blaze angle of 30° on a rotationally-symmetric Schmidt profile. It was used in second order for the wavelength range $43\text{--}94.6\ \mu\text{m}$ and in first order for the wavelength range $94.6\text{--}196.9\ \mu\text{m}$. The FP subsystem, which was situated

in the collimated part of the beam, consisted of a wheel carrying two FP interferometers. The wheel could be set in any of four positions: in one of these, the beam passed straight through the subsystem whilst in another, the beam was completely obscured. In the remaining two positions, one or other FP was placed in the beam and modulated it spectrally. The two FPs covered the wavelength ranges 47–70 μm and 70–196.6 μm respectively. The instrument contained ten detectors made of Ge:Be and Ge:Ga (stressed and unstressed) material and read out by integrating amplifiers: five of these detectors covered the short-wavelength range $\sim 43\text{--}90\ \mu\text{m}$ in nominally 10 μm -wide channels while the others covered the long-wavelength range $\sim 90\text{--}197\ \mu\text{m}$ in nominally 20 μm -wide channels. Five internal illuminators were used to monitor and calibrate the stability of response of the detectors. The single fixed LWS circular field of view was designed to match the diffraction limit of the telescope at 118 μm (i.e. 100'') and was a compromise for the wavelength range of the instrument. In practice, the beam was somewhat narrower than this. Figure 3.9 gives a schematic of the LWS instrument.

LWS observations were taken in four main modes. Two involved use of the grating only: LWS01 (Grating range scan) and LWS02 (Grating line scan); while the other two also used the FPs: LWS03 (FP wavelength range) and LWS04 (FP line spectrum). Observers had to add background observations separately.

- LWS01 took a spectrum over a user-specified range of wavelengths up to the full LWS range. The spectrum could be sampled at 1, 1/2, 1/4 or 1/8 of a resolution element. The spacecraft raster mode could also be used.
- LWS02 took a spectrum around a number (up to 10) of user-specified wavelengths. The user specified the number of resolution elements around each line. An alternative use of this mode was ‘narrow-band photometry’, where the grating was stationary and spectro-photometry was obtained at 10 fixed wavelengths in the LWS range. The spacecraft raster mode could also be used.
- LWS03 took a high-resolution spectrum over a user-specified range of wavelengths between 47.0 μm and 196.7 μm . The user specified the spectral sampling interval. The spacecraft raster mode could also be used.
- LWS04 took a high-resolution spectrum around a number (up to 10) of user-specified wavelengths between 47.0 μm and 196.7 μm . The user specified the spectral scan width and the sampling interval. The spacecraft raster mode could also be used.
- LWS22, LWS23, LWS70, LWS71, LWS72, LWS76: Engineering Data
- LWS99: Non-standard data, mainly used for special calibration purposes

In orbit, the LWS performed very well. The spectral resolution was as expected. The grating wavelength accuracy was $0.25\ \Delta\lambda$ with a long term stability of better than $0.5\ \Delta\lambda$. For both FPs, the wavelength accuracy was better than $0.5\ \Delta\lambda$. The flux calibration for the grating is better than 20%. The effects of charged particle impacts reduced the overall sensitivity of the instrument. Operationally, the biggest concern was the precautionary suspension of LWS use for a time while characteristics of the interchange wheel were further studied; upon resumption, no restrictions were needed on scientific use of the instrument.

More details about LWS are given in *The ISO Handbook, Volume III: LWS – The Long Wavelength Spectrometer*, [68].

3.4.3 The ISO Imaging Photo-Polarimeter: ISOPHOT

The ISOPHOT instrument (Lemke et al. 1996, [110]; Lemke & Klaas 1999, [111]) consisted of three subsystems:

- ISOPHOT-C: two photometric far-infrared cameras, used one at a time, for the wavelength range 50–240 μm . The ‘C100’ camera contained a 3×3 array of Ge:Ga detectors, each with a pixel field of

view of $43.5''$, and 6 filters covering wavelengths up to $105\ \mu\text{m}$. The 'C200' camera used a 2×2 array of stressed Ge:Ga detectors with a pixel field of view of $89''$ and had 5 filters covering wavelengths longwards of $100\ \mu\text{m}$.

- ISOPHOT-P: a multi-band, multi-aperture photo-polarimeter for the wavelength range $3\text{--}110\ \mu\text{m}$. It contained 13 apertures ranging in size from $5''$ to $180''$ and 14 different filters. It had three single detectors, used one at a time, made of Si:Ga, Si:B and Ge:Ga.
- ISOPHOT-S: a dual grating spectrophotometer which provided a resolving power of ~ 90 in two wavelength bands simultaneously ($2.5\text{--}5\ \mu\text{m}$ and $6\text{--}12\ \mu\text{m}$). It contained two 64-element Si:Ga detector arrays with a square entrance aperture of $24'' \times 24''$.

A focal plane chopper with a selectable beam throw of up to $3'$ was also included in ISOPHOT. Selection between the different modes of the various sub-systems was achieved with appropriate settings of three ratchet wheels. Two redundant sets of thermal radiation sources (fine calibration sources, FCSs) were located symmetrically about the centre of the ISOPHOT field of view and were used for calibration and to monitor the time evolution of detector responsivity. Figure 3.10 shows a schematic representation of ISOPHOT.

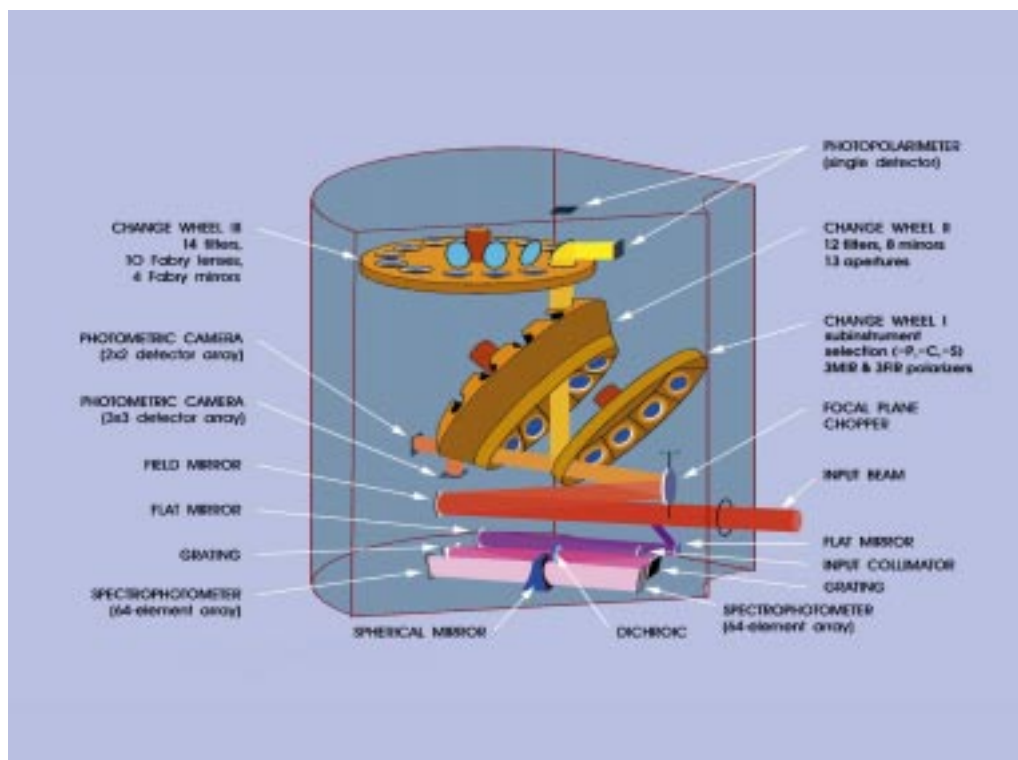


Figure 3.10: *Schematic of the Photo-polarimeter (ISOPHOT).*

ISOPHOT had 11 operating modes, grouped into 4 categories, plus non-standard and engineering modes.

- Photometry: Single pointing and Staring Raster Modes
 - PHT03: Standard mode for multi-filter photometry using ISOPHOT-P detectors. An arbitrary number (up to 14) of filters could be selected plus one aperture per filter. Used in stare, raster or chop modes, the production of maps and scans was possible.

- PHT22: Analogue of PHT-03 for long-wavelength photometry using ISOPHOT-C detectors. Up to 11 filters could be selected; no aperture selection was needed as the field of view was defined by the detector arrays. Used in stare, raster or chop modes, the production of maps and scans was possible.
- PHT05: Absolute photometry using the ISOPHOT-P detectors. Absolute flux calibration was achieved by long internal fine calibration source measurements and the possibility to perform zero level measurements at the time of the sky measurement. The user selected one filter and one aperture.
- PHT25: Absolute photometry using the ISOPHOT-C detectors, i.e. a long wavelength analogue of PHT05. No aperture selection was needed as the field of view was defined by the detector arrays.
- PHT04: Multi-aperture photometry using the ISOPHOT-P detectors. Only one filter could be selected and the minimum number of apertures was 2. Also used in chop mode.
- Photometry: Scanning/Mapping Modes
 - PHT32: Multi-filter mapping using the ISOPHOT-C detector arrays. Designed for high spatial resolution by over-sampling.
 - PHT17/18/19: Sparse mapping with the ISOPHOT-P detectors. A sequence was measured of up to 30 positions, which could be irregularly distributed on the sky within a field of radius 1.5° . The sequence had to start with a PHT17 measurement and end with a PHT19 one; intervening positions used PHT18.
 - PHT37/38/39: Sparse mapping with the ISOPHOT-C detectors, i.e. a long wavelength analogue of PHT17/18/19. No aperture selection was needed as the field of view was defined by the detector arrays.
- Spectrophotometry
 - PHT40: Spectrophotometry simultaneously at wavelengths $2.5\text{--}5\ \mu\text{m}$ and $6\text{--}12\ \mu\text{m}$ using the ISOPHOT-S detector arrays. Staring or chopped observations could be performed.
- Polarimetry
 - PHT50: Polarimetry using the ISOPHOT-P2 detector at $25\ \mu\text{m}$. The target was observed at $25\ \mu\text{m}$ with one aperture ($79''$) through the three different polarisers.
 - PHT51: Polarimetry using the ISOPHOT-C200 detector array at $170\ \mu\text{m}$, i.e. a long wavelength analogue of PHT50.

(Operationally, PHT50/51 were implemented in a different manner to the other modes).
- PHT77: Data taken by the ISOPHOT Serendipity Survey.
- PHT80, PHT81, PHT82, PHT83: Engineering Data with instrument activation sequence and responsivity checks of each detector after curing.
- PHT84: Engineering Data with de-activation sequence, including the PHT-S responsivity check at the end of the science window.
- PHT99: Non-standard data, mainly used for special calibration purposes

In orbit, ISOPHOT worked well; however, establishment of its detection limits and detailed calibration proceeded more slowly than was first expected. This was due to the complexity of the instrument with its many operating modes needing a very detailed stepwise approach with many pieces having to be completed and interlinked. Additionally, the complexity of the sky at far infrared wavelengths made it necessary to develop new dedicated observing strategies. Some of the detectors had reduced sensitivity in flight as compared to pre-launch estimates.

More details are given in *The ISO Handbook, Volume IV: PHT – The Imaging Photo-Polarimeter*, [107].

3.4.4 The ISO Short Wavelength Spectrometer: SWS

The SWS (de Graauw et al. 1996, [62]; de Graauw 1999, [63]) covered the wavelength range 2.38–45.2 μm with a spectral resolving power of the order of 1000–2500. Using also the Fabry-Pérot (FP) etalons, the resolution could be increased to more than 25 000 for the wavelength range 11.4–44.5 μm .

The SWS instrument consisted of two nearly independent grating spectrometers plus two scanning Fabry-Pérot filters. The short wavelength section (SW) used a 100-lines/mm grating in the first four orders covering the range 2.3–12.0 μm . The long wavelength (LW) section had a 30-lines/mm grating in the first two orders covering the range 11–45 μm . The two FPs were at the output of the LW section and used the first three orders of the LW grating. The SWS had three apertures and a shutter system. This allowed use of one of them while keeping the other two closed. For astronomical observations, the spacecraft pointing had to be adjusted to have the target imaged onto the selected aperture. Each aperture was used for two wavelength ranges, one of the SW section and one of the LW section. This was achieved by using ‘reststrahlen’ crystal filters as wavelength-selective beam splitters behind the apertures. The transmitted beams entered the SW section; the reflected beams entered the LW section. The actual spectrometer slits were located behind the beam splitting crystals. Interference filters or crystal filters took care of further order sorting. Depending on wavelength, the aperture sizes for the grating sections ranged from 14" \times 20" to 20" \times 33". Each grating had its own scanner, allowing the use of both grating sections (SW and LW) at the same time, although the observed wavelength ranges were linked. The output of each of the two grating sections was re-imaged onto two small (1 \times 12) detector arrays, located in-line. The materials used for the grating detectors were InSb, Si:Ga, Si:As and Ge:Be, while the FPs used 1 \times 2 elements of Si:Sb and Ge:Be. Figure 3.11 gives a schematic of the SWS instrument.

SWS observations were taken in four main modes. Three involved use of the gratings only: SWS01 (Full grating scan), SWS02 (Grating line profile scan), SWS06 (Grating wavelength range scan); while the fourth used also the FPs: SWS07 (FP line scan). These modes did not include use of the spacecraft raster mode; maps had to be made by concatenating individual pointings (see Section 4.5).

- SWS01 provided a low-resolution full-wavelength grating scan. Different scan speeds (1, 2, 3, 4) could be selected by the user corresponding to resolving powers of the order of 400, 400, 800 and 1600, respectively.
- SWS02 had a scanning scheme optimised to obtain grating scans of individual spectral lines. The user could specify up to 64 different lines in a single observation.
- SWS06 was designed to observe arbitrary wavelength intervals at full resolution. The user could specify up to 64 different ranges in a single observation.
- SWS07 was used for the FP observations. The LW grating section was used as the order sorter and was kept in tune with the FP wavelength to minimise leakage from the adjacent FP orders.
- SWS90, SWS91, SWS92, SWS93, SWS94, SWS95, SWS96, SWS97, SWS98: Engineering Data
- SWS99: Non-standard data, mainly used for special calibration purposes

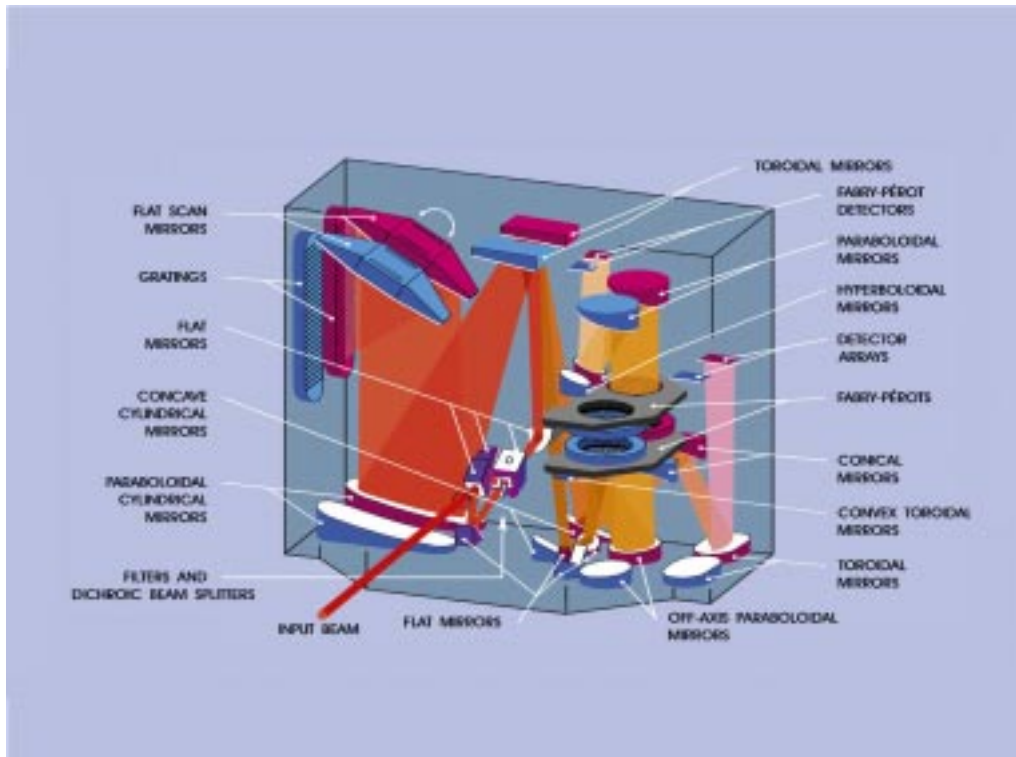


Figure 3.11: *Schematic of the Short Wavelength Spectrometer (SWS).*

In orbit, the instrument behaved extremely well. The performance was in all aspects as expected except for the detector sensitivity where the noise was dominated by effects from particle radiation — initial estimates of the loss in sensitivity were up to a factor of 5. Further analysis of the instrument behaviour is now allowing recovery of some of the loss. The pre-launch goal of a 30% absolute flux calibration accuracy was achieved with stability better than $\sim 5\%$ at the shorter wavelengths and $\sim 15\%$ at the longest. The wavelength calibration (goal: $1/10$ of a resolution element) was $1/8$ (long wavelengths) and $1/16$ (short wavelengths).

More details about SWS are given in *The ISO Handbook, Volume V: SWS – The Short Wavelength Spectrometer*, [108].

Chapter 4

ISO Operations

4.1 The ISO Orbit

ISO's operational orbit had a period of just under 24 hours, an apogee height of 70 600 km and a perigee height of 1000 km (see Figure 4.1). The lower parts of this orbit were inside the Earth's Van Allen belts of trapped electrons and protons. Inside these regions, ISO's scientific detectors were virtually unusable due to effects caused by radiation impacts.

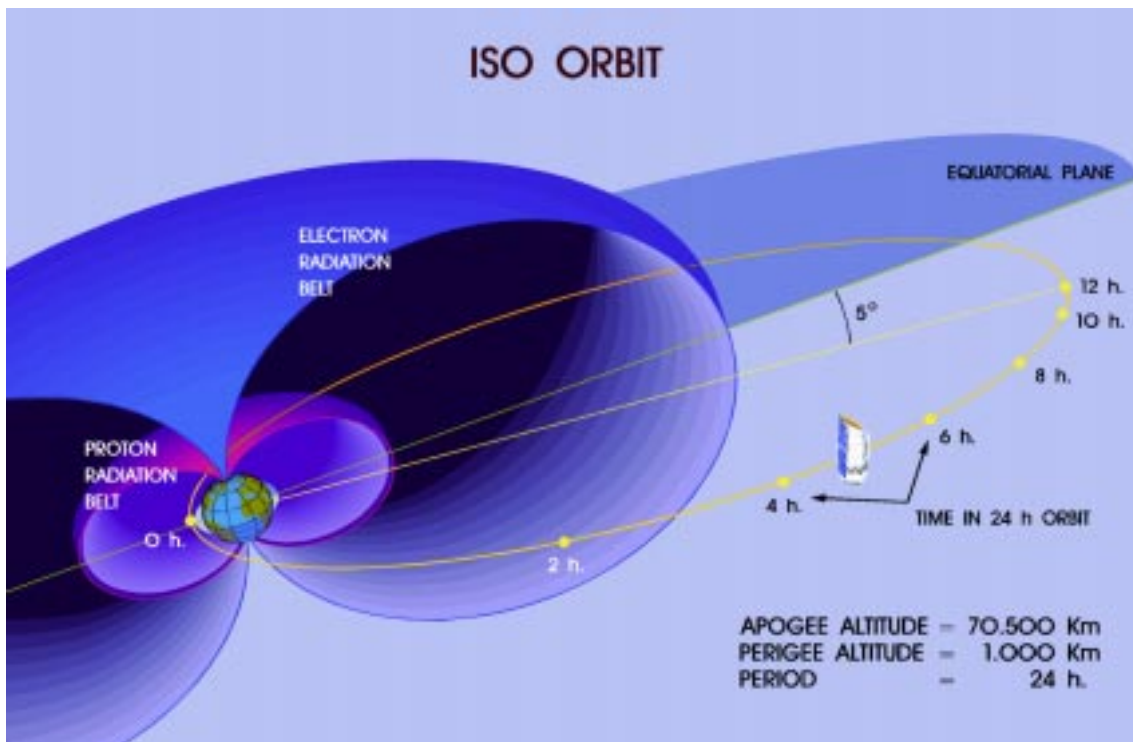


Figure 4.1: *The ISO orbit.*

4.1.1 Orbit phases

The 24 hours satellite orbit can be broken down into six phases:

1. Acquisition-of-Signal (AOS) by VILSPA and satellite activation
2. Operations during the VILSPA science window
3. Handover to Goldstone
4. Operations during the Goldstone science window
5. De-activation and Loss-of-Signal (LOS) at Goldstone
6. Perigee passage

After perigee passage VILSPA re-acquired communications with ISO. There was an activation phase, not usable for scientific activities, when the spacecraft was re-configured, all instruments were switched on and any necessary detector curing took place. These activities continued until the VILSPA science window opened, approximately four hours after perigee. This occurred when ISO was outside the radiation belts and the instruments could operate normally without being affected by the particles in the radiation belts. Normal operations, including scientific observations, then occurred for approximately the next nine hours. Before ISO dropped below the VILSPA horizon, communications were handed over to Goldstone. During this time, lasting a minimum of 15 minutes, instrument re-curing took place, e.g. for ISOPHOT. Because observations could not be performed during this handover period the maximum length of an observation was limited to one of the two periods of normal science operations. While the length of these varied (such that the sum remained the same), generally the VILSPA science window was the longer. Normal observing was then continued from Goldstone.

Finally, as ISO neared the radiation belts approximately twenty hours after perigee, observations ended, the instruments were de-activated and the satellite was configured for perigee passage. Goldstone then lost the spacecraft's signal as it approached perigee.

At the beginning and end of revolutions, the spacecraft was outside the control of the normal pointing system even though scientific data were routinely still being collected. Instead, a number of procedures were used grouped under the name of Programmable Pointing Mode (PPM) intended to avoid violation of Sun and Earth constraints. The PPM ensured that the spacecraft's attitude was maintained with sufficient accuracy for observations to be resumed without need for further calibration.

Prior to launch, assumptions were made as to the detrimental effects on instrument sensitivity of impacts from high energy particles and how these effects would vary with position on the orbit. These models and calculations led to definition of a cut-off altitude of 43 000 km, corresponding to a daily science window of 16 hours. During PV phase however, it became apparent that scientifically useful observations could continue longer than expected. Therefore the science window was extended by 40 minutes from revolution 66 onwards (i.e. approximately 3/4 of the way through PV). It was later found that LWS observations carried out late in the science window were affected by charged particles, the extent of the effect depending on the season. Therefore from revolution 204 onwards the LWS switch-off was rolled back 60 minutes.

4.1.2 Pointing constraints

For thermal (protecting the spacecraft from sunlight) and power (illuminating the solar arrays) reasons and also to prevent straylight from reaching the instruments, there were constraints on the allowed pointing directions for the satellite. ISO always pointed only in a direction between 60° and 120° away from the Sun. Additionally, it was neither pointed closer than 77° to the Earth limb, nor closer than

24° to the Moon. Jupiter was usually kept away from the optical axis by at least 7° unless, of course, Jupiter or one of its moons was the target of an observation. The sum of these constraints meant that, typically, only some 10–15% of the sky was available to ISO at any instant (see Figure 4.2).

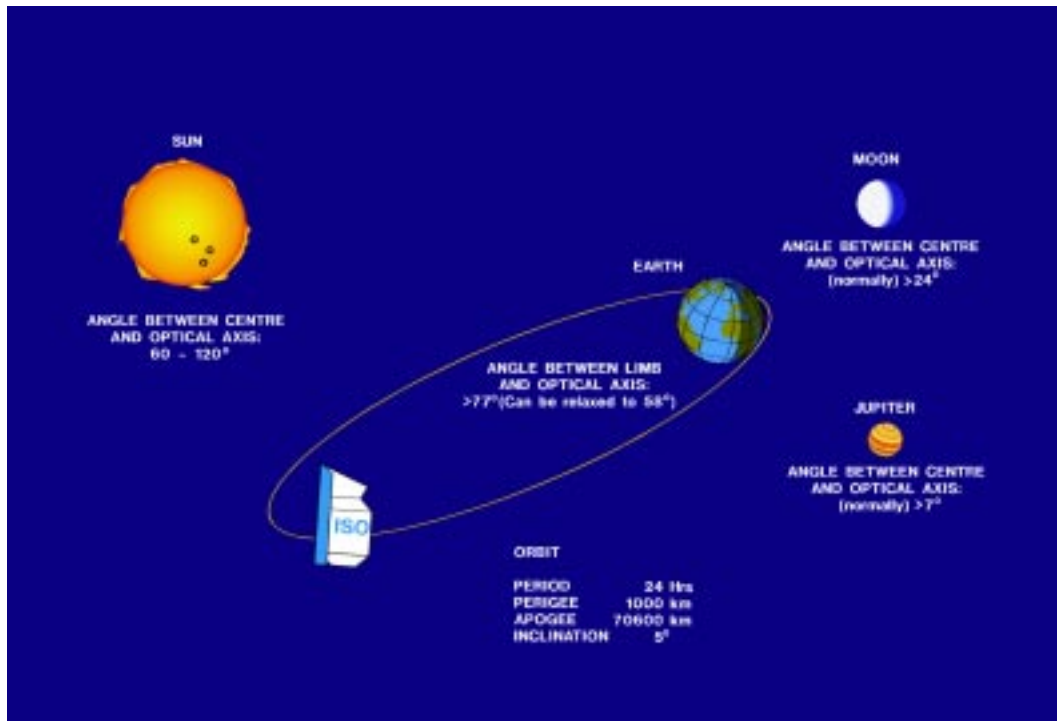


Figure 4.2: *Visibility constraints of ISO.*

The orbit also precessed rather slowly. Thus, in the nominal 18-month long mission, there would have been an area of sky, centred on the Taurus-Orion region, inaccessible to ISO. Happily, the cryogen lasted longer than specified and almost all the sky was visible to ISO at some time during the mission.

4.2 The Ground Segment

The limited lifetime of ISO, the severe sky coverage constraints, the complexity of the scientific instruments, along with the necessity to make many short observations under ground station coverage (no on-board data or command storage for instrument operations was possible) dictated that all operations had to be pre-scheduled in order to maximize the time spent acquiring useful astronomical data. Thus, ISO was operated in a service observing mode with each day's observations being planned in detail up to three weeks in advance.

This operational concept drove the design of the ground segment (Kessler et al. 1996, [95]; 1998, [96]), which consisted of the Spacecraft Control Centre (SCC) and the Science Operations Centre (SOC), both co-located at VILSPA, and two ground stations providing approximately 22 hours/day of real-time support.

The SCC team, within the Directorate of Technical and Operational Support (D/TOS), was responsible for conducting and controlling the flight operations of the spacecraft, including health and safety of the instruments. The SOC team, within the Directorate of Science (D/SCI) was responsible for all aspects of the scientific operations ranging from the issue of the 'Calls for Observing Proposals', through the

scheduling and use of the scientific instruments, to the pipeline data processing, and distribution of the data products. Additional teams, based mainly at the PI institutes, supported the off-line operations of the instruments.

4.2.1 Ground stations

Two ground stations were used to communicate with ISO, providing visibility of the satellite from the ground for the entire scientifically-useful part of the orbit over 16 hours per day. The primary at ESA's Villafranca Satellite Tracking Station (VILSPA, see Figure 4.3), located near Madrid, Spain, and the secondary at Goldstone, USA, provided by the National Aeronautics and Space Administration (NASA). The ISO Spacecraft Operations Center (SOC), based at VILSPA, controlled the satellite via one of the two stations, carrying out the operations in real-time. The orbit of ISO was arranged so that after perigee passage (when ISO was out of view of both ground stations for approximately 30 minutes) the first ground station to re-acquire the ISO signal was VILSPA. Additional resources, enabling ISO to be operated for a longer period per day, were supplied by the Institute of Space and Astronautical Science (ISAS), Japan.



Figure 4.3: *ESA's Villafranca Satellite Tracking Station in Spain (VILSPA).*

4.2.2 The Spacecraft Control Centre (SCC)

The SCC was led by the Spacecraft Operations Manager and, throughout the routine operations phase, there were 28.3 staff in post. Its main responsibility, as already mentioned, was conducting and controlling the flight operations of the spacecraft, including health and safety of the instruments.

After the end of the Launch and Early Orbit Phase (LEOP) — revolutions number 0 to 3 — the satellite control was transferred to VILSPA from the Operations Control Centre (OCC) at ESOC, Darmstadt; all subsequent operations were successfully supported from the SCC.

Starting from manual use of the Flight Operations Plan and associated procedures, operations were gracefully automated during the Commissioning Phase to use, by the end of this phase, a fully pre-programmed Central Command Schedule (CCS) reflecting the output of the Mission Planning Phase 1 (SOC) and the Mission Planning Phase 2 (SCC). This schedule contained all platform and payload commands. On average, some 10 000 commands had to be uplinked to the spacecraft every day. Therefore, only minimum operator intervention was required for spacecraft and instrument operations.

The CCS contained ‘dedicated windows’ during which either spacecraft or science operations could be scheduled. Additionally, ‘event designators’ and ‘keywords’ were defined that triggered certain command operations to be inserted in those windows, when required. A skeleton schedule for a revolution (orbit) is shown in Figure 4.4.

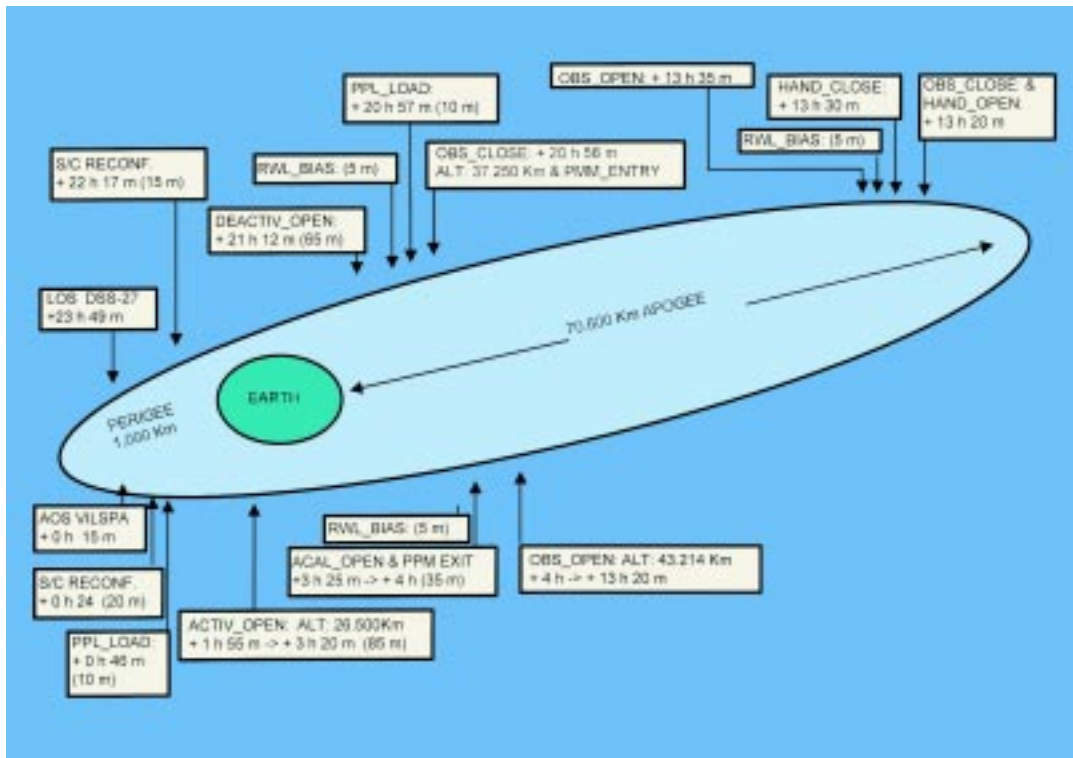


Figure 4.4: Skeleton schedule of ISO activities along an orbit, showing activities from acquisition of signal (AOS) at VILSPA to loss of signal (LOS) from the Goldstone DSS-27 antenna. Times are given in hours and minutes since perigee passage, and the duration of an activity is shown in brackets. Science observations started with the opening of the observation window (OBS_OPEN) about 4 h after perigee passage and continued — with a short break at the time of handover from VILSPA to Goldstone — until OBS_CLOSE nearly 21 h after perigee passage. The instruments were activated/de-activated during specific windows (ACTIV and DEACTIV), which also contained instrument calibration and trend analysis activities. PPL and PPM refer to a programmed pointing mode for autonomous pointings to an uplinked list of safe attitudes. During the ACAL window, various spacecraft attitude calibrations were carried out. Depending on the planned observing programme, the reaction wheels (RWL) had to be biased at various times during the day’s operations.

The baseline approach during routine operations was that all four instruments were activated and deactivated automatically by the schedule, irrespective of whether a particular instrument was scheduled for use in that orbit or not.

To optimise the time available for scientific observations, spacecraft operations and instrument activation/de-activation were placed along an orbit in such a way that they did not use science time (defined as the time the satellite spent outside the main parts of the Van Allen belts). Interleaved manual commanding was, in principle, only required to support ranging, ground station handover, and for a few specific operations of the AOCS. The schedule offered 'hold', 'resume' and 'shift' functions in order to recover from, and to minimise the impact of, spacecraft, instrument or ground segment anomalies. When required, recovery from problems was initiated following the relevant Flight Control Procedures (FCPs) and Contingency Recovery Procedures (CRPs) of the Flight Operations Plan. It is worth noting that approximately 1000 FCPs and 500 CRPs had been written and validated with platform simulator before launch.

During pre-launch testing, it was already realised that the command schedule was highly susceptible to ground segment problems because of the very high scientific instrument command rate. In the event of problems, e.g. when commands could not be verified due to loss of telemetry, the schedule was suspended. In the worst case, a short drop in telemetry could cause the loss of an entire scientific observation of several hours' duration.

Throughout the in-orbit operations, a wide variety of efforts were successfully undertaken by the SCC to prevent or minimise the loss of science. Major improvements included the implementation of an automatic telemetry link re-configuration on the ISO Dedicated Control System, which reduced the impact of telemetry drops considerably. The implementation of the Hipparcos/Tycho Guide Star Catalogue in the Flight Dynamics System (FDS) contributed greatly in solving the guide star acquisition problems encountered early in the mission. In a joint effort between the SOC and the SCC, a new observing mode was implemented for the Long Wavelength Spectrometer, enabling it to gather science data even when not scheduled as the 'prime' instrument.

Another improvement, which made a major contribution to the science output, was the reduction of satellite's absolute pointing error from 4'' during the Commissioning Phase to 1'' level in the Routine Phase, especially since the system specification was < 11.7'' (see Section 5.4.1).

The ISO Mission Control System (see Figure 4.5) performed all aspects connected with operations and safety of the spacecraft, including safety monitoring of the scientific instruments. The hardware of the control system consisted essentially of two VAX 4600 redundant Spacecraft Monitoring and Control computers (ISORT/ISODV), six associated Sun SPARC-20 workstations, associated spacecraft control software, and the mission planning system software as far as Mission Planning 2 was concerned. The system was designated as the ISO Dedicated Control System (IDCS). The FDS consisted of a set of five Sun workstations and dedicated software. These systems were networked on a partially-redundant OPSLAN to prevent single point failures and isolated the SCC from the outside world.

Two redundant micro-VAX 3100-76 computers formed the Operational Data Server system (ODS-1/2). The ODS constituted the interface between the spacecraft control system of the SCC and that of the SOC as far as science real-time data reception in the form of Telemetry Distribution Formats (TDFs) was concerned. The latter contained not only the telecommand history data, but also specially provided derived telemetry parameters. These parameters were used within the SOC for instrument monitoring and control purposes, using the Real-Time Technical Assessment (RTA) and Quick-Look Analysis (QLA) software, which ran on the four instrument workstations (one dedicated per instrument). The ODS was also the interface between the Mission Planning Phase 1 (MPP1) and the SOC and that of the SCC (MPP2) for interchanging mission planning files.

Furthermore, the ODS provided the short history archive of the science telemetry and archived TDFs onto optical disks for access from the SOC Science Data Processing system. The network interface provided the connectivity of the IDCS with the ground stations through the Integrated Switching System (ISS), as part of the OPSNET. Support functions were provided for: Spacecraft Performance Evaluation (SPEVAL), required to determine all aspects of spacecraft performance which could impact the life of the

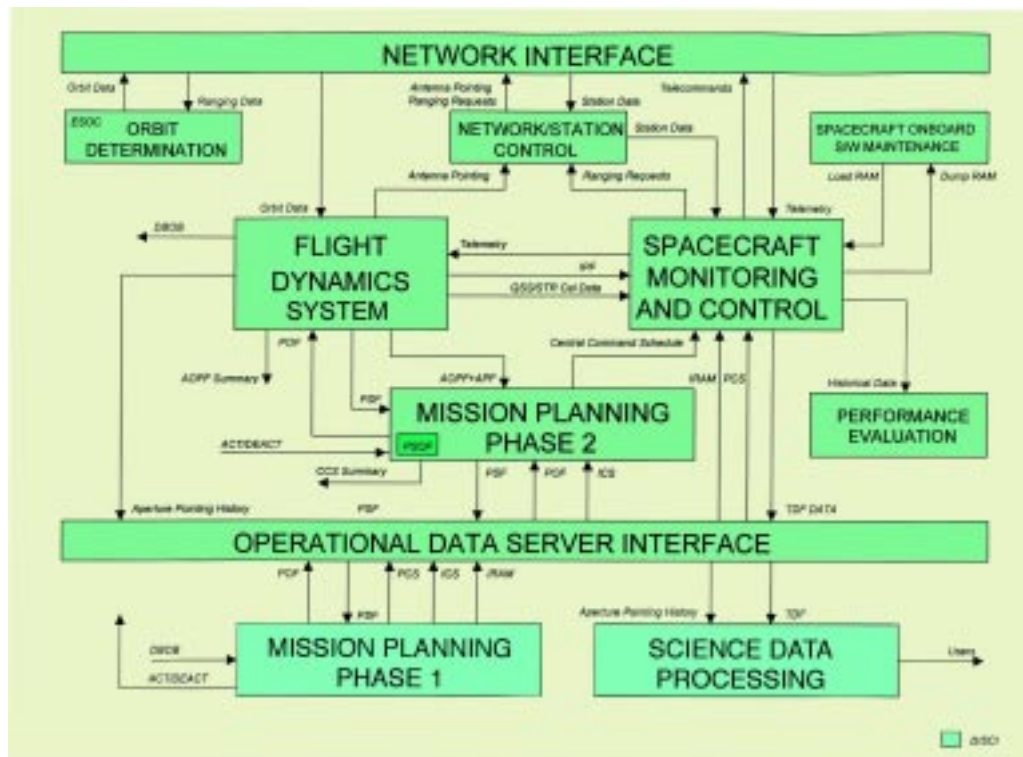


Figure 4.5: *The ISO Mission Control System.*

mission and mission efficiency; and spacecraft on-board software maintenance for the AOCS, STR and the OBDH. Communications Services were provided to support a variety of tasks, such as testing and validating procedures, AOCS and on-board software maintenance and validation, and spacecraft anomaly investigation.

One very significant achievement was the mission extension beyond September/October 1997. During this time, ISO's orbital geometry was such that it underwent eclipses of exceptionally long duration. Additionally, during early September, marginal violations of the Earth constraint on the pointing direction could not be avoided for some minutes each day as ISO went through perigee. Since the spacecraft was required to be operated beyond design specifications with respect to power, Sun and Earth constraints, it was necessary to develop and implement a new operations strategy, which deviated considerably from the well-proven Routine Phase operations concept. In addition to the above, there was a strong requirement from the scientific community to observe the Orion and Taurus regions of the sky, which became visible to ISO during this period for the first time in the mission.

During the period 7 September to 7 October 1997, when the eclipses reached a maximum of 166.5 minutes, i.e. more than twice as long as the baseline design of 80 minutes, the power of the two batteries had to be preserved by switching off non-essential units, by restricting scientific pointings to one observation during eclipse, and by restricting the use of the instruments to two out of four during the peak eclipse period. To ensure proper pointing stability in eclipse, a second 'roll star' was used by the Star Tracker. This star, some 2° away from the guide star, was used to control the gyro drift with respect to the satellite x-axis and hence the telescope boresight. At the same time, the Earth warning and forbidden regions had to be violated, since no constraint-free corridor was left around perigee. This was crucial for the AOCS and therefore for the telescope pointings around perigee. In order to reduce the impact of the penetration into the Earth-constraint region, the Sun constraint had to be relaxed.

of the next three months was made. This process was extremely time- and resource-consuming and never worked quite as expected since one was dealing with a ‘moving target’. In other words, the flexibility offered to the observers to optimise their observing programmes meant that the input changed faster than the plan. This flexibility was necessary and greatly enhanced the scientific return. However, extensive and complex manual work was required to enable ISO to execute successfully nearly 98% of the highest priority observations. Similar missions in the future should be able to generate a representative long term plan within a few days with minimal human intervention.

Next in the production line came the detailed planning of each day’s observations to the level of instrument commands at a granularity of 1 second of time. The goal here was to minimise slews and dead time, and generate efficient schedules while preserving the scientific content (i.e. carrying out the high priority observations). The system worked very successfully and produced schedules with an average efficiency of 92%, where efficiency is defined as the ratio of the time the satellite was accumulating scientific data to the available science time. In fact, the actual efficiency achieved can be considered to be even higher since nearly two-thirds of the time for slewing between targets was used to gather serendipitous data at previously-unsurveyed infrared wavelengths with the photometer, and since the camera and Long Wavelength Spectrometer collected data in parallel modes when the observer has specified use of another instrument. Part of the trick was to do ‘overbooking’. In other words, the mission database was filled up so that it always contained about twice as many observations as could be accommodated during the remaining ISO lifetime. In essence, short lower-grade observations were used to fill in gaps between high-grade ones.

The SOC monitored the instruments in real-time as the observations were executed automatically, and had the capability to intervene manually if necessary. There were few instrument anomalies; typical interventions were, for example, the ‘closing’ of the camera if a bright target entered its field of view. This was required to avoid saturation and its long-lasting effect on the detectors.

The final steps in the production line involved the off-line processing, quality control, archiving and finally the distribution of the data in CD-ROMs. From an operational point of view, the processing and archiving of the data worked flawlessly. Over 10 000 CD-ROMs were shipped to observers. The processing algorithms and calibration were initially far from perfect and, in fact, improvements will still continue for the coming years. However, within one year of launch, an ISO-dedicated issue of *Astronomy and Astrophysics* containing nearly 100 papers, had been published. Given the complexity of the instruments and in particular of the behaviour of the infrared detectors, this can be considered a significant achievement.

One of the major factors in the successful operation of ISO’s sophisticated instruments was the assignment to each of an ‘Instrument Dedicated Team’ (IDT) of experts at VILSPA. The teams’ responsibilities included: the overall maintenance of the instruments (including the real-time monitoring software and procedures); the calibration; and the design and much of the coding and testing of the data processing algorithms. Other experts, back at the Principal Investigator institutes, worked in close cooperation with the SOC’s Instrument Dedicated Teams. These teams were crucial in making instrument operations run smoothly by rapidly diagnosing and fixing anomalies, by optimising the observing modes and by getting the instruments properly calibrated.

Much of the necessary complexity of science operation was embedded in the over one million lines of code of the SOC software. More than 1 700 Software Problem Reports (SPRs) were responded to and over 250 System Change Requests and Extra Wishes (SCREWs) implemented in the course of the mission. This comes on top of the ~ 1000 SPRs and ~ 100 SCREWs implemented pre-launch, during and after the period of integration, tests and simulations. All of the SOC’s software maintenance team had been involved in the development of the SOC software before launch. Such breadth and depth of experience turned out to be a major factor in the success of ISO science operations.

The SOC benefited greatly from having all functions (e.g. from establishing observing programmes to data distribution; from system design to software maintenance) integrated into one centre as this streamlined interfaces and improved communications. For the same reasons, the co-location with the SCC was also very beneficial.

Another key factor was the extensive period of end-to-end tests and simulations through which the entire ground segment software and procedures were exercised prior to launch. Not only was this essential in uncovering bugs not found by lower level tests, but it also ensured that the whole SOC was fully trained and operational at launch. In particular, the full 58 days of the Performance Verification Phase had been scheduled and validated on the software simulator prior to launch. This permitted that, 2.5 months after launch exactly as planned, the Routine Phase could start with two-thirds of the observing modes fully commissioned and ready for use by the scientific community.

4.3 Observing with ISO

4.3.1 Observing strategy

ISO was operated in a pre-planned manner without any significant routine real-time interaction. Thus, all observations had to be specified in full detail by the proposers. For a variety of reasons including efficiency and sky coverage constraints, observing time was distributed on a ‘per observation’ basis as was the case e.g. for EXOSAT, and not on a ‘per shift’ basis as it is the case for many ground-based observatories and for IUE. However, for operational reasons, no guarantees could be given that a particular observation would be executed.

Individual observations (or concatenated chains) were the basic building blocks for the observational schedule, which was built in units of ‘revolutions’. A revolution was one rotation of ISO about the Earth; as ISO’s orbital period was close to 24 hours, a revolution was roughly equivalent to a day. In the schedule — and also in the ISO Data Archive — every observation is uniquely identified by an 8-digit number, called the TDT (for ‘Target Dedicated Time’) number. The first three characters identify the revolution on which it was executed, the middle 3 digits specify the sequence number of the observation in the timeline of this revolution and the last two are an identifying number given to that observation by the observer in the original proposal.

4.3.2 Guaranteed time and open time programmes

Approximately 45% of ISO’s time was reserved for those parties contributing to the development and operation of the scientific instruments and the overall facility, namely: the four Principal Investigators (PI) and their teams, who built the ISO instruments; the five Mission Scientists; the scientific staff of the SOC; and ESA’s international partners in the mission, NASA and ISAS. Definition and coordination of these guaranteed-time observations started some eight years before launch with the definition of the so-called ‘Central Programme’.

The requirement upon this programme was that it would be a ‘balanced and coherent programmeproviding a solid scientific core for the ISO observing programme’. Its publication intended to ‘give an overview of the observing potential of the observatory to enable the submission of top quality, complementary and feasible observing proposals leading to the maximum output of the observation programme’. The programme was unanimously endorsed by the ISO Observing Time Allocation Committee (OTAC).

The complete guaranteed time programme was presented in three paper documents, namely ‘ISO Guaranteed Time Programme Part A: Overview’, ‘ISO Guaranteed Time Programme Part B: Proposal Abstracts’ and ‘ISO Guaranteed Time Programme Part C: Catalogue of Observations’ in April 1994.

In addition to its scientific value, this early start was important both to help define observing modes and also to be able to publish worked examples to the community with the pre-launch call for proposals.

ISO — as an observatory — was open to the astronomical community including expert and non-expert users. Thus, the remaining more than half of ISO’s observing time was distributed to the general community via the traditional method of proposals and peer review. Open time proposers could apply to use any of the spacecraft and instrument modes. Guaranteed time holders were also allowed to apply for open time.

The observations in the guaranteed time programme were reserved and open time proposals were not allowed to duplicate any of these. Checks for duplications were made during the processing of proposals. Duplications were determined by consideration of the target observed, the observing mode used, details of the observation parameters (e.g. size of rasters, wavelength ranges, filters) and the scientific objective. Figure 4.7 shows the distribution of ISO observing time per participating group.

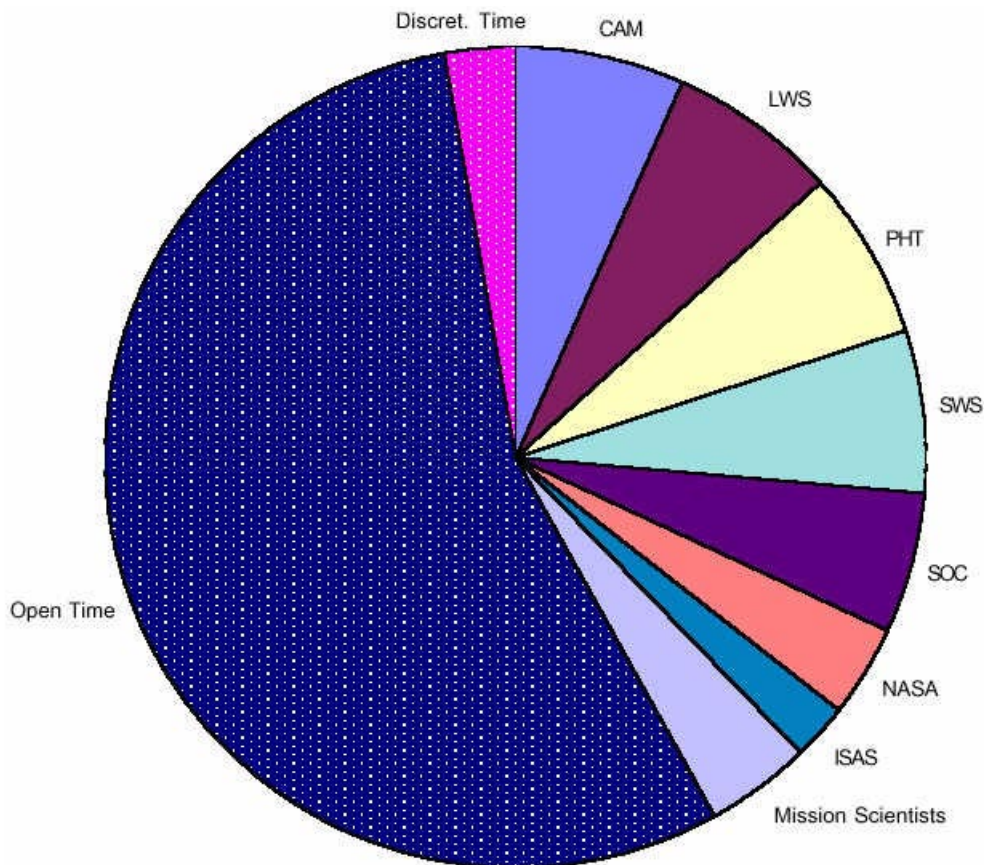


Figure 4.7: *Distribution of observing time per participating group.*

4.3.3 The ISO observing cycle

4.3.3.1 Calls for proposals

In order to distribute the available open time among the members of the astronomical community, one 'Call for Observing Proposals' was issued pre-launch (April 1994) and another 'Supplemental Call' post-launch (August 1996). Both calls, pre- and post-launch, were in principle open only to proposers in ESA member states, the USA and Japan. Over 1 500 proposals, requesting almost four times more observing time than available, were received in response to these calls. Some 40% of the proposals arrived in the last 24 hours before the deadlines.

Pre-launch call

The Pre-launch call solicited proposals for:

- 1) Observing Programmes
- 2) Target of Opportunity teams.

Responses to this call consisted of a Letter of Intent and a so-called ‘Phase 1’ proposal. The following schedule was established for the pre-launch Call:

Issue of Call: April 1994
 Letters of Intent: due 10 June 1994
 Phase 1 Proposals (electronic version): due 19 August 1994
 Phase 1 Proposals (paper version): due 23 August 1994
 OTAC review complete by end November 1994
 Start of Phase 2 data entry: December 1994
 End of Phase 2 data entry: mid-1995
 Launch of ISO: 19 September 1995 (finally, the launch took place on 17 November 1995)

Supplemental call

This supplemental call solicited proposals to be carried out in the period from December 1996 to the end of the mission (April 1998). Although completely new proposals were not excluded, priority was given to proposals aiming at continuing, completing and extending existing ISO observing programmes.

Responses to this call consisted of a ‘Phase 1’ proposal only.

The following schedule was established for the Supplemental Call:

Issue of Call - 5 August 1996
 Phase 1 Proposals (electronic version): due 7 October 1996
 Phase 1 Proposals (paper version): due 9 October 1996
 OTAC review complete by late November 1996
 Start of Phase 2 data entry: end November 1996
 End of Phase 2 data entry: end January 1996.

4.3.3.2 Proposal evaluation and selection

From the observers’ point of view the end-to-end observing process started with the preparation of the ‘Phase 1’ proposals and their submission both in electronic and paper version to the OTAC.

Following each of the two calls above mentioned, the ‘Phase 1’ open time proposals received were evaluated scientifically by an Observing Time Allocation Committee (OTAC) consisting of approximately 35 external scientists. This committee was appointed by the ESA Director of Science, following the recommendation of the Astronomy Working Group. It was headed by an overall Chairman and consisted of seven panels, one for each of the following scientific areas: Solar System, Interstellar Matter, Stellar Physics, Circumstellar Physics, Normal and Starburst Galaxies, Active Galaxies and Quasars, and Cosmology. Each panel consisted of a Panel Chairman and, depending on the scientific area, 3 or 4 members.

In parallel, the electronic versions were imported into a proposal database for statistical analysis and checking for, *inter alia*, duplication with the guaranteed observing programme and with each other, or the distribution on the sky of the requested observations in view of the uneven sky coverage of ISO. The scientific staff of the SOC made also an assessment of the technical feasibility of the proposed observations and sent the results to the OTAC.

After peer review, the ISO OTAC made recommendations on the observing programme to be carried out by ISO via assigning grades either to entire proposals or to individual observations.

The following items were taken into account during the review process:

- scientific case described in the abstract and justification,
- scientific merit and relevance of the proposed observation(s),
- technical feasibility of the observation(s),
- the necessary observing time, and
- oversubscription in particular parts of the sky.

The output of the OTAC review was a list of proposals/observations ranked by scientific merit. OTAC assigned a cut-off grade below which proposals and observations were not carried forward into Phase 2 for further processing.

However, for efficient timelining of observations, the scientific scheduling software needed to work from a pool of observations which significantly overfilled the time available. All these observations had to be fully specified in the database from which the mission planning system worked.

4.3.3.3 Proposal data entry

The Principal Investigators of proposals/observations with grades above the cut-off value (see previous section) moved on to the next phase of the process, the so-called ‘Phase 2’. Here they had to enter full details of their observations into the SOC’s databases. Checking of their inputs was done both by the ‘Proposal Generation Aids’ (PGA) and the ‘Proposal Handling’ (PH) modules.

Prior to launch, this typically involved a visit of around a week to the ‘ISO Proposal Data Entry Centre’, set up in ESTEC (for USA ISO observers, IPAC was designated by NASA as the support centre). The European centre at ESTEC was co-located with the Science Operations Centre during its development phase, prior to moving to Spain and it was operated by scientific and technical staff from the SOC, who assisted visitors in the entry of their data and who checked, as thoroughly as possible, that the observations were both feasible and optimised. It was only after completion of this Phase 2 data entry and checking process that the pre-launch feasibility of the observations was verified. Over 500 astronomers visited ESTEC in the first six months of 1995 and were assisted by resident astronomers and technical assistants in finalising and entering their observational programmes.

Successful proposers of polarisation observations were assigned a Resident Astronomer (if one was not already present on the proposal) who contacted the proposers and discussed with them the details of the observations. These observations were entered via a SOC expert.

After completion of the Phase 2 data entry, and when all was correct, the observations were stored in the ‘Mission Data Base’, a critical element of the overall SOC architecture as it contained full details of all observations that ISO would make. Calibration observations were also stored in the same database but entered by a different route.

The daily timeline of observations was then set up by the ‘Mission Planning Phase 1’ system. This software system used a set of routines (‘AOT logic’) to convert automatically the user-entered parameters (α , δ , wavelength, flux, spectral resolution, observation time or desired signal to noise, etc.) into detailed commands to be finally passed to the Spacecraft Control Centre for transmission to the spacecraft.

Post-launch as experience and confidence grew, visits to ESTEC and IPAC were almost completely replaced by remote logins across the Internet.

During the operational life of ISO, observers were permitted to tune up their programmes — via Internet communications with the Community Support Team at the Science Operations Centre — to take full advantage of results from previous observations and of improving knowledge of how best to use the instruments. In some cases, the different in-orbit detector sensitivities led to changes in the values of observing parameters and in the worst case rendered some observations unfeasible. The visibility constraints were closely related to the launch date and the target lists also had to be adjusted accordingly. The facility was widely used, with — averaged across the entire set of observations — each programme

being updated around three times. Because scientific judgement often had to be involved, checking that updated observations did not duplicate existing ones was a very labour-intensive task.

4.3.4 Community Support

The overall community support task during operations was intended to facilitate scientifically-effective use of ISO and included not only handling all requests for observing time as above described but also providing concise and up-to-date information.

Prior to launch, user documentation (such as observers manuals, data reduction manuals, information notes, etc.) was mainly paper-based. However, during the operations, this completely switched to being web-based. The ISO WWW site (<http://www.iso.vilspa.esa.es/>) opened in 1994 and had over 1 million hits (from non-ESA machines) during operations. Internet rapidly became the essential way of communicating with observers, also through the ISO Helpdesk (helpdesk@iso.vilspa.esa.es) service. The ISO WWW site has been continually upgraded since its creation, e.g. with the addition of galleries of science results and of tools for detailed monitoring of execution of observing programmes. It currently serves every week more than 3000 HTML pages, 6000 images and 2000 documents to 4000 distinct hosts. The ISO Helpdesk has received and answered more than 31000 e-mails as of November 2003 and it is still used by the ISO archive users to retrieve information on the archived data products or to ask questions to the calibration experts on data reduction.

During Post-Operations the ISO Data Centre welcomed and supported more than 135 visitors who wanted to analyse ISO data with the help of an IDC support astronomer and it also organised several workshops and conferences (see Section 1.2).

4.4 Overview of the Scientific Programme

The scientific programme for ISO consisted of more than 1000 individual proposals from nearly 600 principal investigators from the world-wide astronomical community.

About 10% of ISO's time was used for Solar System studies, 23% for the Interstellar Medium (ISM), 29% on Stellar/Circumstellar topics, 27% for Extragalactic observations and 11% for Cosmology (see Figure 4.8).

The full list of accepted and performed proposals is given in Appendix B.

4.4.1 Large survey programmes

There were no restrictions on the duration nor the size of the programmes except those set by the technical constraints of the mission, e.g. sky visibility and the orbit.

The OTAC considered each proposal on its scientific merits without any, a priori, preference for programmes of any specific size.

Taking advantage of this, some ISO programmes were proposed by observers and approved by the OTAC requesting a large amount of observing time. They intended to produce homogenous data sets on large samples of sources in a variety of scientific areas.

Table 4.1 gives an overview of the largest survey programmes.

More details of the survey programmes can be found in '*ISO Surveys of a Dusty Universe*' (Lemke et al. 1999, [112]).

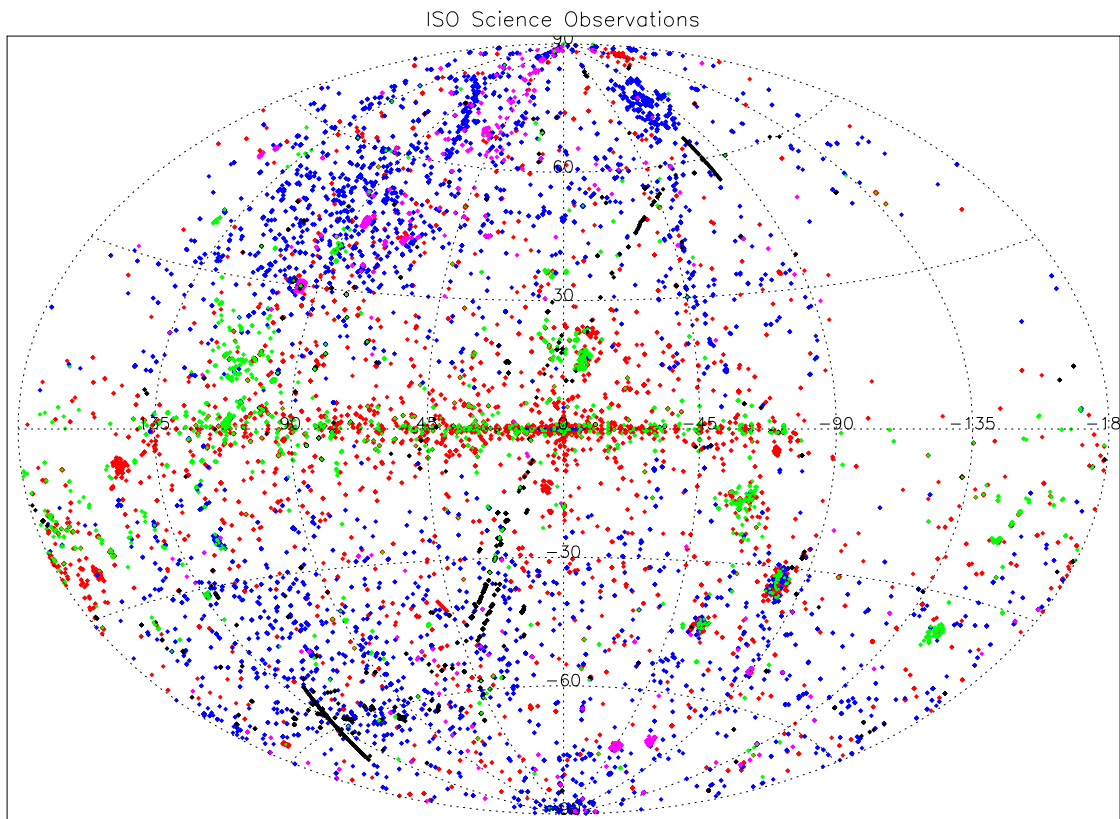


Figure 4.8: *ISO* made more than 30 000 observations, covering all fields of astronomy, literally from comets to cosmology. The observation pointings are depicted in this figure, an Aitoff projection in galactic coordinates. The scientific category of the associated observing proposals are: solar system (black), stellar physics (red), interstellar medium (green), extragalactic (blue) and cosmology (magenta). Noticeable features are e.g., the zodiacal light scans, and the Magellanic Clouds. Due to the stringent pointing constraints *ISO* was in principle precluded to observe the Orion region, but thanks to the extended lifetime, observations could be done on Orion ($l \approx -150^\circ$, $b \approx -20^\circ$) towards the end of the mission.

Table 4.1: *The largest ISO observing programmes, each with 1 % or more of ISO's observing time and together amounting to 15 % of the total time available.*

Programme	PI
European Large Area ISO Survey (ELAIS)	Rowan-Robinson
Spectroscopy of Bright Galactic Nuclei	Genzel
ISOCAM Survey of the Inner Galaxy (ISOGAL)	Omont
ISOCAM Deep Survey Programme	Cesarsky
ISM of Normal Galaxies	Helou
Dust Debris Around Solar Mass Stars	Becklin
Exploring the Full Range of Quasar/AGN Properties	Wilkes
Structure of the FIR Background	Puget

4.4.2 Target of opportunity programmes

In order to maximise ISO's scientific return from unpredictable astronomical events some of which needed rapid reaction times, a number of small teams were also set up to define and prepare the necessary ISO observations for likely Targets of Opportunity (ToO), such as supernovae, novae, bright comets, etc.

These teams prepared generic observations in advance, stored pre-planned observation sequences in the SOC's databases, fine tuned them as needed and were responsible for publishing the data to the community as quickly as possible. Such observations were executed only in the event that the specified phenomenon actually occurred and it was the responsibility of the Principal Investigator of the team to inform the SOC of the occurrence of the phenomenon. Time for any such ToO observations came from the general Open Time.

These ToO proposals were reviewed by OTAC in the same way as other observing proposals. Each selected team contained, *ex officio*, one or more SOC astronomers. These were either included in the original proposal or were added to selected teams. The roles of these SOC staff included co-ordination during definition, responsibility for maintaining the appropriate observations in the SOC's databases and, being the focus at the SOC, during any execution of these observations.

Table 4.2 gives a summary of the performed ToO programmes. These proposals are also contained in Appendix B under Open Time proposals.

4.4.3 Discretionary time programmes

ISO made new and unexpected discoveries and, in many cases, ISO itself was the only facility capable of follow-on investigations of these discoveries. Additionally, compelling new observations became apparent during ISO's in-orbit life. Thus, a small pool of 'discretionary time' was kept available, outside the normal 'Call-Proposal-Review' cycle, for observations that could not have been foreseen at the time of proposal submission. An average of 30 minutes of discretionary time observations per day was foreseen.

To use this discretionary time, a request had to be made to the scientific head of the Observatory, the Project Scientist. Whenever possible, the Chairman of the OTAC was consulted by the Project Scientist before any additional observations were authorised. The Project Scientist reported to the next meeting of OTAC on all discretionary time observations.

Over 150 discretionary time proposals were received during the ISO operational lifetime, 40% of them in the last four months of the mission.

Following a recommendation of the OTAC, after a meeting held on 16 September 1997 where the overall status of the ISO scientific programme was reviewed, recommendations were made concerning use of the extra-time available as a consequence of the longer lifetime of ISO.

The principal conclusions were: that the amount of discretionary time should be significantly increased for the rest of the mission; that an additional ~ 200 hours should be made available to the previously-approved large surveys; and that some 300 hours should be devoted to observations of 'general interest' which should be placed in the public domain without the usual 12 months proprietary period. Thus, about 20 additional proposals on *specific* topics were solicited to the community; these can be recognised in the ISO Data Archive as the programme names all start with 'ZZ'.

4.4.4 Parallel and serendipity programmes

The parallel and serendipity modes were not available to proposers. The data from these modes needed to be taken and reduced in a systematic and completely different manner. This was done by the respective instrument consortia, in collaboration with the SOC, and the data are available now through the ISO Data Archive. Table 4.3 gives an overview of all performed parallel and serendipity programmes of ISO. The parallel data were obtained while other instruments were prime, the serendipity data were taken during slews of the satellite.

Table 4.2: Summary of all performed ToO programmes.

Programme	PI	Observed Targets
Observations of Novae during the ISO Mission	Barlow	Nova Cas 95, Nova Aql 95 Nova Cru 96,...
The Nature of the Superluminal Galactic Source GRS 1915+105: ISO Monitoring of the Most Powerful Source in the Galaxy	Castro-Tirado	GRS 1915+105
The Nature of the Superluminal Galactic Source GRS 1915+105: ISO Observations during the Oct 1997 X-Ray and Radio Outburst	Castro-Tirado	GRS 1915+105
New Soft Gamma-Ray Repeater (SGR 1814–1340): A New IR-Source?	Castro-Tirado	SGR 1814–1340
Studies of High Mass X-ray Binary Systems: Multi-waveband Investigations of such Systems in Outburst	Coe	4U1145–619, 4U1700–37
Observations of Unexpected Comets	Crovisier	P/Hale-Bopp
Spectroscopic Observations of Comets	Crovisier	P/Hale-Bopp
ISO Observations of Cygnus X-3 in Outburst: Infrared Studies of a Flaring Microquasar	Fender	Cyg X-3
Observations of New Novae in Outburst Physics Characteristics and Contributions to the ISM	Gehrz	Nova Aql 95, LMC1 1995, Nova Oph 94, Nova Sco 97,...
ISOPHOT Observations of a Bright Comet Coma: Composition and Dust Production	Grün	P/Hale-Bopp
ISOPHOT Observations of a New Comet: Coma Composition and Dust Production	Grün	P/Hale-Bopp
The Nucleus of a New Bright Comet	Lamy	P/Hale-Bopp, P/Tempel-Tuttle, P/Hartley 2
Observations of Low-Mass X-ray Binaries	Naylor	V404 Cyg, GX1+4
Cometary Comae in the IR: Dimensions, Structures and Composition	Peschke	P/Hale-Bopp
Evolution of the Circumstellar Environment during an FU Ori or EX Lup Outburst	Prusti	FU Ori in Serpens
Dust Formation around R CrB Type Stars at their Minima: Search for Fullerenes	Tanabe	LR Sco, V Cra
The Infrared Counterpart of GRS 1915+105: Observations of Outbursts	Winkler	GRS 1915+105

Table 4.3: *Summary of all performed parallel and serendipity programmes.*

Programme	Wavelength	No. of observations / sky coverage
ISOCAM Parallel	6.0, 6.7, 14.3 μm	> 40 000 observations
ISOCAM Serendipity	6.0, 6.7, 14.3 μm	\approx 10 to 15% sky coverage
ISOPHOT Serendipity	170 μm	\approx 15% sky coverage
LWS Parallel	10 wavelengths: 46 to 178 μm	> 17 000 obs. \approx 1% sky coverage
LWS Serendipity	10 wavelengths: 46 to 178 μm	\approx 10% sky coverage

Most of the parallel and serendipity programmes are explained in detail in ‘*ISO Surveys of a Dusty Universe*’ (Lemke et al. 1999, [112]).

4.5 Overview of Satellite Observing Modes

An ISO observation is a combination of spacecraft and instrument operations. This section describes the available spacecraft observing modes and the overheads involved. An overhead is the time to prepare the satellite and instrument for a new observation or measurement before photons can be collected from the source.

In addition to the spacecraft observing modes the satellite construction constrains observations. The instruments are fixed with respect to the satellite axes (Figure 3.2). Therefore the satellite orientation determines how e.g. apertures are projected on the sky. This may be relevant when the aperture has a rectangular shape, when an array is used or when internal chopping was required. The instrument specific Handbooks provide detailed information about satellite orientation constraints.

Single pointing

The main operational mode of the spacecraft was a three-axis stabilised pointing at a target to carry out one or more observations, followed by a slew to another target.

A single pointing is an observation at a single sky position with a single instrument, which may consist of a series of measurements.

This was the standard mode used to observe ‘normal targets’ (i.e., point sources with fixed celestial coordinates). The coordinate information had to be given with an accuracy of 1'' in Declination and 0.1 s in Right Ascension, the required accuracy at least for the smaller entrance apertures of ISO. IRAS positions were thus generally *not* precise enough for ISO. The instrument specific volumes of the Handbook describe problems encountered when observations were mispointed (for various reasons).

In order to avoid incorrect pointing, proper motion had to be given for objects such as nearby stars, in units of arcseconds per year.

Peaking-up

Peaking-up was originally designed for observations which require higher pointing accuracy, than the accuracy specified for the spacecraft. Since the absolute pointing error (APE) was less than 2.5'' (see Section 5.4), peaking-up was never used. This observing mode is here included purely for historical reasons so that observers may understand the term.

Mapping or rastering

Spectroscopic and continuum maps could be obtained with a series of single pointings using the spacecraft raster mode. A map could contain one scan (one-dimensional mapping) or several scans (two-dimensional mapping). All pointings of a raster map had to lie within an area of 1.5 by 1.5 square degrees. Mapping was available for CAM, PHT and LWS. The observer had to specify the coordinates of the centre position, the number of scan lines (N), the number of points in a scan line (M) and the step sizes in arcseconds.

The latter are the distance between the scan lines and the distance between points in the scan line. Additionally, the observer had to specify the position angle of the scan lines i.e. the orientation of the map (see Figures 4.9 and 4.10).

The number of points in a scanline and the number of scanlines can be any integer between 1 and 32. Setting one of the numbers to 1 specifies a one-dimensional scan. Allowed step sizes were 0,2,3,...,180 arcseconds.

A step size of 0'' in spacecraft z-direction was used to simulate a 'nodding' observation to achieve repeated quasi-staring observations between target and one or more background positions.

The position entered into PGA for a raster map was taken as the center of the grid. Thus a 5×6 raster has its centre at, and therefore the position refers to, raster position (2.5,3).

The raster map parameters refer to:

- M = number points in a scanline
- = number of points in the direction of the orientation
- N = number of scanlines
- = number of points perpendicular to the map orientation (M scanline)

orientation angle

- = the angle between north direction and the direction of the scanline (z-axis), counted anti-clockwise i.e. via east

Figure 4.9 shows an example of an M=4, N=3 raster carried out with orientation angle=0, while Figure 4.10 shows one with an orientation angle of 47°.

Note that all angles are processed in J2000 coordinates.

The orientation angle of a map or a scan is counted from the North direction via East (see Figure 4.10). The values for the orientation angle can be between 0 and 179 degrees. A scan orientation angle of 90 degrees indicates that the scan was obtained going East–West. Note that the orientation angle, held for example in the IIPH keyword ATTROTA, is different from the roll angle of the spacecraft, held for example in the IIPH keywords INSTROLL and CINSTROL. The roll angle indicates how the instrument apertures were placed on the sky and the orientation angle indicates how the raster was performed on the sky.

The map parameters are specified with respect to the equatorial coordinate system (Right Ascension and Declination for a given epoch). The orientation of the spacecraft axes was essentially arbitrary with respect to that system. Since the orientation of the detector arrays (i.e. CAM and PHT-C) and rectangular apertures (for PHT-P) is fixed with respect to the spacecraft axes, the orientation of the array or aperture with respect to the scan line was arbitrary. More details can be found in the CAM and PHT volumes of this Handbook. In some cases the spacecraft coordinate system was requested instead of the equatorial system to align the axes of a map with the spacecraft axes.

For scheduling, mapping was regarded as a single observation. Thus, a map, or a scan, was only scheduled as a whole or not at all.

Mapping was not available for SWS. There, maps were generated by concatenating individual observations together.

During pointings (both single pointings and raster pointings) the AOCS control about the spacecraft y- and z-axes was primarily achieved using the Star-Tracker. The control was to place the guide star on particular Star-Tracker 'set-points' (which were calculated from the star vector, target quaternion and instrument alignments).

In raster mode the movement from one raster point to the next was simply achieved by appropriately changing the Star-Tracker set-points. This means the pointing accuracy of the first position of an $M \times N$

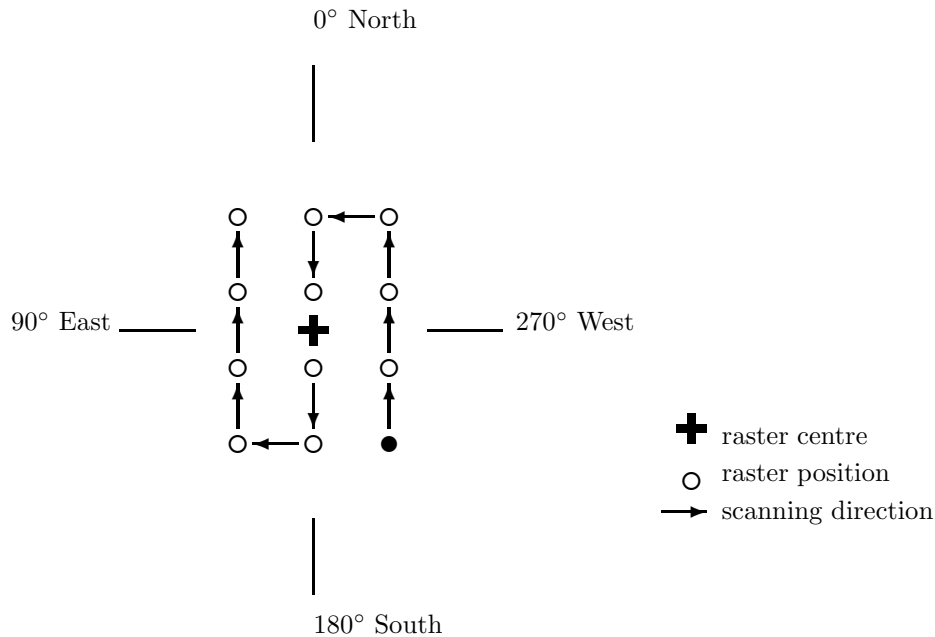


Figure 4.9: Mapping with ISO: This panel shows the sampling procedure for an orientation angle of 0° . The number of scanlines is 3, the number of points in a scanline is 4. The start position of the map is indicated by the filled circle.

raster was set by the absolute pointing accuracy. The relative accuracy between any points in the raster is more difficult to determine. For rasters that did not move the star too much across the field of view of the Star-Tracker the pointing error should be of the order of the pointing jitter. However, for rasters that moved the star substantially across the field of view, the error could reach that of the APE, as the distortion might be different there.

Tracking of solar system objects was accomplished by using a 1-dimensional raster (effectively a time-dependent offset from background stars) and, therefore, raster pointing was not available to observers for designated solar system targets.

Concatenation

Concatenated observations are a chain of observations from the same proposal which had to be performed contiguously in time. All targets of the concatenated observations had to lie in an area of 3 degrees diameter.

For scheduling, concatenated observations were treated as a single unit, i.e. either all observations in the chain were scheduled or none. The underlying rationale for this treatment was that the proposer used concatenation to indicate that scheduling of only a part of these observations was not sufficient to meet the scientific objectives described in the proposal justification.

Note that concatenating observations simply because the pointings were close together in the sky was not a valid argument, since the mission planning system optimised the schedule very efficiently.

In principle up to 99 observations, the maximum allowed per proposal, could be concatenated. However, the more AOTs that were contained in the chain, the longer the duration of the entire observation; once this duration exceeded several hours, it became highly unlikely that the observation could be scheduled.

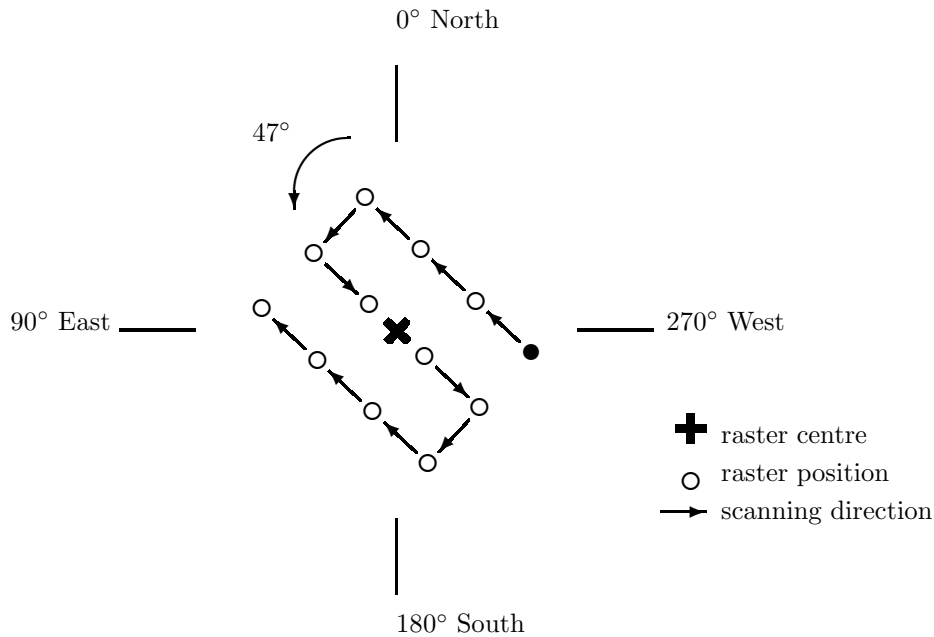


Figure 4.10: Mapping with ISO: This panel shows the sampling procedure for an orientation angle of 47°. The number of scanlines is 3, the number of points in a scanline is 4. The start position of the map is indicated by the filled circle.

Linked observations

If carrying out an observation depends on the results of a previous observation, the corresponding two observations were called 'linked'. The execution of these observations involved intervention by a resident astronomer, as the result of the first observation had to be evaluated on the basis of the specified observer requirements.

Examples of linked observations are:

- A spectrum is to be measured using SWS, provided that the continuum flux of the source, as determined from an observation with PHT, is above a certain limit.
- An image of a certain area is to be taken only if a first image, taken at the position of the expected brightness maximum, yields a positive detection.

A proposal requesting linked observations had to have a strong scientific case and to contain clear and quantitative specifications of the condition under which the later observation should be carried out. For scheduling reasons the later observations were carried out at least three revolutions later.

Archive users are unlikely to come across linked observations as the facility was rarely used during the mission.

Fixed time and periodic observations

Observations were carried out when they could be scheduled conveniently and without leading to large overheads, e.g. in target acquisition. Given the mission planning cycle, the time when an observation of a

target would be scheduled was not known until the detailed schedule had been generated for a particular revolution a few days in advance.

However, there was the possibility to request an observation to be performed on a particular date (i.e. revolution) during the ISO mission. An example for this type of observing request is to observe a Mira variable at a certain phase in the light curve. The proposer specified in the scientific justification when the target was to be observed.

Periodic observations were a generalisation of fixed time observations. In the scientific justification, the proposer specified the date of the first observation, if e.g. the phase of the phenomenon to be observed was important. Additionally, the number of observations to be carried out and the number of days between successive observations had to be given. The small fraction of sky accessible from ISO at any given time rendered some periodic observations impossible.

Special modes

These three special observing modes were used to make additional scientific observations either when the spacecraft was slewing to a new target or when CAM or LWS were not the prime instrument. These modes are the already mentioned:

PHT Serendipity mode: Whenever possible during satellite slews PHT made a survey at $200\ \mu\text{m}$ (Stickel et al. 1999, [154]; 2002, [155]).

CAM Parallel mode: While an observation was carried out with another instrument at a particular sky position, CAM took images on a nearby field separated from the sky position by the 12 or 17 arcmin separation between the instrument apertures in the ISO focal plane (Siebenmorgen et al. 1996, [151]; Ott et al. 2002, [135]).

LWS Parallel mode: While an observation was carried out with another instrument at a particular sky position, LWS observed a nearby field separated from the sky position by the 12 or 17 arcmin separation between the instrument apertures in the ISO focal plane. Data from all LWS detectors were taken at a fixed grating position (Lim 2002, [115]).

These modes were not available to proposers, but the data is available in the ISO Data Archive.

4.6 Overview of Instrument Observing Modes and AOTs

The ISO instruments had some 23 main observing modes, the so-called ‘Astronomical Observation Templates’ or ‘AOTs’. A summary of them is given in Table 4.4.

For historical reasons the AOT numbers are not consecutive. The first column gives the AOT identifier, the second the AOT title and the third column gives the restriction for the AOT if applied to observations of solar system targets. ‘not applicable’ means that this AOT could not be used for solar system observations, ‘single pointing’ means that no raster maps could be performed, ‘staring’ means that the chopper could not be used and ‘one entrance aperture’ in the case for SWS AOTs means that a change of wavelength was not allowed when it involved an automatic change of the entrance aperture.

Table 4.5 shows the relative usage of the four instruments in terms of time and number of observations performed.

Figure 4.11 shows the usage of the different instrument observing modes during the mission. It is interesting to note that 90 % of the observations carried out come from around 50 % of the modes.

Table 4.4: *Overview of the main ISO instrument observing modes, the so-called ‘Astronomical Observation Templates’ or ‘AOTs’.*

AOT	AOT Title	Solar System
CAM01	General Observation	single pointing
CAM03	Beam Switching	not applicable
CAM04	Spectral Observations	single pointing
CAM05*	Polarisation	single pointing
LWS01	Grating Wavelength Range Spectrum	single pointing
LWS02	Grating Line Spectra	single pointing
LWS03	Fabry-Pérot Wavelength Range Spectrum	single pointing
LWS04	Fabry-Pérot Line Spectra	single pointing
PHT03	General Multi-filter Photometry with PHT-P	single pointing, staring
PHT04	General Multi-aperture Photometry with PHT-P	single pointing, staring
PHT05	Absolute Photometry with PHT-P	staring
PHT17	Sparse Map with PHT-P (start AOT)	not applicable
PHT18	Sparse Map with PHT-P (intermediate AOT(s))	not applicable
PHT19	Sparse Map with PHT-P (end AOT)	not applicable
PHT22	Multi-filter Photometry with PHT-C	staring
PHT25	Absolute Photometry with PHT-C	single pointing, staring
PHT32	Multi-filter Map / Linear Scan with PHT-C	not applicable
PHT37	Sparse Map with PHT-C (start AOT)	not applicable
PHT38	Sparse Map with PHT-C (intermediate AOTs)	not applicable
PHT39	Sparse Map with PHT-C (end AOT)	not applicable
PHT40	Spectrophotometry with PHT-S	single pointing, staring
PHT50*	Single Filter Polarimetry with PHT-P	single pointing, staring
PHT51*	Single Filter Polarimetry with PHT-C	single pointing, staring
SWS01	Low-Resolution Full Grating Scan	one entrance aperture
SWS02	Grating Line Profile Scan	one entrance aperture
SWS06	Grating Scan	one entrance aperture
SWS07	Combined Fabry-Pérot Line Scan and SW Grating Scan	one entrance aperture

* Polarisation observations with ISOCAM and ISOPHOT were implemented in operations by a different route than that for the standard ‘AOT-based’ observing modes.

Table 4.5: *Usage of the four ISO instruments by time and by number of observations.*

	CAM	LWS	PHT	SWS
By time:	28%	18%	30%	24%
By # of observations:	26%	12%	49%	13%

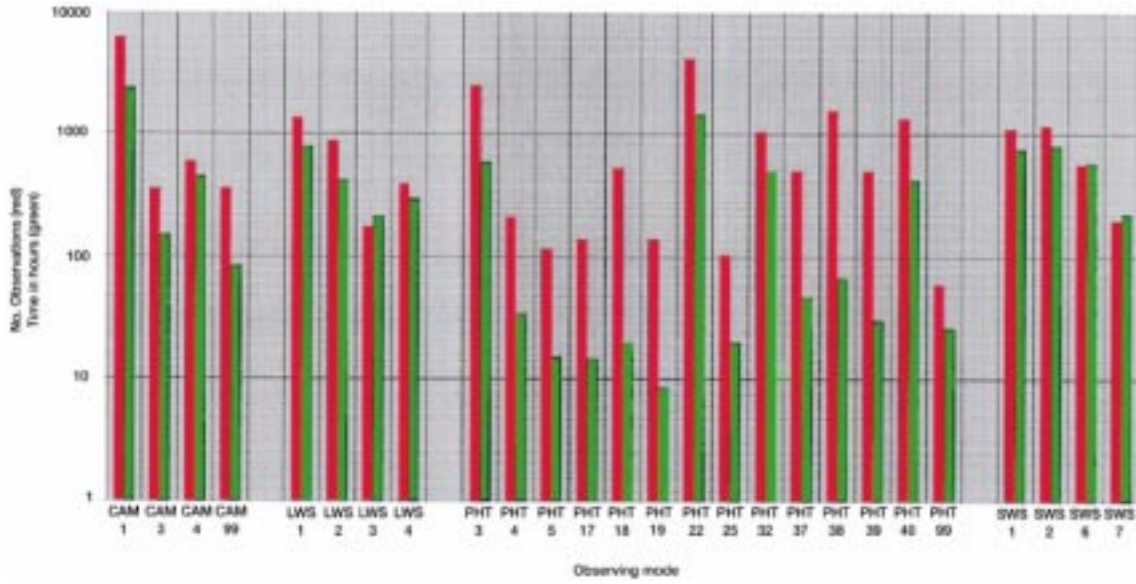


Figure 4.11: Usage of the different observing modes of the four ISO instruments by time (green) and number of observations (red). For an explanation of the observing modes see Section 3.4.

Chapter 5

ISO In-Orbit Performance

5.1 Satellite Operation Performance

ISO operations ran very smoothly from the start. They were well served by a superb spacecraft and by robust instruments which suffered only a few anomalies of relatively minor nature. The mission planning system produced schedules with an average efficiency of 92%. During the routine operations phase, some 50 000 slews were executed in order to carry out over 30 000 observations (including astronomical calibration observations). In total, over 27 000 science observations were carried out successfully for nearly 600 observers corresponding to over 1 000 different research programmes. About 400 hours of science observations were carried out per month with an average of 41 observations per day, but ranging from 6 to 238. The average observation duration was 24 minutes, ranging from 36 seconds (a camera calibration) for the shortest measurements up to 7.6 hours (on Titan) for the longest.

ISO was 1 000 times more sensitive and had 100 times better angular resolution than IRAS at $12\ \mu\text{m}$. The wavelength range was twice as large which enabled observations of the coldest objects. The considerably higher spectral resolution allowed new chemistry and kinematic studies. ISO also provided unique polarisation capabilities. The results have impact on all astronomical topics, from comets to cosmology. All elements of the ground segment also performed excellently, leading to an overall availability of the system during Routine Phase of 98.3% of the time scheduled for science. Taking into account all possible reasons for failure, only 4% of observations were lost. Over 98% of the highest priority observations were successfully executed.

5.2 Cryostat Performance

The effective lifetime of the cryostat was determined by the rate at which the super-fluid helium in the main tank was depleted through venting of gaseous phase helium. This was proportional to the rate at which heat leaked into the cryostat from external sources or was generated by internal sources, such as internal calibration sources, cryomechanisms, etc. To optimise the lifetime of the cryostat it was necessary to minimise the heat dissipated within the cryostat and heat leaks entering the cryostat from external sources. A number of sources of heat input to the cryostat were identified and addressed as follows:

Service Module to Payload Module interface: a major source of heat input to the cryostat was the interface between the Service Module and the Payload Module. This was countered, and effectively eliminated, by allowing a portion of each connecting strut to act as a radiator, diverting Service Module heat into space. Although this considerably reduced the heat input to the cryostat, it came at a penalty of impaired platform stability from transient temperature gradients in the struts.

Instrument electronics: a source of heat within the cryostat were the electronic systems used by the instrument detector and readout systems. Considerable effort went into the development of detectors

which were capable of operating without significant heat dissipation at the extremely cold temperatures within the cryostat. Those systems which could not be developed to these requirements were located in the warm electronics section of the Service Module.

External radiation: the radiation received by the cryostat from sources external to the spacecraft (i.e. Sunlight, Earthlight) would cause net heat flows into the cryostat without the presence of the exterior shielding. This consisted of a sun-shield, multi-layer insulation (MLI) and vapour-cooled radiation shields which, in combination, effectively isolated the interior of the cryostat from heat inputs from sources external to the spacecraft.

An important factor for the planning of ISO's scientific operations was the accurate knowledge of the amount of liquid helium remaining in the tank. The ability to make this 'Direct Liquid Content Measurements' (DLCMs) under microgravity conditions was a novel development for ISO, which relied on the near-infinite thermal conductivity of the superfluid helium. A calibrated heat pulse was introduced into the tank, which increased the temperature of the helium by an amount directly proportional to the mass remaining. Three such measurements (see Section 5.7) were performed at various stages of the mission for estimating the mass flow rate of the boiled-off helium and determine with a better accuracy the lifetime expected for the satellite.

Due to excellent engineering and a fortunate combination of circumstances at launch, the liquid helium supply lasted over 10 months longer than the specified 18 months. Three months came from a prudent safety margin in the engineering calculations of the rate of loss of helium. Two months were the result of favourable circumstances in the launch campaign at Kourou in French Guiana, when, during a technical check of the Ariane 44P launcher, ISO's engineers seized the chance to recharge the helium, and the quick launch that followed meant that the outer parts of the cryogenic system of the spacecraft had little time to warm up in Kourou's tropical climate. Finally, the daily loss of helium turned out to be 17% less than expected, at the lower end of a range of possibilities considered by the engineers, giving another five months of additional life.

This extra lifetime not only led to many more observations but also made it possible to observe the Taurus/Orion region — inaccessible in the nominal mission.

5.3 Optical Performance

5.3.1 ISO Point Spread Function

Early during the Commissioning Phase of the ISO mission, the ISO Point Spread Function (PSF) was measured in order to validate the performance of the telescope optics. The best way of measuring the ISO telescope PSF was to use ISOCAM in one of its configurations which minimised any instrumental effects. For this, calibration data were obtained with a bright point source located at the centre of the detector array, to avoid possible field distortion effects. The micro-scanning mode was used with the minimum allowed raster step size of 2 arcsec in order to obtain the best sampling rate with respect to the limited pixel size of the detector arrays. To avoid the limited resolution of the ISOCAM pixels, a large PSF compared to the pixel size was needed. Thus, the configuration chosen was that of 1.5 arcsec pixel field of view with the LW9 filter at 15 μm . The LW9 filter has the longest reference wavelength of the ISOCAM filters and its bandwidth is smaller than that of LW3 (also centered at 15 μm). Thus, this filter was expected to provide the largest and less blurred PSF.

The obtained data were reduced using the CAM Interactive Analysis (CIA) software (see Salama et al. 2001, [140] for details on the data reduction) and compared with two independent models, the first one based on the Fourier transform of the telescope aperture, and the second one on ray-tracing with Gaussian decomposition of the beam to simulate diffraction (Okumura 2000, [131]).

Figure 5.1 shows the reconstructed PSF measured with a sampling rate of 0.5 arcsec, determined by the pixel size and the micro-scan step size. A concentric hexagonal pattern can be seen, instead of circular

Airy rings, due to the diffraction pattern of the tripod. The tripod introduced a slight difference between y-axis (horizontal in Figure 5.1) and z-axis (vertical) PSF profiles. Figure 5.2 shows the data in graphical form, overlaid with the model based on the Fourier transform of the telescope aperture.

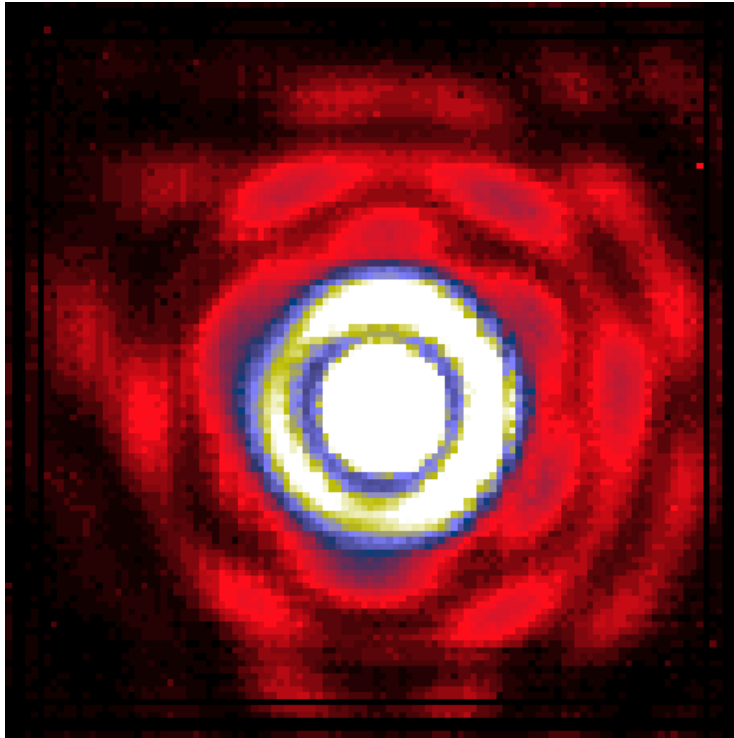


Figure 5.1: *Image of the ISOCAM PSF in the configuration of the minimum instrumental effect.*

The data show an asymmetry in the diagonal direction, easily visible in the brightness distribution of the first ring of the PSF. This asymmetry is observed at all wavelengths and its amplitude is larger at short wavelengths but it is not clear whether it comes from the telescope or from the camera. Laboratory ISOCAM calibration data obtained in the telescope simulator before the satellite launch already showed a small amount of detectable asymmetry above the noise. This suggests that at least a part of the asymmetry may arise from the ISOCAM instrument itself and not from the telescope but it cannot be reproduced with any model parameters setting for the camera. Introducing a slight offset of the secondary mirror of the telescope (M2). also produces an asymmetry but it cannot reproduce the wavelength dependency of its amplitude over the whole range of ISOCAM. This result should be taken with some caution, as all the model parameter space may not have been explored.

Another deviation was found between the model and the observed ISOCAM PSF width, especially at short wavelengths. The modelled PSFs are narrower than the observed ones, which result in a lower value of the flux measured using the PSF model fit compared to that obtained from aperture photometry. However, the SWS instrument did not observe such a large deviation, which suggests that it arises from the ISOCAM instrument.

Similarly to ISOCAM, the other ISO instruments were also used in-flight to determine their effective apertures, required for the calibration of extended sources, and their beam profiles, required for the calibration of point sources observed off-axis. They all reported some asymmetries in their beam profiles (see Salama et al. 2001, [140] and references therein). However, it was not possible to identify whether these are consequences of the telescope PSF or due to other instrument specific effects.

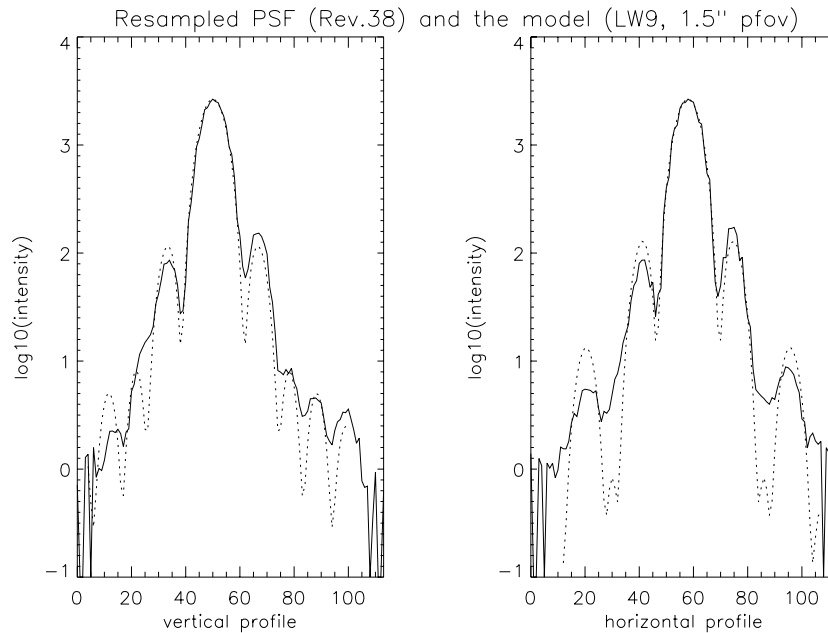


Figure 5.2: Plot of the observed ISOCAM PSF in the configuration of the minimum instrumental effect. The dashed line corresponds to the model based on the Fourier transform of the telescope aperture.

The LWS mean beam profiles and effective apertures were determined for each LWS detector from a series of observations of Mars taken at different positions in the LWS field (Lloyd 2001a, [116]; Lloyd 2001b, [117]). Off-axis observations of Mars revealed narrower than expected profiles as well as the presence of both strong fringes and spectrum fracturing, which produced an asymmetric beam profile. The fringing is known to be produced by the interference between the direct beam from the complex mirror M2 and the reflection from its supporting substrate, but the origin of the spectrum fracturing observed is unknown.

For SWS, raster observations of several bright point sources (HR 5340, γ Dra, NML Cyg, η Car or HR 1457) were used to determine the instrumental beam profiles, which were also found to be narrower than expected and far from flat-topped (Beintema & Salama 2001, [10]). The asymmetries observed are likely produced by internal misalignments between the SWS detectors, especially in the cross-dispersion direction.

Similar measurements were also made with ISOPHOT to derive the instrumental beam profiles and effective solid angles. For PHT-P, dedicated raster observations of bright point sources were confronted with theoretical models of the expected beam profiles revealing strong asymmetries towards the central axis (Müller 2000a, [122]; Müller 2000b, [123]) while for PHT-C, the fraction of the PSF that actually entered a given detector was determined as a function of the source position with respect to the centre of the detector arrays C100 and C200 (Laureijs 1999, [103]). Finally, the beam profiles of the 128 pixels of PHT-S were measured with cross-scans along the spacecraft y- and z-axis of the bright star γ Dra. In the dispersion direction (z-axis) the beam profile was found to be fairly rectangular as expected, while in the cross-dispersion direction (y-axis) the profile was very sharp, with the peak generally deviating from the geometrical centre of the aperture (Herbstmeier et al. 2001, [80]).

Other particular effects on individual instruments related to their optical performance, like the presence of ghosts or the field distortion in ISOCAM, or their response to observations made off-axis or on extended sources, are described in detail in the corresponding instrument specific volumes of the ISO Handbook

and will not be addressed here.

5.3.2 Straylight

In general, the optical performance of the telescope and baffle system was excellent. In order to fulfill the scientific objectives of ISO, stringent straylight requirements were imposed to the optical system. First, the parasitic light level in the focal plane should not exceed 10% of the minimum diffuse astronomical background for the wavelength range from 2.5 to 240 μm . Second, the thermal self-emission from the optical system should also be less than 10% of the minimum diffuse background. Main straylight sources were expected to be the Sun, Earth, Moon, and extremely bright sources like Jupiter.

Several experiments were performed in-orbit using ISOPHOT to verify both the near-field straylight (within 1° radius) and the far-field straylight suppression.

The near-field straylight measurements were taken with PHT-S at 2.5–12 μm , with PHT-P at 25 μm , where the straylight contribution from Earth and Moon are largest, and with PHT-C at 170 μm , the most sensitive band to detect straylight due to thermal self-emission (Lemke et al. 2001, [113]). With PHT-S, measurements performed at a distance of 60'' from the bright source γ Dra (1600–100 Jy) resulted only in a signal consistent with dark current. In the P_25 filter, double cross-scans over Mira (1500 Jy at 25 μm) were performed out to radial distances of 30'. At these distances no additional contribution from the beam profile of the bright source on top of the relatively bright zodiacal light background could be detected. With the C_160 filter, the double cross-scans were performed around Saturn (32 000 Jy at 160 μm). Crossing the source was avoided to prevent memory effects and saturation of the detector. The maximum radial distance was 45'. The radial fall-off of the signals was close to the pre-launch predictions. According to the theoretical models, most of the straylight comes from the tripod support of the secondary mirror, the secondary edge and the secondary mirror surface. An example of the straylight effects induced by very bright sources in PHT22 raster maps is shown in Figure 5.3.

The far-field straylight of the Sun and the Moon were searched for during solar eclipses (Klaas et al. 1998, [99]; Lemke et al. 2001, [113]). For the Sun straylight the telescope pointed at a fixed sky position 60° away, i.e. at the minimum avoidance angle. For the expected drop and rise at the entry and exit of the eclipse phase, an upper limit of 9 mJy at 25 μm and 19 mJy at 170 μm was derived for a 180'' aperture or the sum of the four C200 pixels, respectively. A sequence of 3 successive eclipses were used to assess the Moon straylight. ISO was pointed at three different fixed positions of the sky located at distances of 62° , 49° and 28° with the intention of detecting relative differences in the background levels. Again, the variation was below the detection limit and only upper limits of 100 mJy and 86 mJy were derived at 25 μm and 170 μm , respectively.

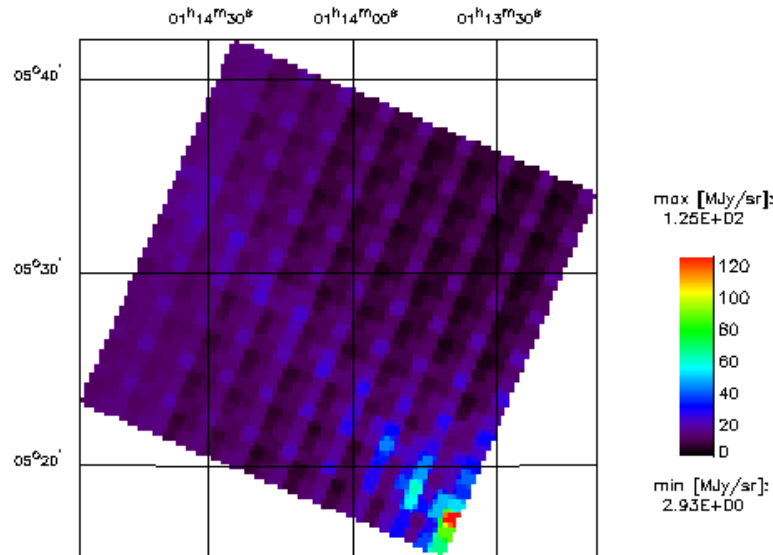
Finally, the measurement of straylight contributions from the Earth was performed with the Earth positioned at 3 different directions relative to the oblique conical sunshade, keeping the limb at the minimum angle allowed from the ISO sky pointing. The observations were designed to detect differences in the measured background level, depending on the Earth illumination into the sunshade. The upper limits derived in this case were of 101 mJy at 25 μm and 526 mJy at 170 μm .

Surprisingly, the 170 μm serendipity survey contributed to our knowledge of instrumental straylight. A composition of all slews relative to Saturn produced after the mission revealed the presence of a very faint straylight ring emission at a distance of 0.7° to 1.0° with Saturn at its centre. The brightness of the ring is $\sim 1\%$ of the central source and was tentatively assigned to grazing reflections at the oversized secondary mirror cover (Lemke et al. 2001, [113]).

In the case of SWS, off-axis responses were measured early in the PV phase on the bright source W Hya, out to a distance of 2'. Later in the mission, specific straylight checks were performed, prompted by scientific needs for a better characterisation of the influence of straylight from Saturn on planetary satellites such as Titan and Europa.

One measurement of straylight rejection was performed during observations of Titan on revolution 384.

KBM2 20-JUN-1997 PHT22
 (RA,Dec)=(1h14m 3.2s, 5°28'38.2") (J2000) TDT No. 58200903
 Filter: 90 μm



QLP_701 - C4LG_40 - PHT Browse 2.0

Figure 5.3: *Straylight observed in a PHT22 raster map taken in the vicinity of Saturn. The planet is located at a distance of 4.5' outside the displayed field close to the lower corner of the image and exactly in the direction indicated by the stripe.*

The spectral line due to C_2H_2 at $13.7 \mu\text{m}$ was measured on Saturn and at a position corresponding to a distance of $3'$. This gave a rejection factor of 10^4 (Salama 1998, [139]).

For LWS, spot checks of the flux entering the instrument at distances of $5'$ and $9'$ from a very strong source like Jupiter were also performed when the LWS was taking the off-source spectra corresponding to Ganymede and Callisto. The results obtained show that there is a good correlation in both cases between the flux measured as a function of the distance to Jupiter and the model of the ISO PSF by Okumura 2000, [131]. However, the measured fluxes are systematically higher than what was expected from the optical model, which could be due either to the fact that Jupiter is not a point source or to the existence of significant wings in the beam profile.

Straylight effects from extended sources in ISOCAM were investigated through observations of zodiacal background regions with three CVF step positions corresponding to the wavelengths of 7.7 , 11.4 and $15 \mu\text{m}$, and all possible pixel field of views. The images obtained show some contamination by straylight which is found to be an important limitation in CVF images, where real physical structures with an average flux per pixel below 10% of the background are hard to detect.

In addition, straylight measurements were also performed in the surroundings of the bright source NML Cyg in revolution 46. Dedicated raster scans around the source with 6 different orientations taken at a distance of $4.6'$ from the ISOCAM field centre showed the presence of a faint straight line pattern and a diffuse excess brightness in the direction of the source. However, the flux of NML Cyg is roughly 3000

to 5000 Jy at the ISOCAM wavelengths while the brightest pixel of the straylight is about 10^{-5} to 10^{-6} times fainter. This corresponds very well with the predicted values in the pre-flight optical modelling (Okumura et al. 1998, [130]).

In CAM parallel observations, images taken in the neighbourhood of very bright sources were also found to show bands of illuminated pixels pointing towards the direction where the bright source was located. The effect is again very small but it can be seen in some cases at distances of several arcmin (see Figure 5.4).

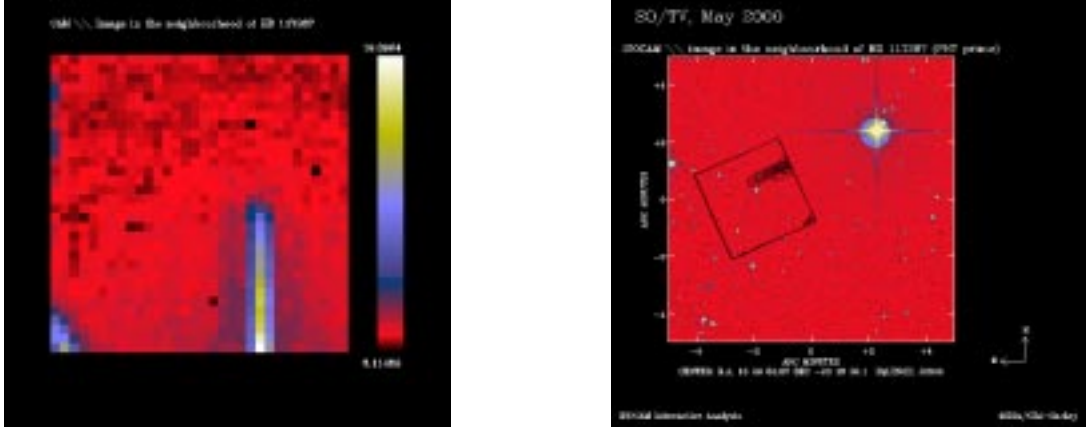


Figure 5.4: *Straylight observed in a CAM parallel image (left panel) in the neighbourhood of the bright Mira variable HD 117287 (the bright star in the right panel). The distance to this source from the centre of the image is about $4'$.*

5.4 Pointing Performance

5.4.1 Pointing accuracy

The standard ISO observing mode was a 3-axis-stabilised pointing at a selected astronomical target, permitting observations for a period up to several hours. Pointing accuracy was defined according to three terms:

1. *Relative Pointing Error (RPE)*: the angular separation between the instantaneous absolute orientation of the satellite fixed axis at a given time and a reference axis defined over 30 s around that time. This is a measure of the jitter of the satellite and is expressed as 2σ , half-cone;
2. *Absolute Pointing Drift (APD)*: the angular separation between the short time average (barycentre of the actual pointing during a given time interval) and a similar pointing at a later time;
3. *Absolute Pointing Error (APE)*: the angular separation between the commanded direction and the actual direction, effectively blind pointing accuracy. It is defined to be:

$$APE = 2 \times \sqrt{\sigma_y^2 + \sigma_z^2} \quad (5.1)$$

Observers may also come across the rarely used term *Average Measurement Accuracy (AMA)*, the angular separation between the actual and the measured orientation of the satellite fixed axis defined instantaneously over a time interval. The requirements for the pointing accuracy in terms of these three definitions are given in Table 5.1, along with the accuracies achieved in-flight.

Pointing and tracking were carried out by the use of one of the two Star-Trackers (STRs) mounted outside the cryostat (the other was not commissioned), the Quadrant Star Sensor (QSS), located on the optical axis of the telescope, and the gyros and reaction wheels controlling movement.

One of the first tasks accomplished during PV was the proper determination of the focal-plane geometry through a series of observations designed to measure the precise locations of the instrument apertures with respect to the QSS boresight.

Any changes in alignment with respect to the nominal focal-plane geometry were expected to be caused by temperature changes of the STR baseplate. It was anticipated that the temperature would vary, and it had been planned to have an update of the pointing quaternion (see Appendix F) at the start of every revolution (on the assumption that the variation within a revolution would be small).

At the beginning of the mission, while the satellite was still cooling down, the measured temperature was far from what was expected, and in the first revolutions SCC finetuned the STR parameters in order to bring any misalignments within the required value.

Before this calibration work was completed in revolution 21 and the data incorporated into the spacecraft's pointing procedures, all pointings were subject to systematic errors in the aperture positions used. Anyone interested in using very early PV observations (few of which contain science data) should therefore do so with caution.

In-flight tests of the satellite pointing during the PV Phase soon revealed a much better performance than that required, with the obtained values of RPE, APD and APE given in Table 5.1. The excellent stability of the ISO spacecraft was mainly due to lower than expected thermoelastic distortions between the STR and the optical axis of the telescope.

In order to check this stability during the mission, any misalignment between the operational STR and the telescope boresight (and by inference the scientific instruments) was determined at the start of every revolution by placing a guide star in the centre of the field of view of the QSS and determining its position in the STR.

A specific calibration programme was designed and executed in revolution 137 to evaluate the ISO pointing performance, by which a number of point-like sources were observed with ISOCAM, since it was suspected that some systematic effects could still be present in the determination of the APE. This was combined with additional observations performed in revolution 264 with a more accurate star selection procedure, based on the Hipparcos star catalogue, and a better determination of the colour-colour relation between visual magnitude (as quoted in the Hipparcos catalogue) and the expected flux in the CAM LW9 filter. As a consequence of this calibration exercise, it was found that there was a clear correlation between pointing offset and position of the guide star in the STR field of view, indicating that there was still room for additional improvements in the ISO pointing accuracy.

As a consequence of the analysis performed, the following measures were taken:

- Improved Sun ephemerides were introduced at the start of revolution 327.
- The STR calibration was updated at the end of revolution 368.
- After revolution 452 the Sun ephemerides were recalculated four times per revolution, instead of once per revolution. These times were: first, during the activation (ACAL) window; second, about halfway between first OBS_OPEN and first OBS_CLOSE; third, just before ground-station handover (first OBS_CLOSE minus 3 minutes); and fourth, halfway between the second OBS_OPEN and the last OBS_CLOSE (see Figure 4.4). This brought the APE below 2".

A further refinement took place later during Post-Operations when the guide star proper motions and differential aberration effects were taken into account, together with a refinement of the ISO Guide Star coordinates via the Hipparcos output catalogue (see Section 5.4.3).

In this way, the APE was reduced to 1.4" in the legacy version of the ISO Data Archive, almost ten times better than specified (cf. specification of <11.7") and the short term jitter was less than 0.5", about five times better than the specification of 2.7" (2σ , half-cone, over a 30 s period of time).

Table 5.1: *Pointing performance.*

Type of pointing error	Required	After PV	After rev. 368	After rev. 452
	[$''$]	[$''$]	[$''$]	[$''$]
Jitter (RPE)	< 2.7	0.5	0.5	0.5
Drift per hour (APD)	< 2.8	< 0.1	< 0.1	< 0.1
Absolute Pointing Error (APE)	<11.7	\approx 2.5	\approx 1.4	< 2.0

Notes:

1. The values are 2σ for the radius of the cone, i.e. the angular separation between the actual and the commanded pointing direction is within these limits 95 % of the time.
2. This pointing performance assumes one calibration per revolution.
3. The accuracies quoted here are from two experiments only and should only be taken as an indication of errors on other revolutions.

The excellence of the pointing performance was especially welcome for the use of small-aperture instruments such as the smaller PHT-P apertures and the SWS. For example, an Absolute Pointing Error of $4''$ would have both limited the photometric calibration accuracy of SWS to about 30% and also compromised its wavelength calibration via an effective shift of one grating scanner step.

A detailed description of the improvements made to the ISO pointing during the Operational Phase and a quantitative assessment of the ISO pointing accuracy reached at the end of the mission can be found in Salama et al. 2001, [140], and Pollock 2001, [137].

5.4.2 Tracking of solar system objects

Observations of Solar System Objects (SSO) were implemented as tracked observations using one or more one-dimensional raster observations, although this technique was subject to some limitations of particular relevance to long SSO observations, in which an often complicated trajectory was approximated by a series of straight-line raster operations.

As the spacecraft pointing was stable at each raster position, data from observations using small apertures (e.g. SWS) were often still sensitive to the variable position of the object within the aperture, correlated with changes in both the raster points as documented in the Instrument Reference Pointing History (IRPH) file and the instantaneous pointing position reported in the Instrument Instantaneous Pointing History (IIPH) file.

From revolution 290 onwards an improved SSO tracking algorithm was used, resulting in smoother SSO tracking. Before then, the spacecraft pointed at the expected position of the SSO and waited until it was $2''$ away before moving to the next pointing. Therefore, the object tended to have an average offset of $1''$ along its path, from the spacecraft's pointing. From revolution 290 the spacecraft was pointed $1''$ ahead of the SSO and not moved until it got $1''$ behind, bringing the average mispointing down to zero and the maximum offset down from $2''$ to just $1''$.

5.4.3 Guide stars and effects on pointing

The properties of the guide stars used as reference for pointing had also an important effect on the pointing accuracy.

A list of guide stars was prepared before the mission based on a pre-release of the Hipparcos catalogue and used for pointing purposes. Guide stars were removed during the mission from the list if the observations

performed using them showed pointing problems.

The apparent visual magnitude limits for the guide stars were between 2 and 8. These limits were set according to the STR sensitivity. For normal observations this meant that there were always at least one, and at most five, guide stars in the field of view ($3^\circ \times 4^\circ$) of the CCD detector inside the operational STR.

The accuracy in the determination of the position of guide stars in the STR field of view was in some cases disturbed by the presence of other stars in their vicinity. If a guide star was detected on the same column of the CCD as a bright star, problems could occur due to CCD blooming. Thus, guide stars were avoided if they were predicted to fall near one.

There were also small differences between the Hipparcos coordinates initially used (based on a preliminary version of this catalogue), which were referred to the J1991.25 epoch, and the ISO catalogue coordinates, referred to J1997.00. This resulted in slight differences in proper motions and parallaxes.

To avoid this problem, the ISO guide star catalogue was cleaned and stars with proper motions larger than $0.5''/\text{yr}$ in the Hipparcos catalogue were removed. In addition, the ISO guide star catalogue was updated every three months with positions of individual stars corrected for proper motion, calculated with respect to the mid of every period.

The residual effects left were very small ($\leq 0.4''$) but still significant in some cases, fortunately only affecting a few nearby guide stars.

Further pointing inaccuracies were introduced when the guide star was far from the centre of the field of view of the CCD (differential aberration) and when the guide star magnitude was near the lower sensitivity limit.

While aberration was thought to be corrected for ISO observations by the fact that guide stars are always close ($< 2.5^\circ$) to the observed target, the differential aberration effect can cause pointing errors up to $0.9''$ if the guide star is away from the instrument optical axis (if ISO's velocity is considered as well, this can become even larger).

The final ISO pointing model used in the legacy pipeline considers the effects of differential aberration, proper motion and parallax of the guide stars used and it also makes use of the latest version available of the Hipparcos catalogue. This way the accuracy of the ISO pointing was improved at the end of the mission to the arcsecond level (see Section 5.4.1).

5.5 Satellite Timing

ISO contained several on-board clocks: one for each instrument and one for the satellite itself. Several time keys derived from these on-board clocks, and also from ground-based clocks, are present in the ISO data (*ISO Architectural Design Document*, [85]). The most prominent ones are the UTC (Universal Time(Coordinated)), the UTK (Uniform Time Key) and the ITK (Instrument Time Key). Also in widespread use is the Ground Station Time (GST), the time when data were received. Note that the abbreviations UTC and GST are often used interchangeably and that GST does NOT refer to Greenwich Sidereal Time.

The GST is contained in each record of the Telemetry Data Format (TDF) archive; it is the time of reception of the start of the format by a ground station. This time is expressed in the Universal Time Coordinated (UTC) scale as two I*4 integers; the first holding the whole number of seconds since midnight at the beginning of 1989; the second holding the remainder in units of 10^{-7} seconds. In some other data structures, the UTC is expressed in other ways, namely *'yydddhhmmss'* and the Modified Julian Date offset in days from 2000.0. These are all exactly equivalent in physical meaning within the given precision; in particular all of them 'stand still' during a leap second.

The spacecraft on-board time is contained in frame zero of each TDF format. It is read from the same oscillator that drives the telemetry encoding, and therefore increments by a fixed amount per TDF format. Experience with other missions has shown that although ideally the spacecraft clock is a very convenient

quantity for a time scale and easy for software to manipulate, it may be subject to discontinuous jumps or resets, and therefore it cannot be used where it is necessary to label data with a unique time, or where a uniformly increasing time is required. The on-board time is thus not used within the Off-Line Processing (OLP) software.

As an alternative that does not suffer such disadvantages, an artificial on-board time called the uniform time key, or UTK, is derived from the GST. It is the UTK that is used to index all products derived from spacecraft telemetry as distinct from instrument telemetry.

The uniform time key (UTK) is defined as follows:

- a normal signed I*4 quantity,
- increasing at a rate of 24 Hz,
- divisible by 48 on a format boundary,
- initialised to zero at a time close to ISO launch,
- having a constant linear relation to the real spacecraft time, as long as the latter increments nominally,
- guaranteed to increase with time, even across a jump of the real spacecraft clock or in the absence of telemetry frame 0.

A continuously increasing time scale is also necessary for labelling instrument telemetry records. While each of the four instruments had its own way to synchronise data with spacecraft telemetry, these have been unified by defining for each an Instrument Time Key (ITK) as follows:

- a normal signed I*4 quantity,
- valid at least over one Target Dedicated Time (TDT), the time spent in one observation of a target,
- set to an arbitrary initial value to ensure that the key does not overflow,
- having a constant linear relation during the TDT to the UTK defined above.

The four ITKs have been defined as follows:

- The CAM ITK is derived from CAM's internal time word in telemetry and the UTK and is expressed in CAM Time Units. This unit is subject to empirical measurement; the value for products before OLP v7.0 was 0.14000498 seconds, after which it was changed to 0.13999950 seconds. The CAM ITK is unique over the whole mission.
- The LWS ITK is in units of 2^{-14} seconds (approximately 6×10^{-5} seconds) and is calculated as a scaled difference of two UTK times. The LWS ITK is unique over a revolution (ISO orbit).
- The PHT ITK is in units of 2^{-14} seconds and is calculated by combining the UTK and the times contained in PHT floating blocks. The PHT ITK is unique over a revolution.
- The SWS ITK is the UTK and is thus in units of 1/24 seconds. The SWS ITK is unique over the whole mission.

For CAM and SWS it is thus possible to label data records with a time key that is unique for the whole mission; for LWS and PHT, the time key should be used in combination with the TDT number.

The relationships between (i) UTC and UTK, and (ii) UTK and ITK are both established for every observation at the beginning of data processing and recorded in the Compact Status file. DERIVE_ERD,

which reformats an observation's raw data into Edited Raw Data (ERD), makes the appropriate clock calibrations easily available in FITS header keywords and labels all ERD records with an instrument time key.

Attention is drawn to possible irregularities in the relations between UTC and UTK and ITK over one observation. The UTC-UTK relationship may not be entirely stable or constant, for one or more of the following reasons:

- 1) During pre-launch ground tests the UTC, which is the TDF format arrival time, was very occasionally not exactly 2 seconds after the preceding format. We are not aware that this ever occurred during operations but users should be aware of the possibility.
- 2) There is a slow systematic change in the UTC due to orbital motion, related to the changing distance between the earth and the spacecraft.
- 3) The UTC is 'real-world' time and thus includes any so-called 'leap seconds' that were added by decree to the last second of a day at the end of June 30 or December 31, in much the same way that leap-years have an extra day. No attempt has been made to deal with such 1-second clock jumps.

Therefore, the following should be borne in mind:

- the TREFxxxx keywords in main science ERD product FITS headers refer only to a single reference time in the observation and cannot be extrapolated to other points in the observation with high precision.
- the UTC should not be used in place of the UTK or ITK for any ISO data analysis purposes.
- the UTC may be used roughly to correlate ISO data with external events, taking account of the heliocentric correction available in the TREFHELx keywords if necessary.
- the UTC can be derived from the UTK only to a precision that reaches 2 seconds in the worst case.

Users should also be aware that a small fraction of data was lost due to regular if infrequent small gaps in the telemetry stream, although most observations escaped such losses.

5.6 Detector Performance

In the following we will address only some general aspects related to the in-orbit performance of the ISO detectors. More details are given in the corresponding instrument specific volumes (II to V) of the ISO Handbook.

5.6.1 Radiation effects

5.6.1.1 Space radiation environment

The performance of infrared detectors in space can be seriously affected by the ionising radiation environment. Charged particles can induce spikes (also known as 'detector glitches'), higher dark current and detector noise as well as an increase level of responsivity.

The space radiation environment in which ISO was operated had four main constituents: geomagnetically trapped protons and electrons, solar protons and galactic cosmic rays (Nieminen 2001, [129]), each with a variable contribution depending both on the time of the mission and on the orbit phase.

The highly elliptic ISO orbit took the spacecraft deep into the Earth's radiation belts in its perigee (~ 1000 km) and to the interplanetary space in its apogee (~ 72000 km). To minimise the effect of

charged particles impacting the ISO detectors at low altitudes, when the spacecraft crossed through the inner Van Allen belt (mainly composed of high-energy protons), the on-board instruments were switched off (see Section 4.2.2). At higher altitudes, during the ISO science window, the spacecraft detectors were mainly affected by galactic cosmic rays, but also by a significant number of interplanetary and outer belt electrons. Additional effects can be produced by electron *bremsstrahlung* in the outer structures of the spacecraft and in the instrument shields, which may in turn give rise to secondary electrons which can also hit the detectors. Actually, some of the ISO instrument teams reported a clear correlation between detector glitches and energetic electron fluxes as observed by the GOES-9 satellite (Heras et al. 2001, [78]) especially at the edges of the science window, i.e. at ISO altitudes comparable to that of GOES-9. Typical electron integral fluxes as a function of ISO orbital time are shown in Figure 5.5 for two energy cut-offs.

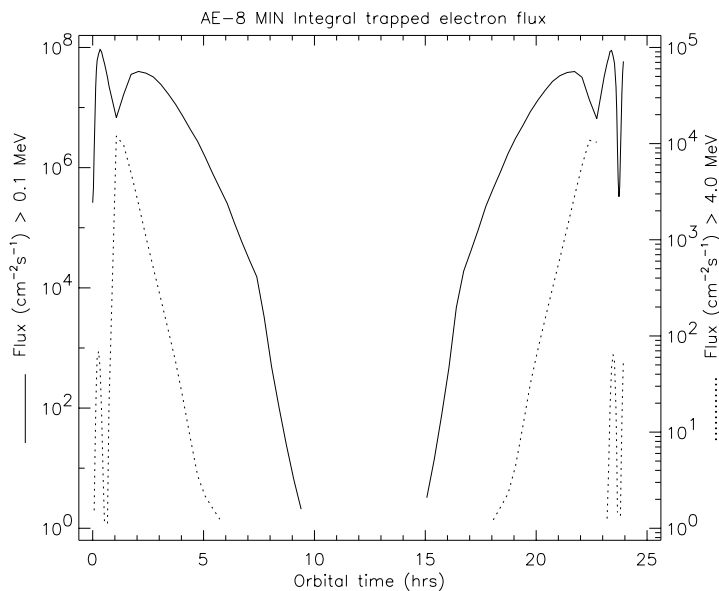


Figure 5.5: *Trapped electron fluxes as a function of ISO orbital time for two energy channels (>100 keV and >4 MeV).*

On the other hand, since the ISO mission was carried out nominally during the solar minimum period, the solar energetic particle contribution was not significant, except for two moderate solar proton events that took place towards the end of the mission: the first, a double-event in November 1997 (revolutions 720–722) during which the proton flux for $E < 10$ MeV and $E < 100$ MeV increased by almost three orders of magnitude and almost one order of magnitude respectively with respect to its average value (see Figure 5.6); and the second, shorter one in April 1998, already during the so-called ‘Technology Test Phase’ after helium boil-off¹. The first event was clearly registered by all four ISO instruments (a detailed description of the effects produced on the detectors is given in Heras 2001, [77]), while the second one had measurable effects on the ISO Star Tracker, as an increased false count rate. Neither of these events contributed significantly to the overall degradation of the satellite in comparison with the long term effect of the constant radiation belt traversals.

During the science observation window the main source of radiation are galactic cosmic rays. They originate outside the solar system, and mainly consist of protons (85%), α -particles (14%), and a smaller component of heavier ions. The major part of these particles cannot be stopped by the spacecraft shielding

¹A third, softer geomagnetic disturbance occurred in April 1996 (revolution 152) which is also visible in Figure 5.6 only at low energies (upper panel)

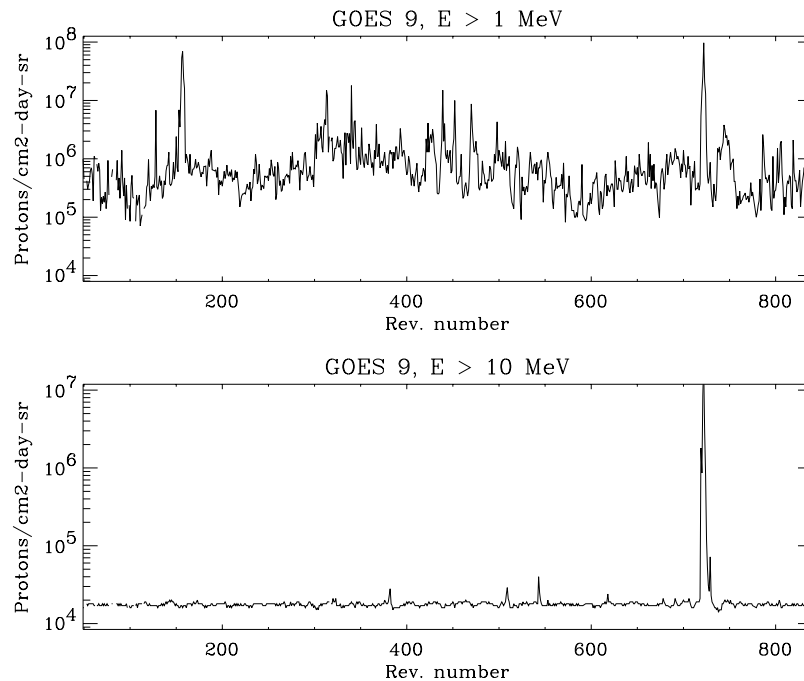


Figure 5.6: *Daily proton fluence measured by the GOES-9 satellite (Space Environment Center, NOAA) during the ISO mission.*

since its differential spectrum peaks roughly between 500 MeV and a few GeV, and are therefore highly penetrating. Due to the high energies involved there is very little that can be done to exclude these effects, and increasing the shielding thickness may in fact be worse since more secondary particles (neutrons, protons, spallation products) can be generated, thus potentially adding to the problem (Nieminen 2001, [129]). The flux of cosmic rays is anticorrelated with the solar activity. This is because during the solar maximum period the expanding heliospheric magnetic field scatters more effectively the arriving charged particles. Apart from the slow variation over the solar cycle (not more than a factor of two in the integral proton fluxes) this radiation environment component is very stable.

5.6.1.2 Glitches in ISO detectors

The main effect produced in the detectors by the space radiation environment is the production of signal spikes or ‘glitches’ caused by particle hits in the detectors. They can have negative or positive polarity and any amplitude between telemetry resolution and saturation.

The detector ‘background’ resulting from the steady cosmic ray bombardment in the science windows, as well as by the energetic electron fluxes in the Earth’s radiation belt and/or from their secondaries form the bulk of the glitches analysed by the four instrument teams.

Upon impinging on the spacecraft, the incident particles can undergo various processes that lead to a modification of the radiation environment as seen at the instrument level. The highly energetic galactic cosmic rays and solar event protons that reach the detectors even after thick shielding leave a trace of ionisation along their track. This can be clearly observed as lines and spots in the detector pixel image, such as in the case of ISOCAM (see Figure 5.7, analysis done by Sauvage 1997, [143]). Numerous secondary particles such as δ -rays and neutrons can also be generated, leading to shower-type particle cascades.

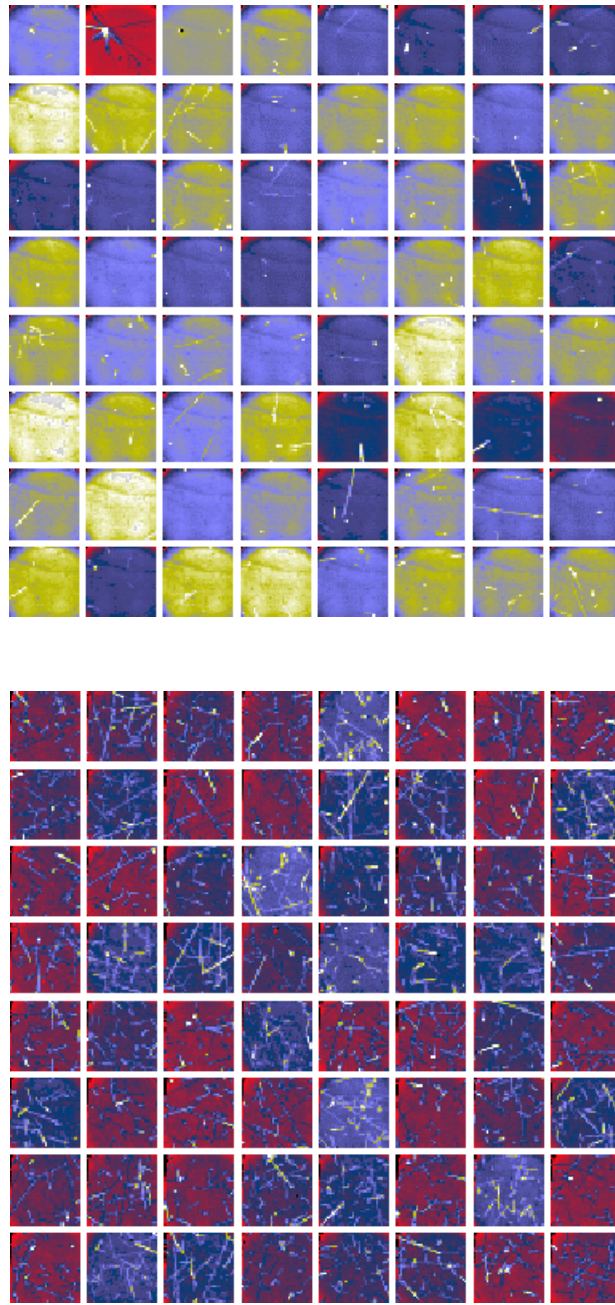


Figure 5.7: Sets of ISOCAM images taken during solar quiet period (upper panel) and during the solar proton event of 4–10 November 1997 (lower panel).

With the minimum shielding of 9 mm Aluminum equivalent, electrons in the outer radiation belt need energies of at least ~ 4 MeV to reach any of the ISO detectors. However, in slowing down in the shielding,

the electrons generate *bremsstrahlung* photons that can be more penetrating than the incident electrons themselves. These electrons and photons may then be observed as an increase in the low-energy part of the glitch spectrum. The average energy deposited by a secondary electron, emitted on absorption of a *bremsstrahlung* photon is 0.1–0.2 MeV in Si and ~ 0.1 MeV in Ge.

Table 5.2 displays the glitch rates per unit area for the different ISO detectors as measured in-orbit. The results show that when comparing values for the same detector material, the observed glitch rates agree within a factor of 2–3.

Table 5.2: Comparison of observed glitch rates and minimum deposited energy in the ISO detectors.

Detector type/ Instrument	Glitch rate [$\text{cm}^{-2}\text{s}^{-1}$]	Minimum deposited energy [keV]
Si:Ga		
CAM	14.9	-
PHT-P1	6.5	1
PHT-S	5.8	1
SWS	10.0	1
Ge:Be		
LWS	6.3	1.9
SWS	17.8	0.95
SWS-FP	10.1	0.95
Ge:Ga		
PHT-P3	10.1	1
PHT-C100	12.5	1
LWS	7.0	1.2
PHT-C200 (stressed)	7.3	1
LWS (stressed)	6.7	1.3

The same analysis can be made for the observed glitch height (deposited energy) distributions. Again, the results obtained are consistent for detectors made of the same material (Heras 2001, [77]).

Considering the diversity of instrument designs, instrumental data and software used, the differences found can be attributed to: i) instrument shielding; ii) cross-talk between detectors, iii) the efficiency in the detection of small glitches, which is particularly important because they are the most numerous; iv) the uncertainty in the values of the photoconductive gain (especially for LWS), which affects the conversion from voltage jumps to energy deposited in the detectors; and v) the number of undetected glitches due to saturation.

Glitch rates per unit area and glitch height (energy deposited) distributions can also be predicted for the different ISO instruments and detectors with the help of Monte-Carlo simulations based on ray-tracing techniques or with full simulations of the physical processes occurring along the track of the incident particles and their secondary particles, taking into account also the local shielding (this second approach was only needed for LWS since for the other three instruments the ray-tracing method provided a fair agreement with in-flight data). A detailed description of the results obtained from these simulations can be found in Heras 2001, [77] and references therein.

The comparison of the observed energy deposited distributions with the results of ray-tracing simulations which model primary cosmic ray-induced glitches only shows a good agreement at high energies, but the peak of the observed distributions at the lowest deposited energies are not reproduced, especially in the Ge:Be detectors. In addition, the observed glitch rates are between 1.5 and 4 times higher than the predicted values. These facts, together with the correlation found between glitch rates and the electron

flux measured by the GOES-9 spacecraft, lead to the conclusion that between 30 and 75% of the observed glitches are caused by δ -rays and other secondary particles produced by cosmic rays and the environment protons and electrons in the detectors and in the instrument and satellite shields (Heras et al. 2001, [78]). Glitches were detected and removed from ISO data following deglitching algorithms implemented in the ISO Off-Line Processing pipeline. In some cases more sophisticated deglitching methods have been provided in the Interactive Analysis software packages. They are described in detail in Heras 2001, [77] and references therein, or in the instrument specific volumes (II to V) of this Handbook and, thus, will not be discussed here.

5.6.1.3 Other radiation induced effects on the detectors

Although radiation effects are mainly recognised by the presence of glitches in the science data, in some cases they are also associated with temporal changes in detector responsivity, dark current levels and noise.

SWS: The space radiation environment affected the long term behaviour of band 3 Si:As SWS detectors, causing their dark current levels, and in some cases, their dark current noise, to increase during the mission. The other SWS detector bands were stable and did not show long term trends. Some of the worse band 3 detectors cured spontaneously (e.g. detectors 34 and 36), that is, their dark currents and noise decreased suddenly to launch levels without apparent reason. Laboratory tests in which Si:As detectors were irradiated with 100 MeV protons during long periods reproduced successfully the in-orbit behaviour. Although no curing procedure could be found, it was decided to operate the detector at a lower bias than initially planned, which reduced the damaging radiation effects and kept the dark currents and noise at acceptable levels during the mission (Heras et al. 2001, [78]).

LWS: A similar behaviour was observed in LWS detectors. Sudden voltage jumps produced by impacts affecting a given integration ramp were followed by a change in the detector responsivity in the following ramps. In addition to these ‘positive’ glitches, ‘negative’ ones have also been found. These caused a sudden decrease in the ramp voltage, and are thought to be produced by hits on the FET. Negative glitches did not appear to affect the detector responsivity (Swinyard et al. 2000, [156]). The overall responsivity of the detectors increased with particle hits during the orbit. To re-normalise the responsivity, the bias current was increased beyond the breakdown voltage for each detector twice in every orbit: a first bias boost on exit from the Van Allen belts; and a second one half way through the 24 hour orbit. Dark currents were not affected by the cosmic rays and remained constant during an orbit. The change in responsivity between bias boosts was monitored by the use of the infrared illuminators. This way it was possible to correct for the overall drift in responsivity with time during an orbit in the processing pipeline.

CAM: In ISOCAM, responsivity variations were also detected after perigee passage due to the very high radiation dose coming from trapped particles in the Van Allen belts. In extensive radiation tests performed before launch it was already found that γ -ray sources, protons and heavy ions impacting the detectors induced a responsivity increase which relaxed in a few hours. The effect was minimised if the photo-conductor was polarised and exposed to a high infrared flux. In-orbit, during the perigee passage, since the instrument was switched-off, a specific power supply kept a bias voltage on the photo-conductors, and the camera was left open to light. The responsivity variation often remained below 5% in the science window. Apart from *common* glitches, other types of glitches were detected in ISOCAM data and classified as: *faders*, where the pixel value decreases slowly until a stabilised value is reached (Figure 5.8); and *dippers*, where the pixel value decreases first below the stabilised value, and then increases slowly until the stabilised value is reached (see Figure 5.9). While *common* glitches are interpreted as induced by both trapped and galactic protons and electrons, *faders* would be induced by energetic protons, electrons and light galactic ions, and *dippers* would be induced by heavy galactic ions (Claret et al. 2000, [25]). The effect of glitches are not so dramatic for SW detectors as for LW detectors. This is because the active zone of the pixel is very thin, $< 10 \mu\text{m}$, so that its volume is very small. Due to the very low energy

needed to create a free carrier pair, the charge generation is equivalent for both SW and LW detectors, but the pixel geometry of the SW array ensures that most of the particles cross only one pixel. After a hit the responsivity of the pixel decays slowly to its previous value. The decay time is the same as for transients due to IR flux changes (see Section 5.6.2). The lower the illumination of the array, the longer the decay time.

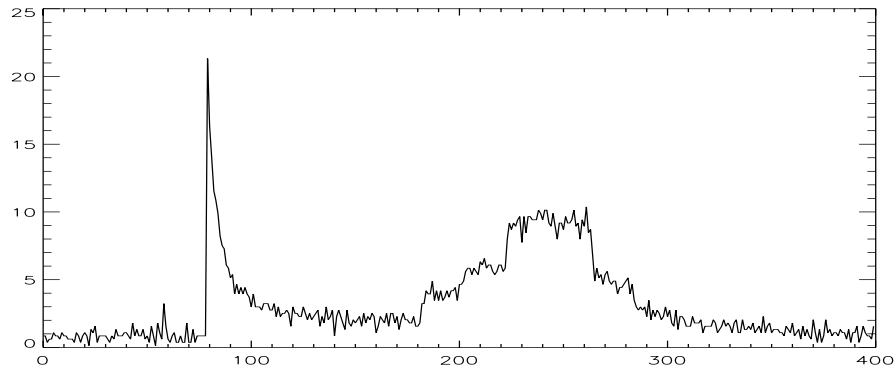


Figure 5.8: *Temporal flux history of a pixel of the LW detector array which was hit by a fader glitch, showing a long tail. The flux in ADU is plotted against time given by the exposure index. The large structure corresponds to a source detection.*

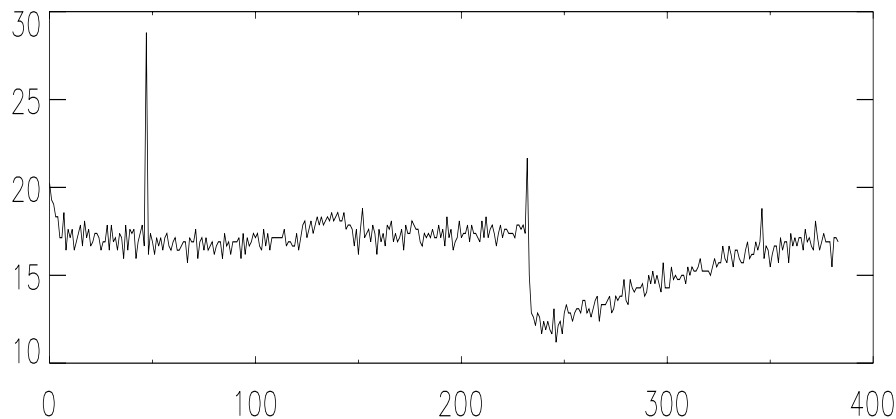


Figure 5.9: *Temporal flux history of a pixel of the LW detector array which was hit by a dipper glitch with a negative tail. The flux in ADU is plotted against time given by the exposure index. Note the gain variation of about 5 ADUs which appears after the second glitch.*

PHT: The continuous hits of high energy particles during the ISO orbit also increased the responsivity of PHT detectors at short term and long term scales. At short term scales the disturbance of an integration ramp after a hit was usually followed by a tail-like signal excess lasting a few integration ramps, which is interpreted as a momentary response variation. At long term scales, already during the pre-flight calibration tests it was found that the responsivity of the detectors increased after exposing them to high energy radiation. The same behaviour was found in-orbit, affecting mostly the responsivity of the Ge-based, low bias voltage far-infrared detectors (P3, C100 and C200), whereas the Si-based, high bias voltage

detectors P1, P2 and PHT-SS showed only small changes in their responsivity. An exception was the PHT-SL array which showed a similar, but less pronounced behaviour as the FIR detectors. This change of responsivity was also found to be correlated in-orbit with the geomagnetic activity and the electron fluxes, increasing systematically (by 20–50%) one or two days after the onset of a geomagnetic storm. P3 and C100 showed the largest changes, followed by C200 (Castañeda & Klaas 2000, [14]). Due to the high radiation doses during perigee passage the responsivities and noise levels of the ISOPHOT detectors were strongly increased before the beginning of every new science window. Therefore, appropriate curing procedures were designed for the different detectors to restore the nominal responsivities. The procedures were applied after the switch-on of the instrument, before the beginning of the science window. For the doped germanium detectors (P3, C100 and C200) they consisted of a combination of bright IR-flashes using one of the FCSs and a bias boost (absolute increase of the bias voltage). For the doped silicon detectors (PHT-SS, PHT-SL, P1 and P2) curing was achieved by exposing the detector to a higher temperature at a reduced bias voltage for a defined period of time. In addition, P1 underwent an infrared flash curing. The doped germanium detectors were much more susceptible to drifts caused by accumulating effects of the high energy radiation impacts. In order to keep their responsivities within the nominal range a second curing procedure was applied around apogee passage in the handover window, when the satellite control was switched from VILSPA (Madrid) to Goldstone (California). Trend analysis performed immediately after the curing procedure showed that the nominal responsivities were re-established with $\pm 2\%$ accuracy for all detectors, if the space environment conditions were stable. On the other hand, low energy glitches also affected the measurements by increasing the dark current level and the detector noise. The consequence was an increase of the minimum measurable signal, or equivalently, a decrease of the sensitivity limit. All these effects are associated with the generation of electron-hole pairs in the bulk of the detectors during the irradiation, and with the capture of the minority carriers by the compensating impurities.

5.6.2 Detector transients

The operation of infrared detectors in space is strongly complicated by memory effects. These detectors are usually doped silicon and germanium bulks with implanted low ohmic contacts used as extrinsic photoconductors and are characterised by a transient response after flux changes.

A large number of such detectors were used on board ISO (see Table 5.3). From this point of view, the ISO satellite was a very interesting laboratory since several technologies and detector materials (Ge:Be, Ge:Ga, In:Sb, CID In:Sb, Si:As, Si:Ga, Si:B) were used to cover a wide spectral range from 2.5 to 240 μm .

Some of these detectors exhibit long time constants and it was usually not possible to wait for current stabilisation when they were exposed in space to sources of infrared emission, making the determination of the input fluxes a very difficult task. Without any correction, the errors induced by the transient effects can be as large as 50% in some cases. However, in some of the ISO detectors and under certain circumstances, the response after a flux change was highly reproducible, which gives sense to look for models and to correct the data for these transient effects.

Before launch, ground-based tests were extensively performed (CAM - Pérault et al. 1994, [136]; PHT - Groezinger et al. 1992, [65]; Schubert et al. 1994, [146]; Schubert 1995, [145]; SWS - Wensink et al. 1992, [164]). Unfortunately, as a result of these ground-based tests it was not possible to develop an accurate model for transients in SWS and CAM. Only for PHT-S a promising non-linear model was proposed (Fouks & Schubert 1995, [54]), that was later corrected to introduce the effect of temperature variations.

During the ISO mission, several linear and non-linear models were suggested for the various ISO instruments and observing modes. It became evident that the models should be non-linear and non-symmetrical and take into account the illumination history of the detector.

Analytical models were developed for infrared detectors by Vinokurov & Fouks 1991, [162], from the non-linear equations describing such detectors (Vinokurov & Fouks 1991, [162]; Haegel et al. 1999, [71]). One of these models, the so-called ‘Fouks-Schubert’ model (Fouks & Schubert 1995, [54]), was the one used for

Table 5.3: *List of the IR detectors on board ISO with indications of type, operating wavelengths (peak or range) and detector topology (individual pixel, linear or matrix array).*

	Detector Name	Type	Wavelength (μm)	Pixels
CAM	SW	CID In:Sb	2.5 – 5.5	32×32
	LW	Si:Ga	4.0 – 18.0	32×32
PHT	SS & SL	Si:Ga	15, (peak)	64×1
	P1	Si:Ga	15, (peak)	1
	P2	Si:B	25, (peak)	1
	P3	Ge:Ga	100, (peak)	1
	C 100	Ge:Ga	100, (peak)	3×3
	C 200	Ge:Ga (stressed)	180, (peak)	2×2
SWS	band 1	In:Sb	2.38 – 4.08	1×12
	band 2	Si:Ga	4.08 – 12.0	1×12
	band 3	Si:As	12.0 – 29.0	1×12
	band 4	Ge:Be	29.0 – 45.2	1×12
	FP band 5	Si:Sb	11.4 – 26.	1×2
	FP band 6	Ge:Be	26.0 – 44.5	1×2
LWS	SW1	Ge:Be	43 – 51	1 detector
	SW2-SW5, LW1	Ge:Ga	50 to 121 (10)	5 detectors
	LW2-LW5	Ge:Ga (stressed)	108 to 197 (20)	4 detectors

describing transients in PHT-S detectors during the ground-based tests, as we have already mentioned. This is a simplified analytical model which is able to reproduce the behaviour of Si:Ga detectors with high accuracy.

The Fouks-Schubert model and the basic equations involved are described in Coulais et al. 2000, [36], and references therein. The Fouks-Schubert formula, which describes the detector behaviour when starting from an unstabilised current J_{n-1}^{end} at the end of block $n - 1$ is:

$$J_n(t) = \beta J_n^\infty + \frac{(1 - \beta) J_n^\infty (J_{n-1}^{end} - \beta J_{n-1}^\infty)}{(J_{n-1}^{end} - \beta J_{n-1}^\infty) + [(1 - \beta) J_n^\infty - (J_{n-1}^{end} - \beta J_{n-1}^\infty)] \exp(-J_n^\infty t / \lambda)} \quad (5.2)$$

where the time t is measured from an arbitrary instant after the flux change at time $t = 0$, β is the instantaneous jump and λ is a constant. The unstabilised current J_{n-1}^{end} before the flux change reflects the history of the detector (stabilisation in block $n - 1$ is achieved when $J_{n-1}^{end} = J_{n-1}^\infty$); J_n^∞ is the steady-state current under the constant incoming flux during block n .

This simple non-linear analytical formula (Equation 5.2), which takes into account the memory effects, describe the processes in the detector bulk, with the use of Fouks' boundary condition (Fouks 1981a, [50]; 1981b, [51]) that describes the properties of the detector contacts. This boundary condition has the form:

$$p(0, t) = p(0, 0) \exp \left[\frac{\Delta E(0, t)}{E_j} \right] \quad (5.3)$$

where $p(z, t)$ is the hole concentration at the plane z measured from the injecting contact placed at the plane $z = 0$, the time t is measured from an arbitrary instant, as in Equation 5.2, $\Delta E(0, t)$ is the change of the near-contact field with time ($\Delta E(0, t) = E(0, t) - E(0, 0)$), and E_j is the injection ability of the

contact. Equation 5.3 allows to describe the contact properties with a high precision (Fouks & Schubert 1995, [54]) and, in addition, to take into consideration additional technological and engineering effects inherent to real detectors (Fouks 1997, [52]).

The use of Equation 5.3, instead of a detailed consideration of the processes which occur inside the near-contact space-charge region, strongly simplifies the description of transient currents. Nevertheless, in general the problem remains rather complex even after this simplification. However, in the case where E_j is much less than the steady-state field in the detector bulk $E_0 = V_0/l$ (where V_0 is the steady-state voltage applied to the detector, l is the inter-contact distance), this description can be additionally strongly simplified, and Equation 5.2 serves as a very exact description for transient currents (Vinokurov & Fouks 1991, [162]). The parameter E_j quantifies the quality of the contacts and depends on the flatness of the donor profile in the near-contact region and is linked to the time constant of the current relaxation. The higher the contact quality, the less is E_j , and the shorter the time constant. In real detectors at liquid helium temperatures E_j is of the order of 10^2 – 10^3 V/m. For Si:Ga detectors E_0 is considerably high, typically 10^5 – 10^6 V/m, which provides a very high accuracy to Equation 5.2. In Ge:Ga detectors E_0 , however, E_0 is of the order of E_j , thus making this formula not so exact.

The other important point lies in the fact that Equation 5.2 is applicable only when the illumination is uniform on the pixel surface. In this case, high photoelectric non-stationary cross-talking between adjacent pixels, that are inherent to such detectors (Fouks & Schubert 1995, [54]), compensate each other, which makes the electric field uniform along the planes z and the used one-dimensional equations true. Under non-uniform illumination the set of one-dimensional equations cannot be used, and Equation 5.2 loses its accuracy (Vinokurov & Fouks 1988, [161]; Vinokurov et al. 1992, [163]).

5.6.2.1 Si:Ga detectors

Several Si:Ga detectors were on board ISO (see Table 5.3): the LW 32×32 matrix array of ISOCAM; the band 2 (a 1×12 linear array) of SWS; and the PHT-SS, PHT-SL and P1 detectors of ISOPHOT.

The LW detectors of ISOCAM present strong transient effects. The worst situations occurred in two cases:

1. illuminating the array after having the detectors in the dark (dark position of the entrance wheel);
2. after a saturating flux.

The first problem could be reduced for the LW array by keeping always light on the array (e.g. with the so-called ‘CAM parallel mode’, see Section 3.6 of the ISO Handbook Volume II on ISOCAM, [11]) and sorting the observations by decreasing fluxes. In addition, dark calibrations were always placed at the end of the observations or in those revolutions without ISOCAM science activity in prime mode.

The transient behaviour of the LW channel has two main components (see Figure 5.10): a short term one which consists of an initial jump typically of about 40–60% of total signal step, followed by a long term drift with small amplitude oscillations (typically 5–10% of the flux) and can last hours (Abergel et al. 2000, [1]; Coulais & Abergel 2000, [35]).

Upward and downward steps are not symmetrical (downward steps are hyperbolic-like) and the short term response at a given time strongly depends on the past of the observation and also on the spatial structure of the input sky (e.g. uniform emission or point sources).

Under quasi-uniform illumination the short term transient response of individual LW pixels can be described by the Fouks-Schubert model with an accuracy around 1% per readout for all pixels except near the edges. (Coulais & Abergel 2000, [35]). This model is fully characterised by the two parameters (β , λ) above mentioned, which are determined for each pixel in the array. No significant changes of these parameters were observed during the whole in-orbit ISO life per pixel, so that only one 32×32 map for each parameter was used when this correction was applied in the data reduction pipeline. In addition, the dispersion found in the values derived from pixel to pixel indicates that:

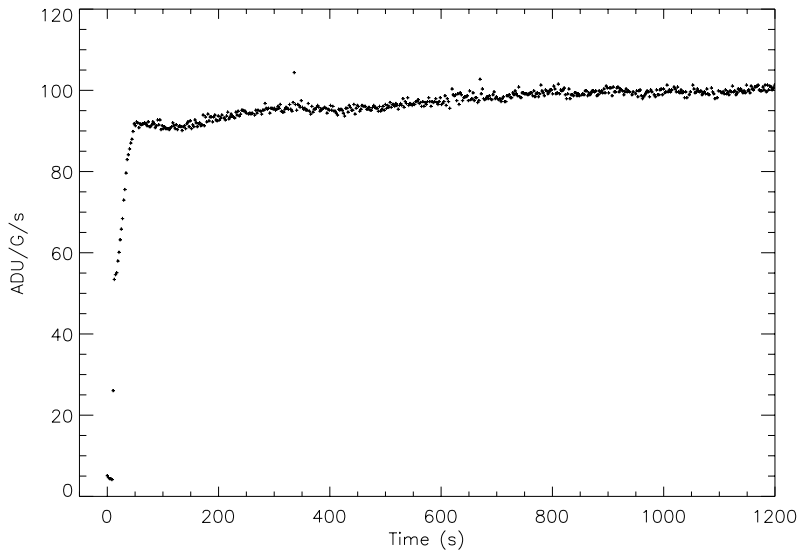


Figure 5.10: *An example of the transient behaviour of LW-CAM detectors. This is an observation which starts just after the switch-on of the instrument at the begin of a revolution. We clearly see the two components of the transient response: the short term transient from time ~ 0 s to ~ 50 s, which is the transient response described by the Fouks-Schubert model and, from ~ 100 s to the end, the response change due to the long term drift.*

1. the bulk quality of the matrix array was rather good and uniform, but
2. the quality of contacts was not uniform and far from theoretical limits.

In the LW array, the pixels are defined only by the electrical field applied between the upper electrode and the bottom 32×32 contacts. As a consequence of the electrical design of the matrix array, the adjacent pixels are always affected by cross-talk effects (Vigroux et al. 1993, [160]). Under uniform illumination these cross-talks compensate each other and can be ignored but this is not the case when the input sky contains strong fluctuations with typical angular scale around the pixel size (e.g. point sources with gradient between pixels typically higher than 20 ADU/s). Thus, the one-dimensional Fouks-Schubert model fails for such point sources, and three-dimensional models are required.

The LW-CAM data contained in the ISO Data Archive are corrected for transients using the ‘standard’ one-dimensional Fouks-Schubert model above described. This means that the results obtained in fields with bright point sources or very steep gradients after applying this correction are not so accurate, although this is still within the few percent level.

Recently, a new simplified three-dimensional model for point source transients has been developed by Fouks & Coulais 2002, [53]. This model uses the same (β, λ) parameters which were used for the uniform illumination case and is able to qualitatively reproduce real point source transients. The model predicts e.g. that, starting from the same initial level, the stronger the source the faster the transient response and the higher the initial overshoot, as it is observed in real data, and it works better for configurations in which the PSF is narrow. A more complicated three-dimensional model, able to account for quantitative effects taking into account the true geometrical and electrical specificities of LW detectors, is still under development

With respect to the remaining effects above mentioned (long term drift, small amplitude oscillations,..) no physical models exist yet to describe the detector behaviour and only empirical dedicated processing methods have been developed so far. Two approaches exist for the extraction of reliable information from

raster observations affected by long term drifts. For the case of faint point sources, as in cosmological surveys, source extraction methods are discussed in Starck et al. 1999, [152] and Désert et al. 1999, [45]. For raster maps with low contrast large-scale structure (as in the case of diffuse interstellar clouds) a long term drift correction method is available in CIA. This method was developed by Miville-Deschênes et al. 1999, [121] and is based on the use of the spatial redundancy in raster observations to estimate and to correct for the long term drift (see Figure 5.11).

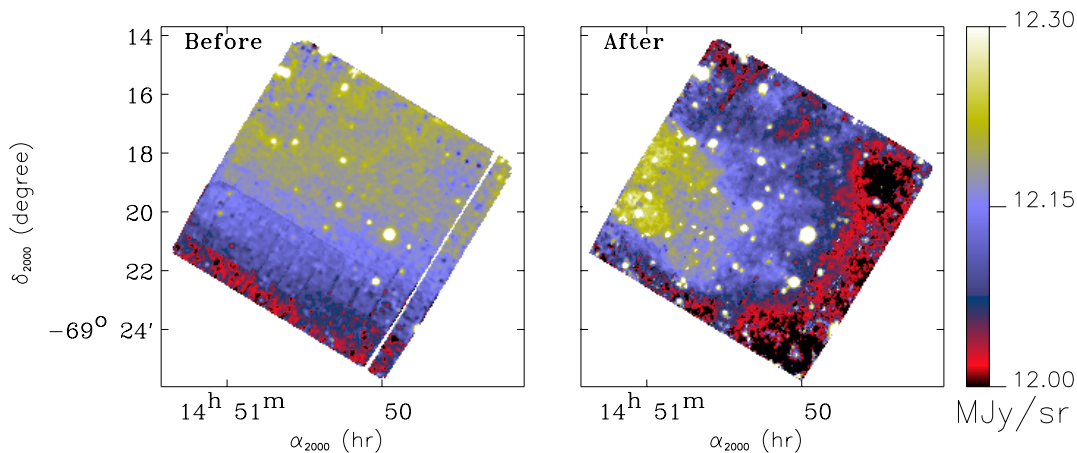


Figure 5.11: When the contrast of the observed object is very low, and when the observations suffer from long term transient effects, it is important to use a correction method based on the spatial redundancy in raster observations. In the present case, the structure of a low contrast diffuse interstellar cloud is recovered (see Miville-Deschênes et al. 1999, [121] for more details).

For ISOPHOT Si:Ga detectors (P1, PHT-SS and PHT-SL detectors), and although a good agreement was achieved between transients and Fouks models during ground-based tests, the application of these models to real in-flight data was unsuccessful. Several facts can explain the change in the behaviour of the detectors:

- the effect of high energetic particles hitting the detectors generated electron-hole pairs resulting in visible glitches and in accumulation of invisible positive (hole) and negative (electron) charges captured in the bulk.
- the electrical curing used in-orbit could not completely restore the detector parameters

Typical drift curves in P1 detectors are shown in Figure 5.12. In case of a flux drop, a signal decay and in case of increasing flux steps, a signal rise is observed. In addition, a hook response during the first 40 seconds is also observed for large positive flux steps. The signal shows a behaviour similar to a strongly damped oscillation around the asymptotic level. For even higher flux steps the signal behaviour can be restricted to an overshoot followed by a slow decay. Doped silicon detectors tend to show a longer stabilisation time than doped germanium detectors (P3, C100 and C200 in the case of ISOPHOT), which can go from just a few seconds to hours. The relative stabilisation time is faster for positive flux steps. and steps at low flux levels take more time to stabilise. In addition, the stabilisation time also depends on the temperature of the detector.

In OLP no sophisticated treatment of transients was applied to staring PHT-P1 observations. Instead, an algorithm was used which determines per chopper plateau whether a significant signal drift is present based on the application of the non-parametric Mann statistical test to the signals (Hartung 1991, [74]). In case such a drift is found, only the last stable part of the chopper plateau is used. Of course, this

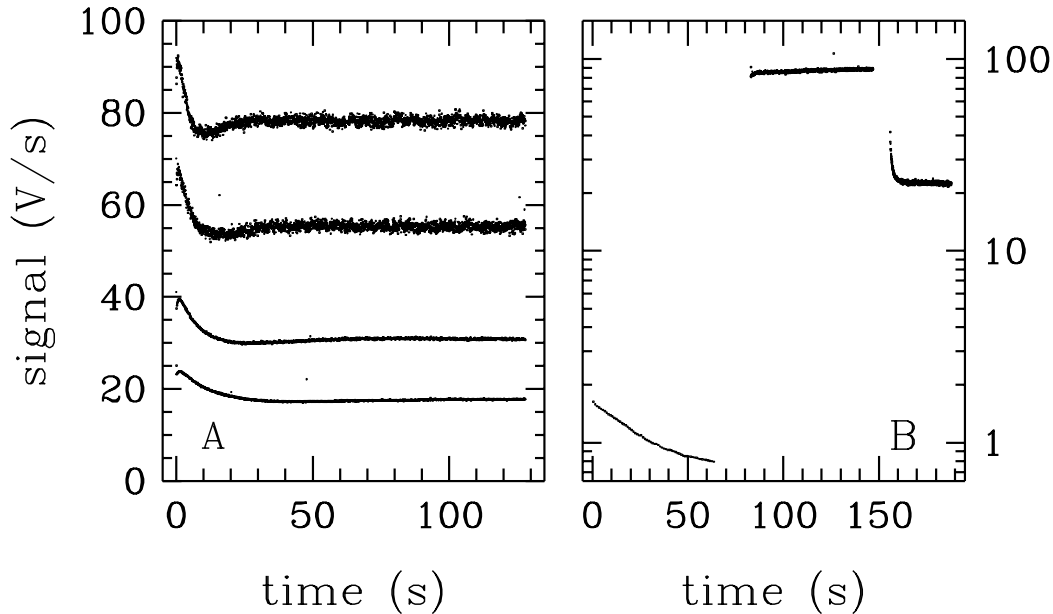


Figure 5.12: *Examples of P1 detector transients. Left panel (A): 4 transient curves after a flux step overplotted in the same graph for comparison, the highest curve corresponds to the largest positive flux step. In all cases the signal prior to each step was the same and had a strength of about 35 V/s. For these flux steps a signal overshoot is detected followed by a strongly damped oscillation. Right panel (B): multi-filter observation of the star HR6705, filter sequence P_16 (64 s integration), P_3.6 (64 s) followed by the P_3.6 (32 s) FCS measurement. Both the P_16 as well as the P_3.6 FCS measurement show a downward drift, with a longer stabilisation time for the fainter P_16 signal.*

correction only works satisfactorily for measurements which are long compared to the stabilisation time. This ‘drift recognition’ method is explained more in detail in Section 7.3 of the ISO Handbook Volume IV on ISOPHOT, [107].

In the case of chopped PHT-P1 observations, non-stabilised signals cause significant losses on the true difference signal. Signal derivation in OLP relies on the analysis of signals from pairs of consecutive readouts rather than signals per ramp. This gives better statistics of the signals per chopper plateau, since in many chopped measurements each chopper plateau covers only a few (typically 4) ramps. To increase further the robustness in determining the difference signal, the repeated pattern of off-source and on-source chopper plateaux is converted into a ‘generic pattern’. The generic pattern consists of only 1 off- and 1 on-source plateau and is generated using an outlier resistant averaging of all plateaux. The shape of the generic pattern determines the correction factors to apply with regard to stabilised staring measurements of a sample of calibration standards.

For PHT-S observations taken in staring mode an alternative approach was developed, known as the ‘dynamic calibration’ method, which performs the calibration measurement by comparing the transient behaviour of the unknown source with that of celestial standards of similar brightness. Then, the transients which show the same time scale and amplitude for both measurements cancel out in the calibration process. This method works only for staring PHT-S observations because the flux history of PHT-S pixels is similar in all observations as they always start with a 32 s dark measurement which is followed by the real measurement. A detailed description of how the flux assignment is performed and the library of calibration standards and model spectra used for the application of this method can be found in García-Lario et al. 2001, [60]. The ‘dynamic calibration’ brings down the errors associated to this observing

mode (sometimes as high as 30%) to just a few percent.

Note that this accuracy is not applicable to raster measurements made with PHT-S, which also generally suffer from transient effects, because the assumption of a flux history similar to that used for the calibration stars is not met for all raster points in a map except for the first one. Thus, only a static spectral response function can be applied in this case. The photometric calibration of each raster point is performed by converting the signal to a flux using an average spectral response function for PHT-S staring observations derived from 40 observations of 4 different standard stars with different brightness.

The same argument is applicable to chopped PHT-S observations. Thus, for this observing mode a ‘drift recognition’ routine similar to the one used for P1 detectors was implemented in OLP to detect the presence of a significant signal transient on a chopper plateau. When a transient is detected, a range of unreliable signals are flagged. The signal so derived is then corrected assuming a spectral response function corrected for chopper losses. The Fouks-Schubert model is not applicable in this case because the sources are usually very faint and the signal-to-noise ratio is too low for the fitting procedure to work properly. Thus, although the possibility exists in PIA of applying the Fouks-Schubert correction to faint sources observed in chopped mode, the above alternative approach was used to calibrate these sources in the automated pipeline. More details on the method applied and the calibration of the standard stars used for this purpose are given in García-Lario et al. 2001, [60].

An overview of the various transient behaviours observed for the different SWS bands as a function of the detector material is shown in Figure 5.13, where we can see that band 2 (Si:Ga) and band 4 (Ge:Be) are those affected by the largest memory effects.

The signature of memory effects in the Si:Ga band 2 of SWS is that the up- and down-scans are different in flux level (up to 20% for sources with fluxes greater than about 100 Jy). The down-scan normally succeeds the up-scan in the AOT and appears to be already ‘accustomed’ to the flux level.

For band 2 SWS data, an adapted version of the Fouks-Schubert model was developed by Do Kester (Kester 2001, [98]) and successfully implemented in the legacy version of the SWS pipeline to correct this band for transient effects as well as in the Observers’ SWS Interactive Analysis (OSIA) software package (version 3.0). The method brings the errors (sometimes up to 20% originally) down to the few percent level.

A complete description of the procedure followed and how the correction was implemented in the pipeline can be found in the ISO Handbook Volume V on SWS, [108]. Additional details are provided in Kester 2001, [98] and García-Lario et al. 2001, [60].

5.6.2.2 Ge:Ga detectors

Several Ge:Ga detectors were also set up for use on board ISO (see Table 5.3): one detector (P3) and two small matrix arrays for PHT (C100 3×3 pixels and stressed C200 2×2 pixels); and several stressed (4) and un-stressed (5) monolithic detectors for LWS. All of these detectors were affected by transient effects which can bias the final photometry typically from 10 to 40%.

As we have already mentioned, the present status of our understanding of transients in Ge:Ga detectors is less favorable than for Si:Ga detectors. Based on the ratio E_0/E_j , Ge:Ga detectors are unfortunately always in an unfavourable domain for the application of the Fouks-Schubert model correction.

At first sight these transients appear easier to model than the Si:Ga ones because they are at first order exponential (Church et al. 1993, [22]). Thus, the use of non-linear models seems to be *a priori* less necessary in order to take into account the memory effects. However, the correction is not as precise as the one obtained for Si:Ga detectors using non-linear models. The expected accuracy of such simplified analytical models, even if the detector is perfect, is only about 10–20 %. The main problem is that some very important characteristics of such detectors are often not well under control (e.g. contact quality). and, thus, each Ge:Ga detector seems to require a peculiar model (Coulais et al. 2000, [36]).

In general, doped germanium detectors show faster stabilisation times than doped silicon ones (typical time scales are 100 s for P3 and C100, 40 s for C200, and 50 to 100 s for LWS detectors). Some of them

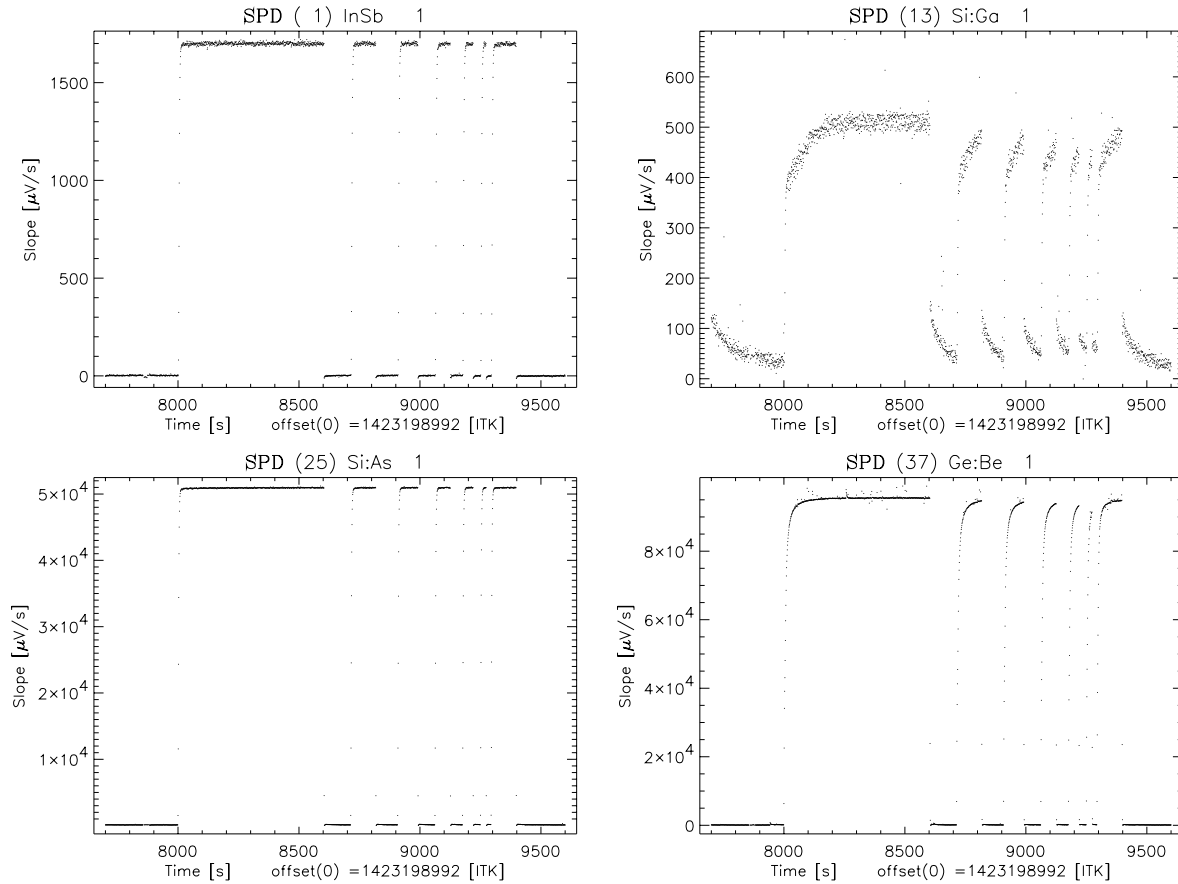


Figure 5.13: *Example of the various transient behaviours observed for the different SWS bands as a function of the detector material (Band 1: InSb; Band 2: Si:Ga; Band 3: Si:As; Band 4: Ge:Be).*

present an initial hook response (quick overshoot) for high upward steps of flux and undershooting after a downward step. The long term response exhibits a time constant which decreases for high fluxes, whereas it strongly increases for low fluxes. This transient component can be well modelled by an exponential function in most cases (Acosta-Pulido et al. 2000, [8]).

Figures 5.14 and 5.15 show the typical transient behaviour observed in P3 detectors at intermediate and low flux levels, respectively. We can see the initial hook response clearly in the intermediate flux example and the longer stabilisation time for low fluxes. In both cases the long term transient behaviour has been modelled with a single exponential function which can be written as:

$$S(t) = S_{\infty} + (S_{ini} - S_{\infty})exp(-t/\tau); \tau = \frac{E}{S_{\infty}^{\alpha}} \quad (5.4)$$

The first analysis shows that τ is inversely proportional to the final signal, S_{∞} , in log-log scale (see Acosta-Pulido et al. 2000, [8]). Therefore, τ can be written as an inverse power law function of S_{∞} . The parameter α describes the behaviour of the transient effects with the illumination and E is a normalisation constant. E and α are parameters which have to be determined for each detector/pixel. In the case of the Fouks-Schubert function α is equal to unity. If the proposed function is a good description of the transient behaviour of the considered detectors, those parameters can be fixed. The stabilised signal

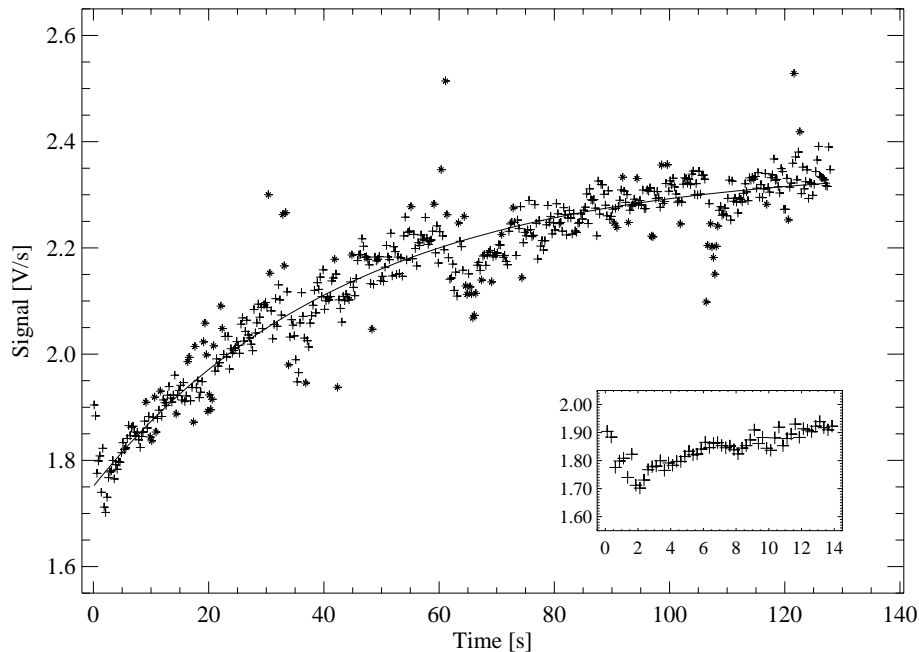


Figure 5.14: *Typical transient behaviour of detector P3 at intermediate flux level (~ 11 Jy at $100 \mu\text{m}$). The measured signals are represented by plus sign symbols. Detected glitches are marked by crosses. The single exponential model is represented by the continuous line through the data points. The initial signal sequence is shown in the inset, where the hook response is clearly recognised.*

is obtained by fitting the above function to the measured signals and leaving S_{ini} and S_{∞} as free fit parameters.

The parameters E and α for the detectors P3, C100 and C200 were determined in-orbit using a large set of long measurements. The measurements were selected if a clear transient behaviour was present, and they were long enough that at the end the photocurrent is close to stabilisation. Nevertheless, this data set may suffer some selection bias: transients with very long time constants (> 1000 s) could not be detected because of the limited observing time; and the flux history may influence the transient as well as the switch-on of the detector every time an observation starts. In the process of determining E and α each measurement was fitted by leaving all parameters free in the above expression and rejecting those fits where the residual rms per degree of freedom was larger than 3.

Table 5.4: *Time constants for the long term transients observed in P3, C100 and C200 detectors derived from the empirical model*

Detector	E	α	r	β
P3	87 ± 8	0.79 ± 0.05	-0.79	~ 0.34
C100	36 ± 3	0.48 ± 0.04	-0.63	~ 0.30
C200	38 ± 2	0.63 ± 0.03	-0.89	~ 0.85

The results obtained from a least square fit are presented in Table 5.4, together with the correlation coefficient r . For P3 and C200 the correlation is very good while it is worse for C100.

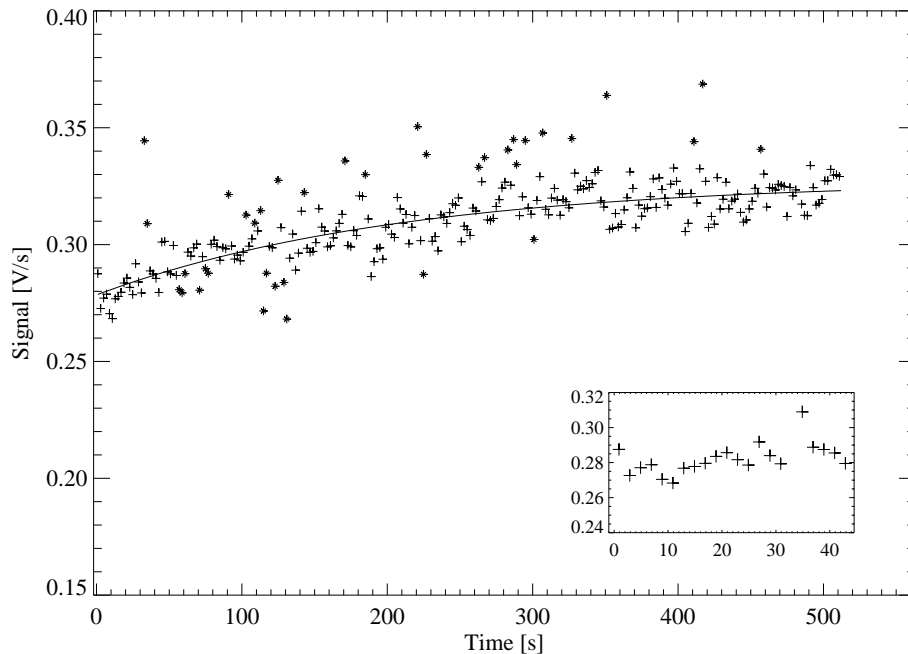


Figure 5.15: Typical transient behaviour of detector P3 at low flux level (~ 2 Jy at $100 \mu\text{m}$). The meaning of the symbols is as in Figure 5.14.

We performed tests using an independent set of measurements other than those used for determining the time constants. The resulting χ^2 distributions are very narrow and peak around 1. The worst case is again the detector C100, for which the χ^2 distribution for all pixels (except pixel 8) is wide and values around 2-3 are frequent. The low frequency noise which affects detectors C100 and P3 when measuring faint targets is likely limiting the goodness of the fit.

According to the values derived and shown in Table 5.4 it is also possible to estimate the fraction of the final signal which is affected by the slow transient component, i.e. the signal difference between the value reached at the initial jump and the final value. The magnitude of this component combined with the time constant determines the accuracy of any measurement after a certain time. For example, a long time constant is not so relevant, if the fraction of the slow component is small compared to the total signal. The magnitude of the slow component can be estimated from the initial jump after a flux change and the knowledge of the final stable current. This has to be derived from chopped measurements where the flux changes are like a step-function. Raster observations cannot be used, because the flux varies gradually as the telescope slews to a different sky position. Results for detectors P3, C100 and C200 are presented in Table 5.4, where β represents the fraction of the total signal difference which is achieved immediately after the flux change. It has been found theoretically that the magnitude of the slow component increases with the photoconductive gain, G (Haegel et al. 1996, [70]). G depends on the material, the electric field and the dimensions of the detector. Detectors P3 and C100 are manufactured of the same material but they have different bias voltages and dimensions, yielding $G[\text{C100}] > G[\text{P3}]$; which is consistent with a larger fraction of the slow component for C100.

We present in Figure 5.16 an example of the application of this single exponential fit model to a measurement taken with detector C100: using the full measurement time of 512 s an error of 6% between the direct measurement of the signal and the model prediction is found. A comparison of the estimates of the final signal using only the first 32 s gives the following results: the value obtained from the ‘drift recognition’ method which is applied in the pipeline is too low by 30%, whereas the value obtained from the empirical model above described is lower by only 12%. This example demonstrates how the use of

this method can significantly improve the photometric accuracy of relatively short measurements.

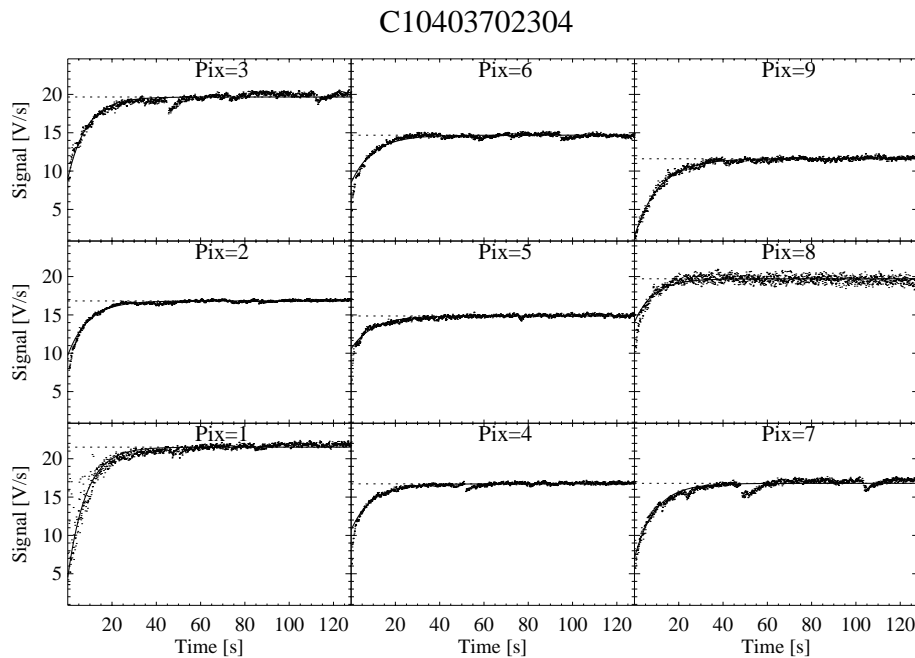


Figure 5.16: *Typical transient behaviour of the nine C100 pixels at high flux level (~ 75 Jy at $80 \mu\text{m}$). The dots represent the measured signals, the solid line the fit and the dashed horizontal line the predicted final signal level.*

Another example, this time applied to detector C200, is shown in Figure 5.17. Again, a single exponential fit has been applied to predict the final signal level with a quite satisfactory result.

However, a detailed analysis of the transient curves, especially for detector C100, reveals the presence of more than one time constant. Solutions consisting on a combination of two (and even three) exponential functions have been found to describe better the drifting curve improving the accuracy of the photometry (Church et al. 1996, [23]; Fujiwara et al. 1995, [56]). Currently, several fitting methods are available in the PIA software used for interactive analysis (Gabriel & Acosta-Pulido 1999, [57]). The main difficulty is to determine the relative importance of the different components.

In the pipeline, a simple ‘drift recognition’ method similar to the one applied in Si:Ga detectors is implemented for PHT-P3 and PHT-C staring observations. If the stability test fails for a given measurement, an empirical solution based on the fitting of an exponential function is tried (Schulz et al. 2002, [148]). Thus, as for the PHT-P1 detectors, the transient correction applied only works satisfactorily for measurements which are long compared to the detector stabilisation time at a given illumination.

In the case of chopped measurements, where non-stabilised signal causes significant losses to the true difference signal, OLP makes use of a ‘pattern recognition’ method similar to the one used also for PHT-P1 detectors. For P3 detectors the accuracy is poor when the fluxes are below between 0.2 and 1 Jy (the exact number depends on aperture size and chopper throw), due to cirrus confusion and the restricted number of sky references longward of $80 \mu\text{m}$. For C100 and C200 the accuracy is also strongly limited when the fluxes detected are below 0.2 Jy and 1 Jy, respectively. In this case the chopper offset correction, being the zero point of the signal correction, is less accurate and the relatively bright sky background and the small number of reference positions make an estimation of the cirrus confusion noise necessary.

Finally, no transient correction was implemented in the pipeline for PHT32 chopped raster maps because of the high interactivity needed in the processing to correct these maps for transient effects. A processing

C20159402607

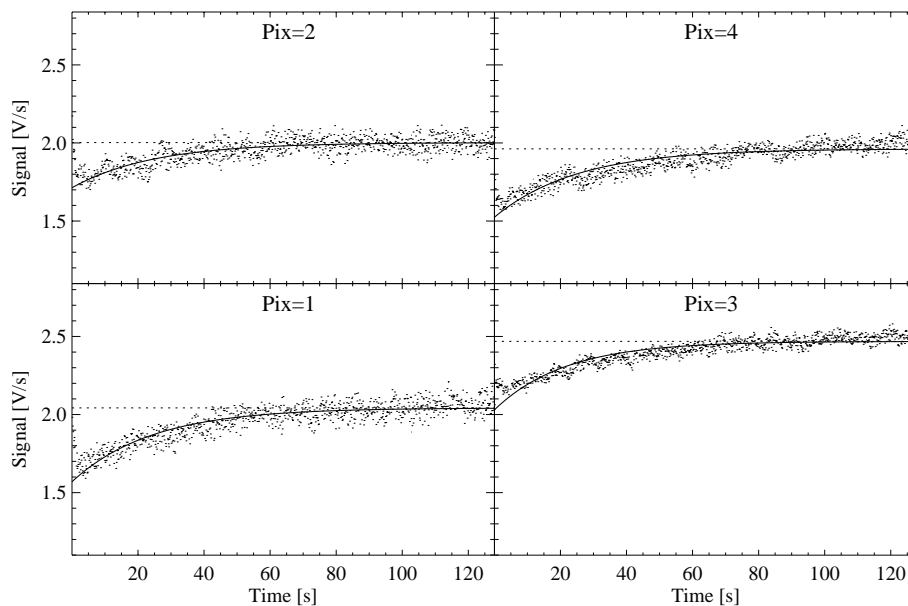


Figure 5.17: Typical transient behaviour of the four C200 pixels at high flux level (~ 60 Jy at $150 \mu\text{m}$). The meaning of the symbols is as in Figure 5.16.

tool including full transient modelling developed by Richard Tuffs (from MPI-Heidelberg) is available in PIA and details on its application to real data can be found in the proceedings of the *ISOPHOT Workshop on P32 Oversampled Mapping*, [149].

LWS Ge:Ga detectors present also memory effects, due to their slow response times (typically tens of seconds, as already mentioned) to changes of illumination (Church et al. 1992, [21]). As for the other Ge:Ga detectors on board ISO the typical transient behaviour of both LWS stressed and unstressed detectors consists of a long term component due to the steady accumulation of particle hits during each revolution and a short term component caused by the changes in flux.

In general, after a flux change, the immediate reaction is quick, and in some cases the detector overshoots, producing the characteristic hook response, but the detector output can take a considerable time to settle the final level. Specific laboratory tests were made before launch (Church et al. 1996, [23]) showing that the detectors actually react on a variety of time scales depending on the initial and final flux levels.

Church et al. 1996, [23] found that the response of LWS Ge:Ga detectors to a step change in flux could be modelled empirically by a function containing three exponential time constants, with typical values of <1 , 5 and 30 seconds (for unstressed Ge:Ga detectors) and 0, 10 and 100 seconds (for stressed Ge:Ga detectors). However, the general behaviour and appearance of the hook response depends on bias and operating temperature, as well as on the flux levels. The main difference between the stressed and unstressed Ge:Ga detectors is in the speed of the hook response (faster in the stressed Ge:Ga detectors). The time constants generally decrease with increasing flux step. In all cases the transient response after a decreasing flux step is faster than the response after an increasing flux step. Kaneda et al. 2001, [92] uses a step and two-component exponential model to fit the step response of these detectors and shows that the transient response time decreases with an increase in both the initial and final incident flux levels.

The in-orbit transient response of the detectors is most clearly seen in the illuminator flashes that provide the basic sensitivity drift calibration. These are steps in flux levels that mirror the laboratory tests, but these sequences are much shorter and not all the effects appear as described above. Sample illuminator

flashes are shown in Figures 5.18 and 5.19 for detectors SW4 (unstressed Ge:Ga) and LW2 (stressed Ge:Ga) respectively, which are those affected by the largest transient effects. For these detectors the slow long term response is the main problem as the flux is still increasing at the end of the flash. SW3 (unstressed Ge:Ga) and LW4 (stressed Ge:Ga) also show the same effect to a lesser extent. The remaining detectors are rather better behaved, e.g. the stressed LW5 (see Figure 5.20), although LW1 (unstressed) and LW3 (stressed) invariably show also a hook response.

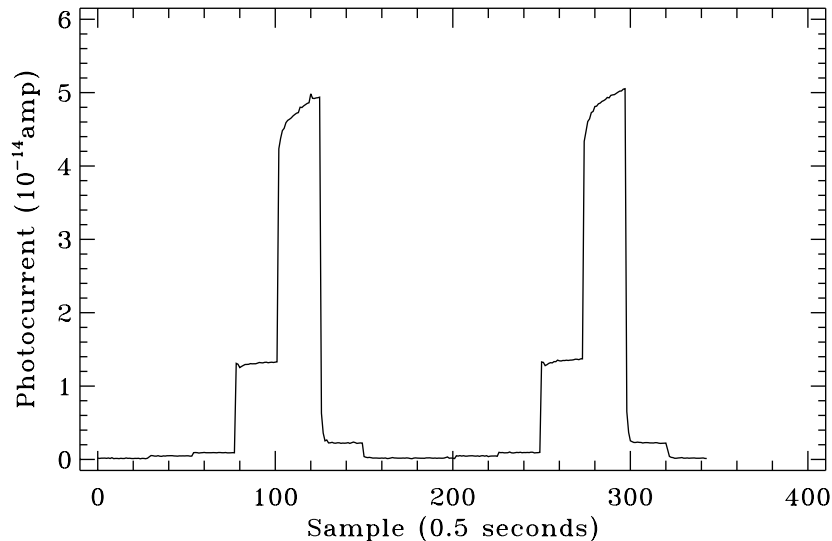


Figure 5.18: *Typical transient behaviour observed in LWS-SW4 (unstressed Ge:Ga) detector under a series of illuminator flashes. This is one of the LWS detectors showing the largest memory effects.*

The effect of the detector transient response on the illuminator flashes is to introduce a non-linearity into the drift correction. The problem is not that the correct illuminator flash level is not reached, but that the detector will respond differently depending on the flux levels involved, so the calibration will be inconsistent. How inconsistent will depend on the change in flux levels and the severity of the detector transient response.

One of the major effects of this transient behaviour is in the determination and application of the so-called ‘Relative Spectral Response Function’ (RSRF). LWS was operated in a mode where the grating was scanned forward and backward through the spectral range. For most detectors the scans pass through steep sided RSRFs and the resultant profiles are clearly split with the photocurrent dependent on scan direction. The transient response of the detectors can be seen in the difference in flux level between forward and backward scans. In general this leads to a distortion of the whole grating profile and of individual line profiles.

The calibration strategy used in the pipeline for the derivation of the LWS RSRF for a given detector was to average all data before dividing by the Uranus model. However when this averaged RSRF is applied in the pipeline it leads to a scan dependent behaviour in the resultant spectra.

Figures 5.21 and 5.22 show the spectrum of Uranus as observed by the SW4 (unstressed Ge:Ga) and LW2 (stressed Ge:Ga) detectors, respectively. We can see that LW2 does show significant differences between the forward and backward scans, while SW4 does not, possibly because of the lower fluxes and the smaller flux changes involved.

The transient behaviour of the LWS detectors can also affect the line flux accuracy. The effect, however, is minor (a few percent) in grating spectra and it has only been detected in the stressed Ge:Ga detectors,

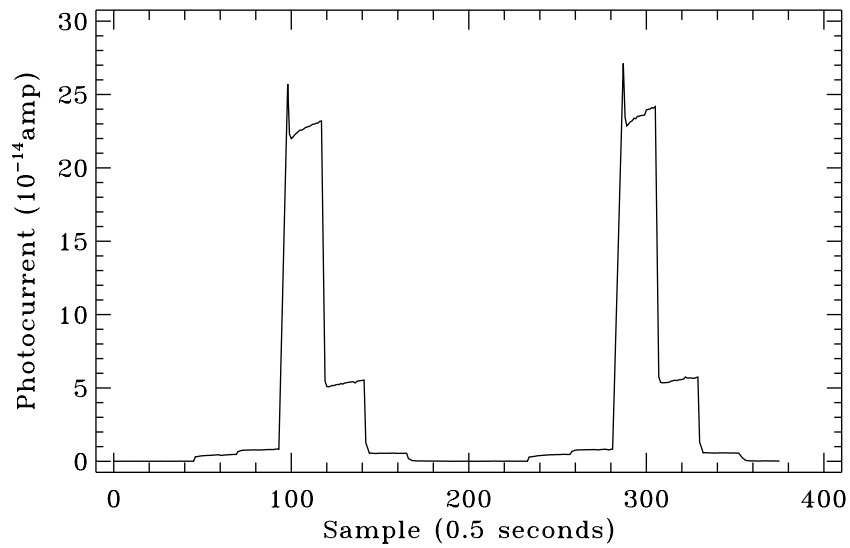


Figure 5.19: *Typical transient behaviour observed in LWS-LW2 (stressed Ge:Ga) detector under a series of illuminator flashes showing an initial hook response and then a slow continuous rise typical of a long time constant.*

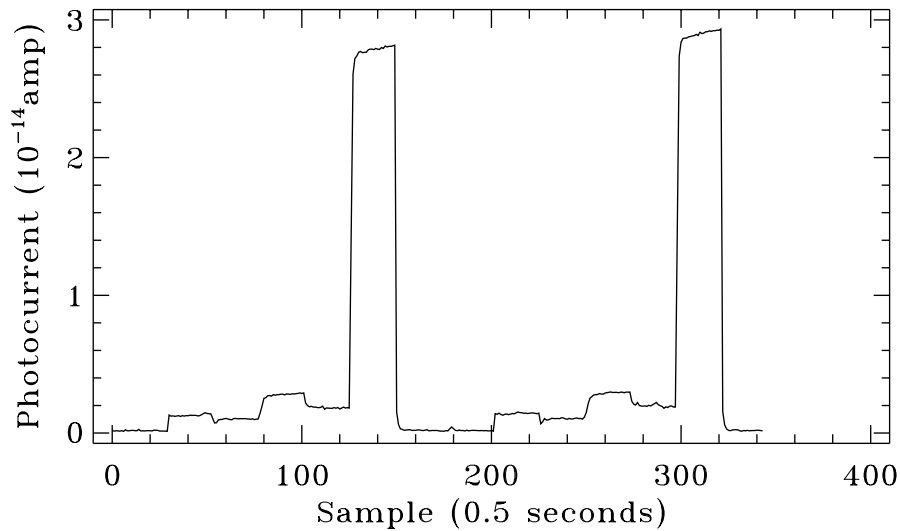


Figure 5.20: *Typical transient behaviour observed in LWS-LW5 (stressed Ge:Ga) detector under a series of illuminator flashes. This is one of the better behaved LWS detectors.*

where it is found to depend on both the line flux and the illumination history.

In the case of Fabry-Pérot observations made with LWS, the line profiles observed using AOT LWS04 are generally asymmetric, with the long wavelength wing at a higher flux level than the short wavelength

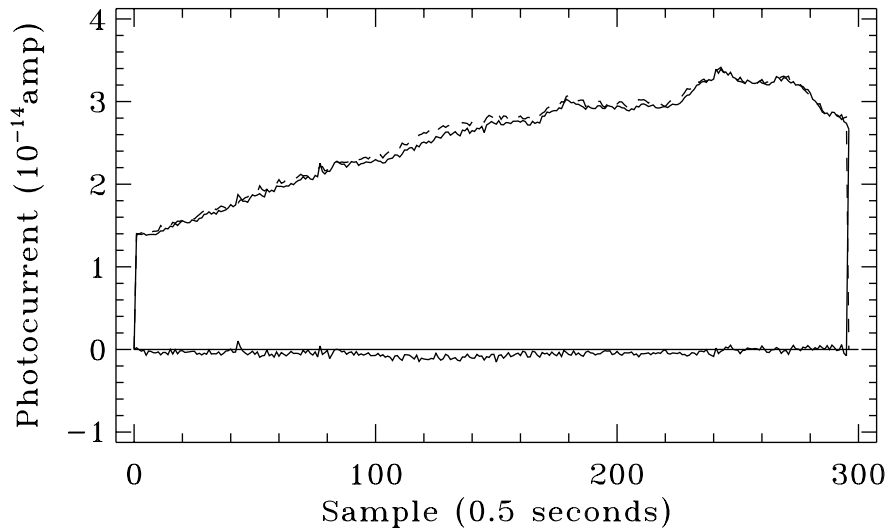


Figure 5.21: *The mean of the forward (solid line) and backward (dashed line) scans in SW₄ (unstressed Ge:Ga) observations of Uranus which contribute to the LWS RSRF, and their difference. The difference reveals the slower reaction to the increasing flux as shown by the illuminator flashes.*

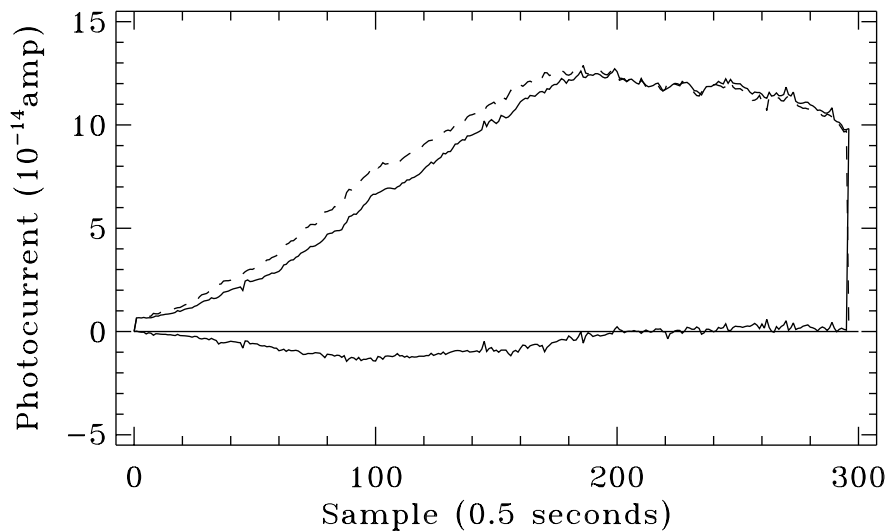


Figure 5.22: *The mean of the forward (solid line) and backward (dashed line) scans in LW2 (stressed Ge:Ga) observations of Uranus which contribute to the LWS RSRF, and their difference.*

one. The effect on line flux depends on the line-to-continuum ratio. For example, for a line with no continuum, the line flux can change by as much as 30%. The effect on the velocity shift is relatively small (about $\pm 3 \text{ km s}^{-1}$). It is also possible that some of the asymmetry observed may be due to loss of

parallelism as the Fabry-Pérot line is scanned.

Various methods for removal of transient effects in LWS detectors have been investigated.

Linear models based on fitting two or three exponentials do not work on a wide dynamical range of these detectors. While it is possible to construct an empirical fit to the transient response of the detectors with a two- or three-component exponential function, the reality is probably more complicated.

There have also been several attempts to provide a physically realistic model of doped germanium detectors able to account for their non-linear behaviour. However, these models are extremely complex and, thus, it is worth to try using analytical simplifications like the Fouks-Schubert model applied to the Si:Ga detectors.

The problem is that the Fouks-Schubert model, as we have already mentioned, is in principle not applicable to Ge-based detectors. In spite of this, a modified version of the Fouks-Schubert model has been developed and applied to several bands of LWS with relative success (Caux 2001, [15]). The routine used to find the Fouks-Schubert parameters is stable, but it still remains to check possible dependences on the spectral shape of the source.

For the time being, and before a solution is given to some still existing problems affecting the determination of the LWS RSRF using the adapted Fouks-Schubert model, a simple method to correct the fluxes has been developed which assumes that the slow upward changes in flux have a single time constant and that the downward changes are instantaneous, reflecting the differences seen in the laboratory experiments and illuminator sequences (Lloyd 2001c, [118]). The time constant is chosen so as to minimise the differences between the forward and backward scans. An example of the results obtained this way is shown in Figure 5.23.

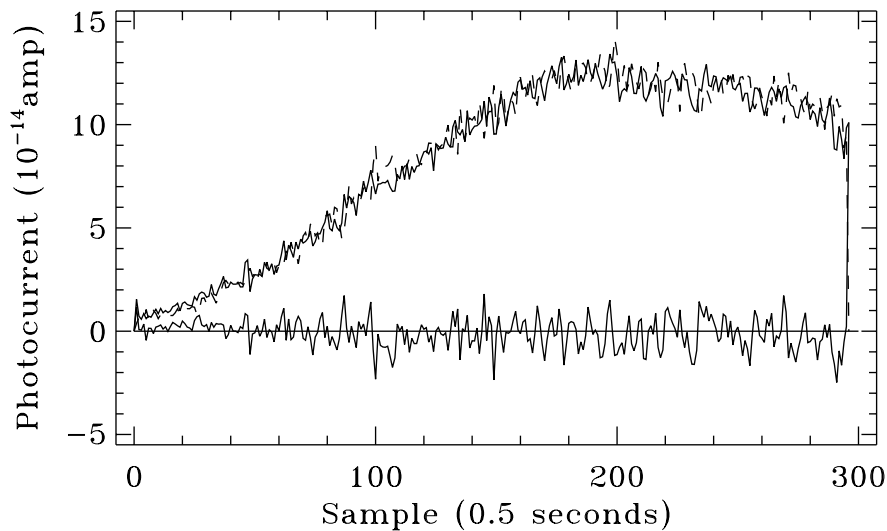


Figure 5.23: *The mean of the forward (solid line) and backward (dashed line) LW2 scans of Uranus after the transient correction has been applied. The time constant used was 6 steps.*

Another possible approach to correct for these memory effects is to use two RSRF functions, each derived only from scans in one direction. Attempts using this calibration strategy have so far led also to promising results.

Unfortunately, no correction is done for transient effects as such in the LWS pipeline. However, there is a plan to include a dedicated routine to perform this correction in the future in the LWS Interactive Analysis

(LIA) software package based on new transient effect corrected RSRFs obtained using the adapted Fouks-Schubert model above mentioned. These new RSRFs differ by just a few percent with respect to the old ones. Some preliminary results on the application of this correction to grating and Fabry-Pérot LWS observations can be found in Caux 2001, [15], where the implications on line flux calibration, wavelength calibration and spectral resolution are discussed.

Meanwhile, efforts on improving the pipeline products have concentrated in finding a correction for the effects observed in the illuminator flashes. Although the illuminator flashes, especially the brightest ones, are not flat, they are very consistent in shape, within the constraints of the transient response. When calculating the drift correction, which is a ratio of the observed illuminator flash to the ‘standard’ one, it is therefore important to use a method that recognises this consistency. The most appropriate method is the one that calculates the ratio on a point-by-point basis. This weighted-average method (explained in detail in Sidher et al. 2001, [150]) is applied in OLP Version 10 to process the illuminator flashes and represents a considerable improvement with respect to previous OLP versions but, unfortunately, it is only valid for the longer duration of the new style of flashes performed after revolution 442. The shorter duration of the old style flashes in observations before ISO revolution 442 often leaves just 3 to 4 points for an individual illuminator, following removal of data points affected by glitches, thus making it almost impossible to apply this method. It is important to note that in OLP Version 10, data from the old style flashes is still processed using the old method and, thus, they are expected to be more affected by transients.

5.6.2.3 Other detectors

The SW CAM CID In:Sb 32×32 matrix array is also affected by a strong transient effect but without instantaneous jump ($\beta=0$), as it can be seen in Figure 5.24. The time lag when responding to a flux variation is attributed to the surface traps in the detector, which need to be filled first with photon-generated charges before the well begins to actually accumulate signal (Tiphène et al. 1999, [157]).

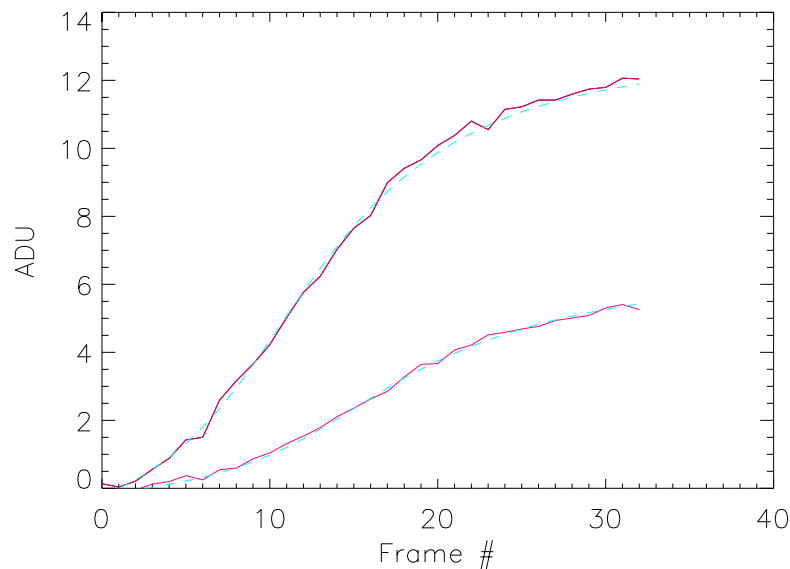


Figure 5.24: *Two examples of the evolution of the signal on two ISOCAM SW pixels after a positive but small flux step (of different magnitude for each pixel). Solid line: evolution of the signal (in ADUs). Dashed line: fit of the signal by the model.*

Although a detailed physical model of this transient behaviour is lacking an empirical model has been developed which reproduces quite well the observed response using only a small set of parameters. The model provides the asymptotic value of the stabilised signal. Unfortunately, because of the limited number of test cases available it is difficult to judge whether the method is generally applicable to the full range of SW CAM data.

PHT-P2 (Si:B) is also affected by transients. An example of P2 detector transients induced by chopper modulation are shown in Figure 5.25. As we can see they also may exhibit a hook response or overshoot after large positive flux steps, like other doped silicon detectors, followed by a slow decay.

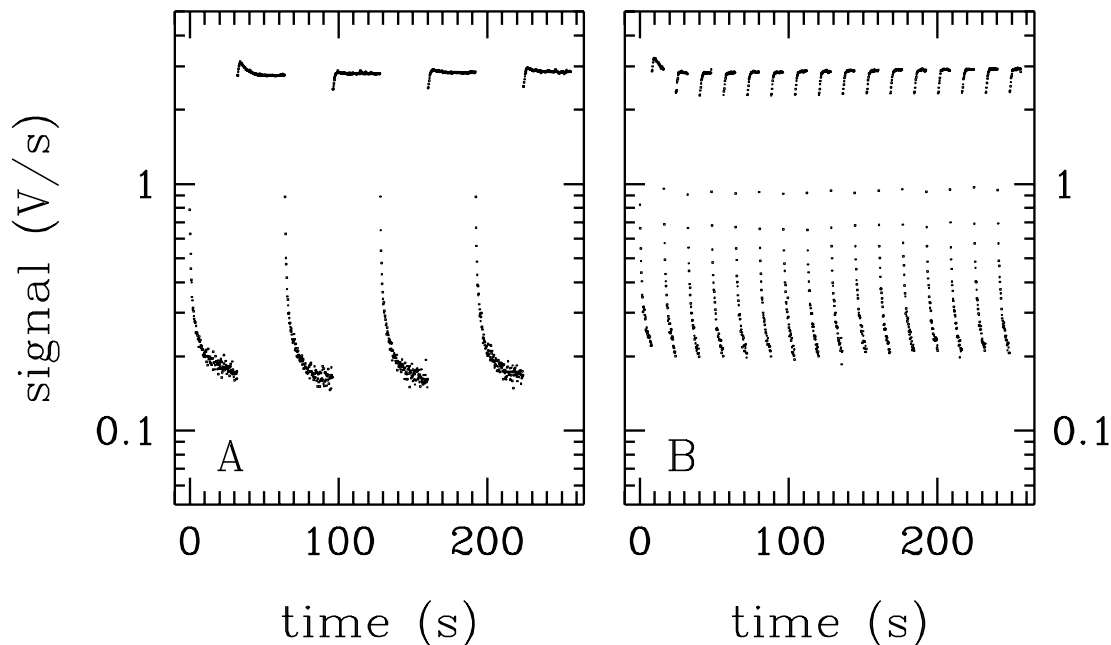


Figure 5.25: *Examples of P2 detector transients induced by the chopper modulation on a very high source-background contrast. Left panel (A): slow (32 s per chopper plateau) chopped measurement on a high source-background contrast. Right panel (B) same source-background contrast as under (A) but with a higher chopper frequency (8 s per plateau). Note the strong overshoot in the first higher plateau; a straight signal average per chopper plateau would underestimate the background subtracted source signal in both cases.*

Figure 5.26 shows the response to an illuminator sequence of the Ge:Be detector SW1 of LWS. This detector is the worst affected by transients in LWS, and exhibits a longer time constant (several minutes) compared to the above described LWS Ge:Ga detectors, which decreases with increasing flux step.

Like other LWS detectors, SW1 also shows significant differences between the forward and backward scans (see Figure 5.27), affecting the spectrum profile and the line flux accuracy, although very few bright lines are observed in the wavelength range covered by this detector (43–51 μm).

The response of the detector to a step change in flux can also be modelled empirically by a function containing three exponential time constants, with typical values of 5, 20 and 200 seconds (Church et al. 1996, [23]) but, again, the initial hook response cannot be reproduced.

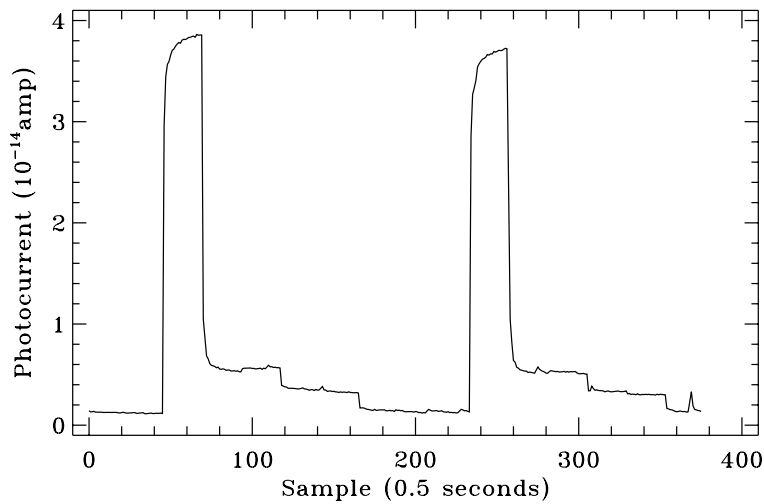


Figure 5.26: Typical transient behaviour observed in LWS-SW1 (Ge:Be) detector under a series of illuminator flashes.

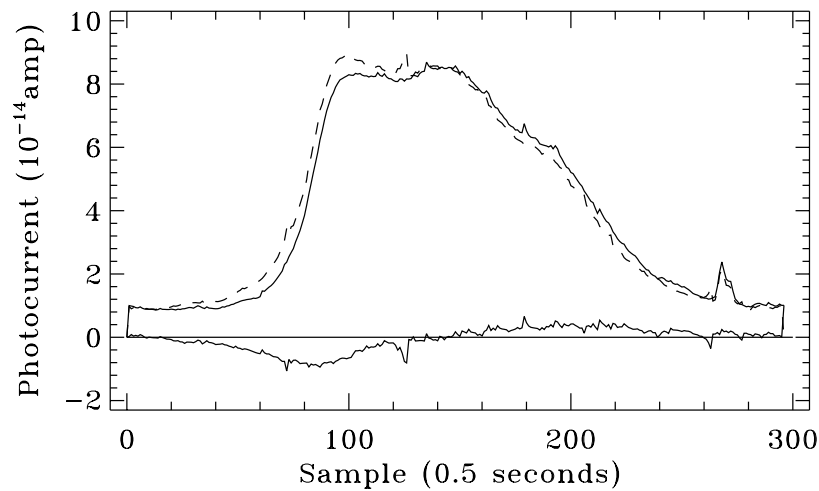


Figure 5.27: The mean of the forward (solid line) and backward (dashed line) scans in the SW1 (Ge:Be) observations of Uranus which contribute to the RSRF, and their difference. The difference reveals the slower reaction to the increasing flux as shown by the illuminator flashes.

Moreover, the adapted Fouks-Schubert model used for the Ge:Ga detectors with relative success simply does not work in this case.

Significant improvements, however, are achieved with the help of the same simple model that was applied to the Ge:Ga detectors (Lloyd 2001, [118]) which assumes that the slow upward changes in flux have a single time constant and that the downward changes are instantaneous, with the time constant chosen as to minimise the difference between backward and forward scans. Figure 5.28 shows the result of applying

this simple model to the SW1 spectrum of Uranus used to derive the detector RSRF.

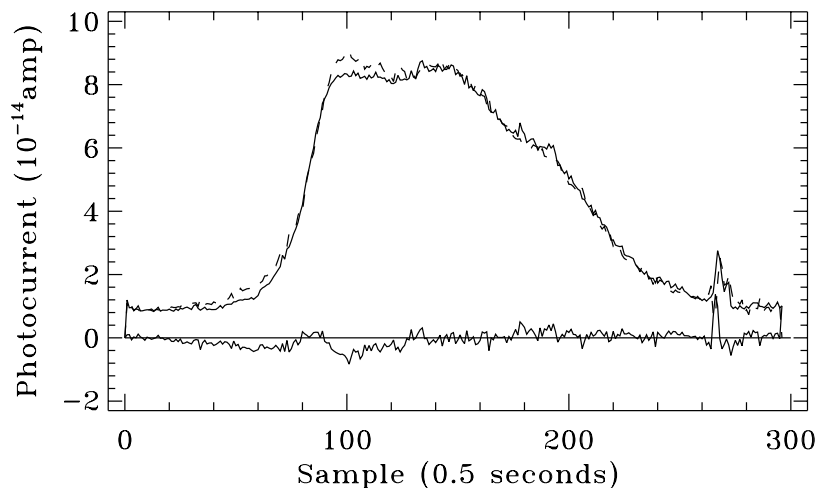


Figure 5.28: *The mean of the forward (solid line) and backward (dashed line) scans in the SW1 (Ge:Be) scans of Uranus after the transient correction has been applied. The time constant used was 1.5 steps. The remaining differences may be due to a dependence of the time constant on the slope of the photocurrent but the largest difference occurs at only one end of the relatively flat plateau section.*

The observations of NGC6302 provide a slightly different test. The means of the forward and backward scans in SW1 are shown in Figure 5.29 where large differences are also observed, similar to those observed in Uranus. The corrected data are shown in Figure 5.30.

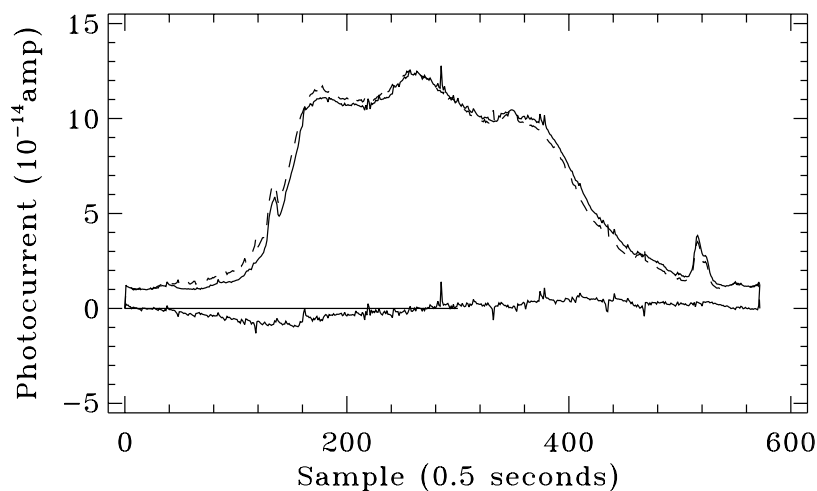


Figure 5.29: *The mean of the forward (solid line) and backward (dashed line) scans of NGC 6302 in the SW1 (Ge:Be) detector, and their difference.*

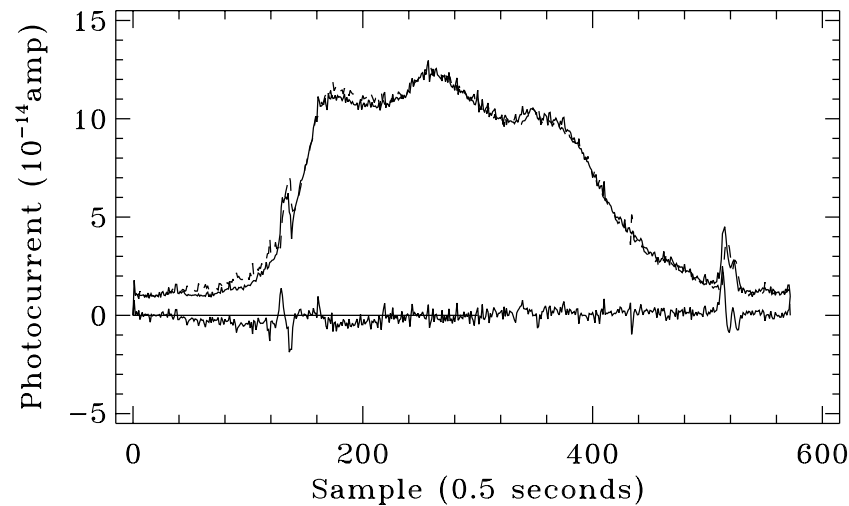


Figure 5.30: *The mean of the forward (solid line) and backward (dashed line) scans in the SW1 (Ge:Be) scans of NGC 6302 after the transient correction has been applied.*

It is clear that this simple model does provide some correction to the data, particularly to the slower changes in flux, but it can still be improved.

Band 4 (Ge:Be) and the two Fabry-Pérot bands (Si:Sb and Ge:Be) of SWS are also affected by memory effects (Wensink et al. 1992, [164]).

Concerning band 4, we know that the Fouks-Schubert model does not work in Ge:Be detectors and up to now, no efficient model has been found to describe these memory effects. As a consequence of this, no correction for memory effects in this band is applied in the pipeline. Efforts are, however, still on-going to try to find an alternative method.

An example of the various effects seen in band 4 is shown in Figure 5.31, an SWS01 speed 4 observation of K3-50. At the start of the up-down scan (at the longer wavelength side) we see a transient. Some detectors, like 37, display a hook effect, some rise faster than others, seeming to get earlier to their relaxed state than the others. At the shorter wavelength there also seems to be some hysteresis effect, where the second part (the down scan in red) seems to stall before getting into the rising mood.

On the other hand, the consequences of transients in the Fabry-Pérot bands (FP in Table 5.3) appear at the present time limited. The main reason for this is that most flux passing through the FP's is weak, in the flux domain where transients are not yet so important. Moreover, FPs could only be operated in one direction, which prevented the up-down strategy to correct for transients. So unless we assume that the FP lines are always symmetrical, or better, that the FP spectrum itself has some *a priori* known characteristics, we cannot disentangle the transients from the spectrum. Thus, a transient correction was never applied.

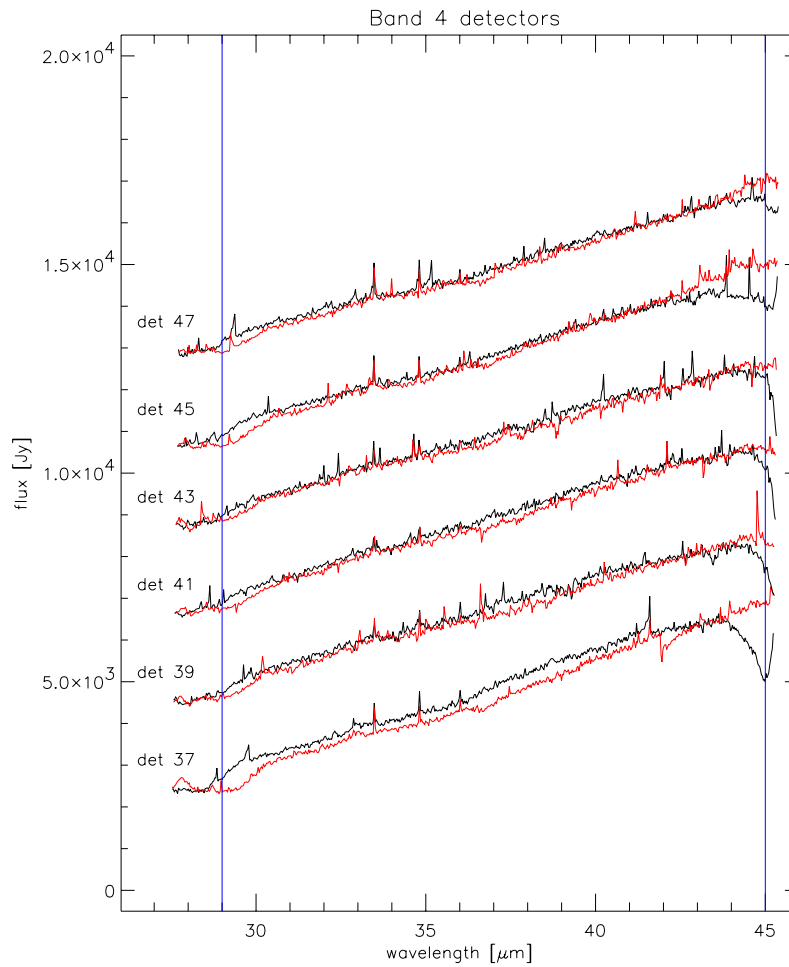


Figure 5.31: *Example of memory effects in band 4 on an up-down scan as seen in an AAR of an SWS01 speed 4. The scans of the different detectors are offset with respect to each other for clarity. At the start of the upscans (black) at the long wavelength side, various memory effects can be seen, some with hooks (detectors 37, 45 and maybe 47). The down scans (red, running from short to longer wavelengths) generally show less transient effect. Still there is some systematic difference between up and down scans around 30 μm which is probably attributable to transients. Which one of the up or down scans is affected is unclear. The blue lines show the official borders of band 4.*

Other detectors on board ISO are completely free of transient effects. This is the case of band 1 (In:Sb) and band 3 (Si:As BIBIB) of SWS (see Figure 5.13).

5.7 Events and Conflicts during Operations

This is a summary list of special events and conflicts between instruments that occurred during the Operational Phase of the mission (some of which have already been mentioned):

Revolution	Event
79	First revolution after PV Phase.
94	PHT-FCS1/TRS2 change in illumination behaviour/brightness increase.
116	AOCS calibration led to shorter science window. Some loss of science due to system crash.
137	ISO pointing performance tests using ISOCAM.
152	Soft geomagnetic disturbance with no impact on science.
161	Tests of the SWS virtual fourth aperture.
173	Tests of LWS parallel mode.
196	As soon as AOS was achieved at the start of the revolution, it was seen that ISO had gone to survival mode and that both the Earth warning and forbidden regions had been traversed by ISO - ISO had viewed the Earth for about 2 minutes. All temperatures were out of range (high) and all scientific operations for the revolution were therefore suspended.
197	Recovery procedures implemented.
198	Normal operations resumed within 36 hours. No damage was done to the satellite.
204	LWS switch-off rolled back 60 minutes.
217	Some LWS tests made during the revolution to verify a command changing the LWS biases.
220	Many small problems affecting a large number of observations. First there were problems with the PPM (Earth constraint was approached closely), then a guide star was not found, and PHT-P2 suffered from latch-up problems
242	Over four hours of observations lost due to problems with the Goldstone antenna.
256	Goldstone problems led to loss of over one hour observations.
263	Goldstone problems led to loss of over one hour observations.
264	ISOCAM and SWS measurements made for ISO pointing tests. Special ISOCAM mode had to be used for the one hour test.
267-268	Goldstone problems led to loss of over ten hours observations.
274	Spacecraft problems (automatic on-board reset) led to the loss of half the revolution.
290	Improved SSO tracking algorithm implemented.
294	The opening of the science window was delayed by 2h 30m due to a planned delta-V manoeuvre (to keep the phase of the orbit correct) and second DLCM, both at the start of the revolution.
301	Nearly six hours of science lost due to spacecraft problems.
317	Long (~6 hours) calibration observation of Uranus affected for 90 min by short Goldstone dropout.
327	Improved Sun ephemerides.
330	Goldstone problems led to 5 observations (80 min) lost.
343	Loss of communications with ISO for 45 min from Goldstone due to high winds.
356	Tests of LWS wheel subsystem plus minor Goldstone problems.
364	ISO went into survival mode at the start of the revolution, leading to a loss of two hours science.
365	Some Goldstone problems leading to loss of 85 min science time.
368	STR calibration updated.
372	Goldstone power failure led to the loss of 5 hours observing. Satellite went into perigee with ISOCAM in wrong mode.

Revolution	Event
373	No anomaly observed with ISOCAM, but one hour observing lost due to one minute of loss of contact with the satellite.
378	LWS activities halted until further notice due to FP interchange wheel problem (positioning difficulties). Next two revolutions could not be replanned. This time was devoted to LWS observations, that were lost.
384	Straylight rejection measurements for SWS.
398	Many telemetry problems due to a thunderstorm around Madrid and Goldstone problems led to the loss of over 100 min science time.
410–412	Tests of ground system for the 366 day year problem (1996 was a leap year). On revolution 411 this caused the loss of one hour of science.
413	Telemetry problems in Madrid and Goldstone caused the loss of two hours of science.
417	Various problems caused the loss of just over one hour of science.
432–435	Manual LWS checks and tests were made to try and solve the wheel problem.
442	LWS operations re-start with one test observation completed successfully.
447	Real re-start of LWS operations with 30 observations completed nominally.
452	Sun ephemerides recalculated four times per revolution, instead of once per revolution to improve ISO pointing accuracy.
470	Lots of minor Goldstone problems lead to the loss of ~ 1 hour of science.
484	Lots of problems at handover leading to 67 min science lost.
522	Loss of over six hours science due to LWS problems (microprocessor and reset).
528	Non-nominal behaviour of SWS led to the loss of 78 min science.
566	Loss of 75 min of science due to a CTV problem.
571	CAM-CVF observations in the Mission Data Base temporarily 'blocked' from the automatic scheduling routines to prevent the strong increase in band 3 dark currents observed in SWS observations performed in the following 30 min.
575	Loss of 100 min science time (SWS observation) due to non-availability of Goldstone.
578	Fire alarm drill on station, Instrument Controller left post as per procedure. No events happened during this time.
602	Almost four hours of science lost due to spacecraft attitude problems - one observation was up to 1.5 degrees off.
603	Many problems with PHT-P2 latch-ups affecting 85 min science. Science observations using PHT-P2 detector suspended.
613	Start of PHT-P2 latch-up tests. Also, many telemetry drops but little impact on the science time.
614	Lots of telemetry drops due to a thunderstorm around VILSPA.
620	Two hours of observations lost due to Goldstone problems.
623	Two hours of observations lost due to Goldstone problems.
637–641	400 min of PHT science time affected or lost due to PHT-P2 latch-up problem.
646	Loss of 81 min science time due to Goldstone problems.
659	End of PHT-P2 latch-up tests.
661–662	PHT straylight tests during eclipse.
664	Start of long (>140 min) eclipses.
668	Loss of 90 min of observations due to Goldstone problems.
672–673	Special PHT straylight measurements during eclipses.
676	Automatic scheduling of CAM-CVF observations resumed. Mission Planning software was updated so that SWS observations were not scheduled any more until after 30 min of a CAM-CVF measurement.
678	Last revolution for which the eclipses lasted longer than 140 min.

Revolution	Event
684	Resumption of PHT-P2 observations.
688	200 min observation lost due to Goldstone problems.
719	LWS wheel tests.
721	~82 min lost due to problems on instrument start-up.
722	Solar flare caused loss of most of the science time due to enhanced glitch rate.
732	284 min science lost due to Goldstone problems.
756	Problems with guide stars caused 60 min of science to be lost.
757	Third DLCM and an orbit correction manoeuvre carried out at the start of the revolution. Problems with Goldstone led to the loss of 185 min science.
764	OTF set to 2'' for all instruments.
777	100 min of science lost due to a combination of errors, plus on the 1997–1998 year change the wrong year entered in the system.
843–844	~90 min of science lost as orbit geometry causes VILSPA antenna to point directly at the Sun (ISO in the VILSPA-Sun line).
851	Problems with a guide star (blemish on CCD) causes 4h 45m of science to be lost.
875	Liquid helium depletion at 21:07 zulu on 8 April 1998.
876–880	Some SWS observations carried out as bands 1 and 2 are still useable.
881–887	Start of SWS post-He observations. SWS used all these revolutions.
888–907	SWS observations interleaved with the Technology Test Phase (TTP).

Chapter 6

ISO Cross-Calibration

6.1 Cross-Calibration Strategy

During the Operational Phase a limited number of sources were observed repeatedly throughout the mission for cross-calibration purposes. The responsibility for instrument calibration rested with the Instrument Dedicated Teams (IDTs) located at VILSPA, and was supported by staff at the home institutes of the instrument teams. Demands from the different instruments and coordination of cross-calibration observations were handled by a dedicated ‘Calibration Liaison’ team.

As a result of these cross-calibration observations, the overall agreement among the major instrument modes was assessed in several occasions during the mission. The observations confirmed that the internal consistency in terms of absolute flux calibration was in general comparable to pre-launch expectations or better and led to the discovery of some calibration problems in the few cases where larger discrepancies than expected were found.

During Post-Operations, an improved cross-calibration plan was set up, based on the use of the whole ISO Data Archive for cross-calibration purposes, extending the analysis to a much larger number of sources. This way it was possible to study specific calibration topics in detail on dedicated subsets as well as to perform statistical analysis of the results obtained after specific calibration improvements were implemented in the pipeline in many cases.

In addition, it was decided to change the global IDC strategy for cross-calibration, from the rather ‘instrument-oriented’ approach which worked quite efficiently during the Operational Phase (but turned out to be inappropriate for Post-Operations) to a more ‘calibration-topic’ oriented organisation. For this, up to eight different Working Groups were established, each one addressing a specific calibration aspect (glitches, beam profiles and pointing, transients, line profiles, polarisation, spectral matching, general photometric calibration and interactive analysis S/W). They were formed by members of the IDC and of the different NDCs, with all instruments represented, plus external contributors from other projects (ASTRO-F, SIRTf, Herschel,...) in many cases.

Their objectives were:

- Verify that, from a global point of view, the calibration of the individual ISO instruments was correct, and ensure a certain level of homogeneity and consistency of the data and how they were calibrated (e.g. compatibility of models, bandpass zero-points, and of calibration philosophy and procedures).
- Identify calibration problems, trigger/recommend further work, propose solutions and monitor the progress made, promoting the transfer of all useful information to the users community (new tools available, caveats,...).

- Compare the results of the different ISO instruments and seek for understanding the inconsistencies found and make similar comparisons with external data from ground-based or space facilities.

The progress made on each calibration topic under analysis was reflected every six months during Post-Operations in a series of *(Cross-)Calibration Status Reports* posted at the IDC web site where information was included on the latest achievements in the calibration of all four ISO instruments with special emphasis on cross-calibration aspects. At the end of the Post-Operations Phase (end of 2001) each of these Working Groups generated a Final Report, containing the final state-of-the-art of ISO calibration regarding each of the calibration problems addressed. All of them have been put together in the *ISO (Cross-)Calibration Final Report*, [59] available at:

<http://www.iso.vilspa.esa/> → ISO Explanatory Library → Performance and Calibration

This organisation turned out to be an ideal platform to exchange knowledge across the boundaries of the ISO instruments. The information gathered and the conclusions derived from the investigations carried out by members of these Working Groups on the many different calibration problems affecting the ISO instruments constitute an extraordinary source of information for other future space projects. Most of these results were presented to the astronomical community at *The Calibration Legacy of the ISO Mission*, [120] conference, held at VILSPA on February 5–9, 2001.

6.1.1 Definition of cross-calibration sources

As we have already mentioned, only a small set of astronomical sources was used during the Operational Phase for cross-calibration purposes. It was composed of a few bright stars (like HR 7310, HR 7341, HR 6436, γ Dra or α Boo), planetary nebulae (NGC 7027 and NGC 6543), galaxies (Mrk 279), asteroids (Cybele, Hygiea) and planets (Neptune). For most of them, observations exist in IDA taken throughout the whole ISO mission with more than one instrument and in many cases covering a wide range of wavelengths.

During Post-Operations, and as part of the new cross-calibration strategy above described, the concept was extended to any source satisfying at least one of the following conditions:

- it should have been observed with more than one instrument/configuration at least once during the ISO mission (for internal cross-calibration purposes)
- infrared data from non-ISO instruments exist (for external cross-calibration)
- accurate models exist against which ISO data can be compared (for absolute flux calibration).

A more detailed description of the selection criteria used to consider a given observation in IDA as suitable for cross-calibration purposes can be found in the *ISO (Cross-)Calibration Final Report*, [59].

6.1.2 Limitations and caveats

Because of the limited common dynamic range between the ISO instruments, not all kind of internal cross-calibration comparisons were possible. In this respect, the cross-calibration of LWS with PHT in the long wavelength range was especially difficult, since the dynamic range overlap between PHT and LWS was very limited.

When comparing results derived from different instruments/detectors we also need to consider the differences in beam and filter profiles as well as in spatial and spectral resolution. This applies both to internal and external cross-calibration.

In addition, in the case of external cross-calibration, results obtained from facilities other than ISO may be based on different absolute calibration systems: different zero-points, different set of astronomical

standards, different models used for the same standards, can introduce an undesired bias which has to be taken into account.

Last, but not least, some of the sources included for analysis may have been observed slightly off-axis, or show unexpected variability or extended emission not previously reported in the literature and, thus, can introduce some noise into the system. This makes cross-calibration even more complicated since individual spectra must be carefully checked one by one before being validated (see Figure 6.1).

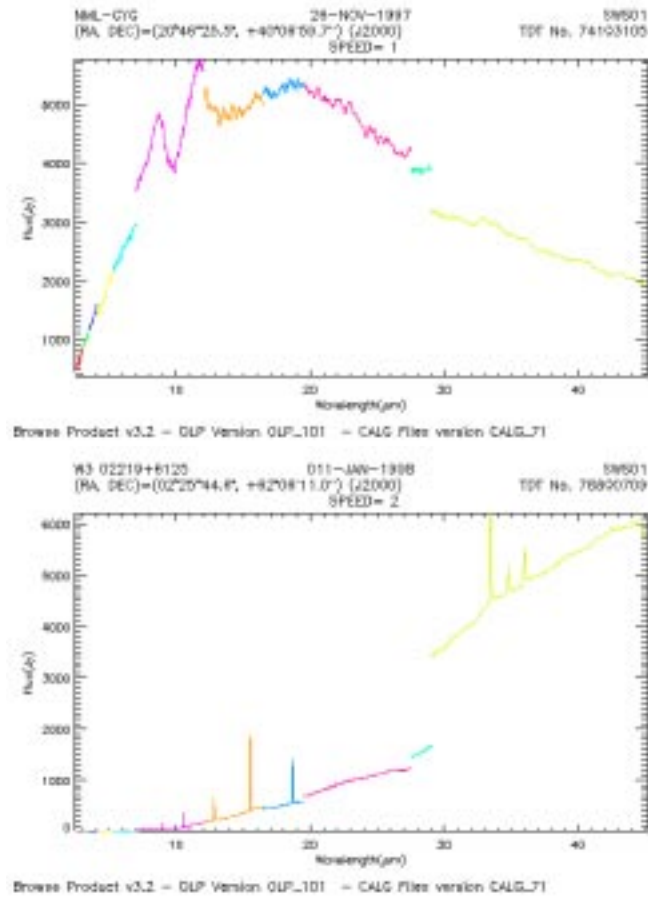


Figure 6.1: Example of the discontinuities observed in SWS spectra as a consequence of a bad pointing (top) compared to the discontinuities due to the extended nature of the source observed (bottom). Note the always positive flux jumps towards longer wavelengths reflecting the progressive increase of the SWS apertures in this latter case.

On the other hand, the accuracy of the absolute flux calibration is always limited by the accuracy of the available models. Stars are too faint in the long wavelength range of ISO (beyond 100 μm) to be used as standards, and asteroids and planets have to be used instead. While stellar models are believed to be accurate to $\pm 5\%$ or better, the uncertainties in asteroid and planet model spectral energy distributions are larger (10–15% level). In the case of asteroids their characterisation is additionally complicated by their variability, which limits the accuracy of the absolute flux calibration of ISO at long wavelengths.

In the following we will present a summary of the main results obtained from a number of internal and external cross-calibration analysis as well as from some consistency checks performed against available models. A more detailed description of how these comparisons were made can be found in the *ISO (Cross)-Calibration Final Report*, [59].

Note that we intentionally exclude from this analysis internal cross-checks made by each instrument team within their own instrument detectors/bands/AOTs. These are addressed in the instrument specific volumes of this Handbook and will not be discussed here.

6.2 Internal Cross-Calibration

6.2.1 Between the ISO spectrometers

6.2.1.1 SWS versus PHT-S

The sample used for this internal cross-calibration comparison comprised around 100 different sources with both SWS (AOT SWS01) and PHT-S (AOT PHT40 either in staring or chopped mode) spectra available in IDA, showing a reasonable signal-to-noise ratio.

The OLP data products were compared in a systematic way since the end of the Post-Operations Phase with every new release of the pipeline. This resulted in the detection of several calibration problems affecting both PHT and SWS calibration that were conveniently reported in the corresponding (*Cross-Calibration Status Report*).

As an example, one of the calibration problems discovered was the effect of poorly modelled molecular features in the spectra of the calibration stars used in the dynamic calibration of PHT-S, before it was implemented in Version 9.0 of the pipeline. Based on the comparison of OLP Version 7 SWS data and staring PHT-S observations of the asteroid Hygiea with the available thermophysical model it was possible to identify the residuals left in the calibrated PHT-S spectra between 8 and 9 μm by SiO features not considered in the original models of the late type stars taken as standards. Only excluding these stars from the generation of the calibration files (and hence accepting a larger gap in the flux range covered by the calibration standards) the spurious features were eliminated in the calibrated spectra. After the correction was introduced in OLP Version 9.0 the agreement between SWS01 and PHT-S staring observations improved significantly.

As of OLP Version 10, the level of agreement reached in terms of absolute flux between these two ISO instruments and observing modes was better than 10–15% for well-behaved data sets (bright, point-like sources not affected by any other known calibration problem). Moreover, the overall shape and even the faintest spectral features were also largely preserved from instrument to instrument (to within the few percent level in most cases) all over the spectral range covered by both instruments.

Figure 6.2 shows some examples which illustrate the good agreement found over a wide variety of sources with different spectral properties, all of them taken from this cross-calibration sample. The plotted spectra are OLP Version 10 data products directly retrieved from IDA corresponding to representative cases of sources showing a ‘blue’ (HR 7310 and HR 6132) or ‘red’ continuum (AFGL 4106 and OH 26.5+0.6), or sources where strong PAH emission bands and/or nebular emission lines (BD +30°3639 and NGC 7027) appear superimposed on the infrared continuum. A very good agreement between both instruments and the IRAS photometry at 12 μm (indicated with a blue square in the plots) is also found.

The examples shown in Figure 6.2 correspond to relatively bright sources observed in all cases with PHT-S in staring mode. For the fainter sources the chopping mode of PHT-S was usually preferred and the behaviour of this mode was also investigated in terms of cross-calibration. The results obtained indicate a similar level of agreement with SWS (10–15%), in spite of the fact that the accuracy achievable with SWS at low flux levels is not expected to be as good.

Figure 6.3 shows two *faint* sources (flux density below 5–10 Jy) observed with SWS and PHT-S. IRAS 16342–3814 was observed with PHT-S in staring mode while IRAS 21434+4936 was observed using triangular chopping. We can see that a very nice agreement exists at absolute flux level as well as in the shape of the individual SWS and PHT-S spectra in both cases. Again, there is also a very good agreement with the IRAS photometry at 12 μm .

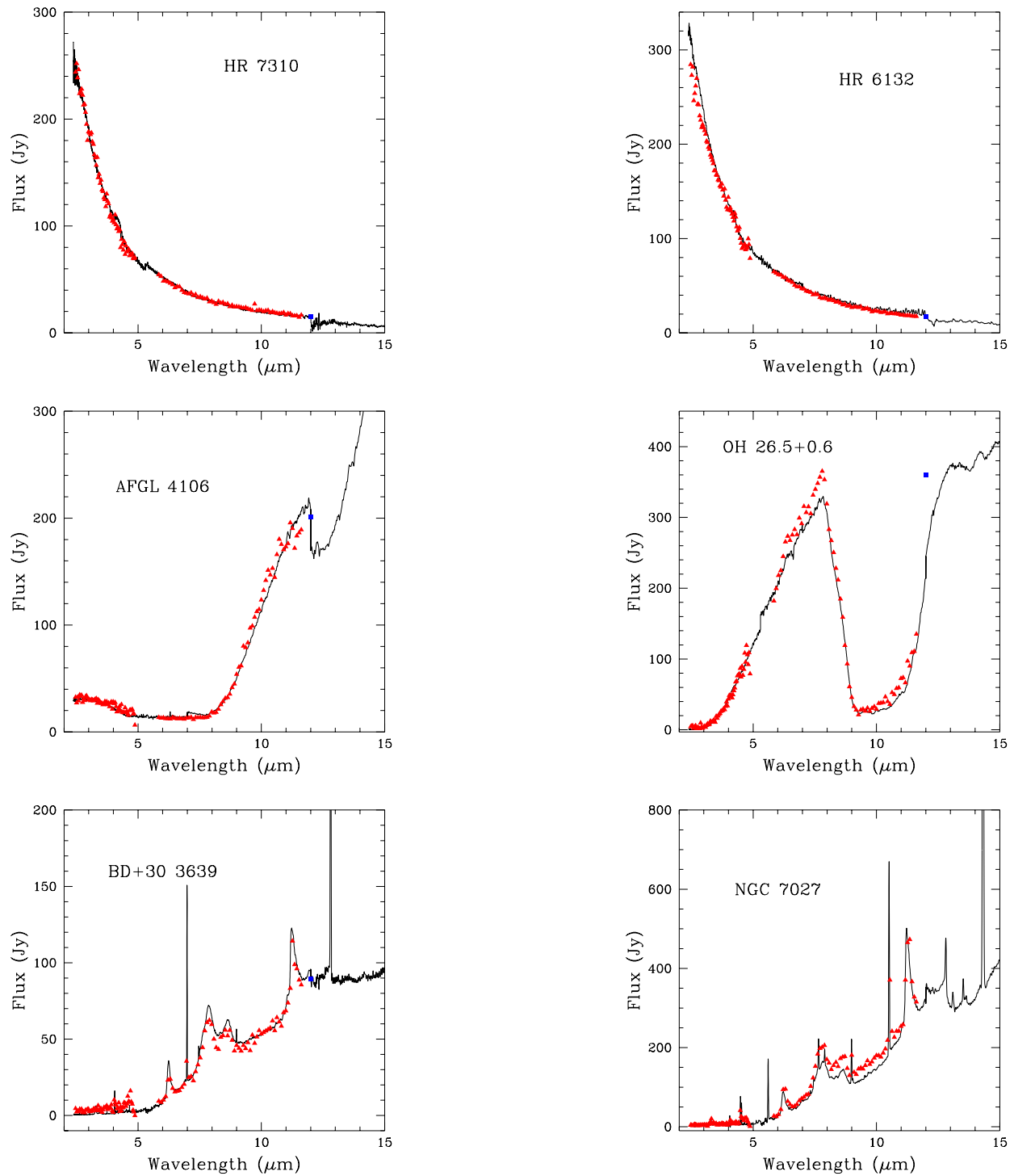


Figure 6.2: *SWS* (black solid line) versus *PHT-S* (red filled triangles) OLP Version 10 spectra of a variety of sources with different spectral properties taken from the cross-calibration sample. The blue squares represent the IRAS photometry at 12 μm when available.

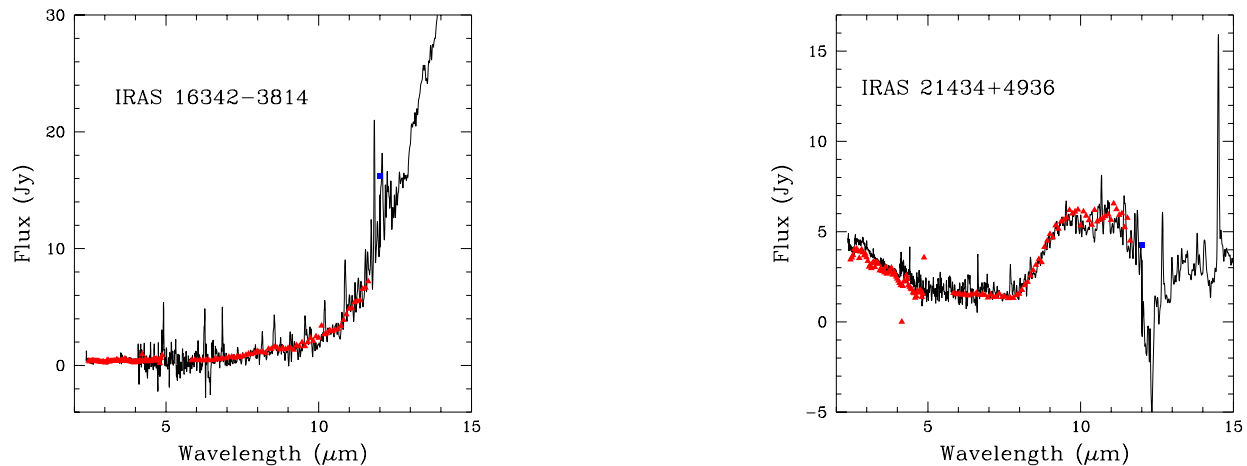


Figure 6.3: Same as Figure 6.2 for two faint sources. Note the effect of an inaccurate dark current subtraction by the pipeline at the blue edge of band 3A ($12.0 \mu\text{m}$) in the SWS spectrum of IRAS 21434+4936. The blue squares represent again the IRAS photometry at $12 \mu\text{m}$.

Outside the overlapping spectral range, a significant jump in flux is detected at the blue edge of band 3A in the SWS spectrum of IRAS 21434+4936 at $12.0 \mu\text{m}$. This is indicating an inaccurate dark current subtraction by the automated pipeline (OLP Version 10). This kind of problem is sometimes observed in the SWS spectra of faint sources and needs to be manually corrected with the use of the SWS interactive software analysis (OSIA) where the right dark current level can be interactively chosen, eliminating the problem.

6.2.1.2 SWS versus CAM-CVF

A similar exercise was performed with a sample of around 20 sources identified in IDA to have SWS (AOT SWS01) and CAM-CVF (AOT CAM04) spectra available with a signal-to-noise ratio enough to be used for cross-calibration purposes.

Again, the OLP data products were compared in a systematic way since the end of the Post-Operations Phase with every new pipeline release since OLP Version 7.

In this case, the main improvement implemented in the pipeline since the start of this cross-calibration analysis was the application of transient corrections based on the Fouks-Schubert method (Fouks & Schubert 1995, [54]) both to SWS01 (band 2) and CAM04 data, which are described in detail in the corresponding instrument specific volumes of this Handbook.

As of OLP Version 10, the level of agreement between SWS01 and CAM04 spectra was in general within 10–15% down to the limits where dark current subtraction (especially for SWS) becomes a significant contribution to the error budget. This statement is valid over the whole spectral range covered by both instruments with the exception of the edges of CAM-CVF scans, which might be affected by transient effects even after the application of the Fouks-Schubert transient correction (this is especially true in the case of bright point sources, for which this correction simply does not work).

Figure 6.4 shows two examples where comparisons are made of CAM04 and SWS01 OLP Version 10 data products directly retrieved from IDA, taken from this cross-calibration sample. They correspond to the bright star HR 7310 (left panel) and to the fainter HD 179218 (right panel), which are representative of the general behaviour observed.

As we can see, the agreement is very good with the only exception of the blue edge of the CAM-CVF spectrum of HR 7310, affected by strong transient effects at the beginning of the measurement. This

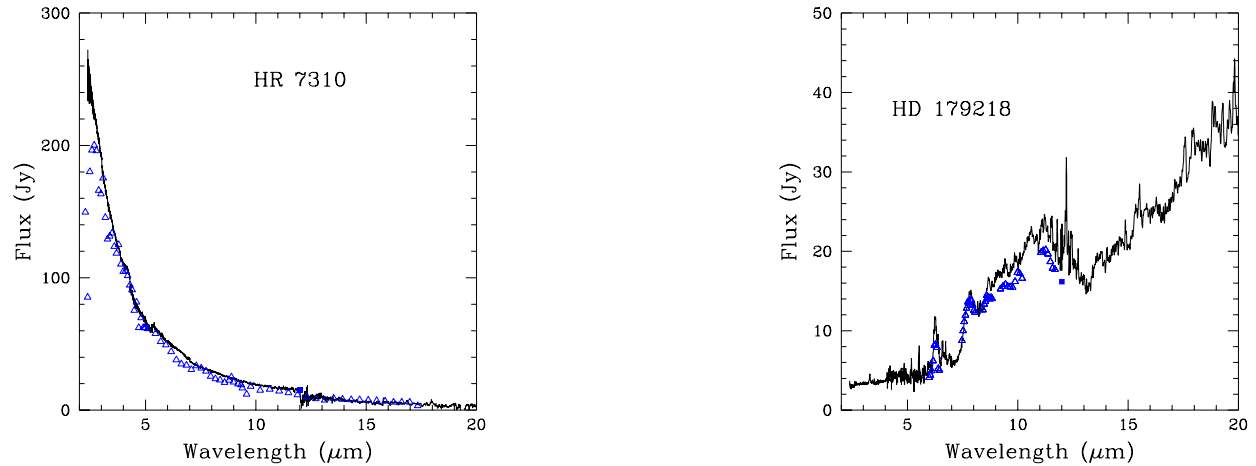


Figure 6.4: *SWS* (black solid line) versus *CAM-CVF* (blue open triangles) OLP Version 10 spectra of two point sources taken from the cross-calibration sample. Note the strong transient observed at the blue edge of the *CAM-CVF* spectra of HR 7310 (left panel). The blue squares represent the IRAS photometry at $12\ \mu\text{m}$.

is, as we have already mentioned, a common feature observed in many cases in *CAM-CVF* spectra of bright sources and its strength depends on the illumination history conditions. It is well known that the Fouks-Schubert correction which is applied in the pipeline only works efficiently for very weak and/or extended sources (i.e. for low flux gradients) and has a neutral effect on bright point sources like HR 7310. Unfortunately, the problem cannot be corrected with the help of CIA.

6.2.1.3 CAM-CVF versus PHT-S

Around 10 other sources were used for a similar internal cross-calibration comparison of *CAM-CVF* (AOT CAM04) and *PHT-S* (AOT PHT40 either in staring or chopping mode).

Figure 6.5 shows two examples where comparisons are made of *CAM04* and *PHT-S* OLP Version 10 data products retrieved from IDA, taken from this small cross-calibration sample. They correspond to the bright star HR 7310 (left panel) and the faint HD 207129 (right panel), which are representative of the general behaviour observed.

Note that for the faint star HD 207129, the background continuum emission is not negligible. In this case, a background measurement available in IDA taken at a position $3'$ away from the central source was used to subtract this contribution. The spectrum shown in Figure 6.5 is the result obtained after subtraction of this background.

We can see once more that a very good level of agreement exists (within 10–15%) in the overall shape and in the absolute flux level determined by the pipeline for *CAM-CVF* and *PHT-S* spectra, as well as between the two instrument observing modes and the IRAS photometry at $12\ \mu\text{m}$.

Again, the main problem is the strong discrepancy observed at the short end of the *CAM-CVF* spectra of both HR 7310 and HD 207129 induced, as we have already mentioned, by transient effects in the ISOCAM detectors.

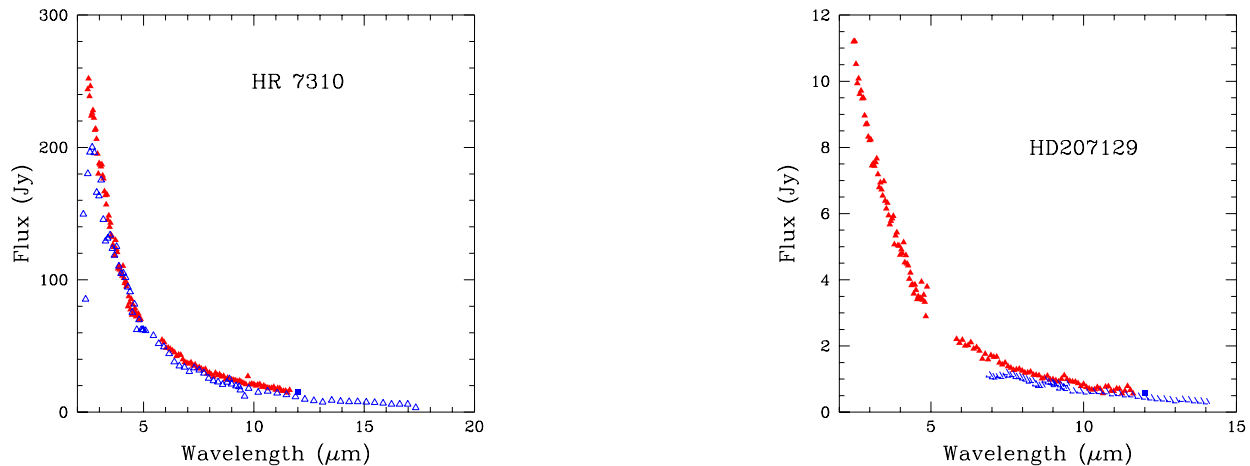


Figure 6.5: *CAM-CVF* (blue open triangles) versus *PHT-S* (red filled triangles) OLP Version 10 spectra of two sources taken from the cross-calibration sample. As usual, the blue squares represent the *IRAS* photometry at $12 \mu\text{m}$.

6.2.1.4 SWS/LWS overlap region

In order to extend our internal cross-calibration analysis to longer wavelengths we also checked the consistency of the absolute flux calibration of SWS (AOT SWS01) and LWS (AOT LWS01) in the overlapping region of these instruments. For this, a total number of 122 common pointings (separated less than $2''$) were selected from IDA for which both SWS and LWS measurements were available with fluxes between 43.7 and $44.4 \mu\text{m}$ higher than 100 Jy .

Sources identified as variable in the literature in this cross-calibration sample were identified and removed from the sample except when the SWS and the LWS measurements were taken on the same revolution (usually one after the other as concatenated observations). Similarly, all sources reported to be extended were also discarded to avoid problems derived from the comparison of fluxes measured through different aperture sizes. In addition, a few other sources were excluded from the analysis because they were identified either as badly pointed (off-axis) or as sources with a possible (not previously reported) extended nature, according to the strong discontinuities observed between SWS bands (see Figure 6.1).

After this purge, the resulting sample still contains around 50 different sources suitable for cross-calibration. A reduced subsample composed of 25 sources (used as test cases) were systematically investigated every time there was a new release of the automated pipeline since OLP Version 7. For each of them the average value of the observed flux density ratio LWS/SWS at $44 \mu\text{m}$ was determined using ISAP (assuming that the source SED shape was of the form $\nu \times f_\nu = \text{constant}$, or equivalently $\lambda \times f_\lambda = \text{constant}$).

As it also happened in other cross-calibration analysis performed during Post-Operations, some calibration problems were identified during the course of this exercise. The most important one in this case was the detection of an anomalous behaviour of the SW1 detector in LWS in all the spectra taken before revolution 237. The flux of this detector appeared systematically underestimated (around 20%) with respect to both the adjacent SW2 detector of LWS and band 4 of SWS. The problem was identified as related to an incorrect treatment by the pipeline of the illuminator flash sequence used by LWS before this revolution and solved in OLP Version 10.1 by applying the necessary modifications in the automated calibration software.

The results obtained as of OLP Version 10 for the 25 test cases above mentioned using ISAP Version 2.1 are listed in Table 6.1. Some examples of the corresponding composite SWS+LWS spectra are shown in Figure 6.6.

Table 6.1: *OLP Version 10 LWS/SWS ratios at 44 μm of the 25 test cases used to analyse the internal consistency between SWS and LWS absolute flux calibration.*

Source	SWS TDT#	LWS TDT#	LWS/SWS	Notes
HD 161796	07100579	07100579	0.95	
HD 101584	07901402	07901520	1.01	
Hen 2–113	07903307	07903229	0.98	
HD 161796	07100579	08001732	1.03	
CPD –56 8032	27301339	08401538	1.03	
IRAS 16342–3814	45801328	08402827	0.94	
Circinus	07902231	10401133	1.26	bad SWS band 4
AFGL 4106	10401225	10401227	0.95	
M 1–78	15901853	15901854	0.90	
CW Leo	19700159	19800158	1.11	
μ Cep	08001274	22002005	1.07	
SAO 34504	26302115	26300513	1.12	bad SWS band 4
IRAS 19114+0002	52000234	31900901	0.96	
OH 26.5+0.6	33000525	33000316	1.01	
VX Sgr	09900171	33100802	1.04	
IRAS 15452–5459	45900615	48800916	1.12	bad SWS band 4
IRAS 16594–4656	45800441	49001642	1.02	
IRAS 19114+0002	52000234	52500861	1.00	
R Dor	58900918	59300644	1.03	
Hen 2–113	07903307	60701891	1.07	
CRL 618	68800561	68800450	0.90	bad SWS band 4
IC 418	82901301	68900805	1.04	
TX Cam	69501070	69501069	1.06	
HD 44179	70201801	70201904	1.00	
IC 418	82901301	86801205	1.03	

If we exclude from the analysis four objects showing calibration problems in band 4 of SWS (those presenting strong mismatches with band 3, indicated in Table 6.1), we can see that the mean LWS/SWS ratio derived from these measurements is $\langle \text{LWS/SWS} \rangle = 1.01$, very close to unity, with a very little dispersion around this value (in most cases the agreement is at the 10% level or better). This is remarkable, if we consider that LWS and SWS were calibrated in a totally different way (LWS calibration is based on Uranus as primary calibrator while SWS band 4 calibration is mainly based on the results of ground-based ILT experiments using blackbody sources).

As a byproduct of this analysis and since some of the objects in this cross-calibration sample were repeatedly observed throughout the mission with either SWS or LWS, it was also possible to perform an independent analysis of the stability of both instruments in terms of absolute flux calibration. The results obtained indicate that both for LWS and SWS the reproducibility was better than 15% in all cases.

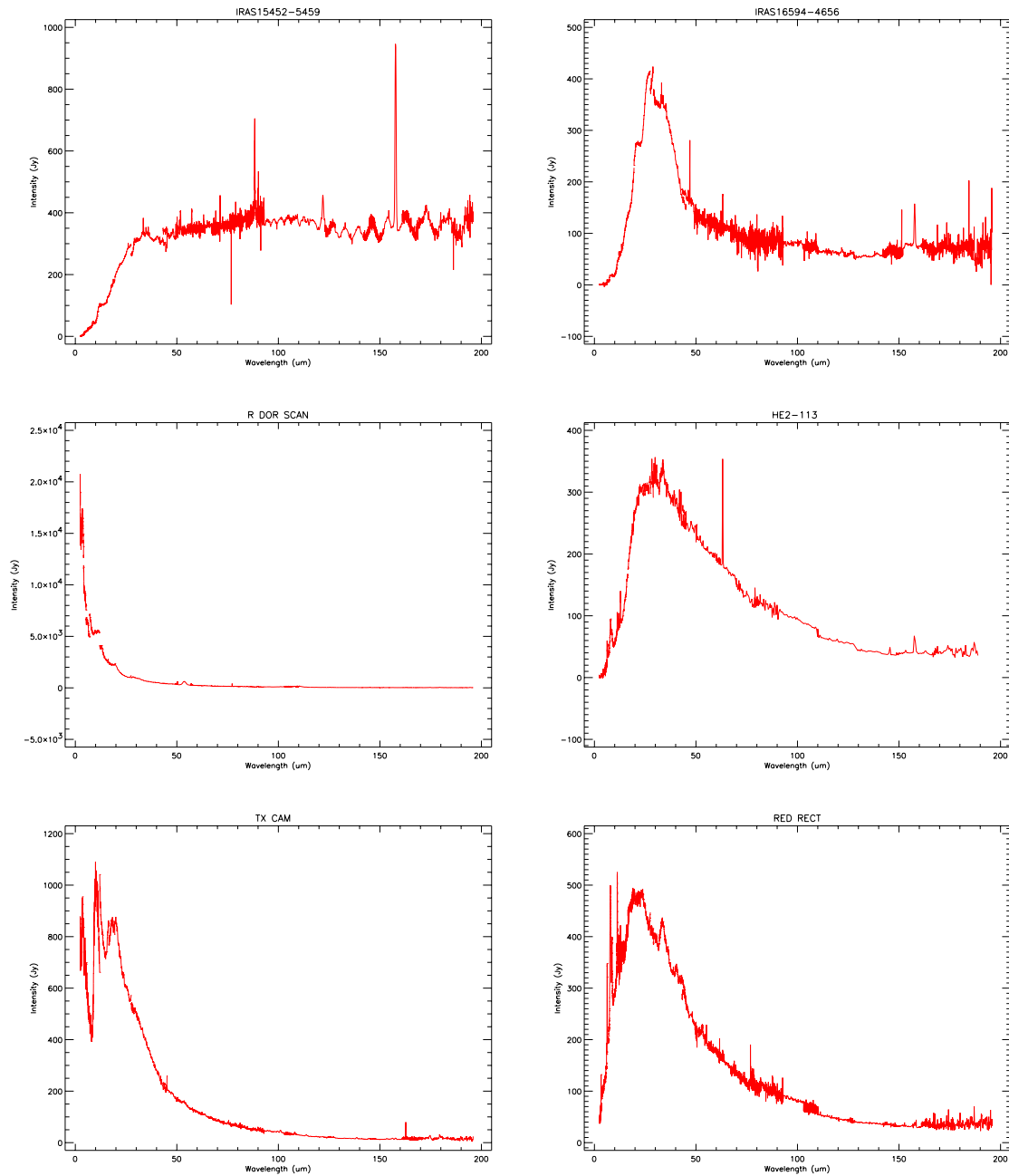


Figure 6.6: *Composite OLP Version 10 SWS+LWS spectra of some of the sources used as test cases for the consistency check between SWS and LWS. Note the excellent match at 44 μm in most cases.*

6.2.2 Filter measurements versus spectroscopy

6.2.2.1 ISOCAM filters versus chopped PHT-S

An excellent agreement is also found when comparing ISOCAM filter measurements with PHT-S spectroscopy. As an example of this, we present here the results obtained from a cross-calibration comparison

performed at a very low flux level (a few mJy) of ISOCAM filter photometry (AOT CAM01) and PHT-S spectroscopy (AOT PHT40) of a sample of 55 Seyfert galaxies reported in Schulz et al. 2000, [147]. Seyfert galaxies in the sample were observed both with ISOCAM LW2 ($6.7 \mu\text{m}$) and LW7 ($9.6 \mu\text{m}$) filters and with chopped PHT-S photometry.

In this case, however, the comparison is not based on OLP Version 10 data products. Instead, calibration was performed using standard CIA and PIA routines starting from ERD. Manual recalibration of the spectra included only glitch de-tailing and transient correction of the chopped PHT-S measurements in a similar way as the Version 10 of the automated pipeline does it. Thus, the expected level of agreement reached in the final products is very similar.

In Figure 6.7 we can see two nice examples of PHT-S and ISOCAM filter measurements of the Seyfert galaxies Markarian 509 (Seyfert 1) and NGC 5953 (Seyfert 2).

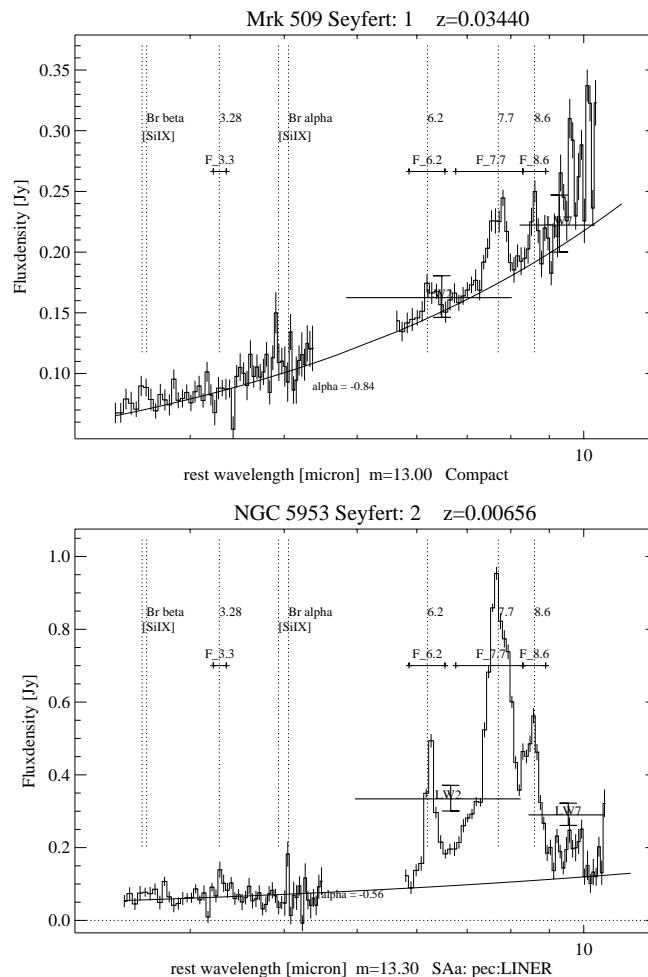


Figure 6.7: PHT-S spectrum and ISOCAM LW2 and LW7 filter measurements of the Seyfert 1 galaxy Mrk 509 and of the Seyfert 2 galaxy NGC 5953. The position of some of the more prominent PAH bands and emission lines are indicated. The two large crosses marked LW2 and LW7 indicate the flux from ISOCAM images with its error and wavelength range. The best fit power-law continuum is shown as a continuous line (taken from Schulz et al. 2000, [147])

The results obtained are very satisfactory since the global median flux ratio (ISOCAM filter/PHT-S) derived from the measurements is: 1.15 for the LW2 measurements and 0.94 for LW7, i.e. ISOCAM

flux densities without colour correction are only 15% higher in LW2 and 6% lower in LW7 than the corresponding PHT-S measurements.

The colour correction for the large bandpass-filter could explain the difference for LW2 up to 10%, as the spectral energy distribution of the Seyfert galaxies observed are red, and with the PAHs contribution in the reddest part of the filter wavelength range. On the other hand, the higher fluxes detected in the LW2 5–8.5 μm filter might also be contaminated by the contribution from the stellar content of the underlying extended galaxy which may still be detectable even for the almost point-like Seyferts, the ISOCAM aperture being wider than the PHT-S one.

6.2.2.2 ISOCAM filters versus SWS

Observations of the Orion bar complex made with CAM-CVF and SWS by Cesarsky et al. 2000, [19] are shown here as an example of this cross-calibration analysis. The spectrum of this region of the sky shows a combination of strong emission features corresponding to PAHs and amorphous silicate grains together with narrow emission lines coming from an ionised region around the isolated O9.5 V star Θ^2 Ori A, as we can see in Figure 6.8.

The simultaneous presence of broad and narrow emission features makes this comparison quite interesting for cross-calibration purposes since it constitutes an excellent laboratory to test the internal consistency of ISO calibration in the presence of emission lines.

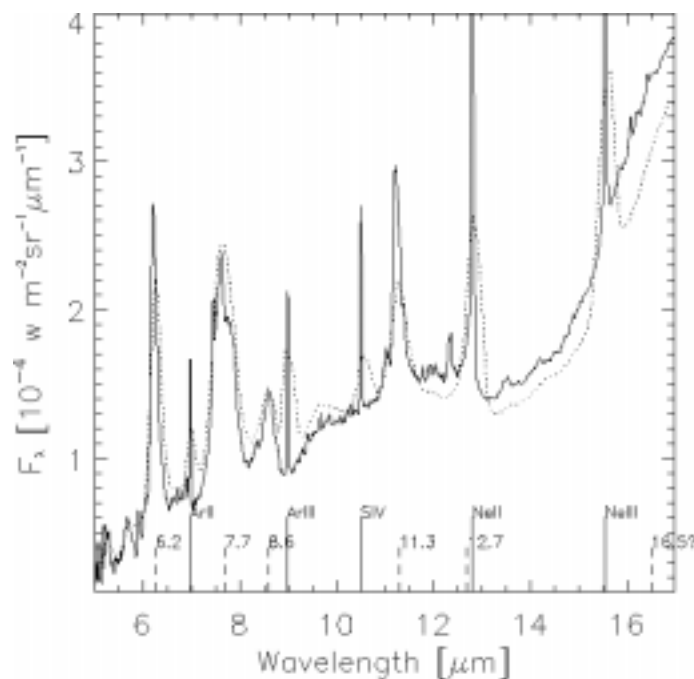


Figure 6.8: SWS spectrum (full line) compared to the CAM-CVF spectrum (dotted line) of the region around Θ^2 Ori A. All the ISOCAM pixels falling in the SWS aperture have been co-added (from Cesarsky et al. 2000, [19]).

The CAM-CVF observations employed the 6'' per pixel field of view of ISOCAM. Full scans of the two CVFs in the LW channel of the camera were performed with both increasing and decreasing wavelength. The results of these two scans are almost identical, showing that the transient response of the detector was only a minor problem for these observations. The raw data were processed using CIA in a standard way and the Fouks-Schubert transient correction was applied to the data resulting in only minor corrections.

The CAM-CVF spectrum of Θ^2 Ori shown in Figure 6.8 was obtained co-adding all the pixels falling within the SWS aperture.

The full range (2.4 to 46 μm) SWS spectrum of the HII region surrounding the star Θ^2 Ori A was reduced with SIA using version 30 of the Cal-G files.

Since the interactive data reduction performed was done in a similar way as Version 10 of the pipeline does it both for ISOCAM and SWS data, the level of agreement reached is expected to be comparable to that obtained using OLP data products. And this was actually found to be excellent, within 20% both for the continuum and for the emission lines.

6.2.2.3 ISOPHOT filters versus ISO spectroscopy

Observations of comet Hale-Bopp taken in October 1996 with ISOPHOT using 4 different detectors (P1, P2, C100 and C200) and 10 filters covering the range between 3.6 and 170 μm by Grün et al. 2001, [66] have been compared with quasi-simultaneous observations taken with PHT-S (Crovisier et al. 1997, [37]), SWS (Crovisier et al. 2000, [38]) and LWS (Lellouch et al. 1998, [109]).

Figure 6.9, taken from Grün et al. 2001, [66] shows the ISOPHOT photometric fluxes together with the PHT-S, SWS and LWS spectra taken on 6–7 October 1996, scaled to a 19'' aperture. This required the application of aperture correction factors which assumed a $1/\rho$ brightness distribution, where ρ is defined as the projected distance from the nucleus. Details on the data reduction of each dataset used in this cross-calibration comparison can be found in the above referenced paper.

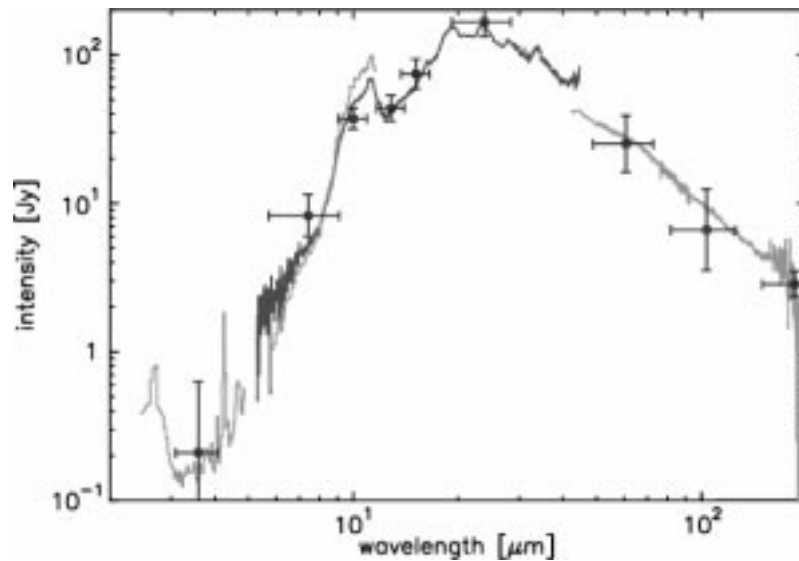


Figure 6.9: Comparison of ISOPHOT photometry (open squares) and the PHT-S, SWS and LWS spectra of Comet Hale-Bopp on 6–7 October 1996. All fluxes have been scaled to a 19' diameter aperture.

In the case of the ISOPHOT filter measurements, background observations were performed with identical instrument settings at the same positions on the sky several days after the comet observations to subtract the contribution from the sky emission to the on-source photometric measurements. All observations were done in single pointing, single filter absolute photometric mode (PHT05 and PHT25).

A reasonable agreement was found between the independently calibrated photometry and spectroscopy in most cases in spite of the many different correction factors applied to the data. These correction factors are needed in the case of ISOPHOT to cope with the different apertures used per filter, positional offsets (observations where the source was not perfectly centred in the aperture), PSF effects on coma

measurements, and the usual colour corrections. For SWS, additional scaling factors were applied to the different bands to make the spectrum continuous; these scaling factors were always close to one.

6.2.2.4 ISOPHOT filters versus LWS

We present here the results obtained from the cross-calibration analysis performed at the long wavelength spectral range covered by ISO between 60 and 200 μm using a combination of PHT-C measurements and LWS01 observations.

As it has already been mentioned before, this comparison is difficult because of the limited common dynamic range and the lack of astronomical sources observed both with PHT-C and LWS suitable for cross-calibration.

Searching the ISO Data Archive it is possible to select around 200 different positions in the sky where ISO observations were performed both with PHT-C filters (photometry beyond 60 μm) and LWS01, corresponding to about 100 different astronomical sources. However, there are very few of them with both PHT and LWS observations of enough quality to derive reliable numbers. In addition, the strong infrared background sometimes completely dominates the measurements especially at the longest wavelengths making cross-comparisons more difficult.

Moreover, we need to purge as usual this cross-calibration sample for bad-pointed observations, variable and extended sources, which at the end limits the number of suitable sources to just 9 common observations which are presented in Tables 6.2 and 6.3. These were the observations selected as test cases for this cross-calibration analysis.

For the derivation of the fluxes quoted in Tables 6.2 and 6.3 we retrieved from the ISO Data Archive the OLP Version 10 PHT-C photometric data together with the corresponding OLP Version 10 LWS spectra. In the case of the PHT-C photometry we just took directly the values provided by the automated pipeline while the LWS spectra were further processed with ISAP Version 2.1 in order to derive the equivalent ‘synthetic photometry’ at 60, 100, 120, 150 and 200 μm .

For this we used the `syn_phot` application in ISAP, which allows the convolution of the ISO LWS spectrum with the transmission profile of the different IRAS PHT-C filters used in the comparison. The programme assigns a monochromatic flux at each of these wavelengths as output under the assumption that the source SED shape is of the form $\nu \times f_\nu = \text{constant}$, or equivalently $\lambda \times f_\lambda = \text{constant}$, in the same way as PHT-C calibration did.

Table 6.2: *List of cross-calibration sources used in the comparison between PHT-C100 and LWS*

Source	C100 60 μm	C100 100 μm	C100 120 μm	LWS 60 μm	LWS 100 μm	LWS 120 μm	IRAS <i>CIRR2</i>
CRL 3068	-	-	70.0	-	-	67.0	1
Y CVn	21.0	10.5	-	14.6	8.3	-	1
HD 161796	-	-	54.8	-	-	54.1	1
R Cas	102	38.5	-	85.5	32.9	-	2
IRAS 16342–3814	-	-	269	-	-	146	4
OH104.9+2.4	84.5	63.0	-	89.2	44.6	-	5
χ Cyg	92.8	50.5	-	82.3	36.6	-	5
μ Cep	112.5	64.0	177.5	108.5	52.9	39.0	5
VX Sgr	-	-	1240	-	-	205	6

In Tables 6.2 and 6.3 the sources have been sorted according to the increasing value of the parameter *CIRR2* as quoted in the IRAS Point Source Catalogue Version 2.1. This is a logarithmic function which describes the contamination expected from background cirrus emission at 100 μm and responds to the equation:

Table 6.3: *List of cross-calibration sources used in the comparison between PHT-C200 and LWS*

Source	C200	C200	LWS	LWS	IRAS
	150 μm	200 μm	150 μm	200 μm	<i>CIRR2</i>
CRL 3068	43.0	23.0	36.5	24.4	1
Y CVn	11.7	7.3	3.0	5.0	1
HD 161796	31.2	17.2	17.4	19.1	1
R Cas	52.7	37.9	13.3	4.7	2
IRAS 16342–3814	221	171	97.0	70.5	4
OH104.9+2.4	246	270	33.2	35.3	5
χ Cyg	161	136	33.3	46.8	5
μ Cep	179.5	147.5	25.8	18.3	5
VX Sgr	1640	1210	216	229	6

$$CIRR2 = \text{int}[(8/3) \times \log(F_c/F_s) + (19/3)] \quad (6.1)$$

where F_c is the cirrus flux and F_s is the source flux (see the *IRAS Explanatory Supplement*, [84]). A value of $CIRR2=1$ corresponds to the cirrus flux being less than 1% of the source flux while $CIRR2$ larger than 5–6 indicates that the flux measurement is probably dominated by the cirrus contribution.

The cirrus contamination effect has clearly been detected in the cross-calibration measurements shown in Tables 6.2 and 6.3, especially beyond 100 μm .

While the consistency between PHT-C and LWS is better than 20–30% in most cases at 60 and 100 μm (detector C-100), we can see that at longer wavelengths (detector C-200) the situation becomes worse and this good level of agreement is only reached by the sources showing a very low value of the $CIRR2$ parameter (and not always). For the rest of the sources in the short list under analysis the cirrus contamination completely dominates the flux detected at 120, 150 and 200 μm . This is clearly reflected by the fact that the flux ratios PHT-C/LWS at these wavelengths closely approach a constant value (between 6 and 8) which is a pure consequence of the difference in size of effective apertures between both instruments.

A similar analysis was carried out by Müller & Lagerros 2002, [127] using a combination of LWS01 grating scans and LWS02 fixed grating observations on a number of asteroids. For this cross-calibration comparison further processing of OLP Version 10 data products was performed using ISAP Version 2.0. In the case of LWS01 grating scans the detector signals were deglitched, σ -clipped ($2.5 \times \text{r.m.s.}$) and averaged. Detectors SW1 to SW5 were then smoothed with the nominal resolution element of 0.29 μm , LW1 to LW5 with a resolution element of 0.6 μm and both scan directions averaged. Observations on a large number of standard sources (planets, asteroids, stars) have shown that the responsivities of the detectors LW1, LW2 and LW3 might be flux dependent. In order to correct for these suspected non-linearities empirical correction values were derived and applied to the asteroid scans (Müller 2001, [124]). The background values were taken from COBE/DIRBE (Hauser et al. 1998a, [75]) weekly maps (25–100 μm) and yearly maps (140–240 μm). LWS solid angles and correction factors for extended sources were taken from the ISO Handbook Volume III on LWS, [68]. Maximal background contributions were 4% for Ceres and up to 50% for Hygiea with the largest influence at long wavelengths.

For the fixed grating LWS02 observations the data reduction was also performed manually taking only the last 100 s of the measurements where the signals were usually stabilised. Dark current subtraction and flux calibration was done in the ISAP command mode. The detector non-linearities and the backgrounds were corrected in the same way as for the LWS01 mode. Maximal background contributions were up to 16% for Ceres, up to about 10% for Pallas and Vesta and up to 40% for Hygiea. The dark current signals in LW4 (160.6 μm) and LW5 (178.0 μm) were in many cases unstable during the integration times and the corresponding fluxes could therefore not be used.

The ISOPHOT observations were calibrated against standard stars and planets only with the help of PIA, using ‘ad-hoc’ Cal-G files excluding intentionally all the asteroids from them (they are also considered calibration standards for ISOPHOT), and treating the asteroid measurements this way as independent scientific observations.

All these observations were compared with thermophysical models of the asteroids (Müller & Lagerros 2002, [127] and references therein), which consider aspects like size, albedo and shape together with the spin vector, a beaming model, thermal inertia and a wavelength-dependent emissivity.

The observations/model ratios are shown in Figures 6.10 to 6.13. It may be interesting to remark here that this cross-calibration comparison comprises a large variety of observing geometries, aspect and phase angles, typically 2–3 orders of magnitude in flux and different background conditions for each asteroid. The observation from the 2 instruments (LWS, ISOPHOT) were taken in different observing modes (LWS01, LWS02, PHT22, PHT25, PHT99) and quite different integration times. They underwent completely different data processing and calibration schemes. Nevertheless, the observations/model representation gives a consistent picture, expressed in ratios close to one. In general no systematic offsets on absolute terms between the instruments or observing modes can be seen with the exception of the well known flux underestimation of the SW1 detector of LWS for observations taken before revolution 237 (some of which are represented in the plots as outliers), corrected in the final Version 10.1 of the LWS pipeline, and a few residual jumps between detector bands which are not yet fully understood.

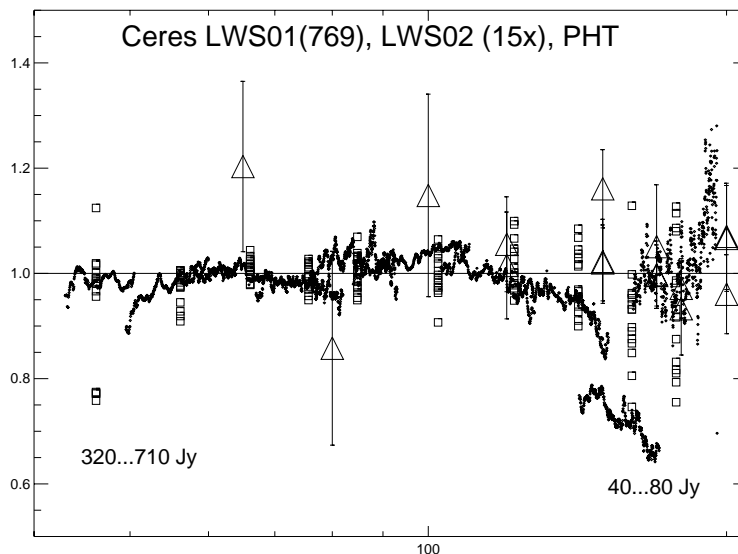


Figure 6.10: *LWS* (fixed grating: squares; grating scans: dots) and *ISOPHOT* (triangles) observations of *Ceres* divided by its thermophysical model. A few *LWS-SW1* fixed grating observations taken before revolution 237 are visible in the plot as outliers as well as a few measurements taken with the *LWS-LW4* and *LWS-LW5* detectors. No other systematic differences between *LWS* and *ISOPHOT* can be seen (from Müller & Lagerros 2002, [127]).

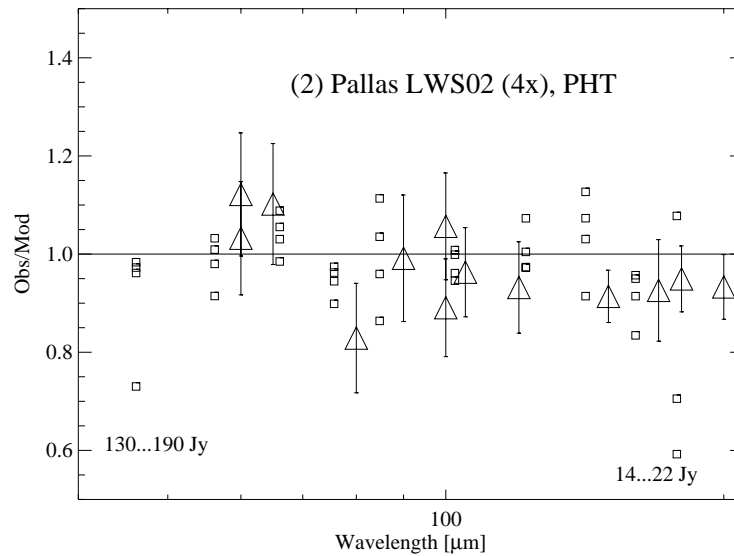


Figure 6.11: *LWS* (fixed grating: squares) and *ISOPHOT* (triangles) observations of *Pallas* divided by its thermophysical model. Only one *LWS-SW1* fixed grating measurement taken before revolution 237 and a couple of individual *LW5* measurements show strong discrepancies with respect to the *ISOPHOT* data and/or the thermophysical model (from Müller & Lagerros 2002, [127]).

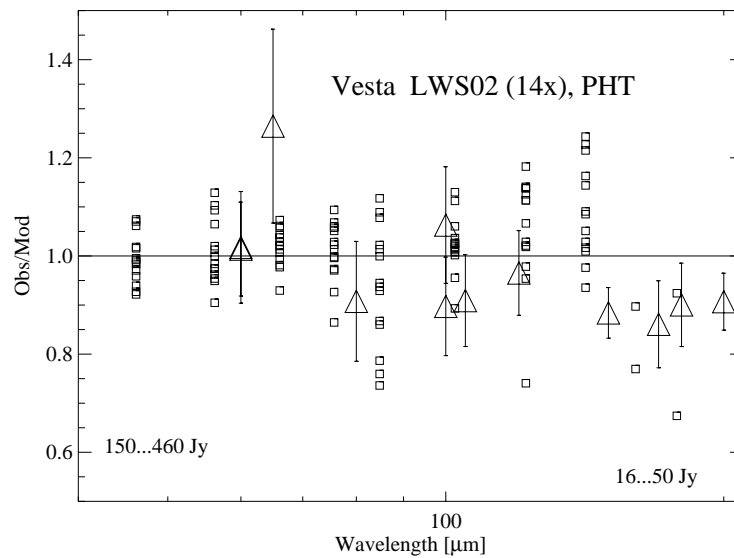


Figure 6.12: *LWS* (fixed grating: squares) and *ISOPHOT* (triangles) observations of *Vesta* divided by its thermophysical model. Again, with the exception of a few measurements at the longest wavelength range, no strong systematic differences between *LWS* and *ISOPHOT* can be seen (from Müller & Lagerros 2002, [127]).

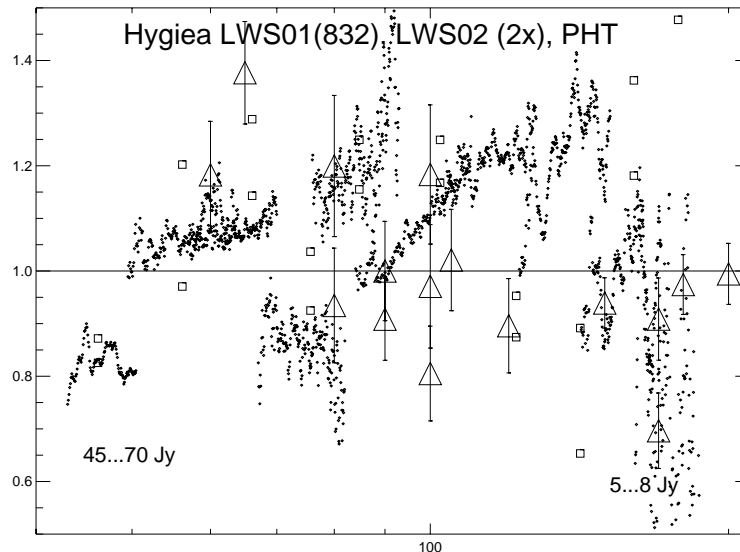


Figure 6.13: *LWS* (fixed grating: squares; grating scans: dots) and *ISOPHOT* (triangles) observations of *Hygiea* divided by its thermophysical model. Note the $\sim 20\%$ discrepancy of the *LWS-SW1* measurements, both taken before revolution 237. Other jumps between *LWS* bands are calibration artifacts. Especially the high quality *ISOPHOT C200* measurements are consistent with the model predictions. Note that the flux level in this case is of only a few Jy at the longest wavelength range, close to the detection limit for *LWS* (from Müller & Lagerros 2002, [127]).

6.3 External Cross-Calibration

6.3.1 Comparison with IRAS

6.3.1.1 SWS versus IRAS photometry

A large number of astronomical sources observed with SWS were also detected by IRAS in the 12 and 25 μm bands and are included in the IRAS Point Source Catalogue.

In order to compare the absolute flux calibration of IRAS and ISO SWS we searched the ISO Data Archive for observations made with ISO at the same positions of the sky, allowing a maximum offset of 1.5'. This way, we found up to 556 different pointings in the ISO Data Archive containing SWS01 observations corresponding to around 400 different IRAS sources.

Unfortunately, many of the sources in this sample had to be discarded because they were known to be slightly extended sources or strongly variable. Extended sources may introduce uncertainty in the results; first, because the SWS calibration is based on point source flux calibration and correction factors are needed to derive their actual absolute flux and, second, because many of these extended sources are usually located in areas of the sky with a complex structure at infrared wavelengths, which complicates even more the problem.

Sources which look extended to SWS are easily recognised because the spectra show strong flux jumps between bands coincident with changes in the aperture size, as we have already shown in Figure 6.1 (bottom panel).

Concerning variability, we know that many of the stars observed by ISO are characterised by their strong photometric variability. Many of them are pulsating stars in the Asymptotic Giant Branch (AGB)

phase evolving into planetary nebulae. Some others are young stellar objects which may also be variable (although in this case the amplitude of the variations in this spectral range is usually not very large).

In spite of all these limitations, we ended up with a list of still more than 250 individual observations susceptible to be used for cross-calibration with the IRAS photometry at 12 and 25 μm , corresponding to more than 100 different astronomical sources, covering a wide range of spectral shapes and brightness.

Each of these 250 individual OLP Version 10 SWS spectra were retrieved from the ISO Data Archive and further processed with ISAP Version 2.1. Basically, bad data points affected by glitches were identified and removed from the spectra using the available tools in ISAP and what we can call ‘ISO SWS photometry’ was performed at 12 and 25 μm with the help of the `syn_phot` application of ISAP, which simply convolves the ISO spectrum with the transmission profile of the IRAS filters at 12 and 25 μm and assigns a monochromatic flux at these two wavelengths under the assumption that the source SED shape is of the form $\nu \times f_\nu = \text{constant}$, or equivalently $\lambda \times f_\lambda = \text{constant}$, in the same way as IRAS did.

In Figure 6.14 we show the results obtained at 12 μm . At first sight, the conclusion is that, in general, ISO SWS synthetic photometry and IRAS photometry at 12 μm are consistent within the 15% level in most cases independent on the flux level considered (from few Jy to several thousand Jy), with only a few sources showing a slightly worse agreement ($\sim 25\text{--}30\%$) at low flux levels (below 25 Jy).

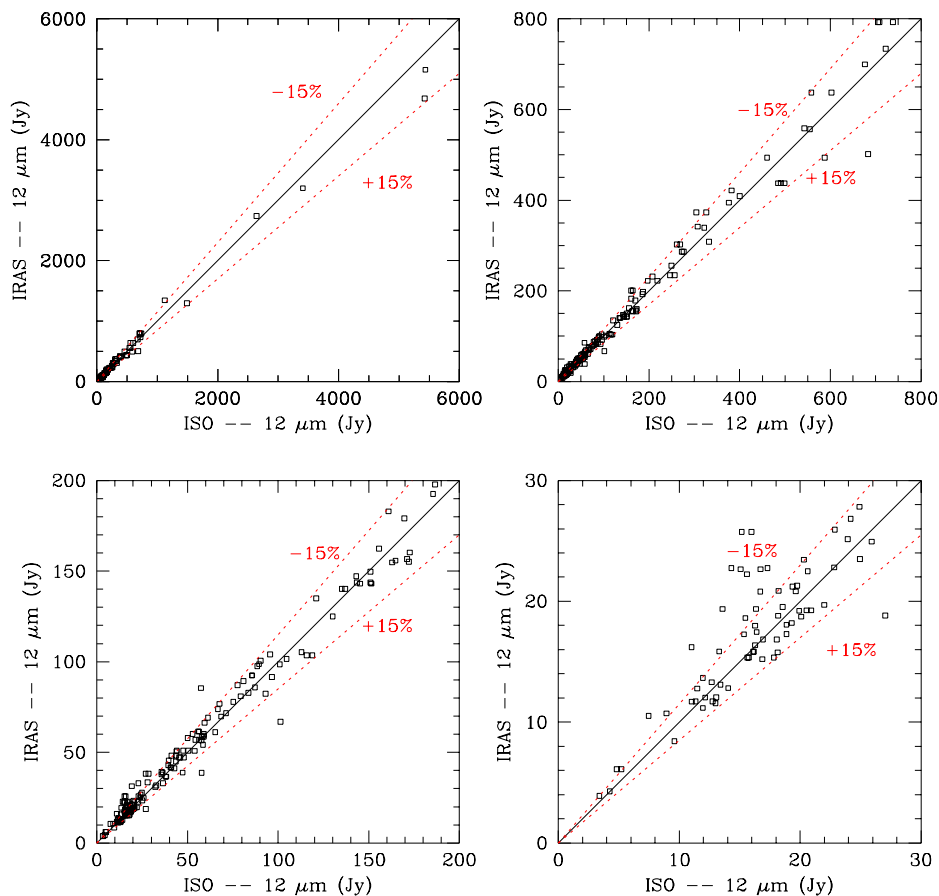


Figure 6.14: *ISO SWS synthetic photometry at 12 μm derived from OLP Version 10 data products compared to IRAS photometry at the same wavelength. The dashed red line represents a 15% discrepancy level*

Figure 6.16 (left panel) shows the distribution of the discrepancies found between the ISO SWS synthetic photometry and IRAS photometry at $12\ \mu\text{m}$. Taking the mean absolute flux level of all the measurements taken with SWS and IRAS at $12\ \mu\text{m}$ the zero-point consistency is found to be better than 2%.

Note that the overall distribution is, however, slightly asymmetric. In the absence of other known calibration problems, the few obvious outliers towards positive values (ISO fluxes overestimated with respect to IRAS) might correspond to variable sources not recognised as such in the sample (and, thus, not purged) detected close their maximum brightness by ISO, while those towards negative values (ISO fluxes underestimated with respect to IRAS) are interpreted as a combination of previously unknown variable sources (caught this time during minimum brightness by ISO) and slightly bad-pointed observations which have partially escaped from detection.

A very similar result is obtained at $25\ \mu\text{m}$, as we can see in Figure 6.15. The level of agreement is again in most cases within 15% for strong sources (above 50 Jy), with very few exceptions, although it becomes also slightly worse for low flux levels (typically within 25–30% for fluxes below 15–20 Jy). Comparing the absolute flux level of all the measurements performed with SWS and IRAS at $25\ \mu\text{m}$ the zero-point consistency is found to be better than 1% (for the derivation of this number, the measurements at $25\ \mu\text{m}$ corresponding to sources with an absolute flux level at this wavelength below 15 Jy were excluded).

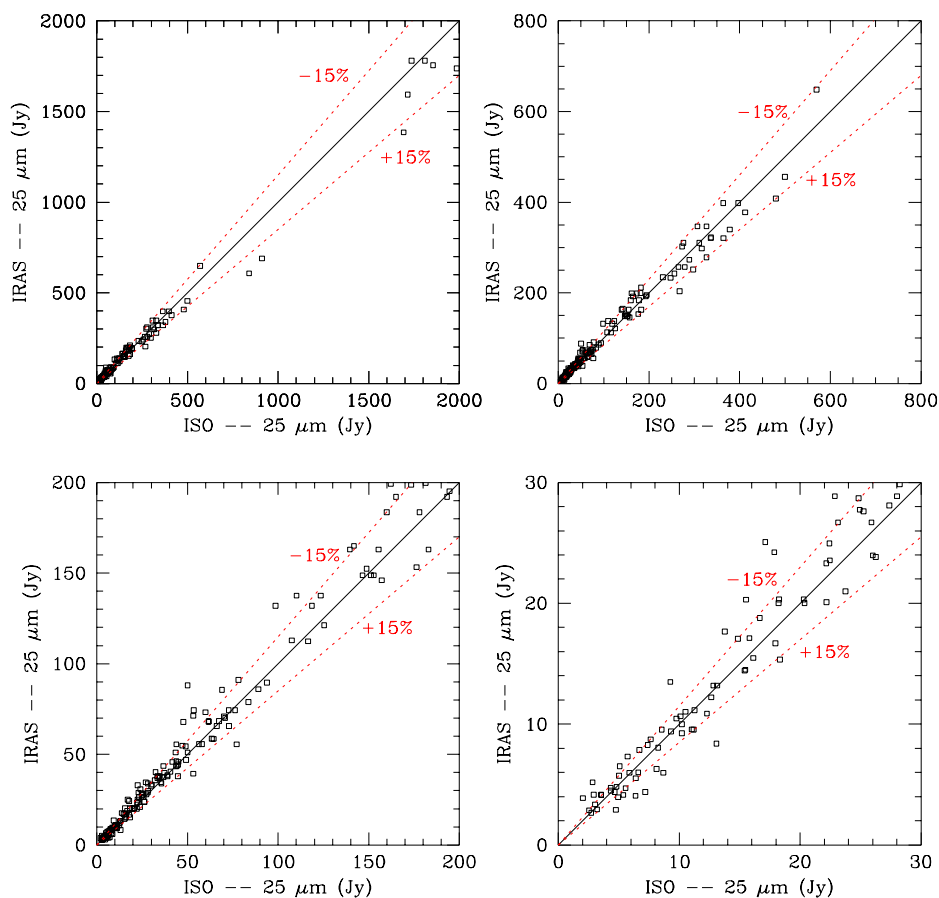


Figure 6.15: *ISO SWS synthetic photometry at $25\ \mu\text{m}$ derived from OLP Version 10 data products compared to IRAS photometry at the same wavelength. The dashed red line represents a 15% discrepancy level.*

In this case, however, the overall distribution of discrepancies plotted in Figure 6.16 (right panel) is not asymmetric, in contrast with what was found at $12\ \mu\text{m}$. The number of strongly underestimated fluxes by ISO with respect to IRAS are in this case more or less similar to the number of overestimations. The few obvious outliers at both sides of the distribution are actually the same sources observed as outliers at $12\ \mu\text{m}$ supporting the hypothesis that they may be variable stars. Thus, we interpret the symmetry observed in this case as the consequence of the smaller number of badly pointed observations at this wavelength, probably because of the larger apertures used by SWS bands 3 and 4, which lowers the probability of missing part of the incoming flux from a point source when it is observed slightly off-axis.

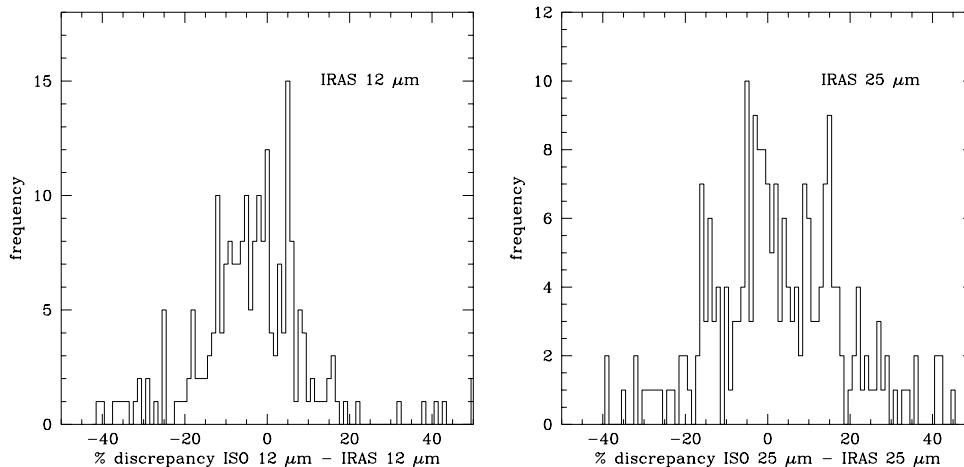


Figure 6.16: *Distribution of the discrepancies found between the ISO SWS synthetic photometry at $12\ \mu\text{m}$ (left) and $25\ \mu\text{m}$ (right) derived from OLP Version 10 data products compared to the IRAS photometry*

6.3.1.2 LWS versus IRAS photometry

A similar analysis was performed by Chan et al. 2001, [20] considering all sources observed with ISO LWS in the grating scan mode (LWS01 AOT) for which there was also available photometry at $100\ \mu\text{m}$ in the IRAS Point Source Catalogue.

In order to compare the absolute flux calibration of IRAS and ISO LWS the ISO Data Archive was searched for observations made with ISO at the same positions of the sky, allowing a maximum offset of $2'$. The objects were selected according to the additional following criteria:

1. IRAS flux density qualities ≥ 2 in the 60 and $100\ \mu\text{m}$ bands
2. LWS data showing no fringes — to avoid sources with a strong cirrus background and/or extended objects
3. $F_\nu(100\ \mu\text{m}) < 1000\ \text{Jy}$ — to avoid detector non-linearities
4. $F_c/F_s < 0.5$, where F_c/F_s is the flux density ratio of cirrus and source
5. IRAS CIRR3 $\leq 254\ \text{MJy/sr}$ and no strong cirrus background on the IRAS Sky Atlas Maps or in the LWS parallel maps at $100\ \mu\text{m}$ (LW1 detector).
6. source is not a known variable source

A total number of 170 different pointings were found in the ISO Data Archive containing LWS01 observations satisfying the above criteria corresponding to 120 different IRAS sources. They all were included in this cross-calibration analysis as test cases, covering a wide range of spectral shapes and brightness.

The OLP Version 10 LWS grating spectra were retrieved from the ISO Data Archive and further processed with ISAP Version 2.1 prior to their comparison with the IRAS photometry at $100\ \mu\text{m}$. Bad data points affected by glitches were removed from the spectra using the available tools in ISAP. A few sources had to be corrected also for the so-called ‘near-infrared leak’. This is an instrumental effect which produces false strong features at $\sim 53\ \mu\text{m}$ and $\sim 105\ \mu\text{m}$ on the LWS spectra of sources with a bright near infrared counterpart. These features can easily be removed by fitting a power-law to the underlying continuum and assuming they have a Gaussian profile, which is a very good approximation to their real shape (see ISO Volume III of the Handbook on LWS, [68] for more details).

ISAP was also used to perform the equivalent ‘ISO LWS photometry’ at $100\ \mu\text{m}$ of all the 120 sources contained in our new cross-calibration sample. This was done using again the `syn_phot` application, which convolves the ISO spectrum with the transmission profile of the IRAS $100\ \mu\text{m}$ filter. This assigns a monochromatic flux at this wavelength under the assumption that the source SED shape is of the form $\nu \times f_\nu = \text{constant}$, or equivalently $\lambda \times f_\lambda = \text{constant}$, in the same way as IRAS did.

The main problem which affects our cross-calibration comparison is the cirrus contamination. The infrared sky is characterised by emission at $100\ \mu\text{m}$ from interstellar dust on all spatial scales. In spite of the restrictions applied to the selected sources, a significant chance exists that some of them can still be affected by components of this long-wavelength emission on point source scale. While the IRAS photometric fluxes quoted in the Point Source Catalogue are already corrected for this background ‘cirrus’ emission, this is not the case of the photometry derived from LWS data, which includes this background contribution. Therefore, it is necessary to apply a correction either to LWS data or to the IRAS photometry before making any cross-calibration comparison.

Two methods can be applied to perform this ‘cirrus correction’. Both recovery procedures are only an approximation:

- **Method 1:** based on the restoration of the original IRAS flux density at $100\ \mu\text{m}$ uncorrected for cirrus (i.e. $F_c + F_s$) using the value of *CIRR2* listed in the IRAS Point Source Catalogue, which is directly related via Equation 6.1 to the value of F_c/F_s . As we have already mentioned in Section 6.2.2.4 *CIRR2* is an integer in the range from 1 to 9. *CIRR2* values less than 4 indicate little or no cirrus contamination. *CIRR2* values larger than 5 indicate the presence of bright cirrus emission heavily contaminating the source photometry.
- **Method 2:** based on the removal of the cirrus contamination from the ISO-LWS synthetic photometry using the *CIRR3* values listed in the IRAS Point Source Catalogue. *CIRR3* is the total surface brightness of the sky surrounding a source in a 0.5° beam at $100\ \mu\text{m}$ clipped to exclude values larger than $254\ \text{MJy/sr}$. LWS calibration is based on point sources, so those that sit on a significant background will require this correction before they can be compared with the IRAS photometric values in the Point Source Catalogue. To perform this correction requires the knowledge of the ISO LWS beam; that is, the effective solid angle of the LWS detectors and the so-called ‘extended source correction factors’, both of which are given in the ISO Handbook Volume III on LWS, [68]. The main problem of this whole procedure is that in regions with bright cirrus emission, the *CIRR3* value may overestimate grossly the true background flux local to the source.

Figure 6.17 shows the distribution of ISO/IRAS flux density ratios at $100\ \mu\text{m}$ as a function of the IRAS flux density at $100\ \mu\text{m}$ in a logarithmic scale using the two different methods above mentioned. The results obtained suggest that, in spite of the uncertainties induced by the sometimes large (and inaccurate) correction factors needed to make this comparison, there is a reasonable good agreement between ISO and IRAS at $100\ \mu\text{m}$ in most cases (within 30%).

However, ISO flux calibration is found to give systematically 12.5% higher fluxes respect to IRAS (if we take the mean value), independent on the method used. A similar discrepancy (11.3%) was reported in

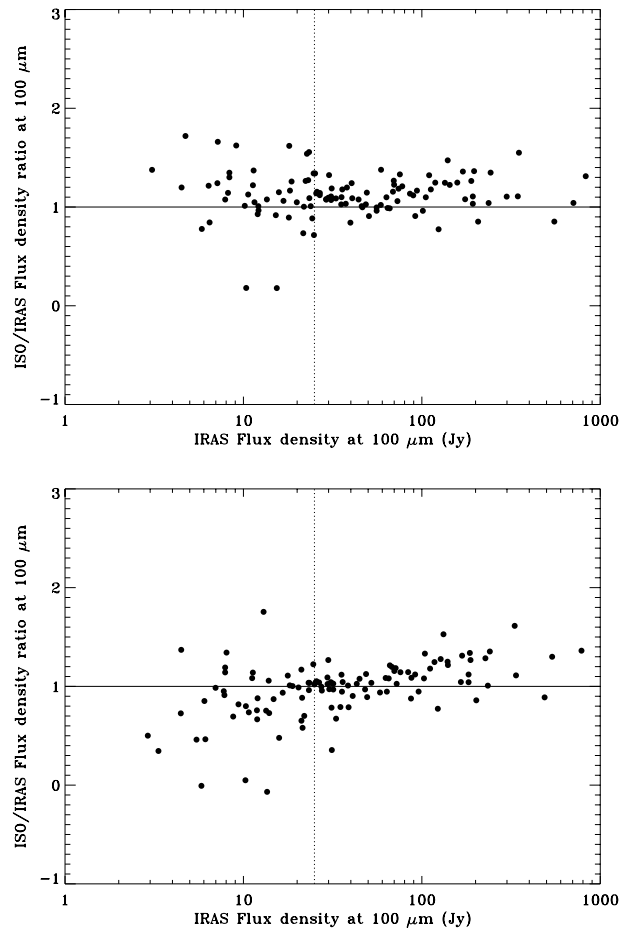


Figure 6.17: *The LWS/IRAS flux density ratios at $100\ \mu\text{m}$ as a function of the IRAS flux density at $100\ \mu\text{m}$ using Method 1 (top) and Method 2 (bottom). The vertical dashed line represents an arbitrary limit below which LWS accuracy becomes dominated by inaccurate dark current subtraction. Note the higher fluxes detected by ISO with respect to IRAS at high flux levels in both cases (from Chan et al. 2001, [20]).*

the *LWS OLP Version 10 Scientific Validation Report* (Lim et al. 2001, [114]), where the calculations were restricted to a short list of low background sources, suggesting that the problem is not related to a wrong background subtraction.

In order to analyse more in detail the problem we have plotted in Figure 6.18 the results of the same cross-calibration comparison in a linear scale and only including sources with IRAS flux densities at $100\ \mu\text{m}$ below 100 Jy using Method 1. Interestingly, the distribution shows the existence of at least 2 different turning points leading to three different regimes. The first regime is followed by sources with ISO fluxes below 25 Jy. These are the sources showing the higher degree of consistency with ISO in terms of absolute flux level, although the dispersion is very high at these low flux levels, as expected, due to inaccurate dark current subtraction. A second regime is followed by sources well detected by ISO with fluxes at $100\ \mu\text{m}$ between 25 and 75 Jy. These sources show systematically 10–15% higher ISO fluxes compared to IRAS with a dispersion of only 20%. And there seems to be even a third regime beyond 75 Jy which shows an even larger systematic discrepancy (up to 20%) with a similar dispersion. The same behaviour, although not shown here, is observed when we use Method 2.

The discontinuities observed are still of unknown origin and may be either in ISO or in IRAS calibration. It is remarkable that the problem seems to be not related with inaccuracy at low flux levels induced

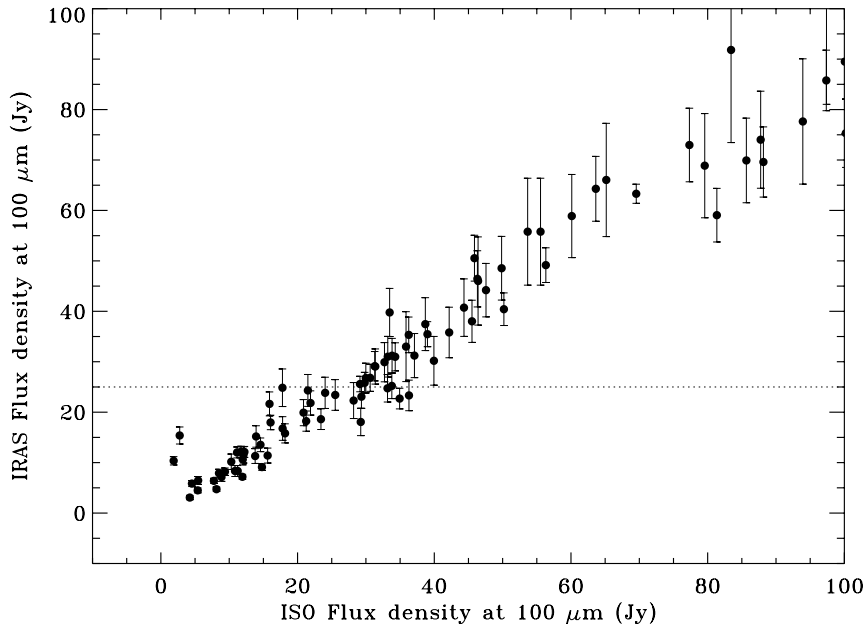


Figure 6.18: *ISO LWS synthetic photometry at 100 μm compared to IRAS photometry at the same wavelength for sources with IRAS flux density at 100 μm less than 100 Jy, using Method 1. The horizontal dashed line represents an arbitrary limit below which LWS accuracy becomes dominated by inaccurate dark current subtraction (taken from Chan et al. 2001, [20]).*

by an inaccurate dark current subtraction since this would just increase the observed dispersion but it would not change the zero-point of the absolute flux calibration. Actually, the strongest discrepancies are observed in the group of the brightest sources.

Neither does the problem seem to be directly correlated with the inaccuracy of the different methods used for cirrus correction, since it equally affects sources with low and high background, as we have already mentioned.

An interesting independent comparison between ISO LWS and IRAS photometry at 60 and 100 μm was carried out by Brauher & Lord 2001, [12] on a large sample of extragalactic sources.

This sample consisted of observations of galaxies taken with the LWS in the grating modes (LWS01 and LWS02) that were reduced in a uniform manner using all of the advanced data reduction techniques of LIA and ISAP starting from OLP Version 7 data products. The galaxy sample comprised nearly all galaxies observed during the ISO mission whose far-infrared emission fell within the 75'' LWS beam and had IRAS Point Source Catalogue detections. There were 155 such galaxies in the ISO Data Archive with 60 μm fluxes ranging from below 1 Jy to 300 Jy.

In this study, a small correction factor was introduced in the derivation of the ISO synthetic photometry at 60 μm with ISAP in order to account for the fraction of the IRAS 60 μm filter not covered by ISO LWS (27–87 μm is the spectral coverage of the IRAS 60 μm filter versus 43–197 μm for LWS). This may introduce some uncertainty in the derived values. Assuming that the majority of the galaxies used for this comparison span a narrow temperature range (30–45 K) the amount of the integrated flux measurement missed by LWS is estimated to vary from 2–8%. Thus, an average correction of 5% to the LWS 60 μm fluxes was applied to all the galaxies in the sample.

The LWS02 60 μm and 100 μm continuum fluxes must also have a secondary correction applied. The fluxes for this AOT were estimated by fitting a 2–5 μm linear baseline through the IRAS filter central

wavelengths, essentially producing a monochromatic flux density. This flux density must be corrected to estimate the flux density IRAS found over its extended passband. Fitting a linear baseline to the spectra overestimates the integrated spectral photometry by 12% at 60 μm and 9% at 100 μm . Thus, the LWS02 fluxes were also corrected for these overestimations accordingly.

After these corrections were applied, the infrared sky background was estimated using IRSKY (images from the all-sky IRAS Survey Atlas with a resolution of 4' in each of the IRAS bands) and then removed from the LWS data, in a similar way as Method 2 described above does it. The background subtracted LWS data were then compared with the IRAS photometry at 60 and 100 μm quoted in the Point Source Catalogue.

Figure 6.19 shows how the LWS and IRAS data compare after a careful reduction with the LWS Interactive Analysis software (LIA), including interactive dark current subtraction, absolute responsivity corrections, as well as manual removal of glitches and fringes.

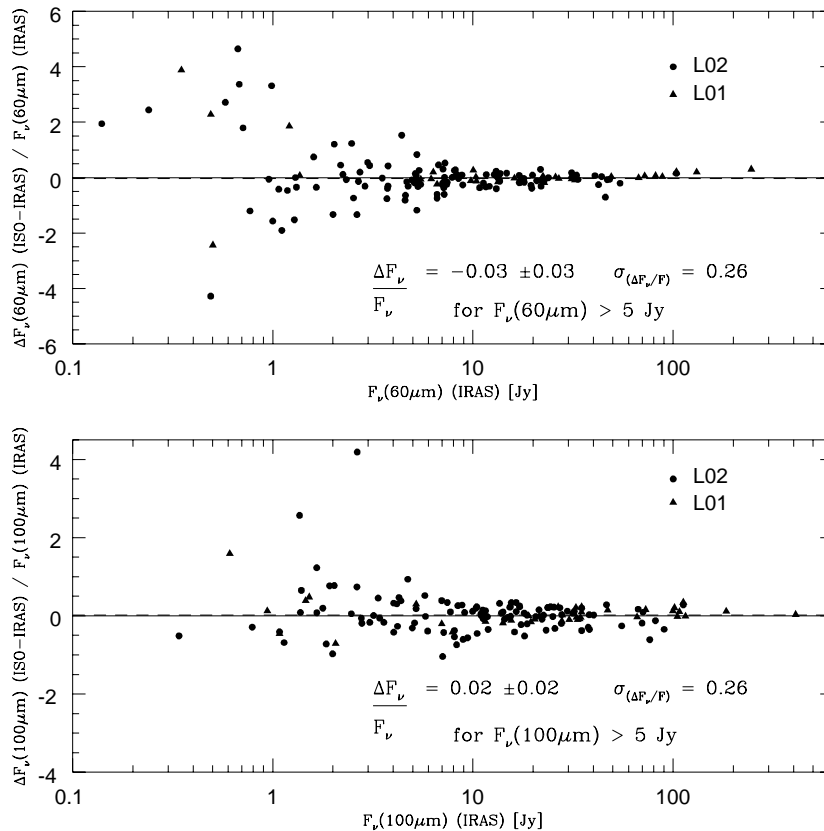


Figure 6.19: *The difference between the LWS and IRAS fluxes at 60 μm and 100 μm . The systematic offsets and dispersions of the LWS01 (triangles) and LWS02 (circles) data with respect to IRAS data are similar. The overall agreement is typically within 26% for fluxes above 5 Jy (from Brauher & Lord 2001, [12]).*

The results obtained suggests an overall good agreement between ISO LWS and IRAS both at 60 and 100 μm , typically within 26% for fluxes above 5 Jy. The ISO fluxes, according to this study are (1) systematically lower than IRAS fluxes by 3% between 5–300 Jy at 60 μm and (2) systematically higher than the IRAS fluxes by 2% between 5–300 Jy at 100 μm . Below 5 Jy the dispersion increases by a factor of two and is attributed to the dark current subtraction errors.

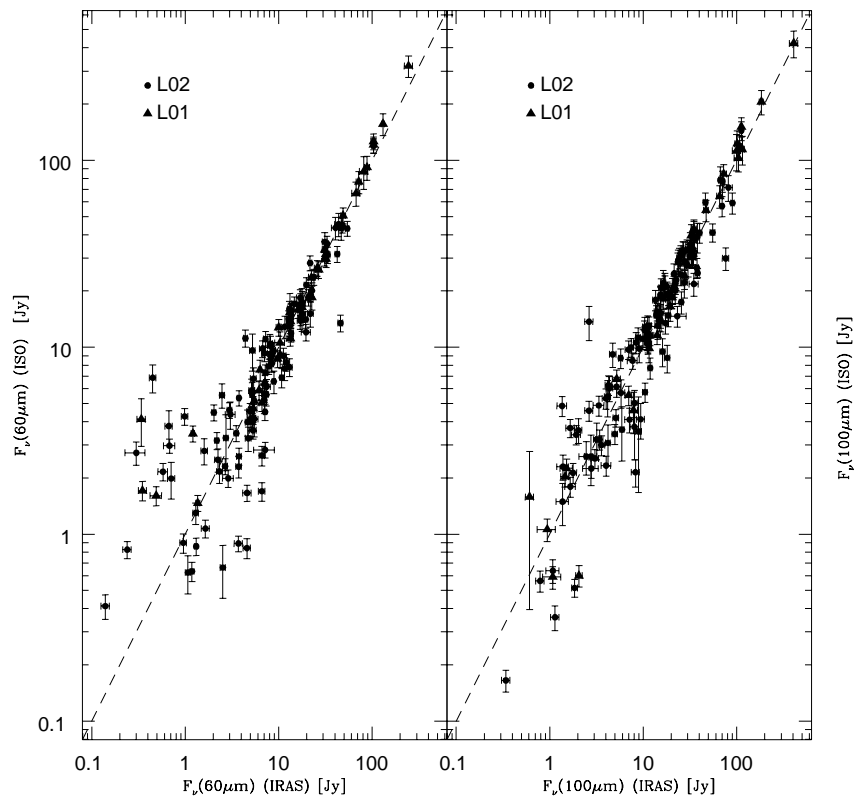


Figure 6.20: *LWS versus IRAS comparison for 60 μm and 100 μm . LWS01 observations are indicated with triangles while LWS02 observations are indicated with filled circles. The IRAS errors come from the Point Source Catalogue, and the ISO errors are a combination of the calibration and measurement uncertainty errors (from Brauher & Lord 2001, [12]).*

However, it is worth to note that if only the brightest sources in the sample are considered (above 25 Jy) the LWS fluxes are found systematically 12% higher than the corresponding IRAS fluxes both at 60 μm and 100 μm . This result is strikingly similar to the offset found at 100 μm by Chan et al. 2001, [20].

The strong discrepancies at high flux levels are more evident in Figure 6.20 where we have plotted the same results in a different format. The discrepancy seems to be of the order of 20–40% for fluxes above 70–80 Jy, supporting our previous findings.

6.3.1.3 ISO composite SWS+LWS spectra versus IRAS photometry at 60 and 100 μm

We can take advantage of the availability of the sample of cross-calibration sources used for the internal comparison between SWS and LWS presented in Section 6.2.1.4 to produce good quality, composite ISO SWS+LWS spectra which can be directly compared with IRAS photometry at 60 and 100 μm . The spectral coverage of the resulting ISO composite spectrum is such that there is no need to apply in this case any correction factor to the IRAS photometry at 60 μm , since the IRAS photometric band is fully covered by ISO when we combine SWS+LWS data in a single spectrum.

The test sample includes 23 sources which are listed in Table 6.4. Note that, unfortunately, we had to exclude from this cross-calibration analysis some of the sources used in the previous comparison. For

instance, this time we could not include the well known variable sources TX Cam or OH 26.5+0.6, observed close in time by ISO with SWS and LWS, but at a completely different epoch with respect to IRAS photometry, taken in 1983–1984. Neither we could use the source IRAS 15452–5459 because of the bad quality of its IRAS photometry at 60 and 100 μm .

Table 6.4: *ISO OLP Version 10.1 synthetic photometry at 60 and 100 μm compared with IRAS photometry*

Source	IRAS 60 μm	IRAS 100 μm^1	IRAS 100 μm^2	ISO 60 μm	ISO 100 μm	IRAS <i>CIRR2</i>	Notes
HD 161796	151.7	48.7	49.2	167.3	56.3	1	
NGC 6543	133.3	62.7	63.3	144.2	72.9	1	
IRAS 19114+0002	515.9	168.1	169.8	674.5	224.3	1	
R Dor	243.5	83.5	84.3	311.1	96.3	1	strong near infrared leak
CRL 618	1036	339.9	343.3	1361	547.4	1	bad SWS band 4
CPD -56 8032	199.1	91.7	93.5	236.5	105.0	2	
CW Leo	5652	922.0	940.0	5297	1247	2	
Circinus	248.7	315.9	322.2	314.6	426.3	2	bad SWS band 4
HD 101584	193.0	104.0	110.2	226.4	132.5	3	
Hen 2-113	176.6	71.3	75.6	217.5	94.7	3	
M 1-78	589.6	408.2	432.7	792.6	592.6	3	
HD 44179	173.1	66.2	70.2	215.1	81.9	3	
IC 418	103.6	31.2	33.1	119.6	35.4	3	
IRAS 16342-3814	290.2	139.4	157.5	262.8	122.1	4	mean of two measurements
SAO 34504	96.6	41.0	46.3	119.1	44.0	4	bad SWS band 4
AFGL 4106	851.8	181.1	239.1	1053	310.4	5	
μ Cep	127.0	49.9	65.9	140.1	52.8	5	strong near infrared leak
IRAS 16594-4656	131.4	34.4	61.2	146.2	78.2	6	
IRAS 21282+5050	33.4	15.0	26.7	38.6	31.4	6	
IRAS 21318+5631	90.0	25.4	44.7	93.8	45.0	6	
α Sco	115.5	31.9	56.1	139.2	53.2	6	bad SWS band 4 & strong near infrared leak
VX Sgr	262.7	82.3	144.9	312.9	197.9	7	

¹ IRAS flux density quoted in the Point Source Catalogue

² restored IRAS flux density including background cirrus emission

At these long wavelengths, and as it was already mentioned in Section 6.3.1.2, one needs to consider very seriously the amount of cirrus contamination in the measurements. In principle, the effect is expected to be strong only at 100 μm in regions of strong cirrus background while the measurements at 60 μm will only be slightly affected. In any case, in order to take this possibility into account and because it can be of help in the analysis, the sources in Table 6.4 have been sorted as a function of the parameter *CIRR2*, previously defined in Equation 6.1, which is directly related with the background emission at 100 μm in the vicinities of the IRAS point source.

For the derivation of the ISO SWS+LWS synthetic photometry at 60 and 100 μm listed in Table 6.4 we used again ISAP Version 2.1. First the corresponding SWS+LWS OLP Version 10.1 spectra were directly retrieved from the ISO Data Archive and combined to create the composite spectra. Then bad data points affected by glitches in both SWS and LWS sections of the composite spectra were removed and the LWS spectra were corrected for near infrared leaks when necessary. Finally the `syn_phot` application of ISAP was used to convolve the ISO spectrum with the transmission profile of the IRAS filters at 60 and 100 μm . This way we derived a monochromatic flux at each of these wavelengths under the assumption that

the source SED shape is of the form $\nu \times f_\nu = \text{constant}$, or equivalently $\lambda \times f_\lambda = \text{constant}$, in the same way as IRAS did.

Figure 6.21 shows the distribution of the derived ISO/IRAS flux density ratios at $60 \mu\text{m}$ as a function of the IRAS flux density at $60 \mu\text{m}$ in logarithmic scale. As we can see the systematic discrepancy between ISO and IRAS photometry at $60 \mu\text{m}$ (of the order of 15%) is confirmed.

The discrepancy cannot be attributed to background contamination since it is not correlated at all with the value of the IRAS *CIRR2* parameter. Instead, there seems to be a clear correlation with increasing flux, similar to that previously found for the sample of extragalactic sources analysed in Section 6.3.1.2. In order to determine whether this systematic discrepancy between ISO and LWS is also found at $100 \mu\text{m}$ we used again the sources in Table 6.4 to perform an independent analysis.

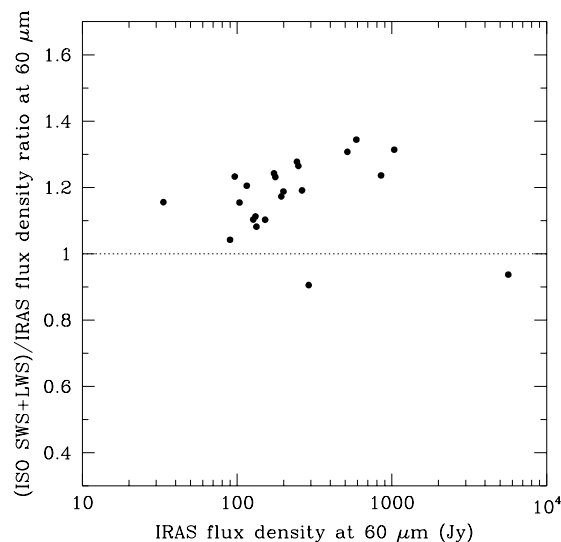


Figure 6.21: *The ISO/IRAS flux density ratios at 60μ as a function of the IRAS flux density at $60 \mu\text{m}$.*

Following the strategy proposed by Josephine Chan in their comparison of ISO data with IRAS photometry at $100 \mu\text{m}$, we used their Method 1, this is, the restoration of the background emission estimated from the *CIRR2* parameter to the quoted IRAS flux density at $100 \mu\text{m}$ in the IRAS Point Source Catalogue Version 2.1, to determine the total cirrus+source flux density. This is the quantity that must be used to compare with the LWS measurements, as LWS measured both source+background emission.

Figure 6.22 shows in logarithmic scale the distribution of ISO/IRAS flux density ratios at $100 \mu\text{m}$ as a function of the restored IRAS flux density at $100 \mu\text{m}$.

Interestingly, we see again the same effect. ISO equivalent fluxes at $100 \mu\text{m}$ are found to be around 20% higher if we take the mean value of all measurements and up to 60% in the most extreme cases. The discrepancies found are not correlated with IRAS *CIRR2*, being equally distributed among sources with low and high background contamination. Surprisingly we find again, instead, what seems to be a clear correlation with the flux level, so that in general the brightest sources are those showing the strongest discrepancies while ISO data and IRAS photometry appear consistent to within the 25% level for sources below 100 Jy.

A plot which combines all the results obtained in the three independent cross-calibration analysis performed at 60 and $100 \mu\text{m}$ between ISO and IRAS here presented is shown in Figure 5.8 of the ISO Handbook Volume III on LWS.

In summary, our conclusion is that both at 60 and $100 \mu\text{m}$ IRAS and ISO agree within a few % in average for sources fainter than 25 Jy, while ISO fluxes are found systematically higher than IRAS fluxes

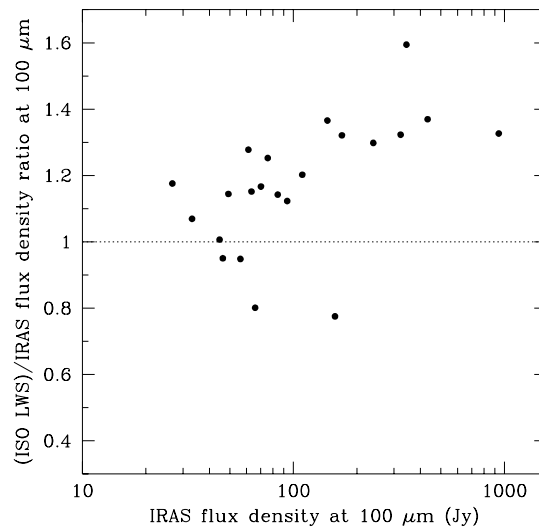


Figure 6.22: *The ISO/IRAS flux density ratios at 100 μ as a function of the restored IRAS flux density at 100 μ for the same calibration sample used in Figure 6.21.*

for sources brighter than 25 Jy. The difference increases from about 15% around 100 Jy, to a level of about 20% for sources up to 400 Jy, and up to 30–50% for sources brighter than 400 Jy.

The reason for this behaviour is not understood. We know it is not due to inaccurate dark current subtraction, nor to cirrus background contamination. A possible cause could be some non-linearities in the infrared detectors. However, the problem could be associated with IRAS data and not with ISO.

Indeed, Figure IV.A.4.2 of the IRAS Explanatory Supplement, [84] does evidence detector non-linearity behaviour and Section VI.B.4.d quotes errors of respectively 30% and 70% at 60 and 100 μ m for sources above 100 Jy.

6.3.1.4 LWS raster scans of extended sources versus IRAS photometry

LWS observations have also been made at a number of positions in the complex Trumpler 14 and 16 fields, and in the direction of the Galactic Centre. LWS data have been compared with the IRAS 100 μ m fluxes at the same positions. All fields contain large areas of extended emission, which although relatively smooth, do change by a factor of ~ 40 within each region.

The point source fluxes (Jy) provided by the LWS pipeline calibration have been converted to extended source fluxes (MJy sr^{-1}) using the correction factors implemented in ISAP Version 2.0.

Figure 6.23 shows the comparison of the converted LWS and IRAS 100 μ m fluxes. As we can see, the results indicate that there is an excellent agreement between the fluxes provided by ISO and the IRAS results. From the analysis of the data we obtain a mean ratio, $\text{LWS/IRAS} = 1.0 \pm 0.1$.

Part of the uncertainty is probably due to the unresolved structure of the sources observed within the beam. This is because the extended source correction factors applied have been derived under the assumption of a smooth and very extended flux distribution. In the real world, structure or embedded sources could produce significant discrepancies from the ideal situation and, with it, differences in flux.

Note also that for fields containing multiple sources the observed flux will depend critically on the precise positions of the sources relative to the optical axis. To recover or model the observed flux requires positional information on the sources and a deconvolution with the PSF and instrumental profile. Indeed, for single point sources observed off-axis a similar procedure is required to recover the correct flux.

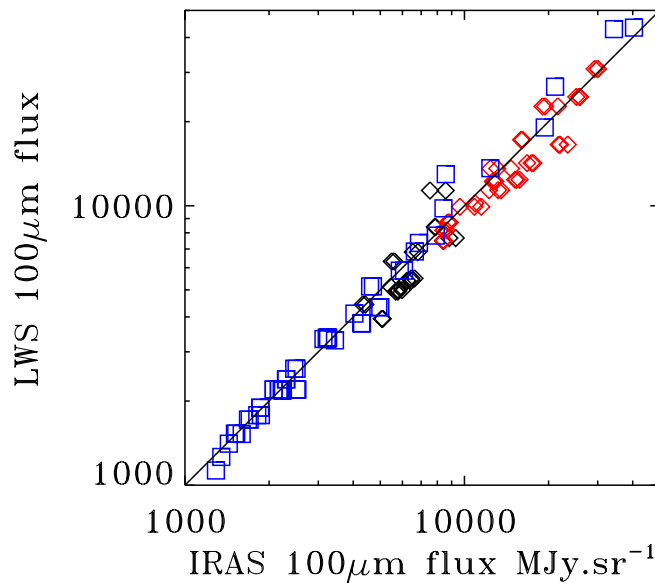


Figure 6.23: Comparison of LWS and IRAS 100 μm fluxes in the Trumpler 14 (red diamonds), Trumpler 16 (black diamonds), and Galactic Centre (blue squares) fields.

6.3.1.5 ISOPHOT-P and -C versus IRAS photometry

The database of ISO observations generated by a project intended to search for Vega-like debris disks around nearby main-sequence stars (Habing et al. 1996, [69]; Laureijs et al. 2002, [106]) has also been used to assess the quality of ISOPHOT photometric calibration.

The sample contains more than 80 main sequence stars that were observed with ISOPHOT at 25, 60, 150 and 170 μm , in order to determine whether the star had an infrared excess indicating the presence of a dusty disk. Unfortunately, the number of stars found with disks was very low: only 8 out of 65 stars observed with ISO showed a significant excess at 60 μm .

The positive point, from the cross-calibration perspective, is that the non-detected stars constitute a nice homogeneous sample of observations which can be used to improve our knowledge of the quality of the observations made with ISOPHOT by comparing the observations with models and with the IRAS photometry of the same sources at 25 and at 60 μm .

The subsample of observations here analysed were performed using the AOT PHT03 (PHT-P detectors) in triangular chopped mode at 25 μm and mini-maps (3×3 with $46''$ steps) centred at the source location at 60 μm using the AOT PHT22, and reflects the status of the PHT calibration as of OLP Version 8.

Figure 6.24 shows the result of the ISO observations compared to the IRAS photometry (when available) of the stars observed at 25 and 60 μm .

As we can see, the level of agreement with IRAS photometry at 25 μm is in most cases better than 25%. The brighter targets ($F_{25} > 1 \text{ Jy}$) appear to have systematically ISO flux densities lower than the IRAS values. This underestimation is expected from the usage of the chopped mode, where a relatively high source-background contrast causes a signal loss due to transient responsivity in the PHT-P detector. On the other hand, the ISO fluxes of the fainter stars ($F_{25} < 300 \text{ mJy}$) appear overestimated with respect to IRAS. The explanation for this overestimation is still not clear but it might be the result of (i) the peculiar transient behaviour of the P2 detector, (2) a low level signal non-linearity, or (3) uncertainties in the IRAS calibration (we have to consider that at these low flux levels we are close to the detection limit of IRAS at 25 μm).

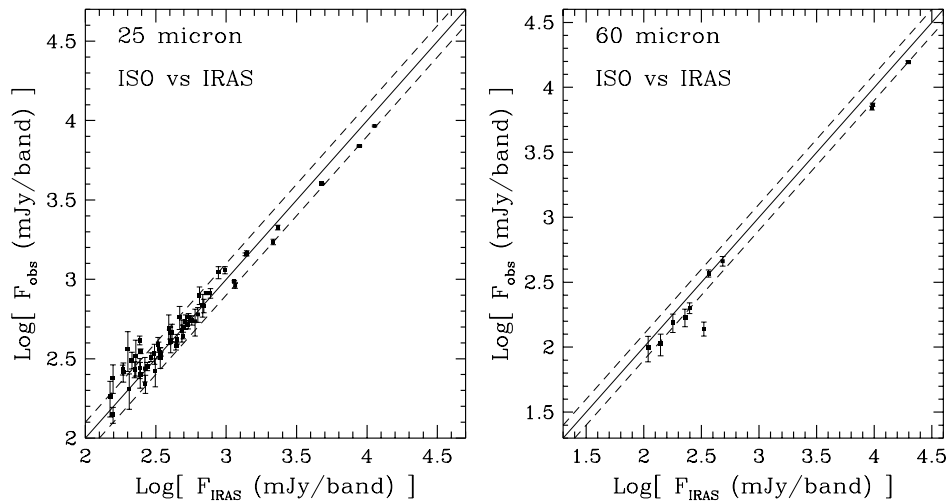


Figure 6.24: The flux densities of the 80 main sequence stars included in the Vega project derived from ISO chopped PHT-P photometry at $25\ \mu\text{m}$ (left) and PHT-C mini-maps at $60\ \mu\text{m}$ (right) are compared to IRAS photometry. (from Laureijs et al. 1999, [105]).

At $60\ \mu\text{m}$ the statistics become poorer. IRAS fluxes are available only for 11 targets. The obvious outlier showing $F_{60,IRAS} \gg F_{60,ISO}$ consists of 3 resolved point sources in the ISOPHOT map. For the remaining detections the correlation is high. However, the ISO observations are systematically ($\sim 25\%$) below the IRAS values. This discrepancy could partially be attributed to the fact that we have assumed point source calibration in the conversion from measured flux in an array pixel to the final target flux. In case of small extended sources the flux would be underestimated for this reason and this is actually what we observe in stars like Vega and β -Pictoris, contained in the sample, which are known to be slightly extended infrared sources.

As a consequence of the calibration upgrades implemented in the latest versions of the ISOPHOT pipeline, the accuracy of chopped PHT-P and PHT-C photometry has further improved significantly.

As an example, we show in Tables 6.5 and 6.6 the photometric data derived from OLP Version 10 for a subset of the stars in the sample above mentioned compared with IRAS photometry and model predictions (Ulrich Klaas, private communication). ISOPHOT and IRAS fluxes are colour corrected.

Table 6.5: OLP Version 10 chopped PHT-P photometry at $25\ \mu\text{m}$ compared to IRAS photometry and model predictions

Source [Jy]	ISOPHOT flux [Jy]	IRAS flux [Jy]	Model flux [Jy]
Sirius	18.52	24.09	21.54
HR7557	5.24	5.76	5.27
HR7310	4.31	3.66	3.40
HR5986	0.68	0.53	0.52
	0.63		
	0.58		
HR5914	0.39	0.41	0.38
HR5447	0.32	0.30	0.26
HR7469	0.25	0.22	0.25

Table 6.6: *OLP Version 10 chopped PHT-C photometry at 60 μm compared to IRAS photometry and model predictions*

Source [<i>Jy</i>]	ISOPHOT flux [<i>Jy</i>]	IRAS flux [<i>Jy</i>]	Model flux [<i>Jy</i>]
Sirius	4.08 4.04	3.73	3.68
HR1654	1.68	1.53	1.61
HR7980	1.25	1.12	1.17
HR7557	0.95	0.95	0.90
HD185144	0.11	0.12	0.10
HR7469	0.06	0.75	0.04

6.3.2 Comparison with MSX

In order to extend the cross-calibration analysis of ISO SWS to observations made with other space facilities than IRAS we performed a similar analysis using this time photometric data provided by the *Midcourse Space Experiment* (MSX; Egan et al. 1999, [48]).

Briefly, MSX was a multi-discipline experiment sponsored by the USA Ballistic Missile Defense Organization. The principal objective of the MSX astronomy experiments was to complete the census of the mid-infrared sky. Experiments were designed to cover the regions either missed by IRAS and COBE/DIRBE or where the sensitivity of IRAS was degraded by confusion noise in regions of high source densities or structured extended emission, including the entire Galactic Plane.

The MSX Point Source Catalogue contains all the point sources detected with signal-to-noise ratio > 3 following criteria very similar to IRAS (detection requires multiple confirmations).

The infrared instrument on MSX was a 35 cm clear aperture off-axis telescope cooled by a single solid H_2 cryostat equipped with Si:As BiB arrays with eight columns of detectors, each with 192 rows of $18'' \cdot 3$ square pixels, and a high sensitivity (0.1 Jy at $8.3 \mu\text{m}$). Two narrow band filters covered the spectral regions centred at 4.29 (B1) and 4.35 (B2) μm , and four broad-band filters covered the spectral regions centred at 8.28 (A), 12.13 (C), 14.65 (D) and 21.34 (E) μm (see Table 6.7).

Table 6.7: *Description of MSX photometric bands*

Band	No active cols.	Isophotal $\lambda[\mu\text{m}]$	50% peak intensity	Isophotal BW[μm]	Zero mag. flux [Jy]	Abs. photom. accuracy	Survey sens. [Jy]	Effective FOV $\Omega_{EFOV} [\times 10^{-9}\text{sr}]$
A	8	8.28	6.8–10.8	3.36	58.49	5%	0.1–0.2	10.6
B ₁	2	4.29	4.22–4.36	0.104	194.6	9%	10–30	14.0
B ₂	2	4.35	4.24–4.45	0.179	188.8	9%	6–18	14.0
C	4	12.13	11.1–13.2	1.72	26.51	3%	1.1–3.1	11.7
D	4	14.65	13.5–15.9	2.23	18.29	4%	0.9–2	11.3
E	2	21.34	18.2–25.1	6.24	8.80	6%	2–6	12.6

In the following analysis we will only consider the broad MSX filters A, C, D and E, which are the most sensitive filters onboard MSX.

About 100 sources with an available SWS01 spectrum in the ISO Data Archive were identified to have their corresponding mid-infrared counterpart in the MSX Point Source Catalogue.

After excluding from this sample all the suspected variable stars and extended sources (as we did for the cross-calibration with IRAS) we ended up with around 50 sources suitable for cross-calibration with MSX at all the above mentioned filters.

The OLP Version 10 SWS spectra of these sources were retrieved from the ISO Data Archive and further processed with ISAP Version 2.1. Bad data points affected by glitches were identified and removed from the SWS spectra using the available tools in ISAP and ISO ‘synthetic photometry’ was performed at the A, C, D and E MSX filters with the help of `syn_phot`. This ISAP application convolves the ISO spectrum with the transmission profile of the corresponding MSX filters assigning a monochromatic flux to each band under the assumption that the SED shape is of the form $\nu \times f_\nu = \text{constant}$, or equivalently $\lambda \times f_\lambda = \text{constant}$.

In Figures 6.25 to 6.28 we show the results obtained. As we can see, they are very similar to the ones obtained in the previous cross-calibration comparison with IRAS data.

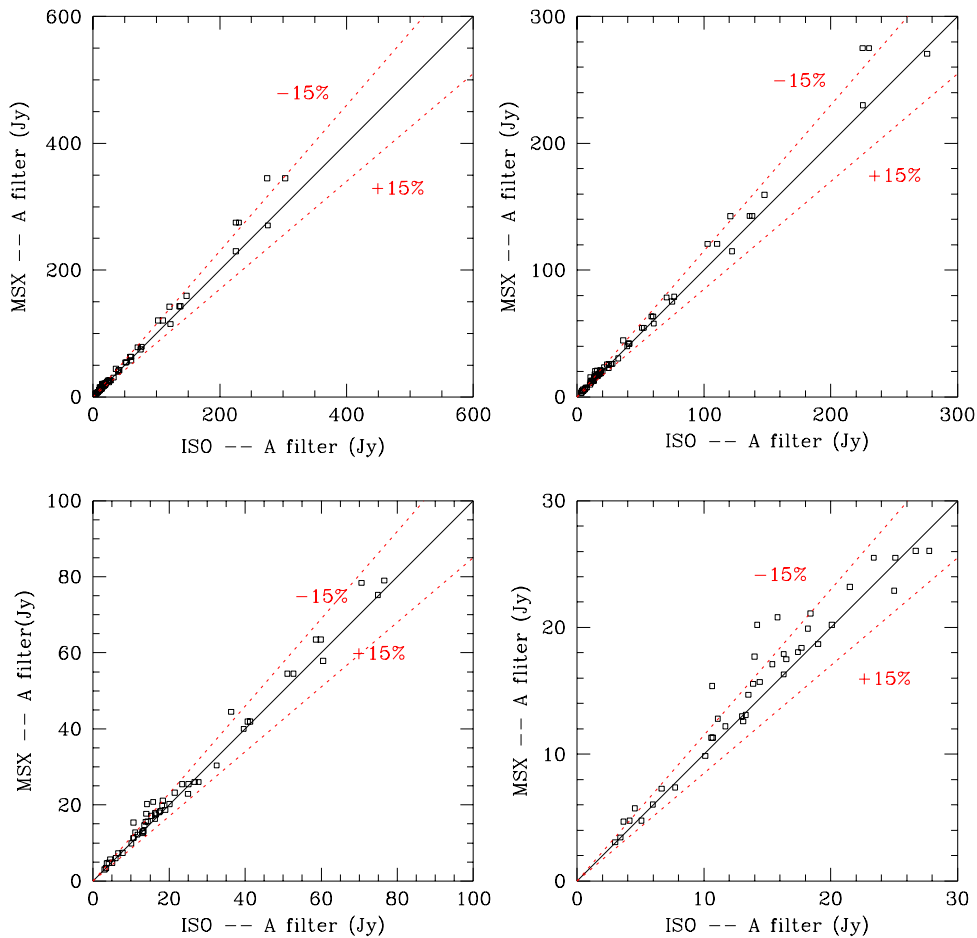


Figure 6.25: *ISO SWS synthetic photometry at 8.28 μm derived from OLP Version 10 data products compared to MSX filter A photometry at the same wavelength. The dashed red line represents a 15% discrepancy level.*

Essentially, the absolute flux calibration of ISO SWS and MSX agrees to within the 10–15% level at all flux levels, with very little degradation even at the lower flux levels.

The few outliers are interpreted as previously unknown variable sources and/or slightly badly pointed observations, similarly to what was observed in the previous comparison with IRAS.

Comparing the absolute flux level of all the measurements performed with ISO and MSX there is a general good agreement in all filters with a zero-point consistency better than 5% in all cases with the exception of filter A (see Figure 6.29), where the distribution of observed discrepancies show a marked asymmetry.

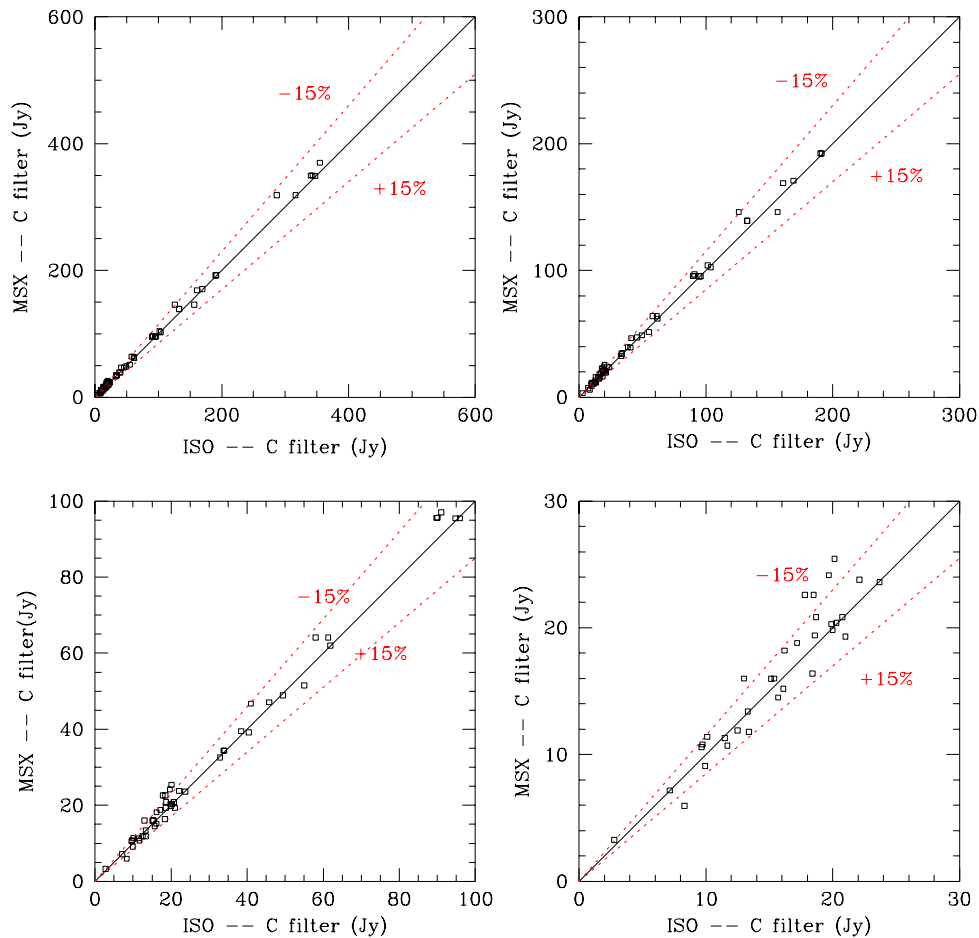


Figure 6.26: ISO SWS synthetic photometry at $12.13\ \mu\text{m}$ derived from OLP Version 10 data products compared to MSX filter C photometry at the same wavelength. The dashed red line represents a 15% discrepancy level.

This asymmetry is most probably due to a higher percentage of badly pointed observations (similarly to what we observed also in the cross-calibration comparison with IRAS at $12\ \mu\text{m}$). Note that this is the filter covering a wavelength range where SWS is most sensitive to small pointing offsets because of the smaller aperture size.

On the other hand, the slightly worse correlation found between ISO SWS and MSX filters D and E (compared to filters A and C) is probably induced by the fact that these filters show a larger overlap with SWS band 3, which is known to be less accurate than SWS band 2 in terms of absolute flux calibration.

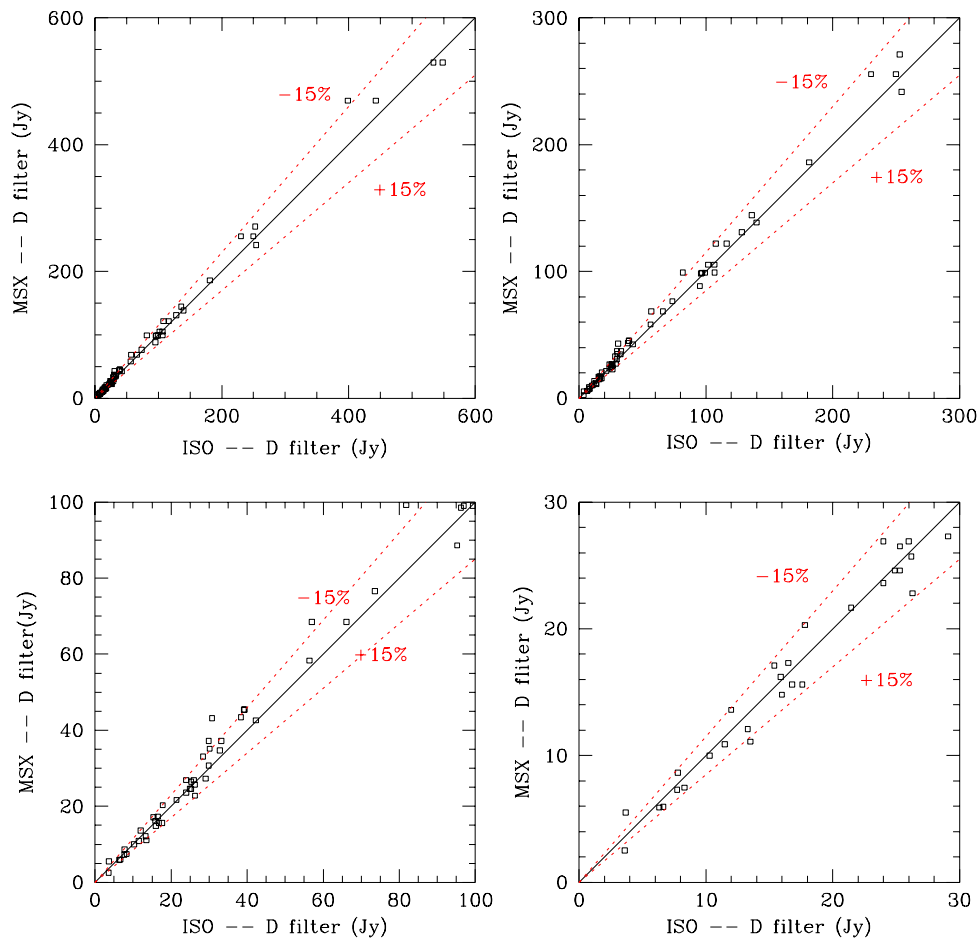


Figure 6.27: ISO SWS synthetic photometry at $14.65\ \mu\text{m}$ derived from OLP v10 data products compared to MSX filter D photometry at the same wavelength. The dashed red line represents a 15% discrepancy level.

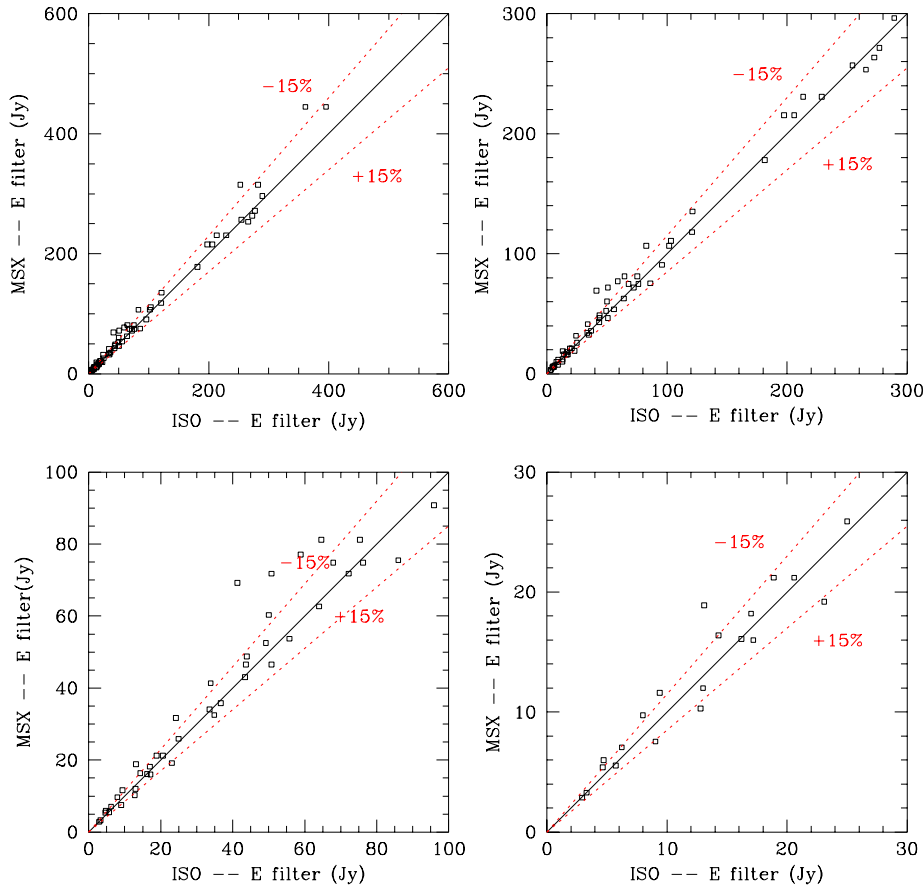


Figure 6.28: *ISO SWS synthetic photometry at $21.34 \mu\text{m}$ derived from OLP v10 data products compared to MSX filter E photometry at the same wavelength. The dashed red line represents a 15% discrepancy level.*

Globally considered, the main difference found with respect to the previous cross-calibration comparison with IRAS is the absence of the strong discrepancies observed at high flux levels between ISO and IRAS data. This supports our hypothesis that the non-linearity problem is in the IRAS calibration at high flux levels.

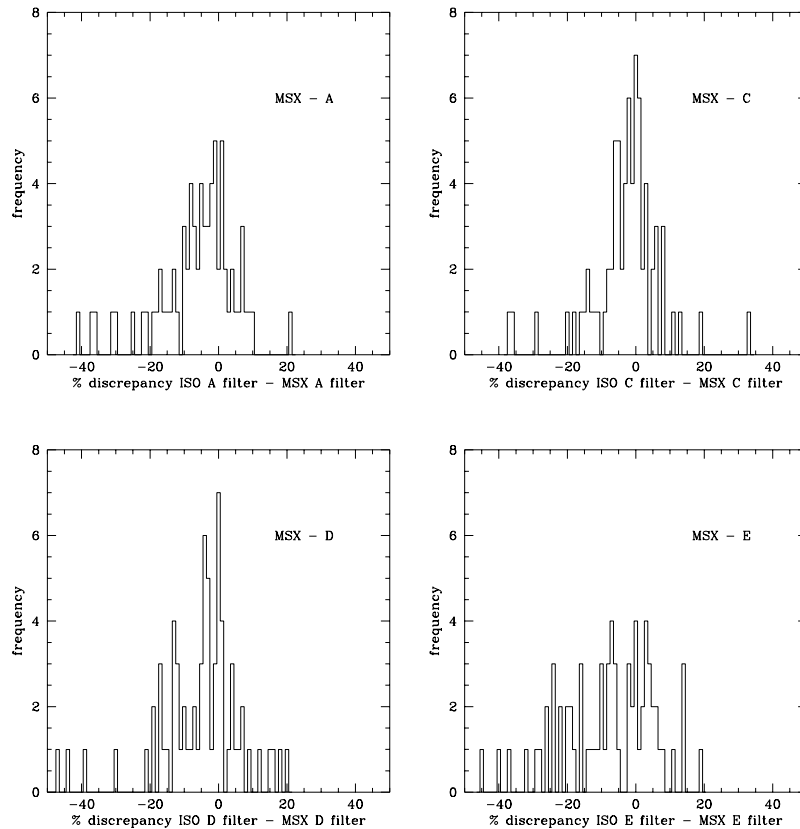


Figure 6.29: *Distribution of discrepancies found between the ISO SWS synthetic photometry at 8.28, 12.13, 14.65 and 21.34 μm , derived from OLP Version 10 data products compared to MSX filter A, C, D and E photometry, respectively.*

6.3.3 Comparison with COBE/DIRBE

ISOPHOT data has also been compared with COBE/DIRBE data as part of our cross-calibration analysis. The *Diffuse Infrared Background Experiment* (DIRBE; Hauser et al. 1998b, [76]) was one of the three instruments onboard COBE (the *Cosmic Background Explorer*), a satellite developed by NASA's Goddard Space Flight Center and launched in November 1989 to measure the diffuse infrared and microwave radiation from the early universe to the limits set by our astrophysical environment.

DIRBE obtained infrared absolute sky brightness maps in the wavelength range 1.25 to 240 μm . Most of this range was also covered by ISOPHOT. However, the comparison between ISOPHOT and COBE/DIRBE data is complicated, mainly because of the vastly different beam sizes (42' FWHM for COBE/DIRBE), as we will see below.

6.3.3.1 PHT-S spectroscopy versus COBE/DIRBE photometry

In order to check the consistency between the absolute flux calibration of COBE/DIRBE photometry and PHT-S spectroscopy we present here a comparison of the absolute surface brightness of the zodiacal light measured by PHT-S and COBE/DIRBE data reported by Dotto et al. 2002, [46].

Figure 6.30 shows the OLP Version 9.0 sky background measurements taken with the long wavelength channel of PHT-S in the vicinities of the asteroids Frigga, Cassandra and Polyxio together with COBE data at 4.9 and 12 μm . Note that the zodiacal light is the dominating background at the PHT-S wavelengths.

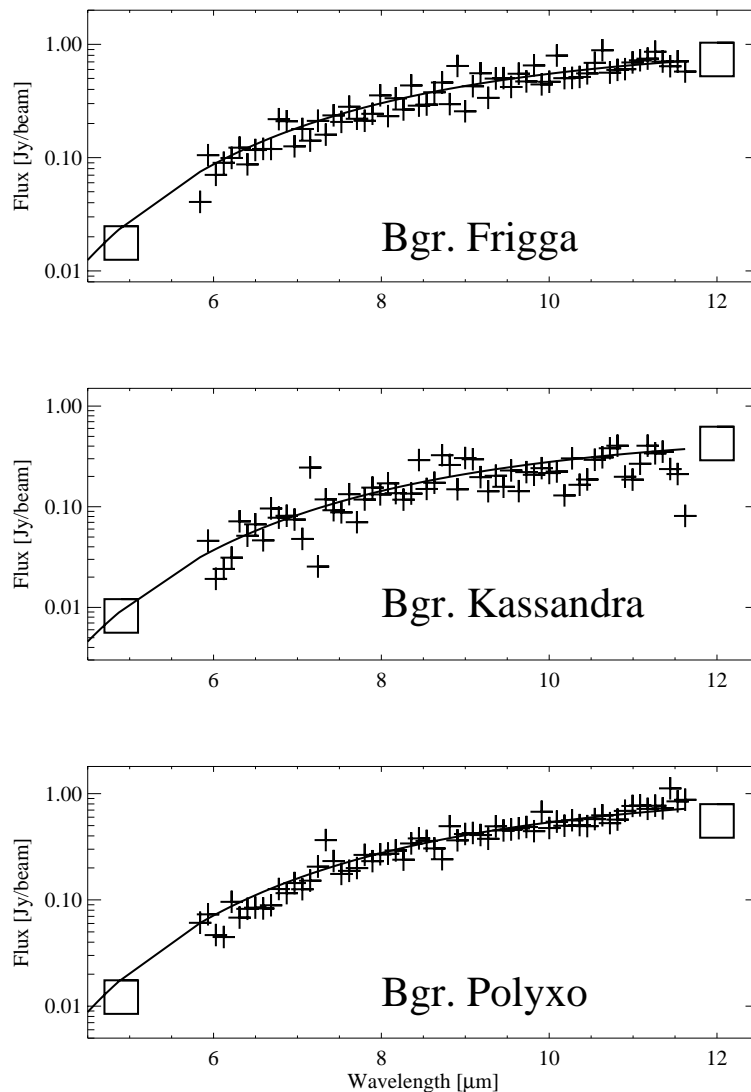


Figure 6.30: Comparison of PHT-S sky background measurements made in the vicinities of the asteroids Frigga, Cassandra and Polyxio (crosses) with COBE data at 4.9 and 12 μm (squares). The solid line corresponds to the fitted blackbody curve (from Dotto et al. 2002, [46]).

As we can see PHT-S is in excellent agreement with COBE data. From the sky background observed we can deduce that the zodiacal light can be well approximated by a blackbody emitting at a temperature of 267 K.

For the short wavelength channel the comparison is not possible because the extremely low flux in this range is below the detection limit of PHT-S. In spite of this we see that the featureless PHT-S spectrum fits nicely between the COBE/DIRBE photometric data points at 4.9 and 12 μm .

Unfortunately, COBE did not cover wavelengths in between 5 and 12 μm , in the range where the brightness of the zodiacal light rises very steeply. However, complementary results obtained with PHT-P and ISOCAM confirm that the zodiacal emission spectrum can be well fitted by a blackbody of 267 K and that the spectrum is featureless between 5 and 16 μm .

6.3.3.2 PHT-C versus COBE/DIRBE photometry

The consistency of the absolute sky brightness derived from ISO C100 maps with COBE/DIRBE data was also verified as part of the OLP Version 8.4 scientific validation of PHT22 staring raster maps (Klaas et al. 2000, [100]).

The mean surface brightness of specific areas of the sky was derived from the full C100 maps used for the flat-field assessment and compared with the surface brightness values in the corresponding filters or adjacent filters of COBE/DIRBE. The use of the full area of the ISOPHOT maps offers the advantage of getting a solid angle coverage comparable to the COBE/DIRBE pixels. However, in most cases the solid angles of the ISOPHOT maps are still considerably smaller than one pixel in COBE/DIRBE. The COBE/DIRBE annual maps were used (since at the wavelengths considered the contribution from the zodiacal light is very small) to determine the fluxes for the DIRBE pixel coincident with the map area centroid. For a check of the large scale variations of the sky background average fluxes of a 1.5 degree circular area were as well determined. ISOPHOT maps containing bright sources were not considered (they would give a considerably higher average surface brightness due to the smaller area considered).

In Table 6.8 we present the results obtained. Except for the different beam sizes a comparison of the ISOPHOT/DIRBE 60 and 100 μm filters is relatively straightforward. In general a good agreement better than 25%, in particular for those maps with comparable sizes to the COBE/DIRBE beam, is found. All larger deviations can be explained by the source structure which is extended over the ISOPHOT map area, but compact inside the COBE/DIRBE beam. The largest outlier shows a similar excess in the C200 range.

Without any correction, the ISOPHOT 90 μm filter maps seem to show a systematic positive surface brightness excess with regard to the DIRBE 100 μm photometry. However, inspection of the COBE/DIRBE SEDs indicates a steep decline in flux between 60 and 100 μm . In fact, the 90 μm ISOPHOT values are practically always in between the 60 and 100 μm DIRBE values. Very often, the surface brightness ratio 60/100 is about 2, i.e. with a linear interpolation between 60 and 100 μm , the 90 μm flux is by 25% higher than the 100 μm flux due to the shape of the SED. Then, also the surface brightness of the 90 μm maps are consistent with COBE/DIRBE within the 25% level. If the discrepancy between the ISOPHOT 90 μm surface brightness and the DIRBE 100 μm surface brightness is small, usually the source SED is reasonably flat between 60 and 100 μm . Whether there is still a positive excess at 90 μm cannot be solved by this kind of study, but needs better matching areas and a proper colour correction of the background SEDs.

From the consistency found in the three filters at 60, 90 and 100 μm and the relative photometric accuracies of all ISOPHOT C100 filters, we conclude that the consistency should also hold for the remaining ISOPHOT filters at 65, 80 and 105 μm . The good correspondance holds for the flux range 4.5 to 400 MJy sr^{-1} .

A similar analysis was also performed by Klaas et al. 2000, [100] for ISOPHOT C200 maps. Since the longest COBE/DIRBE filters (140 and 240 μm) have an internal uncertainty of 20 to 30%, for a subsample of maps with low dynamic range the average fluxes of a 1.5 degree circular area were used, which gives a more robust photometry (this means averaging over 70 COBE/DIRBE pixels).

Table 6.8: Consistency check of C100 map absolute surface brightness with COBE/DIRBE annual map photometry. The solid angle of one COBE/DIRBE pixel is $19.5 \cdot 10^{-5}$ sr. No correction for the wavelength shift between ISOPHOT 90 μm and DIRBE 100 μm filters has been performed which causes for most sky backgrounds a systematic positive excess of the 90 μm flux (see text for details).

OLP product name	filter [μm]	surface brightness [MJy sr $^{-1}$]	solid angle [10^{-5} sr]	DIRBE flux [MJy sr $^{-1}$]	DIRBE filter [μm]	solid angle [10^{-5} sr]	consistency [%]
19002101	60	6.8	0.81	6.6	60	19.5	+2.2
08900102	60	9.5	1.60	6.5	60	19.5	+47
85001219	60	22.8	0.21	22.3	60	19.5	+2.2
13400214	60	39.8	0.22	39.6	60	19.5	+0.6
68300807	60	21.3	6.77	27.2	60	19.5	-22
84403913	60	23.9	1.04	24.5	60	19.5	-2.5
69801101	60	107.4	1.16	122.3	60	19.5	-12
35100809	90	5.1	5.49	3.3	100	19.5	+55
58200903	90	11.8	3.06	12.9	100	19.5	-7.9
19201091	90	4.8	7.30	3.1	100	19.5	+52
86901244	90	5.2	2.75	3.6	100	19.5	+44
41502788	90	8.1	5.10	5.7	100	19.5	+44
09000606	90	11.8	0.77	11.3	100	19.5	+4.4
08901904	90	15.1	0.23	13.6	100	19.5	+11
40100614	90	14.7	6.80	13.3	100	19.5	+10
87001338	90	5.3	2.93	3.6	100	19.5	+47
57501902	90	12.1	1.15	9.7	100	19.5	+25
53700514	90	4.4	0.85	3.7	100	19.5	+21
60002009	90	7.1	4.24	5.2	100	19.5	+37
50000124	90	4.8	8.87	3.3	100	19.5	+43
50100273	90	5.8	8.68	3.5	100	19.5	+68
20701079	90	25.6	0.33	22.8	100	19.5	+12
20800709	90	5.8	3.49	4.0	100	19.5	+46
86800640	90	5.7	2.96	3.6	100	19.5	+60
10101158	100	30.7	1.71	21.0	100	19.5	+46
79401149	100	44.2	0.51	40.6	100	19.5	+9.0
44900714	100	387.7	15.2	440.1	100	19.5	-12
15601578	100	17.4	1.82	6.1	100	19.5	+187
27600420	100	15.4	1.74	12.1	100	19.5	+27
71901220	100	18.5	3.66	16.0	100	19.5	+15
33401134	100	96.4	4.06	49.3	100	19.5	+96

In Table 6.9 we present the results of the comparison. No colour correction with regard to a modified blackbody describing the background spectral energy distribution nor a wavelength correction to better match the COBE/DIRBE filter central wavelength with the ISOPHOT filter central wavelength were performed. Again we have to remark that nearly all the ISOPHOT maps are considerably smaller in area than the solid angle of one COBE/DIRBE pixel. Therefore, structures in the source or background can affect the resulting absolute flux. In case of a flat field, the flux of the centred COBE/DIRBE pixel as well as the 3 degree circular area average is listed to give an impression of the variation of the background (and also the stability of the COBE/DIRBE measurement in one pixel). If the map contains a bright target and is smaller than the COBE/DIRBE pixel, then only the flux of the centred COBE/DIRBE pixel is given.

Taking into account the discrepancies in beam size and the non-correction for different wavelengths of filters and background SEDs, the general agreement is in the order of 20 to 30% at all four filters considered (150, 170, 180 and 200 μm). Restricting the comparison to ISOPHOT maps with comparable solid angles with the COBE/DIRBE measurement, the consistency is confirmed to be better than 25%. This holds for all filters and a surface brightness range between 2.5 and 600 MJy sr $^{-1}$.

Larger deviations between the average ISOPHOT map flux and the COBE/ DIRBE flux only occur for bright central sources which are compact in comparison with the COBE/DIRBE beam. In these cases, the COBE/DIRBE fluxes are always less than the ISOPHOT fluxes, as expected.

Table 6.9: *Consistency check of C200 map absolute surface brightness with COBE/DIRBE annual map photometry. The solid angle of one COBE/DIRBE pixel is $19.5 \cdot 10^{-5}$ sr (see text for details).*

OLP product name	filter [μm]	surface brightness [MJy sr $^{-1}$]	solid angle [10^{-5} sr]	DIRBE flux [MJy sr $^{-1}$]	DIRBE filter [μm]	solid angle [10^{-5} sr]	consistency [%]
56200110	150	3.6	2.91	4.1	140	19.5	-13
56201814	150	22.2	0.42	20.9	140	19.5	+6.2
08900103	150	5.5	1.26	7.7	140	19.5	-29
79400434	170	3.2	3.15	2.2	140	19.5	+45
				2.9	140	215.3	+10
59300101	170	3.5	6.53	3.5	140	19.5	-1.4
				3.4	140	215.3	+4.2
19800208	170	3.2	3.41	5.0	140	19.5	-37
				3.3	140	215.3	-3.6
21001305	170	3.6	3.39	4.1	140	19.5	-12
				3.5	140	215.3	+3.4
79900733	170	6.0	0.50	7.0	140	19.5	-14
33600108	180	2.7	2.50	2.7	140	19.5	-2.6
				2.8	140	215.3	-4.0
33600705	180	4.7	2.55	5.7	140	19.5	-17
				5.7	140	215.3	-17
35100907	180	4.1	4.92	4.5	140	19.5	-8.2
16701206	180	15.0	4.11	12.7	140	19.5	+18
52700412	180	3.2	0.87	3.8	140	19.5	-16
				3.2	140	215.3	+0
85001037	180	8.1	3.78	10.1	140	19.5	-19
				9.3	140	215.3	-13
78200101	200	6.3	28.40	5.3	240	34.45	+20
36803005	200	14.8	0.71	15.5	240	19.5	-4.5
				14.9	240	215.3	-0.9
39602213	200	36.2	6.22	29.2	240	19.5	+24
26101401	200	69.8	11.03	85.4	240	19.5	-18
33401133	200	138.6	3.89	87.6	240	19.5	+58
86101801	200	251.9	5.01	287.9	240	19.5	-13
15601577	200	11.4	1.38	5.9	240	19.5	+95
33300559	200	38.0	6.55	55.7	240	19.5	-32
10101157	200	69.7	1.41	45.2	240	19.5	+54
31000625	200	345.4	1.45	207.8	240	19.5	+66
26701013	200	593.3	15.49	494.5	240	19.5	+20
40900802	200	6.9	1.97	5.6	240	19.5	+23
28001303	200	13.0	2.00	12.8	240	19.5	+1.6

6.4 Comparison with Models

6.4.1 ISOCAM

A small sample of Hipparcos Input Catalogue (HIC, [83]) stars were used throughout the ISO mission to calibrate ISOCAM.

In order to determine the consistency between the measurements and the models used to derive the calibration curves, the fluxes derived from OLP Version 10 data for these stars obtained with multi-filter or CVF observations have been compared with the fluxes predicted by the models. Note that in many cases the same star was observed with various apertures. For this analysis all the available measurements were taken into account.

The fluxes considered here were those included in the CPSL (CAM Point Source List) file, which makes use of an automatic PSF fitting tool to determine the position and the flux of all the detected point sources in the ISOCAM field.

In general, the results obtained show that the consistency with models is within the 15% level in most cases.

However, it is remarkable that many of the flux measurements derived this way are significantly below the model fluxes. This could be the consequence of an incorrect PSF fitting since interactive aperture photometry with CIA generally overrides the problem.

The discrepancies between the mean value of all the measurements taken per star and the corresponding model fluxes are listed in Table 6.10. Globally considered, the results obtained show that the fluxes listed in the CPSL files are systematically $\sim 7\%$ underestimated with respect to the model values.

Table 6.10: *Mean discrepancies found in the photometry of some ISOCAM calibration stars with respect to their models.*

Calibration star	OLP v10
HIC 67485	+2%
HIC 69713	-7%
HIC 70218	-14%
HIC 73005	-18%
HIC 77277	-10%
HIC 85317	+6%
HIC 94376	-12%
HIC 94890	-4%

In Figures 6.31 and 6.32 we show two examples of the results obtained in the case of HIC 67485 and HIC 77277, where the mean errors found were +2% and -10%, respectively.

The full report describing this consistency check can be found in Cesarsky 2002, [18].

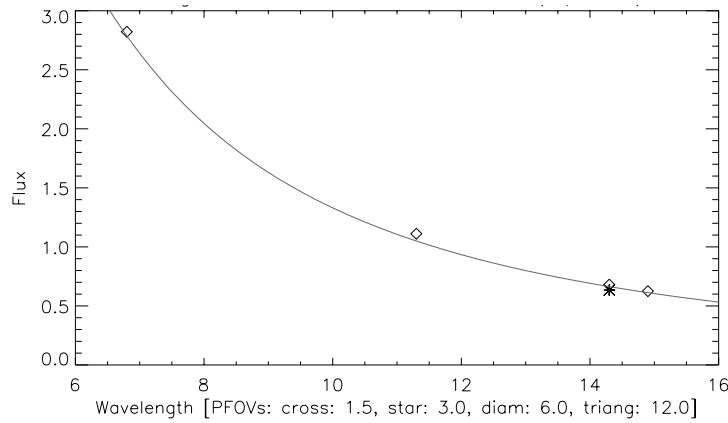


Figure 6.31: Comparison of ISOCAM OLP Version 10 measurements on HIC 67485 with the calibration model.

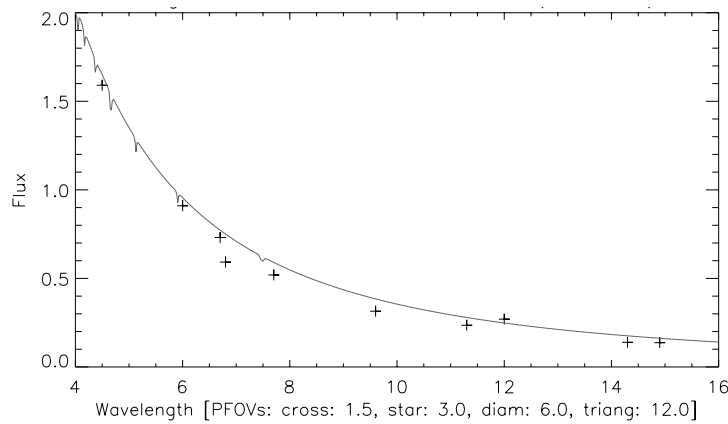


Figure 6.32: Comparison of ISOCAM OLP Version 10 measurements on HIC 77277 with the calibration model.

6.4.2 LWS

Several checks were also made during the process of scientific validation of LWS OLP Version 10 data products against models of planets, asteroids and stars (Lim et al. 2001, [114]). A summary of the main results obtained are presented here:

LWS01 observations of Uranus

LWS photometric calibration is based on Uranus. Thus, a first consistency check was made by comparing Uranus observations versus the model produced by Griffin & Orton 1993, [64].

Table 6.11 shows the average flux for each detector and each observation divided by the average over the model for that detector. The red average row gives the overall average for the period of time covered by type 2 illuminator flashes (revolutions 237 to 442) and the blue row the period of time covered by the type 3 illuminator flashes (after revolution 442). Uranus was not visible during the period when type 1 illuminator flashes were used (before revolution 237).

After manual deglitching the available OLP Version 10 data products were averaged with a 2.5σ clipping using ISAP Version 2.0. Detectors SW1 to SW5 were then smoothed with the nominal resolution element

Table 6.11: *Uranus LWS01 observations averaged per detector versus model predictions as deduced from OLP Version 10 data products for the validation revolutions*

Rev	SW1	SW2	SW3	SW4	SW5	LW1	LW2	LW3	LW4	LW5
321	0.99	0.98	0.98	0.99	0.99	0.99	0.97	0.98	0.96	0.96
328	0.98	0.99	0.98	1.00	0.99	0.99	1.00	0.98	0.99	0.97
335	1.01	1.00	0.99	1.00	1.00	0.98	0.99	0.99	1.00	0.97
349	0.99	1.01	1.01	1.01	1.02	1.01	1.01	0.99	1.01	1.03
356	1.01	1.03	1.02	1.00	0.99	1.01	1.01	1.03	1.00	1.02
Average	1.00	0.99	0.99	0.99						
538	0.96	1.01	0.98	0.98	0.97	0.98	0.98	0.98	0.99	0.98
544	0.99	0.98	0.98	0.99	0.99	0.99	0.98	0.99	1.00	0.99
552	1.03	0.98	0.99	0.99	1.00	1.00	1.04	0.99	1.00	1.01
698	0.98	1.00	1.00	0.99	1.00	1.00	1.00	1.00	0.99	1.01
734	1.01	1.01	1.01	1.02	1.02	1.01	0.99	1.04	1.01	1.02
738	1.04	1.00	1.01	1.00	1.01	1.00	1.00	0.99	1.00	0.99
874	1.00	1.01	1.01	1.02	1.01	1.00	1.01	1.03	1.01	0.98
Average	1.00									

of $0.29 \mu\text{m}$. LW1 to LW5 were smoothed with the nominal resolution of $0.6 \mu\text{m}$ and both scans directions averaged.

Note that within the 15 measurements considered, the change in apparent size of Uranus corresponds to a total flux variation of $\sim 10\%$, which was included in the calculations. The background influence is expected to be less than 0.5% and, therefore, it was not taken into account.

The values obtained show that Uranus does calibrate back to the model and that the calibration is good and repeatable to within a few percent for all detectors.

Looking into the behaviour of each detector more in detail, the same data set for which the results are shown in Table 6.11 were also used to produce Figures 6.33 and 6.34.

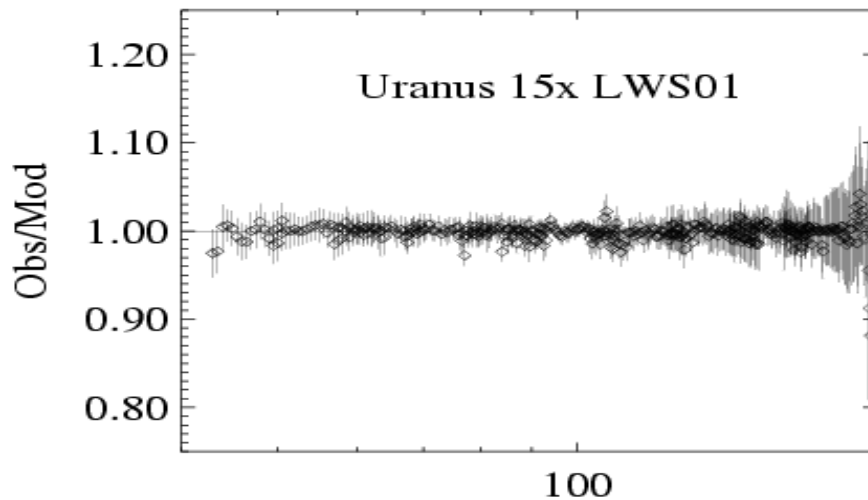


Figure 6.33: *Averaged LWS01 Uranus observations/model ratio for the full LWS wavelength range derived from OLP Version 10 data products.*

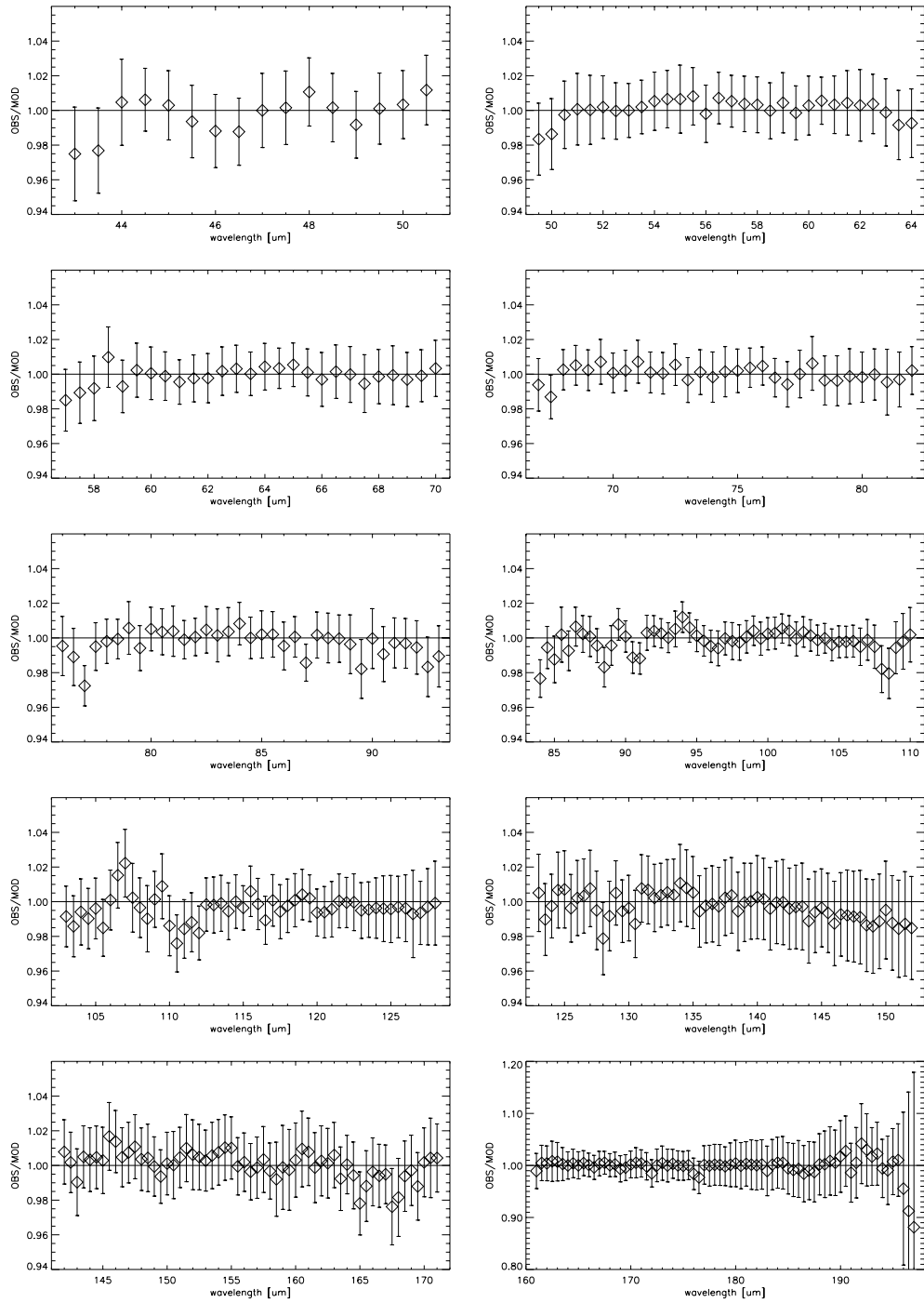


Figure 6.34: Averaged LWS01 Uranus observations/model ratios per detector derived from OLP Version 10 data products. Error bars represent the standard deviation of the 15 measurements considered.

As we can see from the averaged observation/model ratios of all 15 measurements the agreement between Uranus model and the calibrated Uranus observations is in most cases within the 2% level. Only SW1 and SW2 show slightly larger deviations at the short wavelength end, as well as LW5, which shows a larger scatter at the long wavelength end.

In general, the reasons for the deviations might be related to the different ways of calculating Uranus fluxes from the brightness temperature model. However, the fluctuations observed in the SW1 detector may be directly connected with a known problem in the RSRF, which produces a conspicuous double-peaked spectral shape observed not only in the spectrum of Uranus but also in all the astronomical sources inspected in the course of our cross-calibration analysis, including planets, asteroids and stars. The relative error induced by this deficient RSRF amounts to 5–10% in flux and its effect is clearly visible in most LWS spectra, as in the few examples plotted in Figure 6.35.

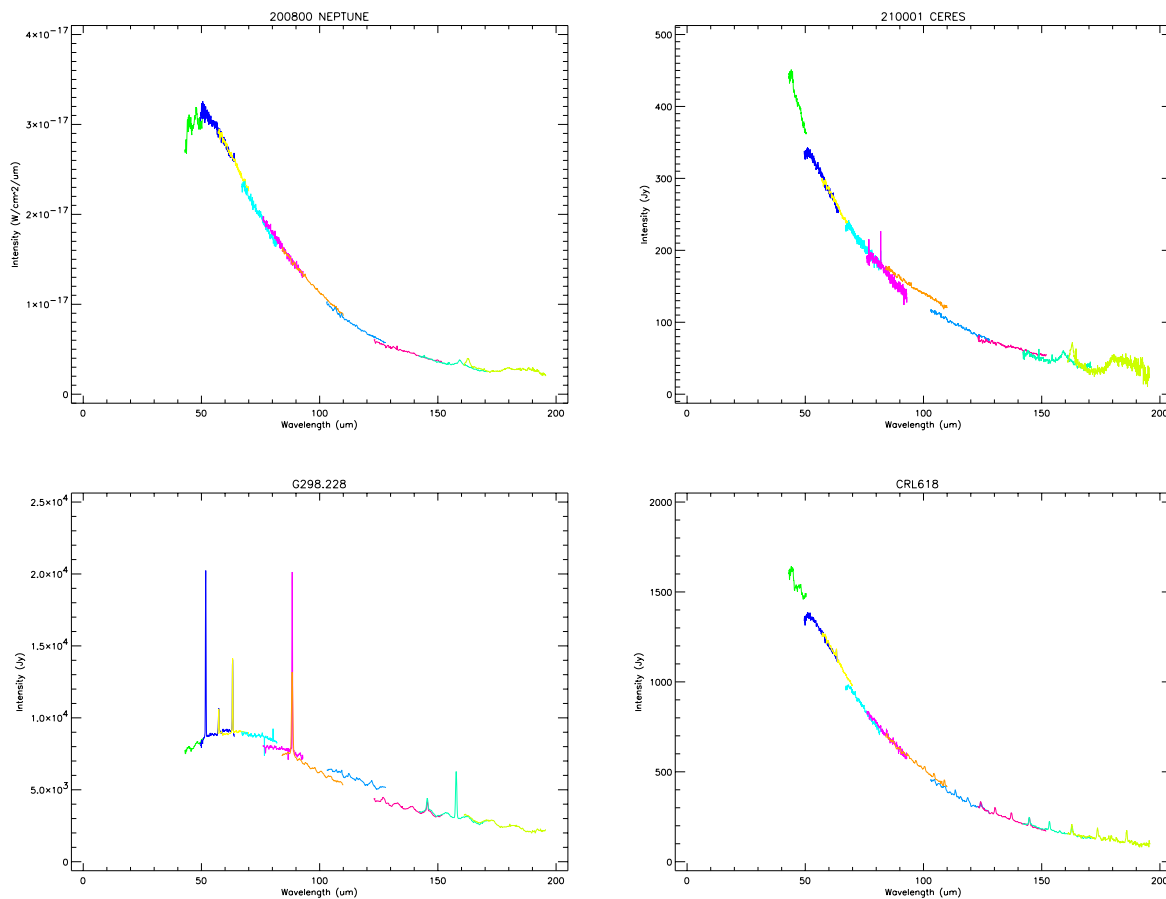


Figure 6.35: Example of OLP Version 10 LWS spectra of planets (Neptune), asteroids (Ceres), HII regions (G298.228) and proto-planetary nebulae (CRL 618) where the conspicuous double-peaked shape of the SW1 detector is clearly seen at the short wavelength end of the spectra in green colour.

LWS02 observations of Uranus

Thirteen different observations of Uranus taken with the AOT LWS02 (fixed grating LWS spectra) were also retrieved from the ISO Data Archive (OLP Version 10 data products) and analysed in order to check the consistency of this observing mode of LWS.

Only the last 100 s of the detector signal were considered in order to avoid transient effects in the beginning of the measurements. After manual deglitching and dark current subtraction using ISAP Version 2.0 (the background values were always smaller than 1% at all wavelengths) we derived the average flux per detector divided by the model.

The agreement found in this case was within the 3% level in general. However, individual observations, especially in SW1 and in the long wavelength detectors LW3, LW4 and LW5 were sometimes off by up to 10% as we can see in Figure 6.36.

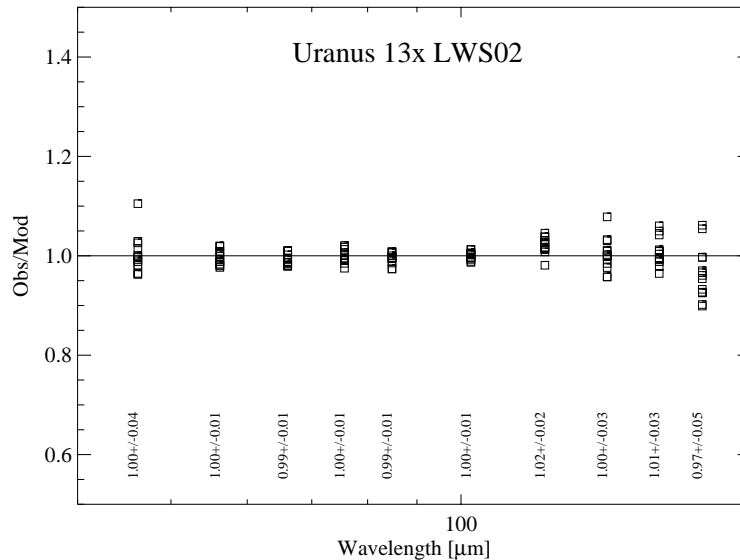


Figure 6.36: Averaged Uranus LWS02 observations/model ratios for the full LWS wavelength range derived from OLP Version 10 data products.

The average ratios per detector and their standard deviation are listed in Table 6.12.

Table 6.12: Averaged Uranus LWS02 observations/model ratios per detector derived from OLP Version 10 data products.

Detector	<Observations/model>	Detector	<Observations/model>
SW1	1.00±0.04	LW1	1.00±0.01
SW2	1.00±0.01	LW2	1.02±0.02
SW3	0.99±0.01	LW3	1.00±0.03
SW4	1.00±0.01	LW4	1.01±0.03
SW5	0.99±0.01	LW5	0.97±0.05

LWS observations of Neptune

Two LWS01 and thirteen LWS02 observations of Neptune retrieved from the ISO Data Archive (OLP Version 10 data products) were analysed in a similar way. The background values for Neptune were again taken from COBE/DIRBE weekly maps (up to $100 \mu\text{m}$) and yearly maps (for wavelengths larger than $100 \mu\text{m}$). The model of Neptune adopted was developed by Orton & Burgdorf (private communication). LWS01 and LWS02 observations of Neptune agree extremely well. In the full scans detector non-linearities appear as jumps between the individual detectors. In the LWS02 mode (see Figure 6.37), detectors SW2, SW3, SW4 and SW5 have been used as references since they seem to give consistent results for all objects. The other detectors are given relative to these 4 detectors. There is a nice agreement between the observations and model predictions but the model seems to underestimate the overall flux detected by 2%. SW1 is systematically 4–8% too low, LW1 a few percent too high. The stressed Ge:Ga detectors LW2 through LW5 are 5–10% too low, with increasing offsets at longer wavelengths. LW5 shows a larger scatter.

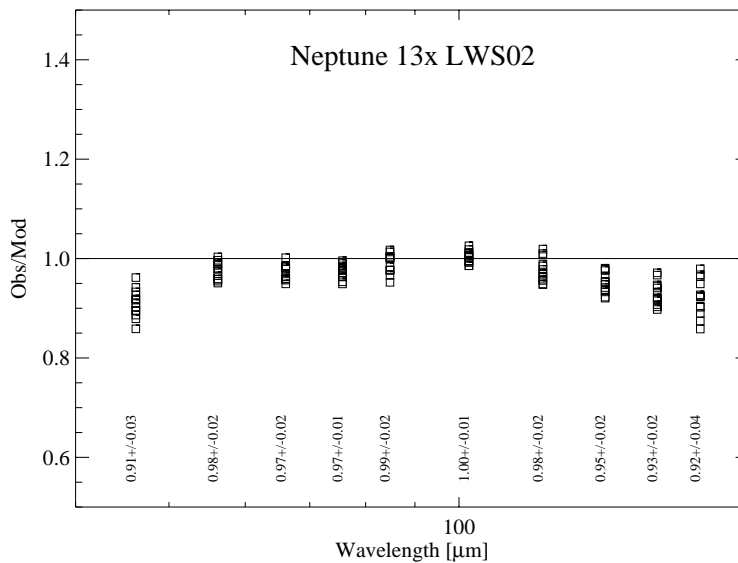


Figure 6.37: Averaged Neptune LWS02 observations/model ratios for the full LWS wavelength range derived from OLP Version 10 data products.

LWS observations of asteroids

The same exercise was performed on a number of asteroids. OLP Version 10 data products were retrieved from the ISO Data Archive and reduced using ISAP Version 2.0 in a similar way as Uranus and Neptune, but here background subtraction becomes quite important. The background values were taken from COBE/DIRBE weekly maps (up to $100 \mu\text{m}$) and yearly maps (for wavelengths larger than $100 \mu\text{m}$). The asteroid models were those produced by Müller & Lagerros 2002, [127].

LWS01 and LWS02 observations agree extremely well. The slight differences found between both observing modes are probably due to transients; LWS02 is less affected by transients since only the last 100 s of each fixed grating position were taken.

- Ceres: A nice agreement (at the 3% level) between observations (15) and model predictions is found for this bright asteroid (see Figure 6.38). SW1 was off in a few cases by up to 20% as expected when observations taken before revolution 237 (the analysis was done before the correction was implemented in OLP Version 10.1). LW1 was on average 6% too high, LW2 5% too low, LW3 15%

too low, while LW4 and LW5 were about 10% too low, but with a larger scatter (10% in LW4 and 20% in LW5).

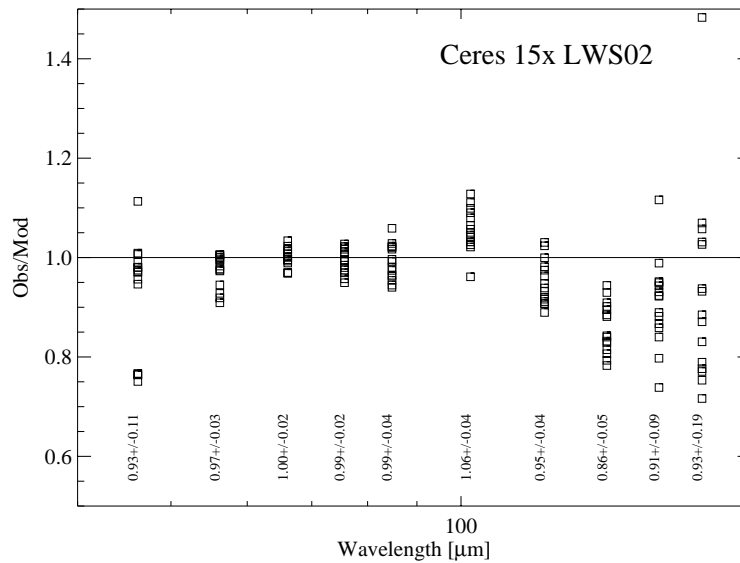


Figure 6.38: *Ceres LWS02 observations/model ratios per detector derived from OLP Version 10 data products. The underestimated SW1 measurements correspond to observations made before revolution 237.*

- Pallas: A nice agreement between observations (4) and model was also found at the 5% level. The SW1 measurement taken before revolution 237 was 15% off, again as expected. LW1 was 10% too high, LW2 12% and LW3 15% too low. Dark current problems in LW4 and LW5 produced too large scatter because of the relatively low flux level of the asteroid at these wavelengths.
- Vesta: The agreement between observations (14) and model predictions is at the 5% level, including SW1 (no observations were taken before revolution 237 in this case). LW1 was found 12% too high, LW2 10% and LW3 15% too low. Again, dark current problems in LW4 and LW5 produced a large scatter at these wavelengths.
- Hygiea: The agreement between observations (2) and model predictions is at the 15% level. SW1 is 15% too low in the observations taken before revolution 237 as expected, LW1 11% too high, LW2 20% too low and LW3 30% too low. This asteroid is the faintest in the sample. Therefore, dark current problems were so strong in the LW4 and LW5 bands that they prevented any kind of analysis at these wavelengths.

LWS01 observations of stars

Stars are among the faintest objects observable with LWS and although detected, the uncertainty in the dark current was in many cases comparable to their flux, particularly at the longer wavelengths. Table 6.13 lists the average observations/model ratios per detector for two of the brightest stars observed with LWS01 as derived from OLP Version 10 data products. The stellar models were taken from the available templates in the Cohen, Walker, Witeborn et al. (CWW) absolute calibration programme (Cohen et al. 1992a, [28]; 1992b, [29]; 1995, [31]; 1996, [32] and 1998, [33]).

The scatter in the values obtained is mainly due to uncertainty in the dark current subtraction. Therefore, no definitive statement can be made about the detector performance, except that the photometric behaviour is still within pre-launch expectations of about 30–50%, even at these very low flux levels.

Table 6.13: *LWS01 observations (averaged per detector) versus model predictions for stars α Boo (Arcturus) and α Tau (Aldebaran). The scatter in the values obtained is mainly due to uncertainty in the dark current subtraction.*

Detector	Arcturus		Aldebaran		
	Rev 448	Rev 608	Rev 818	Rev 848	Rev 861
SW1*	1.15	1.16	0.93	1.14	0.73
SW2*	1.33	1.23	1.12	1.59	1.28
SW3*	1.39	1.27	1.00	1.48	1.44
SW4	0.57	0.71	1.35	1.31	0.83
SW5	1.10	1.08	1.67	1.89	1.58
LW1*	1.42	1.06	1.89	1.37	1.11
LW2*	1.22	1.18	1.53	2.05	2.01
LW3	N/A	N/A	1.50	2.38	1.53
LW4	N/A	N/A	1.49	1.75	-1.05
LW5	N/A	N/A	1.81	1.68	-3.24

* Detectors affected by NIR leaks.

LWS02 observations of stars

Two LWS02 observations of α Boo (Arcturus) were also retrieved from the ISO Data Archive (OLP Version 10 data products) and reduced using ISAP Version 2.0. Background subtraction was again extremely important in this case. The background values were taken from COBE/DIRBE weekly maps (up to 100 μm) and yearly maps (for wavelengths larger than 100 μm), as usual, and they represent up to 50% of the total flux for some detectors. The stellar model was taken from the CWW absolute calibration programme.

As we can see in Figure 6.39 detectors SW1, SW3 and SW4 agree within the 20% level with the model, while LW2 and LW3 are systematically too low (30 and 50%, respectively). Detectors SW2 and LW1 were affected by near infrared leak features.

Others stars like γ Dra were studied but, unfortunately, they were too faint to perform any kind of analysis with the data products provided by the pipeline.

In summary, OLP Version 10 LWS data products of Neptune, the few asteroids studied and α Boo agree nicely with the model predictions. Observational uncertainties are only large for the fainter asteroids and for some of the stars studied, like α Tau or γ Dra, mainly because they are also too faint for LWS.

Appart from the (known) problem affecting detector SW1 before revolution 237, which was corrected in Version 10.1 of the pipeline, detectors LW4 and LW5 usually encounter dark current problems. Manual dark current determinations improve the situation significantly; however, this is only an option for LIA users.

LW1, LW2 and LW3 show systematic effects assuming the COBE derived backgrounds. At the faint end the responsivities possibly depend on the total incoming flux. In the case of LW1 the calibrated fluxes can be up to 15% higher for the faintest sources (as compared to the models). For the stressed detectors LW2 and LW3 the opposite effect is found. Faint sources are systematically underestimated by up to 30% for LW2 and up to 40% for LW3.

A quick comparison with ISOPHOT stressed Ge:Ga detectors reveals the possible nature of this finding. An explanation for the discontinuities observed could come from the known non-linearities shown by stressed Ge:Ga detectors. When going from bright sources (Uranus) to faint sources (stars) the incoming

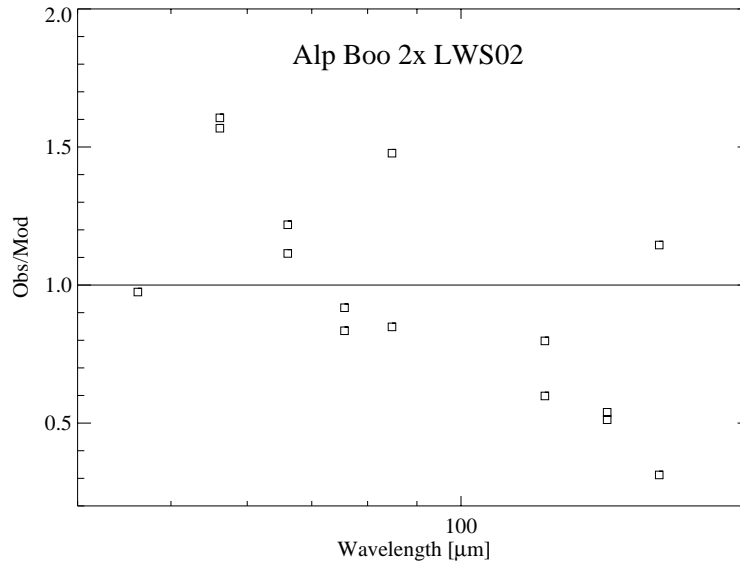


Figure 6.39: *Arcturus* (α Boo) LWS02 observations/model ratios per detector derived from OLP Version 10 data products.

fluxes change by three orders of magnitude. Non-linearity corrections over this flux range can be up to 50% for ISOPHOT. Similar effects could then be expected in LWS detectors.

Although the results are not conclusive, empirical non-linearity corrections have tentatively been derived for LW1, LW2 and LW3, based on the sources here analysed (Neptune, the four asteroids and α Boo). They are available in Müller 2001, [124].

More details on these consistency checks can also be found in Müller & Lagerros 2001, [126].

6.4.3 ISOPHOT

In the case of PHT a large number of consistency checks with models of planets, asteroids and stars were also performed as part of the process of scientific validation of OLP data products (Klaas et al. 2000a, [100]; 2000b, [101]; Klaas & Richards 2002, [102]).

Some of the analysis made are summarised below.

PHT-S staring observations

Staring PHT-S measurements of some of the calibration stars (HR7001 = Vega, HR 5340, HR 7469, HR 7924, HR 7980 and HR 8487) that were used to establish the dynamic relative spectral response function surfaces of Cal-G file PSDYNAMIC were checked in order to determine whether their input model SEDs were correctly reproduced by the pipeline.

OLP Version 10 data products were retrieved from the ISO Data Archive. Once background subtracted, the SEDs of the stars above mentioned were compared with their flux models (see Figure 6.40).

The results obtained show that the absolute accuracy reached is better than $\pm 10\%$ with a relative spectral shape accuracy better than $\pm 20\%$ for the flux range of 1–8000 Jy with the SS-array and for the flux range of 0.2–1800 Jy with the SL-array.

To confirm the accuracy of the observing mode the analysis was extended to a small number of non-calibration stars with similar spectral types as the standard stars above mentioned but different brightness, obtaining very similar results (Klaas & Richards 2002, [102]).

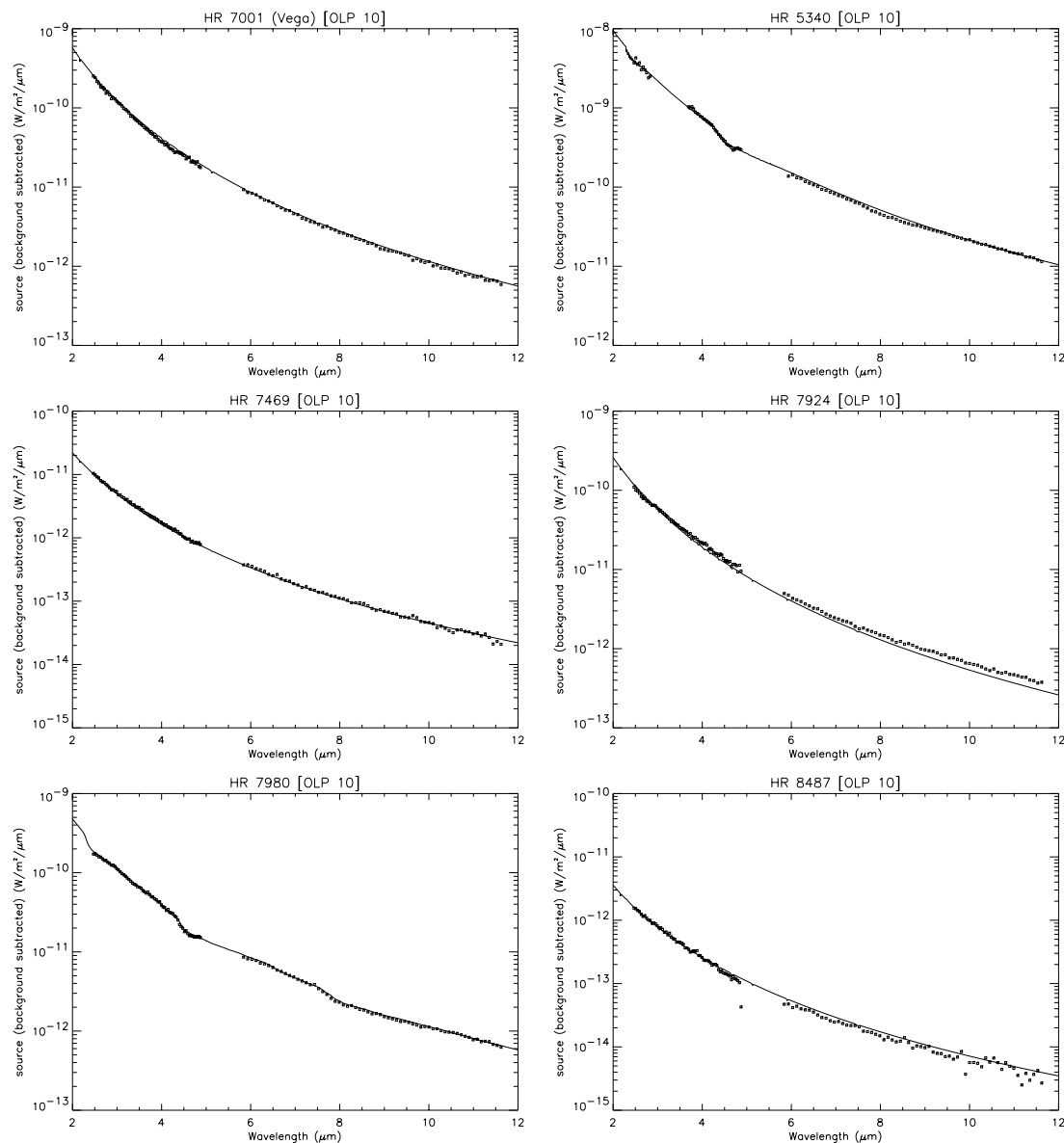


Figure 6.40: Comparison of the staring OLP Version 10.0 PHT-S spectra of HR 7001 (=Vega), HR 5340, HR 7469, HR 7924, HR 7980 and HR 8487 with their model SEDs

PHT-S chopped observations

Measurements of two calibration stars (HR 6817 and HR 6847) which were used to establish the Relative Spectral Response Function for chopped PHT-S calibration were checked in order to determine whether their input model SEDs (provided by Hammersley et al. 1998, [72]) were correctly reproduced by the pipeline. Both calibration stars were measured both in rectangular and triangular chopped modes.

OLP Version 10 data products retrieved from the ISO Data Archive show an excellent agreement with the models (see Figure 6.41). Although not shown in Figure 6.41 there is no significant difference in the results between rectangular and triangular chopped mode. The absolute accuracy and the relative spectral shape accuracy are in both cases better than $\pm 10\%$.

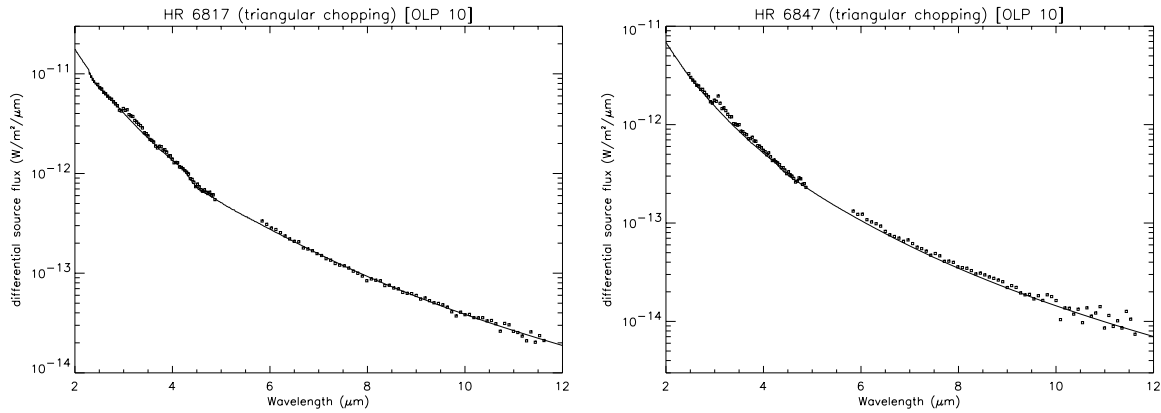


Figure 6.41: Comparison of the chopped OLP Version 10 PHT-S spectra (only the triangular chopping mode results are shown) of the calibration stars HR 6817 (left) and HR 6847 (right) with their models.

As for the staring measurements, the analysis was extended to a small number of non-standard stars with different brightness, obtaining very similar results (Klaas & Richards 2002, [102]).

Multi-filter photometry

The composite spectra from 1 to 35 μm extrapolated to 300 μm provided by Martin Cohen for HR 5340 (α Bootes = Arcturus) and HR 6705 (γ Draconis) were compared with observations of these stars taken with PHT-P and PHT-C in the staring modes PHT03 and PHT22 with all the available filters (except the 3.6 and 4.85 μm filters in the case of HR 5340 because the source saturated the detectors). The comparison plots are shown in Figure 6.42.

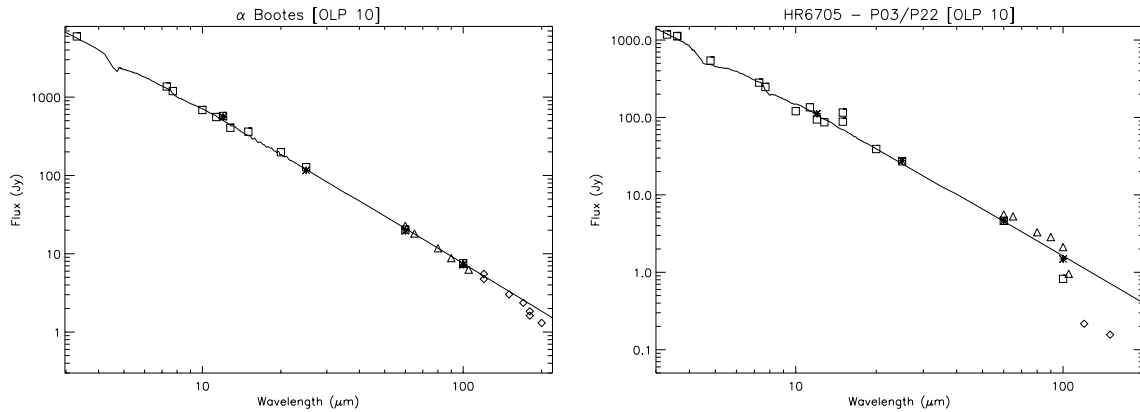


Figure 6.42: Comparison of PHT-P and PHT-C photometry, using the full ISOPHOT filter set, with the composite spectra extrapolated to 300 μm of α Bootes (=HR 5340) (left) and γ Dra (=HR 6705) (right) provided by M. Cohen and with IRAS photometry for OLP Version 10.0 data products. All photometric points were colour-corrected for a 4000 K blackbody. The meaning of symbols is the following: solid line = model; asterisks = IRAS; squares = PHT-P (PHT03) measurements; triangles = C100 (PHT22) measurements; diamonds = C200 (PHT22) measurements.

The conclusion obtained for HR 5340 is that OLP Version 10 photometry gives a good representation of the SED from 3.3 to 170 μm (agreement within 10% in most cases), with still some problems at the

longest wavelengths where the source flux extraction is more difficult because of the strong background. In the case of HR 6705, there is a general good agreement from 3 to 100 μm with the only exception of a measurement at 15 μm affected by strong transients. The C100 filters are systematically high by 20 to 45%. Adopting a default responsivity calibration for these filters gives fluxes which are lower than the model in contrast with the fluxes derived from actual responsivity calibration. The exception is the 105 μm filter which is too low both for actual and default responsivity calibration methods. Very likely this is caused by the background subtraction. For C200 filters, no useful results were achieved. The fluxes are all too low or even negative.

Similar analysis performed on other test cases indicate that reliable photometry with the standard on-off staring mode can be obtained up to a lower flux limit of 0.5 Jy for P1 and P2 detectors, 1.5 Jy for P3 and C100 detectors and 2.0 Jy for C200 with slightly worse accuracies in the case of chopped photometry, more affected by transients. Systematic offsets are only detected for some flux ranges in some filters for staring mode observations as well as for PHT-P photometry in smaller apertures than the standard ones (see Klaas & Richards 2002, [102] for more details).

Absolute photometry

PHT05 and PHT25 (absolute photometry) measurements of the calibration star HR 6705 (γ Draconis) were compared to the model available from Martin Cohen (composite spectrum from 1 to 35 μm extrapolated to 300 μm). The background subtracted, colour-corrected fluxes were compared also with IRAS photometry. The results are shown in Figure 6.43.

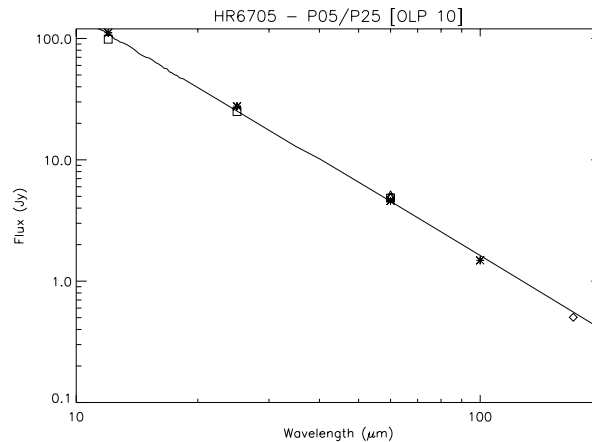


Figure 6.43: Comparison of PHT-P and PHT-C absolute photometry with the composite spectrum of γ Draconis (HR 6705) provided by M. Cohen and with IRAS photometry for OLP Version 10.0 data products. All photometric points are colour-corrected for a 4000 K blackbody. The meaning of the symbols is the following: solid line = model; asterisks = IRAS; squares = PHT-P (PHT05) measurements; triangles = C100 (PHT25) measurements; diamonds = C200 (PHT25) measurements.

The accuracy of the absolute photometry of γ Draconis is better than $\pm 15\%$ for all detectors, even for the 170 μm filter of C200 in contrast to the multi-filter measurement.

A similar analysis was performed with a number of PHT05 observations of HR 2491 (Sirius) covering the range from 3.3 to 25 μm (see Figure 6.44). In this case the accuracy of the absolute photometry achieved was better than 6% for both P1 and P2 detectors (for the 25 μm filter a background measurement was performed and the non-negligible background flux was subtracted from the on-target flux).

Similar results on absolute photometry (PHT05) were found when the comparison was made using observations of α Ari (HR 617) up to 100 μm . The background subtracted, colour-corrected flux values derived from OLP Version 10.0 data products are shown in Figure 6.45.

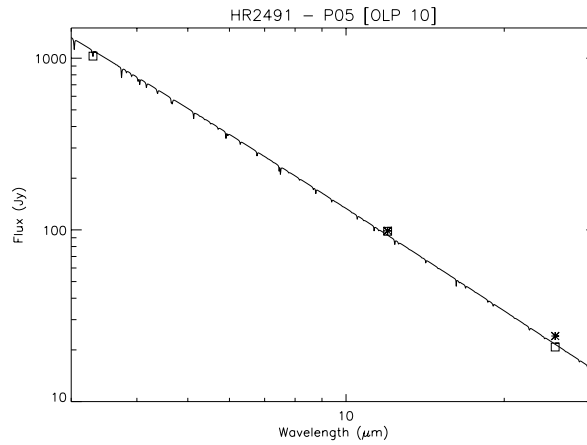


Figure 6.44: Comparison of PHT-P absolute photometry with the composite spectrum of Sirius (HR 2491) provided by M. Cohen and with IRAS photometry for OLP Version 10.0 data products. All photometric points are colour-corrected for a 10000 K blackbody. The meaning of the symbols is the following: solid line = model; asterisks = IRAS; squares = PHT-P (PHT05) measurements.

Accuracies are found to be better than 10% over the full P1 filter range, except for the three filters centred at 4.8, 11.3 and 12.8 μm . The 4.8 μm filter colour correction appears to be not appropriate due to an underlying strong absorption feature. For P2 detectors the background subtraction was performed using COBE/DIRBE fluxes since background measurements were not taken with ISOPHOT. Once this background contribution is removed, the accuracy of the P2 absolute photometry is also found to be better than 10%.

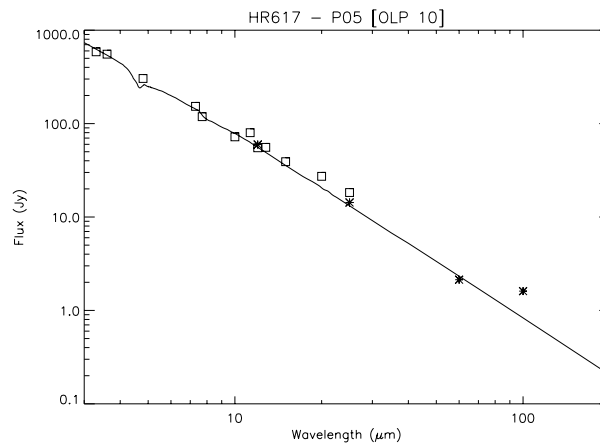


Figure 6.45: Comparison of PHT-P absolute photometry with the composite spectrum of α Ari (HR 617) provided by M. Cohen and with IRAS photometry for OLP Version 10.0 data products. All photometric points are colour-corrected for a 4000 K blackbody. The meaning of the symbols is the following: solid line = model; asterisks = IRAS; squares = PHT-P (PHT05) measurements.

Finally, OLP Version 10 data products corresponding to C200 absolute photometric mode (PHT25) observations of Uranus at 120 and 200 μm were also compared against the Uranus model produced by Griffin & Orton 1993, [64].

Figure 6.46 shows the results obtained where we can see that the measurements are within the 5% level of agreement.

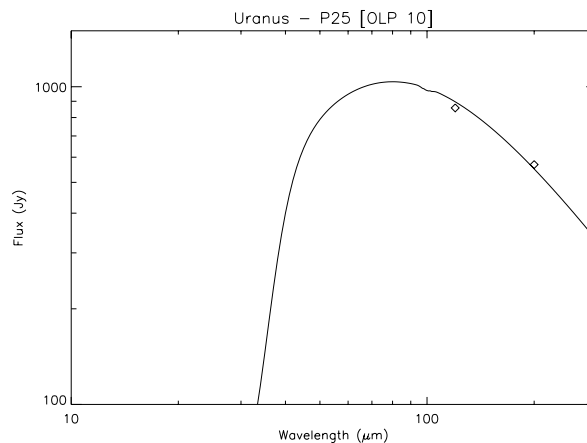


Figure 6.46: Comparison of C200 OLP Version 10.0 absolute photometry of Uranus with the model. All photometric points are colour-corrected for a 60 K blackbody. The meaning of the symbols is the following: solid line = model; diamonds = C200 (PHT25) measurements.

6.4.4 SWS

Detailed cross-calibration comparisons were made by Decin 2001, [40] between a few OLP Version 8.4 spectra of bright stars observed with SWS and their corresponding synthetic spectra from 2.38 to 12 μm derived using the MARCS-code (Gustafsson et al. 1975, [67] and subsequent updates).

The purpose of this study was to determine the origin of the small discrepancies detected between the ISO data and the theoretical spectra, leading both to improvements in the calibration of SWS and on the theoretical description of stellar atmospheres. This data set was used to improve the flux calibration of SWS bands 1 and 2 in OLP Version 10.

The broad-band shape of the relative spectral response function (RSRF) was as of OLP Version 8.4 already quite accurate in band 1. However, some improvements were made at the beginning of band 1A and a fringe pattern recognised at the end of band 1D was also corrected in OLP Version 10. The final accuracy of SWS in band 1 is estimated to be better than 2%.

In band 2 the calibration improved also with respect to previous calibrations in OLP Version 10, but still some problems exist. Due to the new model for memory effect correction based on the Fouks-Schubert model and developed by Do Kester (Kester 2001, [98]) the problems with the memory effects are now under control, at least when the flux jumps are not too high.

By making a comparison between the SWS data and the theoretical models first as a function of the spectral type and then as a function of the absolute flux value (see Figures 6.47 and 6.48) it was possible to distinguish between problems affecting OLP Version 8.4 which were spectral type related -i.e., problems with the theoretical predictions of the model - and problems which were flux, and so memory effect, related. This way it was learned that:

- A bump of $\sim 2.5\%$ in the wavelength range from 4.08–4.30 μm present both in hot and cool stars, in low-flux as well as in high-flux sources is indicative of problems with the RSRF.
- From 4.75 to 4.85 μm , a slight increase ($\sim 1\%$) is noticeable. Once more, an indication of a small problem with the RSRF.

- At the end of band 2A, a quite different behaviour for all the stars emerges. Further inspection indicates that we see a combination of problems with the memory-effect correction, synthetic predictions and, consequently, maybe also with the RSRFs. When we look at Figure 6.47 we can recognize a same — increasing — trend for β Peg, α Cet, β And and α Tau, the coolest stars in the sample and so indicating a problem with the synthetic predictions. This behaviour is however not visible for HD 149447, whose spectral type is in between β And and α Tau. An analogous discrepancy is visible for δ Dra with respect to the stars with almost the same effective temperature. Looking now at Figure 6.48 we see that HD 149447 and δ Dra (together with Vega and α Tuc) have almost the same absolute flux-level in band 2A and show the same trend (decreasing slope) in this plot, indicating a problem with the correction for memory-effects, a statement which is confirmed when we compare the up-scan and down-scan data.

The majority of discrepancies encountered in bands 2B and 2C are due to still existing problems with the memory-effect correction and smaller problems with the RSRFs. This kind of exercise gives us, however, also an idea on the relative accuracy in band 2 for OLP Version 8.4: an accuracy of better than 6%, which is — taking into account the problematic behaviour of the detectors in band 2 — a very good result, which may have been slightly improved in OLP Version 10 with the latest iteration in the determination of the RSRFs.

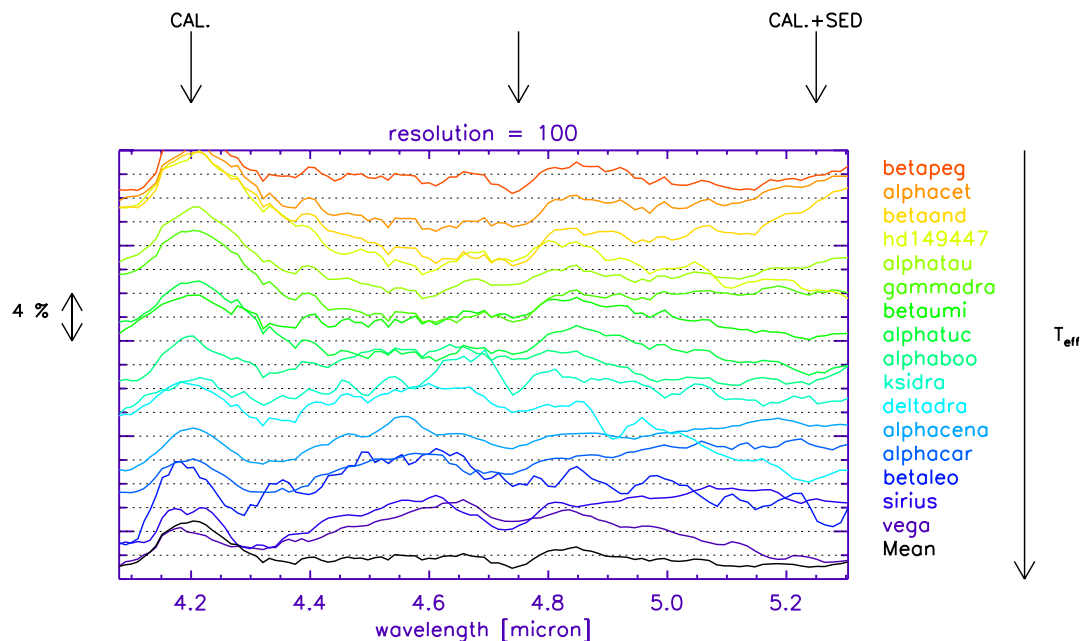


Figure 6.47: Division between OLP Version 8.4 SWS AOT01 data and their theoretical predictions at a resolving power of 100. The synthetic spectra are calculated using as stellar parameters the values determined from band 1 data. In this figure, the stars are ordered by spectral type. The mean of the different, coloured, divided spectra is given in black at the bottom of the figure (from Decin 2001, [40]).

The new set of synthetic spectra resulting from the work by Leen Decin was used to improve the calibration of OLP Version 10, while in OLP Version 8.4 models provided by Martin Cohen were used. Thus, a confrontation between the two sets may be instructive. Several stars are in common between the two samples: i) Vega and Sirius, for which Cohen has constructed a calibrated model spectrum; ii) a composite spectrum (i.e. various observed spectra have been spliced to each other using photometric data) is available for α Cen A, α Boo, γ Dra, α Tau, β And, α Cet and β Peg; iii) a template spectrum (i. e. a spectrum made by using photometric data of the star itself and the shape of a ‘template’ star)

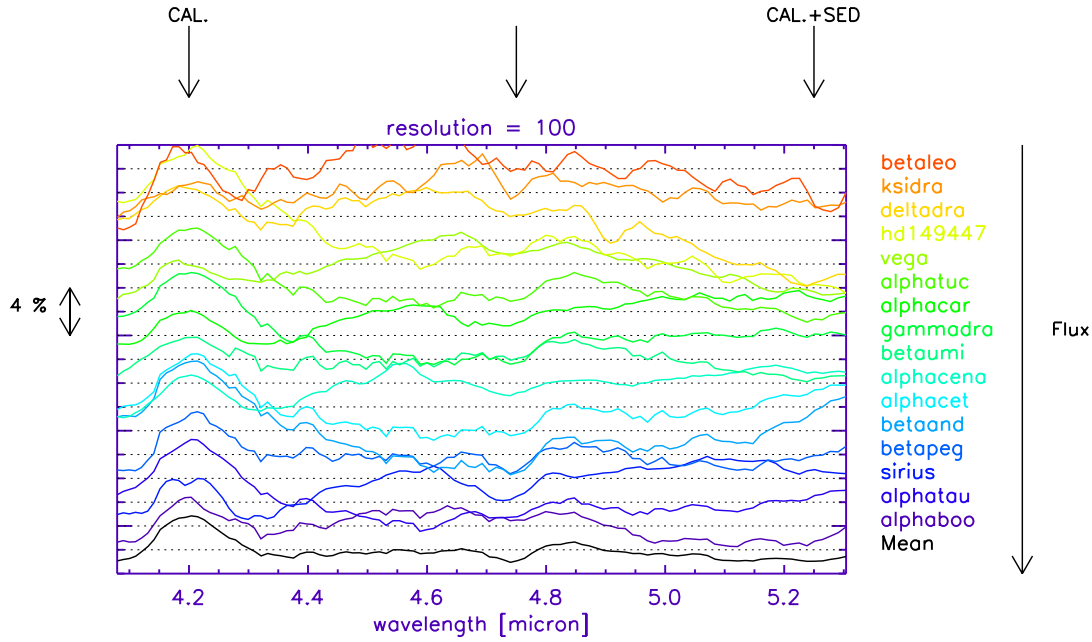


Figure 6.48: Division between OLP Version 8.4 SWS AOT01 data and their theoretical predictions at a resolving power of 100. The synthetic spectra are calculated using as stellar parameters the values determined from the band-1 data. In this figure, the stars are ordered by absolute-flux value. The mean of the different, coloured, divided spectra is given in black at the bottom of the figure (from Decin 2001, [40]).

is built for δ Dra (template: β Gem: K0 III), ξ Dra (template: α Boo: K2 IIIp), α Tuc (template: α Hya: K3 II-III) and HD 149447 (template: α Tau: K5 III). One should notice that for the composite spectrum of γ Dra, no spectroscopic data were available at that time in the wavelength range from $1.2\ \mu\text{m}$ till $5.5\ \mu\text{m}$. The spectrum of α Tau has therefore been used to construct the composite spectrum of γ Dra in this wavelength range.

In order to ensure independency of the absolute-flux level of the SWS data, the angular diameters of the synthetic spectra were determined by using the photometric data of Cohen, JKLM data from Hammersley's GBPP broad-band photometry, IRAS data and some other published photometric data cited in the IA_SED data-base. A comparison between the (high-resolution) synthetic spectra, SEDs of Cohen and used photometric data is given in Figure 6.4.4. The obtained angular diameters θ_d (in *mas*) for the stellar sources are mentioned in the figure.

The most remarkable discrepancies between the two spectra arise in the CO and SiO molecular bands, where the molecular bands are consistently across the sample stronger in the composites of Cohen. Cohen used low-resolution NIR and KAO data to construct this part of the spectrum. Comparing these synthetic spectra with OLP Version 8.4 SWS data (whose calibration is not based on our results) and the high-resolution Fourier Transform Spectrometer (FTS) spectrum of α Boo published by Hinkle et al. 1995, [82] (see Figure 4.5 in Decin 2000, [39]), we did however see that the strongest, low-excitation, CO lines were always predicted as being somewhat too *strong* (a few percent at a resolution of 50000 for the FTS spectrum), probably caused by a problem with the temperature distribution in the outermost layers of the theoretical model (Decin et al. 2003c, [44]). Moreover, a comparison between the high-resolution synthetic spectrum of α Boo with its FTS spectrum shows also a good agreement for the high excitation CO $\Delta v = 1$ lines, the low excitation lines being predicted as too weak. The few percent disagreement between FTS and synthetic spectrum will however never yield the kind of disagreement one sees between the low resolution synthetic spectra and the SED data. The CO $\Delta v = 2$ discrepancy visible in γ Dra

results from using the α Tau observational KAO data. Since α Tau and γ Dra have a different set of stellar parameters, with α Tau having a significant larger amount of carbon, the SED of Cohen for γ Dra displays too strong a CO feature. One should also be heedful of this remark when judging upon the quality of the template spectra for δ Dra, ξ Dra, α Tuc and HD 149447.

As conclusion, we may say that the SED spectra of Cohen are excellent (and consistent) for the absolute calibration of an instrument, but that attention should be paid when using them for relative flux calibration.

This kind of analysis, which has been proven to be very adequate, will be applied also to bands 3 and 4 in the future.

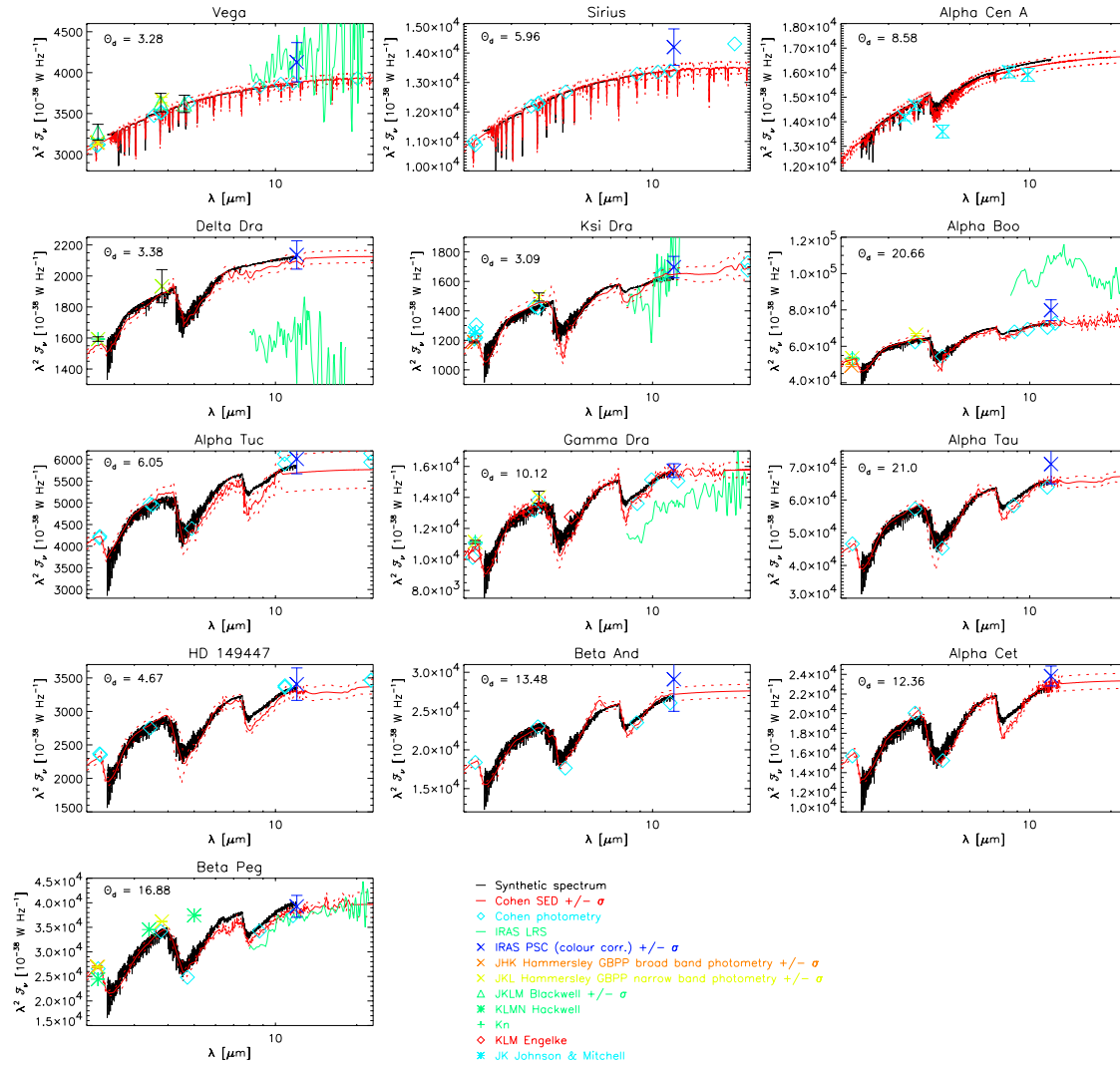


Figure 6.49: Comparison between the synthetic spectra of the standard stellar sources, their SED of Cohen and various photometric datapoints taken from the literature.

6.5 Conclusions

In summary, the results above presented show an overall agreement which exceeds in most cases pre-launch expectations. This applies both to the internal (among the ISO instruments) and external (between ISO instruments and other space missions, like IRAS, MSX or COBE-DIRBE) comparisons made. The consistency found is in general of the order or better than the 10–15% level for what we have called ‘well-behaved’ data sets, with just a few exceptions. In particular the discrepancies between IRAS photometry and ISO synthetic photometry at 60 and 100 μm are shown to be probably related to a problem in the absolute flux calibration of IRAS at high flux levels.

ISO, along with several other missions, was so-well calibrated because they were all underpinned by a common, self-consistent, calibration basis that was already in place at the time of launch.

The clear lesson learned from this success is that one needs a self-consistent common basis as much to bind together the instruments on a given satellite, as to compare transparently with data from different spaceborne, ground-based and airborne facilities. Building on a solid foundation of work from the ground, airplanes and satellites it has been possible to establish a robust infrared calibration framework.

The ISO Ground Based Preparatory Programme (GBPP) was able to deliver a uniform calibration database (photometric data plus spectral energy distributions) of some 400 sources covering the whole sky with an accuracy typically of a few percent which was used mainly for the calibration of the ISO instruments at short wavelengths (Hammersley & Jourdain de Muizon 2001, [73]).

Founded originally on empirical spectra derived from observations on NASA’s Kuiper Airborne Observatory (KAO), the entire calibration context is traceable to emergent spectra from a pair of stellar atmospheric models for Vega and Sirius by Kurucz. The scheme proved very successful in unifying infrared photometry and spectroscopy in the 1–35 μm range for a variety of instruments onboard KAO, IRTS, ISO and MSX and was successfully extended to 300 μm in support of ISOPHOT (Cohen 2001, [34]). Although stars were too faint to calibrate LWS directly, its spectra of several K-giant calibration stars show flux levels and spectral energy distributions to be perfectly consistent (albeit with absolute uncertainties of order 15–20%) with LWS formal calibration from Uranus.

Many connections to IRAS, KAO and between ISO sub-instruments have been established via observations of individual asteroids, which have also provided means to check the absolute photometric calibration and validate the RSRF of the ISO instruments in critical areas, e.g. in the case of late type stellar standards at the CO and SiO fundamental absorption bands (Müller & Lagerros 2001, [126]).

In the near future, this all-sky network of absolute calibrators is expected to be expanded to a far fainter network suitable not only for SIRTf but also for ground-based 8–10 μm class telescopes, still self-consistently.

Chapter 7

The ISO Data Archive (IDA)

ISO was operated as an observatory with the majority of its observing time being distributed to the general astronomical community. One of the consequences of this is that the data set is not homogeneous, as would be expected from a survey. The observational data underwent sophisticated data processing, including validation and accuracy analysis. In total, the ISO Data Archive contains about 30,000 standard observations, 120,000 parallel, serendipity and calibration observations and 17,000 engineering measurements. In addition to the observational data products, the archive also contains satellite data, documentation, data of historic aspects and externally derived products, for a total of more than 400 GBytes stored on magnetic disks. The ISO Data Archive is constantly being improved both in contents and functionality throughout the Active Archive Phase, ending in December 2006.

7.1 Introduction

The ISO Data Archive opened to the external world on December 9, 1998, six months after the end of the operations (Arviset & Prusti 1999, [3] and Arviset et al. 2000, [4]). Through a pioneering user interface based on Java technology, complex queries can be issued to the ISO database. A textual and visual presentation of the data is offered to the users to aid them in selecting observations for retrieval through `ftp`. The ISO Data Archive was designed and developed at the ISO Data Centre in Villafranca del Castillo, Spain, with continuous and fruitful cooperation between users and developers to provide a unique state-of-the art astronomical data archive.

The IDA main characteristics can be summarized as:

- Archive open to the external world via a fast connection to the Internet
- Intuitive and user friendly WWW interface
- Uplink and downlink data held in a single database
- Powerful and complex queries against the observations database
- Configurable results display, including product visualization tools
- Customable product retrieval via a shopping basket
- Choice for direct retrieval of products on disk
- Selection of product level for retrieval
- Product retrieval via `ftp`

- Link between observations and related publications
- Inter-operability with other archives and applications
- Modular and flexible design that can evolve as additional user requirements come along
- Proprietary data - access to each observing programme was restricted to the observing proposals PI's for the first year after its completion.

The ISO Data Archive offers the user a self-contained, fast and powerful interface to all ISO data products. Complex queries can be made against hundreds of database parameters using friendly and modular query panels (general astronomical parameters, observer and proposal, timing constraints, list of targets, pointing and raster map constraints, instrument details, Highly Processed Data Products). The user is helped in the observations selection by a clear and configurable results display that includes quick look data browsing (static GIF icons and postcards and FITS products display), access to auxiliary and ancillary files, access to related observations in the ISO catalogue, on-line help and access to other archives (e.g. IRSA, ADS, CDS). Once logged in, via a simple click, the user can download the data products to his/her local disk for one observation or move this selection to a shopping basket, perform other queries, select other observations and later decide the level of processed products to download (standard datasets or user defined ones, for all or per observation).

The IDA is based on a flexible and open 3-tier architecture design, which main aim is to separate the data from the presentation. The overall system design was decided in early 1997 and has been able to fulfill all new requirements that have been raised since then.

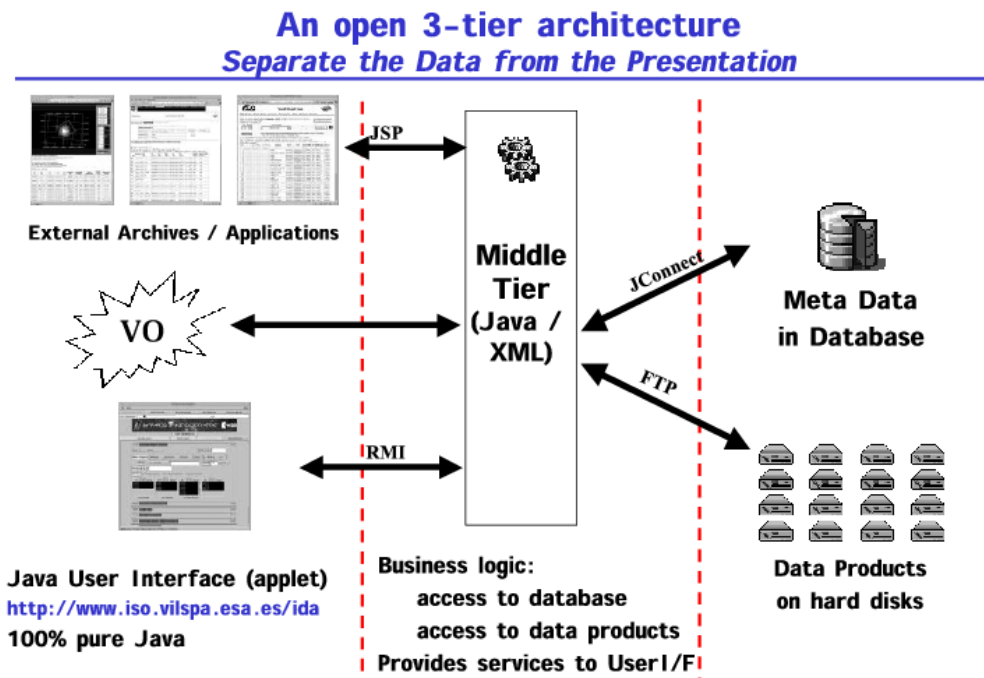


Figure 7.1: *ISO Data Archive 3-tier architecture.*

7.2 IDA Contents

The IDA contains on magnetic disks all the levels of data products, from the reformatted telemetry up to the products fully processed by an automatic pipeline processing chain, as well as quick look browse products, together with ancillary information (engineering, uplink and downlink data). Essential parameters extracted from the data are part of the database allowing complex queries to be made. Also user provided reduced data, catalogues and atlases are archived (the so-called ‘Highly Processed Data Products’ or HPDPs). They are well separated from the pipeline products and are queryable and retrievable in a user-friendly way.

The following paragraphs define in general terms what data and processing tools are archived. More details can be found in Appendix E.

7.2.1 Off-Line products

Every ISO observation was run through an automatic data-analysis pipeline called Off-Line Processing, or OLP, to produce three sets of data products. These correspond to increasing levels of data processing and were extracted from the OLP at successive stages of the pipeline process:

- Edited Raw Data (ERD);
- Science Processed Data (SPD);
- Auto-Analysis Results (AAR);

The type and sophistication of analysis performed for each product set is instrument dependent. Detailed technical descriptions of the contents and formats of data product files and the various types of processing performed are given in the corresponding instrument chapters of the ISO Handbook.

In the ISO Data Archive, products are further classified according to the following scheme:

- Raw Data Products

These are essentially unpacked telemetry in which no data reduction has taken place and thus form the starting point for data analysis performed by OLP or the user’s own system. PHT ERD is an example.

- Basic Science Data Products

These data have been processed further to an intermediate level (with the use of calibration files where necessary), often containing physical units. They are therefore ready for assembly into structures of astronomical significance such as images or spectra by OLP or independently by observers themselves before scientific conclusions can be drawn. For example, the final result of the LWS pipeline is the LSAN file that contains a tabulation of flux in physical units measured during the observation.

- Fully Auto-processed Data Products

These data include a set of coherent, instrument-dependent measurements of images or spectra designed to get as close as possible by automatic means to what could be produced by an astronomer using an interactive analysis system. Where possible, products follow FITS standard conventions

to ease further analysis by standard high-level tools such as IDL or *fv*. They allow the user to carry out initial survey programmes or to make an assessment of the relevance of a given observation to their scientific work, although the limitations must be emphasised of such an automatic procedure which takes no account of the individual circumstances of an observation and involves no scientific judgement. Significantly better results are likely to be achieved using an interactive system. Examples of AAR products are, for the CAM pipeline, individual FITS images in the CMAP file, that are combined where appropriate into mosaics in the CMOS file; a tabulation of sources detected in the images in the CPSL file; and individual source spectra as appropriate in the CSSP file.

7.2.1.1 Scientific validation and accuracy

In addition to the functional validation, the pipeline was also subjected to a ‘scientific validation’ to establish confidence in the processing and calibration of the products. The goals of this scientific validation included, inter alia:

- Confirming that the applied processing had the expected effect(s) on the data
- Establishing that sufficient processing had been applied to the data
- Demonstrating that the processing was reliable, stable and repeatable
- Establishing the level of accuracy of the calibration
- Documenting any known caveats or concerns with the processing and/or calibration
- Demonstrating that, with the information provided in the relevant ISO Handbook sections, user can work from the supplied products to produce publishable results.

The scientific validation of data per AOT and product level is summarized in the specific sections in the ISO Handbook instrument volumes.

Of the 30,000 standard observations in the ISO Data Archive, 89% were performed with modes for which the pipeline was scientifically validated. The remaining 11% (all LWS03 observations and some PHT modes) may still be used for scientific analysis. However, it is strongly recommended to look at the relevant ISO Handbook chapters in order to understand the limitations of the pipeline processing for those modes and consult the ISO Helpdesk as necessary.

For most of the cases, it is possible to improve the data quality of ISO observations by manual data reduction with the different Interactive Analysis (IA) software packages (see Section 1.4.2). Products derived in this way, of higher quality than the pipeline products, can be ingested in the ISO Data Archive in the form of HPDPs (see Section 7.2.3).

7.2.1.2 Quality control

All standard observations in the Routine Phase were individually inspected and an assessment of the quality of the data products was made. Technical flags were assigned to the ISO data products to assess their suitability for delivery to the observers. A detailed description of the flags is given in Appendix E.

The Quality control process was split into three different levels:

- **Level 1:** This was a first quality assessment performed by the Off-line Processing operators according to some simple criteria. A Real Time report provided by the Instrument controllers, an Instrument report automatically generated by the RTA/QLA system and an output log from the Pipeline processing determined that the observation: a) Failed completely and therefore was not delivered and flagged as failed; b) Passed the level 1 assessment being delivered to the proposer and flagged as ‘Good’. c) Was passed to the next quality control level in case of doubt.

- **Level 2:** This was a second quality assessment performed by the Instrument Dedicated Teams to identify the cause of the level 1 check failure and to decide whether the data could be released. The observation was also flagged as ‘failed’ or ‘Good’. In the case of a ‘failed’ observation the QC level 3 could be invoked for rescheduling.
- **Level 3:** The third quality assessment was performed by the Science Team at the SOC. According to the level 1 report and the analysis by the Instrument Dedicated Teams, the Science Team decided whether a failed observation had to re-enter the Mission Planning system for rescheduling.

In addition, an extra level (QC level 4) was invoked when the quality assessment of the observation had to be performed by the proposer. In case of declared failure, the observation could be re-entered into the planning system for execution.

It should be noted that this quality information referred to whether the data were useful from the technical point of view; no attempt was made to judge whether the data served to a particular science goal. During the ISO Active Archive Phase (2002–2006), it is foreseen to enhance the quality information in the ISO Data Archive. ISO products Quality Control statistics are given in Figure 7.2

7.2.2 Browse products after OLP

The ISO Data Archive also provides *browse products* or quick-look data associated to each observation. These products enable users to make informed decisions as to what observations they want to download for detailed astronomical analysis. **These products did not undergo scientific validation nor quality control and should therefore not be used to derive scientific conclusions.**

7.2.3 Highly Processed Data Products

The Highly Processed Data Products (HPDPs) include DATA (images, spectra etc.), which have been processed beyond the pipeline and/or using new, refined algorithms and therefore have been improved to any degree compared to the legacy pipeline products, as well as any resulting CATALOGUES and ATLASES. In July 2003, the ISO Data Archive has been enhanced with the functionality for continuous ingestion of new data, catalogues and atlases, further to screening by the ISO Data Centre. A list of currently available Highly Processed Data Products is generated on-the-fly from the IDA and can be accessed through the ISO Data Center web page at:

<http://www.iso.vilspa.esa.es/> → List of Highly Processed Data Products

Data, catalogues and atlases can be easily queried from the IDA interface.

7.2.4 Other products

The ISO Data Archive also contains auxiliary data (e.g. spacecraft data, mission planning information and diagnostic data), ancillary data (such as space weather), calibration data and other observation specific information. These are described in more detail in Appendix E.

7.3 Database Architecture

The IDA database was designed taking into account all the contents required by the users. From this, a flexible and evolutive Physical Data Model has been built up to design the way the IDA database tables are organised.

The ISO Data Archive architecture is described in the *ISO Data Archive Physical Data Model*, [47]. This gives, for each IDA database table, the fields, the indices, links to other tables and population scripts used.

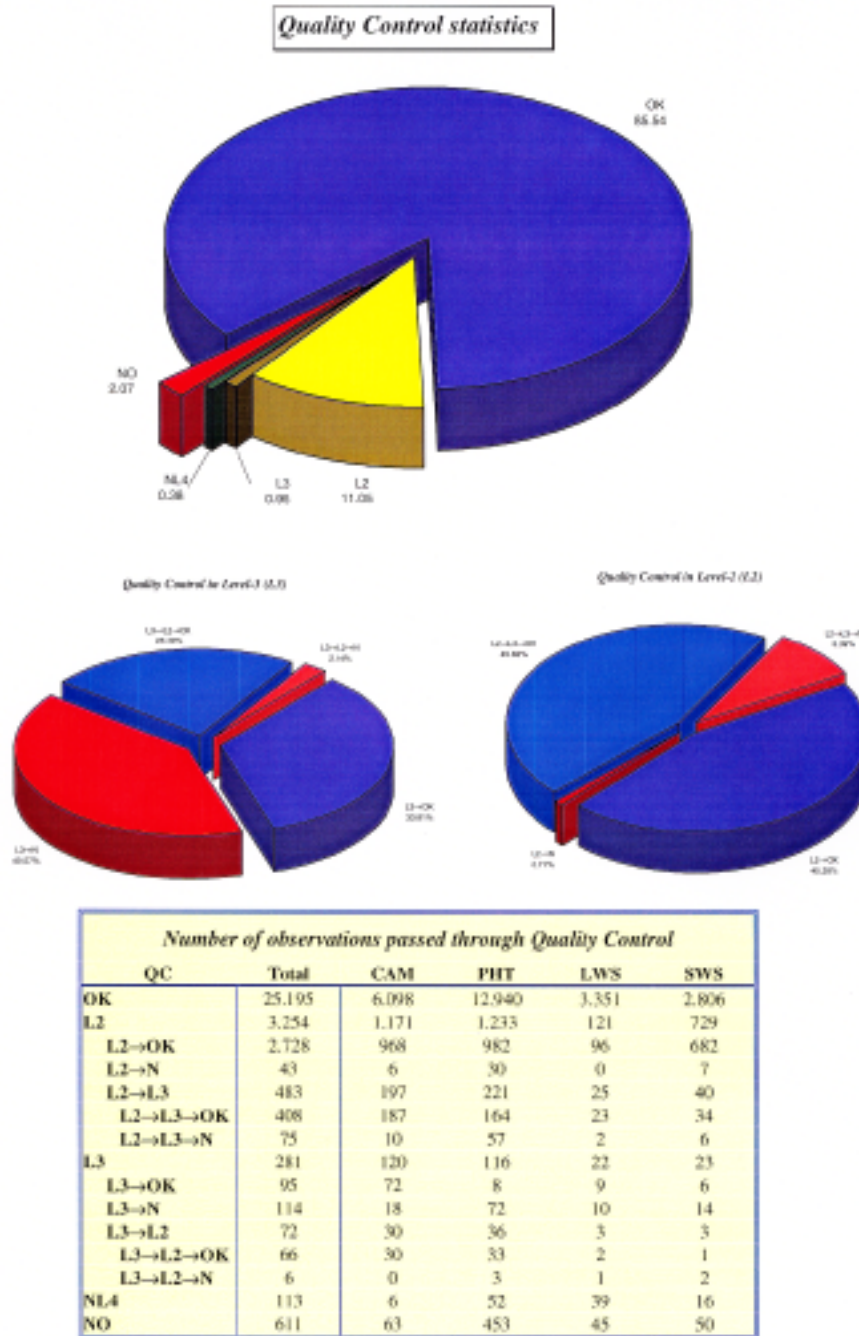


Figure 7.2: ISO pipeline products Quality Control statistics which shows the number of observations which passed through the Quality Control process (from Claes et al. 1998, [24]). An ‘OK’ assessment means that the observation could be processed by the pipeline, partially (until Derive-ERD or Derive-SPD) or fully (until Auto-Analysis). ‘NL 4’ refers to the number of QC L4 cases which were shown to be rescheduling cases. ‘No’ or ‘N’ cases points to pure rescheduling cases in QC L1 (total failure of an observation in QC L1).

7.4 User Interface

In the early stages of the project in 1997, it was decided that the only way to have a powerful graphical user interface meeting all user requirements was to opt for a Java application or ‘applet’ rather than the standard approach based on ‘cgi-bin’ scripts. As a consequence of this, IDA offers one of the most powerful archive interfaces.

7.5 Business Logic/Middle-Tier

While the pipeline processing system produces data products and files and the user only sees the Java interface, all connections between the two other layers are made by the so called ‘Business Logic’ or middle-tier. The use of a middle-tier has a number of advantages. It isolates the interface from the rest of the system and deals with most of the application business logic and complexity. This has the benefit of making the interface lighter and faster and it also means that a number of changes don’t require the users to get a new version of the application. All data transfers between the interface and the middle-tier are compressed which makes the system run faster. This business logic layer is also the way other archives or applications can access the ISO data products and extra files without being required to go through the standard user interface. This has made very easy any inter-operability of IDA in the context of the Virtual Observatories. Another great advantage has been brought by the use of Java in this open 3-tier architecture. The IDA design and code has been re-used to develop other ESA scientific mission archives (e.g. the XMM-Newton Science Archive, first released in April 2002; Arviset et al. 2002, [6]).

7.6 Publication Tracking

This service has been available since the release of IDA Version 3.0, in December 1999. In cooperation with the Infrared Processing and Analysis Center, (IPAC, USA), all major astronomical journals are read for references to ISO. Later on, astronomers at the ISO Data Centre find the specific observations (TDTs) on which the paper is based. This process sometimes involves interaction with the authors, when they are not explicitly mentioned in the paper. The observation details are then entered into IDA, via a dedicated web page called from IDA itself. Paper authors can also enter directly the observations used in their paper using the same system. Further to validation by the IDC, these are entered in IDA. Links between ISO observations and related articles are available in both directions as described in the following section.

7.7 Interoperability Aspects

Prior to the advent of the Virtual Observatory and establishment of associated standards, effort has already been done on improving IDA interoperability with other astronomical archives, through accessing other relevant archives or through providing direct access to the ISO data for external services (Arviset et al. 2001, [5]; Salama et al. 2002a, [141]; Arviset et al. 2003, [7]).

In particular, target name resolution via NED and SIMBAD has been available since the release of the first version of IDA in December 1998. From the list of observations on the IDA interface, users can access the corresponding articles on the ADS WWW mirror at Strasbourg, France. On the other hand, links are provided by ADS to the ISO postcard server for the observations on which a given article is based.

From the ISO postcard, by a simple click, the user can open a browser window to the IRAS archive WWW page located at IPAC, USA that contains the IRAS data covering the region of the sky of the selected ISO observation.

Direct links to the ISO data are also provided, using mechanisms developed to be compatible with the Virtual Observatories. At the time of writing, a subset of ISO observation specific information and data are accessible from the Vizier catalogue browser based at CDS, Strasbourg, France, the NASA HEASARC archive and from ADS. ISO observations are also accessible from the InfraRed Science Archive (IRSA), located at IPAC via a tool showing ISO observations field-of-views, overlaid onto IRAS images.

All these interfaces are being ported to the new Virtual Observatory standards (Simple Image Access Protocol, VOTable, etc...) for the IDA to be fully part of it.

7.8 Using the ISO Data Archive

A short summary follows of the main features of the IDA User Interface. Extensive context-help is available directly for each field in the user interface and a guided tour can be accessed on the ISO Data Center web site at:

<http://www.iso.vilspa.esa.es/> → Guided Tour of the Archive

Access the ISO Data Archive interface

Having reached the ISO Data Archive on the WWW (<http://www.iso.vilspa.esa.es/> → Access the Archive) and having started the Java applet, users can define a query as shown in Figure 7.3.

The *Main query* panel consists of various subpanels, which can be opened to specify parameters against which to query.

The *Principal search criteria* panel, opened by default, allows the general astronomer to query against general parameters such as:

- Target name (as given by the proposer or resolved via NED or SIMBAD)
- Coordinates
- Wavelength ranges
- Type of observing mode (AOT) used by the satellite
- Instrument

Other sub-panels are more specific and allow searches against parameters like:

- Highly Processed Data Products
- Observer or proposal name, proposal text, observation identifier
- Date, time, uplink software version, revolution or phase in orbit
- Target name list
- Observation list
- Raster map parameters
- Instrument specific details parameters

Aimed more at expert users, the interface supports querying of non-standard modes, including engineering data and additional observations obtained in parallel to other instruments or while slewing between targets.

The screenshot shows the ISO Data Archive 6.1 main query panel. The interface includes a menu bar (File, Save, Help), navigation tabs (Query Specification, Latest Results, Shopping Basket, Login/Register, Request Monitor), and a user status bar (User: ASALAMA, Idle). A banner for the Infrared Space Observatory (ISO) and ESA is displayed. The main area is titled "Query Specification" and contains several sections:

- Principal Search Criteria:**
 - Quality: Good
 - TDT Number: 1
 - Search Target By: Name (selected), Type, Equatorial, Galactic, Ecliptic, Radius, etc.
 - Name: for SIMBAD
 - Radius: 5 arcmin
 - Wavelength [µm]:
 - Obs Type: Standard Data (selected), Non-Standard Data, Engineering Data
 - Instrument filters: CAM (All, None), LWS (All, None), PHT (All, None), SWS (All, None)
 - Inc. Parallel, Inc. Serendipity (checkboxes)
- Highly Processed Data Products (HPDP):**
 - Observer, Proposal, OSN
 - Target List
 - Timing Constraints
 - Pointing & Raster Map Constraints
 - CAM Expert Details
 - LWS Expert Details
 - PHT Expert Details
 - SWS Expert Details

Figure 7.3: ISO Data Archive main query panel.

Once the user has completed the search criteria, the query can be executed. The query can also be manually edited to allow expert users to perform more complex queries which are not possible through entering values in search boxes (see Appendix G).

Getting the results

Once a query has been executed, the archive returns the list of observations matching the constraints in the *Latest Results* panel. A subset — sized to fit on the screen — of the returned list of observations will be displayed. The user can scroll through this list using navigational buttons.

ID	Instrument	RA	Dec	Description	Status
HD100546	SRIS01	11h33m25.27s	-70d11'42.2"	low-resolution full grating scan	Scientifically Validated
27601036	CHARLES WEGASTAR	18-Aug-1996 23:21:25	6538 sec	Good	
NGC 5194	FHT32	13h29m51.91s	+47d11'50.2"	Oversampled map	Not Scientifically Validated
36100618	JINAVIES DUSTY GAL	01-Nov-1996 15:38:51	4286 sec	Good	
M16-HST-field	CAM01	18h18m51.10s	-13d49'50.4"	General observation with camera	Scientifically Validated
52000102	GFILSRATM16_HST	19-Apr-1997 03:23:54	1346 sec	Good	
CENTAURUS A	IMS01	13h25m27.58s	-43d01'08.4"	Medium resolution wavelength range	Scientifically Validated
63400464	HRMITH IRS6ALS	11-Aug-1997 02:02:01	2890 sec	Good	
CRAB	CAM04	05h34m31.50s	+82d00'52.7"	CVF spectral observation with camera	Scientifically Validated
83003539	PLAGAGE CAMSR	23-Feb-1998 01:03:53	3420 sec	Good	

Figure 7.4: ISO Data Archive query results panel with associated browse products

Figure 7.4 shows an example of the information displayed for each observation. An icon (one of the browse products) on the right-hand side of the screen gives an immediate visual impression of the data content of the observation. The postcard can be viewed by clicking on the icon. A Survey Products Display Tool (SPDT) allows simple manipulation of the FITS survey products. The amount of information and observations displayed in the *Latest Results* panel can be customised; the main parameters are:

- Target name
- Observing mode
- Coordinates
- Observation type and number
- Field of view
- Wavelength range
- Observer and proposal identification
- Date, time and observation length
- Data quality information

Highly Processed Data Products

The Highly Processed Data Products (HPDPs) are a different kind of products, well distinguished from the homogeneous set of pipeline products. A specific interface has been designed to display and retrieve them in a uniform way. For observations in the *Latest Results* panel having associated HPDPs, a number of options are given to access relevant information and data. A dedicated panel gives the abstracts of all HPDP sets associated to the observation. The following options are given as applicable:

1. Data
Data can be retrieved via direct download on disk.
2. Documentation
If it is a published article, a link is given to the corresponding abstract in ADS, otherwise, a link is provided to a documentation file stored in IDA.
3. The button ‘Add related’ will move all observations pertaining to the given HPDP set to the shopping basket for retrieval of all observations in one go.
More buttons may be highlighted depending on the availability in the given HPDP set:
4. Postcard
An illustration (plot, image) of the reduced observation. This will be obtained by automatically launching your default browser.
5. Atlas
This is defined as illustration of the observations together with other information provided in the HPDP set, such as externally derived Spectral Energy Distributions, stellar models, etc.
6. Catalogue
A new panel will be launched, pointing to the observation specific information. The whole catalogue may be saved on disk or printed.

Observational Details and Related Products

Many additional data products are connected directly to individual observations, but not retrievable in the same way as the observational data (e.g. uplink files and downlink, real-time and instrument reports, proposal abstracts). These products are available under the ‘Details’ and ‘Related’ buttons in the archive and can be saved directly into a file.

Requesting the data

Another innovative and friendly feature of the ISO Data Archive is the wide selection of possibilities offered for the retrieval of data. Once a query has been performed and the user has logged in, observations can be selected for retrieval by moving them to the ‘shopping basket’. The user can then perform other queries, select other observations and add them to the shopping basket. The *Shopping Basket* panel looks very similar to the *Latest Results* one and is similarly configurable. For all observations in the shopping basket, the user can select the level of products to be retrieved, i.e.:

- Raw data
- Basic science
- Fully processed
- Quick-look
- Custom
- HPDP
- All

These choices can be made for all observations as well as per observation and they can be combined. Moreover, through the custom option, users can choose their own set of files to be retrieved.

Once ready for requesting the data, users can press the ‘Submit Request’ button. The User Interface then determines the volume of data, checks whether the daily quota for the user has been exceeded and asks the user for a compression format. The download time by `ftp` (default means of data retrieval) can be estimated if required. The archive processes the data retrieval task and copies the data into an `ftp` public area, where it is stored for a period of seven days. The user is informed by e-mail when and where data is available.

A direct retrieval on disk is also possible for each observation in the Latest Results query panel.

User registration and login

Anybody can query the archive and see results and associated quick-look data. However, before being able to retrieve observations, a username and a password has to be requested and issued. This login mechanism was necessary to protect proprietary data during and shortly after the mission. It also helps in monitoring archive usage and avoids possible disturbances from hackers. Additionally, users have to provide their e-mail address to receive notifications from the archive, when their product report is completed. The user database is also used to maintain close contact with the users community (Matagne 2002, [119]).

Advanced user access the ISO Data Archive database

A specific java applet allows a direct access to the ISO Data Archive metadata via an SQL-applet. The SQL interface allows expert users to perform searches against all queryable contents of the ISO Data Archive, including observation data products, auxiliary data, trend and housekeeping information and many other products. An on-line tutorial is available in the ISO Web site. Worked examples can be found in Appendix G.

Expert users can also create *User Defined Functions* to extract virtual attributes from files external to the database engine. These virtual attributes can then further be used in queries inside the database engine (Wieprecht et al. 1999, [165]).

7.9 Historical Aspects

At the end of ISO operations, in May 1998, all ISO observations (around 900 days of data) were bulk-reprocessed (BKRP) with the latest version of the pipeline and calibration software to produce the first uniform ISO Interim Archive. All products were then stored on CD-ROM jukeboxes.

During the ISO Post-Operations Phase, the data processing and calibration software had been constantly updated and improved at the rate of one major update per instrument per year as the behaviour of instruments was better understood. In order to enable the astronomical community to take advantage of these improvements, an on-the-fly reprocessing facility for all data products was provided through the interface to the archive, for the user to always have the possibility to retrieve the latest version of the data products processed with the latest version available of the pipeline software (Osuna et al. 2000, [133]).

In late 2000, all ISO observations were reprocessed again to produce the ‘New Interim Archive’. As technology had evolved and storage facility had become more affordable, all products were saved on hard disk which allowed faster download of the data.

All ISO data were reprocessed with the final version of the pipeline to produce the so-called ‘Legacy Archive’. This was released at the end of February 2002 and represents the best set of products that can be generated by an overall automated processing chain. All products were put on hard disk and previous Interim Archive and New Interim Archives were discarded.

The ISO Data Archive is constantly enhanced both in contents (Highly Processed Data Products) and functionality throughout the ISO Active Archive Phase, ending in December 2006.

7.10 IDA usage statistics

The usage of the ISO Data Archive is constantly monitored. A snapshot of the statistics at the time of writing is shown in Figures 7.5 to 7.9 (see also Salama 2002b, [142] and Matagne 2002, [119]).

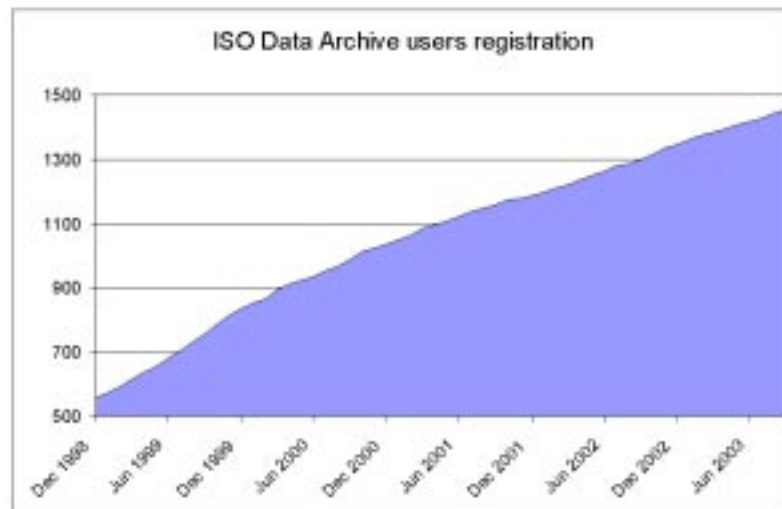


Figure 7.5: *ISO Data Archive users registration. At the time of its first release in December 1998, all ISO proposers were pre-registered. New users are continuously registering. During 2003 the registration rate was about 12 per month.*

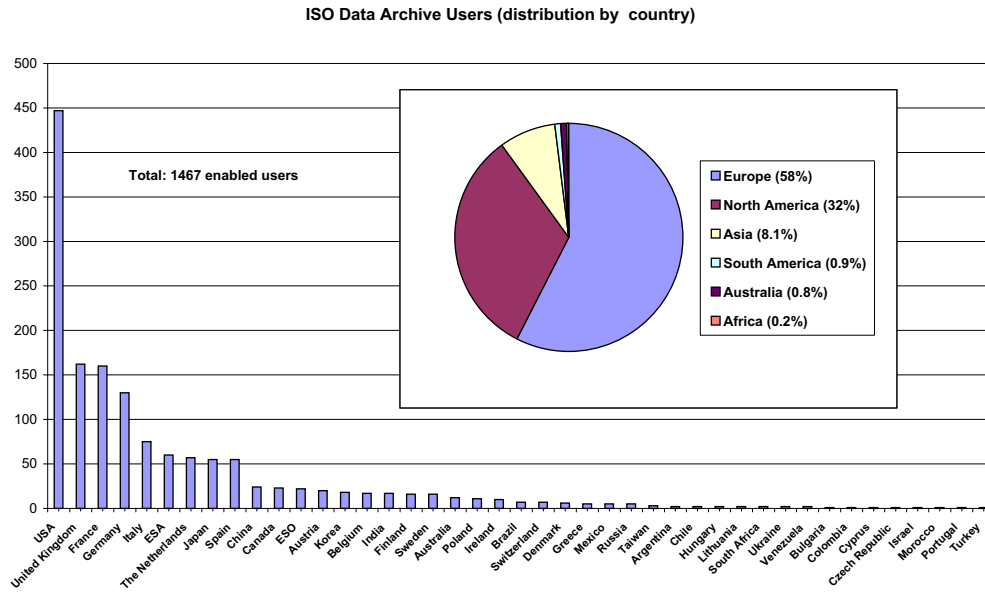


Figure 7.6: ISO Data Archive users distribution by country

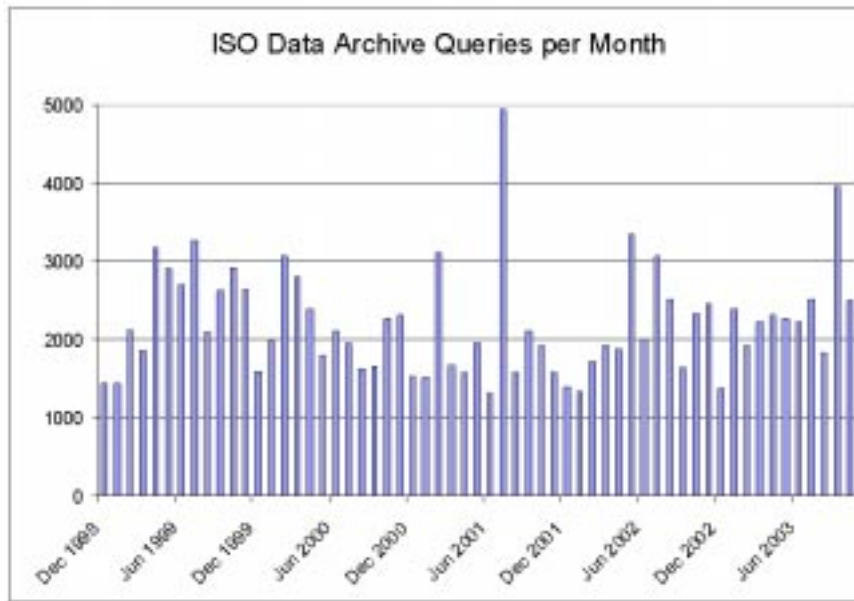


Figure 7.7: ISO Data Archive queries per month. Users do not necessarily need to log in to query the archive database. Only queries from external users are shown here.

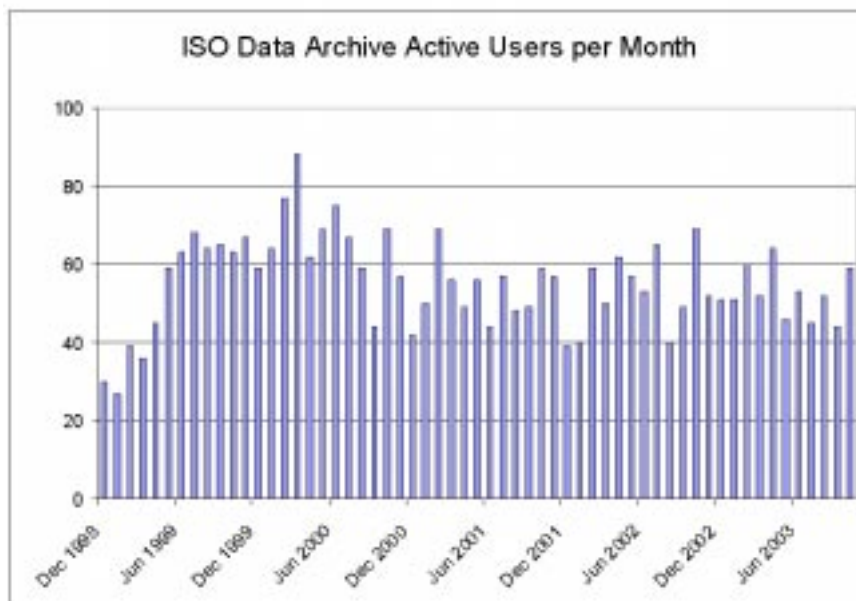


Figure 7.8: *ISO Data Archive active users per month.* A user is here defined to be ‘active’ when a download of at least an observation dataset is performed in the given month. Note that only users external from the ISO Data Centre and the National Data Centres are considered here.

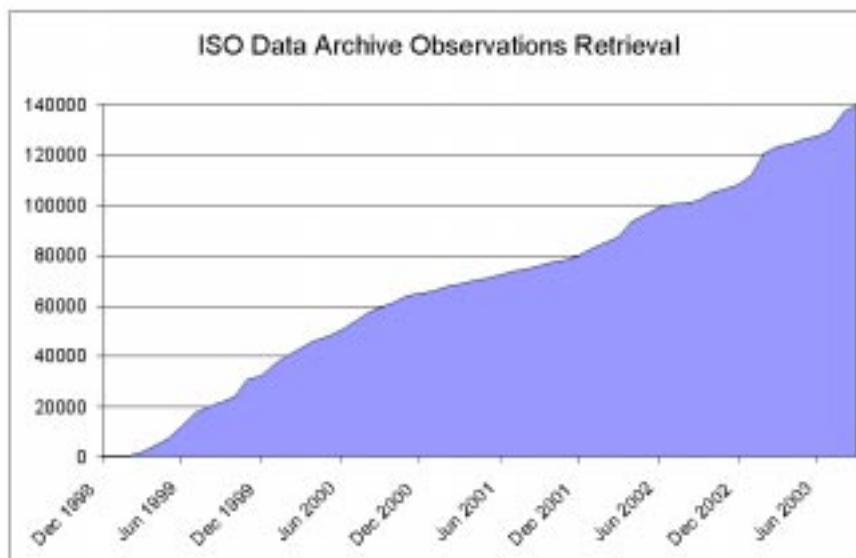


Figure 7.9: *ISO Data Archive observations retrieval.* This plot shows the number of observations downloaded by external users throughout the IDA lifetime. At the time of writing, there has been a download of 4.7 times the equivalent of the scientific content of the archive from the external astronomical community. This factor rises to 8.3, if we also take into account users from the National Data Centres, working with the IDA for both functional and visitor support activities.

Appendix A

Infrared Astronomy

This appendix summarizes the unit conventions used for ISO observations. Some aspects influencing the observations, such as the astronomical background and source confusion are also mentioned.

A.1 Infrared Units

The infrared wavelength range has borrowed units from the surrounding optical and radio (submm) regimes. Both magnitude and flux representations are widely used in the infrared.

Flux density F_ν of a source is defined as the flux per unit frequency. Flux density is the physical unit used for point sources. The unit of flux density is $\text{W m}^{-2} \text{Hz}^{-1}$. For practical purposes in the infrared it is often convenient to scale this SI unit and use Janskys (Jy) instead.

$$1 \text{ Jy} = 10^{-26} \text{ W m}^{-2} \text{Hz}^{-1} \quad (\text{A.1})$$

ISOCAM-CVF and SWS spectra are given in units of Jy/pixel and Jy, respectively in AAR data products. ISOPHOT-S spectra are given in units of $\text{W m}^{-2} \mu\text{m}^{-1}$. The conversion to Jy can be done in the following way:

$$1 \frac{\text{W}}{\text{m}^2 \mu\text{m}} = 10^{13} \frac{\lambda^2}{29.98} \text{Jy} \quad \text{with } \lambda \text{ in } [\mu\text{m}] \quad (\text{A.2})$$

LWS spectra are given in units of $10^{-18} \text{ W cm}^{-2} \mu\text{m}^{-1}$. The conversion to Jansky can be done with the following equation:

$$10^{-18} \frac{\text{W}}{\text{cm}^2 \mu\text{m}} = \frac{\lambda^2}{299.8} \text{Jy} \quad \text{with } \lambda \text{ in } [\mu\text{m}] \quad (\text{A.3})$$

For extended objects, surface brightness B_ν is used instead of flux density. Also background emission, for point sources, is expressed in brightness units. Brightness is defined as the flux density per unit solid angle. The unit of brightness is $\text{W m}^{-2} \text{Hz}^{-1} \text{sr}^{-1}$, but in practice it is often scaled to MJy sr^{-1} .

$$1 \text{ MJy sr}^{-1} = 10^{-20} \text{ W m}^{-2} \text{Hz}^{-1} \text{sr}^{-1} \quad (\text{A.4})$$

The flux density of a point source, in particular for a stellar object, is often given in magnitudes m . In the ISO wavelength range these units are mostly used for ground based measurements below $20 \mu\text{m}$. The conversion to or from magnitudes is performed via the definition of the zero magnitude flux density F_0 , which depends on the wavelength and on the photometric system used. In the case of ISO, the

system zero point is defined by the model spectral energy distribution of Vega (α Lyr), available from <http://www.iso.vilspa.esa.es/>.

The magnitude m of a ground based observation can then be converted into flux density through the formula

$$F_\nu = F_0 10^{-\frac{m}{2.5}}. \quad (\text{A.5})$$

For spectroscopic measurements, the total flux F of a line is often the most interesting quantity. A flux calibrated spectrum may be presented in the form of flux density F_λ ($F_\lambda = \frac{c}{\lambda^2} F_\nu$) as a function of wavelength λ . Flux F of a line of interest can be obtained by subtracting an appropriate continuum flux density level of the spectrum before integrating over the entire line in wavelength λ . The unit of flux is W m^{-2} .

A.2 Astronomical Background Radiation

Background and stray radiation from sources other than the target increase the noise and thus affect the detectability of a continuum or line flux.

Aspects which are related to background radiation and which constraint the sensitivity are:

- the celestial background
- source and cirrus confusion
- straylight from nearby bright sources
- instrumental stray radiation
- high-energy particles

The last three items in this list have already been addressed in detail in Chapter 5.

If the target object was close to strong infrared objects, but not confused with the stronger infrared source, then the background radiation was dominated by emission in the tail of the point spread function of the stronger object. In this case chopping and beam switching techniques generally did not work well. It was then recommended to the observer to consider e.g. observations in scan mode (see Section 4.5) to obtain sufficient information of the stronger source to remove its contribution from the data at the analysis stage.

A.2.1 The celestial background

The two components which contribute most to the celestial background in the infrared are the zodiacal light and the diffuse Galactic emission. Zodiacal light dominates at the shorter ISO wavelengths $\lambda < 50 \mu\text{m}$ with a peak around $25 \mu\text{m}$. The diffuse Galactic emission is more important at the longer wavelengths $\lambda > 100 \mu\text{m}$ with a peak around $200 \mu\text{m}$.

The amount of zodiacal emission depends on wavelength and on the ecliptic coordinates of the object. The closer to the ecliptic plane the more background emission is to be expected. In addition to the dependence on celestial coordinates, zodiacal emission depends also on the satellite orientation: The smaller the solar elongation angle, which for ISO ranges from 120 to 60 degrees, the more zodiacal emission is received. The results obtained with PHT-S, PHT-P and ISOCAM suggest that the zodiacal emission spectrum can be well approximated by blackbodies of 260–290 K, depending on the solar elongation and on the ecliptic latitude (Ábráham et al. 1999, [2]). In addition, ISOCAM CVF and ISOPHOT-S measurements

demonstrated that the spectrum is featureless between 5 and 16 μm . The diffuse Galactic emission has a dependence on Galactic coordinates: Toward the Galactic centre the background radiation is increasing. While the Galactic emission has a significant fraction of intensity in lines and broad spectral features, the zodiacal light is expected to be dominantly continuum radiation.

Both emission components affected the detection of faint sources and it was often desirable to determine the background flux via a reference measurement at a position in the neighbourhood of the source position. The most common methods to obtain reference measurements were beam switching and chopping, which were offered in several AOTs. For some observations the CAM field of view was large enough to image both the source and its background in one frame, thus avoiding beam switching altogether. If a suitable reference position was relatively far from the source position (but still within 3 degrees) the proposer usually prepared two separate observations which were then concatenated (see Section 4.5).

For imaging and spectroscopic observations one of the parameters an observer had to provide was the peak flux density. This included both the emission from the target and the background. For small apertures and strong sources the background contribution was usually negligible. For weaker objects observed with larger apertures (at longer wavelengths) it was necessary to take into account the background emission as discussed in the paragraph below.

For PHT AOTs the background emission was an explicit parameter required for the observations. IRAS maps were considered to be the best source to obtain estimates of the Galactic emission. For estimates at wavelengths outside the IRAS wavelength range, COBE results were recommended. Table A.1 gives some very rough estimates based on COBE data. The values are relative numbers, normalised to the 100 μm flux, and should be used for extrapolation from the IRAS fluxes.

It should be noted that the values in Table A.1 apply to the diffuse interstellar medium only. In molecular cloud complexes the surface brightness at 200 μm may be factors of 5 to 10 higher compared to the diffuse clouds.

Table A.1: *Typical infrared fluxes of interstellar clouds detected with COBE. The results are averages from 10 diffuse clouds and are normalised to the 100 μm flux.*

Wavelength [μm]	Surface Brightness [MJy/sr]
3.5	0.0016
4.9	0.0015
12	0.043
25	0.058
60	0.42
100	1
140	1.99
240	1.40

A proposer had to be aware of all offset corrections made to the data products used. E.g. IRAS maps are often provided with zodiacal emission subtracted. As zodiacal emission might have been the main contributor to the background, it was necessary to take it into account for the total background level estimate. This was not exactly possible as the satellite orientation was not known prior to the actual observation. Therefore a conservative estimate had to be made to avoid saturation. Table A.2 contains for various wavelengths estimates of the maximum zodiacal light contribution as a function of the ecliptic latitude. The ecliptic latitude β can be obtained from Right Ascension α and Declination δ by equation:

$$\sin \beta = \sin \delta \cos 23^\circ 26' - \cos \delta \sin 23^\circ 26' \sin \alpha \quad (\text{A.6})$$

Table A.2: *Maximum zodiacal light contribution in MJy sr⁻¹ with the smallest solar aspect angle possible for ISO (60° except for the ecliptic pole) as a function of the ecliptic latitude β and wavelength λ . The estimates are based on measurements by ZIP (2.5–7.5 μm , Murdock & Price 1985, [128]) and IRAS (12–100 μm), an examination of full IRAS scans obtained with a solar aspect angle $60^\circ < \varepsilon < 61^\circ$ except for the poles for which scans with about 90° solar aspect angle were used). The 200 μm estimate is an extrapolation of the IRAS data.*

λ	2.5	3.5	7.5	12	25	60	100	200
	μm							
$ \beta $								
0°	0.2	0.2	25	75	140	45	25	15
10°				55	100	30	15	
20°				40	70	20	10	
30°				30	50	12	8	
45°				20	35	10	6	
60°				15	30	8	5	
90°	0.2	0.15	4.5	14	25	7	1	0.26

A.2.2 Source Confusion

Source confusion is an additional noise factor closely related to the astronomical background. However, there is a fundamental difference. The sensitivity limit due to confusion is determined by the telescope aperture, observing wavelength and position on the sky. After reaching the confusion limited level, sensitivity cannot be improved by increasing the integration time. With the ISO mission properties and depending on the instrument configurations the confusion limit was reached within a relatively short integration time. Therefore users had to be aware of the limiting source densities as a function of wavelength and the position on the sky. The most important contributors to the confusion limits in the ISO wavelength range are listed below.

- Extragalactic sources dominate the long wavelength end outside the Galactic plane, Magellanic Clouds and nearby star forming regions.
- Small scale structure in cirrus clouds may dominate the longer wavelengths in intermediate Galactic latitudes. The contribution depends heavily on the level of cirrus emission at the position on the sky.
- Old stars dominate at the shorter wavelengths. Their contribution increases toward the Galactic plane and especially toward the Galactic centre (bulge).
- Young stars appear usually in groups. When the line of sight passes through such a group, young stars may dominate the confusion limit in the whole ISO wavelength range. Groups of young stars exist throughout the Galactic plane (the inner Galaxy being more crowded than the outer Galaxy), in the Magellanic Clouds and within nearby star forming regions (in Orion, Ophiuchus, etc.).

For an object away from the Galactic plane ($|\beta| > 20^\circ$) and at wavelengths below 25 μm it was necessary to consider confusion if the estimated flux of the target was less than about 1 mJy. On the Galactic plane the situation is worse (i.e. the confusion limit is higher). At longer wavelengths the approximate limits are: 10 mJy at 60 μm , 50 mJy at 100 μm and 0.1 Jy at 200 μm . However, the level of cirrus may easily change these limits by an order of magnitude depending on the location of the target in the sky. Model dependent estimates of confusion limited flux levels have been presented by Franceschini et al. 1991, [55]

and by Gautier et al. 1992, [61]. Results on the confusion problems, based on ISO results, can be found in Herbstmeier et al. 1998, [79]. A discussion of the models and the consequences for observations with ISO can be found in Puget 1992, [138].

When the expected source flux suggested that confusion noise would be a significant factor, it was important to obtain observations with the highest available spatial resolution. This was achieved by setting the reference measurement (or chopping for PHT) as close as possible to the target position. The best observing strategy for sources with a flux level close to the confusion limit was to obtain fully sampled maps. This was, of course, very expensive as far as observing time is concerned.

A.3 Infrared Astronomical Calibrators

The absolute flux calibration of three of the four ISO instruments (CAM, PHT - at short wavelengths - and SWS) is based primarily on results from the Ground-Based Preparatory Programme (GBPP, Jourdain de Muizon & Habing 1992, [91]; Hammersley & Jourdain de Muizon 2001, [73]) and of the Cohen, Walker, Witeborn et al. (CWW) absolute calibration programme (Cohen et al. 1992a, [28]; 1992b, [29]; 1995, [31]; 1996, [32] and 1998, [33]), and more recently on detailed models provided by Decin et al. 2002, [41]; 2003a, [42]; 2003b, [43] and 2003c, [44]).

The long wavelength filters of PHT also use planets and asteroids to cover the bright and intermediate part of their dynamic range (Müller & Lagerros 1998, [125]; Griffin & Orton 1993, [64]; Orton 2001, [132]). The absolute flux calibration of LWS is based on Uranus as primary source (Sidher et al. 2001, [150]).

A catalogue of calibration source observations as well as many of the reference models used for the calibration of the four ISO instruments are available on-line at the ISO IDC web site:

<http://www.iso.vilspa.esa.es/> → ISO Explanatory Library → Performance and Calibration.

Appendix B

ISO Scientific Observations

In the following sections, the titles, principal investigators and the total observing time (in seconds) of all performed programmes, sorted per scientific area, are summarized. The section has been split up into 2 parts, one for ‘Guaranteed Time Proposals’ (GT) and one for ‘Open Time Proposals’ (OT). This separation is based on the way the proposals were handled and on the availability of observing time under the OT and GT budget. The times are given in seconds for each proposal. More details on the proposals, including the scientific abstracts can be found in the ISO Data Archive. There, searches for proposal categories (European CP observer, American guaranteed time, Japanese guaranteed time, Open time, Calibration observer), scientific categories (Solar System, Interstellar Matter, Stellar Physics, Extragalactic Systems, Cosmology, Calibration), proposal keywords¹, text from proposal abstracts and text from proposal justifications can be done within the *Observer, Proposal, OSN* panel.

Notes:

- In many cases, several proposals with the same PI and on the same topic have been merged to ‘meta-proposals’.
- The scientific categories do not always agree with the OTAC panel structure (in the OTAC the extragalactic proposals were split up into normal galaxies and AGNs).
- The target of opportunity (ToO) proposals are all in the Open Time list.
- Small parts of some proposals were performed under the calibration time budget and not under OT or GT budgets. If PI and title were the same as those corresponding to other OT or GT proposals, the observing times have been added.
- Polarisation observations were done in a special way under the category ‘calibration’, nevertheless they appear in the following lists under OT, since the observing time was taken from the OT budget.

The resulting number of proposals with On-Target Time (OTT) > 0s is 1079.

¹abundances, accretion discs, active galactic nuclei, AGB stars, bipolar outflows, BL Lac objects, brown dwarfs, calibration, circumstellar discs, circumstellar envelope, comet trails, comets, compact galaxies, cooling flows, dark matter, diffuse interstellar medium, dust properties, early-type stars, elliptical galaxies, galactic structure, galaxy clusters, galaxy formation, gravitational lensing, HII regions, interplanetary medium, irregular galaxies, jets, large scale structure, line formation, Magellanic Clouds, molecular clouds, normal galaxies, novae, planetary nebulae, planets, quasars, star formation, starburst galaxies, stellar atmospheres, stellar evolution, stellar winds, supernova remnants, young stellar objects

B.1 Performed Guaranteed Time Proposals

B.1.1 Solar System

Coustenis, A.	Titan: A Study of the Composition and Temperature of the Atmosphere	58078
Crovisier, J.	Spectroscopic Observations of Periodic Comets with LWS and SWS	82232
Davies, J.	Is there Sub-Arcminute Structure in the Zodiacal Bands?	3434
Davies, J.	On the Trail of Tails: Imaging the Trails of Comets P/Kopff, P/Gunn and P/Churyumov-Gerasimenko with CAM	43644
de Graauw, Th.	ISO Observations of Mars	39864
Encrenaz, Th.	Observations of Galilean Satellites and Asteroids with ISO	4214
Feuchtgruber, H.	Search for H ₂ -H ₂ Dimers on Jupiter and Saturn	17848
Feuchtgruber, H.	Titan	15553
Griffin, M.	ISO Spectroscopy of the Giant Planets	344943
Grün, E.	Comet Observations with ISOPHOT: Study of Bare Nuclei, Onset of Activity, Composition of Comets and Dust Production	86080
Heras, A.	Search for Atmospheric Constituents on Jupiter and Saturn Satellites	29073
Leinert, Ch.	Global Mapping, Seasonal Variation and Search for Arcminute Structure of Zodiacal Light	75022
Leinert, Ch.	Properties of Solar System Dust	104296
Morris, P.	SWS Observations of the Zodiacal Light: Solar System Mineralogy	8779
Salama, A.	The Mineralogy and Chemistry of the Major Asteroid Classes	17679
Schulz, B.	Vesta Lightcurve Observations	18925
Sibille, F.	Mapping of Dust and Parent Molecules in Periodic Comets with ISOCAM	23525

B.1.2 Stellar/Circumstellar Physics

Barlow, M.	Abundances in the High-Velocity Outflows from Novae and Early-Type Stars	52895
Barlow, M.	High-Spectral Resolution Observations of Molecules and Atoms in Outflows from Evolved Stars	43052
Barlow, M.	Spectroscopic Observations of Vega-Excess Systems	59408
Barlow, M.	The Far-Infrared Spectra of Cool Evolved Stars, Post-AGB Objects and Planetary Nebulae	342825
Becklin, E.	Dust Debris around Solar Mass Stars	364161
Beckwith, S.	Evolution of Circumstellar Disks around Young Stars	51550
Beckwith, S.	Physical Properties of Circumstellar Disks: Spectral Energy Distributions of Young Stellar Objects	9524
Beintema, D.	Spectroscopy of Planetary Nebulae	102670
Blommaert, J.	Mass-Losing AGB Stars in the Small Magellanic Cloud	20056
Cabrit, S.	Mid-Infrared Dust Emission from Young Stellar Objects: Outflows and Warm Halos	125985
de Jong, T.	A Spectral Study of Bright AGB Stars	86953
Habing, H.	Infrared Flux Densities of Nearby Stars: A Search for Vega-Type Stars	231931
Hammersley, P.	Photometry and Spectroscopy of Normal Stars	35316

Heske, A.	Molecular Bands along the Giant Branches	65637
Hessman, F.	FU Orionis Stars	6404
Izumiura, H.	Mass-Loss in the Late Stage of Stellar Evolution: Deep Infrared Imaging of Dust Shells around AGB Stars	91202
Lamers, H.	Winds and Circumstellar Matter around Hot Luminous Stars	45433
Leinert, Ch.	Binary T Tauri Stars	24214
Leinert, Ch.	Herbig Ae/Be Stars and the Evolution of their Circumstellar Material	29356
Mirabel, I.	Dust Heated by High-Energy Sources	90418
Nordh, L.	A Survey for Young, Low-Mass Stars in Nearby Molecular Clouds	252480
Persi, P.	Infrared Structure of Selected Planetary and Proto-Planetary Nebulae: Spectrophotometric Imaging	49192
Price, S.	Selected Area Galactic Survey	50023
Price, S.	Spectral Characterisation of Bright Infrared Sources	83463
Ray, T.	Infrared Emission from Bipolar Outflows	4766
Ray, T.	The Evolution of Disks around Young Low-Mass Stars	45920
Reipurth, B.	Energy Sources of HH Flows	7990
Rouan, D.	Infrared Structure of Selected Planetary and Proto-Planetary Nebulae: Broad Band Imaging of the Dust Envelope	10923
Russell, S.	Protostars	24826
Salama, A.	ISO Observations of Cataclysmic Variables	133784
Salama, A.	ISO Observations of SS433	11270
Sargent, A.	Planetary/Proto-Planetary Disks: ISOCAM Investigations	71654
Sedlmayr, E.	Variability of Circumstellar Dust Shells around Long-Period Variables	15954
Stencel, R.	The Birth and Death of Planetary Systems	122043
Takashi, T.	Mass-Loss in the Late Stages of Stellar Evolution: Structure of the Outer Atmosphere of Cool Evolved Stars	138192
Tanabé, T.	Mass-Loss in the Late Stages of Stellar Evolution: AGB Stars in the Magellanic Clouds Star Clusters	71548
Telesco, C.	A Search for Brown Dwarfs as Companions to Nearby Stars	34902
Trams, N.	Infrared Photometry of Be Stars	20774
Trams, N.	Mass Loss and Evolution of AGB Stars in the Magellanic Clouds	60849
Trams, N.	The Circumstellar Environment of Evolved Massive Stars	21954
van der Hucht, K.	Winds and Dust Formation by Wolf-Rayet Stars	79797
Waelkens, C.	The Evolution of Proto-Planetary Disks	89538
Walker, H.	Disks and Shells around Post-Main Sequence Stars	43946
Walker, H.	Dust Disks around Vega-Like Stars	68984
Walker, H.	The Infrared Energy Distributions of M-Dwarfs	13960
Waters, L.	The Structure of the Winds of Be Stars	37882
Waters, L.	Transition Objects between Asymptotic Giant Branch and Planetary Nebula	86587
Wesseliuss, P.	Very Young Intermediate-Mass Stars	110268

B.1.3 Interstellar Matter

André, P.	Mid-Infrared Spectral Energy Distribution	55485
Baluteau, J.	Complete LWS Spectral Survey at High-Resolution	229962
Boulanger, F.	Small Particles in the Interstellar Medium	218265
Breitfellner, M.	Search for Interstellar Fullerenes	1020
Caux, E.	Study of the Low Density Components of the ISM: The Diffuse Medium in the Galactic Plane	68174

Cesarsky, D.	Spectral Imaging of H II Region Interfaces and Reflection Nebulae	27417
Cox, P.	Chemical and Physical Characterisation of Compact H II Regions across the Galaxy	139944
Cox, P.	Structure, Physical and Chemical Characterisation of the Dense Parts of the ISM and their Interfaces	108556
Drapatz, S.	Physical and Chemical Conditions in Dense, Warm Interstellar Gas	324046
Emery, R.	Study of Ionised Regions	41240
Gry, C.	Study of the Low Density Components of the ISM: The Interstellar Cirrus	55970
Gürtler, J.	Embedded and Background Infrared Sources for Absorption Mea- surements	14514
Harwit, M.	Measurement of Water Vapor and Oxygen Abundances	146596
Henning, Th.	Circumstellar Matter around Very Young and Massive Stars	24204
Henning, Th.	Star Formation in Molecular Cloud Cores	5373
Joubert, M.	Structure, Physical and Chemical Characterisation of the Dense Parts of the ISM and their Interfaces	37353
Jourdain de Muizon, M.	Solid State Infrared Spectroscopy with ISO	115029
Lagage, P.	Mapping of Supernova Remnants	74614
Laureijs, R.	Exploring the Nature of the Coldest IRAS Sources	23392
Laureijs, R.	Infrared Properties of Compact Sources in the Magellanic Clouds	20578
Laureijs, R.	Small Grains in Reflection Nebula CED 201	13258
Lemke, D.	Addendum to a Large-Scale Map of the Orion Molecular Cloud/Star Formation Complex at 200 μm	7970
Lemke, D.	Interstellar Dust Emission	314849
Lemke, D.	Interstellar Dust Emission: Messier 31	18126
Lemke, D.	Interstellar Dust Emission: Small Magellanic Cloud	80171
Lemke, D.	Interstellar Dust Emission: Taurus Molecular Cloud 1	2644
Mattila, K.	Diffuse Infrared Emission of the Galaxy	36562
Mezger, P.	ISO Observations of the Earliest Evolutionary Stages of Protostars	65639
Mezger, P.	Observations of the Galactic Centre with ISO	124636
Moneti, A.	A Complete Spectrum of the Prototype FU Ori Object FU Orionis	10306
Morris, M.	Large-Scale Shocks in the Galactic Centre and Other Regions	11128
Morris, M.	The Metallicity of Galactic Centre Gas	10254
Olofsson, G.	A Deep Search for Low-Mass Protostellar Objects and Pre-Main Sequence Stars in Nearby Molecular Clouds	39854
Onaka, T.	Observation of Diffuse Interstellar Medium: Spectroscopic Study	216196
Onaka, T.	Observation of Diffuse Interstellar Medium: Far-Infrared Polari- sation Study	6820
Péquignot, D.	Far-Infrared Spectroscopy of Supernova Remnants: Nuclearly Processed Material in Young Supernova Remnants	28008
Pollock, A.	The Morphology of Dust Heated by the SNR G78.2+2.1	6988
Prusti, T.	Solid State Features	976
Prusti, T.	Survey of TMC2 in Taurus	107429
Puget, J.-L.	Spectral Survey of the Cold Interstellar Medium: Search for New Features from Dust, Atom Clusters and Molecule Lines	1890
Roelfsema, P.	Silicate Emission Features towards Ultracompact H II Regions	7506
Roelfsema, P.	The Properties of Dust Emission Features towards Ultracompact H II Regions: The Details of the 5–12 Micron PAH Features	23182
Rouan, D.	Polaro-Imaging of Different Components of the Interstellar Medium and Circumstellar Dust	32092

Saraceno, P.	Pre-Main Sequence Evolution: Outflows and their Interaction with Interstellar Medium	90420
Saraceno, P.	Pre-Main Sequence Evolution: The Early Phase of Star Formation	339508
Saraceno, P.	Pre-Main Sequence Evolution: The Pre Main Sequence Stars	133514
Stark, R.	A Detailed Study of the Carbon and Oxygen Cooling Lines in Translucent Cirrus Clouds	30668
Tamura, M.	Evolution of the High-Density Cores in Molecular Clouds	48894
Tuffs, R.	Observations of Dust and Gas in Supernova Remnants	77470
van Dishoeck, E.	Deuterium in the Galaxy: The HD Abundance as a Function of Galactocentric Distance	16560
van Dishoeck, E.	Molecular Spectroscopy of Gas-Phase Species: A Pilot Study with the SWS	165421
Whittet, D.	Infrared Spectroscopy of Interstellar Dust Absorption	149815

B.1.4 Extragalactic Systems

Barr, P.	Infrared Continuum Variability in BL Lacertae Objects	22898
Barr, P.	The Infrared Flux Distribution of Broad Line Radio Galaxies and the 25 μm Bump in 3C 390.3	7953
Barr, P.	The Polarisation of the Non-Thermal Infrared Continuum in Active Galactic Nuclei	2884
Barthel, P.	The Nature of Broad Line Radio Galaxies	13968
Chini, R.	Emission Mechanisms in Quasars: Radio Loud Quasars and BL Lac Objects	171330
Clavel, J.	ISOPHOT-S and ISOCAM Observations of Seyfert Galaxies: The CfA Sample	138497
de Graauw, Th.	Investigation of the Unified Model of Quasars and Radio Galaxies with Infrared Data	25640
Feuchtgruber, H.	High-Resolution Observations of OH Absorption in the Galactic Centre	17585
Garzón, F.	The Physical Parameters that Control Violent Stellar Bursts	20135
Genzel, R.	Infrared Spectroscopy of Bright Galactic Nuclei and the Connection between Star Formation and AGNs	1069615
Hanlon, L.	Search for a Flaring/Fading Infrared Counterpart to the New Gamma-Ray Burst GRB970111	1078
Helou, G.	The Interstellar Medium of Normal Galaxies: Properties and Evolution	437856
Hippelein, H.	Heating of the Interstellar Medium in Spirals: Mapping of Nearby Galaxies	158486
Joseph, R.	The ISOPHOT Field Galaxy Sample	68067
Klaas, U.	The Infrared Energy Distributions of Ultraluminous Galaxies	51710
Lequeux, J.	A Coordinated Study of Galaxies in the Virgo Cluster	119548
Lequeux, J.	Spectro-Imaging of Individual Star-Forming Regions in Nearby Galaxies	60200
Levine, D.	Determination of SEDs for High-z Ultraluminous Infrared Galaxies Detected in the C. Lonsdale et. al. Filler Survey	30814
Madden, S.	Dust Emission in Irregular Galaxies	74830
Metcalfe, L.	ISO Observations of Blue Compact Galaxies	94174
Miley, G.	Dust in 6C 1908+772	3618
Mirabel, I.	Starburst and Active Galaxies	123792
Moorwood, A.	Deep Imaging of Quasars with ISOCAM	30110

Nakagawa, T.	Mid-Infrared Ne Ionic Lines Survey of Active Galaxies	16258
Nørgaard-Nielsen, H.	Dust in Elliptical Galaxies	54380
Rodríguez Espinosa, J.	Astrophysics of AGN: An ISOPHOT Perspective	64044
Richter, G.	ISOPHOT Observations of an Unbiased Sample of Blue Compact Galaxies	20230
Siebenmorgen, R.	Polarimetry of Ultraluminous IRAS Galaxies: Starbursts or AGN?	7050
Smith, H.	ISO Spectroscopy of Active Galactic Nuclei	305655
Smith, H.	ISO Spectroscopy of Infrared Bright Galaxies	153696
Smith, H.	Spectroscopic Studies of the Galactic Centre Region	140180
Smith, H.	Spectroscopic Studies of the Interstellar Medium in Galaxies	57596
Telesco, C.	Blue Radio Galaxies at Intermediate Redshifts	104006
van der Hulst, J.	Spectral Study of the Interstellar Medium and Star Formation in Nearby Galaxies: Physical Conditions and Composition	137384
van der Werf, P.	Star Formation and Active Nucleus in Distant Radio Galaxies: A Pilot Study	9336
Vigroux, L.	Broad Band Imaging of an Extragalactic H II Region Sample	150694
Vigroux, L.	Infrared Emission from Early-Type Galaxies	88355
Völk, H.	Statistical Sample of Late-Type Galaxies from the Virgo Cluster	108495
Wilkes, B.	Exploring the Full Range of Quasar/AGN Properties	372258

B.1.5 Cosmology

Altieri, B.	The Ultimate CAM Raster on Abell 2390	56981
Bonoli, C.	Star Formation in Barred Spiral Galaxies	78005
Casali, M.	A Search for a Brown Dwarf Halo in an Edge-On Spiral Galaxy and Galactic Clusters	24067
Cesarsky, C.	Deep Imaging of a Sample of X-Ray Galaxy Clusters in Hydra	85607
Cesarsky, C.	ISOCAM Deep Survey Programme (Cosmology)	503359
Franceschini, A.	Deep Imaging of Intermediate and High-Redshift Clusters	237760
Mattila, K.	Measurement of the Extragalactic Infrared Background Radiation	116587
Metcalf, L.	ISO Observations of Gravitationally Lensed Arcs	143082
Nørgaard-Nielsen, H.	ISOPHOT Deep Observations of Selected Area 57	147099
Puget, J.-L.	Structure of the Far-Infrared Background	140322
Stickel, M.	Cold Dust in the Intracluster Medium of Galaxy Clusters	18966
Taniguchi, Y.	A Search for Primeval Galaxies and Quasars	278483

B.2 Performed Open Time Proposals

B.2.1 Solar System

Barbieri, C.	Infrared Observations of Rosetta Asteroidal Targets: Albedo and Diameter Measurements of the Rosetta Target Asteroids	1976
Barucci, A.	Dark, Volatile-Rich Asteroids: Possible Relation to Comets	74127
Beckwith, S.	Search for Dust Debris in the Outer Solar System: Mapping and Fluctuation Search	7374
Bell, J.	Infrared Imaging Spectroscopy of Mars: Constraints on Surface Mineralogy and Volatile Transport	7716
Bell, J.	Infrared Spectroscopy of Phobos and Deimos: Spectral Classification and Constraints on Surface Mineralogy	5824
Bézard, B.	Search for Methyl Radical on Neptune and Saturn	9666
Bézard, B.	Search for Undetected Hydrocarbons on Jupiter and Saturn	3590
Bézard, B.	Search for Undetected Hydrocarbons on Neptune	2102
Bézard, B.	Search for Undetected Photochemical Compounds on Jupiter	6560
Bockelée-Morvan, D.	Study of Carbonaceous Matter in Comets	18114
Colangeli, L.	Cometary Nuclei and Trails Study: Analysis of Comets also in Preparation to Rosetta	22326
Colangeli, L.	Extended Remote Analysis of Coma and Trails: Analysis of Comets also in Preparation to Rosetta	23116
Courtin, R.	A Spectroscopic Investigation of Titan at 5–7 Micrometers	23624
Coustenis, A.	Spectroscopy of the 12.2 and 13.4 Micron Regions on Titan	16428
Coustenis, A.	Spectroscopy of the 15 Micron Region on Titan (CO ₂ and CO)	5384
Coustenis, A.	Spectroscopy of the 16 Micron Region on Titan (C ₄ H ₂ and C ₃ H ₄)	9839
Coustenis, A.	The 3-Micron Window on Titan	27486
Coustenis, A.	The Short-Wavelength Spectrum of Titan	6296
Crovisier, J.	ToO: Observations of Unexpected Comets	82747
Crovisier, J.	ToO: Spectroscopic Observations of Comets	25486
Dermott, S.	Observations of the Earth's Circumsolar Dust Ring	8361
Dermott, S.	Probing the Zodiacal Cloud by Observing the Ecliptic Poles	6666
Drossart, P.	Equatorial Emissions of Hydrocarbons on Jupiter	12708
Drossart, P.	Spectroscopy of the Auroral Regions of Jupiter	10044
Encrenaz, Th.	Jupiter: Latitudinal Variations of Atmospheric Parameters	20052
Encrenaz, Th.	Neptune: Search for PH ₃ and Determination of Tropospheric C/H	33072
Feuchtgruber, H.	Deuterium in the Four Giant Planets	22459
Feuchtgruber, H.	H ₂ O in the Outer Solar System	79859
Fitzsimmons, A.	The Composition of D-Type Asteroids	2910
Fulchignoni, M.	Rosetta Target Asteroids	7368
Grün, E.	ToO: ISOPHOT Observations of a Bright Comet Coma: Composition and Dust Production	24231
Grün, E.	ToO: ISOPHOT Observations of a New Comet: Coma Composition and Dust Production	8732
Harris, A.	Cometary Activity in Asteroids	17952
Ip, W.-H.	A Survey of Kuiper Belt Candidates	102824
Lamy, P.	Observation of Cometary Nuclei	24878
Lamy, P.	ToO: The Nucleus of a New Bright Comet	18054
Larson, H.	Spectroscopic Studies of Volatile-Rich Asteroids	22478
Leinert, Ch.	Mapping of COBE Fields	28518
Lellouch, E.	Deuterium on Jupiter and Saturn	18795
Lellouch, E.	The Surface Temperature of Pluto	34531

Lisse, C.	Large-Scale Observations of Scattered Sunlight and Thermal Emission in the Tails of Bright Periodic Comets	21771
Miller, S.	Forbidden Rotational Spectrum of H_3^+ in the Ionosphere of Jupiter	590
Müller, T.	Polarimetry of Asteroids	9381
Naylor, D.	LWS Grating Observations of HD on Uranus and Neptune	3866
Noll, K.	Titan's Lightcurve at 5 Micron: A Clue to Surface Composition	2330
Oldham, P.	Saturn: Determination of the Tropospheric Methane Abundance Profile	11348
Osip, D.	Spectral Analysis of Carbon-Chain Depleted Comets	10027
Osip, D.	Spectral Analysis of Carbon-Chain Depleted Comets: Spectral Studies of P/Wolf-Harrington	11797
Peschke, S.	ToO: Cometary Comae in the IR: Dimensions, Structures and Composition	3120
Reach, W.	Imaging the Source of Cometary Dust Trails	9629
Reach, W.	Spectrum of the Zodiacal Light	21827
Schmitt, B.	The Composition and Temperature of the Surface of Io	13966
Schulz, R.	Distributed Sources in Cometary Comae: Column Density Profiles of Potential Parent Molecules	12362
Scotti, J.	Characterisation of the Size of Short-Period Comet Nuclei	8934
Stern, A.	A Comprehensive Investigation of the Thermal Properties and Rotational Thermal Variability of the Pluto-Charon Binary and Chiron	7360
Tedesco, E.	Asteroid Size-Frequency Distribution	77003
Thomas, N.	Io's SO_2 Atmosphere and Torus	13461

B.2.2 Stellar/Circumstellar Physics

Abada-Simon, M.	Extension of AE Aquarii's Radio Spectrum to the Far-Infrared: Search for the Synchrotron Spectrum's Turnover Frequency	3418
Ábrahám, P.	Very Cold Dust around Herbig Ae/Be Stars	1962
Alcolea, J.	Dust Distribution around Bipolar PPNe	5570
André, P.	Spatial Structure of the Youngest Protostars: An Absorption Study	16521
Backman, D.	Mapping and Spectroscopy of a Circumbinary Disk: Infrared Studies of an Edge-On Disk Discovered via Coronagraphy	10228
Backman, D.	Terrestrial-Temperature Dust around Cluster 'A' Stars	9503
Backman, D.	Zodiacal Dust in Other Planetary Systems: Search for Hot Dust around Planetary-Perturbation Target Stars	13472
Barlow, M.	FP Observations of Far-Infrared OH Maser Pump Lines	74627
Barlow, M.	High-Resolution Observations of Far-Infrared Water Lines	40643
Barlow, M.	Photometry of a New Sample of Candidate Vega-Excess Sources: Properties of Circumstellar Disks	5222
Barlow, M.	ToO: Observations of Novae during the ISO Mission	34744
Barr, P.	Infrared Observations of Cygnus X-3: What Is the Origin of the Infrared Flares?	4166
Barr, P.	Infrared Properties of Cygnus X-3: Origin of the Infrared Flares and Quiescent Emission	17094
Barrado Navascués, D.	The Infrared Spectrum of Chromospherically Active Stars	4484
Beckwith, S.	Evolution of Circumstellar Disks: A Test of Disk-Regulated Angular Momentum Evolution	13744

Beckwith, S.	Physical Properties of Circumstellar Disks: Spectral Energy Distributions of Young Stellar Objects	60270
Bell Burnell, J.	ISO Observations of Cygnus X-3: Infrared Studies of a ‘Microquasar’	2890
Bergeat, J.	The Environment of Cool Giant Variables: Extensions and Detached Shells on the AGB	19000
Bézar, B.	The Atmospheric Structure of Brown Dwarf Gliese 229 B	10378
Blake, G.	SWS Studies of H ₂ Rotational Lines from YSO Accretion Disks	24463
Blanco, A.	Dust Composition in Carbon Stars	14970
Blommaert, J.	Evolution and Mass Loss of AGB Stars in the Small Magellanic Cloud	36221
Blommaert, J.	The Nature of OH/IR Stars in the Galactic Centre: An Accurate Determination of their Luminosities	57525
Blomme, R.	Clumping in the Stellar Wind of Early-Type Stars	29290
Bockelée-Morvan, D.	Search for CO and CO ₂ Ices towards Vega-Like Stars	4778
Bonnet-Bidaud, J.-M.	Infrared Study of the Peculiar X-Ray Binary Cygnus X-3: Spatial Extent and Energy Distribution of the Infrared Source	6382
Bujarrabal, V.	Atomic Gas in Proto-Planetary Nebulae	73884
Carr, J.	Water in Proto-Planetary Disks	38354
Casali, M.	The Decline of Outflow Activity with YSO Age: A New Approach	24653
Casali, M.	The Disks of Young Stars in Dense Clusters	33380
Cassinelli, J.	Infrared Diagnostics of Temperature Structure in the Atmospheres of Early B-Stars	42550
Cassinelli, J.	The Velocity Structure of Wolf-Rayet Winds from Infrared Line and Continuum Observations	59442
Castro-Tirado, A.	Thermal Imaging of GRO J1744–28 while in Outburst	5994
Castro-Tirado, A.	ToO: The Nature of the Superluminal Galactic Source GRS 1915+105: ISO Monitoring of the Most Powerful Source in the Galaxy	736
Castro-Tirado, A.	ToO: The Nature of the Superluminal Galactic Source GRS 1915+105: ISO Observations during the Oct 1997 X-Ray and Radio-Outburst	12076
Ceccarelli, C.	Major Cooling Lines in Infall around YSOs	30524
Ceccarelli, C.	Map of C- and J-Type Shocks in IRAS 16293–2422	14802
Cernicharo, J.	A Key Spectroscopic Study of CRL 618: Shocked Chemistry in Post-AGB Evolution	7598
Cernicharo, J.	A Study of Water Emission in O-Rich Evolved Stars: The Water Abundance and the ¹⁷ O/ ¹⁸ O Isotopic Abundance Ratio in CSE	27296
Cernicharo, J.	The Molecular Content of IRC+10216 between 2.38 and 196.7 Microns: A Spectroscopic Study of the C-Rich Star IRC+10216	32359
Cherchneff, I.	Observation of Dust Features in Carbon-Rich Wolf-Rayet Stars: A Search for Aromatic and Fullerene Bands in WC Stars	8360
Cherchneff, I.	Observation of Dust Features in R CrB Stars: A Search for Aromatic and Fullerene Bands in R CrB Stars	4404
Chini, R.	ISO Study of Protostars	34928
Clampin, M.	Dust Characterisation in Circumstellar Shells around Evolved, Massive Stars	14130
Clayton, G.	Understanding the Evolution of H-Deficient Stars	19968
Coe, M.	Target of Opportunity Studies of High-Mass X-Ray Binary Systems: Multiwaveband Investigations of Such Systems in Outburst	618
Cohen, M.	PAH Emission Bands in Selected Planetary Nebulae: A Study of the Behaviour with Gas Phase C/O Ratio	7916

Colgan, S.	Infrared Spectroscopy of Black Hole Candidates	8840
Comerón, F.	Brown Dwarf Candidates in Embedded Stellar Populations	19322
Comerón, F.	Brown Dwarf Candidates in the Rho Ophiuchi Cluster	10574
Cox, P.	Spectroscopic Observations of PDRs in Proto-Planetary and Planetary Nebulae	17114
Cox, P.	The Helix Planetary Nebula: A Case Study of a PDR Region	60282
Creech-Eakman, M.	Stellar Plasma to Circumstellar Dust Transformation: The Role of Silicon Monoxide In LPVs	10260
Crifo, F.	Bolometric Magnitude and Effective Temperature of M-Dwarfs	9850
Crifo, F.	Radii, Effective Temperatures and Bolometric Luminosities of Subdwarfs	7982
Currie, D.	Thermal Structure and History of Eta Car	27394
de Jong, T.	High-Resolution Observations of HCN and C ₂ H ₂ Lines in Carbon Stars	10352
de Jong, T.	SWS Observations of O-Rich Circumstellar Shell of Late-Type Stars with the 13 μ m Emission Feature	27820
Decin, L.	Accurate Modelling of Cool-Star Atmospheres	32691
Deguchi, S.	Observations of Halo AGB Stars with ISO SWS for the Purpose of the Future Searches for MACHOs	8820
Deguchi, S.	Observations of Stars with Unusual IRAS LRS Spectra	6471
Deleuil, M.	Origin of the Circumstellar Gas around Beta Pictoris	30336
Dougados, C.	The Embedded Clusters Associated with Young Intermediate-Mass Stars	57390
Doyle, J.	Detectability of Mass Loss from Cool M-Dwarfs	8224
Dufton, P.	H II Regions Associated with Young Galactic Clusters: Comparison of Stellar and Nebular Chemical Compositions	4286
Engels, D.	Infrared Spectral Properties of Young PPN	26702
Engels, D.	The 22 GHz H ₂ O Maser Pump in AGB Stars	38427
Eriksson, K.	A Spectrum of the Envelope around the M-Giant R Doradus	698
Eriksson, K.	Imaging of Dust Shells around Carbon Stars	7008
Eriksson, K.	Spectra of Envelopes around AGB Stars	92254
Evans, A.	An ISO Study of PAH Emission in XX Oph	7440
Evans, A.	Far-Infrared Observations of RV Tauri Stars	5658
Evans, A.	The Far-Infrared Flux Distribution of RS CVn Stars	7604
Eyres, S.	Spectroscopy of Sakurai's Object in Sagittarius: The Evolution of a Final Helium Shell Flash	4958
Eyres, S.	SWS Spectroscopy of Symbiotic Stars	10978
Fajardo-Acosta, S.	Microscan Mapping of Vega-Type Circumstellar Dust	9128
Fender, R.	ToO: ISO Observations of Cygnus X-3 in Outburst: Infrared Studies of a Flaring Microquasar	8824
Fix, J.	ISO Observations of Variable Circumstellar Shells	5699
Forrest, W.	A Search for Brown Dwarfs in the Hyades	81199
Forveille, T.	ISOCAM-CVF Spectrum of the Nearby Brown Dwarf Denis-P J0205–1159	10598
Forveille, T.	ISOCAM-CVF Spectrum of the Newly Discovered Nearby Brown Dwarf Denis-P J0205–1159	5138
Foster, R.	Circumstellar Dust Emission from Millisecond Pulsars	14602
Fusi Pecci, F.	Circumstellar Matter in the Central Region of Globular Clusters	24458
García-Lario, P.	Correlation of Mass and Age with the Far-Infrared Colors of PNe and PPNe	12730
Garzón, F.	Stellar Populations of the Inner Bulge of the Galaxy	1720

Gehrz, R.	Studies of Classical Novae and Related Objects with ISO: Physics Characteristics and Contributions to the ISM	21023
Gehrz, R.	ToO: ISO Spectroscopy of Galactic Novae	51335
Gehrz, R.	ToO: Observations of New Novae in Outburst: Physics Characteristics and Contributions to the ISM	20117
Gerbaldi, M.	Remnant of Circumstellar Matter around Early A-Type Stars in Young Clusters	8692
Goebel, J.	Study of the Population Distribution of the 7 Micron Dust Emission Feature in Oxygen-Rich Stars	31110
Górny, S.	Spectroscopy of Dusty Planetary Nebulae with WR-Type Central Stars	6684
Grady, C.	The Beta Pictoris Phenomenon in Young Stars with Accreting Gas	11794
Griffin, M.	The Far-Infrared Continuum Spectra of Cold Protostellar Sources	12350
Groenewegen, M.	Observations of Mass-Losing Supergiants in the Magellanic Clouds	15280
Groot, P.	ISOCAM 12 Micron Imaging of a Possible GRB970508 Counterpart	7104
Gürtler, J.	Analysis of Dust Envelopes around Evolved Stars	10594
Gürtler, J.	Infrared Imaging of Post-AGB Dust Envelopes	11272
Haas, M.	Physical Conditions in the Circumstellar Envelopes of Supergiants and Other Evolved Stars	41454
Habing, H.	Vega-Type Excess in a Newly Discovered Planetary System	3284
Hammersley, P.	Star Counts in the Galactic Bar	15056
Harrington, P.	Dust in Hydrogen-Poor Planetary Nebulae	11144
Hauschildt, P.	A Spectroscopic Study of the Water Bands in M-Dwarfs	8776
Hawley, S.	Circumstellar Disks and Far-Infrared Luminosity in Active M-Dwarfs	1084
Heinrichsen, I.	High-Resolution ISO Observations of Beta Pictoris	40150
Hirth, G.	Physical Properties of Outflows from Young Stellar Objects: Probing the Circumstellar Environment	10472
Hoare, M.	Ionised Winds from Luminous Young Stellar Objects	8214
Hora, J.	The Spatial Distribution of Cool Dust in Planetary Nebulae	17264
Hrivnak, B.	Spectroscopy of Visible Proto-Planetary Nebulae	29391
Hrivnak, B.	SWS Spectroscopy of Obscured Proto-Planetary Nebulae	5948
Hron, J.	Spectral Variability of Long Period Variables: The Relation between Pulsation, Atmospheric Structure and Dust Formation	72344
Hurley, K.	Study of Soft Gamma Repeater Counterparts	19866
Hurt, R.	Dust Emission from Class 0 Protostars in the Serpens Cloud Core	3134
Hutsemékers, D.	Dust around Luminous Early-Type Stars in Nearby Galaxies	12412
Iverson, R.	Testing the Binary Hypothesis for OH/IR Colour Mimics	11266
Iverson, R.	The Properties of Circumstellar Dust in Symbiotic Miras	7214
Izumiura, H.	Extended Dust Shell around the J-Type Carbon Star RY Draconis	6896
Jameson, R.	A Spectral Atlas for M-Dwarfs	17722
Jiang, B.	The Nature of IRAS LRS Sources without Near-Infrared Detection	6830
Jones, H.	Water Vapour in Cool Dwarfs	37265
Jorissen, A.	A Study of Mass Loss along the AGB and RGB of 47 Tuc	45725
Jorissen, A.	Dust in Binaries Containing Chemically Peculiar Giants: Linking Barium and S-Stars to Post-AGB Stars	5284
Jorissen, A.	Infrared Spectral Classification of S-Stars	14692
Justtanont, K.	SWS Observation of Molecular Lines in NML Cyg	26730
Kaper, L.	Infrared Study of Low-Mass X-Ray Binaries	9092

Kaper, L.	Stellar-Wind Structure in High-Mass X-Ray Binaries	8700
Kastner, J.	Mid-Infrared Polarimetric Imaging of Evolved Star Envelopes	15930
Keenan, F.	Spectroscopy of Hot Halo PAGB Stars and Planetary Nebulae: LS IV –12 111, a PAGB Star Developing a Proto-Planetary Nebula	8948
Kerber, F.	Sakurai’s Object: A New Born-Again Nucleus of a Planetary Nebula	5120
Kerschbaum, F.	Atmospheric Structure of Oxygen-Rich Semiregular and Irregular Variables	9560
Kerschbaum, F.	Atmospheric Structure of Oxygen-Rich Semiregular Variables	9248
Kerschbaum, F.	Spectral Characteristics of the AGB and Post-AGB Phase Objects for the ISO Extended Mission	66979
Klaas, U.	Far-Infrared Polarisation of β Pictoris	6824
Koch-Miramond, L.	Search for Circumstellar Material around Nearby Pulsars: Thermal Emission of Dusty Clouds or Disks around Neutron Stars	13526
Koornneef, J.	A Unique B[e]-Star: ISO Discovers High-Excitation Gas	3028
Koornneef, J.	An Investigation of the Ara Infrared Cluster	2680
Kwok, S.	A Detailed Study of the Unidentified 21 Micron Emission Feature in Post-AGB Stars	4824
Kwok, S.	Spectroscopy of 21 Micron Feature Sources	14315
Kwok, S.	Spectroscopy of Extreme Carbon Stars	9084
Lada, E.	Investigations of the Earliest Stages of Stellar Evolution in Young Embedded Clusters	8096
Lagage, P.	Gas and Dust in the Kepler SNR	5434
Lagage, P.	Polarimetry of Dust Disks around MS and PMS stars	9380
Lagrange, A.-M.	Infrared Study of the Close Herbig Ae/Be Binary System TY CrA	10652
Lambert, D.	FG Sagittae: A New R Corona Borealis Star	8380
Lambert, D.	Infrared Spectroscopy of R Coronae Borealis Stars	48191
Lambert, D.	Testing Model Atmospheres of Cool Dwarf Stars with ISO	18400
Lamers, H.	The Winds of Early-Type Supergiants: The Critical Mass Loss Phase of Massive Stars	39448
Larson, H.	Search for Hydrated Minerals around O-Rich Red Supergiants	3944
Lecavelier, A.	Gaseous Content of a Few Well-Known Beta Pictoris-Like Stars	14504
Leech, K.	ISO Observations of the Pleiades Brown Dwarfs Teide 1 and Calar 3	14129
Leinert, Ch.	Spectral Energy Distribution of Binary T Tauri Stars	15252
Liu, X.-W.	Far-Infrared Fine-Structure Lines in Planetary Nebulae: A Key to Resolving Discrepancies in Abundance Determinations	17370
Loup, C.	Mass-Loss and Evolution of AGB Stars in the LMC: A Mini-Survey	27076
Loup, C.	Mass-Loss and Evolution of AGB Stars in the LMC: Extension of the Mini-Survey to the SMC	34389
Luu, J.	Evolution of Dust in Circumstellar Disks	3826
Manchado, A.	Spectroscopy of Heavily Obscured Post-AGB Stars	8512
Martín-Pintado, J.	The Physical Properties of the Stellar Winds in Selected Radio Stars	10174
Mathieu, R.	Masses of Circumstellar Disks in Pre-Main Sequence Binary Stars	524
Mathieu, R.	Searching for Gaps in the Disks of Pre-Main Sequence Binary Stars	13250
Meixner, M.	Far-Infrared Imaging Dust Halos of Proto-Planetary and Planetary Nebulae: A Study of Mass Loss History	31517
Meixner, M.	Spectroscopy of Atomic Fine-Structure Lines in Evolved Stars: A Study of Planetary Nebula Formation	28705

Meixner, M.	Spectroscopy of Atomic Fine-Structure Lines in GL 618	20866
Metcalfe, L.	Far-Infrared Photometry and CAM-CVF Observations of a Disk around BD +31 643	9910
Millar, T.	Carbon-Bearing Molecules in Oxygen-Rich Stars	28246
Mirabel, I.	Dust Heated by High-Energy Sources (Continuation)	29730
Mirabel, I.	The Galactic Superluminal Source GRS 1915+105: Is the Superluminal Microquasar in a Molecular Cloud ?	7696
Moneti, A.	The Nature of the Pistol, its Star, and the Quintuplet: CAM-CVF and SWS Spectroscopy	15332
Montesinos, B.	The Infrared Energy Distribution of FG Sge	4396
Montmerle, T.	Search for H ₂ and H ₃ ⁺ Infrared Lines Associated with X-Ray Sources Embedded in Molecular Clouds	31456
Morris, P.	Ices towards the Candidate LBV G79.29+0.46	7782
Myers, P.	Warm Dust Imaging of Nearby Low-Mass Protostars	8806
Nakajima, T.	A Search for Brown Dwarf Companions to Young Nearby Stars	7936
Naylor, T.	ToO: Observations of Low-Mass X-Ray Binaries	5534
Neri, R.	A Key Spectroscopic Study of CRL 2688, CRL 618 and NGC 7027: Shocked Chemistry in Post-AGB Evolution	41420
Nguyen-Rieu, Q.	Water Abundance in the Envelope of Optical Oxygen-Rich AGB Stars	12533
Noriega-Crespo, A.	The Star-Forming Region around IRAS 05487+0255: ISOCAM Maps of Stellar Jets and their Sources	2517
Oestreicher, M.	Broadband and Spectrophotometry of Luminous Stars in the LMC: Mass Loss and Evolution of Circumstellar Dust Shells	4004
Oliva, E.	Infrared Coronal Lines and the Intrinsic EUV Spectrum of AGNs: Coronal Lines in AGNs	52290
Oliva, E.	Infrared Spectroscopy of the Most Luminous LMC Supernova Remnant: Infrared Spectroscopy of N 49	6756
Omont, A.	ISOCAM Survey of the Inner Galaxy	553231
Omont, A.	ISOCAM Survey of the Outer Galaxy: Completion of the ISO-GAL 7–15 micron Survey	287300
Onaka, T.	Far-Infrared Polarisation of Diffuse Thermal Emission	9382
Onaka, T.	Time Variation of Circumstellar Envelopes	37196
Oudmaijer, R.	Is Wra 1484 a Hot Post-AGB Star?	3824
Oudmaijer, R.	Post-AGB Stars with Cool Dust Shells	7692
Penny, A.	Dust in Globular Clusters	31046
Pottasch, S.	Determining Planetary Nebulae Central Star Temperatures	18014
Price, S.	Spectral Characterisation of Bright Infrared Sources	34437
Prusti, T.	Variable Infrared Emission from Circumstellar Environment of Young Intermediate-Mass Stars	94033
Prusti, T.	Extended Infrared Emission around Young Stars	23398
Prusti, T.	Search of the Comet-Like Activity in Stars with Non-Periodic Algol-Type Minima	36229
Prusti, T.	ToO: Evolution of the Circumstellar Environment during an FU Ori or EX Lup Outburst	42814
Puxley, P.	The Dust Content of H II Regions	6572
Ramsay, G.	Observations of Magnetic Cataclismic Variables: The Determination of Magnetic Field Strengths	24943
Rauer, H.	Infrared Absorption Features of Extra-Solar Planets: Search for an Extended Envelope around 51 Peg B	37998
Reid, I.	Cocoon Stars in the Magellanic Clouds	14425
Reinsch, K.	Cyclotron Spectroscopy of Magnetic Cataclismic Variables	24624

Rengarajan, T.	Infrared Emission from RS CVn Binaries	2940
Rieke, G.	Low-Mass Pleiades Brown Dwarfs	22990
Roche, P.	Dust Emission Features in Stellar Envelopes	10361
Roche, P.	Spectral Features in Carbon-Rich Stellar Envelopes	8820
Rodono, M.	Infrared Excess in dMe Stars: Existence of a Circumstellar Envelope for Flare Stars	14654
Rodono, M.	Infrared Excess in RS CVn and Algol-Type Binaries: Circumstellar Envelope around Active Binary Stars	2872
Ruiz, M.	ISOCAM Imaging of the Newly Discovered Nearby Brown Dwarf Candidate Kelu 1	4654
Russell, S.	A Statistical Study of the Spectral Energy Distributions of Very Cold IRAS Sources	11082
Sahai, R.	Far-Infrared Spectroscopy of Very Young, Low-Excitation Planetary Nebulae: The Physical and Chemical Evolution of Circumstellar Gas and Dust	10368
Salama, A.	ISO Observation of the New Nova Sgr 1998	5128
Salama, A.	ISO Observations of Old Novae	13007
Salama, A.	Unravelling the Murky Past of the Old Nova GK Per	7246
Schild, H.	Dust in Symbiotic Binaries	29543
Schönberner, D.	Probing Mass Loss Variations of AGB Stars with Detached Shells: Differences in Mass Loss Behavior for C- and O-Rich AGB Stars	27052
Schulte-Ladbeck, R.	Asymmetric Mass Loss in the Upper HR Diagram: The Role of Molecular CO	1080
Schultz, A.	Imaging of Shocked Molecular Hydrogen in Herbig-Haro Objects	7828
Sedlmayr, E.	Variability of Circumstellar Dust Shells around LPVs	1916
Siebenmorgen, R.	Coronagraphic Photometry and Polarimetry of Proto-Planetary Disks	33777
Siebenmorgen, R.	Mid-Infrared Polarimetric Imaging of the Protostellar Candidate HH108MMS	7356
Skinner, C.	CO Observations of Mass-Loss in Low-Mass Post-Main Sequence Stars	24343
Skinner, C.	PAHs and Chromospheres in M-Supergiants	27098
Skinner, C.	Photometry of a New Sample of Candidate Vega-Excess Sources: Properties of Circumstellar Disks	13360
Spyromilio, J.	Infrared Studies of Extremely Young Supernova Remnants: Mid-Infrared Supernova Studies	9966
Stapelfeldt, K.	Dissipation of Gaseous Circumstellar Disks	28953
Stark, R.	The Gas-Dust Connection and Cooling in Proto-Planetary Disks	9880
Stauffer, J.	Dust around 'A' Stars in Young Open Clusters	19500
Stauffer, J.	Dust around Solar-Type Stars in Young Open Clusters	14832
Steele, I.	Photometry of Cluster Low-Mass Stars and Brown Dwarfs	16591
Stencel, R.	ISOPHOT Reobservation of Vega Disk Stars	12848
Stencel, R.	The Birth and Death of Planetary Systems	11800
Strazzulla, G.	Amorphous versus Crystalline Water Ice: Ice Structure in Circumstellar Envelopes	2582
Stringfellow, G.	Replenishment of the Accretion Disk between Outbursts in EXORs: Characterising the Variable Infrared Emission of Accreting YSOs	28998
Szczerba, R.	Detailed Investigation of the 30 Micron Band: Search for the 30 Micron Emitters	26628
Szczerba, R.	Excitation Conditions in Shells of Post-AGB Objects: Search for Precursors of Planetary Nebulae with WR-Type Stars	7998

Szczerba, R.	Infrared Carbon Stars with OH Emission: Transition from O- to C-Rich Stars	5736
Takashi, T.	Dust Formation in the Photospheres of Very Low-Mass Stars from M-Dwarfs to Brown Dwarfs	33968
Takashi, T.	High-Resolution Spectroscopy of CO and SiO in Red (Super)Giants: Physical Structure of the Upper Atmospheres of Cool Evolved Stars	27416
Takashi, T.	Infrared Excesses in Carbon Stars of the Galactic Halo and the LMC: Effect of Metallicity on the Evolution of Carbon Stars	30942
Takashi, T.	Infrared Properties of Very Low-Mass Stars from M-Dwarfs to Brown Dwarfs	32774
Tanabé, T.	A Systematic Study of Unidentified Features in AGB Stars	4850
Tanabé, T.	A Systematic Study on the Properties of Dust Grains around M-Supergiant Stars	9561
Tanabé, T.	Mass-Loss in the Late Stages of Stellar Evolution: AGB Stars in the Magellanic Cloud Star Clusters	8262
Tanabé, T.	Spectrophotometric Observations of AGB Stars in the Magellanic Cloud Star Clusters	36080
Tanabé, T.	ToO: Dust Formation around R CrB-Type Stars at their Minima: Search for Fullerenes	18005
Thum, C.	The Disk of MWC349	5656
Thum, C.	The Recombination Line Maser	31338
Thum, C.	The Recombination Line Maser MWC349: Velocity-Resolved Spectroscopy and Molecular Transitions	36285
Tilgner, C.	SETI: Search for Dyson Spheres	4638
Tinney, C.	The Near- and Far-Infrared Spectra of Very Late M-Stars	33632
Toshikazu, O.	Deep Infrared Observations of Starless Cores in Taurus B213 Region	1132
Trams, N.	Infrared Spectrophotometry and 60 Micron Photometry of LMC and SMC AGB Stars	57894
Trams, N.	The LMC AGB Star IRAS 04496–6958: a Carbon Star with Silicate Dust?	5936
Unger, S.	A Time Variable Plerion: Modelling the Be Star Disk in the Unique Milli-Second Pulsar Binary System PSR B1259–63	3522
van Buren, D.	ISOCAM Search for Pulsar Debris Disks	6272
van de Steene, G.	Accurate Abundance Determination of CNO in PN: An Investigation into the t^2 Problem	13972
van der Hucht, K.	Neon Abundance in Wolf-Rayet Stellar Winds	15801
van der Veen, W.	Imaging of Dust Shells around AGB and Post-AGB Stars	30112
van Dishoeck, E.	Complete SWS/LWS Scans of Young Stellar Objects	28426
van Dishoeck, E.	Further Searches for H ₂ Lines in Circumstellar Disks with the SWS	22188
van Hoof, P.	A Search for PN with Carbon and Oxygen Dust Features	9692
van Hoof, P.	Accurate Abundance Determination of CNO in PN: An Investigation into the t^2 Problem	17502
Volk, K.	Observation of the 21 Micron Feature Prototype IRAS 07134+1005	6168
Volk, K.	Spectroscopy of Featureless, Low-Temperature IRAS Sources	4370
Volk, K.	Study of an Unknown Type of Dust	3052
Volk, K.	Study of Low Temperature, Featureless IRAS Sources	10218
Volk, K.	Study of Unusual 11.3 Micron Feature Sources	5454
Voors, R.	Disks around B[e]-Supergiants	17368

Waelkens, C.	Accurate Modelling of Cool-Star Atmospheres	38324
Waelkens, C.	Circumstellar Chemistry of the Main Sequence Star Beta Pictoris	8796
Waelkens, C.	Circumstellar Matter around High-Latitude Supergiants	5074
Waelkens, C.	Detailed Mineralogy of the Oxygen-Rich Dust around Young Stars	44596
Waelkens, C.	Dust Disks around Young Main Sequence Stars	6908
Waelkens, C.	Jupiters and Circumstellar Dust Disks around Southern G-Dwarfs	52551
Waelkens, C.	Monitoring of the Infrared Emission of HR 4049 and HD 213985	3818
Waelkens, C.	Probing the Vega Phenomenon in Open Clusters: Vega-Type Stars in Clusters	10436
Walker, C.	[C II] Emission as a Probe of Star Formation in Absorption Line Systems: A Study of Star Formation at Intermediate Look-Back Times	5368
Walker, H.	High-Resolution Scans across Vega-Like Dust Disks	8586
Walker, H.	Mapping of R CrB Dust Shells	10964
Walker, H.	Mapping the Environment of Vega-Like Candidates	6713
Walker, H.	Mapping the Environment of Vega-Like Stars	4800
Walker, H.	Spectra of R CrB Dust Shells	1660
Waters, L.	A Proto-Planetary Disk around the Red Rectangle?	8406
Waters, L.	First Detection of Crystalline Silicates in the LMC: Unraveling the Mass Loss History of R 71	13982
Waters, L.	Infrared Spectroscopy of Normal O- and B-Stars: A Search for Low-Density Circumstellar Gas	31730
Waters, L.	Infrared Photometry of K-Stars with Infrared Excess: The Nature of Circumstellar Dust in K-Giants	38757
Waters, L.	Infrared Spectroscopy of OB-Dwarfs: Probing the Outer Layers of the Atmosphere	9894
Waters, L.	Massive Stars in the LMC and SMC: A Study of the Ejecta of B[e]-Stars in the Magellanic Clouds	22702
Waters, L.	Mineralogy of Crystalline Dust: Oxygen Rich Dust Shells in Evolved Stars	62430
Waters, R.	Post-Helium Programme	759232
Wehrse, R.	ISOPHOT Background Observations for M-Dwarfs	14460
Wehrse, R.	Temperature Stratification in Cool Dwarf Atmospheres	15348
Weinberger, R.	Dust in Born-Again Planetary Nebulae	3936
Weinberger, R.	Edge-On Dust Disks in Planetary Nebulae	2608
Weiss, W.	Dust and Gas Environment of Lambda Bootis Stars	16096
Wesselius, P.	Follow-Up SWS Observations on Intermediate-Mass YSOs	11002
Whitelock, P.	A Study of M-Stars with Unusual Mass-Loss Rates	16678
Whitelock, P.	Mass-Loss History of the Lithium-Rich S-Star RZ Sgr	17828
Williams, P.	Structure of Wolf-Rayet Stellar Winds	4844
Willis, A.	The Neon + Magnesium Abundances in WC and WO Stars	64764
Winkler, C.	ToO: The Infrared Counterpart of GRS 1915+105: Observations of Outbursts	21859
Wolstencroft, R.	Chemistry and Mass-Loss History of a Luminous Carbon Star: IRAS 15194–5115	15142
Wright, C.	ISOPHOT Polarisation Observations of Two Bipolar Outflow Sources	4544
Wright, C.	Mid- and Far-Infrared Polarimetry of Young Stellar Objects: Magnetic Fields and Dust Properties	16478
Yamamura, I.	High-Resolution Spectroscopy of IRTS Template Stars	7762
Yamamura, I.	Spectroscopic Observations of High-Velocity Flow of Evolved Objects	21253

Zhang, C.-Y.	Spectroscopy of Dusty Planetary Nebulae	6124
Zijlstra, A.	Carbon Stars and [WC]-Planetary Nebulae in the Sagittarius Dwarf Spheroidal Galaxy	24672
Zijlstra, A.	Spectroscopy of Planetary Nebulae in the LMC	9886
Zinnecker, H.	Are X-Ray Selected Very Young Weak-Line T Tauri Stars Born Naked? A Study of Faint Disks around Low-Mass Stars in an OB Association	21500
Zinnecker, H.	Brown Dwarfs: A Search for Cool Infrared Companions around Nearby Old White Dwarfs	67972
Zinnecker, H.	Remnant Dusty Disks in Lindroos Post T Tauri (PTT) Stars	6614
Zuckerman, B.	Luminosity Class III Stars with Excess Far-Infrared Emission	11936

B.2.3 Interstellar Matter

Abergel, A.	Extinction Curve in Dense Cores	12857
Abergel, A.	Very Cold Dust Imaging	47298
Ábrahám, P.	Investigation of the Cirrus Confusion Noise in a Faint Region near the Draco Cloud	16860
Allamandola, L.	Specific PAH and Amorphous Carbon Structures: The Evolution of Carbon from Carbon Stars to H II Regions	6240
Allamandola, L.	The D/H Ratio in Interstellar PAHs: The Search for Interstellar PADs	8123
André, P.	An ISOCAM Absorption Survey for Dense Clumps within Dark Clouds	29114
André, P.	Magnetic Field Geometry toward Embedded Outflow Sources	40196
André, P.	Spectral Energy Distribution of a Newly-Discovered Protostar in Taurus	5524
André, P.	The Spatial Structure of Protostellar Cores: An Absorption Study	21144
Arendt, R.	Unusual Line and Continuum Emission in the Cas A SNR	18348
Bachiller, R.	Molecular Infrared Lines as Tracers of Infall and Outflow in Star-Forming Cores	35158
Bachiller, R.	The Bipolar Outflows from the Youngest Stellar Objects: Infrared Spectroscopy	38112
Baluteau, J.	Complete LWS Spectral Survey at High-Resolution	36796
Baluteau, J.	LWS High-Resolution Scans of Sgr B2	34817
Bania, T.	Probing the Properties of Southern Hemisphere Galactic H II/PDR/GMC Sources Using ISO Far-Infrared Spectra and AST/RO [C I] Measurements	17420
Bania, T.	Probing the Structure of Nearby Translucent Molecular Clouds: Constraining the Chemistry of High Galactic Latitude Gas	2906
Bania, T.	Probing the Structure of the Nearest Molecular Cloud MBM-12	6850
Bania, T.	Southern Hemisphere High-Latitude Clouds: Constraining the Chemistry of Translucent Gas	13814
Baudry, A.	Detection of OD in Orion A: OD in Hot Molecular Cores	3380
Baudry, A.	Detection of OD in Selected Hot Molecular Cores: OD in Hot Molecular Cores	6896
Baudry, A.	OH in Compact H II Regions	5418
Baudry, A.	OH Spectroscopy of the Dense Gas Surrounding Compact H II Regions: OH in Compact H II Regions	15726
Bernard, J.-P.	Origin of Color Variations in the ISM	59029
Bernard, J.-P.	PAH Destruction around Hot Stars	30018
Bertoldi, F.	High H ₂ Rotational Lines in Orion IRC2 Pk1	4060

Bertoldi, F.	Physical Conditions in Photodissociation Regions	12550
Black, J.	Thermal Structure of Translucent Molecular Clouds	29356
Bontemps, S.	Mid-Infrared Search for Embedded Outflow Shocks around YSOs	24846
Boulanger, F.	A Comparison of Extinction and Emission Properties of Dust	8715
Boulanger, F.	Dust in the Low Density Warm Phases of the Interstellar Medium	17752
Boulanger, F.	Very Small Dust Grains in the Galactic Halo: Dust Destruction in Shocks	10894
Brand, P.	Warm Molecular Hydrogen in the Galaxy	18940
Caux, E.	Atomic Oxygen Absorption against Bright Galactic Sources	10136
Cernicharo, J.	A Search for C ₃ , C ₄ H ₂ , and C ₆ H ₂ in the Interstellar Medium: The Synthesis of Hydrocarbons in the ISM and in the CSM	36066
Cernicharo, J.	A Study of Dust, Atomic and Molecular Emission in Cometary Globules: The Physics of Partially Ionised Globules	18192
Cernicharo, J.	A Study of Dust, Atomic and Molecular Emission in Cometary Globules: The Physics of Partially Ionised Globules in the Trifid	22552
Cernicharo, J.	A Study of Water Emission in Molecular Clouds: The Extent of Water Vapor Emission in Galactic Molecular Clouds	107660
Cernicharo, J.	A Study of Water Emission in Orion: The Extent of Water Vapor Emission in the Orion Cloud	14182
Cernicharo, J.	HH Jets and their Interaction with their Placentary Clouds: HH Jets and Molecular Outflows	20360
Cernicharo, J.	Discovery of a Dust Jet and a Circumstellar Disk in HH1–2	3704
Cernicharo, J.	The Mid- and Far-Infrared Spectrum of Keystone Molecular Clouds: The Molecular Content of Warm and Cold Molecular Clouds	108824
Cernicharo, J.	Warm Dust around Hot Stars: the Ionising Source of the Trifid Nebula	2088
Cesarsky, D.	Dust Emission in Reflection Nebulae	17744
Cesarsky, D.	Supplementary Observations with ISOCAM's CVF: Follow-Up and Complementary Observations	48796
Chrysostomou, A.	Determining the Role of Magnetic Fields in the Disks of YSOs	14380
Chrysostomou, A.	Line Emission from Photodissociation Regions	5137
Clark, F.	Emission from and Destruction of Small Interstellar Dust: High Radiation Environments	11472
Clemens, D.	Are Starless Bok Globules Really Devoid of Stars? ISOCAM Imaging of Starless Bok Globules	27760
Clemens, D.	Dust Temperatures and Densities in Filamentary Dark Clouds: Cold Dust Maps of Globular Filament Clouds	6308
Clemens, D.	Embedded Magnetic Fields in Filamentary Dark Clouds	18197
Clemens, D.	Low Luminosity Protostars and YSOs in Bok Globules: SEDs. Energy Distributions and Source Counts of YSOs in Bok Globules	16750
Colgan, S.	Infrared Spectroscopy of the Great Annihilator	5080
Colgan, S.	The Interaction of Recently Discovered Hot Stars with Galactic Centre Thermal Radio Emission Filaments	6524
Colgan, S.	The Properties of Narrow Recombination Line H II Regions	12022
Comerón, F.	Ultracompact H II Regions in the Large Magellanic Cloud	1082
Cox, P.	A Study of Water Vapour Absorption in Molecular Clouds: Water Vapour Absorption	31330
Cox, P.	Dust Evolution in Planetary Nebulae	19606
Cruikshank, D.	Molecular Nitrogen in Interstellar Ices	9955
d'Hendecourt, L.	Far-Infrared Spectroscopy of Ice Features	13686
d'Hendecourt, L.	Search for Specific Solid State Features from Interstellar Grains	50818

d'Hendecourt, L.	Specific Search for Solid State and Gas Phase Features	4910
d'Hendecourt, L.	Spectroscopy of Carbon-Bearing Molecules in Diffuse ISM	4572
d'Hendecourt, L.	Survey of Solid State Molecular Absorption	21152
Decourchelle, A.	Detailed Comparison of Infrared and X-Ray Emission in Selected Regions of the Cygnus Loop Supernova Remnant	13361
Deharveng, L.	Imaging of a Massive Star-Forming Region: Study of Sh 88B	616
Digel, S.	Abundance Determinations in the Far Outer Galaxy: Infrared Observations of H II Regions	12246
Doi, Y.	Spectroscopy of Interstellar Gas around the Cygnus OB2 Association	6338
Drapatz, S.	Search for Interstellar Molecular Oxygen	6710
Dwek, E.	A Search for the Infrared Signature of Graphite Grains: The 11.52 Micron Graphitic Absorption Feature towards the Galactic Centre	2930
Dwek, E.	Grain Destruction in Intermediate-Velocity Clouds	13624
Dwek, E.	Grain Destruction in Supernova Remnants	12130
Eckart, A.	Probing Shocks and PDRs Using Sulphur-Bearing Molecules	11236
Ehrenfreund, P.	Far-Infrared Observations of Water Ice	11920
Ehrenfreund, P.	Search for Interstellar Fullerenes	7594
Ehrenfreund, P.	Search for Solid Molecular Oxygen and Ozone	10954
Ehrenfreund, P.	Search for Solid O ₂ and O ₃ on Interstellar Grains with ISO	13772
Eisloffel, J.	Rotationally-Excited Molecular Hydrogen in Bipolar Outflows	36708
Eisloffel, J.	The Dusty Envelopes of Deeply Embedded Class 0 Outflow Sources	7736
Engelmann, J.	Interaction of IVC 86+38-44 with the Hot Plasma	1936
Evans, N.	Photoionisation Regulated Star Formation, Cloud Structure, and Tracers of the Neutral ISM	24688
Falgarone, E.	Gas Spectral Diagnostics of the Dust Emission: Color Variations in Interstellar Clouds	47926
Falgarone, E.	Polarisation of Dust Absorption at the Edge of a Dense Core: Magnetic Field Confinement?	47502
Fuente, A.	A Chemical Study of the Hot and Dense Molecular Gas Adjacent to Photodissociation Regions (PDRs)	31671
Fuente, A.	A Chemical Study of the Hot and Dense Molecular Gas Adjacent to the Photon-Dominated Region (PDR) Associated with NGC 7023	36801
Fuente, A.	Study of the Interface Between the Atomic and Molecular Gas in the Reflection Nebulae: NGC 2068 (S), Sgr R1 (A)	30778
Furniss, I.	Observations of Complex H II/Molecular Cloud Structures: The NGC 6334 and NGC 6357 Regions	8794
Gallant, Y.	Crab-Like Supernova Remnants: Imaging, Polarisation and Broad-Band Spectroscopy	16538
Garnett, D.	Sulfur and Neon in Extragalactic H II Regions	18032
Giard, M.	Warm Dust in H II Regions and PDRs	5608
Giard, M.	Water Vapor in Warm Dusty Regions	7338
Goodman, A.	Mapping Magnetic Fields in the Interstellar Medium: Polarimetry at 100 Microns	39067
Gray, M.	Detection of OH Far-Infrared Lasers in Star-Forming Regions: Laser Action in OH at 134.83 and 135.95 Microns	3538
Green, D.	Mapping of 3C 58	7266
Grossmann, V.	Cold Dust and Dust Filaments in a High-Latitude Cirrus Cloud	11220
Guélin, M.	Far-Infrared Emission in the Cepheus A/B Molecular Complex	22218
Gürtler, J.	Infrared Ice Bands towards Young Stars in Chamaeleon	7628

Güsten, R.	Low-Mass Protostars in Globular Filament GF-9: The Physics of Globular Filaments as Sites of Low-Mass Star Formation	32361
Güsten, R.	Study of an Unusual Shock Region in the Galactic Centre: Observation of Shock/Photoionisation Diagnostics toward G0.17-0.04	9698
Haas, M.	A Study of Interstellar Shocks in IC 443	13051
Habing, H.	ISO Observations of Vega-Type Excess in HD 207129	10639
Haikala, L.	Mapping of Cold Dust and Search for Embedded Young Stars	18270
Harvey, P.	Diffraction Limited Imaging of Protostellar Clouds	39675
Harwit, M.	GT Dropped Observations	8844
Heithausen, A.	Ionised Carbon in High-Velocity Clouds	5870
Helmich, F.	Searches for New Interstellar Molecules: CH ₂ and NCCN	8911
Henning, Th.	Dust Spectroscopy of Embedded Infrared Sources in the Magellanic Clouds	13816
Henning, Th.	Search for the 21 Micron Emitters	6840
Herbstmeier, U.	Cirrus Dust Clouds in Hot Plasma G88+36-2	5434
Herbstmeier, U.	Physical Properties of a Cloud Located in the Local Hot Bubble: The Dust	7144
Hüttemeister, S.	Dust Properties of Galactic Centre Clouds	1522
Jackson, J.	Infrared Studies of Massive Young Stars and the ISM: The NGC 6334 Star Formation Region	10310
Jackson, J.	Low Metallicity PDR Diagnostics in the Infrared: A Study of the Dust-Gas Interaction	11636
Jackson, J.	Photodissociated Gas in the NGC 6334 Complex: The Influence of UV Field Strength	7764
Jaffe, D.	Low-Velocity Shocks in the Dense Interstellar Medium	12348
Jansen, D.	The O/OH/H ₂ O Transition in Partially Ionised Globules in IC 1396	872
Jenniskens, P.	The Emission Spectrum of Quiescent Dense Cloud Dust	12105
Joblin, C.	Infrared Emission Features and Interstellar PAH's: The Simple Case of the Reflection Nebula NGC 1333-SVS3	6676
Joblin, C.	Photochemical Evolution of Polycyclic Aromatic Hydrocarbons in the Interstellar Medium	8899
Jourdain de Muizon, M.	Tentative Detection of Solid O ₂ in Interstellar Grain Mantles	10230
Jourdain de Muizon, M.	The Organic Component of Interstellar Dust in Diffuse Clouds	16549
Jourdain de Muizon, M.	Variation of the Dust Composition through the Taurus Cloud: Infrared Spectra of Background Stars toward the Taurus Cloud	39053
Kazuhito, D.	Infrared Properties of YSO Candidates Isolated from Molecular Clouds: Infrared Observations of the Isolated IRAS Point Sources with ISO	5158
Kegel, W.	Methanol-Masers: Pump Mechanism and Possible IRaser-Lines	2888
Kerp, J.	The High-Velocity Cloud 90+42.5-130: The Impact of a High-Velocity-Cloud onto the Galactic Disk	2840
Koornneef, J.	Search for Cold Molecular Hydrogen in the Galaxy	86669
Lahuis, F.	H II Regions in M 33: Supernovae Rates	1526
Langer, W.	Evolution of Pre-Protostellar Core Fragments: Far-Infrared Emission from Core Fragments in L1498	10674
Launhardt, R.	Mid-Infrared Morphology of a High-Mass Protostellar Core: The Case of LBN594-MM	2320
Laureijs, R.	Dust Properties of Cirrus Heated by B-Stars	35224
Laureijs, R.	Properties of Peculiar Molecular Clouds at High-Latitudes	26350

Laureijs, R.	Small Scale Structure and Dust Properties in Cloud Cores	52955
Laureijs, R.	Study of Dust Particles in Bright-Rimmed Clouds	19816
Le Bertre, T.	Interstellar Dust Heated by AGB Stars	60984
Léger, A.	Reflection Nebulae: Photometry and Full Range Spectroscopy	45885
Léger, A.	Search for C60 ⁺ Bands and Long-Wavelength PAH Features	17486
Lemke, D.	Large-Scale Map of the Orion Molecular Cloud/Star Formation Complex at 200 μm	8072
Liljeström, T.	Heating and Cooling of Cirrus and Dark Clouds	8720
Lis, D.	Star Formation in the Galactic Centre Dust Ridge: Search for Embedded Far-Infrared Sources	20672
Liseau, R.	LWS Spectroscopy of the Star-Forming Rho Ophiuchi Cloud: Physical Conditions in the Condensed ‘Absorption Cores’	25574
Liseau, R.	Spectroscopic Mapping of the Rho Ophiuchi Cloud: The Gas and Dust Components of the Star-Forming Core	20008
Liseau, R.	Spectroscopic Mapping of the Serpens Cloud: The Properties of Active and Inactive Cores of Star-Forming Regions	25850
Little, L.	C ⁺ and O Distribution in the Molecular Cloud G34.3+0.2: How Deep Do They Go?	5476
Lutz, D.	The Mid-Infrared Extinction Law Towards the Galactic Centre	10332
Martín-Pintado, J.	On the Properties of the Giant Molecular Clouds in the Neutral Disk	71524
Matsuhara, H.	Far-Infrared Spectroscopy of Galactic Warm Ionised Medium	18236
Mattila, K.	Large-Scale Mapping of the Orion-B Molecular Cloud/Star Formation Complex (Lynds 1630) at 200 μm	11964
Mattila, K.	Search for Compact Very Cold Dust Clouds in the Galaxy	25717
Mattila, K.	Spectrophotometry of Diffuse Dust Emission in the Galaxy: UIR Band Carriers, Small and Large Grains	21054
Megeath, S.	A Search for Deeply Embedded Young Stellar Objects in the NGC 281 West Cluster: A Test for Triggered Star Formation	4016
Merluzzi, P.	Properties of Interstellar Cirrus. Physical Properties of Dust Components in Galactic Cirrus	12004
Mezger, P.	Imaging and Spectroscopy of the Unusual Infrared Source 1742–3005	3454
Mochizuki, K.	Far-Infrared Spectroscopy of M 31: Search for [C II] Deficit	10964
Mochizuki, K.	Far-Infrared Spectroscopy of M 33: Interstellar Physics in a Low Metal Spiral	11886
Molinari, S.	Spectroscopy of Candidate Progenitors of Ultracompact H II Regions	10708
Montmerle, T.	Spectral Features of X-Ray Irradiated Dust	87518
Moritz, P.	Infrared Photometry and Spectroscopy of the Draco Nebula	23841
Morris, M.	Large-Scale Shocks in the Galactic Centre and Other Regions	2090
Murakami, H.	Spectrophotometry of the UIR Bands in the IRTS Field	472
Myers, P.	Warm Dust Imaging of Nearby Young Stellar Objects	7812
Nakagawa, T.	IRTS Follow-On Observation of SNR’s with Far-Infrared Fine-Structure Lines	13320
Neufeld, D.	Far-Infrared Line Emission from Shock Heated Gas in Cepheus: Fabry Pérorot Observations of O I and High-J CO Emissions	9150
Neufeld, D.	Search for Far-Infrared Transitions of Interstellar Hydrogen Halides	3170
Neufeld, D.	Search for Hydrogen Fluoride in OMC–1 and W51	3176
Neufeld, D.	Search for Ultra-High Excitation Rotational Lines of Water: A Probe of the Hottest Molecular Gas in the ISM	3796

Nieten, Ch.	Dust, Clouds and Magnetic Fields in a SW Spiral Arm Region of M 31: A Multi-Wavelength Study of Infrared Emission and Polarisation	19398
Pauls, T.	Far-Infrared Spectroscopy of G159.6–18.5: A Possible Dust-Embedded Supernova Remnant	3948
Péquignot, D.	Far-Infrared Spectroscopy of Nuclearily Processed Material in Young Supernova Remnants	34700
Péroult, M.	Photo-Imaging of Quiescent Molecular Clouds in the Inner Galaxy	16260
Pfau, W.	The Signature of Diffuse Interstellar Bands in Mid-Infrared Emission	4298
Phillips, T.	Oxygen in Molecular Clouds	66080
Pilbratt, G.	CAM Imaging of HST M 16 Field	3222
Pilbratt, G.	ISOCAM M 16 Imaging Follow-Up: CVF Spectro-Imaging	4840
Pilbratt, G.	SWS Spectroscopy of an Unknown Extended Source in the M 16 Area	3824
Prusti, T.	200 Micron Filler Survey for IRAS Sources	25212
Prusti, T.	Bolometric Luminosity Functions of Nearby Star-Forming Regions	15195
Prusti, T.	Circumstellar Environment of Pre-Main Sequence Stars with Variable Extinction	19976
Prusti, T.	Distance to a Cepheid	2574
Prusti, T.	Spectral Energy Distribution of Young Stellar Objects: Star Formation in Molecular Clouds	60256
Puget, J.-L.	Spectral Survey of the Cold Interstellar Medium: Search for New Features from Dust, Atom Clusters and Molecule Lines	47126
Rasmussen, I.	Shock Processing of Dust in Tycho's SNR	26334
Reach, W.	Infrared Emission from the Warm Ionised Medium	19277
Reach, W.	Phase Transitions in Translucent Clouds	20158
Reach, W.	Supernova Interactions with Molecular Clouds and their Influence on X-Ray Remnant Morphology	27406
Richards, P.	Dust in Galactic Open Clusters	11896
Roche, P.	Magnetic Field Structures in Star-Forming Regions	9583
Roelfsema, P.	Element Abundances in Galactic H II Regions	13548
Rubin, R.	An Analysis of Planetary Nebulae: Temperatures, Densities, and Abundances	14374
Rubin, R.	Iron Abundance in the Orion Nebula: Unique Contributions from [Fe III] and [Fe IV] Lines	15050
Rubin, R.	Iron Abundances in Gaseous Nebulae: Unique Contributions from [Fe III] and [Fe IV] Lines	9164
Rubin, R.	ISO Spectral Analysis of Planetary Nebulae: Densities, Temperatures and Abundances	12332
Russell, S.	A Statistical Study of Dust in Magellanic Cloud Supernova Remnants	42706
Russell, S.	The Energy Sources of Molecular Outflows	9578
Sanders, D.	The 135–200 Micron Luminosity of Nearby, Star-Forming GMCs: W3 and NGC 7538	16830
Sandford, S.	A Search for Solid State Ozone (O ₃) in the Ices in Interstellar Dense Molecular Clouds	3412
Sandford, S.	The 11–16 Micron C-H Bending Modes of Interstellar PAHs: Determination of Molecular Symmetries and Abundances	5988
Sandford, S.	The Composition of the H ₂ -Containing Ice and Dust along the Line of Sight to the Unique Object WL5	3454
Saraceno, P.	W28 A2 Revisited	7286

Schutte, W.	Infrared Absorption Features of H ₂ O Diluted in Apolar Ices	3136
Schutte, W.	Infrared Absorption Features of Nitrogen and Sulfur Containing Molecules in Interstellar Ices	13849
Schutte, W.	The 2.75 Micron Feature of Hydrated Silicates	5846
Sellgren, K.	Imaging of Infrared Emission Features in Reflection Nebulae	105536
Serra, G.	Dust and Gas Properties of Extended Cold Cores in the ISM: A Study of Dust Matter Inside Cold Cores	15990
Sibille, F.	Luminosity Functions of Low-Mass Stars in Nearby Molecular Clouds: 60 Micron Photometry of Regions Observed with CAM	30592
Siebenmorgen, R.	Dust Emission of Reflection Nebulae	37250
Siebenmorgen, R.	The Energetics of Extended Emission around Herbig Ae/Be Stars	41840
Smith, M.	Molecular Hydrogen in Bipolar Outflows: High-Vibrational Pure-Rotational Transitions	21796
Smith, M.	Warm CO in the Youngest Protostellar Outflows	6262
Spaans, M.	Far-Infrared Line Observations of Photon Dominated Regions around Cool Stars	21530
Stapelfeldt, K.	The Spectral Energy Distribution of HH 30	5710
Stark, R.	A Protostar in the Southern Ammonia Core of L183?	15704
Stark, R.	Cooling by the Diffuse Cold and Warm Phases of the ISM	3580
Stark, R.	Density Structure and Evolutionary State of TMC-1	24491
Stark, R.	Far-Infrared Line Emission from Galactic High-Latitude Clouds	3110
Stutzki, J.	High-Density PDR Tracers	16056
Stutzki, J.	The Changing Faces of PDRs: Structure, Evolution, and Spectroscopic Characteristics	15854
Stutzki, J.	Trace Species Detected through PDR Emission: A Study of Depletion in the Gas Phase	30805
Tauber, J.	Galactic Distribution of the Isotopic Ratio ¹³ C II/C II	30804
Teixeira, T.	Deuteration in Grain Mantles: The Missing Link	8060
Timmermann, R.	Low-Velocity Shocks in the Dense Medium of Outflows	16932
Tuffs, R.	Observations of Gas and Dust in Supernova Remnants	8238
Tuffs, R.	Polarimetric Imaging of Mid-Infrared Synchrotron Emission in Cas A: A Study of Cosmic Ray Electron Acceleration in a Shell-Type SNR	35887
Tuffs, R.	Polarimetric Mapping of Synchrotron Emission in the Crab Nebula	18300
Unger, S.	Discretionary Time Observations of the SNR 3C 58 Using the ISO Spectrometers	12514
van Buren, D.	Infrared Coronal Lines in Ultracompact H II Regions	5228
van Buren, D.	Stellar Wind Bow Shocks: Laboratories for Dust Shock Processing	4734
van der Hulst, J.	Density and Ionisation Structure of H II Regions	9812
van der Werf, P.	Pressure in the Interstellar Medium of M 33: The Contrast between Arm and Inter-Arm Regions	9893
van Dishoeck, E.	SWS Fabry-Pérot Observations of Highly-Excited H ₂ O Absorption toward Orion IRC2	9142
van Dishoeck, E.	The Chemical State of Southern High-Mass Star-Forming Regions	25980
van Dishoeck, E.	The Chemistry of H ₂ O and CO ₂ in Star-Forming Regions	25950
Verma, R.	Mid-Infrared Imaging of Ultracompact H II Regions/ CO Clumps	2012
Verstraete, L.	Mid-Infrared Spectroscopy of Small Dust Grains around Hot Stars: Photon Processing of Small Grains	41102
Walmsley, C.	Atomic Silicon in Orion	3858
Walmsley, C.	Observation of NH ₃ in Some Hot Molecular Cores	24760
Ward-Thompson, D.	Pre-Protostellar Cores	32256

Ward-Thompson, D.	Pre-Stellar Cores	20806
Wendker, H.	G 79.29+0.46: A New LBV and its Shell: A Surprisingly Perfect Bubble around an LBV	11298
Wesselius, P.	CO ₂ and CH ₄ Ice Absorption Features	22146
Wesselius, P.	Solid ¹² CO ₂ and ¹³ CO ₂ Ice Absorption Features: The Galactic ¹² C/ ¹³ C Abundance Ratio	6448
Wilking, B.	The Nature of Weak Radio Sources in the Rho Oph Cloud Core	13771
Wilson, T.	Molecular Cloud Cores in Orion: Star Formation in Orion	21152
Wooden, D.	Iron-Group Spectroscopy of SN 1987A	6164
Wouterloot, J.	Narrow-Line CO Emission from a Molecular Cloud with Star Formation: Sonic Linewidths from a Star-Forming Region	3240
Wright, C.	Absorption in the Cold ISM toward the Galactic Centre. Molecular Hydrogen	22272
Wright, C.	Formation of Molecular Ice Mantles on Interstellar Dust Grains and the Nature of the Grain Surfaces	4084
Wright, C.	LWS Observations of HD toward the Orion Bar	4498
Wright, C.	SWS Spectrum of the Orion Shock Peak 2	6538
Yates, J.	Observations of Far-Infrared Water Masers in Star-Forming Regions	2530
Yui, Y.	H ₂ Molecule Lines in Rho-Oph Cloud: UV Radiation Field in Dark Clouds	6376
Zavagno, A.	Dust Distribution in Galactic H II Regions	20446
Zavagno, A.	Imaging of a Massive Star-Forming Region: Study of AFGL 4029	1144
Zimmermann, T.	Molecular-Neutral-Ionised Gas Interfaces in L1457: Line Observations of O I (63 μm) and C II (158 μm)	5994

B.2.4 Extragalactic Systems

Aalto, S.	Centre and Disk Spectroscopy of Interacting Galaxies	3724
Acosta-Pulido, J.	Mid-Infrared Imaging of the Starburst Galaxy NGC 6090	9790
Andreani, P.	Far-Infrared Photometry of a Complete Sample of Optically Selected Bright Quasars	35907
Andreani, P.	Spectrophotometry of a Complete Sample of IRAS Galaxies with Millimetric Fluxes, CO and H I Data	11405
Antonucci, R.	Search for CO Absorption in the Cygnus A Torus	39386
Appenzeller, I.	Using Infrared Coronal-Lines as Calorimeters for AGN: Spectroscopy of Sources with Exceptionally High Ionisation	5792
Appleton, P.	Infrared Imaging of Collisional Ring Galaxies	4652
Armus, L.	The Far-Infrared Spectral Energy Distributions of High-Redshift Quasars	3638
Barr, P.	ISO Observations of the Egret Blazars	34946
Barr, P.	Mapping the Molecular Torus in Active Galactic Nuclei	69822
Barr, P.	Multifrequency Monitoring of the Enigmatic Blazar 3C 279	46100
Barr, P.	Target of Opportunity of the Gamma-Ray Flaring Blazar Mkn 501	1384
Barr, P.	Target of Opportunity of the Optical Flaring Quasar BL Lac	3526
Barthel, P.	The Nature of Broad Line Radio Galaxies	6350
Barvainis, R.	An Einstein Ring with Strong Submillimeter Emission	10426
Barvainis, R.	H ₂ Emission from the Molecular Torus in Cygnus A	4366
Barvainis, R.	ISO Observations of the Cloverleaf: A Quasar with CO at z=2.5	29762
Bechtold, J.	Probing Dust in Quasars: Observations of the 9.7 Micron Silicate Feature	7272

Bergvall, N.	Star Formation in Luminous Blue Compact Galaxies	12346
Birkinshaw, M.	Infrared Properties of the Cores of Nearby Radio Galaxies	24165
Boisson, C.	Testing the Unifying Scheme of Active Galactic Nuclei	61759
Bonoli, C.	Infrared Properties of Barred Galaxies	16840
Bonoli, C.	Infrared Properties of Galaxies in Intermediate Redshift Clusters	16122
Bonoli, C.	Star Formation in Ring Galaxies: Dust Properties in Colliding Galaxies	16004
Boulanger, F.	Thermal Balance in the Warm ISM	63510
Bower, G.	Magnetic Field Morphology in Spiral Galaxies: A Study of Polarised Far-Infrared Radiation	9256
Braine, J.	Gas Properties in an Old but Incomplete Merger NGC 660: A Study of Gas Properties in a Polar Ring Galaxy	6538
Braine, J.	Is there Dust in the Intercluster Medium? Dust in Galaxy Clusters	7370
Braine, J.	The Interstellar Medium of a Normal, Isolated, Spiral Galaxy: The ISM in NGC 4414	7095
Brandt, W.	Infrared Line Maps and Longwave Spectra of X-Ray Bright Extragalactic H II Region Galaxies with Superbubbles	8972
Bregman, J.	Are there Hidden Supernovae?	23038
Bregman, J.	Dust in the X-Ray Atmospheres of Elliptical Galaxies	8958
Bregman, J.	The Origin of Dust and PAHs in Elliptical Galaxies	18522
Bregman, J.	The Origin of Mid-Infrared Emission from Elliptical Galaxies	9172
Browne, I.	A New Look at the Synchrotron Emission in Radio-Loud AGN	12742
Calzetti, D.	The Relationship between Dust Absorption and Emission in Galaxies	5048
Carilli, C.	Infrared Imaging of the Optical Emission Line Jet and Optical and H I Shells in Centaurus A	10242
Carilli, C.	Infrared Imaging of the Radio Hot Spots in Cygnus A	7784
Casali, M.	A Search for Cool Halo Emission above NGC 5714 and NGC 5529	40528
Casoli, F.	C II Line Emission in Isolated Galaxies	3534
Casoli, F.	Fine-Structure Line Emission in Selected Regions of M 31	1464
Casoli, F.	Star Formation and Gas Content in Isolated Galaxies: A Reference Sample	38278
Chini, R.	Star Formation Efficiency in Galaxies	27776
Clavel, J.	ISO and mm Observations of Narrow Lines Seyfert 1 Galaxies	15672
Clavel, J.	ISO Observation of the Only Radio Loud Broad Absorption Line Quasar 1556+3517	2786
Clements, D.	The Spectral Energy Distribution of Extreme Ultraluminous IRAS Galaxies	7426
Combes, F.	Bars and Tides in Galaxies: Role of Large-Scale Dynamics on Star Formation	44808
Combes, F.	Spiral Arm in Messier 31: Star-Formation Processes across the Arm	10504
Courvoisier, T.	Far-Infrared Variability of a Large Sample of Quasars	20286
Courvoisier, T.	ISO Spectra of a Sample of AGN	44968
Courvoisier, T.	Polarimetry of Two Radio-Loud Quasars	13640
Cox, C.	Far-Infrared Emission from the Cores of Rich Clusters	9036
Crotts, A.	Evolution of 3–35 Micron Lines from the Formation of SNR 1987A	14190
Davies, J.	The Diffuse Far-Infrared Emission from Spiral Galaxies	30209
de Jong, R.	Surface Density Distribution of Hot and Cold Dust in a Complete Sample of Face-On Spiral Galaxies	11296
Dennefeld, M.	The Nature of High X-Luminosity ROSAT/IRAS Galaxies: Relations with Narrow-Line Seyfert 1 Galaxies	29734

Dennefeld, M.	The Nature of the Faintest IRAS Galaxies and Galaxy Evolution: Follow-Up of IRAS Deep-Field Sources	18642
di Serego Alighieri, S.	Jet-ISM Interactions in Radio Galaxies	7204
Dunlop, J.	An Infrared Comparison of the Host Galaxies of Radio-Quiet Quasars, Radio-Loud Quasars and Radio Galaxies	6894
Edmunds, M.	The Cooling and Composition of Extragalactic H II Regions	16650
Efstathiou, A.	Photometry and Spectroscopy of AGN with Polarised BLR	14838
Egami, E.	SWS Spectroscopy of a Seyfert 2 Warm Ultraluminous Galaxy: IRAS 05189–2524	15414
Egami, E.	SWS Spectroscopy of Molecular Hydrogen Lines in Bright Infrared Galaxies	15758
Elias, J.	Comparison of Mass-Losing AGB Stars in the Magellanic Clouds	7654
Fabian, A.	Cold Gas and Star Formation in Massive Cooling Flows: A Search for the End-Point of the Cooled Gas	92436
Fanti, C.	Medium/Far-Infrared Observations of Compact Steep Spectrum and GHz-Peaked Spectrum Radio Galaxies	41232
Feretti, L.	Rich Clusters with Tailed Radio Galaxies: Dust and Stripping	10142
Fischer, J.	LWS Grating Observations of HD and Other Molecules in Infrared Bright Galaxies	3736
Fosbury, R.	Infrared Properties of Extragalactic Radio Sources: The General Population to High-Redshift	81689
Garnett, D.	Composition and Cooling in Extragalactic H II Regions	44922
Garzón, F.	The Physical Parameters that Control Violent Stellar Bursts	23314
Gavazzi, G.	Infrared Properties of S/Irr Galaxies in the Coma and A1367 Clus- ters: Late-Type Galaxies in Clusters	29776
Genzel, R.	Testing Unified Models with Infrared Spectroscopy	24422
Gerin, M.	The Dust Composition at High-Redshift	17962
Gerin, M.	The Dust Composition in Distant Galaxies	27248
Gilmore, G.	Brown Dwarf Halos of Low Redshift Spiral Galaxies	57652
Gilmore, G.	ISO Colours of the Halos of Normal Galaxies: Confirmation and Origin of Detected Halo Emission	57658
Gómez Álvarez, P.	Infrared Study of High Metallicity Star-Forming Regions	2564
Greenhouse, M.	Infrared Coronal Lines of Active Galactic Nuclei	42994
Gregorini, L.	A Complete Sample of Dumb-Bell Galaxies: Dust inside Interact- ing Systems	10769
Guélin, M.	Matter at the Periphery of Nearby Galaxies: The Dust Compo- nent	19921
Haas, M.	Far-Infrared Map of the Andromeda Galaxy M 31	50889
Haas, M.	Search for Cold Dust in the Normal Spiral Galaxy M 31	9533
Haas, M.	Very Cold Dust in the Dwarf Elliptical Galaxy N 205: Discre- tionary Time Proposal	6301
Hammer, F.	Infrared Studies of Distant Galaxies in Deep Optical and Radio Surveys	122776
Hanlon, L.	Search for a Flaring/Fading Infrared Counterpart to the New Gamma-Ray Burst GRB970111	4442
Hanlon, L.	ToO: Search for Infrared Counterparts to Gamma Ray Bursts	8174
Hansen, L.	Dust in Cooling Flows: Production and Destruction of Dust in X-Ray Gas Environments	26665
Helou, G.	An [O I] Survey in High-Redshift Objects	54153
Helou, G.	Exceptions to the Radio-Infrared Correlation: Radio-Deficient Galaxies	9860
Henkel, C.	An OH Multilevel Study of Megamaser Galaxies: OH Megamasers	11214

Henkel, C.	The Strongest Molecular Hotspot in the Magellanic Clouds: Molecules in the Magellanic Clouds	26844
Higdon, J.	Probing the Star-Forming ISM in Ring Galaxies	2486
Hines, D.	Infrared Fine-Structure Emission in Warm IR-Ultraluminous AGN	21423
Hough, J.	Polarimetry of the Nucleus of Active Galaxies	40266
Hu, E.	Two Extremely Red Galaxies	3618
Iovino, A.	ISO Observations of Compact Groups of Galaxies: A Test to Check their Physical Reality	14445
Ishii, K.	[C II] Observations of Spiral Structures in NGC 300: A Research on Arm-Interarm Contrast in Star-Formation Efficiency	38323
Ivison, R.	A New Window on Galaxy Formation and Evolution	10348
Ivison, R.	The Far-Infrared Luminosity Function of QSOs in the Early Universe	58867
Jaffe, W.	Cool Gas and Dust in Cooling Flows in Clusters of Galaxies	48987
Joseph, R.	The ISOPHOT Field Galaxy Survey	3978
Keel, W.	Dust Emission and Absorption in Backlit Spiral Galaxies	7446
Kegel, W.	OH Megamasers: Pump Mechanism, Possible IRaser-Line	13716
Kegel, W.	OH Megamasers: Pump Mechanism, Possible IRaser-Lines, and the Velocity Field.	30024
Kessler, M.	Search for Flaring/Fading Infrared Counterparts to New Gamma-Ray Bursts	36790
Kidger, M.	The Optical-Radio Polarisation Breakpoint in Blazars	2272
Klaas, U.	The Infrared Spectral Energy Distribution of the Circinus Galaxy: ISOPHOT Broad Band Photometry from 10 to 200 Micron	2568
Knapp, G.	Origin and Evolution of Dust in Elliptical Galaxies: Analysis of Infrared Continuum Emission from 5 to 200 μm	53262
Knapp, G.	Origin and Evolution of Dust in Elliptical Galaxies: ISOPHOT Observations of 10 Galaxies with Nuclear Optical Dust Lanes	11168
Krishna, G.	Gaseous Superdisks in Powerful Radio Galaxies	2588
Krishna, G.	Mid- and Far-Infrared Properties of Nearby Radio-Loud Ellipticals: Radio-Infrared Connection in Bright Active Ellipticals	24670
Krügel, E.	Dust Emission from Radio Galaxies at High-Redshifts	21229
Krügel, E.	The Shape of Grains in the Normal Galaxy N1808	9256
Krüger, H.	Infrared Studies of H II Galaxies with Companions	7782
Kunth, D.	PAH Molecules in Star-Forming Galaxies: Influence of Metallicity and UV Radiation Field	35021
Kunze, D.	Detailed Spectroscopy of the Galactic Centre	28316
Kutner, M.	Molecular Clouds and Star-Forming Regions in the Magellanic Clouds	16132
Leech, K.	A Multiwaveband Study of the Unusual Narrow Line Quasar IRAS 20181–2244	3294
Leech, K.	Is there Dust in $z > 4$ Quasars?	9992
Lemke, D.	Search for Very Cold Dust Outside the Optical Disks of Galaxies	30849
Lequeux, J.	CAM-CVF Observations of the Nuclear Region of M 31	16680
Levine, D.	A Superbubble Surrounding the Quintuplet at the Galactic Centre?	19984
Lo, K.-Y.	Pre-Starbursts in Luminous Infrared Galaxies	15050
Longair, M.	Far-Infrared Photometry of Distant 3CR Radio-Galaxies	8372
Lonsdale, C.	ISO-IRAS Faint Galaxy Survey	253628
Lu, N.	Disentangling the Merging Sequence of Ultraluminous Infrared Galaxies	10166

Lu, N.	IRAS Galaxies with the Coldest Far-Infrared Colors	14766
Luhman, M.	[C II] in Nearby ULIGs: Probing the Starburst Age and the Luminosity Source	7564
Lutz, D.	Exploring with PAH-Features: The Starburst-AGN Connection in Ultra- and Hyper-Luminous Infrared Galaxies	139231
Lutz, D.	Infrared [Fe VII] Lines as Narrow Line Region Diagnostics	7480
Lutz, D.	Spectral Line Mapping of M 82: From Starburst to Quiescent Disk	10868
Macchetto, F.	Exploring the Physical Properties of the Dust Component in Early-Type Galaxies	114045
Macchetto, F.	Imaging of Infrared Counterparts of Extragalactic Radio-Jets	16376
Madden, S.	Effects of Metallicity on Star-Forming Clouds in Irregular Galaxies	32510
Magnier, E.	A Broadband Spectral Study of the Bulge of M 31	4722
Maihara, T.	Far-Infrared Photometry of the Lensed Galaxy MG0414+0534	3682
Maiolino, R.	Imaging Spectroscopy of the Starbursts NGC 4945 and IC 342: Disentangling Star-Forming Regions	17425
Malkan, M.	An Infrared Emission-Line Search for Obscured Active Nuclei: Surveying Four Subsamples of the Strongest Candidates	19916
Malkan, M.	High-Resolution Spectroscopy of the 2 Brightest Seyfert Nuclei: Searching for Dense Gas Orbiting near the Nucleus	28395
Mann, R.	Morphological Disturbance and Star Formation in IRAS Galaxies	15434
Marx, M.	Infrared Spectroscopy of Cool Clouds in the LMC	10434
Mattila, K.	UIR Bands in the Disks of Edge-On Spiral Galaxies	12412
Mazzei, P.	Infrared Properties of Barred Galaxies	13538
McBreen, B.	ISO Observations of Wolf-Rayet Galaxies: H II-Type Galaxy with an AGN Signature	36934
McMahon, R.	Hyper-Luminous Infrared Galaxies	6332
Metcalfe, L.	Infrared Observations of Low Surface Brightness (LSB) Galaxies	45193
Mezger, P.	Observations of the Galactic Centre with ISO	10342
Miley, G.	Dust Emission in an Unbiased Sample of 3CR Galaxies: Obscured Nuclear Activity and Star Formation at $z < 0.5$	50122
Miley, G.	Dust in the Most Distant Radio Galaxies: Spectral Energy Distributions and Luminosities	101182
Mirabel, I.	Starburst and Active Galaxies: Follow-Up Observations	48471
Mittaz, J.	Far-Infrared Observation of X-Ray Selected Emission Line Galaxies from the RIXOS Survey	7824
Moorwood, A.	Energy Source in Ultraluminous Infrared Galaxies: Starbursts or Obscured AGN's in IRAS Galaxies	140181
Moorwood, A.	GT Dropped Observations	10378
Moorwood, A.	Imaging Spectroscopy of the Circinus Galaxy: AGN versus Starburst Ring	7082
Moran, J.	High Spectral Resolution Observations of Megamaser Galaxies	12366
Mouri, H.	Mid-Infrared Spectroscopy of Heavily Obscured IRAS Galaxies	11141
Nakagawa, T.	Large-Scale Multi-Line Spectroscopy of the Galactic Centre: Origins of the Far-Infrared [C II] Line Deficit	25643
Neininger, N.	Mapping the Surroundings of NGC 206: Probing the Dust Processing by a Spiral Arm	2716
Okumura, K.	Diffuse Interstellar Medium in the Magellanic Clouds: Are there PAHs in the Magellanic Clouds?	12676
Okumura, K.	Diffuse Interstellar Medium in the Small Magellanic Cloud: Are there PAHs in the Small Magellanic Cloud?	15416
Oliva, E.	Probing Cool Molecular/Atomic Gas in Cooling Flow cD Galaxies	24044

Oliver, S.	Far-Infrared Studies of a Complete AGN Rich Sample from the Point Source Catalog Redshift Survey	17177
Onaka, T.	A Systematic Study of Infrared Emission from Galaxies: Complementary Study to MIRS/IRTS Observations	43558
Padovani, P.	ISO Observations of Radio-Selected BL Lacs: Observations of the Complete 1 Jy Sample	35292
Pérez-Fournon, I.	Search for Hidden BLR in Seyfert 2 Galaxies: Test of Unification Theories for Seyferts	3952
Pierre, M.	Detailed Insights into the Intracluster Medium of Abell 2256	39314
Poglitsch, A.	Spectral Line Mapping and the Extended Medium in Nearby Galaxies	25659
Prieto, A.	Anisotropy of the Radiation in NGC 5252	12153
Prieto, A.	The CfA Sample of Seyfert Galaxies: Follow-Up Line Spectroscopy with SWS	40282
Puxley, P.	Mid-Infrared Recombination Line Spectroscopy of Bright Galaxies	9324
Quirrenbach, A.	Rapid Infrared Variability of an Extreme BL Lac Object	27144
Rawlings, S.	Far-Infrared Photometry of High-Redshift Radioquasars	27121
Rawlings, S.	Far-Infrared Photometry of Radio Quiet Quasars	43834
Reach, W.	Mapping the Interstellar Cooling Lines in the SMC	21999
Renzini, A.	Far-Infrared Emission in X-Ray Bright and X-Ray Faint Early-Type Galaxies	24573
Rieke, G.	Optically Quiet QSOs	3356
Rieke, G.	Star Formation and Evolution of Seyfert Nuclei	10612
Rieke, M.	Mid-Infrared Output of Quiescent Galaxies	32766
Rieke, M.	Mid-Infrared Output of the Quiescent Galaxy NGC 3115	26457
Rieke, M.	Study of the Far-Infrared Properties of BAL QSOs	19014
Rieke, M.	The Star Formation Rate in Coma E+A Galaxies	7634
Rigopoulou, D.	The Nature and Radiation Field of Ultraluminous IR Galaxies: A Survey Using 6–12 μm Emission Features	6468
Rocca-Volmerange, B.	Galaxy Luminosity Functions by Types from the ESO-Sculptor Redshift Sample	49699
Rodríguez Espinosa, J.	The Spectral Energy Distribution of Seyfert Galaxies: The Centre for Astrophysics Seyfert Sample	24564
Rouan, D.	PAHs/Very Small Grains in Edge-On Galaxies	27135
Rowan-Robinson, M.	Photometry and Spectroscopy of Ultraluminous IRAS Galaxies: The QDOT Sample	46868
Rowan-Robinson, M.	Photometry of Extreme Ultraluminous IRAS Galaxies: The PSCZ Sample	15132
Sanders, D.	Infrared Spectroscopy of an Unbiased Sample of Ultraluminous IRAS Galaxies with $\text{Log}[L_{IR}/L_{Sun}] = 12.3\text{--}13.0$ and $z = 0.1\text{--}0.3$	18676
Sauvage, M.	Hot Dust in the Central Regions of Early-Type Galaxies? A Fast Spectroscopic Survey with ISOCAM	27044
Saxton, R.	Determining the Timescale of Infrared Variability in Blazars	39853
Scoville, N.	ISO Search for H_2 Rotational Transitions in High-Redshift Quasars/Host Galaxies	14898
Shanks, T.	Infrared Properties of X-Ray Selected QSOs and Galaxies	21984
Shields, J.	Infrared Spectroscopy of the Lowest Luminosity Seyfert 1 Nucleus	34762
Siebenmorgen, R.	Polarimetry of Ultraluminous IRAS Galaxies: Starbursts or AGN?	27764
Smith, B.	Mid-Infrared Spectral Imaging of Galaxy Bulges	27843
Smith, B.	The ISM in Low Luminosity Virgo Cluster Spiral Galaxies	7180
Smith, H.	A Spectroscopic Study of OH Lines in Megamaser Galaxies	16624

Smith, H.	Detailed SWS/LWS/PHT-S Spectroscopy of Bright Starburst Galaxies and AGNs	59568
Smith, H.	Excitation and Kinematics of SgrA*: LWS Complete Spectroscopy of Selected Bands	26236
Smith, H.	LWS Molecular Line Observations of M 82 and NGC 253	24910
Smith, H.	The Mid-Infrared Spectral Energy Distribution of Infrared Luminous Galaxies	44470
Soifer, B.	ISO/SWS Observations of Ultraluminous Infrared Galaxies: Probing the Origin of the Luminosity	16056
Spear, G.	The Period-Luminosity Relationship at 12 Microns for LMC Cepheids	30682
Spinoglio, L.	Infrared Energy Distributions and Imaging of Active Galaxies: Towards a Unification Scheme of Active Galactic Nuclei	18145
Spinoglio, L.	Infrared Energy Distributions and Imaging of the Complete Sample: Towards the Unification of Active Galactic Nuclei	56182
Spinrad, H.	MG1019+0535: A Dusty, High-z Radio Galaxy	8714
Sternberg, A.	[Fe II] Emission in Starburst Galaxies and Active Galactic Nuclei	16528
Sternberg, A.	Mid-Infrared Spectroscopy of Liners: The AGN Connection	52720
Stickel, M.	ISOPHOT Follow-Up of Interesting Serendipity Sources	2914
Stockton, A.	Correlations between Far-Infrared Spectra and QSO Host Galaxy Morphology	14910
Sugai, H.	Energy Sources for Emission Lines from Liners: Liners with Broad Balmer Line Components	13086
Sulentic, J.	Star Formation and Secular Evolution in Galaxies: Mixed Morphology Pairs	25211
Tagliaferri, G.	Infrared Continuum Variability of the Highly Variable BL Lac Object PKS 2155–304	25772
Taniguchi, Y.	Star Formation in Hyper-Luminous Infrared Galaxies	10770
Thornley, M.	The Arches Cluster: Probing the Interaction between Massive Stars and the ISM in the Galactic Centre	5748
Thuan, T.	Dust and Infrared Emission in the Extremely Metal-Deficient Blue Compact Galaxy SBS 0335–052	14653
Thuan, T.	The Interstellar Medium in the Young Galaxy System SBS 0335–052 and its Companion	9694
Treves, A.	The Infrared Energy Distribution of the BL Lac Object PKS 2155–304	6493
Trewhella, M.	Dust in Spiral Galaxies: Energy Distribution and Temperature	8070
Tuffs, R.	Heating and Metallicity in the Extended H I Disks around NGC 891 and NGC 6946	21695
Turner, J.	Gas and Dust Properties in Two Nearby Spiral Galaxies: Far-Infrared Continuum Observations of IC 342 and Maffei 2	14592
van Buren, D.	Multi-Wavelength Study of Starburst NGC 3690	18903
van der Hulst, J.	Dust in Shell Galaxies	11567
van der Hulst, J.	Dust Temperatures in Galaxies as Function of their Surface Brightness	26406
van der Hulst, J.	Far-Infrared Observations of Low Surface Brightness Galaxies: Search for Cool Dust in Low Surface Brightness Galaxies	73103
van der Werf, P.	Pressure in the Interstellar Medium of Late-Type Galaxies: Scale Lengths and Multi-Phase Structure	46934
van der Werf, P.	Shocked Molecular Gas in NGC 6240 and Arp 220: Measuring Energy Dissipation and Gas Flow to the Centre	29424

van der Werf, P.	Spectroscopy of Distant Radio Galaxies: Starbursts and Active Nuclei at Redshift One	57890
van der Werf, P.	Stellar Population in the $z=3.5$ Radio Galaxy 6C 1909+722: A Genuine Primeval Galaxy?	10561
Verheijen, M.	An Improved Distance Indicator for Spiral Galaxies: The 2-Parameter Tully-Fisher Relation in Ursa Major	7762
Viallefond, F.	CAM-CVF Observations of NGC 604 in the Nearby Galaxy M 33	8060
Vigotti, M.	The Nature of AGN and Stellar Populations in High-Redshift Powerful Radio Galaxies	12992
Waller, W.	Starburst Anatomy: Infrared Spectral Imaging of Giant H II Regions in M 33	18362
Ward, M.	Centaurus A: Qu'est-ce que c'est?	14052
Ward, M.	Hot Dust in High-Redshift Quasars? Implications for the Presence/Absence of Tori	32547
Ward, M.	Narrow-Line Seyfert 1's: The Infrared Connection	16998
Wehrle, A.	The Energy Emission Mechanism of Gamma-Ray Blazars	3166
Werner, M.	Studies of Wolf-Rayet Galaxies	22376
White, D.	Dust in the Stripped Interstellar Medium of M 86	9976
Willis, A.	Infrared Spectroscopy of Wolf-Rayet Starburst Galaxies	70380
Willner, S.	Abundance Gradient in M 33	14322
Wozniak, H.	High-Resolution Imaging of (Circum-)Nuclear Starburst Galaxies	38009
Wright, G.	Dust Absorption Features in Active Galaxies	14190
Xu, C.	Ionising Flux and Extinction in Closely Interacting Spiral-Spiral Pairs	17232
Xu, C.	Mapping Intergalactic Dust Emission: Compact Groups with Diffuse X-Ray Emission	46704
Xu, C.	Mapping Infrared Enhancements in Closely Interacting Spiral-Spiral Pairs	51643
Yun, M.	Star Formation in Young Infrared Luminous Galaxies	3220

B.2.5 Cosmology

Andreani, P.	Photometry of Cluster Candidates for the Sunyaev-Zeldovich Effect	9468
Barvainis, R.	High-Redshift Primeval Galaxies Lensed by Clusters	8148
Bechtold, J.	The Spectral Energy Distribution of the Proto-Galaxy Candidate MS1512–CB58	8326
Beichman, C.	Search for Dark Matter Halos in Galaxies and Clusters	27908
Bergeron, J.	Far-Infrared Photometry and Spectrometry of Sub-Classes of Radio-Quiet Quasars	13428
Biviano, A.	Early-Type Post-Starburst Galaxies in the Coma Cluster	8934
Biviano, A.	The Infrared Properties of Brightest Cluster Members	8928
Castro-Tirado, A.	ToO: New Soft Gamma-Ray Repeater (SGR 1814–1340): A New IR-Source?	3350
Cesarsky, C.	Ultra-Deep Survey with ISOCAM: Search for Primeval Galaxies and Quasars	46783
Clements, D.	ISO Observations of Low Ionisation BAL Quasars: Ultraluminous IRAS Galaxies and the Nature of Iron Quasars	3374
Cox, C.	The Distribution and Temperature of Dust in Abell 1691	6198
de Zotti, G.	Far-Infrared Evolution of Galaxies: The IRAS Deep Survey Sample	24264

Dunlop, J.	The Formation and Evolution of Elliptical Galaxies	11867
Egami, E.	Search for Primeval Galaxies around $z>4$ Quasars	27680
Elbaz, D.	Galaxy Evolution and Diffuse Far-Infrared Emission in Hickson Compact Groups of Galaxies	37099
Elston, R.	The Nature of Faint Red Field Galaxies	35756
Feretti, L.	Elliptical Galaxies in Rich Clusters: Dust and Stripping	26854
Franceschini, A.	ISO Observations of Candidate Primeval Dusty Galaxies and AGNs: Infrared Photometry of High-Redshift Galaxies	25108
Giard, M.	Infrared Emission of SZ Galaxy Clusters	15940
Goldschmidt, P.	The Physical Causes of Quasar Evolution	19130
González-Serrano, J.	Infrared Photometry of a Complete Sample of B2 Radio Quasars: Properties of Low-Luminosity Radio Quasars	12649
Kawara, K.	ISO Observations around Known Objects at High-Redshift: A Search for Primeval Galaxies around Known Objects	6236
Kawara, K.	ISO Study of Evolution of Quasar Spectra: Spectral Evolution Separated from Luminosity Effect	25280
Kawara, K.	Mid- and Far-Infrared Photometry of High-Redshift QSOs: Dust in High-Redshift QSOs	16654
Keel, W.	Stellar Populations in a Cluster of Galaxies at $z=2.4$	25609
Le Fèvre, O.	Evolution of Galaxies in Very High-Redshift Clusters	49317
Lonsdale, C.	Ultraluminous High-Redshift IRAS Galaxies	11504
Malhotra, S.	Studying Dust in Gravitational Lenses at High-Redshift	3362
Malkan, M.	Dust in Proto-Galaxies: The First Measurements of the Rest-Frame Infrared Emission from Young Galaxies	7388
McHardy, I.	Could Emission from Dust in Clusters of Galaxies Confuse Observations of the Sunyaev-Zeldovich Effect?	5364
McMahon, R.	Dust Masses and the Far-Infrared Properties of the Most Distant Quasars.	6570
Mellier, Y.	Arclets in Three Intermediate Redshift Clusters	25753
Mirabel, I.	Clusters of Galaxies at Early Epochs of the Universe	25454
Mirabel, I.	Continuation of the Search for Clusters of Galaxies at Early Epochs of the Universe	22577
Mobasher, B.	Photometry of Galaxies in Deep Radio-Selected Surveys	34988
Oliver, S.	Evolution in the SED of Ultraluminous IRAS Galaxies	40002
Puget, J.-L.	Deep Survey at 4.5 Micron: Spectrum of Faint Galaxies in the Near-Infrared Cosmological Window	11029
Puget, J.-L.	Structure of the Far-Infrared Background	206595
Rowan-Robinson, M.	A Deep Large-Area Survey with ISO in Open Time	1271242
Rowan-Robinson, M.	A Survey of the Hubble Deep Field with ISO	67560
Rowan-Robinson, M.	An ISO Survey of the Southern Hubble Deep Field	74166
Rowan-Robinson, M.	Photometric Identification of High-Redshift Objects from IRAS FSS Blank Fields	4526
Sams, B.	The Power Source of High- z Ultraluminous Galaxies	28794
Serra, G.	Infrared Emission of SZ Galaxy Clusters	15371
Stickel, M.	Cold Dust in the Intracluster Medium of Galaxy Clusters	5636
van der Werf, P.	Deep ISOCAM Imaging of Faint Blue Galaxies and Microjansky Radio Sources in the Deepest VLA Field	11655

B.3 Performed Discretionary Time Proposals/Calibration

Discretionary Time proposals were performed under the ‘Open Time’ budget and therefore appear under OT in the above lists.

Many interesting scientific targets were also observed during the ‘Performance Verification Phase’, as part of the AOT commissioning and during the mission for specific calibration purposes. All these data are included in the ISO Data Archive and can be retrieved. But, in many cases, it is not easy to use these data and instrument experts should be contacted before one tries to interpret the observations scientifically.

Appendix C

List of Solar System Objects

From the ISO mission planning point of view the solar system targets differed from other astronomical targets. This is due to the fact that solar system objects (SSOs) have no fixed equatorial coordinates. Therefore they were identified by their names in the Mission Data Base and linked to their corresponding ephemerides. The database of ephemerides contains all outer planets, most of their moons, major comets and selected asteroids.

Observations of solar system targets required tracking of the specific object by the spacecraft via a raster observation (see Section 4.5). As the spacecraft raster option was already used for tracking there was no possibility to use the spacecraft raster mode for observations. Therefore, observations of solar system targets in the spacecraft raster mode were forbidden. Additionally, in a certain direction chopping was not feasible. Section 4.6 lists the available AOTs and restrictions with respect to observations of solar system objects. The spacecraft raster capabilities limited observations to objects with an apparent velocity of less than 2 arcminutes per hour with respect to equatorial coordinates.

There are several additional aspects specific to solar system targets (e.g. change of orbital parameters, eclipse of a moon around a planet, change of galactic background or stray radiation level, etc). Users who intend to work with ISO observations of SSOs retrieved from the ISO Data Archive should refer to the documentation available at the ISO IDC web site under:

<http://www.iso.vilspa.esa.es/> → ISO Explanatory Library → ISO Satellite
on ‘Data reduction and analysis of SSO observations’ for further information.

SSOs observed in the solar system tracking mode have associated numbers in the Mission Data Base that were used to identify these targets to the mission planning system, and therefore the ISO Data Archive (IDA) contains both the target name and the associated number in this list, either of which can be used in searching. Table C.1 gives SSO names and ISO generic numbers for all objects observed in this mode during the mission.

Note that other SSOs may have also been observed in non-tracking mode (i.e. fixed pointing), in which case they will appear in the archive solely by the name given by the observer. Non-tracking mode was used when looking at objects such as dust trails, the zodiacal light and Pluto. These sources are, of course, not included in Table C.1.

In addition, many other SSOs have been seen serendipitously in deep ISOCAM images, in large survey programmes, in the CAM parallel survey and in the PHT serendipity mode.

Table C.1: *Objects observed with ISO using the SSO tracking mode.*

Agamemnon	210911	Neptune	200800
Aneas	211172	Nuwa	210150
Aten	212062	Oljato	212201
Callisto	200504	P/Comas Sola	220014
Ceres	210001	P/Elst-Pizarro	220050
Chiron	212060	P/Encke	220004
Cybele	210065	P/Hale-Bopp	220048
Davida	210511	P/Hartley 2	220028
Deimos	200402	P/Helin-Roman-Alu 1	220033
Diomedes	211437	P/Honda-Mrkos-Pajdusakov	220012
Dionysus	213671	P/IRAS	220017
Egeria	210013	P/Kopff	220015
Europa	200502	P/Reinmuth 1	220035
Europa	210052	P/Schwassmann-W. 1	220001
Frigga	210077	P/Shoemaker-Holt 1	220034
Ganymede	200503	P/Tempel-Tuttle	220029
Hebe	210006	P/Wild 2	220020
Hektor	210624	P/Wirtanen	220018
Hestia	210046	P/Wolf-Harrington	220024
Hispania	210804	Palisana	210914
Hygiea	210010	Pallas	210002
Iapetus	200608	Phaethon	213200
Io	200501	Pholus	215145
Juno	210003	Polyxo	210308
Jupiter	200500	Rodari	212703
Jupiter North Pole	200551	Saturn	200600
Jupiter South Pole	200552	Tezcatlipoca	211980
Kassandra	210114	Titan	200606
Lacadiera	210336	Tokio	210498
Mars	200400	Toutatis	214179
Massalia	210020	Uranus	200700
Melete	210056	Vesta	210004
Metis	210009	Wilson-Harrington	214015
Mimistobel	213840		

Appendix D

Satellite Files

This chapter describes all the general data files that can be obtained from the ISO Data Archive related to the satellite as a whole and not to any individual instrument,

For information on instrument specific files the instrument specific volumes (II to V) of the Handbook should be consulted.

D.1 Attitude and Orbit Control System (AOCS)

This file contains raw AOCS data copied from telemetry frames 4, 12, 20 and 28, each of identical layout, used for the derivation of the pointing information included in the IIPH (see Section D.12) and IRPH (see Section D.13) files.

D.1.1 Primary header

The AOCS file contains a primary header with the fields described in Table D.1. In this example non-mandatory fields are filled with example values.

D.1.2 Records

The AOCS file contains records described in Table D.2.

The AOCSFRAM record is described in Table D.3.

Table D.1: *AOCS primary header.*

Keyword	Value	Description
SIMPLE =	T	/
BITPIX =	8	/
NAXIS =	0	/
EXTEND =	T	/
ORIGIN =	'ESA '	/ European Space Agency
TELESCOP =	'ISO '	/ Infrared Space Observatory
COMMENT		Raw AOCS frames
FILENAME =	'AOCS01700101'	/ File name in ISO archive
DATE =	'09/07/95'	/ Creation date
FILEVERS =	'0298 '	/ Version ID in ISO archive
OLPVERS =	'OLP_21 '	/ SOC OLP system version
CALGVERS =	'CALG_31 '	/ SOC OLP CAL-G files version
USERNAME =	'PIPELINE'	/
VERS1 =	'1082/EOHA017'	/ Version ID of each input file
VERS2 =	'1082/EOHI017'	/ Version ID of each input file
VERS3 =	'1082/APPH017'	/ Version ID of each input file
EQUINOX =	2000.0	/ Equinox
TMRATE =	32	/ Telemetry rate in Kbps (Kbits/sec)

Table D.2: *AOCS records.*

Keyword	Number	Format	Description
GEPRTKEY	1	I4	UTK time key
GEPRQUAL ¹	1	I4	Frame quality
AOCSFRAM ²	256	I1	Frame 4, 12, 20 or 28

Notes:

1. The 32-bit integer GEPRQUAL gives the quality of the telemetry frame from which AOCSFRAM was extracted. The most significant bit (bit 31) refers to frame 0, the least (bit 0) to frame 31. A bit set to 1 shows the corresponding frame is bad and should be ignored. e.g. if bit 27 is set to 1, then frame 4 is bad. It is recommended that the AOCSFRAM should be ignored for any non-zero GEPRQUAL.
2. Frames 4, 12, 20 or 28 (the AOCS frames) all have the same layout.

Table D.3: Description of AOCSFRAM field.

Keyword	Number	Format	Description
HEADER	10	I1	Frame header
TKEY	1	I4	AOCS time, TUNIT=0.5s
LAYOUT	1	I2	Frame layout information
ATTQUAT	4	I4	Integer-coded attitude quaternion
FSSX	1	I2	FSS X output data
FSSY	1	I2	FSS Y output data
GYRDATA	4	I2	GYR1-4 output rate data
SASDATA	1	I2	SAS channels 1-9 output
RWSSPD	4	I2	RWL 1-4 speeds (tachometer output)
TORQREQ	3	I2	RWS & RCS torque requests
WDSTAT	1	I2	Watch Dog status word
PDUADIG	1	I2	Branch 1 RCS relay status
PDUBDIG	1	I2	Branch 2 RCS relay status
PDUAMEMR	1	I2	Contents of PDU A memory
PDUBMEMR	1	I2	Contents of PDUB memory
ACCHW	1	I2	ACC H/W status word
AOCSSTAT	1	I2	AOCS status word
MODSDAT	1	I2	Mode specific data
INHISTAT	1	I2	Inhibit status
SCOMSTAT	1	I2	Single word command status
MCOMSTAT	1	I2	Multiple word command status
RMCSTAT	1	I2	RMC status
STRY ¹	1	I2	STR output Y-coordinate of guide star
STRZ ²	1	I2	STR output Z-coordinate of guide star
STRMAGG ³	1	I2	STR output magnitude of guide star
STRSTAT1	1	I2	STR mode status information
STRHC	1	I2	STR health check status
STRHK1	1	I2	STR housekeeping data
REGULAR	20	I1	Regular TM buffer
STRHK2	1	I2	
STRYOUT2	1	I2	
STRZOUT2	1	I2	
STRMAG2	1	I2	
STRYOUT3	1	I2	
STRZOUT3	1	I2	
STRMAG3	1	I2	
STRYOUT4	1	I2	
STRZOUT4	1	I2	
STRMAG4	1	I2	
RASPOID	2	I2	Raster point ID
E_ATTIT	3	I4	Integer-coded attitude error vector
HSENDOR	1	I2	
GSTARIN	1	I2	
IRREGULA	98	I1	Irregular TM buffer
TRAILER	2	I1	Frame trailer

Notes:

1. STRY refers to the position of the star's image on the CCD. It is measured in Star-Tracker instrumental units of $1/7 \mu\text{m}$, which correspond to approximately $0.24''$. The maximum and minimum values are 30106 and -30106 .
2. STRZ refers to the position of the star's image on the CCD. It is measured in Star-Tracker instrumental units of $1/7 \mu\text{m}$, which correspond to approximately $0.24''$. The maximum and minimum values are 22378 and -22378 .
3. This is the visual magnitude of the star, with magnitude 2.0 represented as 0 and 8.0 represented as 120. The resolution is approximately 0.05 mag.

D.2 ISO Operational Guide-Star List (APHSTAR)

This file contains information on the guide stars used by ISO.

D.2.1 Primary header

The APHSTAR file contains a primary header with the fields described in Table D.4. In this example non-mandatory fields are filled with example values.

Table D.4: *APHSTAR primary header.*

Keyword	Value	Description
SIMPLE =	T	/ File does conform to FITS standard
BITPIX =	8	/ Number of bits per data pixel
NAXIS =	0	/ Number of data axes
EXTEND =	T	/ FITS dataset may contain extensions
COMMENT		FITS (Flexible Image Transport System) format defined in
COMMENT		Astronomy and Astrophysics Supplement Series v44/p363,
COMMENT		v44/p371, v73/p359, v73/p365.
COMMENT		Contact the NASA Science Office of Standards and Technology
COMMENT		for the FITS Definition document #100 and other FITS
COMMENT		information.
ORIGIN =	'ESA '	/ Not from central ESA archive
TELESCOP =	'ISO '	/ Infrared Space Observatory
COMMENT		ISO operational guide-star list
FILENAME =	'APHSTAR '	/ File name in archive
DATE =	'1999-11-18'	/ Date of addition to archive
FILEVERS =	'1919 '	/ File version in archive
OLPVERS =	'OLP_80B1'	/ SOC OLP system version
CALGVERS =	'CALG_40 '	/ SOC OLP CAL-G files version
USERNAME =	'APOLLOCK'	/ Product not catalogued
DATE-OLD =	'1999-05-17'	/ Date of original creation by IDT

D.2.2 Records

The APHSTAR file contains records described in Table D.5.

Table D.5: *APHSTAR records.*

Keyword	Number	Format	Description
REFNUM	1	I4	ISO guide-star catalogue reference number
TYC	2	I2	Tycho Catalogue identifier (TYC(3)=1)
HIP	1	I4	Hipparcos Catalogue identifier
VMAG	1	R4	V magnitude
PMOTION	2	I4	Proper motion in (arcsec/yr)*100000
PARALLAX	1	I4	Trigonometric parallax in arcsec*100000
SPARE	4	I1	Spare space

D.3 Aperture Pointing History (APPH)

This file contains the history of the aperture pointing.

D.3.1 Primary header

The APPH file contains a primary header with the fields described in Table D.6. In this example non-mandatory fields are filled with example values.

Table D.6: *APPH primary header.*

Keyword	Value	Description
SIMPLE =	T	/
BITPIX =	8	/
NAXIS =	0	/
EXTEND =	T	/
ORIGIN =	'ESA '	/ European Space Agency
TELESCOP =	'ISO '	/ Infrared Space Observatory
COMMENT		Attributes of instantiated Observations
FILENAME =	'APPH '	/ File name in ISO archive
DATE =	'09/07/95'	/ Creation date
FILEVERS =	'0298 '	/ Version ID in ISO archive
OLPVERS =	'OLP_21 '	/ SOC OLP system version
CALGVERS =	'CALG_31 '	/ SOC OLP CAL-G files version
USERNAME =	'PIPELINE'	/
TSTART =	'96117194942'	/ Start time of interval covered (YYDDDHHMMSS)
TSTOP =	'96118194608'	/ End time of interval covered (YYDDDHHMMSS)
GENTIM =	'96118164552'	/ Time of generation of this file (YYDDDHHMMSS)
REVNUM =	162	/ Revolution number
APHVERS =	1	/ APH version number

D.3.2 Records

The APPH file contains records described in Table D.7.

Table D.7: *APPH records.*

Keyword	Number	Format	Description
SLEWSTA	2	I4	Start time of slew to target as seconds since 1989.0 (UTC) followed by remaining fraction of second
SLEWEND	2	I4	End time of slew to target, as above
RA	1	R8	RA of intended view direction in degrees
DEC	1	R8	DEC of intended view direction in degrees
OTFTHRES	1	R4	On-target flag threshold in arcsec
INSTID	1	A1	Instrument ID (C,L,P,S or Z for QSS)
REQTYPE	1	A1	Type of request: 'P'ointing, 'R'aster or 'T'racking
APERTID	1	I2	Aperture identification: from 0 to 4
NGRID	1	I2	Number of grid points on a scan, from 1 to 32 ²
NRASTER	1	I2	Number of lines in the raster, from 1 to 32 ²
TSLEW1	1	I2	Time to slew and dwell on 1st point ^{1,2}
TSLEW2	1	I2	Ditto for a point on the current line ^{1,2}
TSLEW3	1	I2	Ditto for 1st point on next line ^{1,2}
SCANDIST	1	I2	Distance between points on a scanline. Units are usually arcseconds but if REQTYPE='T' then SCANDIST is defined in units of 0.01 arcseconds ²
LINEDIST	1	I2	Distance between scan lines in arcsec ²
ORIENT	1	I1	Orientation raster flag 0=Raster at an angle ROTATE to North 1=Raster starts parallel to the S/C y-axis
SPARE	5	I1	Spare
ROTATE	1	R4	Rotation of raster pattern, in degrees. 0 < ROTATE < 360
QSSQUAT	4	R8	QSS quaternion for the intended viewing direction. Refers to raster centre if REQTYPE is R or T
MISQUAT	4	R8	QSS/Star-Tracker misalignment quaternion
STARVEC	3	R8	Guide star unit vector
REFSTAR	1	R4	Guide star reference number in catalogue
SOLASPCT	1	R4	Solar aspect angle, in degrees
RPEAMP	1	R4	RPE amplitude, in arcsecs
ATTCONT	1	I1	Attitude continuation flag 1=different aperture but same instrument and target as previous record 0=otherwise
CONTINGE	1	I1	Contingency flag 0=no contingency 1=target attitude not acquired 2=no QSS/STR misalignment available
SPARE2	2	I1	Spare

Note:

1. The unit for this is seconds, however it is stored as an unsigned integer. Zero time is therefore equivalent to 32768.
2. Details of the schedule and directions of individual raster points are calculated and given in the IRPH file.

D.4 Aperture Programmed Pointing History (APPM)

This file contains the history of the aperture pointing when the spacecraft was in Programmable Pointing Mode (PPM), normally around perigee passage. History of the aperture pointing in this mode does not appear in the APPH file. It was routinely used to calculate the evolving pointing history of the spacecraft pointing in the IIPH or CIPH near the beginning and end of an orbit.

D.4.1 Primary header

The APPM file contains a primary header with the fields described in Table D.8. In this example non-mandatory fields are filled with example values.

Table D.8: *APPM primary header.*

Keyword	Value	Description
SIMPLE =	T	/
BITPIX =	8	/
NAXIS =	0	/
EXTEND =	T	/
ORIGIN =	'ESA '	/ European Space Agency
TELESCOP =	'ISO '	/ Infrared Space Observatory
COMMENT		Attributes of instantiated Observations
FILENAME =	'APPM '	/ File name in ISO archive
DATE =	'09/07/95'	/ Creation date
FILEVERS =	'0298 '	/ Version ID in ISO archive
OLPVERS =	'OLP_21 '	/ SOC OLP system version
CALGVERS =	'CALG_31 '	/ SOC OLP CAL-G files version
USERNAME =	'PIPELINE'	/
CREATOR =	'MAKE_APPM v1.0'	/Application that created the file
DATE-OLD =	'1999-08-16'	/ Date of original creation by IDT

D.4.2 Records

The APPM file contains records described in Table D.9.

Table D.9: *APPM records.*

Keyword	Number	Format	Description
POFUTS	1	A11	/ Planned start time of PPM episode
EPISODE	1	A9	/ 'PPM_EXIT' or 'PPM_ENTRY'
INDEX	1	A9	/ PPM index number
APERTURE	1	A2	/ Aperture in use = 'X0'
REQTYPE	1	A1	/ Type of pointing request = 'X'
UTCS	2	I4	/ UTC time key of actual PPM start
UTCE	2	I4	/ UTC time key of actual PPM end
UTKS	1	I4	/ UTK time key of actual PPM start
UTKE	1	I4	/ UTK time key of actual PPM end
RA	1	R8	/ RA of reference PPM direction, in degrees
DEC	1	R8	/ DEC of reference PPM direction, in degrees
ROLL	1	R8	/ ROLL of reference PPM direction, in degrees
STRQ	4	R8	/ Reference Star-Tracker quaternion
REV	1	I4	/ Revolution
LENGTH	1	I4	/ Number of PPM AOCS frames
SPARE	1	8A	/ Spare

D.5 Executed Observation History per AOT (EOHA)

This is the Executed Observation History per AOT file. One of its uses was to transfer what was known as TDATA between the uplink and downlink parts of the system. TDATA, or ‘Transparent Data’, is information about the observation that did not need to be uplinked to the satellite but that was needed to process the data. It was ‘transparent’ (not looked at) to the spacecraft controllers. Such data include the proposer ID, proposal ID, etc. Its main use was in defining the time limits of observations to show how ISO telemetry was divided.

D.5.1 Primary header

The EOHA file contains a primary header with the fields described in Table D.10. In this example non-mandatory fields are filled with example values.

Table D.10: *EOHA primary header.*

Keyword	Value	Description
SIMPLE =	T	/
BITPIX =	8	/
NAXIS =	0	/
EXTEND =	T	/
ORIGIN =	'ESA '	/ European Space Agency
TELESCOP =	'ISO '	/ Infrared Space Observatory
COMMENT		Attributes of instantiated Observations
FILENAME =	'EOHA264 '	/ File name in ISO archive
DATE =	'09/07/95'	/ Creation date
FILEVERS =	'0298 '	/ Version ID in ISO archive
OLPVERS =	'OLP_21 '	/ SOC OLP system version
CALGVERS =	'CALG_31 '	/ SOC OLP CAL-G files version
USERNAME =	'PIPELINE'	/

D.5.2 Records

The EOHA file contains records described in Table D.11.

Table D.11: *EOHA records.*

Keyword	Number	Format	Description
EOHATDTN	1	A6	TDT number
EOHAUTCS	1	A11	UTC start of observation (yydddhhmmss)
EOHAUTCE	1	A11	UTC end of observation (yydddhhmmss)
EOHAINST	1	A1	Prime instrument ID
EOHANCPU	1	A1	# CAM peak-ups (obsolete) Field is always 0
EOHARES	1	A14	Reserved
EOHAAOTN	1	A4	AOT name
EOHAPRID	1	A8	Proposer ID
EOHAPLID	1	A8	Proposal ID
EOHAOSN	1	A2	Observation Sequence Number (OSN)
EOHAPSN	1	A2	Pointing Sequence Number (PSN) (obsolete) Field is always 0
EOHAPCAT ¹	1	A1	Proposal category
EOHACIND	1	A1	Calibration indicator
EOHATNAM	1	A16	Target name
EOHASCAT ²	1	A3	Scientific category
EOHALIND	1	A2	Link indicator
EOHASPAR	1	A5	Spare area within observation description
EOHAAOTV	1	A64	AOT/COT variable information (instrument specific)

Notes:

1. EOHAPCAT indicates the proposal category as entered by the user in PGA. The categories were European GT, NASA GT, ISAS GT, OT or Calibration, and these are coded in EOHAPCAT as the ASCII numbers 1 to 5 respectively.
2. EOHASCAT indicates the scientific category as entered by the user in PGA. The categories were Solar System, Interstellar Matter, Stellar Physics, Extragalactic Systems or Cosmology, and these are coded in EOHASCAT as the ASCII numbers 001 to 005 respectively.

D.5.3 CAM AOT specific information

CAM AOT specific information, kept in the 64 bytes of EOHAAOTV, is described in Table D.12.

Table D.12: *AOTV information for CAM.*

Number	Format	Description
2	I2	Raster size
1	I5	Observation duration in seconds (not including slew)
1	A11	Timestamp of AOT to OCT logic
1	A5	AOT/CO to OCT logic version as xx.yy
1	A5	Unused
1	A34	Unused

D.5.4 LWS AOT specific information

LWS AOT specific information, kept in the 64 bytes of EOHAAOTV, is described in Table D.13

Table D.13: *AOTV information for LWS.*

Number	Format	Description
2	I2	Raster size
1	I5	Observation duration in seconds (not including slew)
1	A11	Timestamp of AOT to OCT logic
1	A5	AOT/CO to OCT logic version as xx.yy
1	A5	Unused
1	I1	FPS use flag '1' yes, '0' no and blank for grating
1	I1	FPL use flag '1' yes, '0' no and blank for grating
1	I2	Spare
1	I2	Total number of spectra to be obtained in this observation
1 ¹	I2	Start detector for an L01 AOT
1 ¹	I2	End detector for an L01 AOT
1 ¹	I4	Start zone to cover the L03 wavelength range
1	I4	End zone to cover the L03 wavelength range
1	I4	First zone for FPL for L03 and L04
1	F8.4	Start wavelength of requested range for L01 and L03
1	F8.4	End wavelength of requested range for L01 and L03

Note:

1. These four bytes are used differently depending on the AOT. If the AOT being described is an L01 then the start and end detectors are placed here (as I2's). If it is an L03 then the start zone is placed here instead (as an I4).

D.5.5 PHT AOT specific information

PHT AOT specific information, kept in the 64 bytes of EOHAAOTV, is described in Table D.14

Table D.14: *AOTV information for PHT.*

Number	Format	Description
2	I2	Raster size
1	I5	Observation duration in seconds (not including slew)
1	A11	Timestamp of AOT to OCT logic
1	A5	AOT/CO to OCT logic version as xx.yy
1	A5	Unused
1	I2	Spare
1	A5	Number of measurements in observation
1	I1	Number of sub-observations making up this observation
1	I1	Calibration Sequence used (1–6)
1	A25	Unused

D.5.6 SWS AOT specific information

SWS AOT specific information, kept in the 64 bytes of EOHAAOTV, is described in Table D.15

Table D.15: *AOTV information for SWS.*

Number	Format	Description
2	I2	Raster size
1	I5	Observation duration in seconds (not including slew)
1	A11	Timestamp of AOT to OCT logic
1	A5	AOT/CO to OCT logic version as xx.yy
1	A5	Unused
1	I7	Radial velocity provided by observer in km/s
1	A27	Unused

D.6 Continuous Executed Observation History (EOHC)

The EOHC file was designed to provide a complete contiguous time history of ISO telemetry without any of the time gaps of the EOHA file.

D.6.1 Primary header

The EOHC file contains a primary header with the fields described in Table D.16. In this example non-mandatory fields are filled with example values.

Table D.16: *EOHC primary header.*

Keyword	Value	Description
SIMPLE =	T	/
BITPIX =	8	/
NAXIS =	0	/
EXTEND =	T	/
ORIGIN =	'ESA '	/ European Space Agency
TELESCOP =	'ISO '	/ Infrared Space Observatory
COMMENT		Continuous Executed Observation History
FILENAME =	'EOHC264 '	/ File name in ISO archive
DATE =	'09/07/95'	/ Creation date
FILEVERS =	'0298 '	/ Version ID in ISO archive
OLPVERS =	'OLP_21 '	/ SOC OLP system version
CALGVERS =	'CALG_31 '	/ SOC OLP CAL-G files version
USERNAME =	'PIPELINE'	/

D.6.2 Records

The EOHC file contains records described in Table D.17.

Table D.17: *EOHC records.*

Keyword	Number	Format	Description
EOHCTDTN	1	A6	TDT number
EOHCUTCS	1	A11	UTC start of observation (yydddhhmmss)
EOHCUTCE	1	A11	UTC end of observation (yydddhhmmss)
EOHCINST	1	A1	Prime instrument ID
EOHCNCPU	1	A1	Obsolete column carried over from EOHA
EOHCRES	1	A14	Reserved
EOHCAOTN	1	A4	AOT name
EOHCPRID	1	A8	Proposer ID
EOHCPLID	1	A8	Proposal ID
EOHCOSN	1	A2	Observation Sequence Number (OSN)
EOHCPSN	1	A2	Obsolete column carried over from EOHA
EOHCPCAT	1	A1	Proposal category
EOHCCIND	1	A1	Calibration indicator
EOHCTNAM	1	A16	Target name
EOHCSCAT	1	A3	Scientific category
EOHCLIND	1	A2	Link indicator
EOHCSPAR	1	A5	Spare area within observation description
EOHCAOTV ¹	1	A64	AOT/COT variable information (instrument specific)

Notes:

1. The EOHCAOTV field is a copy of the EOHAOTV field — see previous section.

D.7 Executed Observation History per ICS (EOHI)

This is the Executed Observation History per ICS (Instrument Command Sequence) file.

D.7.1 Primary header

The EOHI file contains a primary header with the fields described in Table D.18. In this example non-mandatory fields are filled with example values.

Table D.18: *EOHI primary header.*

Keyword	Value	Description
SIMPLE =	T	/
BITPIX =	8	/
NAXIS =	0	/
EXTEND =	T	/
ORIGIN =	'ESA '	/ European Space Agency
TELESCOP =	'ISO '	/ Infrared Space Observatory
COMMENT		Information unconnected to a whole AOT
FILENAME =	'EOHI264 '	/ File name in ISO archive
DATE =	'09/07/95'	/ Creation date
FILEVERS =	'0298 '	/ Version ID in ISO archive
OLPVERS =	'OLP.21 '	/ SOC OLP system version
CALGVERS =	'CALG.31 '	/ SOC OLP CAL-G files version
USERNAME =	'PIPELINE'	/

D.7.2 Records

The EOHI file contains records described in Table D.19.

Table D.19: *EOHI records.*

Keyword	Number	Format	Description
EOHITDTN	1	A6	TDT number
EOHIOSN	1	A2	Observation Sequence Number (OSN)
EOHIUTC	1	A11	UTC of sending associated ICS (yydddhhmmss)
EOHIINST	1	A2	Prime instrument ID, followed by instrument aperture
EOHITDTC	1	A3	TDT Component part
EOHIMSG1	1	A64	AOT specific information on ICS level

D.7.3 CAM AOT specific information

No useful information is kept here for CAM.

D.7.4 LWS AOT specific information

For LWS the useful information contained in EOHIMSG1 is shown in Table D.20.

Table D.20: *LWS EOHIMSG1 contents.*

Check	Character	Contents
Requested S/N ratio	4	
Unused	12	
Spectrum number	I2	Spectrum Number. For line spectra it is the number of the current line being observed. For wavelength ranges it indicates which part of the spectrum is being observed. (The wavelength range may be split into two parts, see AOT_VAR contents and also last three entries in this table.
Scan number	I6	Indicates the current scan number being executed of the total number of scans required.
Zone number	I4	Zone number, only AOTs L03 and L04
Wavelength	8	Wavelength as F8.4. For line spectra this gives the expected wavelength of the line being observed. For wavelength ranges it gives the wavelength of the reference line which determined the overall integration time
Incident Power	8	Incident Power as E8.2. For line spectra this gives the expected power for the line being observed. For wavelength ranges it gives the the power for the reference line which determined the overall integration time
Maximum scan	I4	Maximum Scan half width as I4. Only used in line spectra AOTs (L02 and L04). Maximum number of mechanism steps that could be used to cover the line being observed.
Active Detector	I2	Active Detector. For line spectra and L03 AOTs, the detector number used for the line being observed or measured spectrum. For L01 AOT, the detector corresponding to the reference line used to determine the integration time.
Number of scans	I6	Total number of scans to be completed for the line or part of wavelength range.
Total Scans	I4	Total number of scans per measurement to be completed for the line or part of wavelength range.
Illuminator flash	I4	Number of scans to be made between illuminator flashes for the line or part of wavelength range.

D.7.5 PHT AOT specific information

For PHT the useful information contained in EOHIMSG1 is shown in Table D.21.

Table D.21: *PHT EOHIMSG1 contents.*

Check	Character	Contents
Requested S/N	4	
Type of source	1	Either 'P' for point or 'E' for extended
Unused	11	
Expected source flux	8	
Uncertainty	8	Uncertainty in above
Background	8	Maximum background flux
Subsystem	1	Identifies which subsystem is in use
Measurements	3	Number of measurements with subsystem
Unused	20	

D.7.6 SWS AOT specific information

For SWS the useful information contained in EOHIMSG1 is shown in Table D.22.

Table D.22: *SWS EOHIMSG1 contents.*

Check	Character	Contents
Unused	A16	
Scan type	A1	If 'N' then normal resolution scan If 'L' then low resolution scan If 'R' then reference wavelength
SW Measurement	I2	Measurement number SW section Blank if not applicable
LW Measurement	I2	Measurement number LW section Blank if not applicable
SW detector band	1	Requested SW band. Blank, '1' or '2'
LW detector band	1	Requested LW band. Blank or '3' to '6'
SW Band flux	8	Expected flux in relevant SW band as Jy in F8.2 Blank if not applicable
LW Band flux	8	Expected flux in relevant LW band as Jy in F8.2 Blank if not applicable
Unused	25	

D.8 General Housekeeping (GEHK)

This file contains General Housekeeping data. The most important housekeeping data for an observer is the science housekeeping contained in frame 8. This contains information from the prime instrument.

D.8.1 Primary header

The GEHK file contains a primary header with the fields described in Table D.23. In this example non-mandatory fields are filled with example values.

Table D.23: *GEHK primary header.*

Keyword	Value	Description
SIMPLE =	T	/
BITPIX =	8	/
NAXIS =	0	/
EXTEND =	T	/
ORIGIN =	'ESA '	/ European Space Agency
TELESCOP =	'ISO '	/ Infrared Space Observatory
COMMENT		General HK
FILENAME =	'GEHK26400248'	/ File name in ISO archive
DATE =	'09/07/95'	/ Creation date
FILEVERS =	'0298 '	/ Version ID in ISO archive
OLPVERS =	'OLP_21 '	/ SOC OLP system version
CALGVERS =	'CALG_31 '	/ SOC OLP CAL-G files version
USERNAME =	'PIPELINE'	/
VERS1 =	'0518/EOHA083'	/ Version ID of each input file
VERS2 =	'0518/EOHI083'	/ Version ID of each input file
VERS3 =	'0515/APPH083'	/ Version ID of each input file
EQUINOX =	2000.0	/ Equinox
TMRATE =	32	/ Telemetry rate in Kbps (Kbits/sec)

D.8.2 Records

The GEHK file contains records described in Table D.24.

Table D.24: *GEHK records.*

Keyword	Number	Format	Description
GEPRTKEY	1	I4	UTK time key
GEPRQUAL ¹	1	I4	Frame quality
GEHKGST	2	I4	GST in original TDF record
GEHKFR0 ²	256	I1	Frame 0 (spacecraft housekeeping)
GEHKFR8	256	I1	Frame 8 (science housekeeping)
GEHKFR16 ²	256	I1	Frame 16 (spacecraft housekeeping)
GEHKRPID	3	I1	Raster point ID and validity
GEHKDERP ³	509	I1	(ESOC's) derived parameters

Notes:

1. As in the AOCS file, GEPRQUAL is used to determine the quality of the various frames in the GEHK file. GEPRQUAL is a 32 bit integer. The most significant bit (bit 31) refers to frame 0, the least (bit 0) to frame 31. If the relevant bit for frame x is set to 1 then that frame is bad and should be ignored. e.g. if bit 31 is set to 1, then frame 0 is bad.
2. Frame 0 and 16, containing spacecraft housekeeping, are used to generate ERD but are of no use to the general observer.
3. Similarly, ESOC's derived parameters are unlikely to be of interest to the general observer.

D.8.3 CAM frame 8

No useful information is kept here for CAM.

D.8.4 LWS frame 8

No useful information is kept here for LWS.

D.8.5 PHT frame 8

No useful information is kept here for PHT.

D.8.6 SWS frame 8

Table D.25 describes the bits in frame 8 relevant to SWS. Bits are numbered from 0 (LSB) to 7 (MSB). Some of this information is copied over into the SWS status word SWSPSTAT (see the ISO Handbook Volume V on SWS, [108]).

Table D.25: *SWS frame 8 contents.*

Check	Byte	Bit	Contents
Diffuse calibrator	13	4	If bit set then diffuse calibrator on
Grating calibrator	13	4, 5 and 6	If bit set then grating calibrator on
SW scan in AOT7	13	5	If bit set then SW scan in AOT 7
Grating scan	13	5 and/or 6	If bit set then grating scan
FP	13	5, 6 and 7	If bit set then FP on
Dark current	48	0	If bit set then dark current
Photometric check	46	3	If bit set then photometric check
SW grating run	43	0	If bit set then SW grating running
LW grating run	52	0	If bit set then LW grating running
SW scan direction	43	7	If bit set then SW scan
LW scan direction	52	7	If bit set then LW scan

D.9 General Housekeeping (Sampled) (GSHH)

The GSHH file is a sampled version of the GEHK General Housekeeping file, containing every fifteenth records.

Users should refer to section D.8 for a description of the file. Note that in the GSHH file the record fields are (naturally) named GSHHxxxx rather than GEHKxxxx.

D.10 ISO Guide-Star Hipparcos Catalogue Data (HIPPARCHOS)

This file contains information from the Hipparcos¹ catalogue, [83], for the stars used as ISO guide stars. It is not a full extract of the Hipparcos catalogue, but a subset. Users are recommended to refer to the Hipparcos catalogue for further information on the contents of this file. It was used in some detailed pointing corrections and was not designed to be of use to the general observer.

D.10.1 Primary header

The HIPPARCHOS file contains a primary header with the fields described in Table D.26. In this example non-mandatory fields are filled with example values.

Table D.26: *HIPPARCHOS* primary header.

Keyword	Value	Description
SIMPLE =	T	/
BITPIX =	8	/
NAXIS =	0	/
EXTEND =	T	/
ORIGIN =	'ESA '	/ European Space Agency
TELESCOP =	'ISO '	/ Infrared Space Observatory
COMMENT		ISO guide-star Hipparcos catalogue data
FILENAME =	'HIPPARCHOS'	/ File name in ISO archive
DATE =	'09/07/95'	/ Creation date
FILEVERS =	'0298 '	/ Version ID in ISO archive
OLPVERS =	'OLP_21 '	/ SOC OLP system version
CALGVERS =	'CALG_31 '	/ SOC OLP CAL-G files version
USERNAME =	'PIPELINE'	/
CREATOR	'OLP_CREATE v1.0'	/ Task which created the file
CALIBRAT =	'CAL-G v5.6'	/ Calibration Data release
TIME =	'22:45:59'	/ Time of file creation (hh:mm:ss)
DATE-OLD =	'1999-08-16'	/ Date of original creation by IDT

¹Actually it should have been spelled 'HIPPARCOS', as the space astrometry mission, but a different transcription of the greek name was used in IDA

D.10.2 Records

The HIPPARCHOS file contains records described in Table D.27.

Table D.27: *HIPPARCHOS records.*

Keyword	Number	Format	Description
H1	1	I4	Identifier (HIP number)
H3	1	A12	Identifier RA (J1991.25), as ‘h m s’
H4	1	A12	Identifier Dec (J1991.25), as ‘d m s’
H5	1	R4	Johnson V magnitude, in magnitudes
H8	1	R8	alpha (J1991.25), in degrees
H9	1	R8	delta (J1991.25), in degrees
H11	1	R8	Trigonometric parallax, in mas
H12	1	R8	mu_alpha*, in mas/year
H13	1	R8	mu_delta, in mas/year
H14	1	R8	Standard error in alpha (J1991.25), in mas
H15	1	R8	Standard error in delta (J1991.25), in mas
H16	1	R8	Standard error in pi, in mas
H17	1	R8	Standard error in mu_alpha*, in mas/year
H18	1	R8	Standard error in mu_delta, in mas/year
H19	1	R4	Correlation: alpha*/delta
H20	1	R4	Correlation: alpha*/pi
H21	1	R4	Correlation: delta/pi
H22	1	R4	Correlation: alpha*/mu_alpha*
H23	1	R4	Correlation: delta/mu_alpha*
H24	1	R4	Correlation: pi/mu_alpha*
H25	1	R4	Correlation: alpha*/mu_delta
H26	1	R4	Correlation: delta/mu_delta
H27	1	R4	Correlation: pi/mu_delta
H28	1	R4	Correlation: mu_alpha*/mu_delta
H29	1	I4	Data points rejected, in percent
H30	1	R4	F2 (goodness-of-fit)
H31	1	I4	HIP number
H32	1	R4	BT, in magnitudes
H33	1	R4	sigma(BT), in magnitudes
H34	1	R4	VT, in magnitudes
H35	1	R4	sigma(VT), in magnitudes
H37	1	R4	B–V, in magnitudes
H38	1	R4	sigma(B–V), in magnitudes
H40	1	R4	V–I, in magnitudes
H41	1	R4	sigma(V–I), in magnitudes
H44	1	R4	median(Hp), in magnitudes
H45	1	R4	sigma(Hp), in magnitudes
H46	1	R4	Scatter, in magnitudes
H47	1	I4	Number of accepted transits
H49	1	R4	Magnitude at maximum Hp (5th percentile), in magnitudes
H50	1	R4	Magnitude at minimum Hp (95th percentile), in magnitudes
H51	1	R4	Period, in days

H63	1	I4	Position angle, in degrees
H64	1	R4	Angular separation, in arcseconds
H65	1	R4	sigma(separation), in arcseconds
H66	1	R4	delta(Hp), in magnitudes
H67	1	R4	sigma(delta(Hp)), in magnitudes
H75	1	R4	V-I used for reductions, in magnitudes
H0	1	A1	Catalogue (H = Hipparcos)
H2	1	A1	Proximity flag
H6	1	A1	Coarse variability flag
H7	1	A1	Source of magnitude identifier
H10	1	A1	Reference flag for BT and VT
H36	1	A1	Reference flag for BT and VT
H39	1	A1	Source of B-V
H42	1	A1	Source of V-I
H43	1	A1	Reference flag for colour indices
H48	1	A1	Reference flag for photometry
H52	1	A1	Flag (variability type)
H53	1	A1	Flag (variability tables)
H54	1	A1	Flag (light curves)
H55	1	A10	CCDM Identifier
H56	1	A1	Historical status flag
H57	1	I1	Number of catalogue entries
H58	1	I1	Number of components
H59	1	A1	Double/Multiple Systems Annex flag
H60	1	A1	Astrometric source flag
H61	1	A1	Solution quality
H62	1	A2	Component identifiers
H68	1	A1	Survey flag
H69	1	A1	Chart flag
H70	1	A1	Notes flag
H71	1	A6	HD identifier
H72	1	A10	DM (BD) identifier
H73	1	A10	DM (CoD) identifier
H74	1	A10	DM (CPD) identifier
H76	1	A12	Spectral type
H77	1	A1	Source of spectral type
SPARE	29	A1	Spare space

D.11 ISO Focal Plane Geometry (IFPG)

This file contains information on the offsets of the various instrument apertures with respect to the Quadrant Star Sensor (QSS). It was of fundamental importance in calculating instrument fields of view.

D.11.1 Primary header

The IFPG file contains a primary header with the fields described in Table D.28. In this example non-mandatory fields are filled with example values.

Table D.28: *IFPG primary header.*

Keyword	Value	Description
SIMPLE =	T	/
BITPIX =	8	/
NAXIS =	0	/
EXTEND =	T	/
ORIGIN =	'ESA '	/ European Space Agency
TELESCOP =	'ISO '	/ Infrared Space Observatory
COMMENT		ISO Focal Plane Geometry
FILENAME =	'IFPG '	/ File name in archive
DATE =	'09/07/95'	/ Creation date
FILEVERS =	'0298 '	/ Version ID in ISO archive
OLPVERS =	'OLP_21 '	/ SOC OLP system version
USERNAME =	'PIPELINE'	/
DATE-OLD =	'1996-08-14'	/ Date of original creation by IDT

D.11.2 Records

The IFPG file contains records described in Table D.29.

Table D.29: *IFPG records.*

Keyword	Number	Format	Description
SPARE	17	I1	Spare
INSTID	1	A1	Instrument ID (C,L,P,S)
APERTID	1	I2	Aperture ID (1/2/3)
DY	1	R4	Aperture Y-offset with respect to QSS, in arcmin
DZ	1	R4	Aperture Z-offset with respect to QSS, in arcmin
REV	1	I4	Revolution during which the offsets were measured -1 = EE1 tests -2 = EE2 tests

D.12 Instrument Instantaneous Pointing History (IIPH)

This file details the pointing history of the prime instrument during an observation at a rate of two records per second². Any drift in the pointing is reflected in this file. In anticipation of possible future work, the IIPH's binary table contains all the attitude-related quantities that could conceivably have been variable with time, including, in particular, the Star-Tracker/Quadrant Star Sensor (STR/QSS) misalignment quaternion (MISQ). This misalignment is subject to change due to thermal effects and was thus recalibrated at the beginning of each revolution, though the day-to-day changes were small (less than one arcsecond). The changes during a single revolution, which would cause instruments' pointing direction to drift, were probably even smaller. Although it was not possible to estimate the magnitude of any such drift in routine operations, so that the elements of MISQ are constant in the distributed IIPH files, detailed analysis of high-resolution CAM or SWS data might allow the drift history to be estimated, yielding the evolution of the MISQ.

D.12.1 Primary header

The IIPH file contains a primary header with the fields described in Table D.30. In this example non-mandatory fields are filled with example values.

Table D.30: IIPH primary header.

Keyword	Value	Description
SIMPLE =	T	/ File does conform to FITS standard
BITPIX =	8	/ Number of bits per data pixel
NAXIS =	0	/ Number of data axes
EXTEND =	T	/ FITS dataset may contain extensions
ORIGIN =	'ESA '	/ European Space Agency
TELESCOP =	'ISO '	/ Infrared Space Observatory
COMMENT		Instrument Instantaneous Pointing History
FILENAME =	'IIPH64001226'	/ File name in ISO archive
DATE =	'18/08/97'	/ Creation date
FILEVERS =	'0518 '	/ Version ID in ISO archive
OLPVERS =	'OLP_611 '	/ SOC OLP system version
CALGVERS =	'CALG_31 '	/ SOC OLP CAL-G files version
USERNAME =	'PIPELINE'	/
CREATOR =	'DERIVE_IIPH v6.2'	/ Application that created the file
INSTRUME ¹ =	'PHT '	/ Instrument identifier
ATTRA ² =	266.56054	/ Intended Instrument J2000 Right Ascension (degrees)
ATTDEC ² =	+62.45108	/ Intended Instrument J2000 Declination (degrees)
ATTTYPE ³ =	'R '	/ Type of attitude operation

²Another file called CIPH (CAM Instantaneous Pointing History) is the equivalent file for CAM parallel mode observations only.

ATTOTFTH =	2.0	/ On-target threshold (arcsec)
ATTRNPTS =	3	/ Number of points per raster line
ATTRNLNS =	3	/ Number of raster lines
ATTRDPTS =	92	/ Distance between adjacent points (arcsec)
ATTRDLNS =	92	/ Distance between adjacent lines (arcsec)
ATTRORIE =	1	/ Raster orientation flag (0 or 1)
ATTRROTA =	0.0	/ Rotation of raster pattern (degrees)
ATTGUIDE =	93715	/ Guide star reference number
ATTSAANG =	88.7	/ Solar aspect angle (degrees)
ATTERROR =	0	/ 0=OK, 1=target not acquired, 2=No STR/QSS misalignment
ATTMISQ1 =	0.0000000	/ STR/QSS misalignment quaternion Q(1)
ATTMISQ2 =	-0.0004555	/ STR/QSS misalignment quaternion Q(2)
ATTMISQ3 =	-0.0002231	/ STR/QSS misalignment quaternion Q(3)
ATTMISQ4 =	0.9999999	/ STR/QSS misalignment quaternion Q(4)
ATTINSQ1 =	0.0000000	/ QSS/Instrument alignment quaternion Q(1)
ATTINSQ2 =	-0.0000181	/ QSS/Instrument alignment quaternion Q(2)
ATTINSQ3 =	0.0012427	/ QSS/Instrument alignment quaternion Q(3)
ATTINSQ4 =	0.9999992	/ QSS/Instrument alignment quaternion Q(4)
INSTRA =	266.13155	/ Reference instrument J2000 right ascension (degrees)
INSTDEC =	+62.42157	/ Reference instrument J2000 declination (degrees)
INSTROLL =	127.70	/ Reference instrument J2000 roll angle (degrees)
CINSTRA =	266.13155	/ Corrected reference instrument J2000 right ascension
CINSTDEC =	+62.42157	/ Corrected reference instrument J2000 declination
CINSTROL =	127.70	/ Corrected reference instrument J2000 roll angle
VERS1 =	'0518/IRPH08300207'	/ Version ID of each input file
VERS2 =	'0518/AOCS08300207'	/ Version ID of each input file

Notes:

1. During activation the INSTRUME keyword refers to the QSS.
2. Intended RA & Dec of instrument viewing direction in degrees. For SWS it refers to whichever slit is being used, for ATTYPE 'R' or 'T' it refers to the centre of the raster pattern.
3. Type of attitude operation: 'P' for fine pointing; 'R' for raster; and 'T' for SSO tracking.

D.12.2 Records

Each record in the IIPH file has the fields described in Table D.31. All observations will result in a file of many entries – two every second.

Table D.31: IIPH records.

Keyword	Number	Format	Description
UTK	1	I4	UTK time key
UTC	2	I4	UTC time key
RPID	2	I1	Raster pointer ID
APERTURE ¹	1	A2	Aperture in use
OTF	1	I1	On-target flag. 0=Off target, 1=On target
FILTER	1	I1	Attitude filter applied. 0=None, 1=AOCS, 2=Other
SPIKE	1	I1	Attitude spike flag. 0=OK, 1=warning, 2=not defined
SPARE	13	I1	Spare space
ATTQ	4	R8	Instantaneous attitude quaternion
RA ²	1	R8	Right ascension, in degrees
DEC ²	1	R8	Declination, in degrees
ROLL ²	1	R8	Roll angle, in degrees
CORQ	4	R8	Corrected attitude quaternion
CRA	1	R8	Corrected right ascension, in degrees
CDEC	1	R8	Corrected declination, in degrees
CROLL	1	R8	Corrected roll angle, in degrees
STRQ	4	R8	Instantaneous Star-Tracker quaternion
XRA	1	R8	Instantaneous right ascension, in degrees
XDEC	1	R8	Instantaneous declination, in degrees
XROLL	1	R8	Instantaneous roll angle, in degrees

Notes:

1. During spacecraft activation the APERTURE keyword contains 'Z0', the aperture of the QSS.
2. RA , DEC and ROLL are all measured in degrees — RA is not measured in hh:mm:ss. See the definition in Appendix F of RA, DEC and ROLL.

D.13 Instrument Reference Pointing History (IRPH)

This file details the complete set of reference sky positions that apply to an observation³. A staring observation has one record per aperture; a raster observation has one record per raster point per raster. As the name suggests, these directions provide the reference points for the calculation of the OTF in the IIPH.

D.13.1 Primary header

The IRPH file contains a primary header with the fields described in Table D.32. In this example non-mandatory fields are filled with example values.

Table D.32: *IRPH primary header.*

Keyword	Value	Description
SIMPLE =	T	/ File does conform to FITS standard
BITPIX =	8	/ Number of bits per data pixel
NAXIS =	0	/ Number of data axes
EXTEND =	T	/ FITS dataset may contain extensions
ORIGIN =	'ESA '	/ European Space Agency
TELESCOP =	'ISO '	/ Infrared Space Observatory
COMMENT		Instrument Reference Pointing History
FILENAME =	'IRPH08300207'	/ File name in ISO archive
DATE =	'12/02/96'	/ Creation date
FILEVERS =	'0518 '	/ Version ID in ISO archive
OLPVERS =	'OLP_242 '	/ SOC OLP system version
CALGVERS =	'CALG_31 '	/ SOC OLP CAL-G files version
USERNAME =	'PIPELINE'	/
CREATOR =	'DERIVE_IPH v2.0'	/ Application that created the file
INSTRUME ¹ =	'CAM '	/ Instrument identifier
ATTRA ² =	266.56054	/ Intended Instrument J2000 Right Ascension (degrees)
ATTDEC ² =	+62.45108	/ Intended Instrument J2000 Declination (degrees)
ATTTYPE ³ =	'R '	/ Type of attitude operation
ATTOTFTH =	10.0	/ On-target threshold (arcsec)
ATTRNPTS =	3	/ Number of points per raster line
ATTRNLNS =	3	/ Number of raster lines
ATTRDPTS =	92	/ Distance between adjacent points (arcsec)
ATTRDLNS =	92	/ Distance between adjacent lines (arcsec)
ATTRORIE =	1	/ Raster orientation flag (0 or 1)
ATTRROTA =	0.0	/ Rotation of raster pattern (degrees)
ATTGUIDE =	93715	/ Guide star reference number
ATTSAANG =	88.7	/ Solar aspect angle (degrees)
ATTERROR =	0	/ 0=OK, 1=target not acquired, / 2=No STR/QSS misalignment

³Another file called CRPH (CAM Reference Pointing History) is the equivalent file for CAM parallel mode observations only.

ATTMISQ1 =	0.0000000	/ STR/QSS misalignment quaternion Q(1)
ATTMISQ2 =	-0.0004555	/ STR/QSS misalignment quaternion Q(2)
ATTMISQ3 =	-0.0002231	/ STR/QSS misalignment quaternion Q(3)
ATTMISQ4 =	0.9999999	/ STR/QSS misalignment quaternion Q(4)
ATTINSQ1 =	0.0000000	/ QSS/Instrument alignment quaternion Q(1)
ATTINSQ2 =	-0.0000181	/ QSS/Instrument alignment quaternion Q(2)
ATTINSQ3 =	0.0012427	/ QSS/Instrument alignment quaternion Q(3)
ATTINSQ4 =	0.9999992	/ QSS/Instrument alignment quaternion Q(4)
INSTRA =	266.13155	/ Reference instrument J2000 right ascension (degrees)
INSTDEC =	+62.42157	/ Reference instrument J2000 declination (degrees)
INSTROLL =	127.70	/ Reference instrument J2000 roll angle (degrees)
CINSTRA =	266.13155	/ Corrected reference instrument J2000 right ascension (degrees)
CINSTDEC =	+62.42157	/ Corrected reference instrument J2000 declination (degrees)
CINSTROL =	127.70	/ Corrected reference instrument J2000 roll angle (degrees)
VERS1 =	'0518/EOHA083'	/ Version ID of each input file
VERS2 =	'0518/EOHI083'	/ Version ID of each input file
VERS3 =	'0515/APPH083'	/ Version ID of each input file
VERS4 =	'0456/IFPG'	/ Version ID of each input file
VERS5 =	'1047/ISTR'	/ Version ID of each input file
VERS6 =	'1047/SOLUN'	/ Version ID of each input file
VERS7 =	'1350/ORBIT'	/ Version ID of each input file

Notes:

1. During spacecraft activation the INSTRUME keyword refers to the QSS.
2. Intended RA & Dec of instrument viewing direction in degrees. For SWS it refers to whichever slit is being used, for ATTYPE 'R' or 'T' it refers to the centre of the raster pattern.
3. Type of attitude operation; 'P' for fine pointing; 'R' for raster; and 'T' for SSO tracking.

D.13.2 Records

Each record contains the fields described in Table D.33.

Table D.33: *IRPH records.*

Keyword	Number	Format	Description
RA0	1	R8	Raster centre reference right ascension, in degrees
DEC0	1	R8	Raster centre reference declination, in degrees
ROLL0	1	R8	Raster centre reference roll angle, in degrees
SPARE	1	I1	Spare space
TYPE	1	A1	Type of pointing operation
RPID	2	I1	Raster pointer ID
UTC ¹	1	I4	UTC of start of observation, in seconds, since 1989.0
STRQ	4	R8	Star-Tracker point quaternion
INSQ	4	R8	QSS/aperture alignment quaternion
RPQ	4	R8	Raster point quaternion
RA ²	1	R8	Uncorrected raster point reference right ascension, in degrees. It is derived from the APPH file
DEC ²	1	R8	Uncorrected raster point reference declination, in degrees
ROLL ²	1	R8	Uncorrected raster point reference roll angle, in degrees
CORQ	4	R8	Raster point correction quaternion
CRA	1	R8	Corrected raster point reference right ascension, in degrees
CDEC	1	R8	Corrected raster point reference declination, in degrees
CROLL	1	R8	Corrected raster point reference roll angle, in degrees
OTFT	1	R4	On-target flag threshold, in arcsec
APERTURE ³	1	C2	Instrument/aperture combination (e.g. 'S3')
FILLER	2	I1	For alignment

Note:

1. The UTC start time in the IRPH is the time at which the satellite starts to slew and point towards the raster point in question.
2. RA, DEC and ROLL are all measured in degrees — RA is not measured in hh:mm:ss. See the definition in Appendix F of RA, DEC and ROLL.
3. During activation the APERTURE keyword contains 'Z0', the aperture of the QSS.

D.14 ISO Star-Tracker Calibration Data (ISTR)

This file contains information on the operational Star-Tracker.

D.14.1 Primary header

The ISTR file contains a primary header with the fields described in Table D.34. In this example non-mandatory fields are filled with example values.

Table D.34: *ISTR* primary header.

Keyword	Value	Description
SIMPLE =	T	/
BITPIX =	8	/
NAXIS =	0	/
EXTEND =	T	/
ORIGIN =	'ESA '	/ European Space Agency
TELESCOP =	'ISO '	/ Infrared Space Observatory
COMMENT		ISO Star-Tracker calibration data
FILENAME =	'ISTR'	/ File name in ISO archive
DATE =	'09/07/95'	/ Creation date
FILEVERS =	'0298 '	/ Version ID in ISO archive
OLPVERS =	'OLP_21 '	/ SOC OLP system version
CALGVERS =	'CALG_31 '	/ SOC OLP CAL-G files version
USERNAME =	'PIPELINE'	/
DATE-OLD =	'1997-07-14'	/ Date of original creation by IDT

D.14.2 Records

The ISTR file contains records described in Table D.29.

Table D.35: *ISTR* records.

Keyword	Number	Format	Description
F	1	R8	Focal length, in metre
DFY	1	R8	Focal length fractional error Y-component
DFZ	1	R8	Focal length fractional error Z-component
X10	1	R8	FSS-Z misalignment parameter
DX10	1	R8	FSS-Z misalignment parameter error equivalent angle, in arcsec
STRX	1	R8	STR-X misalignment, in degrees
DSTRX	1	R8	STR-X misalignment error, in arcsec
REV	1	I4	Revolution after which the measurements apply
UTC	1	I4	UTC after which the measurements apply, in seconds since 1989.0
SPARE	16	I1	Spare space

D.15 ORBIT

The ORBIT file contains all the information needed to reconstruct the orbital parameters of the ISO spacecraft. As it is not merely a tabulation of data conforming to the FITS standard but also contains, for example, variable numbers of interpolation coefficients, some accompanying software is required for its proper use. The subroutine MC_ORBIT, listed at the end of this section may be used for this purpose.

This file holds also compressed and detailed information about the complete history of the spacecraft's geocentric position and velocity. For the convenience of observers, at three times during an observation (at the start, middle and end) ISO's heliocentric velocity and velocity towards the target is determined from this file and inserted in the headers of the corresponding instrument data files as described in the instrument specific volumes (II to V) of this Handbook. These data are kept in two sets of three keywords, TREFHEL1,2,3 and TREFDOP1,2,3, along with the corresponding UTC and orbital phase, kept in the TREFCOR1,2,3 and TREFPHA1,2,3 keywords. Note that the spacecraft velocities reported do not include any component of the velocity of the target, SSO or otherwise.

D.15.1 Primary header

The ORBIT file contains a primary header with the fields described in Table D.36. In this example non-mandatory fields are filled with example values.

Table D.36: *ORBIT* primary header.

Keyword	Value	Description
SIMPLE =	T	/
BITPIX =	8	/
NAXIS =	0	/
EXTEND =	T	/
ORIGIN =	'ESA '	/ European Space Agency
TELESCOP =	'ISO '	/ Infrared Space Observatory
COMMENT		Compressed orbit file
FILENAME =	'ORBIT'	/ File name in ISO archive
DATE =	'07/07/98'	/ Creation date
FILEVERS =	'1350 '	/ Version ID in ISO archive
OLPVERS =	'OLP_632 '	/ SOC OLP system version
CALGVERS =	'CALG_31 '	/ SOC OLP CAL-G files version
USERNAME =	'PIPELINE'	/
COMMENT		This file contains ISO orbit data. It can only be interpreted using the software 'MCRORB' within the MC package, or using similar software supplied directly by ESOC.

D.15.2 Records

The ORBIT file contains records described in Table D.37.

Table D.37: *ORBIT* records.

Keyword	Number	Format	Description
ORBITDAT	1	A80	Orbit parameters (composite structure)

D.15.3 MC_ORBIT subroutine

This section lists the FORTRAN subroutine used to read the ORBIT file above described. There is only one call in this subroutine that needs explanation, that of MCRPR.

```
CALL MCRPR (LFILE, RECORD, 80, EOF, BUFFER)
```

reads from unit number LFILE (I*4) record number RECORD (I*4). This record is expected to be 80 bytes long. If, on return, the logical EOF is true it indicates that the requested record was out of the range of the file, otherwise the record is placed in BUFFER (in this case C*80).

```

SUBROUTINE MC_ORBIT(DAY,KODE,LFILE,IERROR,NSAT,X,REVNUM)
C+++++
CP ORBIT: RETRIEVAL ROUTINE FOR COMPRESSED LTOF/STOF ORBIT FILE,
C     delivered under the original name of "ORBIT" by ESOC/OAD.
C
C The following changes have been made by J. Sternberg to the original
C routine supplied by ESOC/OAD in March 1995.
C   1. Name changed to MC_ORBIT (= MC package convention).
C   2. Every formatted READ statement was converted to an UNformatted READ
C      (MCRPR) followed by an internal READ, keeping the same statement
C      numbers for the FORMAT, "END=" and "ERR=" labels.
C   3. NEXT_RECORD was introduced, to keep track of file position,
C      because ORBIT is a direct access file instead of sequential.
C   4. A REWIND statement was replaced by an assignment of NEXT_RECORD to 1.
C   5. IMPLICIT statement was completed for all initial letters, due to
C      /WARNINGS option being in use.
C Anyone outside the SOC trying to use this routine could de-integrate it
C from the MC package, by reversing the above-mentioned changes, i.e. by
C removing everything to do with MCRPR, LFILE_BUFFER, and NEXT_RECORD.
C
C OAD's UPDATE OF 1994/08/30
C OAD's UPDATE OF 1995/03/24: REMOVE REFERENCE TO CLUSTER
C                           CHANGE SEARCH FOR FIRST BLOCK RECORD
C                           RETURN EARLIEST/LATEST DATES IF INVALID DAY
C
C INPUT:
CI DAY (R*8) = MODIFIED JULIAN DAY, FROM 2000, FOR THE STATE VECTOR

```

```

CI  KODE (I*4) = NUMBER OF COMPONENTS OF STATE VECTOR = DIM. OF ARRAY
C      X(); = 3 FOR S/C POSITION, = 6 FOR POSITION & VELOCITY
CI  LFILE (I*4) = LOGICAL NUMBER OF INPUT DATA FILE
C  OUTPUT:
CO  IERROR (I*4) = RETURN CODE: 0=NO ERROR, 1='DAY' TOO EARLY, 2=TOO
C      LATE, 3=TIME GAP IN DATA, 4=WRONG VALUE OF 'KODE',
C      5=FILE CONTENT INCONSISTENT, 6=READ ERROR FROM DATA FILE
CO  NSAT (I*4) = SATELLITE NUMBER: FROM 1 to 99
CO  X(KODE) (R*8) = SPACECRAFT POSITION, KM (AND VELOCITY, KM/S)
CO      IF 'IERROR' = 1 THEN X(2) = EARLIEST TIME (MJD2000)
CO      IF 'IERROR' = 2 THEN X(3) = LATEST TIME (MJD2000)
CO  REVNUM (R*8) = REVOLUTION NUMBER
C
CF  READS A SEQUENTIAL FORMATTED FILE WITH LOGICAL NUMBER 'LFILE'
C-----
      IMPLICIT REAL*8(A-H,O-Z), INTEGER*4(I-N)
      DIMENSION Y(6),COEFF(10,6),X(KODE)
      CHARACTER*3 CH3
      INTEGER*4 LFILE_BUFFER(20)    !added by JRS, for integration with MC
      CHARACTER*80 CFILE_BUFFER    !added by JRS, for integration with MC
      EQUIVALENCE (LFILE_BUFFER, CFILE_BUFFER) ! for integration with MC
      INTEGER*4 NEXT_RECORD        !added by JRS, for integration with MC
      LOGICAL*4 EOF                !added by JRS, for integration with MC
C  INITIALISE FILE NUMBER TO FORCE FILE READING AT FIRST CALL
      DATA MFILE/-9999/
C
C  PARAMETERS SAVED INSIDE ROUTINE: NSATIN,MFILE,DAYFIR,DAYLAS,Y(),
C  RDIST,COEFF(,),KOEFF,DAYBEG,DAYEND,EPOCH,REVEPO,SMAXIS,OMOTIN
      SAVE
C
C  INITIALISE ERROR CODES
      IERROR = 0
      IF(KODE .LE. 0) GOTO 504
      IF(KODE .GT. 6) GOTO 504
C
C  ALWAYS REWIND IF A NEW FILE NUMBER IS USED
      IF(LFILE .NE. MFILE) GOTO 10
C
C  CHECK IF 'DAY' IS INSIDE LAST READ RECORD BLOCK
      IF(DAY .GT. DAYEND + 1.D-4) GOTO 20
      IF(DAY .GE. DAYBEG - 1.D-4) GOTO 70
C
C  INITIALISE THE READING FROM THE FILE
10   DAYFIR = 99.D9
      DAYLAS = 99.D9
      MFILE = LFILE
C  REWIND LFILE          !Commented out by JRS, since not correct for MC
      NEXT_RECORD = 1    !Added by JRS, to replace REWIND
C
20   CONTINUE
C  READ 1ST RECORD IN A BLOCK
      CALL MCRPR (LFILE, NEXT_RECORD, 80, EOF, LFILE_BUFFER)

```

```

        NEXT_RECORD = NEXT_RECORD + 1
        IF (EOF) GOTO 509
        READ (CFILE_BUFFER,41,ERR=506) NSATIN, CH3
41  FORMAT(I3,A3)
C   IF: CH3 IS ' P' OR ' R' THEN THIS IS 1ST RECORD IN A BLOCK
        IF(CH3.NE.' P' .AND. CH3.NE.' R') GOTO 20
        NSAT = NSATIN
C
C   READ 2ND RECORD IN THE BLOCK
CF  NREC = RECORD IDENTIFICATION, SHALL BE = 200 + NSATIN
CF  DAYBEG = BEGIN TIME OF THE RECORD (MJD)
CF  DAYEND = END TIME OF THE RECORD (MJD)
CF  EPOCH = EPOCH OF REFERENCE STATE VECTOR (MJD)
CF  REVEPO = REVOLUTION NUMBER AT EPOCH
CF  SMAXIS = SEMIMAJOR AXIS FOR THE KEPLER ORBIT
CF  OMOTIN = INVERSE MEAN MOTION FOR THE KEPLER ORBIT
        CALL MCRPR (LFILE, NEXT_RECORD, 80, EOF, LFILE_BUFFER)
        NEXT_RECORD = NEXT_RECORD + 1
        IF (EOF) GOTO 509
        READ (CFILE_BUFFER,42,ERR=506)
        &NREC, DAYBEG, DAYEND, EPOCH, REVEPO, SMAXIS, OMOTIN
42  FORMAT(I3,2F12.6,F15.9,F11.3,2F13.5)
C   CHECK CONSISTENCY OF FILE
        IF(NREC .NE. 200 + NSATIN) GOTO 505
        IF(DAYBEG .GT. DAYEND) GOTO 505
C
C   DAYFIR = START TIME OF 1ST RECORD ON 1ST BLOCK ON THE FILE - MARGIN
        DAYFIR = DMIN1(DAYFIR, DAYBEG - 1.D-4)
C   ERROR RETURN IF 'DAY' IS BEFORE START OF FILE (WITH MARGIN)
        IF(DAY .LT. DAYFIR) THEN
            X(2) = DAYFIR
            GO TO 501
        ENDIF
C   ERROR RETURN IF THERE IS A GAP FROM LAST BLOCK (WITH MARGIN)
        IF(DAYBEG .GT. DAYLAS) GOTO 503
C   DAYLAS = END TIME OF LAST READ RECORD BLOCK + MARGIN
        DAYLAS = DAYEND + 2.D-4
C
C   CONTINUE READ IF 'DAY' IS AFTER END OF THIS RECORD BLOCK
        IF(DAY .GT. DAYEND + 1.D-4) GOTO 20
C   REWIND WHEN 'DAY' IS EARLIER THAN START OF PRESENT RECORD BLOCK
        IF(DAY .LT. DAYBEG - 1.D-4) GOTO 10
C
C   READ 3RD RECORD IN THE BLOCK
CF  NREC = RECORD IDENTIFICATION, SHALL BE = 300 + NUMBER OF POL. COEFF.
CF  Y(6) = REFERENCE STATE VECTOR FOR KEPLER ORBIT (KM, KM/S)
CF  RDIST = S/C EARTH CENTRE DISTANCE AT EPOCH
        CALL MCRPR (LFILE, NEXT_RECORD, 80, EOF, LFILE_BUFFER)
        NEXT_RECORD = NEXT_RECORD + 1
        IF (EOF) GOTO 505
        READ (CFILE_BUFFER,43,ERR=506) NREC, Y, RDIST
43  FORMAT(I3,3F11.3,3F11.7,F11.3)

```

```

C CHECK CONSISTENCY OF FILE
  IF(NREC .GT. 310) GOTO 505
  IF(NREC .LT. 300) GOTO 505
C KOEFF = NUMBER OF POLYNOMIAL COEFFICIENTS, BETWEEN 0 AND 10
  KOEFF = NREC - 300
C
C IF THERE ARE NO COEFFICIENTS IN THIS BLOCK
  IF(KOEFF. LE. 0) GOTO 70
  DO 60 K = 1,KOEFF
CF NREC = RECORD IDENT. = KOEFF + 11*K
CF COEFF(10,6) = MATRIX WITH UP TO 10 COEFFICIENTS OF THE CHEBYSHEV
CF POLYNOMIAL FOR EACH OF THE 6 COMPONENTS OF THE STATE VECTOR
  CALL MCRPR (LFILE, NEXT_RECORD, 80, EOF, LFILE_BUFFER)
  NEXT_RECORD = NEXT_RECORD + 1
  IF (EOF) GOTO 505
  READ (CFILE_BUFFER,44,ERR=506) NREC,(COEFF(K,I),I=1,6)
44  FORMAT(I3,3F11.3,3F11.7)
C
C CHECK CONSISTENCY OF FILE
  IF(11*K + KOEFF .NE. NREC) GOTO 505
60  CONTINUE
C END OF BLOCK READING SEQUENCE, PROVIDE OUTPUT DATA
70  CONTINUE
C
C TIME CONVERTED TO DIFFERENCE IN MEAN ANOMALY
  DMANOM = (DAY - EPOCH)*864.D2/OMOTIN
C ORBIT NUMBER
  REVNUM = REVEPO + DMANOM/6.2831853072D0
C
C START MODELLING KEPLER ORBIT
  ARIN = SMAXIS/RDIST
  ARM = (RDIST - SMAXIS)/SMAXIS
  RVWAM = (Y(1)*Y(4) + Y(2)*Y(5) + Y(3)*Y(6))*OMOTIN/SMAXIS**2
C CALC. OF ECC. ANOMALY BY NEWTON'S ITERATION
  TAM = DMANOM - RVWAM
  COMP = 1.D-7 + 1.D-10*DABS(TAM)
  B = TAM
C ITERATIONS TO SOLVE KEPLER'S EQUATION:
  DO 130 ITER = 1,15
  GO = DCOS(B)
  G1 = DSIN(B)
  BET = TAM - ARM*G1 + RVWAM*GO
  D = (BET - B)/(1.DO + ARM*GO + RVWAM*G1)
  B = B + D
C THIS GIVES THE ACCURACY 1.D-14 IN B & THE G'S
  IF(DABS(D) .LE. COMP) GOTO 140
130  CONTINUE
C NO CONVERGENCE, ERROR RETURN
  GOTO 505
140  CONTINUE
  GO = GO - D*G1

```

```

      G1 = G1 + D*GO
      G2 = 1.DO - GO
      G3 = B - G1
      FX = 1.DO - G2*ARIN
      GX = (DMANOM - G3)*OMOTIN
C
      K = MINO(KODE,3)
      DO 150 J = 1,K
150   X(J) = FX*Y(J) + GX*Y(J+3)
C
      IF(KODE .LE. 3) GOTO 170
      RX = DSQRT(X(1)**2 + X(2)**2 + X(3)**2)
      FT = -G1*SMAXIS*ARIN/(OMOTIN*RX)
      GT = 1.DO - G2*SMAXIS/RX
      DO 160 J = 4,KODE
160   X(J) = FT*Y(J-3) + GT*Y(J)
C   END OF MODELLING KEPLER ORBIT
170   CONTINUE
C
C   CHECK IF POLYNOMIAL COEFFICIENTS ARE REQUIRED (1 IS NOT WORTH WHILE)
      IF(KOEFF .LE. 1) GOTO 600
C   MID-POINT & SCALE FACTOR FOR CHEBYSHEV POLYNOMIAL
      DAYMID = 0.5D0*(DAYBEG + DAYEND)
      SCALE = 4.DO/(DAYEND - DAYBEG)
C   ADD CHEBYSHEV POLYNOMIAL TO KEPLER STATE VECTOR
      S = SCALE*(DAY - DAYMID)
      PA = 1.DO
      P = S*0.5D0
C
C   'KODE' = NUMBER OF COMPONENTS OF THE STATE VECTOR
      DO 200 J = 1,KODE
200   X(J) = X(J) + COEFF(1,J) + COEFF(2,J)*P
C
      IF(KOEFF .LE. 2) GOTO 600
      DO 210 L = 3,KOEFF
      PB = PA
      PA = P
      P = S*PA - PB
      DO 210 J = 1,KODE
210   X(J) = X(J) + COEFF(L,J)*P
230   CONTINUE
C
      GOTO 600
C   ERROR RETURNS; IERROR = 5, 6, 4, 3, 2 OR 1
509   CONTINUE
C   END-OF-FILE ONLY IF AT LEAST ONE RECORD HAS BEEN READ
      IF(DAYLAS .LT. 1.D9) THEN
          X(3) = DAYLAS
          GOTO 502
      ENDIF
505   IERROR = -1
506   IERROR = IERROR + 2

```

```
504 IERROR = IERROR + 1
503 IERROR = IERROR + 1
502 IERROR = IERROR + 1
501 IERROR = IERROR + 1
C FORCE A RE-INITIALISATION OF READ AT NEXT CALL AFTER AN ERROR
  MFILE = -9999
600 RETURN
  END
```

D.16 ISO Guide-Star Tycho Catalogue Data (TYCHO)

This file contains information from the Tycho catalogue, [83], for the stars used as ISO guide stars. This file is not a full extract of the Tycho catalogue, but a subset. Users are recommended to refer to the Tycho catalogue for further information on the contents of this file. It was used in some detailed pointing corrections and was not designed to be of use to the general observer.

D.16.1 Primary header

The TYCHO file contains a primary header with the fields described in Table D.38. In this example non-mandatory fields are filled with example values.

Table D.38: *TYCHO* primary header.

Keyword	Value	Description
SIMPLE =	T	/
BITPIX =	8	/
NAXIS =	0	/
EXTEND =	T	/
ORIGIN =	'ESA '	/ European Space Agency
TELESCOP =	'ISO '	/ Infrared Space Observatory
COMMENT		ISO guide-star Tycho catalogue data
FILENAME =	'TYCHO '	/ File name in ISO archive
DATE =	'09/07/95'	/ Creation date
FILEVERS =	'0298 '	/ Version ID in ISO archive
OLPVERS =	'OLP_21 '	/ SOC OLP system version
CALGVERS =	'CALG_31 '	/ SOC OLP CAL-G files version
USERNAME =	'PIPELINE'	/
CREATOR	'OLP_CREATE v1.0'	/ Task which created the file
CALIBRAT =	'CAL-G v5.6'	/ Calibration Data release
TIME =	'22:59:29'	/ Time of file creation (hh:mm:ss)
DATE-OLD =	'1999-08-16'	/ Date of original creation by IDT

D.16.2 Records

The TYCHO file contains records described in Table D.39.

Table D.39: *TYCHO* records.

Keyword	Number	Format	Description
T1	3	I2	TYC identifier
T0	1	C1	Catalogue (T = Tycho)
T2	1	C1	Proximity flag
T3	1	C12	Identifier RA(J1991.25), as 'h m s'
T4	1	C12	Identifier Dec(J1991.25), as 'd m s'

T5	1	R4	Johnson V magnitude
T6	1	C4	Blank
T8	1	R8	alpha(J1991.25), in degrees
T9	1	R8	delta(J1991.25), in degrees
T11	1	R8	Trigonometric parallax, in mas
T12	1	R8	mu_alpha*, in mas/year
T13	1	R8	mu_delta, in mas/year
T14	1	R8	Standard error in alpha(J1991.25), in mas
T15	1	R8	Standard error in delta(J1991.25), in mas
T16	1	R8	Standard error in pi, in mas
T17	1	R8	Standard error in mu_alpha*, in mas/year
T18	1	R8	Standard error in mu_delta, in mas/year
T19	1	R4	Correlation: alpha*/delta
T20	1	R4	Correlation: alpha*/pi
T21	1	R4	Correlation: delta/pi
T22	1	R4	Correlation: alpha*/mu_alpha*
T23	1	R4	Correlation: delta/mu_alpha*
T24	1	R4	Correlation: pi/mu_alpha*
T25	1	R4	Correlation: alpha*/mu_delta
T26	1	R4	Correlation: delta/mu_delta
T27	1	R4	Correlation: pi/mu_delta
T28	1	R4	Correlation: mu_alpha*/mu_delta
T29	1	I4	Data points rejected, in percent
T30	1	R4	F2 (goodness-of-fit)
T31	1	I4	HIP number
T32	1	R4	BT, in magnitudes
T33	1	R4	sigma(BT), in magnitudes
T34	1	R4	VT, in magnitudes
T35	1	R4	sigma(VT), in magnitudes
T37	1	R4	B-V, in magnitudes
T38	1	R4	sigma(B-V), in magnitudes
T41	1	R4	S/N ratio, in magnitudes
T44	1	R4	V(T) scatter, in magnitudes
T45	1	R4	Magnitude at maximum VT (5th percentile), in magnitudes
T46	1	R4	Magnitude at minimum VT (95th percentile), in magnitudes
T7	1	C1	Source of magnitude identifier
T10	1	C1	Reference flag for astrometry
T36	1	C1	Reference flag for BT and VT
T40	1	I1	Astrometric quality flag
T42	1	C1	Source of astrometric data
T43	1	I1	N(photom)
T47	1	C1	Variability (from GCVS/NSV)
T48	1	C1	Variability (from Tycho)
T49	1	C1	Duplicity (from Tycho)
T50	1	C1	Flag (epoch data)
T51	1	C2	CCDM component Identifier
T52	1	I4	PPM identifier
T53	1	I4	HD identifier
T54	1	C10	DM (BD) identifier
T55	1	C10	DM (CoD) identifier
T56	1	C10	DM (CPD) identifier
T57	1	C1	Notes flag
T39	1	C1	Blank
SPARE	36	I1	Spare space

Appendix E

IDA content details

E.1 Off-Line Products

The ISO Data observational products consist of:

Data obtained using AOTs

Most of the scientific observations and many calibration observations have been performed using pre-defined Astronomical Observation Templates (AOTs).

Data Obtained Using Non-Standard Commanding

Many data, especially those obtained during the Performance Verification Phase, from activation sequences and from calibration observations, have been obtained using non-standard commanding. Data obtained using the Calibration Uplink System are an example. Since all these data are of scientific interest, usually the same range of products as defined for AOT-derived data are available. An exception is PHT, for which only ERD is available for these observations (including the two polarisation modes PHT50 & PHT51).

Parallel and Serendipity Data

CAM, PHT and LWS have data which were obtained when the instrument itself was not prime, such as during slews or when other instruments were in staring or raster mode. A suitable range of raw and processed data, as far as possible mirroring of those for AOT-derived data, have been defined and archived. Again, for PHT serendipity mode only ERD data are available.

An overview of the files per product level for each instrument can be found in Tables E.1, E.2 and E.3.

Table E.1: *List of files per product level 'Raw Data'*

Satellite		
IRPH		Instrument Reference Pointing History
IIPH		Instrument Instantaneous Pointing History
CRPH		CAM Reference Pointing History (for parallel mode data only)
CIPH		CAM Instantaneous Pointing History (for parallel mode data only)
CAM		
CSTA		CAM Compact Status
CUFF AAR		CAM User-Friendly log File
CPER ERD		CAM parallel Edited Raw Data
CIER ERD		CAM Image Edited Raw Data
LWS		
LSTA		LWS Compact Status
LIER ERD		LWS Illuminator ERD file
LGER ERD		LWS grating scan ERD file
LSER ERD		LWS FPS scan ERD file
LLER ERD		LWS FPL scan ERD file
LXER ERD		LWS CLO ERD file
LWHK ERD		LWS housekeeping ERD file
LSPD SPD		LWS SPD
LIPD SPD		LWS Illuminator Processed Data
LWGH SPD		LWS glitch history file
PHT		
PSTA		PHT Compact Status
PSTI		PHT serendipity mode Compact Status
P1ER ERD		PHT C100 Edited Raw Data
P2ER ERD		PHT C200 Edited Raw Data
PPER ERD		PHT-P Edited Raw Data
PSER ERD		PHT-S Edited Raw Data
P2ES ERD		PHT C200 Serendipity ERD
PC1D SPD		PHT C100 dark currents
PC2D SPD		PHT C200 dark currents
PP1D SPD		PHT-P1 dark currents
PP2D SPD		PHT-P2 dark currents
PP3D SPD		PHT-P3 dark currents
SWS		
SSTA		SWS Compact Status
SWER ERD		SWS Edited Raw Data
SWSP SPD		SWS Standard Processed Data
SWGK SPD		SWS Glitch History Data

Table E.2: *List of files per product level 'Basic Science'*

Satellite		
IRPH		Instrument Reference Pointing History
IIPH		Instrument Instantaneous Pointing History
CRPH		CAM Reference Pointing History (for parallel mode data only)
CIPH		CAM Instantaneous Pointing History (for parallel mode data only)
CAM		
CSTA		CAM Compact Status
CUFF AAR		CAM User-Friendly log File
CISP SPD		CAM Standard Processed Data
CPSP SPD		CAM parallel Standard Processed Data
LWS		
LSTALWS		Compact Status
LIPD SPD		LWS Illuminator Processed Data
LSAN AAR		LWS Automatic Analysis Results
LSNR AAR		LWS AAR data, no responsivity correction
LIAC AAR		LWS illuminator results summary
LSCA AAR		LWS scan summary file
LGIF AAR		LWS scan group information file
PHT		
PSTA		PHT Compact Status
PSTI		PHT serendipity mode Compact Status
P1ER ERD		PHT C100 Edited Raw Data
P2ER ERD		PHT C200 Edited Raw Data
PPER ERD		PHT-P Edited Raw Data
PSER ERD		PHT-S Edited Raw Data
P2ES ERD		PHT C200 Serendipity ERD
SWS		
SSTA		SWS Compact Status
SWAA AAR		SWS Auto Analysis Results

Table E.3: *List of files per product level ‘Fully Auto-Processed Products’*

CAM		
CMAP AAR	ISOCAM maps of IR flux vs celestial position	
CPSL AAR	CAM Point-Source List	
CSSP AAR	CAM Source Spectrum	
CCIM AAR	CAM calibration images in detector coordinates	
CGLL AAR	CAM Glitch List	
CJAM AAR	CAM Jitter, Memory and Stabilisation information	
CUFF AAR	CAM User-Friendly log File	
CMOS AAR	ISOCAM celestial IR mosaic	
LWS		
LSAN AAR	LWS Automatic Analysis Results	
LSNR AAR	LWS AAR data, no responsivity correction	
LIAC AAR	LWS illuminator results summary	
LSCA AAR	LWS scan summary file	
LGIF AAR	LWS scan group information file	
PHT		
PPAP AAR	PHT-P point source photometry	
PPAE AAR	PHT-P extended source photometry	
PPAS AAR	PHT-P scan & slew photometry	
PLAP AAR	PHT-SL point source spectroscopy	
PLAE AAR	PHT-SL extended source spectroscopy	
PLAS AAR	PHT-SL Raster mode spectroscopy	
PSAP AAR	PHT-SS point source spectroscopy	
PSAE AAR	PHT-SS extended source spectroscopy	
PSAS AAR	PHT-SS Raster mode spectroscopy	
PCAP AAR	PHT-C point source photometry	
PCAE AAR	PHT-C extended source photometry	
PCAS AAR	PHT-C scan & slew photometry	
PGAI AAR	PHT Photometric Image	
PGAU AAR	PHT Uncertainty Image	
PGAT AAR	PHT Exposure Image	
SWS		
SWAA AAR	SWS Auto Analysis Results	

E.1.1 Quality flags

At the time of writing, the following quality categories are present in the ISO Data Archive:

- General:
 - Good: No technical problems.
 - Unknown: The quality assessment was not made for non-standard observations. ‘Unknown’ appears for all AOT99 observations (except CAM99), parallel & serendipity and engineering modes.
 - Never Executed

- Processing problems:
(problems encountered during the different pipeline processing steps; a number of products are missing)
 - Raw and basic science data OK: The first two levels of data products have been derived. Auto-processed data missing.
 - Raw data OK: Only the first level of data products could be derived. Basic science data and auto-processed data missing.
 - No science data available: No data products could be derived.
- Real-Time problems:
(problems during operations of satellite, instruments or with the communication link)
 - TM drop: The data are heavily affected by an interruption of the telemetry.
 - Poor pointing: The actual pointing was significantly off the target, or the target was not acquired at all.
 - Instrument malfunction: The data are heavily affected by a problem in one of the instrument components.

Further information on all events during a specific ISO revolution can be found in the ‘Real-Time Revolution Reports’ (RRPs), in the Observations Details panel.

E.2 Browse Products after OLP

E.2.1 Survey products

These are fully reduced standard data sets, either FITS images or ASCII FITS tables, for survey-type work. Although these products contain fully reduced data, it must be emphasised that the processing is done in a standard and automatic way which does not involve any scientific judgement. These products may serve for statistical or survey-type analysis of large samples.

E.2.2 Icons and postcards

These are static representations in GIF-format of the survey products. Icons are small images intended to give an impression of the data: photometry, an image or a spectrum. Postcards are essentially enlarged icons with annotations added to give users an impression of the flux levels and wavelengths covered. Icons and postcards facilitate a quick-look to scan the data for their particular purposes and identify which data need to be retrieved. These should never be used for scientific work. The postcards are also used to give a quick look impression of the ISO data for a given observation when browsing through ISO information from other archives/databases, in the framework of the Virtual Observatories, within the so-called Postcard Server. Through calling a URL / Java Server Page (JSP) containing the ISO observation identifier, it returns the ISO postcard (GIF image) of this observation and ancillary information embedded into an HTML page (e.g. the observation quality flag or the status of validation of the observation mode used. Links are also provided to specific sections of the ISO Handbook.

A short description follows of the main, instrument-dependent, characteristics of the browse products. More details can be found in the relevant instrument volumes of the ISO Handbook.

1. CAM

Survey Products

These products are the equivalent of the AAR, giving the image from the CMOS file when it exists and CMAP otherwise.

Icons and Postcards

The postcard is the image of the survey product projected in RA,DEC coordinates. It contains a grey-scale coded wedge to indicate flux levels. The icon is a small version of the CMAP/CMOS image shown in detector coordinates. For the CAM spectral observations (CAM04) the mean image of all wavelengths is displayed; the spectrum shown is that of the innermost 10×10 pixels. Up to four multi-filter or multi-PFOV measurements (for a given observation) are shown inside the corresponding icon.

2. LWS

Survey Products

The following processing steps are applied to the standard AAR LSAN file:

- (a) Remove all data points with bad status
- (b) Clip outliers
- (c) Remove individual scans which are inconsistent with the majority of the scans
- (d) Average the remaining scans for each detector.

It should be noted that the resulting spectrum is not stitched together nor is it averaged across detectors. Also, no defringing is applied.

Icons and Postcards

Postcard and icon are spectra. In the case of a raster map only the spectrum of the central point is presented.

3. PHT

Survey Products

The survey product is the equivalent of AAR. No survey product is derived for polarisation observations.

Icons and Postcards

Depending on the observing mode, postcards and icons are: spectrum or flux per filter against wavelength plots (single or multi-filter staring observations with PHT-P, spectrophotometry with PHT-S) flux against aperture size (multi-aperture photometry), image (single filter raster maps with PHT-P and PHT-C) or mosaic (raster map with PHT-S, multi-filter image for PHT-P and PHT-C)

4. SWS

Survey Products

The following processing steps are applied to the standard AAR file:

- (a) Remove all data points with bad or unreliable status
- (b) Flatfield the data such that all detectors are scaled to the same level
- (c) Clip outliers using sigma clipping
- (d) Rebin the data to a grid with the nominal resolution

Icons and Postcards

Postcard and icon are spectra which are presented in a mosaic form when the observation contains more than one wavelength range.

E.3 Other Products

E.3.1 Auxiliary data

Data needed for processing observational data

All spacecraft and instrument data needed to process observational data from the Raw Data level onwards are archived. [Spacecraft pointing and velocity data are examples.]

Mission-planning data

All data needed for the planning of observations, including proposal data abstracts, are archived. [PH reports, the Mission Data Base, the ISO Log and CAL-U files are examples.]

Diagnostic data

All spacecraft and instrument data needed for diagnostic and trend-analysis purposes are archived. [QLA reports and data needed to correlate observational data with orbital position are examples.]

E.3.2 Ancillary data

Space weather

Space weather reports, obtained from external sources, are archived.

E.3.3 Observation details and associated files

There are many observational details and associated files connected to each individual observation in the archive. For example, observation identifiers of all concatenated observations or raster parameters used by the spacecraft when making a celestial map are given in a short summary. Many associated files, which were mainly used for planning of observations and uplink, are also available. Most of them are only for expert usage. The following give a short summary of associated files:

POF:	Planned Observation File
ICS:	Instrument Command Sequence
CUS4_ICPT:	Calibration Uplink System Instrument Calibration Parameter File
CUS4_ICS:	Calibration Uplink System Instrument Command Sequence
CUS4_IDSDB:	Calibration Uplink System Instrument Default Setting Data Base
CUS4_VERBS:	Calibration Uplink System Verbs
RRP:	Real time Revolution Report
ISR:	Instrument Station Report
COIF:	Calibration Observation Input File
COB:	Calibration Observation Batch
CO_PARAM:	Calibration Observation Parameters
CO_LIST:	Calibration Observation List
TIMELINE FILE:	Calibration Observation scheduling instructions (PHT specific)
IPF:	Output file of the program PHTAOT (PHT specific)

Additionally, the proposals abstracts are available for most of the observations. All these products can help to understand and/or interpret specific aspects of a measurement.

E.3.4 Calibration data

All versions of derived calibration data which have been used to process the observational data from the Raw Data level onwards are archived. [Cal-G files are an example].

E.3.5 Historical and chronological data

All data needed to reconstruct the chronology of the mission are archived.

E.3.6 Documentation

All documentation existing in electronic or widely-distributed hard-copy form is archived.

E.3.7 Software

A number of software packages are available to the community to reduce and analyse ISO data. These include: ISOCAM Interactive Analysis (CIA); ISOPHOT Interactive Analysis (PIA); Observers' SWS Interactive Analysis (OSIA); LWS Interactive Analysis (LIA); and ISO Spectroscopic Analysis Package (ISAP). They all can be obtained through the ISO Data Center web pages at:

<http://www.iso.vilspa.esa.es/> → ISO Data Analysis Software. .

Appendix F

Quaternions

Some explanation of how the pointing (as given in the IIPH and other similar files) is calculated is presented here.

The attitude of a satellite is usually expressed by astronomers (and by FITS standard) in terms of the 3 angles: *RA*, *DEC* and *ROLL*, that specify the orientation of the instrument in the inertial J2000 frame. *RA* and *DEC* are the usual astronomical equatorial coordinates specified in degrees, while *ROLL* is the angle, measured anticlockwise, between north and the spacecraft z-axis (see Figure 3.2). This uses the normal astronomical definition of East (to the left).

Operationally, on the other hand, attitudes are specified in terms of 4-component ‘quaternions’:

$$Q = (Q(1), Q(2), Q(3), Q(4)) \quad (\text{F.1})$$

that provide the most concise representation of the series of rotations that are required to specify the satellite attitude. For a rotation of *D* degrees about an axis specified by the direction cosines *l*, *m*, *n* the quaternion components are given by

$$Q(1) = l \times \sin(D/2) \quad (\text{F.2})$$

$$Q(2) = m \times \sin(D/2) \quad (\text{F.3})$$

$$Q(3) = n \times \sin(D/2) \quad (\text{F.4})$$

$$Q(4) = \cos(D/2) \quad (\text{F.5})$$

The resultant quaternion, Q_{ab} , of successive rotations Q_a and Q_b is the product of a 4×4 matrix, each of whose elements is one of the elements of Q_b , and the 4×1 matrix representation of Q_a , i.e.:

$$Q_{ab} = Q_a \times Q_b = \begin{vmatrix} Q_b(4) & Q_b(3) & -Q_b(2) & Q_b(1) \\ -Q_b(3) & Q_b(4) & Q_b(1) & Q_b(2) \\ Q_b(2) & -Q_b(1) & Q_b(4) & Q_b(3) \\ -Q_b(1) & -Q_b(2) & -Q_b(3) & Q_b(4) \end{vmatrix} \begin{vmatrix} Q_a(1) \\ Q_a(2) \\ Q_a(3) \\ Q_a(4) \end{vmatrix} \quad (\text{F.6})$$

The Attitude and Orbit Control System (AOCS) delivers instantaneous estimates of the Star-Tracker quaternions *STRQ* that define the STR J2000 pointing. These have to be combined with the STR/QSS misalignment quaternions *STRQSSQ* and with any of the QSS/Instrument alignment quaternions (one per aperture):

- $QSSCAMQ$
- $QSSLWSQ$
- $QSSPHTQ$
- $QSSWSQ$

[\times any raster point quaternion RPQ] to give a resultant quaternion, Q , that defines the orientation of an instrument in the inertial frame.

Thus, for example:

$$(CAM)Q = [RPQ \times] QSSCAMQ \times STRQSSQ \times STRQ \quad (F.7)$$

defines the orientation of the (CAM) x-, y- and z-instrument axes. If $\langle i \rangle$, $\langle j \rangle$ and $\langle k \rangle$ are the instrument axis unit vectors in the J2000 inertial frame, then:

$$\begin{aligned} \langle X \rangle &= (Instrument)Pointingdirection \\ &= (RA, DEC) \end{aligned} \quad (F.8)$$

$$\langle Y \rangle = (Instrument)y - axis \quad (F.9)$$

$$\langle Z \rangle = (Instrument)z - axis \quad (F.10)$$

where

$$\langle X \rangle = \cos(DEC) * \cos(RA) * \langle i \rangle + \cos(DEC) * \sin(RA) * \langle j \rangle + \sin(DEC) * \langle k \rangle \quad (F.11)$$

$$\sin(DEC) = 2 * (Q(1) * Q(3) - Q(2) * Q(4)) \quad (F.12)$$

$$\cos(RA) * \cos(DEC) = Q(1) * Q(1) - Q(2) * Q(2) - Q(3) * Q(3) + Q(4) * Q(4) \quad (F.13)$$

$$\sin(RA) * \cos(DEC) = 2 * (Q(1) * Q(2) + Q(3) * Q(4)) \quad (F.14)$$

$$\cos(ROLL) * \cos(DEC) = -Q(1) * Q(1) - Q(2) * Q(2) + Q(3) * Q(3) + Q(4) * Q(4) \quad (F.15)$$

$$\sin(ROLL) * \cos(DEC) = 2 * (Q(1) * Q(4) + Q(2) * Q(3)) \quad (F.16)$$

These instantaneous attitude estimates are given in the IIPH columns XRA, XDEC and XROLL.

Appendix G

IDA SQL-Queries: Worked Examples

Here are some worked examples of IDA SQL-queries based on the current data model¹.

The SQL-applet which allows expert users to perform these queries is available at the IDC web site under:
<http://www.iso.vilspa.esa.es/> → Access the Archive → SQL Queries

To fully understand these examples it is necessary to know the definitions and the structures of the *ISO Data Archive Physical Data Model*, [47].

1. Find all ISO observations of NGC 7582:

```
select observations.obsno
  from observations
  where observations.target = 'NGC 7582'
```

2. Find all SWS02 observations of HR6705 (wildcarding is important for name searches):

```
select observations.obsno
  from observations
  where observations.target like '%HR%6705%'
```

3. Find all SWS01 observations at $0 < \text{RA} < 6\text{h}$ and $\text{DEC} > 30^\circ$:

```
select distinct observations.obsno
  from planning_info p, observations
  where observations.aotname = 'S01'
  and p.orgra > 0
  and p.orgra < 6
  and p.orgdec > 30
  and p.obsno = observations.obsno
```

NOTE: orgra is in hours and orgdec in degrees. We assume that the observations made, apertures used, are points. The above query can be performed, better, via the browse/request applet interface. This interface will make use of the 'positions' table, the actual aperture sizes, and the downlink (IRPH) coordinates.

¹These examples were produced by John Dowson.

4. Find all SWS01 observations with exposure time > 1.5 hours:

```
select observations.obsno
  from observations
 where observations.aotname = 'S01'
 and observations.utc_end - observations.utc_start > 5400
```

5. Find all SWS01 observations with 40 min < exposure time < 1 hour:

```
select observations.obsno
  from observations
 where observations.aotname = 'S01'
 and (observations.utc_end - observations.utc_start) > 2400
 and (observations.utc_end - observations.utc_start) < 3600
```

6. Find all SWS06 observations of 'HR6705 GAMMA-DRA' from SWS_CAL with exposure time between 30 and 40 minutes:

```
select observations.obsno
  from observations
 where observations.aotname = 'S06'
 and observations.target = 'HR6705 GAMMA-DRA'
 and obsid = 'SWS_CAL'
 and (observations.utc_end - observations.utc_start) > 1800
 and (observations.utc_end - observations.utc_start) < 2400
```

7. Find all SWS data from revolution 79:

```
select observations.obsno
  from observations
 where observations.institid = 'S'
 and observations.revno >= 079
```

NOTE: assumed that 'data' means all FITS product files (filename and version). The above query can be performed, better, via the browse/request applet interface.

8. Find all SWS data with start time between 04 Feb 1996 12:00:00 (date1) and 04 Feb 1996 18:00:00 (date2):

```
select observations.obsno
  from observations
 where observations.institid = 'S'
 and observations.utc_start > date1
 and observations.utc_start < date2
```

NOTE: date1 and date2 should be converted to UTC in seconds since 1989.

9. Find all SWS02 observations which include a line at rest wavelength between 17.91 and 17.93 μm :

```
select distinct observations.obsno
  from observations, wavelengths
 where observations.aotname = 'S02'
   and wavelengths.lower > 17910
   and wavelengths.lower < 17930
   and wavelengths.obsno = observations.obsno
```

10. Find all SWS02 observations that include both a line in the rest wavelength range 12.8–12.85 and a line in the range 15.5–15.6 μm :

```
select o1.obsno
  from observations o1, wavelengths w1
 where o1.aotname = 'S02'
   and (w1.lower > 12800
   and w1.lower < 12850)
   and w1.obsno = o1.obsno
   and exists
   (select * from observations o2, wavelengths w2
    where o2.aotname = 'S02'
     and (w2.lower > 15500
     and w2.lower < 15600)
     and w2.obsno = o2.obsno
     and o1.obsno = o2.obsno)
```

11. Find all SWS observations following a CAM-CVF measurement:

```
select obsno, utc_end, aotname into #sws1
  from observations
 where aotname in ('C01','C03','C04')

select obsno, fltr_cvf, beam into #sws2
  from cam_measurement
 where fltr_cvf in (12,11)

select distinct s1.obsno, s1.utc_end into #sws3
  from #sws1 s1, #sws2 s2
 where s1.aotname= 'C04' or ((s1.aotname = 'C01' or s1.aotname = 'C03')
   and (s2.fltr_cvf = 12 or (s2.fltr_cvf = 11 and (s2.beam=3 or s2.beam=4))))
   and s1.obsno=s2.obsno

select o.obsno, o.utc_start, s3.utc_end from observations o, #sws3 s3
 where o.instdid = 'S' and abs(o.utc_start - s3.utc_end) < 120
   and prodqlty != 'J'
```

NOTE: Assumes that 'following' means 'within 120 seconds of'

12. Find all SWS02 observations which requested S/N in excess of 200 (easy, but only useful if proposers were careful...):

```
select distinct observations.obsno
  from observations,
  sws_measurement s
 where observations.aotname = 'S02'
    and s.sgnr_req > 200
    and observations.obsno = s.obsno
```

13. Find all PHT40 observations from RGENZEL since revolution 600:

```
select observations.obsno
  from observations
 where aotname = 'P40'
    and obsid = 'RGENZEL'
    and revno >= 600
```

14. Find all CAM observations which changed the gain during one observation:

```
select obsno
  from cam_cstat
 group by obsno having count(distinct cstagain) > 1
```

15. Find all CAM parallel data + IxPH files where HUGO is the observer of the prime instrument:

```
select obsno from observations where obsno-1 in (
  select obsno from observations where cam_par_flag = 'Y' and
  obsid like '%HUGO%')
```

NOTE: This gives the observations that match, these must then be added to the shopping basket and the type of data requested specified.

16. Find all LWS02 observations where LVDT \leq 1000:

```
select distinct o.obsno from observations o, lspd l where
  aotname = 'L02' and lspdglvp <= 1000.0
  and o.obsno = l.obsno
```

17. Find all LWS04 observations using detector LW5:

```
select distinct o.obsno from observations o, lspd l where
  aotname = 'L04' and l.lspdadet = 512 and o.obsno=l.obsno
```

18. Find all LWS observations of the 88 μ m line on detector SW5 with FPS:

```
select distinct l.obsno from wavelengths w, liac l
 where lower <= 88000 and upper >= 88000
    and countno=5 and liacwhap=0
    and w.obsno = l.obsno
```

19. Find all occurrences of the total number of ramps in an LWS scan being less than x (LSCA file):

```
select obsno, lscanrmt, lscaitks, lscaitks from lsca where lscanrmt < x
```

20. Find all LWS observations containing more than 20 scans (LSAN file):

```
select distinct obsno from lsan where (lsan.scanb + lsan.scanf) > 20
```

21. Find all LWS observations where all scans are done in the forward direction (LSCA file):

```
select distinct obsno from lsca where obsno not in
(select distinct obsno from lsca where lscadir != 0)
```

22. Find all occurrences of the last flash in an LWS observation having an LW2 responsivity correction factor above x (LIAC file):

```
select obsno, liaciks, liacike from liac where liacres7 > x
```

23. Find all occurrences of the LWS dark current for SW1 being greater than x (LIAC file):

```
select obsno, liaciks, liacike from liac where liacbk1 > x
```

24. Find all occurrences of the LWS absolute responsivity correction factor for any detector greater than x when the wheel is in the FPL position:

```
select obsno, liaciks, liacike from liac where liacwhap = 2 and
liacres1 > x or liacres2 > x or liacres3 > x or liacres4 > x or liacres5 > x
or liacres6 > x or liacres7 > x or liacres8 > x or liacres9 > x
or liacres10 > x
```

25. Find all occurrences of the LWS responsivity drift slope for SW3 being above x:

```
select obsno, lgifitks, lgifitke from lgif where lgif2rel3 > x
```

26. Find all CAM LW3 rasters with 1.5'' pixel field of view (pfov), which have a raster dimension > 4x4 and at least 25 readouts per position:

```
select distinct o.obsno from observations o, cam_cstat c,
cam_measurement m, raster_map r
where c.cstafltw=125 and
m.pfov = 1.5 and
r.m*r.n > 16 and
c.cstaread >= 25 and
o.obsno = c.obsno and
o.obsno = m.obsno and select distinct o.obsno from observations o, cam_cstat c,
cam_measurement m, raster_map r
```

```

where c.cstafwtw=125 and
m.pfov = 1.5 and
r.m*r.n > 16 and
c.cstaread >= 25 and
o.obsno = c.obsno and
o.obsno = m.obsno and
o.obsno = r.obsno

```

```

select distinct o.obsno from observations o, cam_cstat c, aph a,
obs_pointing p
where o.obsno=p.obsno and p.pointing_id = a.pointing_id and
o.obsno = c.obsno
and c.cstafwtw=125 and c.cstalns=192 and a.scan_dist*a.linedist > 16
and c.cstaread >= 25
o.obsno = r.obsno

```

```

select distinct o.obsno from observations o, cam_cstat c, aph a,
obs_pointing p
where o.obsno=p.obsno and p.pointing_id = a.pointing_id and
o.obsno = c.obsno
and c.cstafwtw=125 and c.cstalns=192 and a.scan_dist*a.linedist > 16
and c.cstaread >= 25

```

27. Find all CAM raster observations longer than 1 hour, which started at the latest 2 hours after activation:

```

select distinct t1.obsno, (t1.utc_end - t1.utc_start)
from observations t1, raster_map where
t1.obsno = raster_map.obsno and
(t1.instid = 'C') and
(t1.utc_end - t1.utc_start > 3600) and
exists (select * from observations t2 where
(t2.aotname='C60' or t2.aotname='C61') and
(t1.utc_start - t2.utc_end) < 7200)

```

Or, alternatively:

```

select distinct t1.obsno, (t1.utc_end - t1.utc_start)
from observations t1, aph a, obs_pointing p where
t1.obsno = p.obsno and p.pointing_id = a.pointing_id and
(a.reqtype = 'R') and (t1.instid = 'C') and (t1.type != 'C') and
(t1.utc_end - t1.utc_start > 3600) and
exists (select * from observations t2 where
(t2.aotname='C60' or t2.aotname='C61') and
(t1.utc_start - t2.utc_end) < 7200)

```

NOTE: The second query is probably better as it uses the aph to distinguish a raster observation. This is generally more accurate than using the raster_map table as this only contains planned uplink values (and so obs which did not go through PGA into the Uplink MDB, such as C99, will not be included). Note,

that this query also explicitly excludes CAM parallel observations
 - these could easily be included if wanted.

28. Find all CAM parallel data + IxPH files for LWS rasters > 2 hours observing time with a dimension > 3x3:

```
select distinct obsno from observations where type='C' and obsno-1 in (
  select o.obsno from observations o, raster_map r where instid='L'
  and r.m*r.n > 9
  and utc_end - utc_start > 7200
  and o.obsno = r.obsno )
```

NOTE: Again, this query can also (better) be performed using the aph table.

29. Find all LWS raster observations longer than 1 hour which started at the latest 2 hours after activation:

```
select o.obsno from observations o, raster_map
  where o.obsno = raster_map.obsno and
  (o.instid = 'L') and
  (o.utc_end - o.utc_start > 3600) and
  exists (select * from observations o2 where
  (o2.aotname='C60' or o2.aotname='C61') and
  (o.utc_start - o2.utc_end) < 7200)
```

Or, alternatively:

```
select o.obsno from observations o, aph a, obs_pointing p
  where o.obsno = p.obsno and p.pointing_id = a.pointing_id and
  a.reqtype='R' and (o.instid = 'L') and type = 'S' and
  (o.utc_end - o.utc_start > 3600) and
  exists (select * from observations o2 where
  (o2.aotname='C60' or o2.aotname='C61') and
  (o.utc_start - o2.utc_end) < 7200)
```

NOTE: This query is restricted to science observations - this could easily be modified to also return LWS parallel observations.

Appendix H

Acronyms

AAP	Active Archive Phase
AAR	Auto-Analysis Results
ADS	Astrophysics Data System
AGN	Active Galactic Nuclei
AMA	Average Measurement Accuracy
AOCS	Attitude and Orbit Control Subsystem
AOPF	Augmented Operations Plan File
AOS	Acquisition-Of-Signal
AOT	Astronomical Observation Template
AOTL	AOT Logic
APD	Absolute Pointing Drift
APE	Absolute Pointing Error
APF	Attitude Parameter File
APHSTAR	ISO operational guide-star list
APPH	APerture Pointing History
APPM	Aperture Programmed Pointing History
AST/RO	Antarctic Submillimeter Telescope and Remote Observatory
BAL	Broad Absorption Line
BIBIB	Back Illuminated Blocked Impurity Band (Detector type)
BKRP	BulK ReProcessing
BLR	Broad Line Region
CAL-G	Calibration General
CAL-U	Calibration Uplink
CAM	The ISO Camera
CAM-CVF	CAM Circular Variable Filter
CCD	Charged Coupled Device
CCS	Central Command Schedule
CD-ROM	Compact Disk - Read-Only Memory
CEA	Laboratoire du Commissariat à l'Energie Atomique (at Saclay)
CEST	Central European Summer Time
CIA	CAM Interactive Analysis
CID	Charge Injection Device
CIDT	CAM Instrument Dedicated Team
CIST	CAM Instrument Science Team

CMAF	ISOCAM Celestial IR image
CMOS	ISOCAM Celestial IR mosaic
CO	Calibration Observation
COB	Calibration Observation Batch
COBE	COsmic Background Explorer
COIF	Calibration Observation Interface File
COT	Calibration Observation Template
CPSL	CAM Point Source List (an AAR product)
CRE	Cold Readout Electronics
CRP	Contingency Recovery Procedure
CSE	Circumstellar Envelope
CSH	Compact Status History
CSM	Circumstellar Medium
CSSP	ISOCAM Source Spectra
CUS	Calibration Uplink System
CVF	Circular Variable Filter
CVV	Cryo Vacuum Vessel
DBOB	Data Base of Observable Bins
DEC	Declination
DIDAC	Dutch ISO Data Analysis Centre (at SRON in the Netherlands)
DIRBE	Diffuse Infrared Background Explorer (onboard COBE)
DLCM	Direct Liquid Content Measurement
DM	Development Model
D/SCI	Directorate of Science of ESA
DT	Discretionary Time
D/TOS	Directorate of Technical and Operational Support of ESA
ELAIS	European Large Infrared Area Survey
ELS	Earth Limb Sensor
EOH	Executed Observation History
EOHA	Executed Observation History per AOT
EOHC	Continuous Executed Observation History
EOHI	Executed Observation History per ICS
ERD	Edited Raw Data
ESA	European Space Agency
ESO	European Southern Observatory
ESOC	European Space Operations Centre
ESTEC	European Space Research and Technology Centre
EUV	Extreme Ultraviolet
EXOSAT	ESA X-Ray Observatory SATellite
FCP	Flight Control Procedure
FCS	Fine Calibration Source
FD	Flight Dynamics
FDD	Flight Dynamics Division
FDS	Flight Dynamics System
FET	Field-Effect Transistor
FIR	Far InfraRed ($> 50 \mu\text{m}$)
FITS	Flexible Image Transport System
FOV	Field Of View
FP	Fabry Péro

FPG	Focal Plane Geometry
FPL	Long Wavelength Fabry-Pérot for LWS
FPS	Short Wavelength Fabry-Pérot for LWS
FPU	Focal Plane Unit
FSS	Fine Sun Sensor
ftp	file transfer protocol
FWHM	Full Width Half Maximum
GEHK	General Housekeeping
GIF	Graphics Interchange Format
GMC	Giant Molecular Cloud
GOES-9	Geostationary Operational Enviromental Satellite-9
GSHH	General Housekeeping (sampled)
GST	Ground Station Time
GT	Guaranteed Time
HEASARC	High Energy Astrophysics Science Archive Research Center
HH	Herbig-Haro
HK	HouseKeeping
HPDP	Highly Processed Data Product
HST	Hubble Space Telescope
HTML	Hyper-Text Mark-up Language
H/W	Hardware
IA	Interactive Analysis
IAS	Institut d'Astrophysique Spatiale (at Orsay)
ICS	Instrument Command Sequence
ID	IDentifier
IDA	ISO Data Archive
IDC	ISO Data Centre
IDCS	ISO Dedicated Control System
IDL	Interactive Data Language
IDPD	ISO Data Product Document
IDT	Instrument Dedicated Team
IFPG	ISO Focal Plane Geometry
IIPH	Instrument Instantaneous Pointing History
ILT	Instrument Level Tests
IMEC	Interuniversity Micro Electronics Center (at Leuven, Belgium)
INTEGRAL	INTErnational Gamma-Ray Astrophysics Laboratory
IPAC	Infrared Processing and Analysis Center
IPC	Industrial Policy Committee
IRAS	InfraRed Astronomical Satellite
IRPH	Instrument Reference Pointing History
IRPSS	ISO Remote Proposal Submission System
IRSA	NASA/IPAC Infrared Science Archive
IRTS	Infrared Telescope in Space
ISAP	ISO Spectroscopic Analysis Package
ISAS	Institute of Space and Astronautical Science (of Japan)
ISM	InterStellar Medium
ISO	Infrared Space Observatory
ISOCAM	The ISO CAMera
ISOGAL	ISOCAM survey of the Inner Galaxy

ISOPHOT	The ISO PHOTo-Polarimeter
ISOSDC	ISO Spectrometer Data Centre (at MPE-Garching)
ISS	Integrated Switching System
IST	ISO Science Team
ISTR	ISO Star TRacker
ITK	Instrument Time Key ($=2^{-14}$ s)
KAO	Kuiper Airborne Observatory
LEOP	Launch and Early Orbit Phase
LHe	Liquid Helium
LIA	LWS Interactive Analysis
LIDT	LWS Instrument Dedicated Team
LIST	LWS Instrument Science Team
LMC	Large Magellanic Cloud
LOS	Loss-Of-Signal
LPV	Long Period Variables
LRS	Low Resolution Spectrograph (IRAS)
LSAN	LWS Auto-Analysis results
LWS	The ISO Long Wavelength Spectrometer
MAU	Million Accounting Units
MDB	Mission Data Base
MIR	Mid InfraRed ($5 - 50 \mu\text{m}$)
MIRS	Mid-Infrared Spectrometer (on board IRTS)
MISQ	Misalignment Quaternion
MLI	Multi-Layer Insulation
MSX	Midcourse Space Experiment
MPE	Max-Planck Institute for Extraterrestrial Physics
MPIA	Max-Planck Institute for Astronomy
MPIfR	Max-Planck Institute for Radioastronomy
MPIK	Max-Planck Institute for Nuclear Physics
MPP1	Mission Planning Phase 1
MPP2	Mission Planning Phase 2
NASA	National Aeronautics and Space Administration (of US)
NDC	National Data Centre
NED	NASA/IPAC Extragalactic Database
NIR	Near InfraRed ($< 5 \mu\text{m}$)
OBDH	On-Board Data Handling
OCC	Operations Control Centre (at ESOC)
OCT	Observatory Command Template
ODS	Operational Data Server
OLP	Off-Line Processing
OPSNET	Operations Network
OSIA	Observers SWS Interactive Analysis
OSN	Observation Sequence Number
OSS	Optical Support Structure
OT	Open Time
OTAC	Observing Time Allocation Committee
OTF	On-Target Flag

OTT	On-Target Time
PAH	Polycyclic Aromatic Hydrocarbon
PCS	Permanent Command Sequences
PDEC	Proposal Data Entry Centre (at ESTEC)
PDR	Photo-Dissociation Region
PDS	Product Distribution System
PFM	Proto-Flight Model
PFOV	Pixel Field Of View
PGA	Proposal Generation Aids
PH	Proposal Handling
PHT	see ISOPHOT
PHT-C	PHT Camera Arrays
PHT-P	PHT Photopolarimeter
PHT-S	PHT Spectrophotometer
PI	Principal Investigator
PIA	PHT Interactive Analysis
PIDT	PHT Instrument Dedicated Team
PN	Planetary Nebula
POF	Planned Observation Files
POPS	Post-Operations (Phase)
PPM	Programmable Pointing Mode
PPN	Proto-Planetary Nebula
PSF	Planning Skeleton File
PSF	Point Spread Function
PV	Performance Verification (Phase)
QC	Quality Control
QLA	Quick Look Analysis
QMW	Queen Mary and Westfield College (at London)
QSO	Quasar (Quasi-Stellar Object)
QSS	Quadrant Star Sensor
RA	Right Ascension
RAL	Rutherford Appleton Laboratory
RAM	Random Access Memory
RF	Radio Frequency
RIXOS	ROSAT Internation X-Ray/Optical Survey
r.m.s.	root mean squared
ROE	Royal Observatory of Edinburgh
ROSAT	Röntgensatellit (German X-Ray space observatory)
RP	Routine Phase
RPE	Relative Pointing Error (pointing jitter)
RPID	Raster Point ID
RPQ	Raster Point Quaternion
RRP	Revolution Report
RSRF	Relative Spectral Response Function
RTA	Real-Time Technical Assessment
SAP	Service d'Astrophysique (at CEA - Saclay)
SAS	Sun Acquisition Sensor
S/C	Spacecraft

SCC	Spacecraft Control Centre
SCP	Satellite Commissioning Phase
SCREW	Software Change Requests and Extra Wishes
SED	Spectral Energy Distribution
SETI	Search for Extra-Terrestrial Intelligence
SI	International System of Units
SIA	SWS Interactive Analysis
SIAP	Simple Image Access Protocol
SIDT	SWS Instrument Dedicated Team
SIMBAD	Set of Identifications, Measurements And Bibliography for Astronomy Data
SMC	Small Magellanic Cloud
S/N	Signal-to-Noise (ratio)
SNR	Supernova Remnant
SOC	Science Operations Centre
SOST	Spacecraft Operations Science Team
SOT	Science Operations Team
SPC	Science Programme Committee
SPEVAL	Spacecraft Performance EVALuation
SPD	Standard Processed Data
SPDT	Survey Product Display Tool
SPR	Software Problem Report
SQL	Structured/Standard Query Language
SRON	Space Research Organisation of the Netherlands
SSO	Solar System Object
STR	Star TRacker
S/W	Software
SWS	The ISO Short Wavelength Spectrometer
TDATA	Transparent Data
TDF	Telemetry Data/Distribution Format
TDT	Target Dedicated Time
TM	TeleMetry
ToO	Target of Opportunity
TOS	Technical and Operational Support
TRS	Thermal Radiation Source
TTP	Technology Test Phase
UDF	User Defined Function
UIR	Unidentified Infrared Bands
UK	United Kingdom
UKIRT	United Kingdom Infra-Red Telescope (Hawaii)
USA	United States of America
UTC	Universal Time (Coordinated)
UTK	Uniform Time Key
VCS	Vapour-cooled radiation Shields
VILSPA	Villafranca Satellite Tracking Station in Spain
VLA	Very Large Array
VO	Virtual Observatory
WWW	World Wide Web

x-axis	Roll in the S/C control frame
XMM-Newton	X-ray Multi-Mirror Telescope
y-axis	Pitch in the S/C control frame
YSO	Young Stellar Object
z-axis	Yaw in the S/C control frame
ZIP	Zodiacal Infrared Project

Bibliography

- [1] Abergel A., Miville-Dechênes M.A., Désert F.-X., Pérault M.X., Aussel H. & Sauvage M. 2000, *The transient behaviour of the long wavelength channel of ISOCAM*, ExA 10, 353
- [2] Ábrahám P., Leinert C., Acosta-Pulido J.A., Schmidtbreick L. & Lemke D. 1999, *Zodiacal light observations with ISOPHOT*, in ‘The Universe as Seen by ISO’, Eds. P. Cox & M.F. Kessler, ESA SP-427, 261
- [3] Arviset C. & Prusti T. 1999, *The ISO Data Archive*, ESA Bulletin No. 98, 133
- [4] Arviset C., Dowson J., Hernández J., Plug A., Osuna P., Pollock A. & Saxton R.D. 2000, *The ISO Data Archive*, in ‘Astronomical Data Analysis Software and Systems (ADASS) IX’, Eds. R.J. Brunner, S.G. Djorgovski & A.S. Szalay, ASP Conf. Ser. 216, 191
- [5] Arviset C., Hernández J. & Prusti T. 2001, *The ISO Data Archive and Links to Other Archives*, in ‘Virtual Observatories of the Future’, ASP Conf. Ser. 225, 165
- [6] Arviset C., Hernández J., Dowson, J. & Osuna P. 2002, *Re-use of the ISO Data Archive to Build the XMM-Newton Science Archive*, in ‘Astronomical Data Analysis Software and Systems (ADASS) XI’, ASP Conf. Ser. 281, 247
- [7] Arviset C., Dowson J., Hernández J., Osuna P. & Venet A. 2003, *Interoperability of ESA Science Archives*, in ‘Astronomical Data Analysis Software and Systems (ADASS) XII’, Eds. H.E. Payne, R.I. Jedrzejewski & R.N. Hook, ASP Conf. Ser. 295, 47
- [8] Acosta-Pulido J.A., Gabriel C. & Castañeda H.O. 2000, *Transient effects in ISOPHOT data: status of modelling and correction procedures*, ExA 10, 333
- [9] Batten A.J. & Stephenson C.A. 1998, *ISO: In-orbit Calibration of the AOCS Sensors and Maximisation of Pointing Performance*, in ‘12th International Symposium on Spaceflight Dynamics’, ESA SP-403, 245
- [10] Beintema D.A. & Salama A. 2001, *Beam profile analysis of SWS*, in ‘The Calibration Legacy of the ISO Mission’, Eds. L. Metcalfe et al., ESA SP-481 (in press)
- [11] Blommaert J., Siebenmorgen R., Coulais A. et al. 2003, *The ISO Handbook: Volume II, CAM – The ISO Camera* ESA SP-1262, SAI-99-057/Dc, Version 2.0
- [12] Brauher J.R. & Lord S.D. 2001, *The ISOLWS-IRAS cross-calibration of extragalactic sources*, in ‘The Calibration Legacy of the ISO Mission’, Eds. L. Metcalfe et al., ESA SP-481 (in press)
- [13] *Call for Experimental and Mission Scientist Proposals*, Paris July 1984, ESA SCI(84)
- [14] Castañeda H.O & Klaas U. 2000, *Recognition of Space Weather Impact on the Isophot Detectors*, ExA 10, 369

- [15] Caux E. 2001, *Transient effects correction for LWS Detectors*, in ‘The Calibration Legacy of the ISO Mission’, Eds. L. Metcalfe et al., ESA SP-481 (in press)
- [16] Cesarsky C.J., Abergel A., Agnèsè P. et al. 1996, *ISOCAM in flight*, A&A 315, L32
- [17] Cesarsky C.J. 1999, *ISOCAM: first assessment after the end of the mission*, in ‘The Universe as Seen by ISO’ Eds. P. Cox & M.F. Kessler, ESA SP-427, 45
- [18] Cesarsky D.A. 2002, *Validation Report for CAM OLP Version 10*, Version 0.3, March 2002 (see ISO documentation under <http://www.vilspa.esa.es>)
- [19] Cesarsky D., Jones A.P., Lequeux J. & Verstraete L. 2000, *Silicate emission in Orion*, A&A 2000, 358, 708
- [20] Chan S.J., Lloyd C., Swinyard B.M. & Lim T. 2001, in ‘The Calibration Legacy of the ISO Mission’, Eds. L. Metcalfe et al., ESA SP-481 (in press)
- [21] Church S.E., Price M.C., Griffin M.J. et al. 1992, *Non-linear effects in doped-Germanium photoconductors for the ISO Long Wavelength Spectrometer*, in ‘Photon Detectors for Space Instrumentation’, ESA SP-356, 261
- [22] Church S.E., Griffin M.J., Price M.C., Ade P.A.R., Emery R.J. & Swinyard B. 1993, *Performance characteristics of doped-Ge photoconductors for the Infrared Space Observatory Long Wavelength Spectrometer*, Proc. SPIE 1946, 116
- [23] Church S.E., Price M.C., Haegel N.M., Griffin M.J. & Ade P.A.R. 1996, *Transient response in doped germanium photoconductors under very low background operation*, Applied Optics 35, 1597
- [24] Claes P., Pérez-Olea D.E., Verdugo E. et al. 1998, *ISO Science Operations Centre (SOC) Off-Line Operations Group Routine Phase Statistics*, ISO internal document No. ISO/TN/98-6036, Issue 1.1
- [25] Claret A., Dzitko H., Engelmann J. & Starck J.-L. 2000, *Glitch effects in ISOCAM Long Wave detector*, ExA 10, 305
- [26] Clegg P.E., Ade P.A.R., Armand C. et al. 1996, *The ISO Long-Wavelength Spectrometer*, A&A 315, L38
- [27] Clegg P.E. 1999, *The ISO Long-Wavelength Spectrometer: description, performance and highlights*, in ‘The Universe as Seen by ISO’, Eds. P. Cox & M.F. Kessler, ESA SP-427, 39
- [28] Cohen M., Walker R.G., Barlow M.J. & Deacon J.R. 1992a, *Spectral irradiance calibration in the infrared. I - Ground-based and IRAS broadband calibrations*, AJ 104, 1650
- [29] Cohen M., Walker R.G., Witteborn F.C. 1992b, *Spectral irradiance calibration in the infrared. II - α Tau and the recalibration of the IRAS low resolution spectrometer*, AJ 104, 2030
- [30] Cohen M., Witteborn F.C., Carbon D.F., Augason G., Wooden D., Bregman J. & Goorvitch D. 1992c, *Spectral irradiance calibration in the infrared. III - The influence of CO and SiO*, AJ 104, 2045
- [31] Cohen M., Witteborn F.C., Walker R.G., Bregman J. & Wooden D. 1995, *Spectral Irradiance Calibration in the Infrared. IV - 1.2–35 micron spectra of six standard stars*, AJ 110, 275
- [32] Cohen M., Witteborn F.C., Carbon D.F., Davies J.K., Wooden D. & Bregman J. 1996, *Spectral irradiance calibration in the infrared. VII - New composite spectra, comparison with model atmospheres, and far-infrared extrapolations*, AJ 112, 2274

- [33] Cohen M., Witteborn F.C., Roush T., Bregman J. & Wooden D. 1998, *Spectral irradiance calibration in the infrared. VIII - 5–14 micron spectroscopy of the asteroids Ceres, Vesta and Pallas*, AJ 115, 1671
- [34] Cohen M. 2001, *Stellar calibration in the infrared: extending the legacy of the KAO, ISO and MSX to SIRTf and beyond*, in ‘The Calibration Legacy of the ISO Mission’, Eds. L. Metcalfe et al., ESA SP-481 (in press)
- [35] Coulais A. & Abergel A. 2000, *Transient correction of the LW-ISOCAM data for low contrasted illumination*, A&ASS 141, 533
- [36] Coulais A., Fouks B.I., Giovannelli A., Abergel A. & Sée J. 2000, *Transient response of IR detectors used in space astronomy: what we have learned from ISO satellite*, Proc. SPIE 4131, 205
- [37] Crovisier J., Leech K., Bockelée-Morvan D. et al. 1997, *The infrared spectrum of comet Hale-Bopp*, in ‘First ISO workshop on analytical spectroscopy’, Eds. A.M. Heras, K. Leech, N.R. Trams & M. Perry, ESA SP-419, 137
- [38] Crovisier J., Brooke T.Y., Leech K. et al. 2000, *The thermal infrared spectra of comets Hale-Bopp and 103 P/Hartley 2 observed with the Infrared Space Observatory*, in ‘Thermal Emission Spectroscopy and Analysis of Dust Disks and Regoliths’, Eds. M.L. Sitko, A.L. Sprague & D.K. Lynch, ASP Conf. Ser. 196, 109
- [39] Decin L. 2000, Ph.D. Leuven University, Belgium
- [40] Decin L. 2001, *Stellar models in IR calibration*, in ‘The Calibration Legacy of the ISO Mission’, Eds. L. Metcalfe et al., ESA SP-481 (in press)
- [41] Decin L., Waelkens C., Eriksson K., Gustafsson B., Plez B. & Sauval A.J., Van Assche, W. & Vandebussche B. 2000, *ISO-SWS calibration and the accurate modelling of cool-star atmospheres. I. Method*, A&A 364, 137
- [42] Decin L., Vandebussche B., Waelkens C., Eriksson K., Gustafsson B., Plez B., Sauval A.J. & Hinkle K. 2003a, *ISO-SWS calibration and the accurate modelling of cool-star atmospheres. II. General Results*, A&A 400, 679
- [43] Decin L., Vandebussche B., Waelkens C., Eriksson K., Gustafsson B., Plez B. & Sauval A.J. 2003b, *ISO-SWS calibration and the accurate modelling of cool-star atmospheres. III. A0 to G2 stars*, A&A 400, 695
- [44] Decin L., Vandebussche B., Waelkens C., Decin G., Eriksson K., Gustafsson B., Plez B., Sauval A.J. 2003c, *ISO-SWS calibration and the accurate modelling of cool-star atmospheres. IV. G9 to M2 stars*, A&A 400, 709
- [45] Désert F.-X., Puget J.-L., Clements D., Pérault M., Abergel A., Bernard J.P. & Cesarsky C. 1999 *A classical approach to faint extragalactic source extraction from ISOCAM deep surveys. Application to the Hubble Deep Field*, A&A 134, 342
- [46] Dotto E., Barucci M.A., Müller T.G., Brucato J.R., Fulchignoni M., Mennella V. & Colangeli L. 2002, *ISO observations of low and moderate albedo asteroids*, A&A 393, 1065
- [47] Dowson J. 2001, *ISO Data Archive Physical Data Model*, SAI/97-107/Dc, Version 4.0
- [48] Egan M.P., Price S.D., Moshir M.M., Cohen M. & Tedesco E. 1999, *The Midcourse Space Experiment Point Source Catalog Version 1.2 Explanatory Guide*, Technical Report AFRL-VS-TR-1999-1522
- [49] Eggel H., Schaap H. & Bagnasco G. 1995, *The ISO Scientific Instruments – Technical Highlights*, ESA Bulletin No. 84, 59

- [50] Fouks B.I. 1981a, *Injection properties of contacts to high-resistivity semiconductors. I*, Sov. Phys. Semicond. 15, 974,
- [51] Fouks B.I. 1981b, *Injection properties of contacts to high-resistivity semiconductors. II*, Sov. Phys. Semicond. 15, 980
- [52] Fouks B.I. 1997, *Theory of photoresponse of low-background IR detectors*, Proc. SPIE 3122, 441
- [53] Fouks B.I., Coulais A. & Normand J. 2002, *Accurate physical model for direct modelling of point source transients for ISOCAM LW detector*, in 'Exploiting the ISO Data Archive. Infrared Astronomy in the Internet Age', Eds. C. Gry, S.B. Peschke, J. Matagne et al., ESA SP-511 (in press)
- [54] Fouks B.I. & Schubert J. 1995, *Precise theoretical description of photoresponse for detectors of ISOPHOT's Si:Ga array*, Proc. SPIE 2475, 487
- [55] Franceschini A., Toffolatti L., Mazzei P., Danese L. & de Zotti G. 1991, *Galaxy counts and contributions to the background radiation from 1 micron to 1000 microns*, A&AS 89, 285
- [56] Fujiwara M., Hiromoto N. & Araki K. 1995, *Moderate-fast response of the Ge:Ga photoconductors*, Proc. SPIE 2552, 421
- [57] Gabriel C. & Acosta-Pulido J. 1999, *The ISOPHOT Interactive Analysis (PIA)*, in 'The Universe as seen by ISO', Eds. P. Cox & M.F. Kessler, ESA SP-427, 73
- [58] Gabriel C., Acosta-Pulido J., Heinrichsen I. et al. 1997, *The ISOPHOT Interactive Analysis PIA, a calibration and scientific analysis tool*, in 'Astronomical Data Analysis Software and Systems (ADASS) VI', Eds. G. Hunt & H.E. Payne. ASP Conf. Ser. 125, 108
- [59] García-Lario P. (Ed.) 2003, *ISO (Cross-)Calibration Final Report*, IDC Report, Version 2.1 (see ISO documentation under <http://www.vilspa.esa.es>)
- [60] García-Lario P., Acosta-Pulido J., Coulais A., Kester D. & Caux E. 2001, *Transients Working Group Final Report*, IDC report, SAI/2000-057/Rp
- [61] Gautier T.N., Boulanger F., Péroult M. & Puget J.L. 1992, *A calculation of confusion noise due to infrared cirrus*, AJ 103, 1313
- [62] de Graauw Th., Haser L.N., Beintema D.A. et al. 1996, *Observing with the ISO Short-Wavelength Spectrometer*, A&A 315, L49
- [63] de Graauw Th. 1999, *Summary of ISO SWS performance and science highlights*, in 'The Universe as Seen by ISO', Eds. P. Cox & M.F. Kessler, ESA SP-427, 31
- [64] Griffin M.J. & Orton G.S. 1993, *The near-millimeter brightness temperature spectra of Uranus and Neptune*, Icarus 105, 537
- [65] Grözinger U., Kirches S., Lemke D., Schubert J., Schulz B. & Wolf J. 1992, *Characterization of detectors and calibration of the ISOPHOT experiment*, in 'Photon Detectors for Space Instrumentation', ESA SP-356, 329
- [66] Grün E., Hanner M.S., Peschke S.B. et al. 2001, *Broadband infrared photometry of comet Hale-Bopp with ISOPHOT*, A&A 377, 1098
- [67] Gustafsson B., Bell R.A., Eriksson K. & Nordlund Å 1975, A&A 42, 407
- [68] Gry C., Swinyard B., Harwood A. et al. 2003, *The ISO Handbook: Volume III, LWS – The Long Wavelength Spectrometer*, ESA SP-1262, SAI-99-077/Dc, Version 2.1

- [69] Habing H.J., Bouchet P., Dominik C. et al. 1996, *First results from a photometric infrared survey for Vega-like disks around nearby main-sequence stars*, A&A 315, L233
- [70] Haegel N.M., Newton C., Simoes J.C. & White A.M. 1996, *Modelling of Transient Response in Far-Infrared Photoconductors* in '30th ESLAB Symposium: Submillimeter and Far-Infrared Space Instrumentation', ESA SP-388, 15
- [71] Haegel N.M., Simoes J.C., White A.M. & Beeman J.W. 1999, *Applied Optics* 38, 1910
- [72] Hammersley P.L., Jourdain de Muizon M., Kessler M.F. et al. 1998, *Infrared standards for ISO. I. A new calibration of mid-infrared photometry*, A&AS 128, 207
- [73] Hammersley P. & Jourdain de Muizon M. 2001, *The development of stellar photometric standards for ISO*, in in 'The Calibration Legacy of the ISO Mission', Eds. L. Metcalfe et al., ESA SP-481 (in press)
- [74] Hartung J. 1991, *Statistik - Lehr und Handbuch der angewandten Statistik*, R. Oldenburg Verlag
- [75] Hauser M.G., Arendt R.G., Kelsall T. et al. 1998a, *The COBE Diffuse Infrared Background Experiment (DIRBE) search for the Cosmic Infrared Background. I. Limits and detections*, ApJ 508, 25
- [76] Hauser M.G., Kelsall T., Leisawitz D. & Weiland J. (Eds.) 1998b, *COBE Diffuse Infrared Background Explorer (DIRBE) Explanatory Supplement*, Version 2.3. COBE Ref. Pub. No. 98-A (Greenbelt, MD: NASA/GSFC)
- [77] Heras A. 2001, *ISO/FIRST Glitches Working Group Final Report*, IDC report, SAI/2001-013/Rp
- [78] Heras A., Wieprecht E., Nieminen P. et al. 2001, *Summary of the SWS detector radiation effects*, in 'The Calibration Legacy of the ISO Mission', Eds. L. Metcalfe et al., ESA SP-481 (in press)
- [79] Herbstmeier U., Ábrahám P., Lemke D., et al. 1998, *Small-scale structures in the far-infrared background*, A&A 332, 739
- [80] Herbstmeier U., Ábrahám P., Héraudeau P., et al. 2001, *Beam profiles of ISOPHOT detectors*, in 'The Calibration Legacy of the ISO Mission', Eds. L. Metcalfe et al., ESA SP-481 (in press)
- [81] Hildebrand R.H., Dotson J.L., Dowell C.D. et al. 1999, *The Far-Infrared Polarization Spectrum: First Results and Analysis*, ApJ 516, 834
- [82] Hinkle K., Wallace L. & Livingston W. 1995, *Infrared atlas of Arcturus spectrum, 0.9–53 microns*, PASP 107, 1042
- [83] *The Hipparcos and Tycho Catalogues*, 1997, ESA SP-1200
- [84] 'Infrared Astronomical Satellite (IRAS) Catalogs and Atlases Explanatory Supplement' Vol. 1, 1998. Eds. C.A. Beichman, G. Neugebauer, H.J. Habing, P.E. Clegg & T.J. Chester. NASA RP-1190
- [85] *ISO Architectural Design Document* 1994, ESA Document ISO-SSD-9105
- [86] *ISO Assessment Study*, Paris, October 1979, ESA SCI(79)6
- [87] *ISO Launch and Early Orbit Phase & Satellite Commissioning Phase Report*, ESOC Document D/TOS-ISO-LEOP/SCP/JF Issue 1.0, October 31, 1997
- [88] *ISO Pre-Phase A Study*, Paris, November 1980, ESA SCI(80)9
- [89] *ISO Report on the Phase A Study*, Paris, November 1982, ESA SCI(82)6

- [90] *ISO Telescope Design Specification*, Aerospatiale, ESTEC Document number ISO.DS.B130.034
- [91] Jourdain de Muizon M. & Habing H.J. 1992, *The ISO Ground-based Preparatory Programme Working Group*, in ‘Infrared Astronomy with ISO. L’astronomie infrarouge et la mission ISO’, Eds. Th. Encrenaz & M.F. Kessler, 129. Nova Science Publishers, Commack, N.Y.
- [92] Kaneda H., Akazaki M., Okamura Y., Nakagawa T. & Yamamura I. 2001, *Laboratory measurements of transient behaviour of stressed Ge:Ga detectors*, in ‘The Calibration Legacy of the ISO Mission’, Eds. L. Metcalfe et al., ESA SP-481 (in press)
- [93] Kessler M.F., Heske A., Metcalfe L. & Salama A. 1995, *The ISO Mission – A Scientific Overview*, ESA Bulletin No. 84, 43
- [94] Kessler M.F. 1995, *Using ISO*, ESA Bulletin No. 84, 73
- [95] Kessler M.F., Steinz J.A., Anderegg M. et al. 1996, *The Infrared Space Observatory (ISO) mission*, A&A 315, L27
- [96] Kessler M.F., Clavel J. & Fälker J. 1998, *Looking Back at ISO Operations*, ESA Bulletin No. 95, 87
- [97] Kessler M.F. 1999, *The ISO mission: past and future*, in ‘The Universe as Seen by ISO’, Eds. P. Cox & M.F. Kessler, ESA SP-427, 23
- [98] Kester D. 2001, *Memory effects and their correction in SWS Si:Ga detectors*, in ‘The Calibration Legacy of the ISO mission’. Eds. L. Metcalfe & M.F. Kessler, ESA SP-481 (in press)
- [99] Klaas U., Lemke D., Kranz T. et al. 1998, *Infrared straylight measurements of the ISO telescope*, Proc. SPIE 3354, 996.
- [100] Klaas U., Radovich M., Wilke K. & Richards P. 2000a, *Report on the PHT Scientific Validation for OLP Version 8.4*, SAI/1999-041/Rp, Version 2.0
- [101] Klaas U., Wilke K., Kiss C., Radovich M. & Richards P. 2000b, *Report on the PHT Scientific Validation for OLP Version 9.0*, SAI/2000-014/Rp, Version 2.0
- [102] Klaas U. & Richards P. 2002, *Report on the PHT Scientific Validation for OLP Version 10.0*, Version 1.0, 9 April 2002 (see ISOPHOT documentation under: <http://www.iso.vilspa.esa.es>)
- [103] Laureijs R.J. 1999, *Point spread function fractions related to the ISOPHOT C100 and C200 arrays*, IDC Report, Version 1.0, 29 June 1999 (see ISOPHOT documentation under: <http://www.iso.vilspa.esa.es>)
- [104] Laureijs R. & Siebenmorgen R. (Eds.) 1999, *ISO Polarisation Observations*, ESA SP-435, December 1999
- [105] Laureijs R.J et al. 1999, *A systematic search for Vega-like stars with ISO*, in ‘Astrophysics with Infrared Surveys: A Prelude to SIRTf’, Eds. M.D. Bica, R.M. Cutri & B.F. Madore, ASP Conf. Series 177, 359
- [106] Laureijs R.J., Jourdain de Muizon M., Leech K. et al. 2002, *A 25 μ m search for Vega-like disks around main-sequence stars with ISO*, A&A 387, 285
- [107] Laureijs R.J., Klaas U., Richards P.J., Schulz B. & Ábrahám P. 2002, *The ISO Handbook: Volume IV, PHT – The Imaging Photo-Polarimeter*, ESA-SP1262, SAI-99-069/Dc, Version 2.0
- [108] Leech K., Kester D., Shipman R., et al. 2002, *The ISO Handbook: Volume V, SWS – The Short Wavelength Spectrometer* ESA SP-1262, SAI/2000-008/Dc, Version 2.0

- [109] Lellouch E., Crovisier J., Lim T. et al. 1998, *Evidence for water ice and estimate of dust production rate in comet Hale-Bopp at 2.9 AU from the Sun*, A&A 339, L9
- [110] Lemke D., Klaas U., Abolins J. et al. 1996, *ISOPHOT - capabilities and performance*, A&A 315, L64
- [111] Lemke D. & Klaas U. 1999, *ISOPHOT - performance, results and outlook*, in 'The Universe as Seen by ISO', Eds. P. Cox & M.F. Kessler, ESA SP-427, 51
- [112] Lemke D., Stickel M. & Wilke K. (Eds.) 1999, 'ISO Surveys of a Dusty Universe', LNP 548, Springer 2000
- [113] Lemke D., Klaas U. & Kranz T. 2001, *Straylight in ISOPHOT?*, in 'The Calibration Legacy of the ISO Mission', Eds. L. Metcalfe et al., ESA SP-481 (in press)
- [114] Lim T., Hutchinson G., Chan S.J. & Müller T. 2001, *LWS OLP 10 Scientific Validation Report*, (see LWS documentation under: <http://www.iso.vilspa.esa.es>)
- [115] Lim T. 2002, *The scientific potential of the LWS parallel and serendipity modes*, in 'Exploiting the ISO Data Archive. Infrared Astronomy in the Internet Age', Eds. C. Gry, S.B. Peschke, J. Matagne et al., ESA SP-511 (in press)
- [116] Lloyd C. 2001a, *The ISO LWS beam profile*, in 'The Calibration Legacy of the ISO Mission', Eds. L. Metcalfe et al., ESA SP-481 (in press)
- [117] Lloyd C. 2001b, *Fringing and spectrum fracturing in ISO LWS observations*, in 'The Calibration Legacy of the ISO Mission', Eds. L. Metcalfe et al., ESA SP-481 (in press)
- [118] Lloyd C. 2001c, *A simple approach to transient correction in ISO LWS data*, in 'The Calibration Legacy of the ISO Mission', Eds. L. Metcalfe et al., ESA SP-481 (in press)
- [119] Matagne J. 2002, *The Infrared Space Observatory Users Community*, in 'Exploiting the ISO Data Archive. Infrared Astronomy in the Internet Age', Eds. C. Gry, S. Peschke, J. Matagne et al., ESA SP-511 (in press)
- [120] Metcalfe L. et al. (Eds.) 2001, *The Calibration Legacy of the ISO Mission*, ESA SP-481 (in press)
- [121] Miville-Deschênes M.A., Boulanger F., Abergel A. & Bernard P. 2000, *Optimising ISOCAM data processing using spatial redundancy*, A&AS 146, 519
- [122] Müller T. 2000a, *ISOPHOT Aperture Profiles and Background Measurements*, in 'ISO Beyond Point Sources: Studies of Extended Infrared Emission', Eds. R.J. Laureijs, K. Leech & M.F. Kessler, ESA SP-455, 33
- [123] Müller T. 2000b, *ISOPHOT Aperture Sequences on Point- and Extended Sources*, in 'ISO Beyond Point Sources: Studies of Extended Infrared Emission', Eds. R.J. Laureijs, K. Leech, M.F. Kessler, ESA SP-455, 41
- [124] Müller T. 2001, *Non-linear detector response of LWS LW-Detectors*, IDC Report SAI/2001-042/Rp, December 2001
- [125] Müller T. & Lagerros J.S.V. 1998, *Asteroids as far-infrared photometric standards for ISOPHOT*, A&A 338, 340
- [126] Müller T. & Lagerros J.S.V. 2001, *Asteroids as calibration standards in the thermal infrared - Applications and results from ISO*, in 'The Calibration Legacy of the ISO Mission', Eds. L. Metcalfe et al., ESA SP-481 (in press)

- [127] Müller T. & Lagerros J.S.V. 2002, *Asteroids as calibration standards in the thermal infrared for space observatories*, A&A 381, 324
- [128] Murdock T.L. & Price S.D. 1985, *Infrared measurements of zodiacal light*, AJ 90, 375
- [129] Nieminen P. 2001, *The in-orbit radiation environment and its effects on space-borne instrumentation*, in ‘The Calibration Legacy of the ISO Mission’, Eds. L. Metcalfe et al., ESA SP-481 (in press)
- [130] Okumura K., Pérault M. & Longval Y. 1998, *Ghosts in ISOCAM Images*, CAM Internal Report issued 4 November 1998 (see CAM documentation under <http://www.iso.vilspa.esa.es>)
- [131] Okumura K. 2000, *The ISO Point Spread Function and CAM Beam Profiles*, in ‘ISO Beyond Point Sources: Studies of Extended Infrared Emission’, Eds. R.J. Laureijs, K. Leech & M.F. Kessler, ESA SP-455, 47
- [132] Orton G.S. 2001, *Planetary spectra as calibration references*, in ‘The Calibration Legacy of the ISO Mission’, Eds. L. Metcalfe et al., ESA SP-481 (in press)
- [133] Osuna P., Arviset C., Saxton R.D., Pollock A. & Verdugo E. 2000, ‘*On-the-Fly*’ *Calibration System for the ISO Data Archive*, in ‘Astronomical Data Analysis Software and Systems (ADASS) IX’, Eds. N. Manset, C. Veillet & D. Crabtree, ASP Conf. Series 216, 195
- [134] Ott S., Abergel A., Altieri B. et al. 1997, *Design and Implementation of CIA, the ISOCAM Interactive Analysis System*, in ‘Astronomical Data Analysis Software and Systems (ADASS) VI’, Eds. G. Hunt & H.E. Payne, ASP Conf. Series 125, 34
- [135] Ott S., Siebenmorgen R., Schartel N. & Vö T. 2002, *Status and scientific potential of the ISOCAM parallel mode survey*, in ‘Exploiting the ISO Data Archive. Infrared Astronomy in the Internet Age’, Eds. C. Gry, S.B. Peschke, J. Matagne et al., ESA SP-511 (in press)
- [136] Pérault M., Désert F.-X., Abergel A., et al. 1994, *Infrared Space Observatory camera calibration facility and pre-flight characterisation*, Optical Engineering 33, 762
- [137] Pollock A.M.T. 2001, *The treatment of pointing data in the ISO pipeline*, in ‘The Calibration Legacy of the ISO Mission’, Eds. L. Metcalfe et al., ESA SP-481 (in press)
- [138] Puget J.L. 1992, *Interstellar Medium — Part One*, in ‘Infrared Astronomy with ISO. L’astronomie infrarouge et la mission ISO’, Eds. Th. Encrenaz & M.F. Kessler, 271. Nova Science Publishers, Commack, N.Y.
- [139] Salama A. 1998, *SWS Beam Profiles and ISO Pointing*, SWS Internal Report issued 9 September 1998 (see SWS documentation under <http://www.iso.vilspa.esa.es>)
- [140] Salama A., Beintema D., Lloyd C. et al. 2001, *Beam Profiles and Pointing Working Group Final Report*, IDC report, SAI/2001-027/Dc
- [141] Salama A., Arviset C., Hernández J., Dowson J. & Osuna P. 2002a, *The ISO Data Archive and Interoperability with Other Archives*, in ‘Astronomical Data Analysis Software and Systems (ADASS) XI’, Eds. D.A. Bohlender, D. Durand & T.H. Handley, ASP Conf. Series 281, 58
- [142] Salama A., Arviset C., Dowson J., Hernández J., Osuna P. & Venet A. 2002b, *The ISO Data Archive: Overview of scientific content and use*, in ‘Exploiting the ISO Data Archive. Infrared Astronomy in the Internet Age’, Eds. C. Gry, S. Peschke, J. Matagne et al., ESA SP-511 (in press)
- [143] Sauvage M. 1997, *A short assessment of the impact of revolution 722 Solar Flare on ISOCAM*, CAM Internal Report, version 2 issued 21 November 1997 (see CAM documentation under <http://www.iso.vilspa.esa.es>)

- [144] Saxton R.D., Arviset C., Dowson J. et al. 1998, *The ISO Post-Mission Archive*, in ‘Astronomical Data Analysis Software and Systems (ADASS) VII’, Eds. R. Albrecht, R.N. Hook & H.A. Bushouse, ASP Conf. Series 145, 438
- [145] Schubert J. 1995, *Die Eichung des Infrarot-Gitterspektrometers in Satelliten-Experiment ISOPHOT und die Korrektur der Transienten seiner Detektoren*, Ph.D. Thesis, Max-Planck Institut für Astronomie, Heidelberg.
- [146] Schubert J., Roth G., Wolf D., Lemke D. & Fouks B.I. 1994, *Correction and curing of in-orbit induced non-ideal behaviour of ISOPHOT’s photodetectors*, Proc. SPIE 2268, 283
- [147] Schulz B., Clavel J., Altieri B. et al. 2001, *PHT-S spectroscopy of Seyfert galaxies*, in ‘ISO Beyond Point Sources: Studies of Extended Infrared Emission’, Eds. R.J. Laureijs, K. Leech & M.F. Kessler, ESA SP-455, 245
- [148] Schulz B., Huth S., Laureijs R.J. et al. 2002, *ISOPHOT – Photometric calibration of point sources*, A&A 381, 1110
- [149] Proceedings of the *ISOPHOT Workshop on P32 Oversampled Mapping*, held on 12–16 February 2001 and 12–16 March at the ISO Data Centre, Villafranca del Castillo, Madrid, Spain, and on 26–30 March 2001 at the Infrared Processing & Analysis Center (IPAC), USA. ESA SP-482, B. Schulz, N. Lu & S.B. Peschke (Eds.)
- [150] Sidher S.D., Swinyard B.M., Griffin M.J., Orton G.S., Burgdorf M. & Lim T. 2001, *Empirical aspects of the LWS photometric calibration*, in ‘The Calibration Legacy of the ISO Mission’, Eds. L. Metcalfe et al., ESA SP-481 (in press)
- [151] Siebenmorgen R., Abergel A., Altieri B. et al. 1996, *First results from the ISOCAM parallel mode*, A&A 315, L169
- [152] Starck J.L., Aussel H., Elbaz D., Fadda D. & Cesarsky C. 1999, *Faint source detection in ISOCAM images*, A&AS 138, 365
- [153] Steinz J. & Linssen A. 1995, *The ISO Programme*, ESA Bulletin No. 84, 67
- [154] Stickel M., Lemke D., Toth L.V. et al. 1999, *The ISOPHOT serendipity far-infrared sky survey — a status report*, in ‘The Universe as Seen by ISO’, Eds. P. Cox & M.F. Kessler, ESA SP-427, 839
- [155] Stickel M., Lemke D., Klaas U., Krause O., Toth V., Vavrek R., Hotzel S. and the CISS consortium 2002, *The scientific potential of the ISOPHOT serendipity sky survey*, in ‘Exploiting the ISO Data Archive. Infrared Astronomy in the Internet Age’, Eds. C. Gry, S.B. Peschke, J. Matagne et al., ESA SP-511 (in press)
- [156] Swinyard B., Clegg P., Leeks S., Griffin M., Lim T. & Burgdorf M. 2000, *Space Operation and Performance of Doped Germanium Photo-Conducting Detectors in the Far Infrared: Experience from the ISO LWS*, ExA 10, 157
- [157] Tiphène D., Rouan D., Epstein G. & Le Coupancec P. 2000, *Modelling transient effects in the IR array of the Short Wavelength channel of ISOCAM, the camera on board the ISO satellite*, ExA 10, 347
- [158] Vandenbussche B., Beintema D.A., de Graauw Th. et al. 2002, *The ISO SWS post-helium atlas of near infrared stellar spectra*, A&A 390, 1033
- [159] van Duinen R., Courtin R., Fitton B., de Graauw Th., Harries J., Jennings R.E., Joseph R., Künzi K.F., Magun A., Moorwood A.F.M., Salinari P. & Wrixon G.T. 1979, *A Mission Proposal to the European Space Agency for an Infrared Space Observatory* (see ISO documentation under <http://www.iso.vilspa.esa.es>)

- [160] Vigroux L.G., Cesarsky C.J., Boulade O. et al. 1993, *ISOCAM – the Infrared Space Observatory camera: results of testing and calibrations*, Proc. SPIE 1946, 281
- [161] Vinokurov L.A. & Fouks B.I. 1988, *Spreading of the current in a photosensitive medium exhibiting an extrinsic photoconductivity*, Sov. Phys. Semicond. 22, 1258
- [162] Vinokurov L.A. & Fouks B.I. 1991, *Non-linear response of extrinsic photoconductors*, Sov. Phys. Semicond. 25, 1207
- [163] Vinokurov L.A., Zaletaev N.B., Kocherov V.F. & Fouks B.I. 1992, *Spreading of time dependent photocurrent in Si:Ga*, Sov. Phys. Semicond. 26, 433
- [164] Wensink J.W., Luinke W., Beintema D.A., et al. 1992, *Characteristics of the ISO Short Wavelength Spectrometer detectors*, in ‘Photon Detectors for Space Instrumentation’, ESA SP-356, 339
- [165] Wieprecht E., Vandenbussche B., Wiezorrek E. et al. 1999, *User Defined Functions for the ISO Post Mission Archive*, in ‘Astronomical Data Analysis Software and Systems (ADASS) VIII’, Eds. D.M. Mehringer, R.L. Plante & D.A. Roberts, ASP Conf. Series 172, 249
- [166] Wright C.M. & Laureijs R.J. 1999, *ISOPHOT Polarimetry of Young Stellar Objects*, in ‘ISO Polarisation Observations’, Eds. R. Laureijs & R. Siebenmorgen, ESA SP-435, December 1999
- [167] Ximénez de Ferrán S. 1995, *The ISO Spacecraft*, ESA Bulletin No. 84, 51

Index

- AAR, 179
- acknowledgements, 7
- Active Archive Phase, 26
- ADS, 183
- AMA, 79
- AOCS, 30, 37, 39, 67, 235, 285
- AOCSFRAM, 235
- AOTs, 40, 70
- APD, 79
- APE, 79
- APHSTAR, 238
- APPH, 240
- APPM, 242
- astronomical calibrators, 197

- background radiation, 194
- baffles, 30, 35
- beam profiles, 74
- BKRP, 189
- browse products, 181, 281
- business logic, 183

- calibration proposals, 231
- CAM, 21, 30, 37, 70, 74, 78, 83, 89, 93, 107, 123, 126, 158, 246, 250, 255, 261
 - cross-calibration, 122, 128
 - description, 41
 - observing modes, 41
 - parallel mode, 40
 - performance, 42
 - survey products, 282
- celestial background, 194
- chronology, 28
- CIA, 11
- cirrus confusion, 196
- COBE/DIRBE, 153, 155
 - cross-calibration, 153
- Commissioning Phase, 20
- concatenated observations, 68
- costs, 16
- cross-calibration, 117
 - external, 134
 - internal, 120
 - models, 158
- cryostat subsystem
 - description, 32
 - performance, 73
- CVV, 33

- Data Analysis Software, 11
- detectors
 - curing, 89
 - dark current, 89
 - glitches, 84, 86
 - noise, 89
 - performance, 84
 - responsivity, 89
 - transients, 91
- development model, 16
- dimensions, 29
- discretionary time
 - programme, 64
 - proposals, 231
- documentation, 6

- Earth Limb Sensor, 30, 37
- EOHA, 244
- EOHC, 248
- EOHI, 250
- ERD, 84, 179

- fixed time observations, 69
- focal plane geometry, 35, 260
- Fouks-Schubert model, 91
- FSS, 37

- Ge:Ga detectors, 97
- GEHK, 253, 256
- GOES-9, 86
- ground
 - segment, 51
 - stations, 51, 52
- GSHH, 256
- GST, 82
- guaranteed time
 - programme, 58
 - proposals, 200

- guide stars, 81, 238, 257, 275
- HEASARC, 183
- helium tank, 30, 33
- Highly Processed Data Products , see HPDPs
- HIPPARCHOS, 257
- HPDPs, 180, 181, 187
- icon, 186, 281, 282
- ICS, 250
- IDA, 177
 - ancillary data, 283
 - auxiliary data, 283
 - basic science level, 179, 279
 - contents, 179, 277
 - fully auto-processed level, 179, 280
 - interoperability, 183
 - observation details, 284
 - physical data model, 181
 - quality flags, 180, 280
 - queries, 184
 - raw data level, 179, 278
 - shopping basket, 188
 - user interface, 183
- IFPG, 35
- IIPH, 67, 81, 261, 285, 286
- in-orbit performance, 73
- industrial consortium, 14
- infrared units, 193
- Interim Archive, 189
- IRAS, 134, 137, 142, 145, 146, 183
 - cross-calibration, 134
- IRPH, 81, 264
- ISAP, 11
- ISOCAM , see CAM
- ISOPHOT , see PHT
- ISTR, 267
- ITK, 82
- java applet, 183
- large surveys, 62
- Launch and Early Orbit Phase, 20
- Legacy Archive, 189
- LIA, 11
- linked observations, 69
- LWS, 21, 30, 37, 70, 75, 78, 83, 89, 102, 108, 137, 145, 159, 246, 251, 255
 - cross-calibration, 124, 129, 130, 142
 - description, 43
 - observing modes, 44
 - parallel mode, 40
 - performance, 44
 - serendipity mode, 40
 - survey products, 282
- MC_ORBIT, 269
- middle-tier, 183
- MLI, 33
- model development, 16
- MSX
 - cross-calibration, 148
- National Data Centres, 9
- NED, 183
- observing
 - cycle, 59
 - modes, 40
 - mapping, 66
 - parallel, 40, 64
 - per instrument, 70
 - rasters, 66, 67, 81
 - satellite, 66
 - serendipity, 40, 64
 - strategy, 58
 - time, 58
- OLP, 179, 277
- on-board clocks, 82
- open time
 - programme, 58
 - proposals, 205
- operational events, 112
- Operational Phase, 20
- optical subsystem
 - description, 34
 - parameters, 35
 - performance, 74
- ORBIT, 268
- orbit
 - description, 49
 - phases, 50
 - science window, 50
- orientation angle, 67
- OSIA, 11
- OSS, 33
- OTAC, 60
- OTF, 264
- parallel mode, 40, 64, 70
- payload module, 21, 30
- Performance Verification Phase, 22, 80
- periodic observations, 69
- Phase A, 13, 28
- Phase B, 14, 28
- Phase C/D, 14, 28

- PHT, 21, 30, 37, 50, 70, 76, 77, 81, 83, 90, 95, 98, 108, 123, 126, 146, 153, 155, 167, 169, 170, 247, 252, 255
 - cross-calibration, 120, 129, 130
 - description, 44
 - observing modes, 45
 - performance, 47
 - serendipity mode, 40
 - survey products, 282
- PIA, 11
- point spread function, 74
- pointing
 - constraints, 37, 50
 - files, 261, 264, 285
 - jitter, 68, 79
 - modes, 39
 - performance, 79
- Post-Helium Phase, 24
- Post-Operations Phase, 25
- postcard, 186, 281, 282
- PPM, 242
- pre-Phase A, 13, 28
- principal investigators, 17
- project organisation, 13
- proposals
 - calibration, 231
 - calls, 59
 - data entry, 61
 - discretionary time, 231
 - evaluation, 60
 - guaranteed time, 200
 - open time, 205
 - selection, 60
- profflight model, 16
- publications
 - guidelines, 6, 9
 - inventory, 9
 - tracking, 183
- QSS, 30, 35, 37, 80, 260–263, 265, 266
- quality control, 180, 280
- quaternions, 67, 261, 285
- radiation effects, 84, 89
- roll angle, 67
- Routine Phase, 22
- RPE, 68, 79
- RPQ, 286
- satellite
 - development, 13, 14
 - files, 235
 - performance, 73
- SCC, 19, 51, 52
- science
 - operations, 19
 - team, 17
 - window, 50
- scientific
 - apertures, 35
 - instruments, 40
 - observations, 199
 - programme, 62
 - validation, 180
- serendipity mode, 40, 64, 70
- service module, 21, 30
- Si:Ga detectors, 93
- SIAP, 184
- SIMBAD, 183
- SOC, 19, 51, 56
- source confusion, 196
- spacecraft
 - operations, 19
 - subsystems, 32
 - velocity, 268
- SPD, 179
- SPDT, 186
- SQL queries, 188, 287
- SSOs, 81, 233, 262, 265
- Star-Tracker, 30, 37, 67, 80, 237, 261, 267
- straylight, 30, 34, 77
- STRQ, 285
- STRQSSQ, 285
- Sun Acquisition Sensor, 30
- sunshade, 30, 35
- survey products, 281, 282
- SWS, 21, 30, 37, 67, 70, 76, 77, 81, 83, 89, 97, 111, 247, 252, 255
 - cross-calibration, 120, 122, 124, 128, 129, 134, 142, 172
 - description, 47
 - observing modes, 47
 - performance, 48
 - survey products, 283
- targets of opportunity, 64
- TDATA, 244
- TDF, 82
- TDT, 250
- Technology Test Phase, 24, 85
- telescope mirrors, 35
- timing, 82
- Transition Phase, 25
- TYCHO, 275
- UTC, 82

UTK, 82

VCS, 33

Virtual Observatory, 27, 183

VizieR, 183

VOTable, 184

zodiacal light, 153